

Synthesis and Characterization of Polymeric Glycoconjugate Mimetics

Inaugural Dissertation

for the attainment of the Title Doctor Rerum Naturalium in the Faculty of Mathematics and Natural Sciences at the Heinrich Heine Universität Düsseldorf

Düsseldorf

presented by

Melina Irene Feldhof

Düsseldorf, April 2025

Institute of Organic Chemistry and Macromolecular Chemistry at the Heinrich-Heine Universität Düsseldorf

Published by permission of the Faculty of Mathematics and Natural Sciences at the Heinrich-Heine Universität Düsseldorf

Supervisor: Prof. Dr. Laura Hartmann

Co-Supervisor: apl. Prof. Dr. Sander Smits

Date of oral examination: 27.11.2025

Statuary declaration

I, Melina Irene Feldhof, hereby sincerely affirm that I have written my dissertation independently and without any unauthorized assistance from third parties, in accordance with the 'Grundsätze zur Sicherung guter wissenschaftlicher Praxis an der Heinrich-Heine-Universität Düsseldorf. This dissertation has not been submitted in its present or similar form to any other institution, nor have any previous attempts at doctoral candidacy been undertaken by me.

Düsseldorf,

_____

(Melina Irene Feldhof)

Acknowledgement

Mein besonderer Dank gilt Prof. Dr. Laura Hartmann, die mir die Möglichkeit gegeben hat, in ihrem Arbeitskreis zu promovieren. Ihre Begeisterung, Motivation und Leidenschaft für Forschung und Lehre waren für mich stets ein Vorbild. Sie hat mir nicht nur ermöglicht, meine eigenen Ideen weiterzuverfolgen, sondern mich auch dabei unterstützt, sowohl fachlich als auch persönlich zu wachsen. Ich bin sehr dankbar, Teil ihres Teams zu sein.

Ich möchte zudem apl. Prof. Sander Smits für die Übernahme der Zweitkorrektur dieser Dissertation danken.

Ich möchte auch Frau Dr. Monir Tabatabai meinen herzlichen Dank aussprechen für ihre Unterstützung, ihr Vertrauen, die inspirierenden Gespräche und vor allem die jahrelange, wirklich schöne Zusammenarbeit im Makro-Praktikum.

Mein weiterer Dank richtet sich an Frau Stephanie Scheelen, Frau Michaela Kitza und Frau Sonja Coors, auf deren Unterstützung ich immer zählen könnte und unsere Zusammenarbeit mir immer viel Freude bereitet hat.

Ebenfalls bedanken möchte ich mich bei meinen Kooperationspartner*innen am Institute of Physical Chemistry, Universität Freiburg und hier besonders bei Rebecca Schlatterer und Dr. Bizan Balzer. Vielen Dank für die produktive Zusammenarbeit und den engen fachlichen Austausch.

Ein besonderer Dank geht an Sandro Sperzel, der durch seine fachlich hervorragende Bachelorarbeit einen wichtigen Beitrag zu Projekten dieser Arbeit geleistet hat und mit dem die Zusammenarbeit auch auf persönlicher Ebene immer eine große Bereicherung war.

Außerdem möchte ich mich bei all meinen weiteren Studierenden bedanken: Sarah Klaus, Katrin Glücks, Melanie Hälsig, Simone Kreiskott, Jacob Nachtwey, Jolana Both, Ben Raunitschke und Henri Koch. Die Zusammenarbeit in jedem einzelnen Projekt, sei es eine Bachelor-, Master- oder Forschungsarbeit, hat mir immer unglaublich viel Spaß gemacht und war stets eine der größten Motivationen für mich. Diese Zeiten waren eine immense Bereicherung, die ich niemals missen möchte.

Ein sehr großer Dank geht an die gesamte Arbeitsgruppe Hartmann und Schmidt. Ihr alle habt diese Zeit unvergesslich werden lassen. Unser einzigartiger Zusammenhalt in der Küche, auf den Klassenfahren und nicht zu vergessen im Sozialraum hat meine Promotion so besonders gemacht. Danke Nicole und Nina für die beste und verrückteste Bürozeit, danke Miriam, Lorand und Ulla dafür, dass wir über die Zeit wirklich gute Freunde geworden sind und danke Janita, Melanie und Jacob für die letzten wirklich schönen Monate. Ganz besonders will ich aber Luca-Cesare Blawitzki für seine grandiosen Ideen, seine Motivation, seinen Spaß und am wichtigsten für seine Freundschaft danken – ohne dich wäre die Zeit an der HHU einfach nicht dasselbe gewesen.

Abschließend richtet sich mein größter Dank an meine Freunde und Familie. Ich bin einfach dankbar für jeden Moment, ihr seid die Besten – ich habe euch alle so unglaublich lieb. Ganz besonders danke ich meinen Eltern, Claudia & Michael und natürlich auch Heike & Volker, meiner Schwester Anne, ihrem Freund Niklas und meinen Großeltern Renate & Horst – ihr seid die liebevollste und ehrlichste Familie auf der Welt. Jede/r einzelne ist mir auf ihre/seine Weise ein großartiges Vorbild und ich kann mich immer auf euch verlassen. Am Schluss gilt der wohl größte Dank Max, ich danke dir für alles – du unterstützt und inspirierst mich und bist gleichzeitig mein größter Ruhepol. Ich liebe dich.

Ich danke euch dafür, dass ihr mir die Möglichkeiten, das Vertrauen und die Freiheiten gegeben habt die selbstbewusste und glückliche Frau zu werden, die ich heute bin.

„Opa, jetzt haben wir das Kapitel geschafft – was machen wir jetzt?“

Table of content

1 Introduction 1
1.1 The Glycocalyx and its Glycan-Conjugates 1
1.1.1 Glycan-Mediated Interactions 3
1.2 Variety of Glycomimetics – Synthesis and Applications 5
1.2.1 Glycooligomers and -polymers as Glycomimetics 6
1.2.2 Brushed and Star-Shaped Glycopolymer Mimetics and Synthesis 13
1.2.3 Glycomimetic Protein-Polymer Conjugates and their Synthesis 17
1.2.4 Glycocalyx engineering 19
2 Aims and Outlines 21
3 Results and Discussion (Publications/Drafts) 25
3.1 Thiol-selective native grafting from polymerization for the generation of protein-polymer conjugates 25
3.2 Site-Specific Polymer-Protein-Polymer Conjugates for the Preparation of Dual Responsive Multilayer Nanoparticles 37
3.3 Highly Branched Sulfated Glycopolymers as Mucin Mimetics 51
3.4 Sequence-Defined Oligoamidoamines as Macroinitiator for Thiol-Induced, Light-Activated Controlled Radical Polymerization of Star-Shaped Glyco-block-copolymers 65
4 Conclusion and Outlook 81
5 References 89
6 Supporting Informations 103
6.1 Methodical section 103
6.2 Supporting Information - Thiol-selective native grafting from polymerization for the generation of protein-polymer conjugates 105
6.3 Supporting Information - Site-Specific Polymer-Protein-Polymer Conjugates for the Preparation of Dual Responsive Multilayer Nanoparticles 159
6.4 Supporting Information - Highly Branched Sulfated Glycopolymers as Mucin Mimetics 227
6.5 Supporting Information - Sequence-Defined Oligoamidoamines as Macroinitiator for Thiol-Induced, Light-Activated Controlled Radical Polymerization of Star-Shaped Glyco-block-copolymers 303

Abstract

The glycocalyx is a carbohydrate-dense layer enveloping endothelial cells that mediate various biological functions including cellular communication and pathogen detection. Specific glycan motifs, like proteoglycans or glycoproteins, initiate a first contact with other cells or during pathogen adhesion. However, many of the underlying mechanisms of such glycan-mediated contacts are not fully understood, yet. One major limitation is an access to more complex glycan conjugates due to their low stability, rapid degradation, and challenges in isolation and characterization. Glycomimetics - synthetic mimics of natural glycans - offer a promising alternative and are commonly used as models to gain new insights into the biological functions of natural glycan motifs, such as glycoproteins or mucins. Therefore, new synthetic strategies are developed in this thesis that give access to advanced glycomimetic structures by combining both: synthetic and biopolymers as scaffolds for the presentation of different glycomimetics (Figure 1).

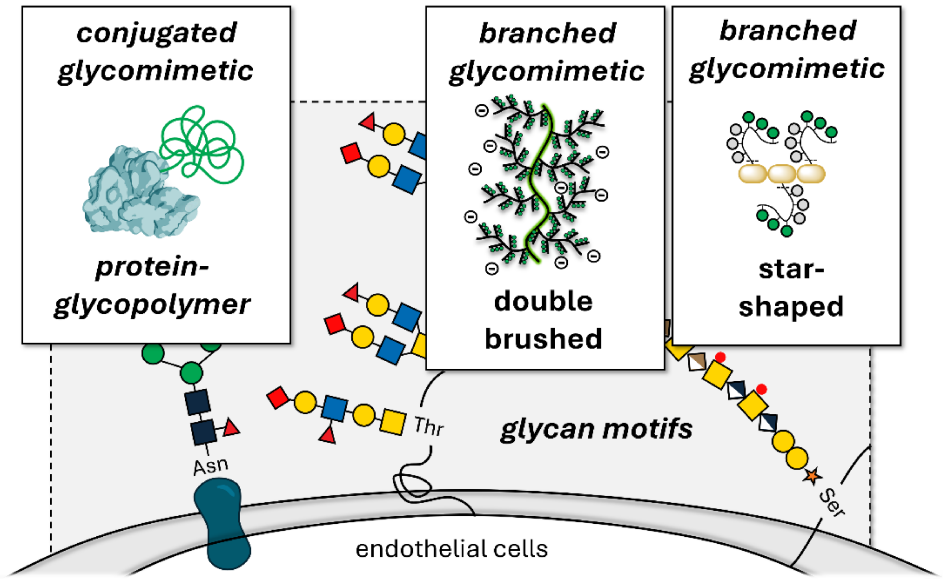


Figure 1: Schematic representation of glycomimetics, alongside the natural glycan blueprints.

First, mimicking the glycosylation of proteins, a new strategy to attach glycopolymers to proteins, was established. Using proteins as macroinitiators in the previously established thiol-induced, light-activated controlled radical polymerization (TIRP) provides straightforward access to a side-selective glycosylation of native proteins. This approach was here first applied using the proteins *bovine serum albumin* (BSA) and *candida rugosa lipase* (CRL) – an enzyme – for a direct grafting-from approach initiated at thiols from

specific cysteine residues of the protein. Different types of polymers including hydrophilic poly(2-hydroxyethyl acrylate) (pHEAA), temperature-responsive poly(N-isopropylacrylamide) (pNIPAM) as well as glycopolymers for mimicking glycosylation were successfully attached to the protein. All protein-polymer conjugates retain the protein's natural structure and function, which was demonstrated in functional protein assays. The enzyme-polymer conjugates maintain their enzymatic activity, and the conjugation with pNIPAM enhances this activity following a temperature-induced aggregation of the conjugates. The BSA-glycopoylmer conjugates allow a straightforward application for surface coatings through physisorption of the BSA on glass slides and thereby give access to glycosurfaces e.g., for protein screening and detection.

Building onto this first set of conjugates, a so-called rebridging agent was introduced here to allow for the introduction of a second polymer. Hence, a second TIRP enables site-specific conjugation of another different polymer to native proteins. In particular pNIPAM decorated BSA that contains the newly designed rebridging agent followed by TIRP give highly defined pNIPAM-BSA-glycopolymer conjugates. These structures form nanoclusters with a glycopolymer corona above the lower critical solution temperature (LCST) and enable the reversible formation of a second protein corona through interaction with specific glycan-recognizing lectins, which creates the formation of a polymer-protein-polymer-lectin multilayered nanoparticle. This synthetic approach enables a dual responsive multilayer nanoparticle that can undergo a stepwise or a one-step disassembly, depending on the stimuli – temperature below LCST or high affinity competing ligands. Interestingly, aggregation behavior can now also be fine-tuned by mixing different pNIPAM-protein-glycopolymer conjugates. By controlling the binding/non-binding glycopolymer ratio during nanoparticle formation, either a still defined particle corona or a large cluster formation is formed.

Another class of glycan-protein-conjugates uses the protein as linear scaffold for the high-density presentation of branched glycan side chains leading to heavily brushed glycan conjugates such as the mucins. Mucins create a protective layer around epithelial surfaces, like those in the respiratory system, to protect them against pathogens. The newly developed mucin mimetics within this thesis are crafted to replicate natural

structures more closely using an innovative double-brushed polymer topology. By integrating solid-phase synthesis of sequence-specific glycooligomers with their attachment to polyactive ester frameworks, which is followed by full sulfation to introduce the anionic charges that are also found in natural mucins, a library of glycopolymers including linear, brushed, and double-brushed glycopolymers was synthesized. This synthetic approach allows precise control over structural parameters such as side chain length, number and branching, carbohydrate type, and sulfation. Together with the groups of Prof. Karg and Dr. Balzer the physicochemical properties of the mucin mimetics, such as hydration, adhesion, and extended conformation on (hydrophilic) surfaces were analyzed via light and neutron scattering, as well as single molecule and imaging force spectroscopy. Only glycomimetic polymers with double-brush architecture can effectively mimic mucin-specific properties, such as a strong extended conformation and the capacity to adhere to (hydrophilic) surfaces.

Finally, fully synthetic glycopolymers with star-like topology were synthesized within this thesis combining sequence-defined macroinitiators accessible through standard solid phase chemistry and TIRP. In comparison to previously known initiators, such as small molecules or proteins with a single thiol group, the macroinitiators presented herein facilitate three-site simultaneous TIRP under controlled conditions. This core-first, one-pot/two-step method offers versatility in the precise design of core and polymer chain structures, enabling significant variability and control over structural parameters like the number, density, and length of the polymer chains. Such star-shape glycopolymers have great potential for targeted drug delivery and for use as antibacterial and antiviral therapeutics.

List of Publications and Author Contributions

Publications included in this thesis

M. I. Feldhof, S. Sperzel, L. Bonda, S. Boye, A. Braunschweig, U. I.M. Gerling-Driessen, L. Hartmann

„*Thiol-selective native grafting from polymerization for the generation of protein–polymer conjugates*"

Chemical Science, 2024, 15 (40), 16768-16777

DOI: 10.1039/D4SC04818K

Impact Factor: 7.6 (2023)

Author contribution: Collaborative project development. Synthesis and characterization (^{1}H-NMR, SDS-PAGE, Ellman's Assay, CD, DSC, IR) of the protein-polymer conjugates. Conducting enzyme activity studies and binding studies on surfaces and in solution. Collaborative writing of the manuscript.

M. I. Feldhof, S. Walber, S. Sperzel, S. Boye, U. I.M. Gerling-Driessen, L. Hartmann

"*Site-Specific Polymer-Protein-Polymer Conjugates for the Preparation of Dual Responsive Multilayer Nanoparticles*"

Small, 2025, 2500531

DOI: 10.1002/smll.202500531

Impact Factor: 13 (2023)

Author contribution: Collaborative project development. Synthesis and characterization (^{1}H-NMR, ^{13}C-NMR, SDS-PAGE, Ellman's Assay, CD, DLS) of the rebridging-agent and bifunctionalized polymer-protein-polymer conjugates. Conducting all core-multi-shell hybrid nanocluster experiments including the corresponding binding studies. Conducting fluorescence microscopy and SEM measurements. Collaborative writing of the manuscript.

M. I. Feldhof,‡ R. Schlatterer,‡ F. Strahl, J. Garthe, S. Prévost, S. Schmidt, M. Karg, B. Balzer, L. Hartmann

"*Highly branched sulfated glycopolymers as mucin mimetics"*

Journal of the American Chemical Society, 2025, 147,36, 32698 – 32709

DOI: 10.1021/jacs.5c08232

Impact Factor: 15.7 (2024)

Author contribution: Collaborative project development. Synthesis and characterization (SEC, ^{1}H-NMR, ^{19}F-NMR) of the linear, brush and double-brush glycopolymers. Conducting dynamic light scattering experiments. Collaborative writing of the manuscript.

‡authors contributed equally

Publications under preparation included in this thesis

M. I. Feldhof, B. Raunitschke, J. Both, S. Boye, L. Hartmann

"*Sequence-Defined Oligoamidoamines as Macroinitiator for Thiol-Induced, Light-Activated Controlled Radical Polymerization of Star-Shaped Glyco-block-copolymers*"

Author contribution: Collaborative project development. Development of the synthetic methodology, collaborative synthesis and characterization of the star-shaped glycopolymers. Collaborative writing of the manuscript.

Publications not included in this thesis

P. B. Konietzny, J. Freytag, M. I. Feldhof, J. C. Müller, D. Ohl, T. Stehle, L. Hartmann

"*Synthesis of Homo- and Heteromultivalent Fucosylated and Sialylated Oligosaccharide Conjugates via Preactivated N-Methyloxyamine Precision Macromolecules and Their Binding to Polyomavirus Capsid Proteins*"

Biomacromolecules 2022, 23 (12), 5273-5284

DOI: 10.1021/acs.biomac.2c01092

Impact Factor: 6.2 (2022)

Conferences

M. I. Feldhof, S. Sperzel, L. Bonda, S. Boye, A. Braunschweig, U. I.M. Gerling-Drissen, L. Hartmann

"*Protein-Polymer conjugates via a new photo-induced controlled radical grafting-from polymerization on native proteins*"

Macromolecular Colloquium Freiburg, 26.-27. February 2024

1 Introduction

1.1 The Glycocalyx and its Glycan-Conjugates

The glycocalyx is a complex, carbohydrate-dense layer that envelops endothelial cells composed of glycolipids especially proteoglycans or glycoproteins, that is known to be involved e.g., in pathogen adhesion, mediating cellular communication and regulating immune responses.[1, 2] These multifaceted roles, which extend beyond the mechanical barrier function of the carbohydrate-dense layer, underscore the glycocalyx relevance in both physiological (cell-cell-interactions) and pathological states (cell-pathogen-interactions).[3-5] Specifically, different glycan-conjugates of the glycocalyx, illustrated in Figure 2, have been identified and studied for their biological function.

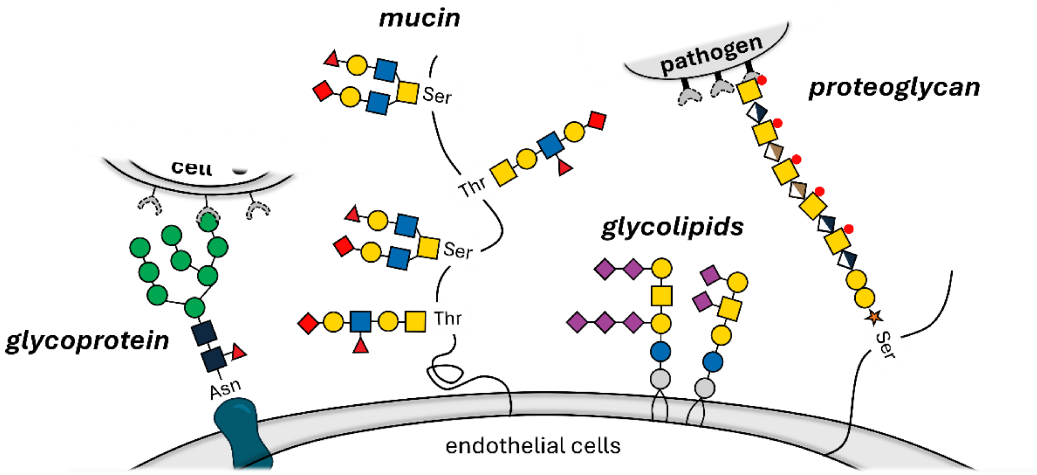


Figure 2: Schematic presentation of a cellular glycocalyx containing glycoprotein, mucin, glycolipids and proteoglycan.

Glycoproteins and proteoglycans or mucins are varieties of glycosylated proteins, which are essential components of the glycocalyx and exhibit fundamental differences in glycan structure, function, and their biological role. The nature of glycosylation can influence glycan stability by protecting against proteolysis and contributes to interactions with other biomolecules which is investigated within the context of medical research.[6-14] For instance, glycoproteins such as the spike protein of SARS-CoV-2 are crucial for viral entry into host cells, underscoring their significance in both health and disease.[15]

Glycoproteins are typically covalently attached with short, branched glycans (< 20 monosaccharides), whereas proteoglycans are characterized by one or more highly unbranched and negatively charged glycosaminoglycan (GAG) chains.[16-18] GAGs, made of

repeating disaccharide units, are complex and diverse.[17] Aside for hyaluronic acid (HA), GAGs are typically sulfated and include heparin sulfate or heparan sulfate (HS) which are the most prevalent GAGs on endothelial cells, comprising over 50% of endothelial proteoglycans.[19-22]

The most common glycans present on eukaryotic membranes are classified into *N*- and *O*-linked glycans, showcasing in Figure 3 and show high complex and diverse glycan structures in terms of length, composition and geometry, such as branching.[23] This glycosylation class is determined by the linkage between the initial sugar of the glycan and the protein.[24] Furthermore, many glycan structures undergo additional enzymatic reactions, modifying them with sulfates, phosphates, or acetates.[25]

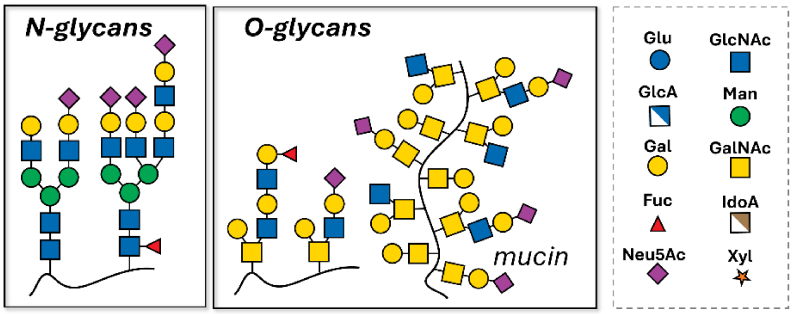


Figure 3: Examples of N-glycan and O-glycan structures and the ten primary specific monosaccharides components of human glycan: Glucose (Glu), galactose (Gal), N-acetylglucosamine (GlcNAc), N-acetylgalactosamine (GalNAc), fucose (Fuc), xylose (Xyl), N-acetylneuraminic acid (Neu5Ac), glucoronic acid (GlcA), mannose (Man) and iduronic acid (IdoA).[6, 26-29]

N-linked glycans are attached to the nitrogen atom of asparagine (Asn) residues and in contrast, *O*-linked glycans are bound to the oxygen atom of either serine (Ser) or threonine (Thr) amino acids.[23] Protein glycosylation is a process that occurs during and after translation, facilitated by enzymes known as glycosyl- and oligosaccharyltransferases.[30] *N*-glycosylation occurs co-translationally, with glycans like mannose units being added during protein biosynthesis. These glycans are then trimmed and sequentially linked with additional monosaccharides, depending on available glycosyltransferases, ensuring proper protein folding and function.[31] *O*-linked glycans usually begin with an *N*-acetylgalactosamine (GalNAc) unit.[18, 31] *O*-glycosylation, a post-translational modification occurring in the Golgi apparatus, involves adding glycans to the protein after biosynthesis.[23, 32] These glycans are essential for the structure, cell protection, and signal transduction. Mucins, large glycoproteins that form protective mucus barriers on

epithelial surfaces, represent prominent examples of extensively *O*-glycosylated proteins.[33-38]

Mucins exhibit high glycosylation density (> 50 mass%), incorporating negative charges through sialyl or sulfate groups.[39-42] The negatively charged nature of polysaccharides in combination with their hydroxyl groups enable substantial water absorption, hereby creating a water-coordinated layer resulting in a gel-like texture.[36, 42] This unique property enables the provision of a protective barrier on epithelial surfaces, facilitating hydration and functioning as a primary defense mechanism against pathogens.[43, 44] Further, Mucins modulate endothelial cell behavior by linking lubrication to adhesion characteristics, while also contributing to immune response by affecting interactions between endothelial and immune cells during inflammation and tissue repair.[45, 46] This complexity facilitates mucin physisorption via *van der waals* forces, hydrophobic and electrostatic interactions, and hydrogen bonds.[35, 47, 48] Studies have demonstrated that mucins exhibit increased expression in various pathological conditions, including adenocarcinomas such as colorectal cancer and lung cancer, as well as chronic obstructive pulmonary disease (COPD).[49-52] As a result, glycoproteins are the subject of extensive research not only for their role in pathogenesis but also for their potential utility as diagnostic tools and specifically as tumor markers.[53]

1.1.1 Glycan-Mediated Interactions

The interaction between specific glycans and their corresponding glycan-binding proteins (GBPs) are mediating processes on cell surface.[54, 55] These GBPs can be categorized into proteins that bind to sulfated glycosaminoglycans (sGAG binding proteins) and lectins, which typically bind to the specific, terminal epitopes of cell surface-associated glycans.[55] sGAG-binding proteins interact through electrostatic forces between negatively charged sulfate and uronic acid components in sGAGs and positively charged amino acid clusters, influenced by secondary interactions like *van der waals* forces or hydrogen bonding.[54, 56] In addition to cellular processes that depend on sGAG-binding proteins interacting with cell surface glycans, numerous pathogens exploit sGAGs in their glycocalyx to adhere to host cells. Exemplary, the SARS-CoV-2 spike protein binds to heparan sulfate on respiratory cells, facilitating transfer to host receptors and infection.[54,

[57] Lectins can be further classified into various categories based on their carbohydrate recognition domains (CRDs), with *C*-type lectins being the most common category.[58, 59] *C*-type lectins, defined by their calcium-dependent carbohydrate-binding, can be classified into single-CRD or dual-CRD lectins based on the number of CRDs and their binding capacities.[60] The interaction between a carbohydrate epitope and its specific lectin is characterized by reversibility and generally weak affinity, resulting in binding constants ranging from µM to mM.[61-63] Analogous to the variation in the number of CRDs, biological systems can present multiple carbohydrates to induce stronger binding, a phenomenon known as multivalency.[64, 65] The multivalent presentation of CRDs or carbohydrates results in enhanced binding avidity, wherein the overall binding enthalpy exceeds the cumulative enthalpy of individual binding interactions.[63, 64, 66] As shown in Figure 4, four distinct effects significantly influence the enhanced avidity through multivalently presented binding partners: the *chelate effect*, the *cluster effect*, *statistical rebinding*, and *steric shielding*.[65, 67]

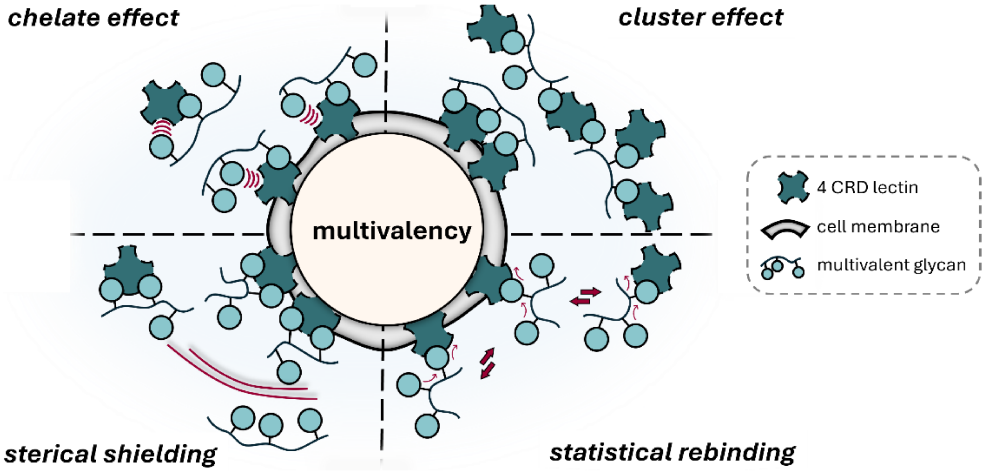


Figure 4: Schematic presentation of the four multivalent effects, including: chelate effect, cluster effect, statistical rebinding, and steric shielding.

The *chelate effect* involves multiple ligand molecules binding simultaneously to various receptor sites, which depends on both: the number of interactions and the spatial arrangement of the ligands.[68, 69] For instance, if the distance between the carbohydrate ligands aligns with those of the receptor's binding sites, the probability of simultaneous binding increases, thereby boosting binding affinity.[70] When multiple carbohydrates are presented, they can bridge multiple binding sites simultaneously on one or several lectins, resulting in a cooperative binding effect that enhances overall affinity which is

known as the *cluster effect*.[68, 71] *Statistical rebinding* results from the close proximity of multiple ligand groups, facilitating the rapid exchange of a bound ligand with another nearby ligand, thereby reducing the dissociation rate of the interaction.[72] The *steric shielding effect* of multivalency refers to the effect wherein the presence of multiple ligand groups on a multivalent scaffold impedes or inhibits the access of competing ligands or inhibitors to the binding sites on a receptor.[73, 74]

Gaining a better understanding of natural glycan variety and their role in mediated interactions is crucial for the development of new therapeutics. Typical limitations of natural glycans, such as their low stability, rapid degradation, and the challenges associated with their isolation and characterization can be overcome by using so-called glycomimetics.[75]

1.2 Variety of Glycomimetics – Synthesis and Applications

Glycomimetics - synthetic structures mimicking natural glycans and glycan-conjugates - have been established as a promising alternative as model compounds in fundamental as well as applied studies.[76-78] Advanced glycomimetic systems aim at mimicking the complexity of natural glycan structures based on their highly diverse carbohydrate composition, associated charges and topology such as branching patterns or length.[78] Glycomimetics can be strategically designed to target specific molecular interactions critical for pathogen interactions, thus providing a foundation for e.g. antiviral strategies.[79] Focusing on terminal epitopes of natural glycans, key binding sites for cell-cell or cell-pathogen interactions, provides a good starting point for synthesizing specific glycomimetics, allowing their imitation as rational, biomimetic constructs.[80] The variety of defined synthetic approaches enable a precise, uniform, and adjustable design of glycomimetics in terms of spatial arrangement of carbohydrates, length and size.[78] As a result, various synthetic models find applications, such as glycooligomers,[81-85] glycopolymers,[81, 86-89] glycodendrimers,[64] nanoparticles[90, 91] or proteins[92-94] and glycan-decorated micelles.[95, 96] All these biomimetic structures can result in enhanced affinities and selectivity for particular lectins with their rational design, as demonstrated for example by developing glycomimetics targeting.[97, 98] The current state of synthetic methodologies that mimic natural glycans, especially glycooligo- and polymers and

brushed or star-shaped glycopolymers, as well as glycoproteins with a high level on structural complexity, will be focused in the following parts of this introduction and is schematically presented in Figure 5.

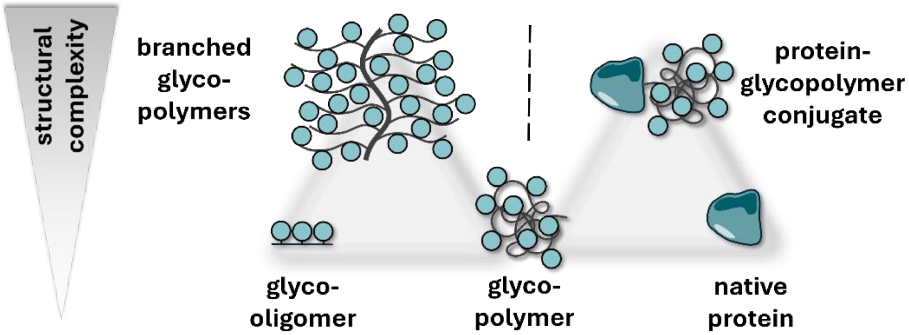


Figure 5: Schematic representation of glycomimetic structures such as glycooligomers, - polymers or native proteins and of more complex structures such as brushed glycopolymers and protein-polymer conjugates.

1.2.1 Glycooligomers and -polymers as Glycomimetics

The various scaffolds for glycomimetics have been introduced and will be further elaborated upon in the subsequent sections, employing a bottom-up approach in terms of complexity. The smallest structures discussed are glycooligomers, which enables sequence-specific synthesis of glycomimetics incorporating carbohydrates. These structures display specific distances and compositions, enabling targeted investigation,[99] although with limitations in molecular size. Consequently, using glycopolymers as large scaffold enables the synthesis of large glycomimetic structures with high molecular weights. When these two approaches are combined, the complexity is increased, resulting in branched glycopolymers, demonstrated in Figure 5. The following section will focus on two particular synthetic methods – solid-phase synthesis and controlled radical polymerizations – to enable a more detailed understanding on the techniques used for synthesizing sequence-defined oligomers and controlled polymers.

Solid Phase Synthesis to derive Controlled Glycomimetics

Solid-phase synthesis (SPS) is used to derive sequence-defined glycooligo(amidoamines) by tailored synthetic building blocks taking into account established peptide synthesis protocols, premiered by Merrifield in the 1963.[84, 85, 100] This technique ensures precise control over architecture including sequence, spacing

between ligands, valency which are crucial factors for lectin binding specificity. Numerous examples show that the resulting glycomimetics act as high-affinity glycomimetics in lectin binding and cell-based studies.[81-85]

SPS involves coupling reactants to a solid support, which enables the iterative assembly of building blocks, simplifying purification processes, as excess reagents can be removed through simple washing techniques, eliminating the need for extensive chromatographic procedures.[101, 102] The general procedure of solid-phase synthesis includes three fundamental parts: I. functionalization of an insoluble carrier resin, II. cleavage of a temporary protecting group, and III. coupling of a carboxyl-functionalized, *N*-protected building block.[101] The sequential construction of building blocks through repeated coupling and deprotection steps ultimately yields the sequence-defined oligomers, which are built from the *C*- to the *N*-terminus.[101] Due to its broad applicability and synthetic importance, SPS can now be conducted using automated peptide synthesizers, which reduces time requirements and facilitates easier scaling up.[101, 103]

Hartmann's enhanced solid phase polymer synthesis (SPPoS) employs various resins and linkers, enhancing the synthesis of more complex organic molecules. This method emphasizes versatility and efficiency, aiding in the creation of combinatorial libraries and complex organic structures with diverse functionalities.[76, 104-107] A key distinction is in the types of reactions performed: Merrifield's method focuses on peptide bond formation, whereas Hartmann's SPPoS supports a broader range of reactions, including coupling reactions and functional group transformations, thus expanding synthetic possibilities.[107]

The Hartmann group frequently utilizes a polystyrene resin with a rink-amide linker as the solid support, which yields a *C*-terminal primary amide upon peptide cleavage from the resin.[101, 108] This choice of linker influences the synthesis strategy and the selection of terminal and permanent protecting groups.[101, 109, 110] The temporary 9-fluorenylmethoxycarbonyl (Fmoc) protecting group, which is orthogonal to the acid-labile rink-amide linker, has been established as a reliable coupling strategy.[111, 112] Fmoc deprotection is accomplished using secondary amines such as piperidine, resulting in a free amine at the *N*-terminus. [112] To couple a new building block in the subsequent step, the coupling reagent PyBOP is frequently employed in conjunction with the sterically

hindered base DIPEA.[116] Excess reagents are subsequently eliminated through simple wash cycles, and the *N*-terminus of the newly inserted building block is protected by another Fmoc group, which can be cleaved again. This method facilitates the iterative construction of highly functional, sequence-defined oligoamidoamides. Figure 6 summarizes the characteristic aspects of the SPPoS approach.

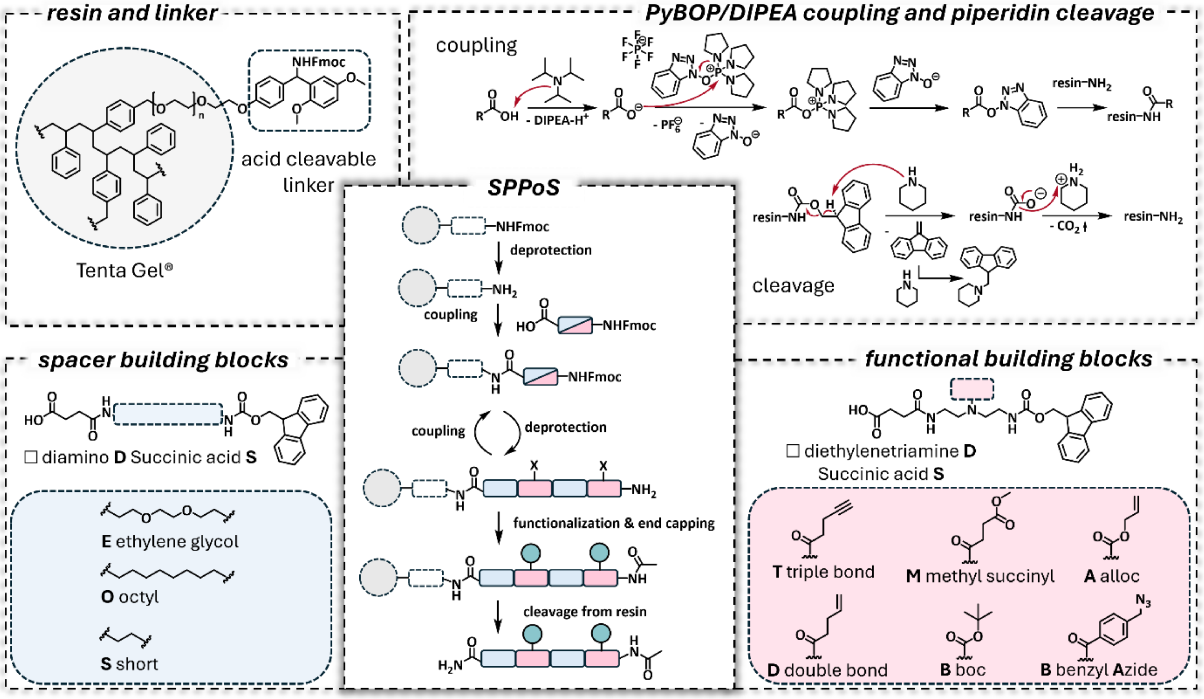


Figure 6: Summary of the key aspects of SPPoS, such as resin and linker, coupling and cleavage conditions and the differences between spacer and functional building block.

SPPoS employs custom-designed synthetic building blocks featuring a Fmoc-protected primary amine and a free carboxylic acid, tailored to their specific roles. These blocks are classified as spacer or functional blocks based on their intended function in the scaffold. Spacer blocks, like EDS and ODS, modify the backbone's polarity and regulate distances between ligands. EDS increases hydrophilicity, while ODS enhances hydrophobicity without altering ligand spacing.[107] Orthogonally protected functional handles in the backbone enable site-specific functionalization, such as adding fluorophores for microscopy or branching points to modify glycan mimetic architecture.[113] Combining these blocks with unmodified or modified α-amino acids enables for the addition of peptide motifs or functionalities like thiol groups through cysteine units.[81] Functional blocks, such as alkyne-functionalized TDS or azide-functionalized BADS, provide side chain functionalities for subsequent modifications via copper(I)-catalyzed azide-alkyne

cycloaddition (CuAAC).[107] When utilizing multifunctional building blocks, i.e., those with a second functionality in the side chain, this functionality is protected from undesired side reactions by a permanent protecting group. Consequently, the temporary and permanent protecting groups must be orthogonal to each other, meaning they must be selectively cleavable in the presence of other protecting groups.

Summarizing, this modular approach of SPPoS enables the synthesis of highly defined synthetic glycomimetics. These mimetics allow for precise modification of various aspects, including the valency and spacing between ligands, the flexibility and polarity of the backbone, the overall structural architecture, and the incorporation of additional functional handles. SPPoS faces challenges in synthesizing high molecular weight structures due to secondary interactions between the increasing sequence and the resin, leading to coiling and aggregation.[114] This prevents quantitative coupling and deprotection, increasing error sequences and reducing yield and purity.[114] As a try to address this, methods such as thiol-ene conjugation of individual oligoamidoamides have been utilized in a step-growth polymerization approach[81] or a split and combine approach give access to branched glycoamidoamides.[115]

Alternatively, controlled polymerization methods and polymer analogous reactions are commonly employed,[116, 117] as they facilitate the synthesis of defined polymer scaffolds with complex side chains allowing a closer look into the influence of glycopolymer conformation.

Controlled Radical Polymerizations and Polymer Analogue Reaction

Controlled radical polymerizations (CRP) have emerged as a promising approach in the synthesis of glycopolymers, with brushed glycopolymers representing a significant subclass within this field. Glycopolymers find applications in various areas, including pathogen detection and inhibition, cancer research, and tissue engineering.[92, 118-120] Therapeutic applications have already been demonstrated, as exemplified by the antiviral properties of some mimetics showing prophylactic effects against viral infections, including SARS-CoV-2.[79] Advancements in CRP techniques, particularly reversible addition-fragmentation chain transfer (RAFT), photoinduced electron/energy transfer reversible addition-fragmentation chain transfer polymerization (PET-RAFT), atom

transfer radical polymerization (ATRP), nitroxide-mediated radical polymerization (NMP), ring opening polymerization (ROP) and thiol-induced, light-activated controlled radical polymerization (TIRP) have facilitated the synthesis of glycopolymers with precisely defined structures, controlled molecular weight, and low dispersity. These characteristics are essential for their application in biomedical fields.[62, 121, 122] One of the key advantages of CRP techniques is their capacity to synthesize glycopolymers that exhibit specific interactions with biological systems. This specificity is largely attributed to the multivalent nature of glycopolymers, which enables stronger binding interactions with lectins due to the "glycocluster effect".[62, 123] The ability to fine-tune the structure and composition of glycopolymers using CRP techniques opens new opportunities for creating materials that can effectively interact with biological targets, thereby enhancing therapeutic efficacy and highlighting their importance in the intersection of polymer science and glycobiology.[121, 124] RAFT employs a chain transfer agent (CTA), usually a thiocarbonyl compound, to reversibly capture growing radicals, imparting "living" polymerization traits.[125, 126] This enables customized polymerization of polymer architecture and functionality.[127-129] It also provides notable versatility and control over polymer properties but has drawbacks, such as side reactions and sensitivity to environmental conditions like oxygen.[129, 130] In the PET-RAFT process, a photocatalyst absorbs light energy and transfers it to the RAFT agent, generating radicals to initiate polymerization. Utilizing visible light, this eco-friendly method is compatible with various functional monomers.[131, 132] Key advantages include oxygen tolerance and precise polymer growth regulation through controlled light exposure.[126, 133-135] However, the need for a photocatalyst can complicate the reaction setup and introduce additional variables, like limited aqueous solubility and tedious purification to manage.[136, 137] ATRP employs reversible activation and deactivation of radical species, allowing the creation of polymers with precise structures, predictable molecular weights, and narrow polydispersity indices. Using a transition metal catalyst, usually copper, the process transfers a halogen atom from a dormant polymer chain to a radical, generating a new active radical and regenerating the dormant species.[138-140] ATRP is highly effective for controlled polymer synthesis, providing substantial benefits in structural control and functionalization.[141-144] Nonetheless, issues with catalyst management and reaction

conditions need to be resolved to maximize its potential in polymer chemistry.[138-140, 145, 146] NMP is a controlled/living radical polymerization method using reversible deactivation with nitroxyl radicals. Polymer radicals are reversibly capped by a stable nitroxide, creating a dormant alkoxyamine species, enabling control over molecular weight and low dispersity through reversible activation-deactivation equilibrium.[147] Compared to other controlled radical polymerization methods, NMP often exhibits slower polymerization kinetics, potentially restricting its industrial use.[148] ROP cleaves a cyclic structure to form a linear polymer via anionic, cationic, or radical mechanisms, producing high molecular weight polymers with controlled architecture. Cyclic esters like lactide and ε-caprolactone can be polymerized into biodegradable polyesters, which is important for biomedical applications.[149-151] This process often occurs under mild conditions, with lower temperatures and shorter reaction times than other polymerization methods, benefiting sensitive monomers.[151-153] However, side reactions such as transesterification can occur, compromising control over molecular weight and polydispersity.[150, 154] TIRP means, that thiols act as initiators, activating polymerization upon light exposure, typically using photoinitiators like $Ir(ppy)_3$ and radical initiator TPO.[104, 155] It describes the formation of active polymer chain ends and their equilibrium with dormant species, dependent on light and catalysts. Owing to its viability under mild conditions and its capacity to enable the polymerization of various readily accessible thiols, TIRP broadens the spectrum of controlled, light-initiated polymerization techniques. This technique enables the synthesis of low-dispersity polymers and complex architectures, including block copolymers.[155] However, challenges such as light permeation and reaction optimization remain to be addressed to fully exploit the technique's potential across various applications. Figure 7 below summarizes the essential aspects of several relevant CRPs.

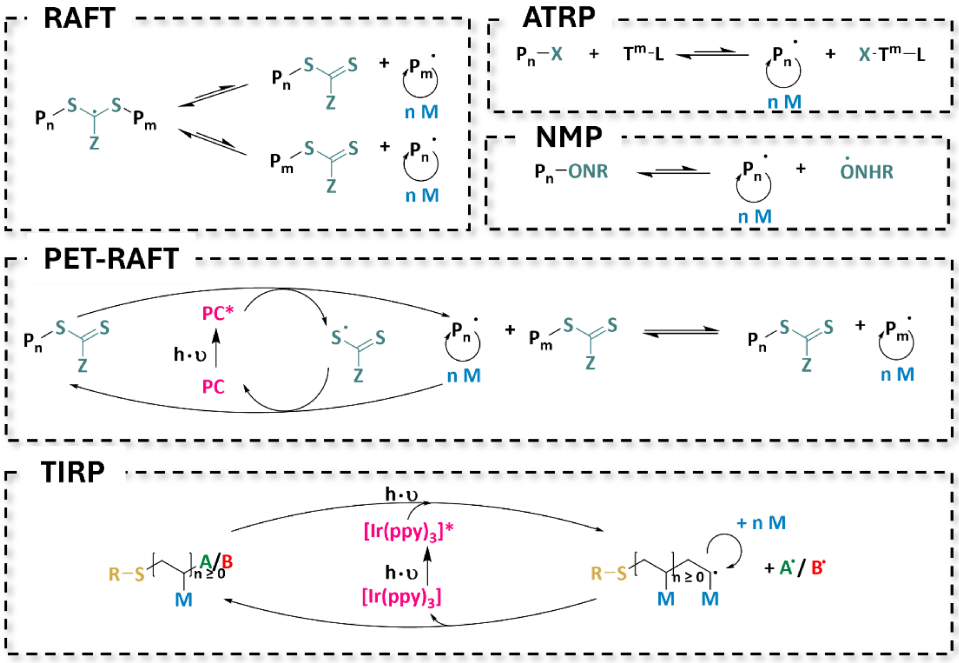


Figure 7: Overview of some relevant controlled radical polymerization methods.

Further, the special case of polymer analogue reaction, or post-polymerization modification involves replacing a polymer's functional group with another. This process incorporates specific functionalities, enhancing polymer performance and utility in areas like biomedicine or glycobiology.[156-158] Key modifications include hydrogenation, ester conversion, etherification, chlorination, sulfonation, cyclization, and cross-linking of synthetic and natural polymers.[159] Gauthier et al.[160] investigated post-polymerization modification techniques that involve directly polymerizing monomers with selective side chains, which can later be converted into various functional groups under mild conditions and high yields. This method is especially beneficial for creating polymers with tailored functionalities.[160] Polymers with active ester groups form a distinct class that is particularly suitable for polymer analog transformation. These specialized polymers contain reactive ester moieties capable of participating in substitution reactions with nucleophiles. The chemistry of active esters, especially pentafluorophenyl (PFP) and *N*-acryloxysuccinimide (NAS), is widely used for post-polymerization modification. Eissa et al.[161] synthesized amphiphilic glycopolymers from pentafluorophenyl acrylate. This results in glycopolymers that could form nanoparticles with surface sugar moieties, suggesting potential applications as antimicrobial agents.

The introduction of CRPs and polymer analogue reactions allows for precise regulation of polymerization processes, which is essential for synthesizing glycopolymers as glycomimetics. As a result, CRPs established significant methods for the further incorporation of glycopolymers into complex systems, such as glycopolymer conjugates. It is important that glycopolymer conjugation is conducted in a controlled manner to maintain biological functions and effectiveness.[123] The CRP techniques outlined here focus on the importance and creation of linear glycopolymers. However, examining the topology of natural glycan models like mucins reveals that most glycans exhibit branched structures. To enhance our understanding of synthesizing these formations, the next section will investigate the synthesis of branched and star-shaped glycomimetic polymers.

1.2.2 Brushed and Star-Shaped Glycopolymer Mimetics and Synthesis

It has been shown that the topology of glycopolymers affects their biological activity such as their binding avidity and even specificity.[162, 163] Looking back at the natural blueprints, two subclasses of branched glycopolymers can be differentiated, showcasing in Figure 8: glycopolymers mimicking proteoglycans (long, highly unbranched and negatively charged GAG chains) and glycopolymer mimicking mucins (short, highly branched sialic acid and sulfated glycans). Emphasizing the topology of these two structural categories acts as a guide for selecting branched glycomimetics.

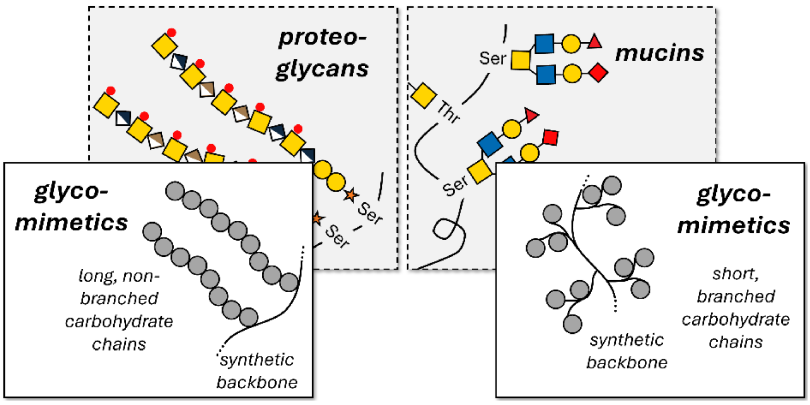


Figure 8: Comparison of the schematic natural glycan models and the resulting mimetic structural characteristics.

Brush-like glycopolymers are a type of glycopolymer characterized by polymer chains grafted onto a separate backbone, creating a "brush" structure. Brush-like glycopolymers are superior to linear glycopolymers in accessibility and functionality due to their higher

packing density from branched structures which results in an more stretched conformation, whereas linear glycopolymers often adopt coiled conformations in solution, impairing their recognition capabilities.[62, 164, 165] Ribeiro et al.[166] summarizes several examples that brushed glycopolymers exhibit a higher binding affinity to lectins compared to their two linear counterparts and preventing non-specific adhesion of proteins and cells. Their architecture enhances interactions with biomolecules like proteins and lectins for drug delivery, biosensing, and tissue engineering while creating biomimetic surfaces mimicking the glycocalyx essential for cell signaling.[165, 167] Brush-like polymers can be synthesized via *grafting-(on)to*, *grafting-from*, and *grafting-through* approaches which is graphically shown in Figure 9.

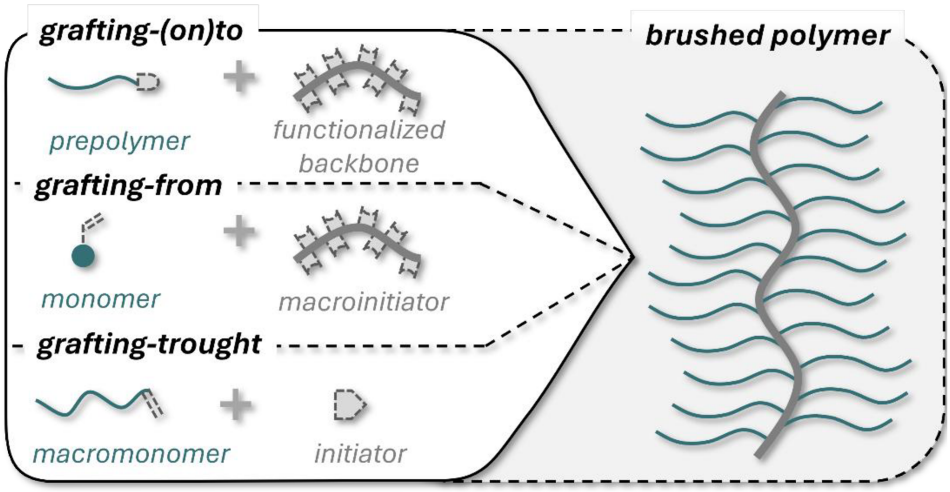


Figure 9: Schematic illustration of the three major approaches for brush-like polymer synthesis.

Each approach has unique characteristics, advantages and disadvantages affecting the polymer's architecture and properties: *grafting-(on)to* technique attaches pre-synthesized polymer chains to another polymer backbone, allowing flexible side chain design as they can be independently synthesized before attachment.[168, 169] This method is beneficial for achieving specific functionalities and using polymers incompatible with grafting conditions. However, it often results in lower grafting densities due to steric effects, where attached chains hinder the addition of more chains.[170] In the *grafting-from* approach, polymer chains are synthesized directly from a macroinitiator like polymers or macrooligomers, enabling high grafting densities and control over side chain length.[169] This method is effective for producing thick polymer brushes with well-defined structures. However, steric hindrances may limit the maximum grafting density and

reduce the overall polymer mass.[169] The *grafting-through* technique polymerizes macromonomers with a polymerizable backbone and a reactive end group for substrate attachment, enabling concurrent polymer chain growth and surface attachment.[169] This can result in high grafting densities and well-defined brush structures and is beneficial for creating complex architectures like block copolymers.[171] Nevertheless, the limited availability of suitable macromonomers and their removal during purification make this approach more complex compared to grafting-from and grafting-to methodologies.[172] Shamout et al.[116] synthesized brush-like glycopolymers via *grafting-(on)to* featuring monodisperse, sequence-defined side chains that mimic the structure of proteoglycans. These glycopolymers were evaluated for their interactions with Concanavalin A, demonstrating their usefulness in studying carbohydrate-protein interactions. Park et al.[165] designed glycopolymer brushes displaying *N*-acetyllactosamine glycan oligomers to bind specific lectins, emphasizing the role of multivalent presentation in improving lectin interactions, crucial for biosensing and targeted drug delivery applications. Wang et al.[164] synthesized branched glycopolymer brushes through chemoenzymatic methods, which serve as artificial glycocalyx for specific lectin binding and revealed a high specific binding capacity for Concanavalin A.

Star-shaped glycopolymers are a further unique class of glycopolymers with branched architecture, consisting of multiple arms radiating from a central core. As well as brush-like structures, star-like glycopolymers also exhibit increased multivalency and enhanced binding strength with target biomolecules.[173] These star-like glycopolymers allow simultaneous interactions with multiple binding sites on target proteins and show tunability in size based on hydrodynamic properties. The diameter of star-shaped glycopolymers increases with the number of arms, crucial for applications in drug delivery with controlled release and immunomodulation.[174-177] Zhang et al.[178] demonstrated the use of water-soluble star-shaped glycopolymers as nanocontainers to encapsulate hydrophobic drugs effectively for targeted delivery of anti-HIV drugs. The synthesis of star-shaped polymers can be achieved via *core-first*, *arm-first*, and *coupling-onto* methods, each offering distinct control over molecular structure and functionality,[179, 180] see Figure 10. In the *arm-first* approach, the polymer arms are initially synthesized before being permanently linked together, resulting in the formation of a star

polymer. A limitation is the variable number of arms on the core and the presence of linear chains that must be removed.[180-183] In the *core-first* approach, the core initiates star polymer synthesis, primarily through controlled processes like RAFT or ATRP.[182, 184-186] The *coupling-onto* strategy attaches end-functionalized linear polymers to a central core, facilitating controlled polymerization and ensuring high coupling efficiency.

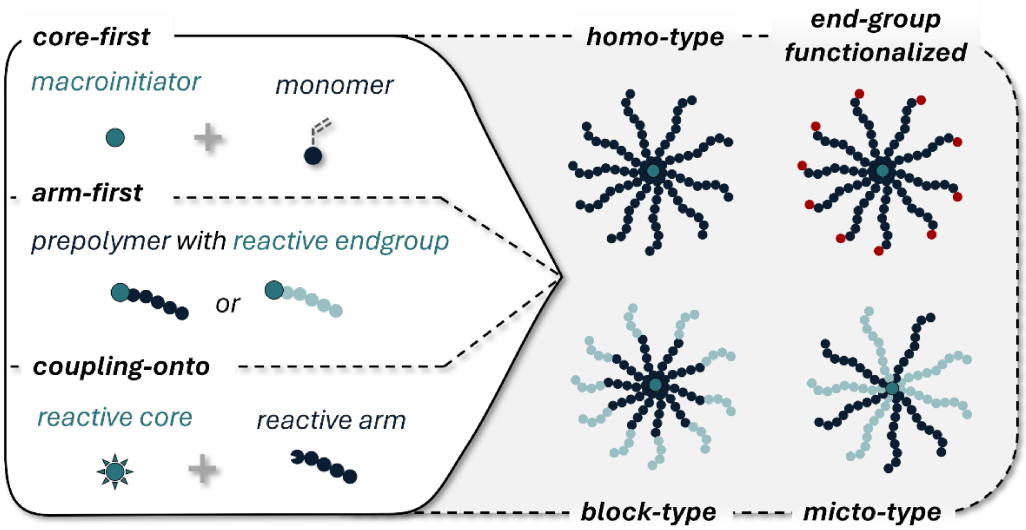


Figure 10: Schematic illustration of the three major approaches for star-polymer synthesis and the resulting star-polymer types.

Based on these synthesis routes, it is possible to distinguish different structural classes of star polymers: *homo-type* star polymers consist of only one monomer type, which can be extended by end-group functionalization.[187] *Micto-type* stars consist of different arms, but each arm is a homopolymer. In *block-type* star polymers, one monomer type is at the core, followed by the second type, resulting in core-shell architectures.[187] These polymers exhibit higher compactness and segmental density near the core, leading to reduced viscosities and greater solubility compared to linear structures of the same molecular weight.[188, 189] The replication of these macromolecules is influenced by factors such as topology (arrangement and number of arms), monomer composition, and the core's chemical nature.[184, 189] The core links at least three linear polymers (arms) to form a star-shaped polymer. Nagao et al.[162] developed star-shaped glycopolymers to target influenza viruses, demonstrating their ability to inhibit hemagglutination and prevent viral aggregation and infection, highlighting their potential as antiviral agents. Monaco et al.[177] developed multi-armed star-shaped glycopolymers with precisely controlled core sizes

and arm lengths, which showed improved lectin interactions and potential for drug encapsulation. Chen et al.[176] examined how molecular weight and branching of star-shaped glycopolymers affect lectin binding affinity because glycopolymer architecture influences biological interactions, important for biosensing and targeted therapies.

The glycomimetics introduced here up to this point represent some initial strategies to address natural complexity. Nevertheless, most glycans are anchored on proteins and are not directly attached to the cell membrane.[2] This also glycomimetic structures are explored for their conjugation onto protein systems, thereby increasing the overall complexity of the mimetic systems. This complexity opens up new challenges for synthesis and analysis, which will be explored in detail in the next section.

1.2.3 Glycomimetic Protein-Polymer Conjugates and their Synthesis

Glycan modification on proteins aims to introduce carbohydrate components and mimic the structure and function of naturally occurring glycoproteins.[92] Naturally occurring glycosylation is crucial for protein structure, function, and interaction partner recognition.[92, 190] Substantial advancements in synthetic glycoprotein development now shows significant promise in various biomedical and biotechnological fields, such as the development of vaccines and the delivery of drugs.[93] These conjugates offer improved resistance to high temperatures, storage stability, salt compatibility and low pH conditions.[191-198] Lin and Kasko[199] created multivalent glycopolymer conjugates to strengthen lectin interactions, thereby enhancing binding affinity and specificity and demonstrate promising applications for targeted drug delivery and biosensing. Lee et al.[200] created end-functionalized glycopolymers that mimic chondroitin sulfate proteoglycans. These glycopolymers were utilized to produce microarrays for studying protein interactions, specifically focusing on the binding of monoclonal antibodies to glycan motifs. Droumaguet and Nicolas[201] showcased the application of glycopolymer-conjugated BSA to highlight the potential of protein-glycopolymer conjugates for immunological applications by enhancing complement activation through the lectin pathway. Figure 11 summarizes some core elements of protein-polymer conjugates, highlighting their broad applicability and investigating into structural property enhancements.

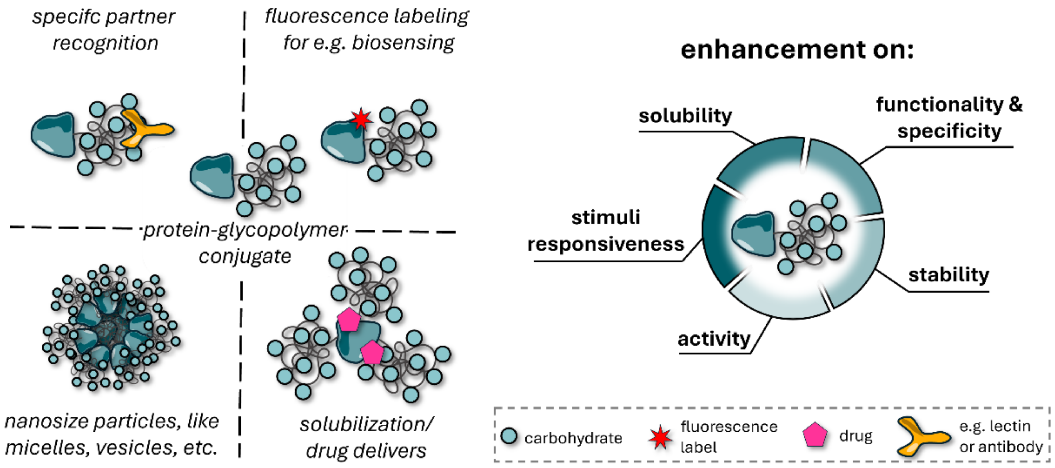


Figure 11: Highlighting protein-polymer conjugates broad applicability and structural property enhancements.

Two common methods for creating protein-polymer conjugates over a two-step procedure are: pre-functionalizing the protein with an initiator for a *grafting-from* approach or conjugating a pre-synthesized polymer to the protein using a *grafting-to* approach.[202, 203] Significant challenges associated with the *grafting-to* approach include the complexity of purification processes required to separate unconjugated polymer chains, as well as low conjugation efficiency, primarily due to the steric hindrance of the components.[202, 203] The primary limitation of the *grafting-from* approach is the risk of protein inactivation and denaturation, for example, caused by organic solvents and elevated temperatures, during initiator introduction or polymerization.[202, 203] Meanwhile, several approaches successfully circumvent this issue, demonstrating initiator conjugation and subsequent polymerization in aqueous buffer solutions[92, 204-208] or through photo-induced polymerizations that minimize potential damage to protein structure, thereby preserving bioactivity.[209-211] In both grafting approaches, protein modification generally involves reactions with amino acid side chain functional groups, like those in lysines (Lys) or cysteines (Cys), which interact with amines, thiols, carboxylic acids or succinimides.[92, 197, 212] However, the presence of multiple side residues, like lysines, in most proteins often results in a heterogeneous mixture with varying conjugation sites and quantities, limiting their biomedical applications.[213] Site-specific functionalization needs bioorthogonal groups to specific amino acids (e.g., *N*- or *C*-terminus, free cysteines, disulfides, or non-natural amino acid sites), allowing selective and efficient conjugation, which typically demand advanced synthetic techniques, like

CRP.[213, 214] Figure 12 illustrates diverse grafting and conjugation opportunities for protein modification to integrate an initiator or polymer.

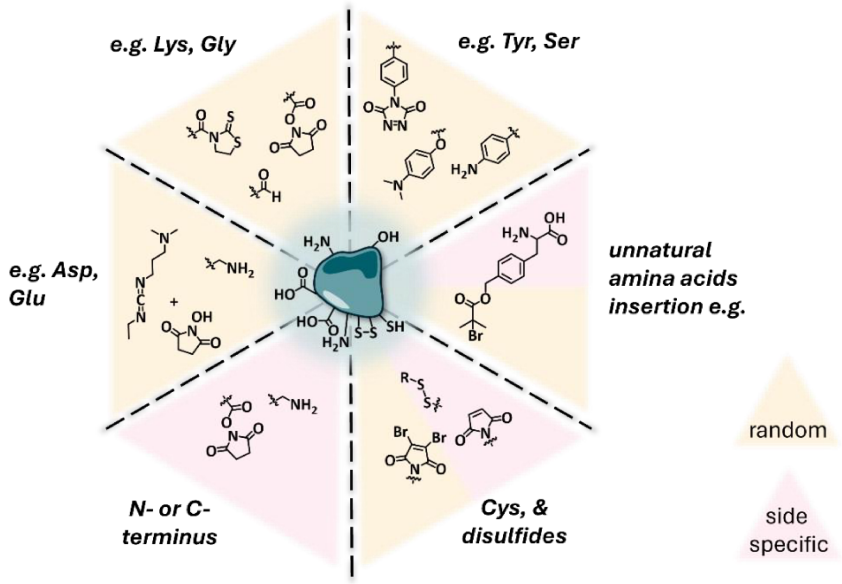


Figure 12: Summary of divers grafting and conjugation opportunities for protein modification for initiator or polymer integration.

Consequently, it is essential to regulate the quantity and positioning of polymer chains in the conjugates, as well as the polymer composition, dispersity and chain length. There are various options for controlled polymerization. The most common methods for synthesizing protein-polymer conjugates include ATRP,[215-220] RAFT,[136, 221-223] PET-RAFT[211] and single electron-transfer living radical polymerization (SET-LRP).[207] Ideally, a conjugated polymer should enhance the native protein properties without altering its structure or blocking an enzyme's active site.[224, 225] The development of protein-polymer conjugates is in the focus of research to achieve precise site-specific conjugation, control over stoichiometry, and high-yield products with innovative functions.[226]

1.2.4 Glycocalyx engineering

Most of the glycomimetic systems discussed so far demonstrate selective carbohydrate-protein interactions in solution or on surfaces, both of which represent simplified models for glycocalyx-oriented studies. While the investigations show promising initial results for glycomimetic structures, they completely disregard the natural environment in which glycan structures form bonds in the native cell membrane.[227] K. Godula[1] introduced the term "glycoscape," which defines the role of carbohydrates within the extremely dense

and heterogeneous surface of the glycocalyx, the nature of epitope presentation, and the dynamics of these through the membrane and associated locality. To incorporate aspects of 3D complexity into glycomimetic studies, initial investigations were conducted under the term glycocalyx engineering. The aim is to replicate the complexity of the glycocalyx, which can be achieved through two different approaches. The initial approach involves replacing native cell membrane glycans through chemo-enzymatic, genetic or metabolic methods, which often results in extensive alterations and limited spatial organization.[1, 228-232] For this purpose, in the second approach, a process known as *de novo* glycocalyx engineering, lipid-anchored glycomimetics can be strategically incorporated to initiate controlled modifications or replace specific structural classes. This approach offers the significant advantage of allowing glycomimetic structures to be examined for their binding behavior under natural conditions.[1] Hudak et al.[233] integrated sialylated glycopolymers into cancer cell lines via a lipid component, demonstrating that increased cell surface sialylation conferred protection against natural killer cell-mediated cytotoxicity. Kamil Godula's group developed phospholipid-functionalized mucin-mimetic glycopolymers to create a screening platform for Influenza A virus (IAV) inhibitors and to position them on red blood cell surfaces.[234] This method enables the study of how macromolecular displacement in the glycocalyx influences the binding efficiency of glycan-binding proteins.[235]

Although these models better simulate natural processes, they quickly become too complex to yield meaningful insights into the relationships between individual structures and their binding behavior. Thus, it is reasonable to reconsider and reconstruct glycomimetic structures based on key features, then progressively integrate them into glycan-decorated protocells.[236]

2 Aims and Outlines

Today, the significance of the glycocalyx, a heterogeneous and dynamic dense layer of glycosylated proteins and lipids on eukaryotic cells, in areas such as cellular communication, adhesion, and pathogen invasion is well-understood. However, our understanding of the mechanistical details e.g., of cell-cell or cell-pathogen interactions mediated by glycan conjugates of the glycocalyx is still limited.

Synthetic glycan-conjugate systems, known as glycomimetics, are designed to imitate, simplify, and control interactions with proteins or cells and thereby offer a valuable tool to gain new insights into structure-activity correlations and binding mechanisms. However, most glycomimetics do not yet fully capture the inherent complexity of native cellular glycocalyces and their glycan conjugates such as glycoproteins or proteoglycans.

The goal of this study is to synthesize and characterize structurally more complex, yet highly controlled glycomimetics with a special focus on glycoproteins including mucin mimetics based on glycopolymers. These mimetics will be then applied to gain initial insights into their topology and specific binding behavior as a contribution to existing research on the development of glycocalyx mimetics.

The initial section will focus on synthesizing specific protein-glycopolymer conjugates using the recently introduced controlled polymerization method, thiol-induced, light-activated controlled radical polymerization (TIRP) (Figure 13). Previous investigations have established TRIP as a novel approach for small initiator molecules in solution. This research is aiming to extend this method to high-molecular-weight initiators, such as proteins and enzymes, to access glycopolymers-protein conjugates that offer a way for selectively introducing artificial glycosylation. This method will thus allow for the straightforward, mild and selective conjugation of glycopolymers in aqueous buffers while preserving the native structure and activity of the protein, without requiring prior protein modification.

Building on this first strategy, the introduction of a so-called rebridging agent is intended to expand the incorporation of an additional defined polymer through TIRP while preserving the native protein structure. This approach will yield bifunctional polymer-

protein-polymer conjugates with two distinct polymers attached to a single protein. Such controlled designs can then facilitate the development of advanced property materials, enabling the formation of highly controlled multilayered polymer-protein-polymer nanoparticles by stimuli-responsive self-assembly.

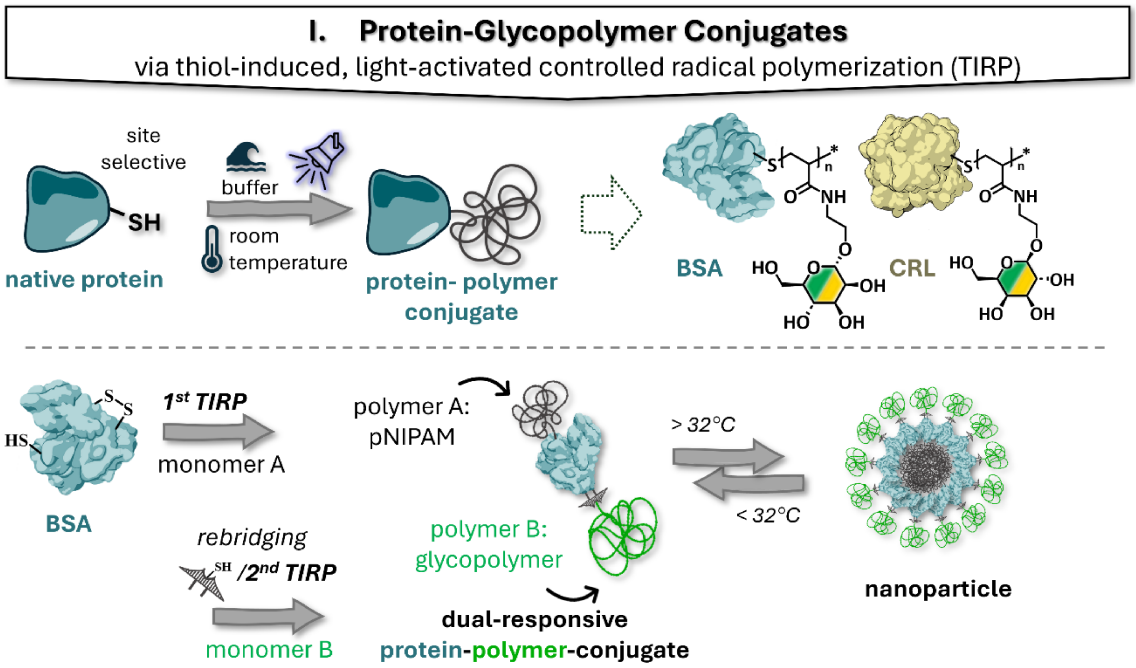


Figure 13: Overview of the TIRP-based protein-glycopolymer conjugate - first part of this thesis.

The subsequent section will concentrate on the synthesis and structural characterization of well-defined, high-molecular-weight, sulfated double-brushed glycopolymers by combining SPPoS with polymer analog reactions (Figure 14). These polymers will be designed to mimic the properties of glycopolymer part of native mucins, specifically *O*-glycosylated large glycoproteins, in terms of their high degree of branching, anionic charges, hydration, conformation, and adhesion characteristics.

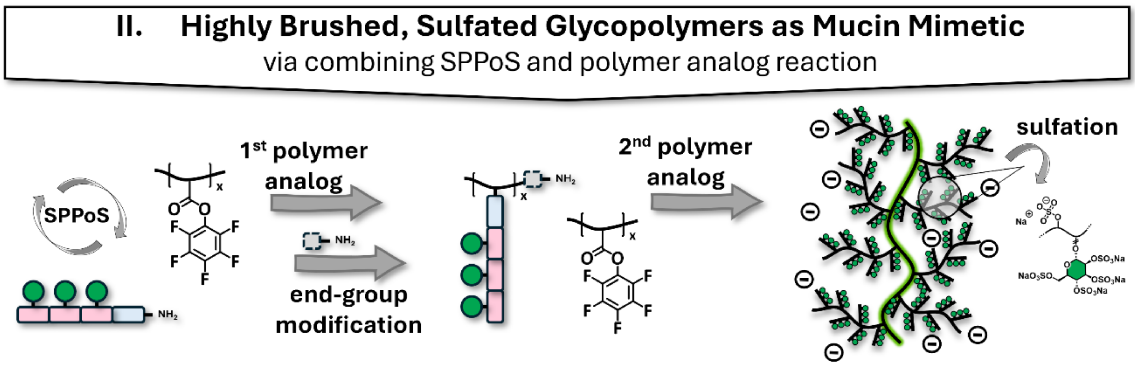


Figure 14: Overview of the SPPoS and polymer analog reactions – second part of this thesis.

Accordingly, in addition to establishing the synthesis strategy, mucin characteristic-oriented experiments will be conducted in collaboration with the research groups of Prof. Karg and Dr. Balzer. These experiments will focus on determining adhesion properties, as well as gathering initial evidence of hydration and conformation properties through small-angle neutron scattering (SANS) and atomic force microscopy (AFM) measurements.

The concluding part will evaluate the potential of TIRP as its transitions from utilizing basic initiators to adopting macroinitiators for the creation of star-shaped glycopolymers, representing another form of branched glycomimetics (Figure 15). The design of these star-shaped glycopolymers will involve the synthesis of macroinitiators through standard SPPoS, with TIRP enabling the development of both homopolymer and blockcopolymer branches. This polymerization approach will be designed to offer extensive variability and precise control over structural features such as the number, density, and length of the polymer chains.

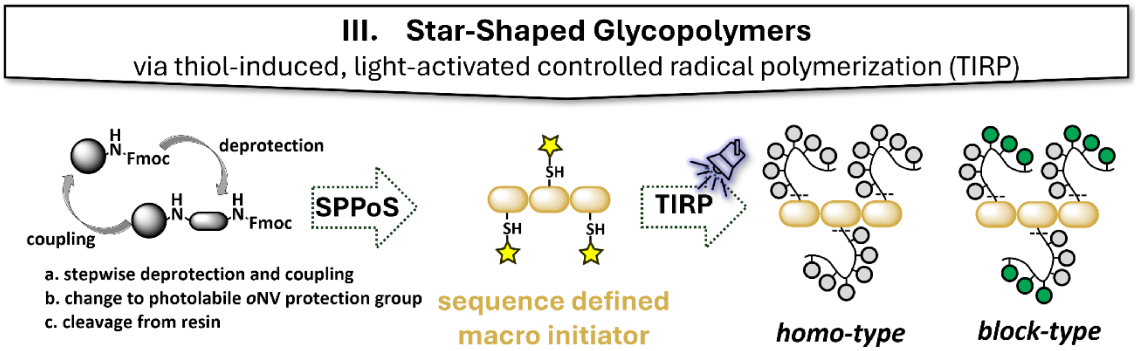


Figure 15: Overview of star-shaped glycopolymer – third part of this thesis.

3 Results and Discussion (Publications/Drafts)

3.1 Thiol-selective native grafting from polymerization for the generation of protein-polymer conjugates

Authors: Melina I. Feldhof, Sandro Sperzel, Lorand Bonda, Susanne Boye, Adam B. Braunschweig, Ulla I. M. Gerling-Driessen and Laura Hartmann

Journal: Royal Society of Chemistry

Issue: **2024**, *15*, 16768-16777

Type of Paper: Edge Article

Impact Factor: 7.6 (2023)

DOI: 10.1039/D4SC04818K

First author contribution:

Collaborative project development. Synthesis and characterization (^{1}H-NMR, SDS-PAGE, Ellman's Assay, CD, DSC, IR) of the protein-polymer conjugates. Conducting enzyme activity studies and binding studies on surfaces and in solution. Collaborative writing of the manuscript.

Reprinted with permission from Royal Society of Chemistry.

Copyright © 2024 Royal Society of Chemistry.

Chemical Science

ROYAL SOCIETY OF CHEMISTRY

EDGE ARTICLE

View Article Online
View Journal

Check for updates

Cite this: DOI: 10.1039/d4sc04818k

All publication charges for this article have been paid for by the Royal Society of Chemistry

Open Access Article. Published on 18 September 2024. Downloaded on 9/26/2024 12:32:12 PM. This article is licensed under a Creative Commons Attribution 3.0 Unported Licence.

Thiol-selective native grafting from polymerization for the generation of protein–polymer conjugates†

Melina I. Feldhof,[a] Sandro Sperzel,[a] Lorand Bonda,[a] Susanne Boye,[b] Adam B. Braunschweig,[cde] Ulla I. M. Gerling-Driessen*[f] and Laura Hartmann*[f]

Protein–polymer conjugates combine properties of biopolymers and synthetic polymers, such as specific bioactivity and increased stability, with great benefits for various applications from catalysis to biomedicine. Furthermore, polymer conjugation can mimic important posttranslational modifications of proteins such as glycosylation. There are typically two approaches to create protein–polymer conjugates: the protein is functionalized in advance with an initiator for a *grafting-from* method or a previously produced polymer is conjugated to the protein *via* a *grafting-to* method. In this study, we present a new approach that uses native proteins and allows for direct *grafting-from* using a thiol-induced, light-activated controlled radical polymerization (TIRP) that is initiated at thiols from specific cysteine residues of the protein. This straightforward method is employed to introduce polymers onto proteins and enzymes without any prior protein modifications, it works in aqueous buffer and maintains the protein's native structure and activity. The resulting protein–polymer conjugates exhibit high molar masses and low dispersities. We demonstrate the versatility of this approach by introducing different types of polymers such as hydrophilic poly(2-hydroxyethyl acrylate) (pHEAA), temperature-responsive poly(*N*-isopropylacrylamide) (pNIPAM) as well as glycopolymers mimicking the natural protein glycosylation and enabling selective interactions. We present successful combinations of the protein and polymer functions *e.g.*, temperature-induced aggregation leading to an increase in enzyme activity and the introduction of artificial glycosylation inducing specific protein–protein cluster formation and giving straightforward access to glycosurfaces. Based on this straightforward, potentially scalable yet highly controlled synthesis of protein–polymer conjugates, various areas of applications are envisioned ranging from biomedicine to material sciences.

Received 19th July 2024
Accepted 17th September 2024

DOI: 10.1039/d4sc04818k

rsc.li/chemical-science

Introduction

Protein–polymer conjugates are materials with a broad spectrum of applications in biotechnology, catalysis or even laundry detergents due to their improved properties, such as salt compatibility, storage stability and resistance to high temperatures or low pH conditions.[1–8] The first PEGylated BSA conjugates found commercial applications as immunogenicity reducing drugs already in 1977.[9] Today, at least 15 protein-PEG conjugates have been approved by the Food and Drug Administration (FDA) for therapies against diseases including hepatitis C, leukemia, blood cancer or autoimmune diseases.[9,10] Protein–polymer conjugates are obtained by covalent linkage of a polymer and protein of choice, while retaining the protein's natural structure and function.[11–14] Protein–polymer conjugates have opened new opportunities, especially in biomedical applications, as they offer a unique opportunity of salvaging the biological activity of native proteins and combining this with the advantageous properties of synthetic polymers, such as improved solubility, prolonged circulation time in the blood stream, reduced immunogenicity and improved biocompatibility.[15–19] Furthermore, conjugation of polymers can mimic posttranslational modifications of proteins such as their glycosylation. This has been explored extensively through the introduction of hydrophilic polymers such as poly(ethyleneglycol) (PEG) *e.g.*, to increase protein stability.[20–24] Using

[a]*Department of Organic and Macromolecular Chemistry, Heinrich-Heine-University Düsseldorf, Universitätsstraße 1, 40225 Düsseldorf, Germany*

[b]*Center Macromolecular Structure Analysis, Leibniz-Institut für Polymerforschung Dresden, Hohe Str. 6, 01069 Dresden, Germany*

[c]*Advanced Science Research Center, Graduate Center, City University of New York, 85 St. Nicholas Terrace, New York, NY 10031, USA*

[d]*PhD Programs in Chemistry and Biochemistry, Graduate Center, City University of New York, 65 5th Avenue, New York, NY 10016, USA*

[e]*Department of Chemistry, Hunter College, 695 Park Avenue, New York, NY 10065, USA*

[f]*Institute for Macromolecular Chemistry, University of Freiburg, Stefan-Meier-Str. 31, D-79104 Freiburg i.Br., Germany. E-mail: laura.hartmann@makro.uni-freiburg.de; ulla.gerling-driessen@makro.uni-freiburg.de*

† Electronic supplementary information (ESI) available: Detailed information on the materials and methods used as well as additional microscopic images and data about activity assays of CRL, carbohydrate–lectin binding studies in solution and on the surface. See DOI: https://doi.org/10.1039/d4sc04818k

© 2024 The Author(s). Published by the Royal Society of Chemistry

Open Access Article. Published on 18 September 2024. Downloaded on 9/26/2024 12:32:12 PM. This article is licensed under a Creative Commons Attribution 3.0 Unported Licence.

biofunctional polymers such as glycopolymers in protein–polymer conjugates to also affect bioactivity through the polymer component of the conjugate has been studied much less so far.[25–31]

The synthesis of protein–polymer conjugates distinguishes between *grafting-to* and *grafting-from* approaches.[32,33] The *grafting-to* method involves the synthesis of a polymer followed by a subsequent conjugation of the polymer to the protein, allowing a simple and straightforward polymer synthesis and characterization. The major challenges with this method are low conjugation efficiency due to the high steric demand of the two components and complex purification procedures to separate conjugation products carrying different numbers of polymer chains on one protein.[32,33] In contrast, the *grafting-from* approach uses polymerization from the protein *via* an initiator that is previously inserted into the protein structure. This typically results in higher yields of the protein–polymer conjugate due to lower steric demand of the monomers and growing chain during polymerization.[32,33] However, the major limitation of this approach is the potential denaturation and inactivation of proteins due to the chemical conditions *e.g.*, organic solvents and higher temperatures, during the introduction of the initiator moiety or the polymerization itself.[34,35] Recent work by Maynard *et al.*,[36] Haddleton *et al.*,[37] Velonia and Anastasaki *et al.*[13] and Matyjaszewski *et al.*[38] circumvents this and showed the successful conjugation of an initiator and later polymerization also in aqueous buffer solutions. Another important development has been the use of photo-induced polymerization methods to derive protein-conjugates by light at specific wavelengths can minimize potential damage to the protein structure, thus preserving bioactivity.[39–41] Nevertheless, these processes are still two-step procedures and the immediate use of the protein as *e.g.*, isolated from a biotechnological process or biological sources is not possible. For both grafting methods, protein modification usually proceeds *via* the functional groups of the amino acids side chains, such as lysines or cysteines, that can react with succinimides, thiols, amines, or carboxylic acids.[1,34,42] Since most proteins present several of these residues, this typically results in a mixture of products where conjugation sites and numbers can vary and such dispersity can limit applications *e.g.*, in biomedicine.[16] In contrast, site-specific functionalization involves the insertion of bioorthogonal groups at specific amino acids *e.g.*, the N- or C-terminus, free cysteines, disulfides, or at selected sites that allow insertion of unnatural amino acids to enable selective and efficient initiator or polymer conjugation, but these approaches often require advanced synthetic methodologies.[15,16]

In addition to the positioning and number of polymer chains in the conjugates, polymer chain length, dispersity and composition (*e.g.*, copolymers and functional side and end groups) needs to be controlled. As controlled polymerization methods for the preparation of protein–polymer conjugates, mainly atom transfer radical polymerization (ATRP),[43–48] reversible addition–fragmentation chain-transfer polymerization (RAFT),[49–52] single electron-transfer living radical polymerization (SET-LRP),[37] photoinduced electron/energy transfer reversible addition–fragmentation chain transfer polymerization (PET-RAFT)[41] and ring opening polymerization (ROP)[53] have been used. Ideally, the conjugated polymer should not significantly modify the structure of a native protein or in the case of an enzyme interfere or block the active site, yet at the same time the polymer should bring in additional properties and functions, such as solubilization or shielding.[14,54] Today, the design and synthesis of protein–polymer conjugates are still subject to extensive research that aims at achieving site-specific conjugation, stoichiometric control, and high-yield conjugation products with new and advanced function,[55] and also continue to be pursued to gain new insights into protein–protein interactions.[56,57]

Here, we introduce for the first time a *grafting-from* approach using native proteins without the need for any prior modifications while still enabling site-selective and highly controlled polymerization by employing a thiol-induced, light-activated controlled radical polymerization (TIRP) (Fig. 1). Our approach uses gentle polymerization conditions, suitable for a variety of proteins, potentially also less stable proteins, retaining their native structure and thus function, and allows for site selective modification addressing free thiols, which gives access to highly controlled protein–polymer conjugates.

Results and discussion

The recently introduced TIRP is a potentially controlled radical polymerization that can be initiated from various low molecular weight thiol initiators, such as tritylthiol.[58] We now explore this method for the first time on high molecular weight thiol initiators, specifically the free thiols of cysteines in a protein (Fig. 2A). We chose *bovine serum albumin* (BSA) as protein initiator, as it contains exactly one free cysteine at position ′34.[59] Four different acrylamide derivatives were chosen as monomers based on previously optimized TIRP conditions and to demonstrate the versatility of our approach in generating protein–polymer conjugates of different types. Specifically, p(HEAA) as a well-established hydrophilic, biocompatible polymer with non-immunogenic, anti-fouling, and non-toxic properties,[60–62] p(NIPAM) as a non-toxic and temperature-responsive polymer[63–66] and two glycopolymers derived from

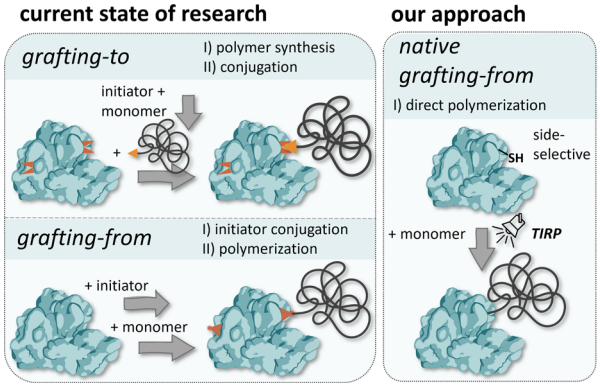


Fig. 1 Overview of well-known systems for the preparation of protein–polymer conjugates and comparison with our approach.

© 2024 The Author(s). Published by the Royal Society of Chemistry

Open Access Article. Published on 18 September 2024. Downloaded on 9/26/2024 12:32:12 PM. This article is licensed under a Creative Commons Attribution 3.0 Unported Licence.

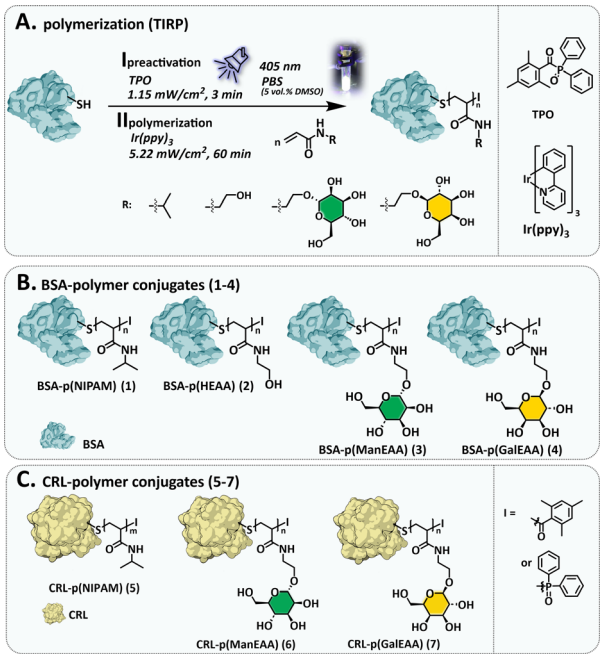


Fig. 2 (A) Illustration of the general set up for the synthesis of TIRP based protein–polymer conjugates and approach values. (B) BSA based protein–polymer conjugates **1–4**. (C) CRL based enzyme–polymer conjugates **5–7**.

mannose (Man) and galactose (Gal) acrylamide monomers to install artificial glycosylation[67] were polymerized from BSA (Fig. 2B). In addition to using BSA as an initiator, we chose the enzyme *Candida rugosa lipase* (CRL), with one free cysteine at position ′217 [68] to test whether both, the protein structure as well as its function (enzyme activity) are maintained after polymer conjugation (Fig. 2C). BSA is already a well-established protein known for its particularly good adhesion properties and CRL was selected for its reliable evidence of enzymatic activity. These two proteins were also chosen because of their free accessible thiol. However, this approach is not limited to proteins that already carry free cysteines. Recombinant protein expression methods allow easy modification of protein sequences, offer a straightforward opportunity to introduce cysteine residues as natural amino acids into a protein structure[69–71] and thus make them amenable to the here presented native *grafting-from* approach.

TIRP-based native *grafting-from* polymerization on the proteins was carried out at room temperature in nitrogen-deoxygenated phosphate buffer (10 mM, pH 7.4). The photoinduced radical polymerization takes place under deoxygenated conditions to minimize oxygen-induced side reactions. The radical initiator diphenyl(2,4,6-trimethylbenzoyl)phosphine oxide (TPO) and tris(2-phenylpyridine)iridium, iridium catalyst were pre-dissolved in DMSO and diluted with the buffer to obtain a final concentration of 5% DMSO, which is known to not affect the native structure of proteins.[72] In the pre-activation step I (Fig. 2A) the TPO/protein mixture is irradiated at low intensity (1.15 mW cm^{-2}) for three minutes to form the activated protein initiator, immediately followed by step II, adding monomer and Ir catalyst and irradiating for one hour (5.22 mW cm^{-2}). The formed protein–polymer conjugates were isolated by dialysis against PBS buffer.

Details on the characterization of the conjugates by ^{1}H-NMR, IR, asymmetrical flow field flow fractionation with light scattering detection (AF4-LS), SDS-PAGE, Ellman's Assay, circular dichroism (CD) and differential scanning calorimetry (DSC) are displayed in the ESI.† ^{1}H-NMR and IR spectroscopy were used to demonstrate the successful formation of the different acrylamide polymers. The separation of protein–polymer conjugates is usually challenging due to high number of different functionalities. The use of AF4-LS[56,73] enabled us to efficiently separate the three populations of BSA (monomeric BSA, BSA dimer or trimer/multimer), BSA–polymer conjugates and allowed the determination of absolute molar masses, dispersities and hydrodynamic radii (see ESI†). This gentle separation technique reduces sample degradation risk and permits the analysis of sensitive biomolecules like proteins and nucleic acids, which could be damaged by the shear forces in GPC.[74] The shift towards increased molar masses verified the successful attachment of the polymers to BSA **1–4** (Fig. 3A). Furthermore, AF4-LS measurements confirmed that the protein–polymer conjugates **1–4** obtained molar masses in the range that were expected for the conjugation of one polymer chain per BSA according to a controlled polymerization. Molar mass distributions (Fig. 3B) showed a subtle shoulder for conjugates **1**, **3**, and **4** in the lower molar mass region, which indicates the presence of some remaining unconjugated BSA. This is explained by the fact that not all BSA molecules present

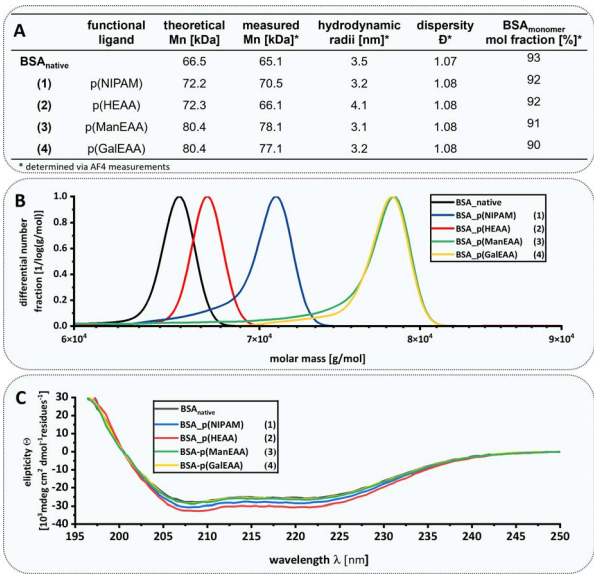


Fig. 3 (A) Summary of analytical data for monomeric BSA population of protein–polymer conjugates **1–4** *via* AF4-LS in PBS buffer (pH 7.4 at 25 °C). (B) Molar mass distributions obtained by AF4-LS: comparison of the individual molar masses of monomeric BSA population protein–polymer conjugates **1–4**. (C) Presentation of CD spectra of BSA–polymer conjugates **1–4** for investigation of structural properties. The measurements were performed in PBS buffer (pH 7.4, at 20 °C) with an exact concentration of 251 μg mL^{-1} adjusted by the Pierce assay.

Open Access Article. Published on 18 September 2024. Downloaded on 9/26/2024 12:32:12 PM. This article is licensed under a Creative Commons Attribution 3.0 Unported Licence.

free thiols. In agreement with literature values,[75] approximately 54% of the theoretically available thiols of BSA were detected as accessible initiators for polymerization by using Ellman's assay.[76] After polymer conjugation, we observed a significant decrease of free thiols (Fig. S47†). CD measurements[77] confirmed that the native structure of BSA is maintained (Fig. 3C). Thermal protein denaturation of the protein–polymer conjugates determined the degree of unfolding by measuring the ellipticity at 222 nm at increasing temperatures. The results demonstrated no changes in protein stability for the conjugates **2–4** and a rather small increase in stability for the BSA–p(NIPAM) (**1**) conjugate (Fig. S42†). In addition, DSC measurements were performed (see ESI†) confirming an increase in thermal stability for the conjugate **1**, which is in accordance with previous observations for other, similar protein–polymer conjugates.[78,79] In order to analyze the polymer alone without the protein it was grafted from, protein–polymer conjugates were subjected to thermal amino acid degradation and the polymer was subsequently isolated by dialysis and analyzed by ^{1}H-NMR and IR (see data for BSA–p(NIPAM) conjugate **1** in the ESI, Fig. S69 and S70†). For conjugates **2–4** pHEAA and glycopolymers were also degraded under the applied conditions and therefore did not allow for additional analysis of the polymer alone (data not shown). To further demonstrate that polymer conjugation maintains not only the structure but also function of the protein, we chose an enzyme – lipase CRL – for polymer conjugation *via* TIRP. CRL is widely used in pharmaceutical and biotechnological applications due to its selective hydrolysis of ester bonds.[80–82] Three CRL–polymer conjugates carrying either p(NIPAM) (**5**), or glycopolymers p(ManEAA) (**6**) or p(GalEAA) (**7**) were prepared. CRL activity was determined by photometric quantification of the hydrolysis of *p*-nitrophenol acetate to *p*-nitrophenol and acetic acid (Fig. 4A).[83] Correct conformation as well as an accessible active site are vital factors for proper enzyme function.[81,82]

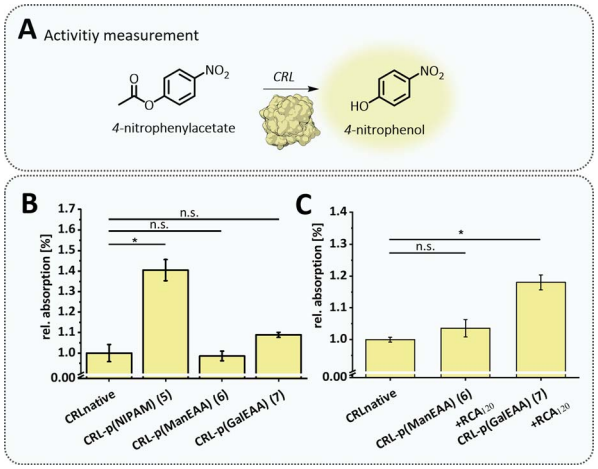


Fig. 4 (A) Illustration of the activity/ester cleavage of the enzyme CRL. All thiol detections were performed in reaction buffer: 0.1 M sodium phosphate, pH 8.0, containing 1 mM EDTA. Ellman's stock solution of 4 mg mL^{-1} Ellman's reagent and a 0.75 mM protein stock solution were prepared in reaction buffer. The assay is performed in triplicate with an incubation time of 15 min and absorbance is measured at 412 nm. (B) Comparison of the activity of the native enzyme CRL and the conjugates **5–7**. (C) Comparison of native CRL with CRL–polymer conjugates **6** and **7** incubated with lectin RCA_{120}. Data were evaluated using one-way ANOVA analysis followed by Bonferroni correction (* <0.05).

To directly compare activity of the native enzyme and the respective polymer conjugates, measured adsorption values of the activity assay were normalized to the standard activity of the native, unconjugated enzyme, which represents 100% native activity. We observed that the enzyme activity of CRL remained unaffected in the conjugates **6** and **7** carrying the glycopolymers (Fig. 4B). However, we noticed a significant increase of about 40% in the activity for the CRL–p(NIPAM) conjugate **6**. A similar effect was previously observed for CRL–p(NIPAM) conjugates in non-aqueous solvents obtained by a *grafting-to* method.[84] The authors explain this by the hydrophobic character of the polymer, which interacts with the CRL lid and thus supports a conformation that is suitable for catalysis. We attribute our own observation to another phenomena, possibly in addition to the previous suggestion, and to the fact that the activity assay was carried out at 30 °C, which is close to the LCST of the CRL–p(NIPAM) conjugate **5** (32 °C, Fig. S56†). The increase in the activity at elevated temperatures could be the result of cluster formation of this conjugate.

This finding inspired us to start looking into different areas of applications for the protein–polymer conjugates now available from the native *grafting-from* method. Applications have been chosen that demonstrate the successful preservation as well as combination of properties of both, protein and polymer. First, to confirm aggregation induced increase in enzymatic activity of CRL, we used the galactose-specific lectin *Ricinus communis agglutinin I* (RCA_{120}) to induce clustering of the CRL–p(GalEAA) conjugate (**7**) while the CRL–p(ManEAA) conjugate (**6**) served as negative control with RCA_{120} not binding to Man (Fig. 4C). Cluster formation between CRL–p(GalEAA) (**7**) and RCA_{120} was confirmed by turbidity measurements, while CRL–p(ManEAA) (**6**) showed no interaction with RCA_{120} (Fig. S53†). Indeed, we observed that the enzymatic activity of the CRL–p(GalEAA) conjugate increased significantly, by approximately 20%, when clustering is induced by the lectin, whereas the activity of the CRL–p(ManEAA) conjugate remained unaffected. Thus, conjugation of the glycopolymer enabled not only an increase in stability but the specific formation of a protein–protein complex and thus tuning the enzyme activity.

Indeed natural glycosylation of proteins plays a key role for their structure, function and the recognition of other interaction partners.[34,85] Glycopolymers are simple mimetics of natural glycoconjugates and have found wide application in biomedical research *e.g.*, for the detection and inhibition of pathogens, in tumor biology and tissue engineering.[29,34,67,86,87] To this end, conjugation of glycopolymers to proteins can serve as "artificial" glycosylation.[34] Indeed, protein–glycopolymer conjugates have demonstrated great potential for various biomedical and biotechnological applications *e.g.*, in vaccine development and drug delivery.[25] TIRP-based native *grafting-from* approach now gives access to protein–glycopolymer conjugates in a one-step procedure and enables the combination of the protein's

 © 2024 The Author(s). Published by the Royal Society of Chemistry

Open Access Article. Published on 18 September 2024. Downloaded on 9/26/2024 12:32:12 PM.
This article is licensed under a Creative Commons Attribution 3.0 Unported Licence.

properties and function with the specific binding of the glycopolymer.

To further demonstrate this, we used the two different BSA–glycopolymer conjugates BSA–p(ManEAA) (**3**) and BSA–p(GalEAA) (**4**) to study the interactions of the protein–polymer conjugate with two lectins – Gal-recognizing RCA_{120} and Man-recognizing *Concanavalin A* (ConA). Selective binding and protein–protein complex formation was studied by turbidity measurements[88,89] demonstrating cluster formation between BSA–p(ManEAA) (**3**) and ConA, and between BSA–p(GalEAA) (**4**) and RCA_{120}, respectively. To confirm that cluster formation is driven by the glycopolymer–lectin interactions, α-methyl-mannose and galactose were used as competitive inhibitors enabling full dissolution of the previously formed clusters (Fig. 5A and B). The strength of carbohydrate–lectin interaction can be estimated by determining the concentration (5.61 ± 0.38 μM) at which the half-maximal turbidity is reached for BSA–p(ManEAA) conjugate (**3**) (Fig. S44†). Considering that approximately 84% of the molecular weight of the conjugate is the protein, it is feasible to determine a value for the half-maximal turbidity that solely pertains to the carbohydrate units, amounting to 0.94 ± 0.06 μM (Fig. S45†). This value of the BSA–p(ManEAA) conjugate is similar to the concentration of pure p(ManEAA) polymer in solution (1.05 ± 0.06 μM) (Fig. S46†), suggesting that an equivalent binding affinity was achieved with the same amount of Man units in solution as in the conjugate. Hence, the conjugation did not affect the binding affinity of the carbohydrate ligands.

BSA is often used in the passivation of surfaces based on its high adherence *e.g.*, to glass. Here we made use of this property to demonstrate an easy and effective immobilization of our protein–glycopolymer conjugates on glass surfaces and derived glycofunctionalized surfaces. Glycofunctionalized surfaces are commonly used *e.g.*, in glycan arrays[90] or for the detection and isolation of pathogens and tumor cells[91–93] but usually require more complex synthetic procedures. Using a simple half-coating dip approach (schematic representation in the ESI, S60†), either native BSA and a BSA–glycopolymer conjugate or combinations of both BSA–glycopolymer conjugates were adsorbed next to each other on a glass surface. Fluorophore-labeled lectins ConA (Alexa 647) and RCA_{120} (FITC) were used to determine the specific glycopolymer–lectin interaction *via* fluorescence microscopy. Inhibition competition assays using soluble glycopolymers p(ManEAA) (***S7***) and p(GalEAA) (***S8***) were performed to confirm selectivity of the protein–glycopolymer interactions. While in solution, the addition of the monosaccharide-based inhibitors (α-methylmannose and galactose) resulted in dissociation of the conjugate-lectin clusters, the addition of these inhibitors to the surfaces did not result in the release of the respective lectins from the BSA–

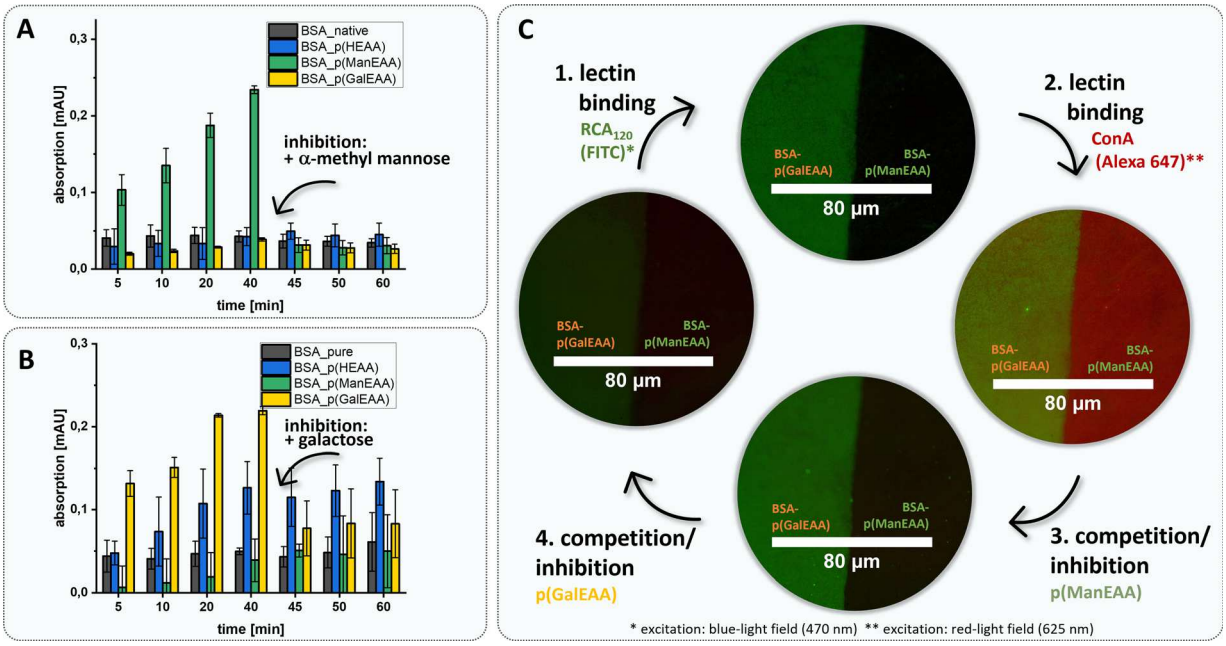


Fig. 5 Presentation of ligand–receptor competition inhibition assay in solution and on surface. (A) Turbidity measurements were performed at 420 nm at room temperature (20 °C). 120 μL of all structures **S5**, **2**, **3** und **4** (5 μM) were mixed with ConA (50 μM) and measured after 5, 10, 20 and 40 min. Inhibitor p(ManEAA) **S7** (30 mM) was then added and measured for another 5, 10, and 20 min. (B) Turbidity measurements were performed at 420 nm at room temperature (20 °C). 120 μL of all structures **S5**, **2**, **3** und **4** (5 μM) were mixed with RCA_{120} (50 μM) and measured after 5, 10, 20, and 40 min. Inhibitor p(GalEAA) **S8** (30 mM) was then added and measured for another 5, 10, and 20 min. (C) Microscopic images of the surface ligand–receptor interaction using the half-side dip approach with conjugate **4** *vs.* **3** (1 mg mL^{-1} in LBB buffer). The microscope images are a stack of blue (470 nm)– and red (625 nm)-light excitation. (1) The half–half carbohydrate coated surface was first incubated with the Gal-recognized lectin RCA_{120}-FITC (5 μM) for 30 min. (2) After washing the surface with LBB it was incubated with Man-recognized lectin ConA-Alexa 647 (5 μM) for another 30 min. The following inhibition step (3) with p(ManEAA) **S7** (15 mM) and (4) with p(GalEAA) **S8** (15 mM) can also be comprehended microscopically.

Open Access Article. Published on 18 September 2024. Downloaded on 9/26/2024 12:32:12 PM. This article is licensed under a Creative Commons Attribution 3.0 Unported Licence.

polymer conjugates. Presumably, the dense presentation of multivalent glycopolymer ligands on the surface requires stronger or multivalent competitors to disrupt the lectin binding.[94] Furthermore, steric shielding of the glycopolymer ligands, as well as favoured statistical rebinding events, are likely factors to contribute to the strong lectin binding on glycopolymer-presenting surfaces. Therefore, as inhibitors, glycopolymers p(ManEAA) (***S7***) and p(GalEAA) (***S8***) were employed to enable competitive lectin release from the glycopolymer-coated surfaces (Fig. 5).

Fluorescence microscopy confirmed homogeneous surface functionalization and simultaneous yet specific binding of RCA_{120}-FITC and ConA-Alexa 647 to the BSA–p(GalEAA) (**4**) and BSA–p(ManEAA) (**3**) coated parts of the surface, respectively. Through inhibition with soluble glycopolymers, either of the lectins can be released from the surface in presence of the other lectin staying bound. Thus, this demonstrates the straightforward use of BSA–glycopolymer conjugates to derive glycofunctionalized surfaces for specific ligand-mediated receptor interactions.

Conclusions

In summary, protein–polymer conjugates are an important class of biomolecules with a great variety of applications in the biomedical or the material sciences. Yet, deriving protein–polymer conjugates with currently available *grafting-to* and *grafting-from* polymerization methods is limited by low yields, poor conjugation site control and the need for artificial initiators. Here, we now present a mild *grafting-from* polymerization method using the native protein for the generation of various protein–polymer conjugates. We show that the native structure and function of proteins is retained and is suitable for the conjugation of various polymers including high molecular weight glycopolymers giving straightforward access to introducing artificial glycosylation. We already demonstrate a variety of potential applications of protein–polymer conjugates and protein–glycopolymer conjugates which can be further extended into areas such as catalysis, material sciences, biotechnology and biomedicine which can now benefit from the mild, simple, and rapid yet controlled and potentially also scalable methodology of TIRP with native proteins.

Experimental

Standard protocol for preparation of BSA polymer conjugates *via* TIRP

500 mg (7.69 μM) *Bovine Serum Albumin* was dissolved in 5 mL phosphate buffer (PBS 10 mM, 2.7 mM potassium chloride and 137 mM sodium chloride at pH 7.4) and deoxygenated with nitrogen for 20 min. Then, 1.3 mg (3.75 μmol) of diphenyl(2,4,6-trimethylbenzoyl) phosphine oxide (TPO) was dissolved in 0.1 mL dimethyl sulfoxide (DMSO) and slowly added to the protein solution, which was subsequently deoxygenated for another 20 min. 50 equivalents (375 μM) of the corresponding vinyl monomer was separately dissolved in PBS (50 mg mL^{-1}) and 0.05 mol% (relative to the monomer, 0.18 μmol) of tris(2-phenylpyridine) iridium catalyst (Ir-Cat.) was dissolved in 0.1 mL DMSO and added before the whole solution was deoxygenated for 20 min. The protein/TPO solution was then irradiated for 3 min under the UV lamp ($\lambda = 405$ nm) at an intensity of 114 mW cm^{-2}. After this, the monomer/Ir-Cat. mixture was added and irradiated for another 60 min at 5700 mW cm^{-2}. The reaction mixture was then purified by dialysis (exclusion volume 50 kDa) and lyophilized.

Standard protocol for preparation of CRL polymer conjugates *via* TIRP

200 mg (3.47 μM) *Candida rugosa lipase* was dissolved in 4 mL PBS buffer and deoxygenated with nitrogen for 20 min. Then, 0.6 mg (1.73 μmol) of TPO was dissolved in 0.2 mL DMSO and slowly added to the protein solution, which was subsequently deoxygenated for another 20 min. 50 or 200 equivalents, respectively (174 μM resp. 694.6 μM) of the corresponding vinyl monomer were separately dissolved in PBS (50 mg mL^{-1}) and 0.05 mol% (relative to the monomer, 0.09 μmol resp. 0.35 μmol) of tris(2-phenylpyridine) iridium catalyst (Ir-Cat.) were dissolved in 0.2 mL DMSO and added before the whole solution was deoxygenated for 20 min. The protein/TPO solution was then irradiated for 10 min under the UV lamp ($\lambda = 405$ nm) at an intensity of 5700 mW cm^{-2}. After this, the monomer/Ir-Cat. mixture was added and irradiated for another 60 min at 5700 mW cm^{-2}. The reaction mixture was then purified by dialysis (exclusion volume 50 kDa) and lyophilized.

Pierce-protein-assay

Protein concentrations were determined using a Pierce 660 nm Protein assay. Therefore, 1 mg mL^{-1} stock solutions (PBS) of all protein polymer conjugates were prepared. Native BSA served as a standard to determine the calibration curve (2000 μg mL^{-1}, 1000 μg mL^{-1}, 500 μg mL^{-1}, 250 μg mL^{-1}, 125 μg mL^{-1}, 62.5 μg mL^{-1}, and 31.25 μg mL^{-1}). All measurements were performed in 96-well plates (Greiner®, polystyrene, F-bottom, transparent, 382 μL total volume per well) as triplicates. In each case, 10 μL of the corresponding sample was presented and mixed with 150 μL of the dye solution. The plate was shaken at 20 °C for 1 min and then incubated for 5 min at the same temperature. Absorbance is measured at 660 nm using the microplate reader (CLARIOstar®) and based on the values the corresponding protein concentrations are adjusted.

Ellman's assay

The Ellman's assay was performed according to the manufacturer's instructions. All thiol detections were performed in reaction buffer: 0.1 M sodium phosphate, pH 8.0, containing 1 mM EDTA. In addition, Ellman's stock solution of 4 mg mL^{-1} Ellman's reagent and a 0.75 mM protein stock solution were prepared in reactions buffer. The assay was performed in triplicate determination using the Microplate Reader. For this procedure, 196 μL of the buffer was mixed with 20 μL of the protein stock solution followed by 4 μL of the Ellman's stock solution and incubated for 15 min. The absorbance was measured at 412 nm and the amount of accessible thiols was

 © 2024 The Author(s). Published by the Royal Society of Chemistry

Open Access Article. Published on 18 September 2024. Downloaded on 9/26/2024 12:32:12 PM. This article is licensed under a Creative Commons Attribution 3.0 Unported Licence.

determined based on a previously established calibration curve. This resulted in 54% free thiols for the native BSA, which was in agreement with previously reported data.[42,95] For CRL, a value of 95% free thiol was detected, which corresponds to one thiol per protein.

Turbidity assay

For the measurement of protein–protein clustering by specific ligand–receptor interactions in solution, absorbance spectra were measured as triplicates on a microplate reader. Specific ligand–receptor interactions in the protein–protein clusters were determined based on quantifying the turbidity of the solution. Absorbance spectra (λ = 420 nm) were measured as triplicates in lectin binding buffer (LBB, 50 mM sodium chloride, 1 mM manganese(II) chloride tetrahydrate, 1 mM calcium chloride and 10 mM HEPES dissolved in ultrapure water at a pH of 7.4). Initially, 120 μL of the native BSA and each BSA–polymer conjugate (50 μM) were provided at the beginning. Then, 40 μL of the respective lectin (5 μM, ConA and RCA_{120}) was added and the absorbance was measured after 5, 10, 20 and 40 min, respectively. Subsequently, 40 μL of the inhibitor (30 mM, αMeMan for ConA and galactose for RCA_{120}) was added and absorbance was measured after 5, 10 and 20 min, respectively. For the purposes of reference, 40 μL of LBB were added to 120 μL of native BSA (50 μM) for the competition experiment, and an additional 40 μL of LBB were added for the inhibition experiment.

Determination of the half-maximum turbidity

The half-maximal turbidity was determined from a concentration series measurement of the turbidity assay (performed in triplicates). A 5 μM solution of ConA (in LBB buffer) was prepared and the corresponding amount of ligand solution (in LBB) was added, resulting in the final concentrations to be measured: for BSA–p(ManEAA) (***3***): 0 μM, 0.125 μM, 0.25 μM, 0.5 μM, 0.75 μM, 1 μM, 1.5 μM, 2 μM, 2.5 μM, 5 μM, 10 μM, 15 μM, 20 μM and for p(ManEAA) (***S7***): 0.75 μM, 1 μM, 1.5 μM, 2 μM, 2.25 μM, 2.5 μM, 2.75 μM, 3 μM, 3.25 μM, 3.5 μM, 4 μM, 4.5 μM, 5 μM. After adding the ligand and incubating for 20 minutes, the absorbance was measured at 420 nm. The absolute values of the absorbance were corrected according to the reference (only ConA in LBB) and normalized between zero and one. Each of the triplicate measurements was individually plotted logarithmically against the concentration and fitted *via* the Hil1. The mean value and the standard deviation of the corresponding concentration at 50% absorption were determined as the value of the half-maximum turbidity.

Competition-inhibition assay on glass surface of protein–polymer conjugates

For the fluorescence images, a half-sided dip coating approach was used, in which first one half of the glass surface is dipped in the solution containing BSA or a BSA–polymer conjugate followed by coating of the entire surface with a different BSA polymer conjugate (1 mg mL^{-1} in LBB buffer). For this approach, ibidi® μ-Slide 18-Well Glass Bottom plates were used. Initially, the glass surface was pre-cleaned and activated in the Ozone Cleaner for 30 min. Then, 20 μL of the first sample was incubated on the slanted glass surface (ESI Fig. S61A†) for 30 min at 100 rpm. Afterwards the coated side was washed five times with 20 μL LBB and subsequently the entire chamber was incubated with 80 μL of a different sample for 30 min at 100 rpm in a balanced state. Afterwards, the entire chamber was washed five times with LBB and covered with 90 μL of LBB. To this solution, 10 μL of the appropriate lectin (5 μM) was added and incubated for 30 min at 100 rpm before the surface was washed five times with LBB to remove the excess lectin. For the fluorescence spectroscopy measurements, the chambers were filled with 80 μL of LBB. To perform the lectin release studies, 45 μL of LBB were mixed with 45 μL of the corresponding inhibitor polymer ***S7***, ***S8*** (15 mM) and added to the chamber. After incubation for one hour at 100 rpm the surface was washed five times with LBB.

Activity measurements of CRL–polymer conjugates

Activity measurements of CRL-based samples were performed in NaH_2PO_4 buffer (100 mM, pH 7.3) in an adapted protocol from Margesin *et al.*[83] Additionally, a 100 mM 4-nitrophenyl acetate (pNPA) stock solution was prepared in isopropanol. The different CRL–polymer conjugates as well as the native CRL were freshly prepared as 17 μM solution in NaH_2PO_4 buffer and vortexed to give a suspension.

Assay I. 1 mL of conjugates ***5***, ***6***, and ***7*** were gently heated in a water bath to 30 °C for 10 min before adding 1 μL of the pNPA stock solution and incubating at 30 °C for additional 10 min. Samples were then cooled to 0 °C in an ice bath for 10 min and centrifuged at, 2000 rpm (2 °C) for 5 min before triplicate absorbance measurements were performed for each sample.

Assay II. 133 μL of a 5 μM RCA_{120} solution in LBB was assed to 400 μL of the 17 μM conjugate solutions (***6*** and ***7***) and incubated for 20 min. Native CRL sample was supplemented with 133 μL of NaH_2PO_4 buffer instead of a lectin to obtain equal dilutions. Subsequently, all samples were heated in a water bath to 30 °C for 10 min before adding 1 μL of the pNPA stock solution and incubating for additional 10 min at 30 °C. Samples were then cooled to 0 °C in an ice bath for 10 min and centrifuged at 2000 rpm (2 °C) for 5 min before triplicate measurements were performed for each sample. Activity values represent the measured absorption maxima of the hydrolase cleavage product, *p*-nitrophenol at 400 nm. All absorption values were normalized between zero and one.

Thermal amino acid degradation

50 mg of the corresponding conjugate was dissolved in 6 M HCl, boiled for six hours at 110 °C under reflux, neutralized with NaOH and the polymer was isolated *via* dialysis (exclusion volume: 1 kDa) and freeze-dried.

Data availability

The data supporting this article have been included as part of the ESI.†

Open Access Article. Published on 18 September 2024. Downloaded on 9/26/2024 12:32:12 PM. This article is licensed under a Creative Commons Attribution 3.0 Unported Licence.

Author contributions

M. F.: investigation (lead), methodology (lead), validation, writing – original draft preparation. S. S.: investigation (supporting). L. B.: investigation (supporting). S. B.: investigation (supporting), methodology (supporting). A. B.: conceptualization (supporting). U. G.-D.: investigation, methodology (supporting), validation, supervision (equal), writing – review & editing (equal). L. H.: conceptualization (lead), funding acquisition, methodology (supporting), project administration, supervision (equal), writing – review & editing (equal).

Conflicts of interest

There are no conflicts to declare.

Acknowledgements

Thanks to the CeMSA@HHU (Center for Molecular and Structural Analytics @ Heinrich Heine University) for recording the mass-spectrometric and the NMR-spectroscopic data. We would also like to thank Christine Beuck und Peter Bayer (AG Bayer University of Duisburg-Essen, Center for Medical Biotechnology and Structural and Medical Biochemistry) for providing access to the CD spectrometer. A. B. acknowledges the US National Science Foundation (DMR-2212139) and the Air Force Office of Scientific Research (FA9550-23-1-0230) for funding.

References

1 B. S. Lele, H. Murata, K. Matyjaszewski and A. J. Russell, *Biomacromolecules*, 2005, **6**, 3380–3387.
2 C. Y. Fu, Z. G. Wang, Y. T. Gao, J. Zhao, Y. C. Liu, X. Y. Zhou, R. R. Qin, Y. Y. Pang, B. W. Hu, Y. Y. Zhang, S. P. Nan, J. R. Zhang, X. Zhang and P. Yang, *Nat. Sustain.*, 2023, **6**, 984–994.
3 T. A. Wright, R. C. Page and D. Konkolewicz, *Polym. Chem.*, 2019, **10**, 434–454.
4 Y. J. Wang and C. Wu, *Biomacromolecules*, 2018, **19**, 1804–1825.
5 R. J. Mancini, J. Lee and H. D. Maynard, *J. Am. Chem. Soc.*, 2012, **134**, 8474–8479.
6 C. Cummings, H. Murata, R. Koepsel and A. J. Russell, *Biomacromolecules*, 2014, **15**, 763–771.
7 E. P. DeBenedictis, E. Hamed and S. Keten, *ACS Nano*, 2016, **10**, 2259–2267.
8 S. L. Baker, A. Munasinghe, B. Kaupbayeva, N. R. Kang, M. Certiat, H. Murata, K. Matyjaszewski, P. Lin, C. M. Colina and A. J. Russell, *Nat. Commun.*, 2019, **10**, 4718.
9 A. Abuchowski, T. van Es, N. C. Palczuk and F. F. Davis, *J. Biol. Chem.*, 1977, **252**, 3578–3581.
10 Y. Q. Hou and H. Lu, *Bioconjugate Chem.*, 2019, **30**, 1604–1616.
11 R. Duncan, *Nat. Rev. Drug Discovery*, 2003, **2**, 347–360.
12 R. P. Welch, H. Lee, M. A. Luzuriaga, O. R. Brohlin and J. J. Gassensmith, *Bioconjugate Chem.*, 2018, **29**, 2867–2883.
13 A. Theodorou, E. Liarou, D. M. Haddleton, I. G. Stavrakaki, P. Skordalidis, R. Whitfield, A. Anastasaki and K. Velonia, *Nat. Commun.*, 2020, **11**, 1486.
14 E. M. Pelegri-O'Day, E. W. Lin and H. D. Maynard, *J. Am. Chem. Soc.*, 2014, **136**, 14323–14332.
15 X. Liu and W. Gao, *Angew Chem. Int. Ed. Engl.*, 2021, **60**, 11024–11035.
16 J. H. Ko and H. D. Maynard, *Chem. Soc. Rev.*, 2018, **47**, 8998–9014.
17 P. Zhang, F. Sun, S. J. Liu and S. Y. Jiang, *J. Controlled Release*, 2016, **244**, 184–193.
18 S. Liang, Y. Liu, X. Jin, G. Liu, J. Wen, L. L. Zhang, J. Li, X. B. Yuan, I. S. Y. Chen, W. Chen, H. Wang, L. Q. Shi, X. Y. Zhu and Y. F. Lu, *Nano Res.*, 2016, **9**, 1022–1031.
19 K. L. Heredia and H. D. Maynard, *Org. Biomol. Chem.*, 2007, **5**, 45–53.
20 Y. Wu, D. Y. Ng, S. L. Kuan and T. Weil, *Biomater. Sci.*, 2015, **3**, 214–230.
21 P. B. Lawrence and J. L. Price, *Curr. Opin. Chem. Biol.*, 2016, **34**, 88–94.
22 A. Rondon, S. Mahri, F. Morales-Yanez, M. Dumoulin and R. Vanbever, *Adv. Funct. Mater.*, 2021, **31**, 2101633.
23 J. M. Harris and R. B. Chess, *Nat. Rev. Drug Discovery*, 2003, **2**, 214–221.
24 C. Li, T. Li, X. Tian, W. An, Z. Wang, B. Han, H. Tao, J. Wang and X. Wang, *Front. Pharmacol*, 2024, **15**, 1353626.
25 M. Ahmed, P. Wattanaarsakit and R. Narain, *Eur. Polym. J.*, 2013, **49**, 3010–3033.
26 J. Sun, J. Guo, L. Zhang, L. Gong, Y. Sun, X. Deng and W. Gao, *J. Controlled Release*, 2023, **356**, 175–184.
27 Y. Cui, Z. Li, L. Wang, F. Liu, Y. Yuan, H. Wang, L. Xue, J. Pan, G. Chen and H. Chen, *J. Mater. Chem. B*, 2016, **4**, 5437–5445.
28 T. Lipinski, P. I. Kitov, A. Szpacenko, E. Paszkiewicz and D. R. Bundle, *Bioconjugate Chem.*, 2011, **22**, 274–281.
29 J. Geng, G. Mantovani, L. Tao, J. Nicolas, G. Chen, R. Wallis, D. A. Mitchell, B. R. Johnson, S. D. Evans and D. M. Haddleton, *J. Am. Chem. Soc.*, 2007, **129**, 15156–15163.
30 H. Zhang, J. Weingart, V. Gruzdys and X.-L. Sun, *ACS Macro Lett.*, 2016, **5**, 73–77.
31 Y. Miura, in *Comprehensive Glycoscience*, Elsevier, 2nd edn, 2021, pp. 250–262.
32 W. G. Zhao, F. Liu, Y. Chen, J. Bai and W. P. Gao, *Polymer*, 2015, **66**, A1–A10.
33 M. S. Messina, K. M. M. Messina, A. Bhattacharya, H. R. Montgomery and H. D. Maynard, *Prog. Polym. Sci.*, 2020, **100**, 101186.
34 Y. Miura, *J. Mater. Chem. B*, 2020, **8**, 2010–2019.
35 B. S. Sumerlin, *ACS Macro Lett.*, 2012, **1**, 141–145.
36 K. M. Mansfield and H. D. Maynard, *ACS Macro Lett.*, 2018, **7**, 324–329.
37 Q. Zhang, M. Li, C. Zhu, G. Nurumbetov, Z. Li, P. Wilson, K. Kempe and D. M. Haddleton, *J. Am. Chem. Soc.*, 2015, **137**, 9344–9353.
38 S. Averick, A. Simakova, S. Park, D. Konkolewicz, A. J. Magenau, R. A. Mehl and K. Matyjaszewski, *ACS Macro Lett.*, 2012, **1**, 6–10.

 © 2024 The Author(s). Published by the Royal Society of Chemistry

Open Access Article. Published on 18 September 2024. Downloaded on 9/26/2024 12:32:12 PM. This article is licensed under a Creative Commons Attribution 3.0 Unported Licence.

39 G. Szczepaniak, M. Łagodzińska, S. Dadashi-Silab, A. Gorczyński and K. Matyjaszewski, *Chem. Sci.*, 2020, **11**, 8809–8816.
40 R. A. Olson, J. S. Levi, G. M. Scheutz, J. J. Lessard, C. A. Figg, M. N. Kamat, K. B. Basso and B. S. Sumerlin, *Macromolecules*, 2021, **54**, 4880–4888.
41 B. S. Tucker, M. L. Coughlin, C. A. Figg and B. S. Sumerlin, *ACS Macro Lett.*, 2017, **6**, 452–457.
42 K. L. Heredia, D. Bontempo, T. Ly, J. T. Byers, S. Halstenberg and H. D. Maynard, *J. Am. Chem. Soc.*, 2005, **127**, 16955–16960.
43 W. A. Braunecker and K. Matyjaszewski, *Prog. Polym. Sci.*, 2008, **33**, 165.
44 H. Wei, J. A. Pahang and S. H. Pun, *Biomacromolecules*, 2013, **14**, 275–284.
45 B. Gerland, A. Goudot, G. Pourceau, A. Meyer, S. Vidal, E. Souteyrand, J. J. Vasseur, Y. Chevolot and F. Morvan, *J. Org. Chem.*, 2012, **77**, 7620–7626.
46 K. Matyjaszewski, *Macromolecules*, 2012, **45**, 4015–4039.
47 J. Nicolas, V. San Miguel, G. Mantovani and D. M. Haddleton, *Chem. Commun.*, 2006, 4697–4699.
48 A. Theodorou, D. Gounaris, E. Voutyritsa, N. Andrikopoulos, C. I. M. Baltzaki, A. Anastasaki and K. Velonia, *Biomacromolecules*, 2022, **23**, 4241–4253.
49 L. Barner, C. Barner-Kowollik, T. P. Davis and M. H. Stenzel, *Aust. J. Chem.*, 2004, **57**, 19–24.
50 P. De, M. Li, S. R. Gondi and B. S. Sumerlin, *J. Am. Chem. Soc.*, 2008, **130**, 11288–11289.
51 C. Boyer, V. Bulmus, J. Q. Liu, T. P. Davis, M. H. Stenzel and C. Barner-Kowollik, *J. Am. Chem. Soc.*, 2007, **129**, 7145–7154.
52 Y. Huang, X. Li, Y. C. Zhang, Z. W. Shi, L. Zeng, J. B. Xie, Y. C. Du, D. Lu, Z. G. Hu, T. Cai and Z. T. Luo, *ACS Appl. Mater. Interfaces*, 2021, **13**, 44488–44496.
53 B. R. Spears, J. Waksal, C. McQuade, L. Lanier and E. Harth, *Chem. Commun.*, 2013, **49**, 2394–2396.
54 K. Ciepluch, A. Radulescu, I. Hoffmann, A. Raba, J. Allgaier, D. Richter and R. Biehl, *Bioconjugate Chem.*, 2018, **29**, 1950–1960.
55 Y. Pang, J. Y. Liu, Y. Z. Qi, X. H. Li and A. Chilkoti, *Angew. Chem., Int. Ed.*, 2016, **55**, 10296–10300.
56 B. Kaupbayeva, S. Boye, A. Munasinghe, H. Murata, K. Matyjaszewski, A. Lederer, C. M. Colina and A. J. Russell, *Bioconjugate Chem.*, 2021, **32**, 821–832.
57 B. Kaupbayeva, H. Murata, G. S. Rule, K. Matyjaszewski and A. J. Russell, *Biomacromolecules*, 2022, **23**, 3831–3846.
58 L. Bonda, D. J. Valles, T. L. Wigger, J. Meisner, A. B. Braunschweig and L. Hartmann, *Macromolecules*, 2023, **56**, 5512–5523.
59 T. Peters, *Adv. Protein Chem.*, 1985, **37**, 161–245.
60 J. J. Zhang, S. W. Xiao, M. X. Shen, L. Sun, F. Chen, P. Fan, M. Q. Zhong and J. T. Yang, *RSC Adv.*, 2016, **6**, 21961–21968.
61 C. Zhao, Q. Chen, K. Patel, L. Y. Li, X. S. Li, Q. M. Wang, G. Zhang and J. Zheng, *Soft Matter*, 2012, **8**, 7848–7857.
62 H. X. Wu, L. Tan, Z. W. Tang, M. Y. Yang, J. Y. Xiao, C. J. Liu and R. X. Zhuo, *ACS Appl. Mater. Interfaces*, 2015, **7**, 7008–7015.
63 B. Trzebicka, R. Szweda, D. Kosowski, D. Szweda, L. Otulakowski, E. Haladjova and A. Dworak, *Prog. Polym. Sci.*, 2017, **68**, 35–76.
64 P. S. Stayton, T. Shimoboji, C. Long, A. Chilkoti, G. Chen, J. M. Harris and A. S. Hoffman, *Nature*, 1995, **378**, 472–474.
65 R. Jalababu, S. S. Veni and K. V. N. S. Reddy, *J. Drug Delivery Sci. Technol.*, 2018, **44**, 190–204.
66 I. Y. Galaev and B. Mattiasson, *Trends Biotechnol.*, 1999, **17**, 335–340.
67 Y. Miura, Y. Hoshino and H. Seto, *Chem. Rev.*, 2016, **116**, 1673–1692.
68 P. Grochulski, Y. Li, J. D. Schrag, F. Bouthillier, P. Smith, D. Harrison, B. Rubin and M. Cygler, *J. Biol. Chem.*, 1993, **268**, 12843–12847.
69 E. A. Hoyt, P. M. Cal, B. L. Oliveira and G. J. Bernardes, *Nat. Rev. Chem*, 2019, **3**, 147–171.
70 G. Hannig and S. C. Makrides, *Trends Biotechnol.*, 1998, **16**, 54–60.
71 A. Schütz, F. Bernhard, N. Berrow, J. F. Buyel, F. Ferreira-da-Silva, J. Haustraete, J. Van den Heuvel, J.-E. Hoffmann, A. De Marco and Y. Peleg, *STAR Protoc.*, 2023, **4**, 102572.
72 A. Pabbathi, S. Patra and A. Samanta, *ChemPhysChem*, 2013, **14**, 2441–2449.
73 B. Kaupbayeva, H. Murata, K. Matyjaszewski, A. J. Russell, S. Boye and A. Lederer, *Chem. Sci.*, 2021, **12**, 13848–13856.
74 W. Michael, H. Stephan, T. Anja and F. Alfred, *Anal. Chem.*, 2014, **86**(11), 5201–5210.
75 D. Bontempo, K. L. Heredia, B. A. Fish and H. D. Maynard, *J. Am. Chem. Soc.*, 2004, **126**, 15372–15373.
76 G. T. Hermanson, *Bioconjugate Techniques*, Academic Press, 2013.
77 N. J. Greenfield, *Nat. Protoc.*, 2006, **1**, 2876–2890.
78 C. M. Riccardi, K. S. Cole, K. R. Benson, J. R. Ward, K. M. Bassett, Y. Zhang, O. V. Zore, B. Stromer, R. M. Kasi and C. V. Kumar, *Bioconjugate Chem.*, 2014, **25**, 1501–1510.
79 T. Zhang, W. An, J. Sun, F. Duan, Z. Shao, F. Zhang, T. Jiang, X. Deng, C. Boyer and W. Gao, *Nano Lett.*, 2022, **22**, 8294–8303.
80 S. Benjamin and A. Pandey, *Yeast*, 1998, **14**, 1069–1087.
81 J. G. Mala and S. Takeuchi, *Anal. Chem. Insights*, 2008, **3**, 9–19.
82 E. Vanleeuw, S. Winderickx, K. Thevissen, B. Lagrain, M. Dusselier, B. P. A. Cammue and B. F. Sels, *ACS Sustainable Chem. Eng.*, 2019, **7**, 15828–15844.
83 R. Margesin, G. Feller, M. Hammerle, U. Stegner and F. Schinner, *Biotechnol. Lett.*, 2002, **24**, 27–33.
84 X. Y. Hou and Q. H. Shi, *Chin. J. Chem. Eng.*, 2023, **62**, 182–191.
85 E. Lisowska, *Cell. Mol. Life Sci.*, 2002, **59**, 445–455.
86 B. Voit and D. Appelhans, *Macromol. Chem. Phys.*, 2010, **211**, 727–735.
87 U. I. M. Gerling-Driessen, M. Hoffmann, S. Schmidt, N. L. Snyder and L. Hartmann, *Chem. Soc. Rev.*, 2023, **52**, 2617–2642.
88 C. Gerke, M. F. Ebbesen, D. Jansen, S. Boden, T. Freichel and L. Hartmann, *Biomacromolecules*, 2017, **18**, 787–796.

Open Access Article. Published on 18 September 2024. Downloaded on 9/26/2024 12:32:12 PM.
This article is licensed under a Creative Commons Attribution 3.0 Unported Licence.

89 J. E. Gestwicki, C. W. Cairo, L. E. Strong, K. A. Oetjen and L. L. Kiessling, *J. Am. Chem. Soc.*, 2002, **124**, 14922–14933.
90 D. J. Valles, Y. S. Zholdassov, J. Korpanty, S. Uddin, Y. Naeem, D. R. Mootoo, N. C. Gianneschi and A. B. Braunschweig, *Angew. Chem.*, 2021, **133**, 20513–20520.
91 W. Li, H. Wang, Z. Zhao, H. Gao, C. Liu, L. Zhu, C. Wang and Y. Yang, *Adv. Mater.*, 2019, **31**, 1805344.
92 C. Schneider, D. F. Smith, R. D. Cummings, K. F. Boligan, R. G. Hamilton, B. S. Bochner, S. Miescher, H.-U. Simon, A. Pashov and T. Vassilev, *Sci. Transl. Med.*, 2015, **7**, 269ra261.
93 C. D. Rillahan and J. C. Paulson, *Annu. Rev. Biochem.*, 2011, **80**, 797–823.
94 F. Jacobi, A. C. de la Calle, S. Boden, A. Grafmüller, L. Hartmann and S. Schmidt, *Biomacromolecules*, 2018, **19**, 3479–3488.
95 J. Janatova, J. K. Fuller and M. J. Hunter, *J. Biol. Chem.*, 1968, **243**, 3612–3622.

© 2024 The Author(s). Published by the Royal Society of Chemistry

3.2 Site-Specific Polymer-Protein-Polymer Conjugates for the Preparation of Dual Responsive Multilayer Nanoparticles

Authors:	M. I. Feldhof, S. Walber, S. Sperzel, S. Boye, U. I.M. Gerling-Driessen, L. Hartmann
Journal:	Small
Issue:	**2025**, 2500531.
Type of Paper:	Research Article
Impact Factor:	13 (2023)
DOI:	10.1002/smll.202500531

First author contribution:

Collaborative project development. Synthesis and characterization (^{1}H-NMR, ^{13}C-NMR, SDS-PAGE, Ellman's Assay, CD, DLS) of the rebridging-agent and bifunctionalized polymer-protein-polymer conjugates. Conducting all core-multi-shell hybrid nanocluster experiments including the corresponding binding studies. Conducting fluorescence microscopy and SEM measurements. Collaborative writing of the manuscript.

Reprinted with permission from Small.

Copyright © 2025 Small.

Check for updates

RESEARCH ARTICLE

NANO · MICRO small
www.small-journal.com

Site-Specific Polymer-Protein-Polymer Conjugates for the Preparation of Dual Responsive Multilayer Nanoparticles

*Melina I. Feldhof, Simon Walber, Sandro Sperzel, Susanne Boye, Ulla I.M. Gerling-Driessen, and Laura Hartmann**

Protein-polymer-based materials demonstrate high potential in advanced applications. However, controlled combinations of multiple proteins and polymers to obtain multimaterial systems is limited due to the complexity of retaining protein structure and function and achieving high structural control for the polymers simultaneously. Here, the first combination of a rebridging agent and thiol-induced, light-activated controlled radical polymerization (TIRP) is introduced to directly enable site-specific conjugation of two different polymers to native proteins. Specifically, poly(*N*-isopropyacrylamide) (pNIPAM) is attached to bovine serum albumin (BSA), followed by incorporation of a new rebridging agent, and initiating a second TIRP to introduce a glycopolymer, giving highly defined pNIPAM-BSA-glycopolymer conjugates. Above the lower critical solution temperature (LCST), nanoparticles with a glycopolymer corona are formed. The addition of a glycan-specific lectin leads to the formation of a second protein corona and so-called multilayer nanoparticles. Depending on the sequence of stimuli, the particles can either undergo a step-wise or one-step disassembly. Furthermore, by controlling the ratio of binding/non-binding glycopolymers in the multilayer nanoparticles, either distinct nanoparticles or large clusters can be formed. Thus, dual-responsive multilayered polymer-protein nanoparticles are now accessible with controlled and programmable material properties such as assembly and disassembly while maintaining the protein's native structure and thus function.

1. Introduction

Recently, proteins have gained increasing interest for the use in material applications as biobased alternative to fuel-based polymeric materials.[1] In order to optimize properties and obtain materials with specific functions, proteins are either enhanced, e.g., through biological engineering or through chemical modifications to optimize properties beyond the original protein itself.[2] Protein-polymer conjugates are a well-established class of such modified proteins and are widely recognized for their relevance in various applications, from medical applications of protein drugs to the use of enzymes in biocatalysis.[3] Proteins alone would often be insufficiently stable, e.g., for prolonged circulation times in vivo or under non-aqueous conditions for catalysis;[3c,4] whilst polymers alone do not provide the advanced functionality of proteins. It is the combination of both, polymer and protein, that enables the desired properties and functions.[3i,5] However, in order to achieve such synergism, proteins and polymers have to be linked in a way that does not affect the protein structure and allows high control over the polymer, e.g., in terms of dispersity, chain length and site-selective attachment to the protein.[3b] Controlled design of protein-polymer conjugates then allows to derive materials with advanced properties as is demonstrated in this study for the preparation of multilayer protein-polymer nanoparticles from the stimuli-responsive self-assembly of highly controlled polymer-protein conjugates.

Nanoparticles are defined as colloidal structures in nanometer range (1–1000 nm in diameter) that can be generated, e.g., through emulsification, thermal structuring, hydrophobic interactions, and nanoprecipitation.[4a,6] Nanoparticles composed exclusively of proteins exhibit inherent biocompatibility and biodegradability, which reduces the potential for toxicity and adverse immune responses.[6b,7] However, these nanoparticles exhibit notable stability limitations, which can be enhanced by incorporating polymers.[7] Site-selective polymer-protein conjugation with, e.g., thermal- or pH-responsive polymers are well known for the stimuli-responsive self-assembly of protein-based nanoparticles.[8] For instance, poly(*N*-isopropyl acrylamide) (pNIPAM) conjugated proteins self-assemble into nanoparticles

M. I. Feldhof, S. Sperzel
Department of Organic and Macromolecular Chemistry
Heinrich-Heine-University Düsseldorf
Universitätsstraße 1, 40225 Düsseldorf, Germany
S. Walber, U. I. Gerling-Driessen, L. Hartmann
Institute for Macromolecular Chemistry
University of Freiburg
Stefan-Meier-Str. 31, D-79104 Freiburg i.Br., Germany
E-mail: laura.hartmann@makro.uni-freiburg.de
S. Boye
Advanced Macromolecular Structure Analysis
Leibniz-Institut für Polymerforschung Dresden
Hohe Str. 6, 01069 Dresden, Germany

The ORCID identification number(s) for the author(s) of this article can be found under https://doi.org/10.1002/smll.202500531

© 2025 The Author(s). Small published by Wiley-VCH GmbH. This is an open access article under the terms of the Creative Commons Attribution License, which permits use, distribution and reproduction in any medium, provided the original work is properly cited.

DOI: 10.1002/smll.202500531

below their lower critical solution temperature (LCST),[9] while poly(2-(diisopropylamino)ethyl methacrylate) conjugated proteins form pH-responsive nanoparticles,[8b] both featuring a hydrophobic core and a hydrophilic protein shell. Although polymer-protein conjugates demonstrate significantly improved stability, they also exhibit limitations in terms of potential loss of protein functionality and complexity of synthesis.[10]

Typically, the synthesis of protein-polymer conjugates involves controlled polymerization methods, such as atom transfer radical polymerization (ATRP)[3g,11] or reversible addition–fragmentation chain-transfer (RAFT)[3a,12] performing either a grafting-to or grafting-from synthesis.[13] However, challenges in controlled polymerizations include potential protein denaturation and inactivation due to chemical conditions such as organic solvents or high temperatures.[14] More recent advances introduced the use of aqueous[3f,15] or light-activated polymerizations[16] and particularly the combination of both, recently introduced by Haddleton[15b] and Velonia and Anastasaki,[3f] which minimizes potential damage to the protein structure and thus preserves bioactivity. In our own work, we have recently introduced a new synthetic methodology to give straightforward access to site-specific conjugation of polymers to native proteins and enzymes without any prior protein modifications and maintaining the protein's native structure, stability and activity by using thiol-induced, light-activated controlled radical polymerization (TIRP).[17]

However, so far, this method only allowed for polymer conjugation on native proteins presenting a free thiol side chain and introducing the same polymer at all available positions. Here, we now present a new strategy that gives straightforward access to highly controlled, multifunctional protein-polymer conjugates presenting site-selectively two different polymers on one protein. To do so, we combine TIRP and so-called rebridging agents,[18] now allowing also disulfide groups in the protein structure to be accessed for TIRP. Rebridging agents, e.g., based on bissulfones,[19] disubstituted maleimides like bromomaleimides,[18c] arsenous acids,[20] dibromopyridazinediones,[21] alkynes,[22] allyl sulfones,[23] or diethynyl phosphonites[24] are well-established for introduction of functional handles into the disulfide bond of native proteins thereby retaining the protein structure and function.[25] For this study, we developed a new rebridging agent, based on a symmetrical dibromomaleimides, allowing us to introduce an additional free thiol residue without compromising the original disulfide bond. The symmetrical design ensures that after intramolecular disulfide reduction of the rebridging agent, both fragments are chemically identical, even if potentially the rebridging agent would react by bridging two proteins in the first insertion step. In short, the protein – here bovine serum albumin (BSA) is first site-selectively functionalized with one type of polymer at the free cysteine residue (Cys'34) using TIRP.[17] Next, exactly one of the intramolecular disulfide bridges of the protein is opened by reduction and the rebridging agent is introduced. However, at this time, we do not know which one of the disulfide bonds is accessed as this would require more complex protein analysis. This newly introduced thiol is then used in a second TIRP introducing a second type of polymer. Thus, to the best of our knowledge, we present for the first time the preparation of polymer-protein-polymer conjugates where two different polymers are site-selectively, covalently attached to a protein. We demonstrate the variability of this approach by introducing two different functional polymers at two selected positions in the protein structure – pNIPAM for temperature-induced nanoparticle formation and glycopolymers for ligand-induced formation of a lectin corona – and how this enables the formation of dual responsive multilayer nanoparticles (**Figure 1**). We can also demonstrate, that the lectin corona protects the nanoparticles against temperature-induced disassembly and only in the presence of high affinity competing ligands, nanoparticles disassemble back into single polymer-protein conjugates. This dual responsive formation of multilayer nanoparticles opens new opportunities in the development of functional, protein-based materials, e.g., for biomedical applications such as drug delivery, or the use of enzymes as advanced biocatalysts.

2. Results and Discussion

2.1. Synthesis of Protein-Polymer and Polymer-Protein-Polymer Conjugates

As protein for polymer functionalization, we chose well-studied BSA as it is extensively used for various applications.[26] We first synthesized BSA-pNIPAM conjugates with different polymer length (**1–3**) and BSA-p(*N*-hydroxyethyl acrylamide) (BSA-pHEAA) (**4**) using TIRP on native BSA, see **Figure 2A**.[17] Protein-polymer conjugates were analyzed by ^{1}H-NMR spectroscopy, asymmetric flow field flow fractionation with light scattering detection (AF4-LS), circular dichroism (CD), sodium dodecyl sulfate-polyacrylamide gel electrophoresis (SDS-PAGE), infrared (IR) spectroscopy and dynamic light scattering (DLS) (see Supporting Information). As previously demonstrated,[17] also for these conjugates polymer conjugation does not affect the protein structure and stability. To introduce a second, different polymer chain at another position in the protein, we developed a new type of rebridging agent that allows us to introduce another free thiol into the protein. We chose the rebridging process, as this has been shown to preserve the 3D structure of the protein and thereby also the protein's function.[18a] Rebridging agents, e.g., based on bissulfones,[19] disubstituted maleimides like bromomaleimides,[18c] arsenous acids,[20] dibromopyridazinediones,[21] alkynes,[22] or allyl sulfones[23] are well-established for introduction into a disulfide bond of native proteins thereby retaining the protein structure and function but also introducing an orthogonal functional group for selective conjugation to the protein.[25] Here we developed a new rebridging agent allowing us to introduce an additional free thiol residue without compromising the original disulfide bond. Notably, disulfide bonds are integral to the structural integrity and 3D conformation of proteins, thus a simple reductive opening of the disulfide to achieve a free thiol would likely result in a destabilization of the protein structure and thus loss of function.

The new rebridging agent was obtained by reacting cystamine with bromoacetyl bromide in aqueous sodium hydroxide solution to obtain intermediate structure **5** and subsequent reaction with 2,3-dibromomaleimide to final rebridging agent **6** (Figure 2B, see Supporting Information for analytical data and further information on the synthesis). The symmetrical design of the rebridging agent is intended to prevent the formation of two products during

© 2025 The Author(s). Small published by Wiley-VCH GmbH

16136829, 0, Downloaded from https://onlinelibrary.wiley.com/doi/10.1002/smll.202500531 by Universitäts- Und Landesbibliothek Düsseldorf, Wiley Online Library on [10/03/2025]. See the Terms and Conditions (https://onlinelibrary.wiley.com/terms-and-conditions) on Wiley Online Library for rules of use; OA articles are governed by the applicable Creative Commons License

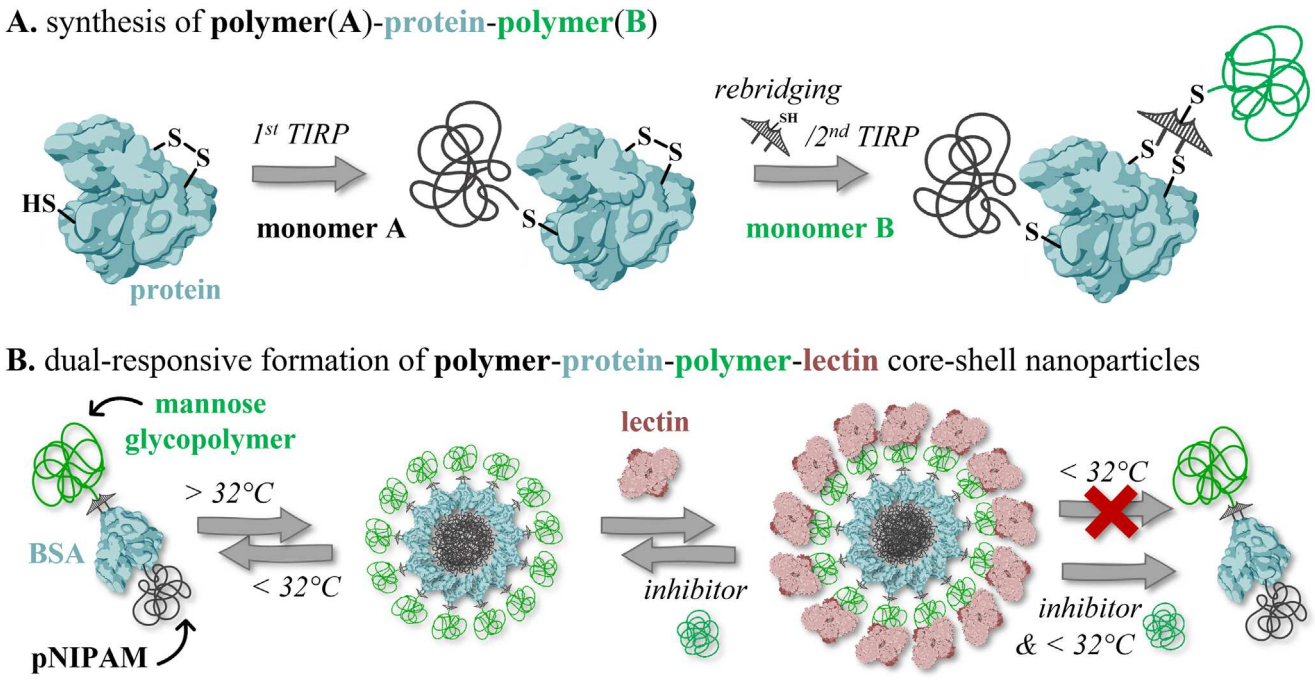


Figure 1. A) Schematic representation of the synthesis of polymer(pNIPAM)-protein-polymer via 1st TRIP followed by first 2nd TIRP introduced by the rebridging agent. B) Schematic representation of dual responsive formation of multilayer (core-shell) nanoparticles. Potentially, particles have a separated or mixed BSA-pNIPAM core above the LCST. In this schematic drawing this is, however, depicted as a core-shell structure only for simplicity reasons. At this time, we have no experimental evidence to proof which type of core (core-shell or mixed) is formed. This type of schematic drawing is used throughout the manuscript.

conjugation, thereby enabling the uniform modification of the proteins. Dibromomaleimide was chosen as the reactive group as it forms irreversible linkages, making retro-Michael deconjugation highly unlikely and persists even after hydrolysis, ensuring the stability of the rebridged protein during further application and analysis.[27]

Introduction of the rebridging agent into the BSA-pNIPAM conjugate **1** and BSA-pHEAA conjugate **4** was achieved following a protocol by Heredia et al.[28] which allows for the reduction of only one of the native disulfide bonds of BSA by using 10 equivalents of tris(2-carboxyethyl)phosphine (TCEP) as reducing reagent, as is also confirmed by an Ellman's Assay (see Supporting Information for further information). After removal of the reducing agent, the rebridging agent (**6**) was added. Successful conjugation was monitored by ultraviolet–visible (UV/Vis) spectrophotometry and fluorescence measurements (Supporting Information), as the formed rebridged protein is UV active with an intrinsic fluorescence, as exemplified by O'Reilly et al.[29] Next, to release the free thiol required for TIRP, 10 eq. TCEP as reducing agent was added again, and removed again through dialysis, the second polymerization was performed using TIRP at previously developed reaction conditions. As monomers, acrylate-modified mannose (**S1**), and acrylate-modified galactose (**S2**) was used to modify the BSA-pNIPAM precursor (**1**) and NIPAM were

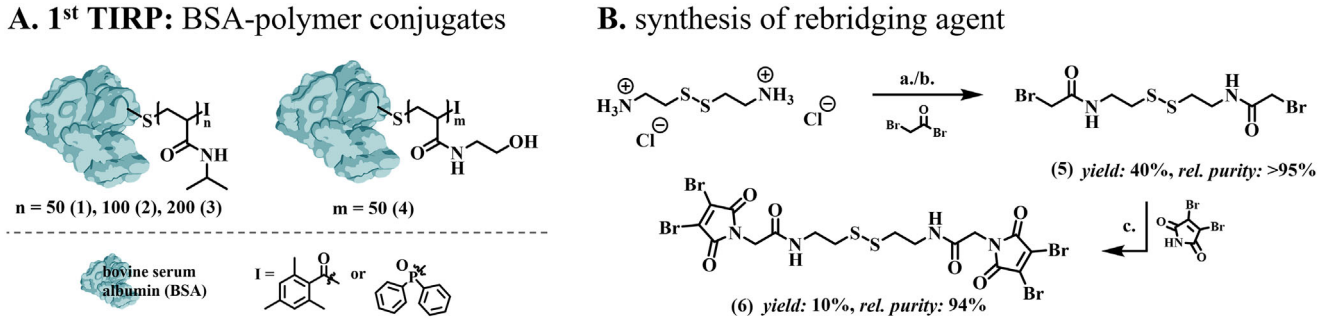
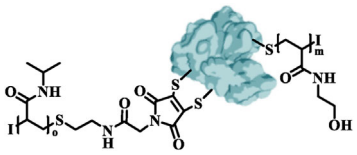
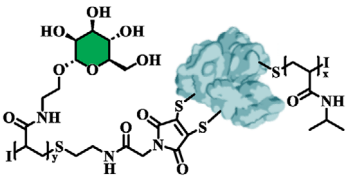
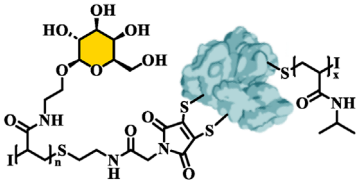


Figure 2. A) Presentation of the TIRP-based synthesized BSA-pNIPAM conjugates (**1**–**3**) and BSA-pHEAA conjugate (**4**). B) Synthesis of the rebridging agent (**6**) for conjugation to BSA-polymer precursor **1** and **4** to produce defined bifunctionalized, protein-polymer conjugates. The yields and relative purities are presented as percentages. The relative purity was determined using LC-MS. Reaction conditions: **a**. NaOH, H_2O, 15 min, RT, **b**. $CDCl_3$, 2 h, RT, **c**. K_2CO_3, THF, N_2, 2 h, RT.

© 2025 The Author(s). Small published by Wiley-VCH GmbH

16136829, 0, Downloaded from https://onlinelibrary.wiley.com/doi/10.1002/smll.202500531 by Universitäts- Und Landesbibliothek Düsseldorf, Wiley Online Library on [10/03/2025]. See the Terms and Conditions (https://onlinelibrary.wiley.com/terms-and-conditions) on Wiley Online Library for rules of use; OA articles are governed by the applicable Creative Commons License

Table 1. Presentation of the defined biofunctionalized BSA-polymer conjugates synthesized via rebridging in combination with TIRP: non-functional system (**7**) and two glycopolymer conjugates bases a mannose (**8**) and galactose (**9**). Visualization of potential hydrolysis of the conjugated rebridging agent.[27b]

Sample Labeling	Structure	1st Polymer	2nd Polymer
pHEAA-BSA-pNIPAM (**7**)		pHEAA	pNIPAM
pNIPAM-BSA-pMan (**8**)		pNIPAM	pMan
pNIPAM-BSA-pGal (**9**)		pNIPAM	pGal

used to modify the BSA-pHEAA (**4**) precursor. After polymerization, all protein-polymer (**7–9**) conjugates were purified via dialysis (**Table 1**).

Successful polymerization and formation of polymer-protein-polymer conjugates were confirmed by proton nuclear magnetic resonance (^{1}H-NMR), AF4-LS, and CD spectroscopy (see Supporting Information for further information). AF4-LS[30] was found to be effective in gently separating the different BSA populations (monomeric BSA, BSA dimer, and trimer/multimer), and corresponding BSA–polymer conjugate.[17] By analyzing the structures presented here, the analysis simplifies its approach by concentrating on the molar masses of the monomeric population while similar trends are observed in the dimer fractions (see Supporting Information for further information). AF4-LS measurements confirmed that the protein–polymer conjugates (**7–9**) with two different polymers obtained higher molar masses in comparison to the initial BSA-polymer conjugate (**1** or **4**) **Figure 3A**.

We confirmed by CD measurements that also after rebridging and second polymerization the conformation of the protein was retained, see Figure 3B (see also Supporting Information).

2.2. Nanoparticle Formation from Defined Polymer-Protein-Polymer Conjugates

Based on the different types of polymers we introduced into to protein-polymer and polymer-protein-polymer conjugates, we can now use two different stimuli to induce the formation of aggregates. On the one hand, temperature induced aggregation

A. asymmetric flow filed-flow fractionation with light scattering detection

	1st polymer (precursor)	2nd polymer	Mn$^{theor.}$ [kDa]	Mn$^{measur.}$ [kDa]*	Man/Gal content
(**1**)	NIPAM	-	72.2	70.5	-
(**4**)	HEAA	-	72.3	66.1	-
(**7**)	HEAA	NIPAM	69.0	69.0	-
(**8**)	NIPAM	Man	77.4	73.4	11
(**9**)	NIPAM	Gal	77.4	74.8	16

* determined via AF4-LS

B. circular dichroism

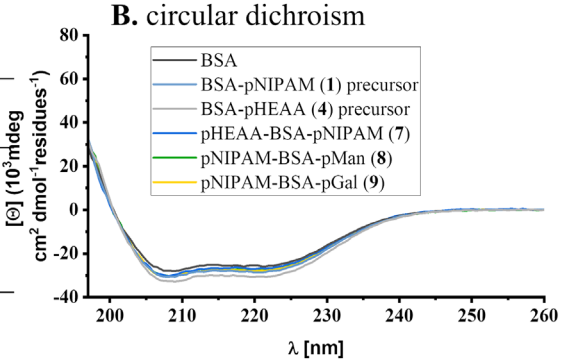


Figure 3. A) Analytical data for molar masses of monomeric BSA population of protein–polymer conjugates **1**, **4**, **7–9** via AF4-LS in PBS buffer (pH 7.4 at 25 °C). The theoretical molecular weights were determined based on the measured AF-4 data of the precursors, taking into account the intended polymer length. B) Presentation of CD spectra of BSA, BSA–polymer precursor **1**, **4**, and bifunctionalized rebridged structures **7–9** for investigation of structural properties. The measurements were performed in PBS buffer (pH 7.4, at 20 °C) with an exact concentration of 251 µg mL^{-1} adjusted by the Pierce-Protein-Assay.

© 2025 The Author(s). Small published by Wiley-VCH GmbH

16136829, 0, Downloaded from https://onlinelibrary.wiley.com/doi/10.1002/smll.202500531 by Universitäts- Und Landesbibliothek Düsseldorf, Wiley Online Library on [10/03/2025]. See the Terms and Conditions (https://onlinelibrary.wiley.com/terms-and-conditions) on Wiley Online Library for rules of use; OA articles are governed by the applicable Creative Commons License

Table 2. Summary of all data determined via DLS of the synthesized conjugates **1**–**4** (c = 0.5 mg mL^{-1}) and native BSA. The corresponding DLS runs are shown in the Supporting Information.

Structure	Mn [kDa][a]	< LCST [20 °C]		temp.Ramp [min]	> LCST [44 °C]		LCST[d] [°C]
		D_h[nm][b]	PdI[b]		D_h[nm][c]	PdI[c]	
(**1**)	50	10.6 ± 0.3	0.35 ± 0.02	2	130 ± 0.3	0.10 ± 0.01	35.5
				10	136 ± 0.9	0.14 ± 0.01	35.2
				20	189 ± 0.4	0.19 ± 0.01	33.6
(**2**)	100	16.1 ± 0.39	0.56 ± 0.01	2	130 ± 0.7	0.05 ± 0.02	35.0
				10	165 ± 0.9	0.04 ± 0.02	33.6
				20	363 ± 0.2	0.13 ± 0.02	33.3
(**3**)	200	17.2 ± 0.61	0.48 ± 0.01	0	156 ± 0.1	0.04 ± 0.01	35.8
				2	158 ± 0.9	0.06 ± 0.01	34.9
				10	186 ± 0.8	0.11 ± 0.01	33.7
				20	260 ± 0.1	0.16 ± 0.01	32.4
(**4**)	50	10.7 ± 0.19	0.35 ± 0.01	2	14.8 ± 1.	0.23 ± 0.15	–
				10	12.9 ± 1.8	0.23 ± 0.06	–
				20	13.1 ± 0.1	0.20± 0.07	–
BSA native	66.5	8.2 ± 0.32	0.17 ± 0.04	2	8.44 ± 0.1	0.23 ± 0.01	–
				10	9.34 ± 0.2	0.26 ± 0.02	–
				20	9.30 ± 0.0	0.26 ± 0.00	–

[a] determined via AF4/SEC measurements; [b] determined via DLS ninefold measurements; [c] determined via DLS triplicate measurements; [d] LCST calculation via Hill 1 Fit.

from the LCST behavior of the pNIPAM chains is possible. On the other hand, recognition and binding of glycopolymers by a lectin (carbohydrate-recognizing protein) leads to the formation of glycopolymer-protein complexes.[17]

First, we studied the temperature dependent cluster formation of the BSA-pNIPAM precursors **1**–**3** with varying chain length of the pNIPAM (50, 100, or 200 repeating units). The temperature-induced aggregation and nanoparticle formation was investigated using DLS in phosphate buffered system (pH 7.4). As expected, all protein-polymer conjugates show higher hydrodynamic diameter (D_h) than the native BSA. We observe no aggregation based on LCST for native BSA or BSA-pHEAA (**4**) (further information in SI). For all BSA-pNIPAM conjugates, temperature-dependent cluster formation is clearly observed. The formed clusters have very low dispersities (PdI = 0.03–0.25) and can be completely restored to their initial non-aggregated state by lowering the temperature again below the LCST (**Table 2**).

LCST of the conjugates is in the range of 32.4–35.8 °C and thus close to the LCST of free pNIPAM chains[31] and comparable protein-pNIPAM conjugate systems in the literature.[32] Size of the nanoparticles can be tuned in the range from 130 to 363 nm by varying the molar mass of the pNIPAM, the heating ramp, and the weight concentration of the conjugates in solution (see **Figure 4**).

Next, we investigated the temperature-induced clustering of the polymer-protein-polymer conjugates (**8**,**9**). The revealed hydrodynamic diameters for pMan-BSA-pNIPAM conjugate **8** and pGal-BSA-pNIPAM conjugate **9** show hydrodynamic diameters below LCST (20 °C) of 62 and 71 nm, respectively. This substantial increase in hydrodynamic diameter in comparison to the BSA-pNIPAM precursor with 10.6 nm is attributed to the hydrate shell of the glycopolymer and supports the successful formation of a polymer-protein-polymer conjugate. Furthermore, conjugates **8** and **9** exhibit lower critical solution temperatures at 34.3 °C and 34.8 °C, respectively, compared to BSA-pNIPAM **1** at 35.5 °C. Studies on other materials combining pNIPAM and carbohydrates have shown that increased hydrophilicity by incorporating carbohydrates in pNIPAM conjugates can lead to a decrease in the LCST, which is potentially attributed to faster elimination of the pNIPAM hydration layer due to the H-bonds of the carbohydrates.[33] We observe this effect in our systems, attributed to the presence of hydrophilic glycopolymers in the protein-polymer-protein conjugates. We hypothesize that in the polymer-protein-polymer cluster above LCST, the nanoparticles have a glycopolymer corona while the pNIPAM and BSA form the core of the clusters – potentially also as core-shell or a mixed core structure. Presentation of the glycopolymers on the outside of the clusters should thus also allow us to add a second protein – a carbohydrate recognizing lectin – that can now bind to the nanoparticles forming another layer or shell.

To study this, we utilized the model lectin Concanavalin A (Con A) which is well characterized for its specific binding to mannose ligands such as in the Man-presenting glycopolymers of conjugate **8**. We start with the pMan-BSA-pNIPAM (**8**) conjugate below the LCST at 28 °C (LBB buffer, pH 7.4) showing an initial hydrodynamic diameter of 69 nm. This size can likely not only be attributed to carbohydrate-induced hydration but may also be affected by the formation of pre-assembled structures driven by hydrogen bonding. Above the LCST (38 °C, 2 min ramp) nanoparticles with hydrodynamic diameters of 196 nm are formed, presenting glycopolymer chains with an average of 11 mannose side

© 2025 The Author(s). Small published by Wiley-VCH GmbH

16136829, 0, Downloaded from https://onlinelibrary.wiley.com/doi/10.1002/smll.202500531 by Universitäts- Und Landesbibliothek Düsseldorf, Wiley Online Library on [10/03/2025]. See the Terms and Conditions (https://onlinelibrary.wiley.com/terms-and-conditions) on Wiley Online Library for rules of use; OA articles are governed by the applicable Creative Commons License

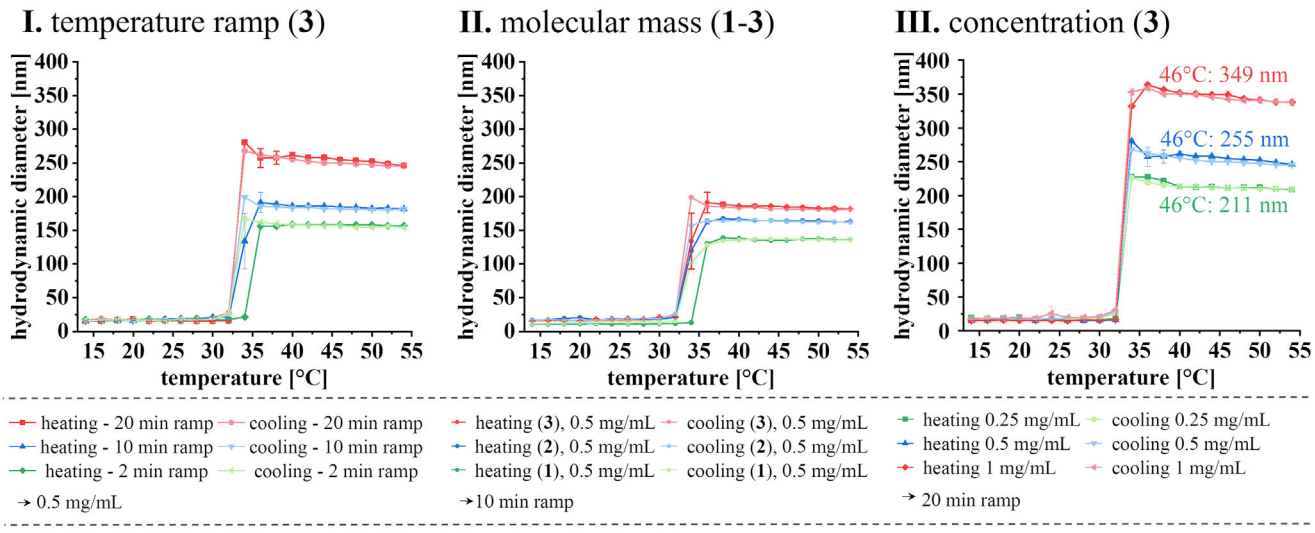


Figure 4. Comparison of the DLS measurement results with respect to the **I**: molar mass (**1**–**3**), **II**: temperature ramp effect (1–3), **III**: concentration (**3**) of the conjugates: BSA-pNIPAM (**1**), BSA-pNIPAM (**2**), BSA-pNIPAM (**3**) in PBS buffer (pH 7.4).

chains per polymer chain (degree of polymerization). Then we added ConA in LBB buffer pH 7.4 and observed a further increase in size of the nanoparticle to now 52 nm. ConA alone has a hydrodynamic diameter of ≈8.8 nm,[34] thus in the formed nanoparticles roughly three ConA molecules have attached in the formation of the lectin corona in height.

This Man to ConA ratio aligns with previous studies from Haddleton et al.[35] examining the number of ConA (7 units) binding sites on mannose-based glycopolymers (23 mannose units) with an acrylate backbone under identical measurement conditions. Consequently, the data obtained for the three ConA units on the corona indicates a near-maximum loading of the cluster. The formation of nanoparticles was further validated by fluorescence microscopy using fluorescently labeled ConA (Figure 6B). When adding ConA to conjugate **8** below the LCST (28 °C) and only then increasing the temperature above the LCST, similarly sized nanoparticles are formed. This nicely demonstrates that nanoparticle formation is controlled by the design of the polymer-protein-polymer conjugates rather than cluster formation conditions. To confirm that formation of conjugate-lectin clusters is based on specific interactions, inhibition experiments through addition of free pMan were performed. A decrease in size back to D_h of 191 nm was observed, which corresponds to the size of the cluster without ConA above LCST and thus confirms the complete removal of the lectin from the cluster. Specificity is also demonstrated from the negative control experiment using pGal-BSA-pNIPAM conjugate (**9**) as ConA does not bind to galactose. Indeed, here no increase in nanoparticle size is observed upon addition of ConA. Overall, we can show that through the conjugation of two distinct polymers to BSA, we can achieve dual-responsive aggregation behavior and form-controlled polymer-protein nanoparticles.

Finally, we investigated whether – similar to the stepwise formation of the nanoparticles from the two distinct assembly stimuli – we can also disassemble the nanoparticles in a controlled manner. Such reversible, stimuli-responsive aggregation and nanoparticle formation has great relevance for the potential future applications of these materials, e.g., for drug encapsulation and release. As control experiment, we already showed that addition of excess of free pMan leads to selective disassembly of the lectin corona. As expected, when reducing the temperature below the LCST, the nanoparticle disassembles completely back into the non-aggregated polymer-protein-polymer conjugates. Interestingly, when starting again from the multi-shell nanoparticles with lectin corona and first reducing the temperature below the LCST, no change in the hydrodynamic diameter of the nanoparticles is observed (**Figure 5BII**). Thus, the lectin corona stabilizes the clusters against disassembly. Stabilized nanoparticles can also be visualized and confirmed by fluorescence microscopy using fluorescently labeled Alexa^{647}-ConA as well as by SEM (see **Figure 6C,D**), with the nanoparticle being stable for several days (see Supporting Information).

Only when we add pMan as inhibitor, do we observe disassembly, now immediately into the free polymer-protein-polymer conjugates. Thus, depending on the sequence of the applied stimuli (temperature, glycan inhibitor) we can control the disassembling process either in a stepwise fashion or in a spontaneous complete disassembly back into the free conjugates.

To confirm this finding, we also performed microscopy studies using fluorescently labeled Alexa^{647}-ConA and scanning electron microscope (SEM) images, see Figure 6.

2.3. Binding and Non-Binding Carbohydrate Mixed Multi-Shell Hybrid Nanoparticle

This study has demonstrated the capability to generate and stimuli-control highly defined multi-shell nanoparticles from polymer-protein-polymer conjugates made accessible through TIRP in combination with a new rebridging agent. Specifically, we used pNIPAM to induce temperature-dependent nanoparticle formation, followed by using the glycopolymers in the corona of the nanoparticle presenting either mannose- or galactose to specifically bind lectins and thereby add a second protein shell

© 2025 The Author(s). Small published by Wiley-VCH GmbH

16136829, 0, Downloaded from https://onlinelibrary.wiley.com/doi/10.1002/smll.202500531 by Universitäts- Und Landesbibliothek Düsseldorf, Wiley Online Library on [10/03/2025]. See the Terms and Conditions (https://onlinelibrary.wiley.com/terms-and-conditions) on Wiley Online Library for rules of use; OA articles are governed by the applicable Creative Commons License

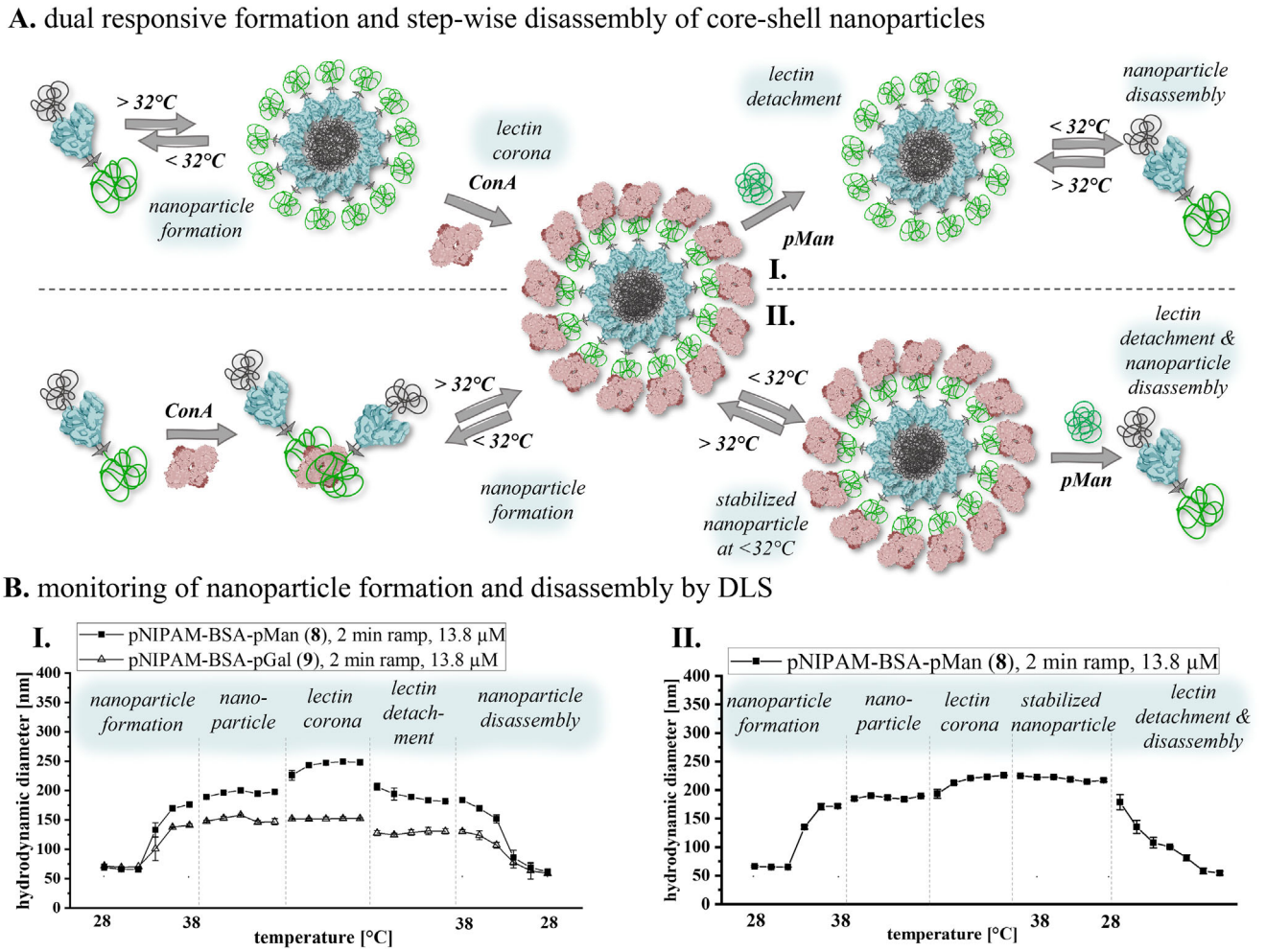


Figure 5. A) Schematic demonstration of two ways for thermally switchable core-multi-shell hybrid nanoparticle formation with presentation of hydrophilic carbohydrate polymers on the surface for specific binding to the lectin ConA. In addition, the schematic disassembly of the lectin corona above the LCST followed by the thermal disassembly of the cluster or the nanoparticle stabilized by the lectin below the LCST. B) **I**. Comparison of DLS measurements of mannose- and galactose-based bivalent systems. Formation of the defined cluster owing to the thermosensitive polymer conjugate. Thereupon, the formation of a specific interaction with ConA, exclusively the mannose-based cluster, and the associated increasing hydrodynamic diameter. The galactose-based cluster did not interact with lectin. Thereafter, detachment with the pMan polymer (**S3**) and decreasing D_h before the defined cluster is dissolved again by lowering the temperature. **II**. The difference from set-up I is that after the addition of ConA, the temperature is first lowered (< LCST) and the cluster can thus be fixed. Only then is the inhibitor added, and the entire cluster is dissolved.

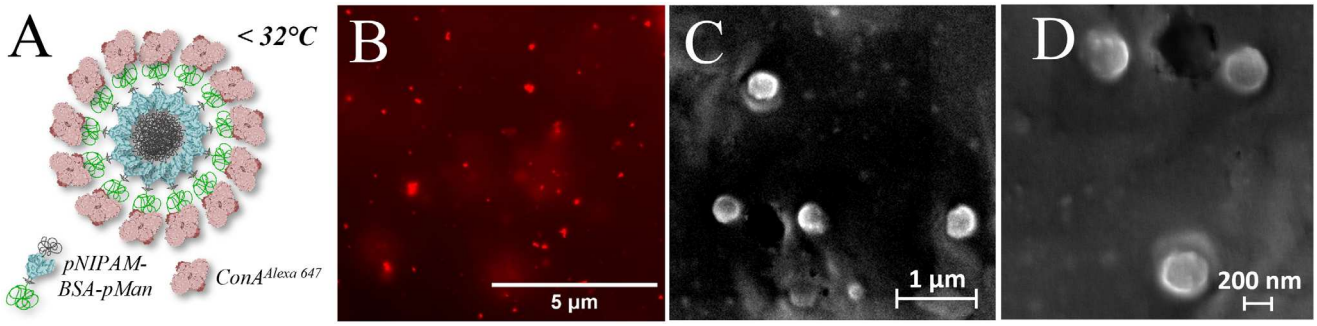


Figure 6. A) Schematic demonstration of the investigated state over fluorescence microscopy and SEM. B) Fluorescence image of the pNIPAM-BSA-pMan (**8**) below the LCST with addition of the lecin ConA$^{Alexa\ 647}$ Fluorescence image (excitation: 641 nm, emission: 690 nm). C./D. SEM images of pNIPAM-BSA-pMan (**8**) fixed via ConA as nanoparticles in LBB below the LCST with concentrations at 0.46 µM.

© 2025 The Author(s). Small published by Wiley-VCH GmbH

16136829, 0, Downloaded from https://onlinelibrary.wiley.com/doi/10.1002/smll.202500531 by Universitäts- Und Landesbibliothek Düsseldorf, Wiley Online Library on [10/03/2025]. See the Terms and Conditions (https://onlinelibrary.wiley.com/terms-and-conditions) on Wiley Online Library for rules of use; OA articles are governed by the applicable Creative Commons License

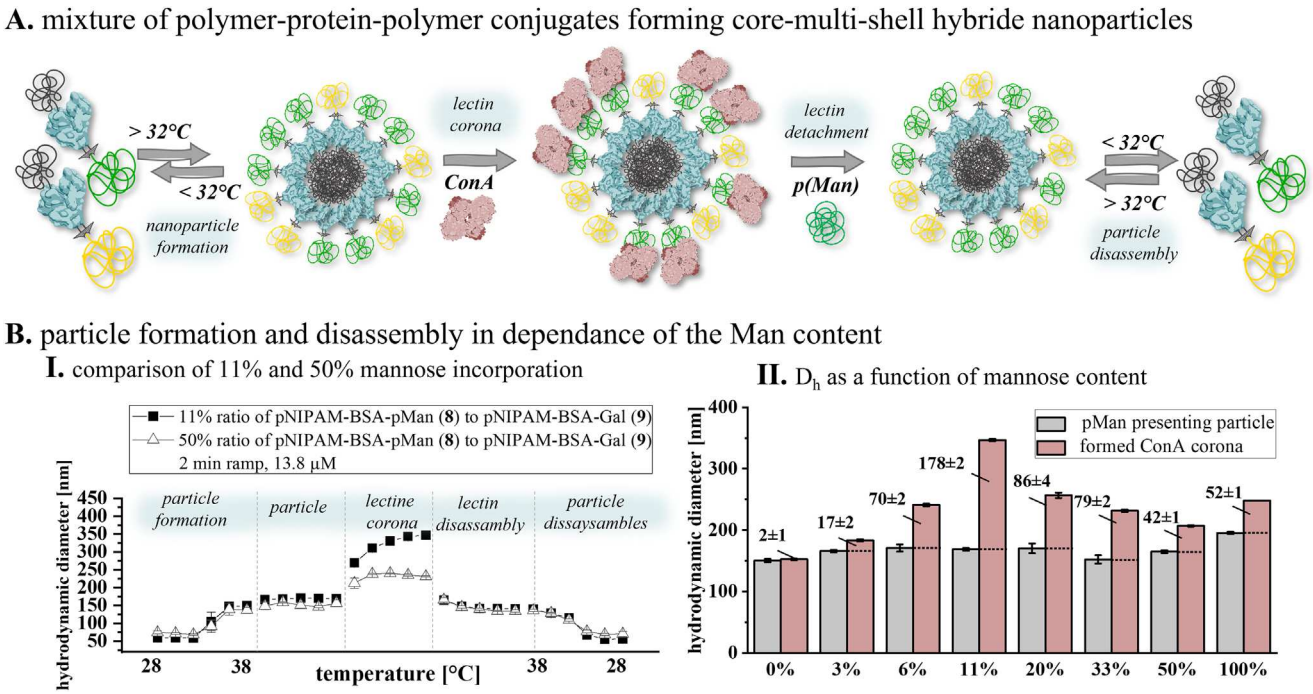


Figure 7. A) Schematic demonstration of core-multi-shell hybrid nanoparticle formation out of a mixture of mannose (**8** – binding ligand) or galactose (**9** – non-binding ligand) bifunctionalized protein-polymer conjugates. B) **I**. Comparison of DLS curves between 11% and 50% mannose (**8**) ratio in comparison to galactose (**9**) (LBB buffer, 13.8 µM, 2 min ramp). **II**. Plot of hydrodynamic diameter bevor and after ConA adding and the corresponding increase in D_h at different mannose to galactose ratios. All experimental data are available in detail in the SI, including cluster formation and inhibition of lectin.

to the nanoparticles. Since both types of conjugates, mannose- or galactose-presenting nanoparticles, are derived from the same BSA-pNIPAM precursor, it is now also feasible to combine these two conjugates while maintaining controlled nanoparticle formation. One of the key binding mechanisms of carbohydrate-lectin interactions is multivalent binding. Single carbohydrate interactions are typically weak (in the µM to mM) range.[36] Nature uses the multivalent presentation of such low affinity carbohydrates, e.g., in glycoprotein conjugates to ensure high avidity and high selectivity binding.[36c,37] However, an increase in binding through multivalent interactions is not achieved through a simple "the more the better" principle. Rather it is well understood, that the combination of binding and non-binding carbohydrates in both, natural and mimetic glycoconjugates plays a key role in maximizing multivalent binding.[38] From mixing the two polymer-protein-polymer conjugates with mannose or galactose-functionalization, respectively, we can now easily vary the ratio of the two carbohydrates in the resulting nanoparticle and study the effect on lectin binding, **Figure** 7A.

Different ratios of conjugates **8** and **9** were mixed in solution (0, 3, 6, 11, 20, 33, 50, or 100% of mannose-conjugates mixed with the corresponding percentage of the galactose-conjugates) and then treated under the same aggregation conditions as previously established for the single conjugate systems (first increasing the temperature above the LCST, followed by addition of ConA). For samples containing no (0%) or only 3% of mannose-conjugate, we observe nanoparticles that correspond in size to the clusters prior to ConA addition, with a slight increase for the 3% samples (Figure 7BII). The increase in hydrodynamic diameter of nanoparticles formed at 50% quite are similar to those formed from all mannose conjugates (100%). Interestingly, for nanoparticles formed with 6–33% mannose-conjugates we observe increasing hydrodynamic diameters with increasing mannose-conjugate contents. This can be explained by more ConA binding to the polymer-protein-polymer nanoparticles which is in line with previous observations where lower density of binding carbohydrates, e.g., among non-binding epitopes in glycopolymers, has enabled more lectin binding.[38a,c,39] Notably, the sample with 6% mannose incorporation exhibits no reduction in hydrodynamic diameter, suggesting that the ConA content remains unchanged. This indicates that a minimal quantity of binding ligand may be adequate to attract the maximum amount of lectin. The 11% sample shows an increase of noticeable 178 nm after ConA addition, which suggests that factors beyond the increased ConA content, such as the limited availability of mannose ligands, may also be playing a role. We hypothesize that ConA with its four binding sites bridges mannose ligands from two different nanoparticles, which is supported by our hydrodynamic diameter measurements. DLS measurements over various mannose ratios exhibit a predominantly monomodal distribution before and after lectin addition, suggesting well-defined, uniform nanoparticles. Only the 11% sample displays a broad, multimodal distribution by lectin corona building, indicating diverse conformations and supporting the hypothesis of lectin-bridged nanoparticles (see Supporting Information). To proof that cluster formation is still induced by specific carbohydrate-lectin interactions, inhibition experiment by adding mannose-presenting free glycopolymer were performed

© 2025 The Author(s). Small published by Wiley-VCH GmbH

16136829, 0, Downloaded from https://onlinelibrary.wiley.com/doi/10.1002/smll.202500531 by Universitäts- Und Landesbibliothek Düsseldorf, Wiley Online Library on [10/03/2025]. See the Terms and Conditions (https://onlinelibrary.wiley.com/terms-and-conditions) on Wiley Online Library for rules of use; OA articles are governed by the applicable Creative Commons License

again and show full disassembly of cluster aggregates for all systems. We also observed that the kinetics of disassembly are different for different mannose-to-galactose ratios in the clusters, however, we will need more advanced time-resolved measurements to study this further.

3. Conclusion

We introduce the site-specific conjugation of two different polymers – pNIPAM and glycopolymer – to native proteins by combining a novel rebridging agent and TIRP giving access to dual-responsive multilayer nanoparticles with stimuli-triggered self-assembly and disassembly. First, temperature-induced aggregation of pNIPAM leads to the formation of nanoparticles that are stabilized by a glycopolymer corona. A second protein corona can then be added by leveraging specific glycopolymer-lectin interactions. This outer particle corona of a non-covalently bound lectin efficiently protects the nanoparticles from temperature-induced disassembly. Thus, depending on the sequence of stimuli, the particles can be disassembled in a step-wise or one-step fashion. Furthermore, from mixing polymer-protein conjugates presenting different types of glycopolymers – lectin binding and non-binding – at defined ratios, the formation of defined multilayer nanoparticles or large nanoparticle clusters can be controlled. This novel approach expands the functionality of protein-based materials, which can now also be transferred to enzymes in future research, opening new possibilities for applications, e.g., in drug delivery or biocatalysis.

4. Experimental Section

Standard Protocol for Introducing the Rebridging Agent on Previous Synthesized BSA-Polymer Conjugates and Reduction of the Disulfide Bridge from the Rebridging Agent: 40 mg (0.6 µmol) of BSA-p(HEAA) (**4**) or BSA-pNIPAM (**1**) conjugate was dissolved in 1.5 mL PBS buffer. To this, 100 µL of a 60 mM (10 eq.) tris(2-carboxyethyl)phosphine (TCEP) stock solution in PBS buffer was added and stirred for 10 min at room temperature. The solution was briefly purified via dialysis (exclusion volume 50 kDa, refilled to 1.5 mL with PBS), followed by a second addition of 100 µL of TCEP stock solution (60 mM in PBS) and further stirring for 10 min at room temperature. The remaining TCEP residues were completely removed by repeated purification with deoxygenated PBS buffer via dialysis (exclusion volume 50 kDa, refilled to 1.5 mL with PBS). Ten equivalents of TCEP were used based on Heredia et al.'s demonstration that one disulfide bridge is opened under these conditions.[28] To the reduced protein, 50 µL (1 eq.) of the rebridging stock solution (12 mM in DMSO) was added and stirred for 10 min, producing a yellow coloration upon successful conjugation. The protein was then purified again via dialysis (exclusion volume 50 kDa, refilled to 1.5 mL with PBS) to remove the unconjugated rebridging agent. To reduce the rebridging agent's disulfide bridge, the following steps were repeated three times: the protein conjugate was adjusted to 1.5 mL with PBS buffer, mixed with 100 µL of TCEP stock solution (60 mM in PBS), stirred for 10 min, and rapidly purified via dialysis (exclusion volume 50 kDa, refilled to 1.5 mL with PBS). The protein conjugate was subsequently dialyzed three more times with PBS buffer only and lyophilized.

Standard Protocol for Preparation of Functionalized BSA-Polymer Conjugates via TIRP: 50 mg (0.77 µmol) BSA-pNIPAM-r.b. (**8**) was dissolved in 2 mL PBS buffer and deoxygenated with nitrogen for 20 min. Subsequently, 0.13 mg (0.38 µmol) TPO in 20 µL DMSO was added to the protein solution and deoxygenated for another 20 min. Separately, 25 eq. (18.8 µmol) of the vinyl monomer were dissolved in PBS (50 mg mL^{-1}), and 0.05 mol% (0.0095 µmol) Ir-Cat. in 20 µL DMSO was added before deoxygenation for 20 min. The protein/TPO solution was irradiated for 3 min under a UV lamp ($\lambda = 405$ nm) at 114 mW cm^{-2}. Then, the monomer/Ir-Cat. mixture was added and irradiated for 60 min at 5700 mW cm^{-2}. The reaction mixture was purified by dialysis (exclusion volume 50 kDa) and lyophilized.

Table 3. Summary of the volumes for the mixed measurements.

Mannose Content	Mannose Conjugate (8) [13.8 µM] [µL]	Galactose Conjugate (9) [13.8 µM] [µL]
50%	200	200
30%	133.3	266.7
20%	80	320
11%	44.4	355.6
6%	23.5	376.5
3%	12.1	387.9

DLS Experiments for Particle Formation: Hydrodynamic diameters of thermally induced particles were measured for homovalent conjugates BSA-pNIPAM (**1**-**3**) in polystyrene cuvettes from SARSTEDT at concentrations of 1, 0.5, and 0.25 mg mL^{-1} in PBS buffer. Measurements were conducted cyclically, with a forward run (14–54 °C) followed by a return run (54–14 °C). Samples were tested at different heating rates, with a temperature increment of 2 °C and equilibration times of 2, 10, and 20 min between steps.

DLS Experiments for Particle Formation in Combination with Competition-Inhibition Assay in Solution of Heterovalent BSA-Polymer Conjugates and the Mannose and Galactose Mixed Particle: The double-switchable systems for "I ConA inhibition before particle dissociation" were evaluated using hydrodynamic diameters via DLS measurements in four phases. First, 400 µL (13.8 µM in LBB: 50 mM sodium chloride, 1 mM manganese (II) chloride tetrahydrate, 1 mM calcium chloride, and 10 mM HEPES in ultrapure water, pH 7.4) of the conjugate was placed in a SARSTEDT polystyrene cuvette and heated above the LCST from 28 to 38 °C, with a 2 min equilibration between temperature steps. Subsequently, five measurements were taken at 38 °C with the same equilibration time. In the second phase, 30 µL of ConA solution (5 µM in LBB), preheated to 38 °C, was added, followed by five measurements at 38 °C. In phase three, 100 µL (15 mM) of the pMan (**S3**) inhibitor solution was added at 38 °C, and five more measurements were taken at 38 °C. In the final phase, the temperature was reduced from 38 to 28 °C with a 2 min equilibration between steps.

For the second experiment, "II Lectin stabilized particle below LCST followed by inhibition," phases one and two were identical to the first experiment. However, in phase three, the temperature was reduced from 38 to 28 °C with five measurements taken with a 2 min equilibration, stabilizing the ConA particle below LCST. In phase four, 100 µL (15 mM) of the pMan (**S3**) inhibitor was added at 28 °C to dissolve the specific binding and the particle.

For the mixed systems, the measurement approach was similar to the four phases of "I ConA inhibition before particle dissociation," except that phase one included mixtures of conjugates **8** and **9**. Additionally, a measurement was conducted with 11% mannose in an acetate buffer (100 mM sodium acetate, 100 mM sodium chloride, 5 mM calcium chloride, and 5 mM manganese (II) chloride tetrahydrate, pH 5.2). The ratios are provided in the following **Table 3**:

*UV/Vis and Fluorescence Measurements of BSA-pNIPAM-r.b. (**8**)*: UV/Vis and fluorescence measurements were conducted to verify the conjugation of the rebridging agent to the conjugates. UV/Vis was measured in quartz cuvettes from 200–800 nm. Fluorescence was measured using a microplate reader with an excitation of 396.5 ± 25 nm and an emission range of 480 ± 10 to 605 ± 10 nm. As references, absorbance and fluorescence were independently measured from the conjugate (14 µM in PBS with 10 µL DMSO, deoxygenated with N_2) and the pure rebridging agent (**6**) (14 µM in PBS). Next, 1 mg of the BSA-polymer conjugate was dissolved in 1 mL of 140 µM (10 eq.) tris(2-carboxyethyl)phosphine hydrochloride (TCEP) solution, deoxygenated for 10 min, and its absorbance and

© 2025 The Author(s). Small published by Wiley-VCH GmbH

16136829, 0, Downloaded from https://onlinelibrary.wiley.com/doi/10.1002/smll.202500531 by Universitäts- Und Landesbibliothek Düsseldorf, Wiley Online Library on [10/03/2025]. See the Terms and Conditions (https://onlinelibrary.wiley.com/terms-and-conditions) on Wiley Online Library for rules of use; OA articles are governed by the applicable Creative Commons License

fluorescence were measured. Then, 10 µL of the rebridging agent stock solution (1.4 mM in DMSO) was added, and absorbance was measured. As the highest absorbance occurred at ≈20 min, fluorescence was also measured at this time.

Fluorescence Microscope: Fluorescence images were taken in µ-Slides 8 Well with glass bottom from ibidi, after 30 min of ozone cleaning. The glass surface was blocked with 1 mg mL^{-1} BSA for 15 min to prevent unspecific interactions, followed by washing five times with LBB. The chamber was then filled with 100 µL pNIPAM-BSA-pMan (**8**) (4.6 µM in LBB), heated at 1 °C min^{-1}, and equilibrated for 20 min at 38 °C. Subsequently, 5 µL of a 5 µM ConA stock solution in LBB was added and equilibrated for another 20 min. The temperature was reduced to 28 °C at 1 °C min^{-1}, and after 20 min of equilibration, 20 µL of the pMan (**S3**) inhibitor stock solution (15 mM in LBB) was added and equilibrated for another 20 min. To test particle formation with ConA added below the LCST, 5 µL ConA (5 µM in LBB) was added to 100 µL pNIPAM-BSA-pMan (**8**) (4.6 µM in LBB) at 28 °C, then the temperature was raised to 38 °C at 1 °C min^{-1}.

SEM Imaging: Samples for SEM were prepared similarly to DLS experiments, but after adding lectin to fix the particles, the solution was removed and diluted from 4.6 to 0.46 µM with LBB buffer at 38 °C. The solutions were then dried on 10-well coverslips, sputtered with gold, and measured.

Standard protocols for a) preparation of BSA-polymer conjugates via TIRP, b) Pierce-Protein-Assay, c) SDS-PAGE, d) CD measurements, and e) AF4-LS measurements have already been published by Feldhof et.al.[17]

Supporting Information

Supporting Information is available from the Wiley Online Library or from the author.

Acknowledgements

The authors would like to acknowledge the Center for Advanced Imaging (CAi) at Heinrich Heine University and especially Steffen Köhler for performing the sample preparation and the imaging at the transmission electron microscope. The authors thank the Institute of Experimental Medical Physics at HHU for providing the Epifluorescence IX83 microscope from Olympus. Thanks to the CeMSA@HHU (Center for Molecular and Structural Analytics @ Heinrich Heine University) for recording the mass-spectrometric and the NMR-spectroscopic data. The authors would also like to thank Christine Beuck and Peter Bayer (AG Bayer University of Duisburg-Essen, Center for Medical Biotechnology and Structural and Medical Biochemistry) for providing access to the CD spectrometer. SW and LH also thank the Deutsche Forschungsgemeinschaft (DFG, German Research Foundation) for financial support through the livMatS Cluster of Excellence under Germany's Excellence Strategy (EXC-2193/1-390951807).

Open access funding enabled and organized by Projekt DEAL.

Conflict of Interest

The authors declare no conflict of interest.

Data Availability Statement

The data that support the findings of this study are available from the corresponding author upon reasonable request.

Keywords

dual responsive multilayer nanoparticles, ligand-receptor interaction, polymer-protein-polymer conjugates, rebridging agent, thiol-induced light activated controlled radical polymerization (TIRP)

Received: January 14, 2025
Revised: February 18, 2025
Published online:

[1] a) A. Miserez, J. Yu, P. Mohammadi, *Chem. Rev.* **2023**, *123*, 2049; b) A. J. Capezza, R. Mezzenga, *Biomacromolecules* **2024**, *25*, 4615.
[2] a) M. Bilal, H. M. Iqbal, S. Guo, H. Hu, W. Wang, X. Zhang, *Int. J. Biol. Macromol.* **2018**, *108*, 893; b) T. Nagamune, *Nano Convergence.* **2017**, *4*, 9; c) J. A. Shadish, C. A. DeForest, *Matter* **2020**, *2*, 50.
[3] a) C. Boyer, V. Bulmus, J. Q. Liu, T. P. Davis, M. H. Stenzel, C. Barner-Kowollik, *J. Am. Chem. Soc.* **2007**, *129*, 7145; b) Y. J. Wang, C. Wu, *Biomacromolecules* **2018**, *19*, 1804; c) K. L. Heredia, H. D. Maynard, *Org. Biomol. Chem.* **2007**, *5*, 45; d) S. L. Kuan, Y. Z. Wu, T. Weil, *Macromol. Rapid Commun.* **2013**, *34*, 380; e) A. Theodorou, P. Mandriotis, A. Anastasaki, K. Velonia, *Polym. Chem.* **2021**, *12*, 2228; f) A. Theodorou, E. Liarou, D. M. Haddleton, I. G. Stavrakaki, P. Skordalidis, R. Whitfield, A. Anastasaki, K. Velonia, *Nat. Commun.* **2020**, *11*, 1486; g) A. Theodorou, D. Gounaris, E. Voutyritsa, N. Andrikopoulos, C. I. M. Baltzaki, A. Anastasaki, K. Velonia, *Biomacromolecules* **2022**, *23*, 4241; h) J. Nicolas, G. Mantovani, D. M. Haddleton, *Macromol. Rapid Commun.* **2007**, *28*, 1083; i) R. Raveendran, Y. D. Xu, N. Joshi, M. H. Stenzel, *Pure Appl. Chem.* **2022**, *94*, 983; j) Z. Liu, C. Dong, X. Wang, H. Wang, W. Li, J. Tan, J. Chang, *ACS Appl. Mater. Interfaces.* **2014**, *6*, 2393; k) Z. H. Li, Y. Y. Jiang, K. Wust, M. Callari, M. H. Stenzel, *Aust. J. Chem.* **2020**, *73*, 1034; l) J. Kaltbeitzel, P. R. Wich, *Angew. Chem., Int. Ed.* **2023**, *62*, 202216097.
[4] a) A. O. Elzoghby, W. M. Samy, N. A. Elgindy, *J. Controlled Release.* **2012**, *157*, 168; b) S. Liang, Y. Liu, X. Jin, G. Liu, J. Wen, L. Zhang, J. Li, X. Yuan, I. S. Chen, W. Chen, *Nano Res.* **2016**, *9*, 1022; c) X. Liu, W. Gao, *Angew. Chem., Int. Ed.* **2021**, *60*, 11024.
[5] J. Ge, E. Neofytou, J. Lei, R. E. Beygui, R. N. Zare, *Small* **2012**, *8*, 3573.
[6] a) X. Chen, G. Lv, J. Zhang, S. Tang, Y. Yan, Z. Wu, J. Su, J. Wei, *Int. J. Nanomed.* **2014**, *9*, 1957; b) K. DeFrates, T. Markiewicz, P. Gallo, A. Rack, A. Weyhmiller, B. Jarmusik, X. Hu, *Int. J. Mol. Sci.* **2018**, *19*, 1717; c) J. W. Chung, K. Lee, C. Neikirk, C. M. Nelson, R. D. Priestley, *Small* **2012**, *8*, 1693; d) H. Zhong, B. Zhao, J. Deng, *Small* **2023**, *19*, 2300961.
[7] S. Hong, D. W. Choi, H. N. Kim, C. G. Park, W. Lee, H. H. Park, *Pharmaceutics* **2020**, *12*, 604.
[8] a) D. Moatsou, J. Li, A. Ranji, A. Pitto-Barry, I. Ntai, M. C. Jewett, R. K. O'Reilly, *Bioconjugate Chem.* **2015**, *26*, 1890; b) P. Li, M. Sun, Z. Xu, X. Liu, W. Zhao, W. Gao, *Biomacromolecules* **2018**, *19*, 4472.
[9] a) F. Wei, H. Zheng, C. Gao, J. Tian, J. Gou, H. I. Hamouda, C. Xue, *J. Agric. Food Chem.* **2024**, *72*, 13943; b) G. Han, J.-T. Wang, X. Ji, L. Liu, H. Zhao, *Bioconjugate Chem.* **2017**, *28*, 636.
[10] a) E. M. Pelegri-O'Day, E.-W. Lin, H. D. Maynard, *J. Am. Chem. Soc.* **2014**, *136*, 14323; b) Y. Pang, J. Liu, Y. Qi, X. Li, A. Chilkoti, *Angew. Chem., Int. Ed.* **2016**, *55*, 10296.
[11] a) K. Matyjaszewski, *Macromolecules* **2012**, *45*, 4015; b) J. Nicolas, V. San Miguel, G. Mantovani, D. M. Haddleton, *Chem. Commun.* **2006**, *45*, 4697.
[12] a) P. De, M. Li, S. R. Gondi, B. S. Sumerlin, *J. Am. Chem. Soc.* **2008**, *130*, 11288; b) L. Qiu, X. Han, C. Xing, U. Glebe, *Small* **2023**, *19*, 2207457.
[13] a) M. S. Messina, K. M. Messina, A. Bhattacharya, H. R. Montgomery, H. D. Maynard, *Prog. Polym. Sci.* **2020**, *100*, 101186; b) W. Zhao, F. Liu, Y. Chen, J. Bai, W. Gao, *Polymer* **2015**, *66*, A1.
[14] a) Y. Miura, *J. Mater. Chem. B* **2020**, *8*, 2010; b) B. S. Sumerlin, *ACS Macro Lett.* **2012**, *1*, 141.
[15] a) K. M. Mansfield, H. D. Maynard, *ACS Macro Lett.* **2018**, *7*, 324; b) Q. Zhang, M. Li, C. Zhu, G. Nurumbetov, Z. Li, P. Wilson, K. Kempe, D. M. Haddleton, *J. Am. Chem. Soc.* **2015**, *137*, 9344; c) S. Averick,

 © 2025 The Author(s). Small published by Wiley-VCH GmbH

16136829, 0, Downloaded from https://onlinelibrary.wiley.com/doi/10.1002/smll.202500531 by Universitäts- Und Landesbibliothek Düsseldorf, Wiley Online Library on [10/03/2025]. See the Terms and Conditions (https://onlinelibrary.wiley.com/terms-and-conditions) on Wiley Online Library for rules of use; OA articles are governed by the applicable Creative Commons License

A. Simakova, S. Park, D. Konkolewicz, A. J. Magenau, R. A. Mehl, K. Matyjaszewski, *ACS Macro Lett.* **2012**, *1*, 6.
[16] a) G. Szczepaniak, M. Łagodzińska, S. Dadashi-Silab, A. Gorczyński, K. Matyjaszewski, *Chem. Sci.* **2020**, *11*, 8809; b) R. A. Olson, J. S. Levi, G. M. Scheutz, J. J. Lessard, C. A. Figg, M. N. Kamat, K. B. Basso, B. S. Sumerlin, *Macromolecules* **2021**, *54*, 4880; c) B. S. Tucker, M. L. Coughlin, C. A. Figg, B. S. Sumerlin, *ACS Macro Lett.* **2017**, *6*, 452.
[17] M. Feldhof, S. Sperzel, L. Bonda, S. Boye, A. Braunschweig, U. I. Gerling-Driessen, L. Hartmann, *Chem. Sci.* **2024**, *15*, 16768.
[18] a) M. W. Jones, R. A. Strickland, F. F. Schumacher, S. Caddick, J. R. Baker, M. I. Gibson, D. M. Haddleton, *J. Am. Chem. Soc.* **2012**, *134*, 1847; b) F. F. Schumacher, M. Nobles, C. P. Ryan, M. E. B. Smith, A. Tinker, S. Caddick, J. R. Baker, *Bioconjugate Chem.* **2011**, *22*, 132; c) M. E. B. Smith, F. F. Schumacher, C. P. Ryan, L. M. Tedaldi, D. Papaioannou, G. Waksman, S. Caddick, J. R. Baker, *J. Am. Chem. Soc.* **2010**, *132*, 1960.
[19] S. Brocchini, S. Balan, A. Godwin, J.-W. Choi, M. Zloh, S. Shaunak, *Nat. Protoc.* **2006**, *1*, 2241.
[20] P. Wilson, A. Anastasaki, M. R. Owen, K. Kempe, D. M. Haddleton, S. K. Mann, A. P. Johnston, J. F. Quinn, M. R. Whittaker, P. J. Hogg, *J. Am. Chem. Soc.* **2015**, *137*, 4215.
[21] N. Trattnig, Z. Li, G. P. Bosman, P. Kosma, G. J. Boons, *ChemBioChem* **2022**, *23*, 202200408.
[22] N. Griebenow, A. M. Dilmaç, S. Greven, S. Bräse, *Bioconjugate Chem.* **2016**, *27*, 911.
[23] T. Wang, A. Riegger, M. Lamla, S. Wiese, P. Oeckl, M. Otto, Y. Wu, S. Fischer, H. Barth, S. L. Kuan, *Chem. Sci.* **2016**, *7*, 3234.
[24] C. E. Stieger, L. Franz, F. Körlin, C. P. Hackenberger, *Angew. Chem., Int. Ed.* **2021**, *60*, 15359.
[25] S. L. Kuan, T. Wang, T. Weil, *Chem. Eur. J.* **2016**, *22*, 17112.
[26] H. Zhang, N. Huang, G. Yang, Q. Lin, Y. Su, *OncoTargets Ther.* **2017**, *8*, 63311.
[27] a) A. Wall, K. Nicholls, M. B. Caspersen, S. Skrivergaard, K. A. Howard, K. Karu, V. Chudasama, J. R. Baker, *Org. Biomol. Chem.* **2019**, *17*, 7870; b) J. P. M. Nunes, M. Morais, V. Vassileva, E. Robinson, V. S. Rajkumar, M. E. B. Smith, R. B. Pedley, S. Caddick, J. R. Baker, V. Chudasama, *Chem. Commun.* **2015**, *51*, 10624; c) P. A. Szijj, C. Bahou, V. Chudasama, *Drug Discov. Today Technol.* **2018**, *30*, 27.
[28] K. L. Heredia, D. Bontempo, T. Ly, J. T. Byers, S. Halstenberg, H. D. Maynard, *J. Am. Chem. Soc.* **2005**, *127*, 16955.
[29] M. P. Robin, P. Wilson, A. B. Mabire, J. K. Kiviaho, J. E. Raymond, D. M. Haddleton, R. K. O'Reilly, *J. Am. Chem. Soc.* **2013**, *135*, 2875.
[30] a) B. Kaupbayeva, S. Boye, A. Munasinghe, H. Murata, K. Matyjaszewski, A. Lederer, C. M. Colina, A. J. Russell, *Bioconjugate Chem.* **2021**, *32*, 821; b) B. Kaupbayeva, H. Murata, K. Matyjaszewski, A. J. Russell, S. Boye, A. Lederer, *Chem. Sci.* **2021**, *12*, 13848.
[31] M. Heskins, J. E. Guillet, *J. Macromol. Sci. Chem.* **1968**, *2*, 1441.
[32] M. Li, P. De, S. R. Gondi, B. S. Sumerlin, *Macromol. Rapid Commun.* **2008**, *29*, 1172.
[33] a) Y. Hu, Y. Shin, S. Park, J.-p. Jeong, Y. Kim, S. Jung, *Polymers* **2022**, *15*, 122; b) T. J. Paul, S. Rübel, M. Hildebrandt, A. K. Strzelczyk, C. Spormann, T. K. Lindhorst, S. Schmidt, *ACS Appl. Mater. Interfaces* **2019**, *11*, 26674.
[34] C. Boss, E. Meurville, J. M. Sallese, P. Ryser, *J. Membr. Sci.* **2012**, *401*, 217.
[35] Y. Gou, J. Geng, S. J. Richards, J. Burns, C. Remzi Becer, D. M. Haddleton, *J. Polym. Sci., Part A:Polym. Chem.* **2013**, *51*, 2588.
[36] a) J. Aretz, E.-C. Wamhoff, J. Hanske, D. Heymann, C. Rademacher, *Front. Immunol.* **2014**, *5*, 323; b) S. S. Ting, G. Chen, M. H. Stenzel, *Polym. Chem.* **2010**, *1*, 1392; c) R. T. Lee, Y. C. Lee, *Glycoconjugate J.* **2000**, *17*, 543.
[37] a) S. Liese, R. R. Netz, *ACS Nano* **2018**, *12*, 4140; b) J. J. Lundquist, E. J. Toone, *Chem. Rev.* **2002**, *102*, 555.
[38] a) G. Yilmaz, C. R. Becer, *Front. Bioeng. Biotechnol.* **2014**, *2*, 39; b) D. Ponader, P. Maffre, J. Aretz, D. Pussak, N. M. Ninnemann, S. Schmidt, P. H. Seeberger, C. Rademacher, G. U. Nienhaus, L. Hartmann, *J. Am. Chem. Soc.* **2014**, *136*, 2008; c) J. L. J. Blanco, C. O. Mellet, J. M. G. Fernández, *Chem. Soc. Rev.* **2013**, *42*, 4518; d) L.-C. Blawitzki, N. Bartels, L. Bonda, S. Schmidt, C. Monzel, L. Hartmann, *Biomacromolecules* **2024**, *25*, 5979.
[39] a) A. Miyachi, H. Dohi, P. Neri, H. Mori, H. Uzawa, Y. Seto, Y. Nishida, *Biomacromolecules* **2009**, *10*, 1846; b) Y. Nishida, H. Uzawa, T. Toba, K. Sasaki, H. Kondo, K. Kobayashi, *Biomacromolecules* **2000**, *1*, 68.

© 2025 The Author(s). Small published by Wiley-VCH GmbH

16136829, 0, Downloaded from https://onlinelibrary.wiley.com/doi/10.1002/smll.202500531 by Universitäts- Und Landesbibliothek Düsseldorf, Wiley Online Library on [10/03/2025]. See the Terms and Conditions (https://onlinelibrary.wiley.com/terms-and-conditions) on Wiley Online Library for rules of use; OA articles are governed by the applicable Creative Commons License

3.3 Highly Branched Sulfated Glycopolymers as Mucin Mimetics

Authors: Melina I. Feldhof,‡ Rebecca Schlatterer,‡ Friederiek Strahl, Jonathan Garthe, Sylvain Prévost, Stephan Schmidt, Matthias Karg, Bizan N. Balzer, Laura Hartmann

Journal: Journal of the American Chemical Society

Issue: **2025**, 47, 36, 32698–32709.

Type of Paper: Research Article

Impact Factor: 15.7 (2024)

DOI: 10.1021/jacs.5c08232

First author contribution:

Collaborative project development. Synthesis and characterization (SEC, ^{1}H-NMR, ^{19}F-NMR) of the linear, brush and double-brush glycopolymers. Conducting dynamic light scattering experiments. Collaborative writing of the manuscript.

‡ authors contributed equally

Reprinted with permission from J. Am. Chem. Soc. **2025**, 147, 36, 32698–32709. Copyright © 2025 American Chemical Society.

JACS
JOURNAL OF THE AMERICAN CHEMICAL SOCIETY

Open Access
This article is licensed under CC-BY 4.0

pubs.acs.org/JACS
Article

Highly Branched Sulfated Glycopolymers as Mucin Mimetics

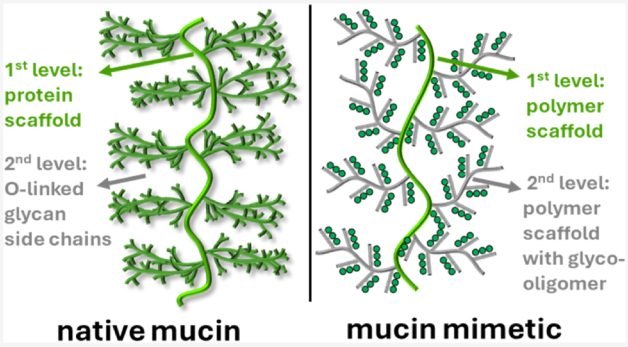
Melina I. Feldhof,◆ Rebecca Schlatterer,◆ Friederike Strahl, Jonathan Garthe, Sylvain Prévost, Stephan Schmidt, Matthias Karg, Bizan N. Balzer,* and Laura Hartmann*

Cite This: J. Am. Chem. Soc. 2025, 147, 32698−32709

Read Online

ACCESS | Metrics & More | Article Recommendations | Supporting Information

ABSTRACT: Mucins are highly complex glycoproteins that form protective and lubricating barriers around epithelial surfaces, e.g., in the respiratory tract, to protect against pathogens. The isolation and purification of natural mucins without compromising their structure and thus their properties remain challenging. Glycopolymers as mucin mimetics have shown great potential in biomedical research, for example, in mucosal barrier enhancement and respiratory disease treatment, or in improving surface lubrication and adhesion properties. Here, we introduce double-brushed mucin mimetic glycopolymers, replicating for the first time a structural design that more closely imitates key architectural features of natural mucins. By combining solid-phase synthesis of sequence-defined glycooligomers and their attachment onto polyactive ester scaffolds, we enable access to a library of linear, brushed, and double-brushed glycopolymers with controlled variations of structural parameters, such as overall chain length, number, and length of branches, as well as number of carbohydrates and degree of sulfation. By using light and neutron scattering as well as atomic force microscopy-based single-molecule force spectroscopy and imaging, we can demonstrate that the double-brushed architecture is responsible for successfully mimicking critical mucin properties, such as their adhesion to hydrophilic surfaces and an extended conformation, properties that are not achieved with single-brushed or linear analogues. Thus, our findings show that double-brushed sulfated glycopolymers effectively replicate key characteristics of natural mucins, advancing their potential as mucin models, as well as for use in biomedical applications.



Downloaded via DUESSELDORF LIBRARIES on December 7, 2025 at 10:41:46 (UTC).
See https://pubs.acs.org/sharingguidelines for options on how to legitimately share published articles.

INTRODUCTION

The glycocalyx is a carbohydrate-dense layer on endothelial cells composed of glycoconjugates, such as glycolipids and proteoglycans, known to be involved in various biological functions and processes, such as pathogen adhesion, cellular communication, immune responses, and for its protective function.[1,2] In particular, mucins, high molecular-weight *O*-linked glycoproteins, form protective hydrogels on epithelial surfaces, shielding cells, e.g., against attachment of pathogens.[3−7] Mucin molecules are also highly important in the lubrication of various tissues to reduce friction, e.g., in the lung, via hydration lubrication, and as a sacrificial layer. For this, mucin hydration properties are crucial, as water molecules are coordinated by mucins and undergo exchange in response to shear forces, facilitating smooth movement. The hydration lubrication of mucins is enhanced by their high degree of glycosylation, carrying negative charges from sialic acid and sulfated saccharides.[4−6,8,9] This high degree of glycosylation is achieved by a brush structure with a protein core presenting a high density of branched oligosaccharide side chains. Influenced by these structural features, mucins build up strongly adhering sacrificial layers on underlying substrates or tissue, which are integral to their protective properties, reducing wear. The sacrificial layer mechanism involves the ability of mucins to dissipate energy upon force application, preventing damage to underlying substrates or tissue.[5,9−12] Thus, mucin hydration, lubrication and protective properties are also closely tied to their adhesion characteristics, with mucin physisorption mediated via van der Waals forces, hydrophobic- and electrostatic interactions and hydrogen bonds.[4,9,11] Since the isolation, study and potential application of natural mucins is limited by the high dispersity of mucins from different sources and challenges in isolating purified samples or synthesis of natural mucins,[13] synthetic mimetics of mucins have been developed, e.g., based on anionically charged polymers, glycopolymers and hydrogels.[14−18] Synthetic glycopolymer mimetics have been designed to replicate key features of mucins, such as their negative net charge, molecular weight, presence of hydrophobic segments, and disulfide cross-linking.[4,9,11] They have been successfully used as a versatile class of adhesive polymers and model systems to provide

Received: May 15, 2025
Revised: July 30, 2025
Accepted: August 12, 2025
Published: August 28, 2025



ACS Publications
© 2025 The Authors. Published by American Chemical Society

https://doi.org/10.1021/jacs.5c08232
J. Am. Chem. Soc. 2025, 147, 32698−32709

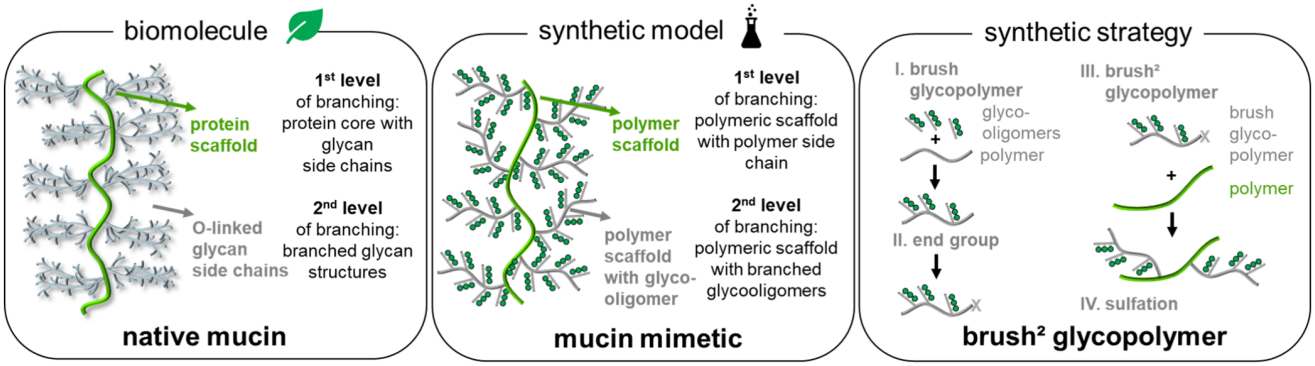


Figure 1. Schematic representation comparing native mucins and mucin mimetics based on the presented double-brushed glycopolymers and the synthetic strategy to derive two levels of branching.

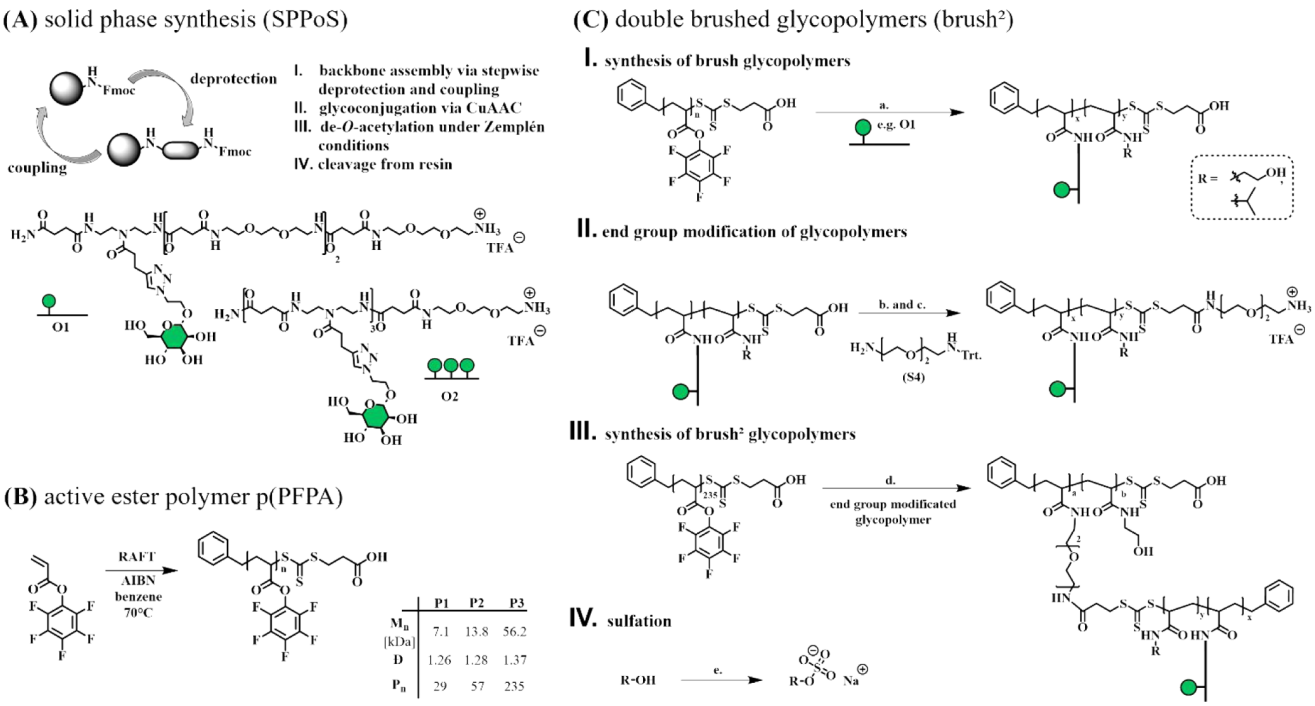


Figure 2. Polymer and oligoamidoamide synthesis for double-brushed glycopolymers. (A) Schematic of Fmoc peptide coupling via solid-phase synthesis for monovalent- (**O1**) and trivalent- oligoamidoamide (**O2**). (B) RAFT polymerization of p(PFPA) with 29 (**P1**), 57 (**P2**), and 235 (**P3**) repetition units. (C) Synthetic route for double-brushed glycopolymers: I. synthesis of brush glycopolymers − a. p(PFPA) **P1** or **P2** in DMF, 40 °C, pH > 8 with NEt_3, oligoamidoamide **O1** or **O2** incorporated at 15% ratio, stirred 24 h followed by quenching with excess ethanolamine or isopropylamine, stirred 24 h at 40 °C, precipitated in cold acetone or diethyl ether, purified by dialysis. II. end group modification of glycopolymers − b. glycopolymer in DMF, terminal carboxylic acid preactivated with EDC*NHS chemistry, linker (**S4**) added, stirred 24 h at room temperature, purified by dialysis − c. dissolved in DMF, diluted with DCM, Trt. protecting group cleaved with 95% TFA and 5% TIPS for 1 h, amine-functionalized polymer precipitated in diethyl ether. III. synthesis of brush^2 glycopolymers − d. product from II. in DMF, swelled 1h at pH > 8 (NEt_3). p(PFPA) **P3** (number of repeat units = 235) in DMF, 40 °C, pH > 8 with NEt_3, swollen product from II. added at 5% ratio, stirred 24 h, followed by quenching with excess ethanolamine, and stirred 24 h at 40 °C. Brush^2 glycopolymer precipitated in cold acetone, purified by dialysis (MWCO 50 kDa). VI. sulfation − e. 40 eq TMA*SO_3 per OH-group in DMF, stirred 24 h at 70 °C, aqueous sodium acetate solution (10 wt %) added at 0 °C, dialyzed (cutoff: 50 kDa).

insights into the functional role of mucins, e.g., in pathogen adhesion.[19,20] Based on the brush topology of natural mucins, also mucin mimetic polymers have been developed in various brush-type structures, including branching, dendrimers, or hydrogel formation.[14,21−25] However, when looking more closely at the natural mucin structure, we find that this exhibits two levels of branching: First, the oligosaccharide side chains themselves are branched structures with monosaccharides as branching points. Second, these side chains are then positioned in a brush-type structure on the protein core (Figure 1). Mucin mimetic glycopolymers so far have included only one level of branching, neglecting the branching within the oligosaccharide side chains. Here, we introduce double-brushed glycopolymers by combining the solid-phase synthesis of sequence-defined glycooligomers. We mimic the oligosaccharide motifs with polyactive ester scaffolds for the conjugation of these glycooligomers to achieve the second level of branching. This results in what we call double-brushed or brush^2 glycopolymers (Figure 1). Based on the topology, we characterize these glycopolymer mimetics as mucin mimetics;

https://doi.org/10.1021/jacs.5c08232
J. Am. Chem. Soc. 2025, 147, 32698−32709

however, they also contain features such as higher sulfation and charge density that can be attributed to sulfated glycosaminoglycans (sGAGs) or sGAG-conjugates such as proteoglycans. This is indeed one of the advantages of these mimetic systems, where we can create non-natural hybrids and, from the controlled variation of structural parameters, gain knowledge that also supports the fundamental understanding of the natural blueprints.

The preparation of brush glycopolymers can be achieved mainly via three strategies: (a) a *grafting-to* approach, where a presynthesized polymer with a reactive end group is attached to the reactive side chain of another polymer, (b) a *grafting-from* approach, where a polymer chain is growing from a macroinitiator, usually another polymer with several initiator units in the backbone, and (c) a *grafting-through* approach, where macromonomers, polymer chains with, e.g., vinyl end groups are polymerized to obtain a brushed polymer.[26,27] Glycopolymers synthesized via postmodification reactions, such as *grafting-to*, provide a flexible method to customize their properties for applications such as selective interactions with lectins, cellular receptors, or other biomolecules.[28] These reactions involve adding specific functional groups to preformed polymers, enabling precise control over the glycopolymer structure and properties.[29,30] Additionally, postmodification allows for the introduction of various carbohydrate residues, adjustment of ligand density, and optimization of the spatial arrangement of functional groups, all of which influence interactions with biological targets.[31] Well-established strategies to perform postpolymerization use click chemistry, such as azid-alkyne, thiol−ene, or maleimide, isocyanate-amin, epoxide-alcohol, and transesterification reactions.[32,33] Especially, the transesterification of an active ester polymer, such as poly*N*-hydroxysuccinimide (pNHS) and polypentafluorophenyl (pPFP), is very efficient without competing side reactions and can be performed under neutral conditions, at low temperatures, without the requirement for inert reaction conditions or addition of catalysts.[34,35] Here, we combine sequence-defined, glycan-functionalized oligomers via solid-phase synthesis and controlled polyactive ester scaffolds to mimic the double-brushed, hydrophilic glycopolymer part of native mucins, key in the mucosal barrier for biolubrication and protection against pathogens.[7,36−38] While our current focus is on the hydrophilic region, these findings lay the groundwork for including additional functional features and toward future applications, e.g., in wound healing, mucosal barrier enhancement, and respiratory disease treatments. Furthermore, we will include the use of our mucin mimetics in the development of glycocalyx mimetics to extend on our previous work, systematically exploring the structural features of glycoconjugates and their effect on dynamic glycan-mediated attachment.[39,40]

RESULTS AND DISCUSSION

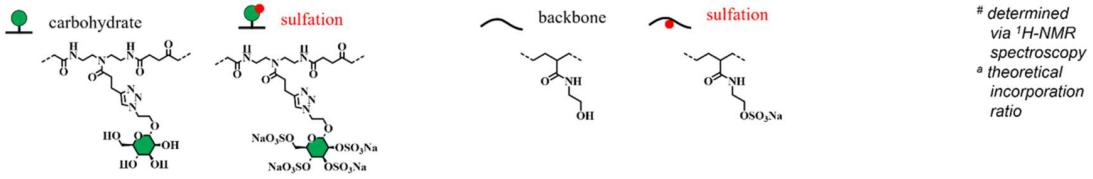
Synthesis Strategy for Double-Brushed (Brush^2) Mucin Mimetics. Our synthetic strategy follows a three-step (**A**−**C**) procedure (Figure 2). Specifically, first sequence-defined glycooligoamidoamines **O1** and **O2** are synthesized via solid-phase polymer synthesis (SPPoS). In short, in SPPoS, tailor-made building blocks representing artificial fluorenylmethoxycarbonyl protecting group (Fmoc) protected amino acids or highly defined synthetic building blocks are assembled on a solid support, in particular, a TentaGel resin, through stepwise addition reactions, giving access to monodisperse, sequence-defined scaffolds. By the selection of the appropriate building block, various functionalities can be individually designed. We have previously introduced the building blocks EDS[41] (ethylene glycol-diamine-succinic acid, 1-(9*H*-fluoren-9-yl)-3,14-dioxo-2,7,10-trioxa-4,13-diazaheptadecan-17-oic acid), to tune length and hydrophilicity, and TDS[42] (triple-bond diethylenetriamine-succinic acid, 1-(fluorenyl)-3,11-dioxo-7-(pent-4-ynoyl)-2-oxa-4,7,10-triazatetra-decan-14-oic acid) to provide a functional side-chain alkin-functionality for further functionalization. Mannose-azide ligands can then be attached via a CuAAC followed by de-*O*-acetylation under Zemplén conditions.[43] Importantly, glycooligomers need to carry a free terminal amine group for later conjugation onto the active ester polymer scaffolds. To accomplish this, the *N*-terminal Fmoc protecting group of the terminal building block is cleaved before the glycooligomer is retrieved from the resin. In total, two glycooligomers, **O1** and **O2**, with controlled variation of length and the number of mannose units, are obtained in high purity and analyzed via ^{1}H-NMR, RP-HPLC-MS, MALDI, and HR-ESI (Figure 2A, and Supporting Information). In the second step (Figure 2B), poly(pentafluorophenyl acrylate) active esters p(PFPA) scaffolds are synthesized via reversible addition−fragmentation chain-transfer (RAFT), employing benzylsulfanylthiocarbonylsulfanyl propionic acid (BSTPA) as a RAFT agent, following established protocols.[25,44,45] Overall, three p(PFPA)s (**P1**−**P3**), varying in chain length, are obtained (Figure 2B) with degrees of polymerization of 29 (7.2 kDa), 57 (13.8 kDa), and 235 (56.2 kDa), respectively, showing narrow dispersities ($Đ$ = 1.26−1.37) (Supporting Information). These active ester polymers are additionally quenched with ethanolamine (**P4**−**P6**) to simplify the analysis and both the p(PFPA) (**P1**−**P3**) and the quenched p(HEAA) polymers (**P4**−**P6**) are analyzed using ^{1}H-NMR, ^{19}F-NMR, and SEC (see Supporting Information).

In the third step of our synthetic strategy, we utilize postpolymeric reactions to create highly brushed glycopolymers with controlled variations in the degree and length of branching, carbohydrate functionalization, and negative charges. The used synthesis route of the double-brushed polymers (brush^2) is built up chronologically in four steps **I**−**IV**, which is shown as an example in Figure 2C. Step **I.** The synthesized **O1** and **O2** are incorporated in a 15% ratio in the p(PFPA) derivatives **P1** and **P2**, while all other PFP functionalities are quenched with ethanolamine or in a second sample with isopropylamine. Thereby, p(*N*-2-hydroxyethyl acrylamide) and p(*N*-isopropylacrylamide) main chain polymers with glycooligomer side chains are derived. P(NIPAM) is a thermoresponsive polymer that undergoes reversible phase transitions at physiological temperatures. In our mucin mimetics, this enables modulation of the polymer conformation, analogous to temperature-dependent changes in viscosity and interactions also observed with native mucins, and allows us to study this feature in more detail in future studies.[4] The brush glycopolymers produced in this step then serve as side chains to synthesize the targeted double-brushed (brush^2) structures. In order to use the brushed polymers as side chains on another polyactive ester scaffold and derive double-brushed glycopolymers, they have to be modified at the terminal carboxylic acid (step **II**). For this purpose, a linker molecule (**S4**), based on 2,2′-(ethylenedioxy)bis(ethylamine), is employed, which is triphenylmethyl (Trt) protected on one side and can be conjugated to the carboxylic acid of the polymer

https://doi.org/10.1021/jacs.5c08232
J. Am. Chem. Soc. 2025, 147, 32698−32709

Table 1. Summary of All Synthesized Linear and Brush Glycopolymers (P7−P24) and Brush[2] Glycopolymers (B1−B17)

structure type	label	$Pn_{precursor/arm\ length}$	oligomeric precursor	$N_{side\text{-}chain}$[#]	$N_{mannose}$[#]	sulfation[#]	quencher	topology	Mn [kDa][#]
brush glycopolymer (e.g.)	$_{2}E_{29}$ P7	29	O1	2	2	no	H_2N OH	brush	5.9
	$_{6}E_{29}$ P8	29	O2	2	6	no	H_2N OH	brush	5.3
	$_{2}I_{29}$ P9	29	O1	2	0	no	H_2N	brush	5.9
	$_{6}I_{29}$ P10	29	O2	2	6	no	H_2N	brush	7.0
	$_{6}E_{57}$ P11	57	O1	6	6	no	H_2N OH	brush	13.8
	$_{18}E_{57}$ P12	57	O2	6	18	no	H_2N OH	brush	15.5
	$_{6}I_{57}$ P13	57	O1	6	6	no	H_2N	brush	13.7
	$_{18}I_{57}$ P14	57	O2	6	18	no	H_2N	brush	13.6
brush[2] glycopolymer (e.g.)	$_{22}E^{2}_{29}$ B1	29	O1	11	22	no	H_2N OH	brush[2]	99.1
	$_{66}E^{2}_{29}$ B2	29	O2	11	66	no	H_2N OH	brush[2]	92.0
	$_{22}I^{2}_{29}$ B3	29	O1	11	22	no	H_2N OH	brush[2]	98.5
	$_{66}I^{2}_{29}$ B4	29	O2	11	66	no	H_2N OH	brush[2]	112.1
	$_{66}E^{2}_{57}$ B5	57	O1	11	66	no	H_2N OH	brush[2]	193.4
	$_{198}E^{2}_{57}$ B6	57	O2	11	198	no	H_2N OH	brush[2]	182.3
	$_{66}I^{2}_{57}$ B7	57	O1	11	66	no	H_2N OH	brush[2]	192.3
	$_{198}I^{2}_{57}$ B8	57	O2	11	198	no	H_2N OH	brush[2]	191.6
	$_{22}E^{2}_{29}$ B9	29	O1	11	22	yes	H_2N OH	brush[2]	164.6
	$_{66}E^{2}_{29}$ B10	29	O2	11	66	yes	H_2N OH	brush[2]	163.6
	$_{66}E^{2}_{57}$ B11	29	O1	11	66	yes	H_2N OH	brush[2]	131.0
	$_{198}E^{2}_{57}$ B12	29	O2	11	198	yes	H_2N OH	brush[2]	164.2
	$_{22}I^{2}_{29}$ B13	57	O1	11	22	yes	H_2N OH	brush[2]	307.9
	$_{66}I^{2}_{29}$ B14	57	O2	11	66	yes	H_2N OH	brush[2]	319.2
	$_{66}I^{2}_{57}$ B15	57	O1	11	66	yes	H_2N OH	brush[2]	244.3
	$_{198}I^{2}_{57}$ B16	57	O2	11	198	yes	H_2N OH	brush[2]	273.1
controls (e.g.)	$_{11}E_{235}$ P15	235	O1	11	11	no	H_2N OH	linear	37.7
	$_{33}E_{235}$ P16	235	O2	11	33	no	H_2N OH	linear	37.7
	$_{11}I_{235}$ P17	235	O1	11	11	no	H_2N	linear	40.8
	$_{33}I_{235}$ P18	235	O2	11	33	no	H_2N	linear	38.9
	$_{11}E_{235}$ P19	235	O1	11	11	yes	H_2N OH	linear	64.4
	$_{33}E_{235}$ P20	235	O2	11	33	yes	H_2N OH	linear	68.3
	$_{11}I_{235}$ P21	235	O1	11	11	yes	H_2N	linear	45.7
	$_{33}I_{235}$ P22	235	O2	11	33	yes	H_2N	linear	47.5
	$_{0}E_{235}$ P23	235	-	-	-	no	H_2N OH	linear	26.8
	$_{0}I_{235}$ P24	235	-	-	-	no	H_2N	linear	27.3
	$_{0}E^{2}_{57}$ B17	75	-	5[a]	-	no	H_2N OH	brush[2]	46.0



brush via EDC*NHS chemistry. In step **III**, the synthesized amine functional brushed glycopolymer is consequently incorporated at a 5% ratio on the higher molecular weight p(PFPA) (**P3**) precursor, followed by quenching unreacted PFP functionalities with ethanolamine. The derived brush[2] glycopolymers are isolated by precipitation in diethyl ether, purified by dialysis, and characterized by ^{1}H-NMR and ^{19}F-NMR. To mimic the negative charges of natural mucin polymers, brush[2] polymers **B1−B8** are then globally sulfated (step **IV**) following previously established protocols[46] and the sulfation is proven by characteristic proton shifts through ^{1}H-NMR (see Supporting Information for further details on the synthesis and analytical data). All synthesized structures, listed in Table 1, follow uniform nomenclature. The capitalized letter describes the quencher or the main part of the glycopolymer side chain backbone (E = ethanolamine, I = isopropylamine). The exponent (top right) indicates whether a structure is present as a brush glycopolymer (no designation) or as a double-brushed glycopolymer (brush[2]). The lower index (right) indicates the length of the glycopolymer side chains in brush[2] glycopolymers or the general polymer length in brushed or linear structures, the lower index (left) indicates the

https://doi.org/10.1021/jacs.5c08232
J. Am. Chem. Soc. 2025, 147, 32698−32709

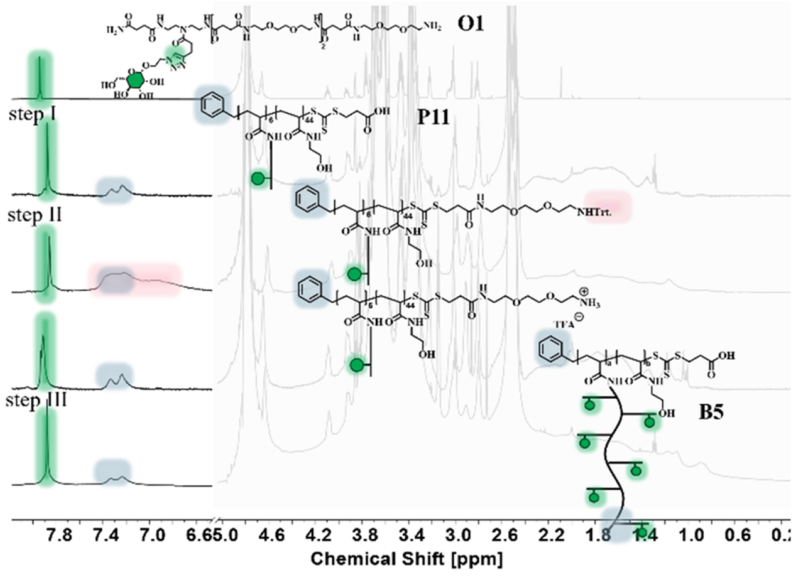


Figure 3. Comparison of the individual synthesis steps from oligoamidoamine to brush[2]. The characteristic triazole protons are marked in green, the aromatic protons of the RAFT initiator in blue, and the Trt protecting group in red. The backbone and main side chain signals are grayed out, as they only make a limited contribution to explaining the conversion step. These spectra are shown here only as examples and focus on the characteristic peaks to demonstrate the synthesis route. A more detailed analysis of the ^{1}H-NMR spectra is shown in the Supporting Information.

number of sugar units in relation to the entire polymer, and sulfation is marked by the addition of an asterisk (*) at the top left position.

^{1}H NMR is also used to calculate and confirm the incorporation efficiency of the functionalities in the linear, brush, and brush[2] polymers, as well as the overall number of carbohydrates per polymer and the molecular weights (Table 1). The obtained brush glycopolymers (**P7**−**P14**) are isolated, purified via dialysis, and analyzed via ^{1}H-NMR, whereby the incorporation ratio of the corresponding oligoamidoamine is determined based on the correlation between triazole protons of the oligoamidoamine and the aromatic protons of the RAFT initiator. The successful conversion of all PFP-active functionalities is confirmed by ^{19}F-NMR (see Supporting Information). The integration ratio of the brush[2] structures is calculated as follows: protons assigned to the triazole unit in the glycooligomers are put in relation to the aromatic protons assigned to the RAFT initiator. The number of mannose units is calculated from the results of the incorporation ratio of the glycopolymer. Figure 3 exemplary showcases the analysis strategy of structure **B5** by ^{1}H-NMR that allows one to follow the individual reaction steps. By comparing the ^{1}H-NMR of **O1** with the product from step **I**, **O1** is successfully incorporated with six repeat units. Subsequently, the Trt-protected linker (**S4**) is conjugated, which can be qualitatively confirmed by the increase in signal width in the aromatic region (highlighted in pink here). After subsequent Trt cleavage with 95% TFA, the brush glycopolymer bears a terminal amine for further conjugation. The incorporation of **P11**, a side-chain brush glycopolymer with one mannose molecule per oligoamidoamine, necessitates that the triazole signal in brush polymer **B5** exhibits a corresponding proton count. When the integral sums of the aromatic compounds in both the side chain glycopolymers and the brush[2] end are compared, the consistency of the proton number is verified.

To determine the efficiency of the sulfation reaction in obtaining sulfated brush[2] glycopolymers via ^{1}H-NMR, the chemical shift of the triazole proton before and after sulfation is considered (Supporting Information). Based on the sulfate groups, the change of the electrochemical environment (shielding) has the greatest impact on the chemical shift, toward a lower field, of the triazole protons and the anomeric center of mannose. Table 1 presents the final structures obtained, along with their respective yields. For comparison, nonglycosylated homopolymers—linear and brushed—are synthesized using exclusively ethanolamine or isopropylamine to functionalize the PFPA precursor. Additionally, single-brush glycopolymers with glycooligomer side chains presenting one or three mannose units are obtained by using the same high molecular weight PFPA precursor as for the brush[2] glycopolymers (Table 1).

Properties of Highly Branched Sulfated Glycopolymers as Mucin Mimetics. After the successful establishment of the synthetic protocol to derive a series of linear, single-brushed, brush[2], and globally sulfated glycopolymers, we investigated their ability to mimic key features of natural mucins, such as hydration, conformation, and adhesion. Mucins have shown characteristic sacrificial layer formation on different substrates and so-called hydration lubrication. Although the hydrophobic folded regions of mucins are essential for the sacrificial layer formation, in particular on hydrophobic substrates,[12] these domains are not within the scope of this study. We focus on mimicking the hydration, conformation, and adhesion properties of the glycosylated domains of mucins, which are crucial for the adhesion and thus sacrificial layer formation.[11,12]

Dynamic light scattering (DLS) and small-angle neutron scattering (SANS) experiments are carried out to obtain insights into the conformation and the hydration state of brush[2] glycopolymers. From DLS, the hydrodynamic diameters of all brush[2] (**B1**−**B17**) and control structures (**P15**−**P24**) are revealed, ranging from 66 to 184 nm (see Supporting Information for detailed information). These first experiments show that brush[2] structures with longer brushed glycopolymer

https://doi.org/10.1021/jacs.5c08232
J. Am. Chem. Soc. 2025, 147, 32698−32709

side chains consistently exhibit larger hydrodynamic diameters in comparison to those with shorter brushed glycopolymer side chains. This is independent of the type of quencher introduced during synthesis (ethanolamine or isopropylamine) and overall carbohydrate content. This supports the expectation that larger brushed glycopolymer side chains lead to increased hydrodynamic diameters and can even induce extended bottlebrush rather than random coil conformations.[47] The brush[2] structures with sulfation exhibit approximately similar size ranges for their hydrodynamic diameter as brushed heparan sulfate derivatives reported in the literature.[48] For glycopolymers with a p(NIPAM) backbone, we can also study the potential LCST behavior. Therefore, all samples containing p(NIPAM) backbones are measured at 20 °C (below LCST) and 40 °C (above LCST), respectively. Glycopolymers exhibit larger hydrodynamic diameters above the LCST (40 °C). This increase is mainly due to the aggregation of polymer chains, driven by enhanced hydrophobic interactions and the transition from a solvated to a collapsed state. Such behavior is well-known for thermoresponsive polymers and is affected by their molecular architecture and environmental conditions.[49−51] To gain further insights, selected polymers are additionally analyzed by SANS. Detailed information on the experimental conditions can be found in the Supporting Information. To further investigate the conformation differences in the polymer structures of differently brushed glycopolymers, experiments are conducted with a brush[2] glycopolymer (**B6**) and a linear control glycopolymers (**P15**). These measurements allow us to resolve the individual polymer strands due to the chosen q range (Figure 4).

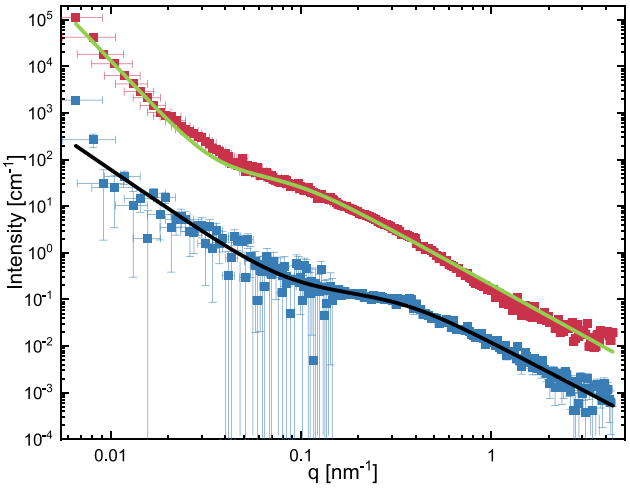


Figure 4. Radially averaged scattering profiles obtained from SANS measurements performed in D_2O with 5 mg/mL at 25 °C. Red squares correspond to data recorded from sample **B6**, while blue squares correspond to sample **P15**. The profile of **B6** is offset vertically by multiplication by a factor of 10 for the sake of clarity. Solid lines correspond to fits to the data. The incoherent background scattering was subtracted.

Both scattering profiles can be described by three contributions: a q-independent incoherent background, a sharp increase in scattering intensities toward low q, which can be described by a power law, and a polymer form factor, which is accounted for by a generalized Gaussian coil model.[52] The form factor is based on the random walk description of a polymer, as first described by Flory.[53,54] This model considers the radius of gyration R_g of the polymer coil, the (excluded volume parameter) solvent parameter ν, and the forward scattering of the neutrons. The compositions of the fits are shown in detail in the Supporting Information. The fits to the data, shown as solid lines in Figure 4, describe the experimental data well. Some small deviations arise for branched sample **B6** in the low q region. These deviations could arise from the occurrence of larger particle aggregates present in the sample lying just outside the q range. Both fits can be described with similar solvent parameters of ν = 0.44 (**B6**) and ν = 0.47 (**P15**), respectively. This parameter suggests that the interactions between polymer and solvent are slightly unfavorable. The steep increase below q = 0.05 nm^{-1} can be described by a power law, wherein the exponent is correlated to the solvent parameter ν as $n = 1/\nu \approx 2.2$ for polymer coils.[55] The coils have a radius of gyration R_g of 4.6 (**P15**) and 17.7 nm (**B6**), respectively. The increase in size with increasing molecular weight is in good agreement with theoretical calculations following the theory of Mark−Houwink-Kunh-Sakurada.[56] Following this theory, the size of the polymer depends on the molecular weight through the equation $R_g \sim M_W^{\nu}$. Thus, the DLS and SANS findings demonstrate size differences between conventional brushed and our newly introduced brush[2] glycopolymers. For mucins, their high level of hydration behavior is attributed to their hydrophilic carbohydrate components.[36] We find similar properties for our mucin mimetics, as we observe that the measured radii of gyration are considerably smaller than the radii of hydration, consistent with previous literature on mucin (e.g., MUC5AC: R_g = 187 nm, R_H > 1 μm).[57,58] This indicates that these novel brush[2] structures mimic natural mucins with respect to their conformational and hydration behavior.

Natural mucins form strongly adhering sacrificial layers on cellular substrates. The sacrificial layer mechanism depends on mucin molecules rapidly detaching and reattaching, linking their lubrication behavior to their adhesion characteristics.[5,8,9,59] Also, their lubrication and protective properties are closely linked to their adhesion. We investigate in the following the adhesion properties of our mucin mimetics using selected samples via AFM-based single-molecule force spectroscopy (SMFS). Specifically, we examine the influence of mannose and sulfated mannose on the desorption (dead-hesion) force of the here presented 2-hydroxyethyl acrylate (HEAA)-based glycopolymers. Using SMFS to investigate polymer interaction with solid substrates in liquid environment is well established,[60−67] and has been successfully applied also for natural mucins.[12]

Single polymers are covalently attached to an AFM cantilever tip (see Supporting Information), using a functionalization protocol that has been established and successfully applied in multiple studies.[68−73] The functionalized tip is then approached to a bare, freshly cleaved mica surface in water. After the polymer is brought into contact with the mica (dwell time: 1.0 s), the cantilever is retracted (usually at a velocity of 1.0 μm s^{-1}) until the polymer desorbs from the surface (Figure 5a). We measure desorption forces at a defined pulling velocity, which allows us to compare different polymers, as previously done in SMFS experiments.[65,74,75] Furthermore, we apply strict criteria to isolate single-molecule desorption events in force−extension curves. This includes the selection of characteristic force−extension curves, showing clear single-molecule desorption motifs.[76,77] We observe single-molecule desorption events, such as plateaus of constant force (Figures

https://doi.org/10.1021/jacs.5c08232
J. Am. Chem. Soc. 2025, 147, 32698−32709

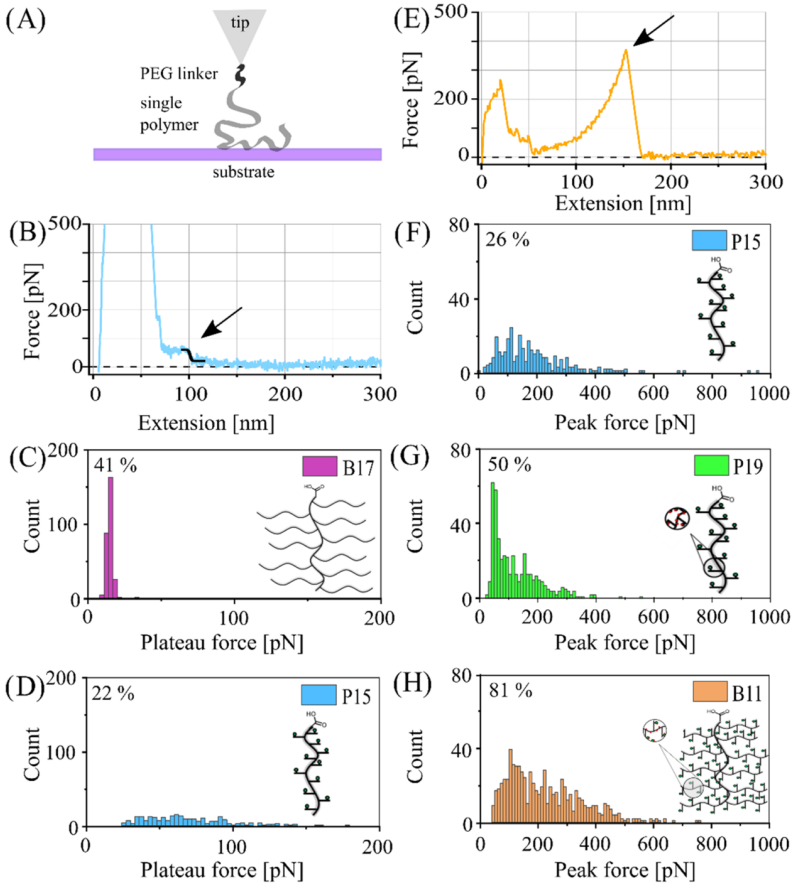


Figure 5. AFM-based single-molecule desorption. (A) Scheme of the covalent attachment of a single polymer to an AFM cantilever tip via EDC*NHS chemistry using poly(ethylene glycol) (PEG) linkers and exemplary force−extension curves with (B) a plateau of constant force (for structure **P15**) or (E) with a force peak (for structure **B11**) as desorption motif, measured in water. The desorption motifs are indicated with arrows. Usually, approach and retraction velocities of 1.0 μm s^{-1}, a dwell time toward the surface of 1.0 s, and a sampling rate of 5 kHz are taken. Adhesion peaks at small extensions (at the beginning of the retraction process) are due to the unspecific adhesion of the whole cantilever tip and the underlying substrate. (C,D) Plateau forces of **B17** (brush^2, no carbohydrates, nonsulfated -41% of all obtained curves show single-molecule interaction events, 289/700 curves) and **P15** (linear, carbohydrates, nonsulfated -22% plateaus, 258/1200 curves). (F−H) Peak forces of **P15** (linear, carbohydrates, nonsulfated -26% peaks, 314/1200 curves), **P19** (linear, carbohydrates, sulfation -50% peaks, 447/900 curves), and **B11** (brush^2, carbohydrates, sulfated -81% peaks, 731/900 curves).

5b−d and S111) or desorption events represented by peaks, wherein the polymer is stretched between the AFM cantilever tip and the mica surface until detachment (Figures 5e−h and S111).[64,74,77,78] We further performed control measurements (Figure S111) with purely poly(ethylene glycol) (PEG) functionalized cantilevers to differentiate between force responses resulting from the investigated glycopolymers and from the PEG-linker system. It has been shown by Kienle et al.[65] that plateaus are the result of surface-mobile polymers, independent of the polymer architecture, whereas peaks are due to surface-immobile polymers, which depend on the polymer architecture, in particular on the side chain structure.

Negative control brush^2 polymer **B17**, without any mannose, shows exclusively plateaus of constant force as the desorption motif with a desorption force of only (15 ± 3) pN (Figure 5c). By contrast, brush polymer **P15** reveals a mix of plateaus and peaks as a desorption motif, with the plateaus exhibiting higher forces of around 100 pN (Figure 5d). The presence of plateaus is a sign of a high polymer mobility and dispersion forces acting between the polymer and mica. The occurrence of peaks is observed for all tested glycopolymer structures **P15**, **P19**, and **B11**. Their force−extension curves mainly exhibit peaks with peak forces up to 800 pN (Figure 5f−h). They all contain either mannose (nonsulfated glycopolymers e.g., **P15**) or statistically sulfated mannose (sulfated glycopolymers, e.g., **P19** and **B11**). This might lead to a decrease in mobility and a higher desorption force due to an increase of specific directional bonds. In particular, the polymer−substrate interaction is strengthened by the high density of hydroxyl in the mannose units, which increases the number of potential interaction sites and enables multivalent binding.[66] This density can be varied and controlled through brush architecture and the introduction of carbohydrate motifs. When compared to brush^2 polymer **B17** with no mannose, the potential hydrogen bond density (normalized based on the backbone length) increases slightly for brush glycopolymers **P15** and **P19**, by a number of $\rho_{P15,P19} = 0.6\frac{\text{H-bonds}}{\text{nm}}$, reaching its maximum increase by $\rho_{B11} = 3.6\frac{\text{H-bonds}}{\text{nm}}$ for the brush^2 glycopolymer **B11**. This increase of potential interaction sites reasonably explains not only the increase of the desorption force but also the increase of the interaction frequency for brush^2 glycopolymer **B11** in comparison to the other glycopolymers (Figure 5h). Furthermore, in water, a hydration

https://doi.org/10.1021/jacs.5c08232
J. Am. Chem. Soc. 2025, 147, 32698−32709

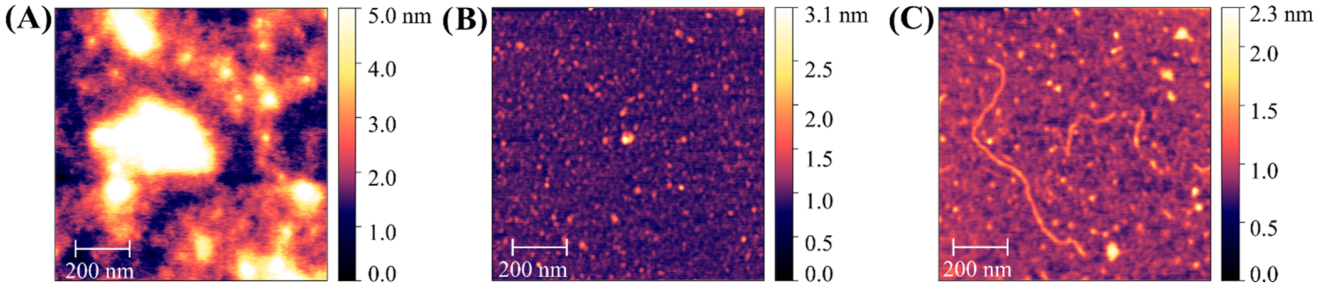


Figure 6. AFM topography images (size: 1 μm^2) revealing different conformations of (A) brush^2 glycopolymer **B17** without mannose, (B) brush glycopolymer **P19** with sulfated mannose, and (C) brush^2 glycopolymer **B11** with sulfated mannose. All polymers are deposited from a 0.1 $\mu g\ mL^{-1}$ polymer solution in water and then dried under vacuum. Images are obtained in air.

layer is present on mica, giving rise to a short-range repulsive force.[79] This hydration force opposes adsorption. However, the energetic costs of removing this hydration layer from mica can be compensated by favorable polymer−substrate interactions such as H-bonding and entropy gain by release of the hydration layer,[60,80] which is also feasible for the glycopolymers based on the presence of hydroxyl groups. Additionally, the hydroxyl groups in mannose are neutral but polar, leading to the possibility of dipole-charge interaction with the negatively charged mica. This is further facilitated by the HEAA backbone, adding a large polyamide domain with additional H-bonding sites to overcome hydration barriers for adsorption.[81] For comparison, experiments at increased ionic strength in buffer (10 mM HEPES, 50 mM NaCl, pH 7.0) with **P15** and **B11** on mica showed no desorption events (Figure S112), suggesting blocking of H-bonding by HEPES and hydrated salt ions.[82]

Furthermore, by comparing brush glycopolymer **P15** and its sulfated counterpart **P19**, we can deduce the influences of the sulfates on the desorption behavior. Both polymers have the same structure, but **P19** contains statistically sulfated mannose, making it polyanionic. In general, mica in water is also polyanionic, therefore one would expect dominant ionic repulsion between sulfated structures and mica, unless multivalent cations such as Mg^{2+} or Ca^{2+}were present.[73,83] However, previous studies have shown that negatively charged carbohydrates[60] or proteins[84] can also adsorb on mica in the absence of multivalent cations. This could be explained by solvent water molecules promoting hydrogen bonds between the sulfates and mica, i.e., a water-mediated attractive interaction between like-charged motifs.[85−87] In addition, local charge heterogeneity[88] (neutral vs negatively charged portions) facilitates the formation of hydrogen bonds. This is similar to mucins, where a multivalent interaction of the polyanionic, glycosylated chain (e.g., via chelate formation, hydrogen bonding, or electrostatic interaction) has been observed on steel.[11] Furthermore, positive counterions (Na^+) could be present in our polymer solutions, a remnant from the synthesis process, where the sulfurtrioxide trimethylamine complex (TMA^*SO_3) for sulfation is quenched with sodium acetate. Such ions partially screen the sulfates, reducing long-range electrostatic repulsion. As the nonsulfated **P15** and sulfated **P19** reveal the same range of desorption forces, it is likely that their adhesion on a hydrophilic surface, such as mica, can be mainly attributed to the mannose units, while attractive and repulsive contributions of the sulfate groups might largely compensate each other.

To gain further insight into the interaction between the glycopolymers and the surface, selected structures are investigated in more detail with respect to their mica surface adsorbed conformations, in contrast to our previous investigations using DLS and SANS, which were performed in solution. The conformations of the presented polymers are influenced by their interaction with the mica surface, which, in turn, depends on the brush structure. Figures 6 and S113 show exemplary images of the polymers **B11**, **B17**, and **P19** analyzed by AFM-based imaging on mica (deposited in solution, dried, and imaged in air), showing compact conformations for brush glycopolymer **P19** and extended conformations for brush^2 polymer **B11** (see Supporting Information, Figure S113 for more images). The AFM images further support an increase of polymer−substrate interactions for brush^2 glycopolymers, corresponding to the increase in hydrogen bond density (see above). Brush^2 polymer **B17** (Figure 6a), without any mannose, shows a high degree of self-aggregation, whereas the glycopolymers **P19** and **B11** (Figure 6b,c), containing mannose, form smaller or, in the case of **B11**, even linear aggregates, preferring mica substrate interaction over aggregation. We observe linear chains reaching several hundred nm for brush^2 glycopolymer **B11**, which cannot correspond to a single molecule based on the molecular weight but is attributed to aggregation, where one molecule is connected to the next one forming a linear chain, possibly due to intermolecular hydrogen bonds. Such highly extended chain conformations on mica have been observed before for the linear, polyanionic polysaccharide hyaluronan.[89−93] Here, the linear conformation might result from both the branched geometry of **B11** and the electrostatic repulsion of the sulfate groups, leading to both a rather extended chain conformation and to a larger interaction area with the mica substrate.

AFM topography images in Figures 6c and S113 support the SMFS data, where the brush^2 polymer **B11** shows an extended and flat conformation on mica (deposited in solution, dried, and imaged in air). Thus, the contact area of **B11** is increased, which could also increase adhesion.[65,67] This increase in contact area is most probably due to mannose: both **B11** and **B17** share the same branching topology and both are sulfated; however, **B17** does not carry any mannose and shows a coiled conformation (Figure 6a). Hence, mannose seems to increase not only the contact area but also the ability for multivalent binding.

CONCLUSIONS

We introduce the synthesis of double-brushed glycopolymers as mucin mimetics by combining the solid-phase synthesis of

https://doi.org/10.1021/jacs.5c08232
J. Am. Chem. Soc. 2025, 147, 32698−32709

sequence-defined glycooligomers and their conjugation onto polyactive ester scaffolds. First, we demonstrate the straightforward access to a library of linear, brushed, and double-brushed (or brush^2) glycopolymers with controlled variations of structural parameters, such as branching, their brushed glycopolymer side chain length and number, carbohydrate content, and sulfation. Subsequently, selected structures are analyzed for their physicochemical properties, focusing on features that are characteristic of the unique behavior and function of natural mucins, such as their hydrodynamic size and adhesion properties. Specifically, we use DLS, SANS, AFM-based SMFS, and imaging to confirm that indeed brush^2 glycopolymers successfully mimic key interaction parameters of mucins. We show that glycopolymer adhesion increases with branching sugar content, as it allows for multivalent binding due to hydrogen bonds, similar to the glycoprotein mucin, where multivalent interactions of the polyanionic, glycosylated chain are observed. AFM imaging reveals a highly linear conformation of sulfated brush^2 glycopolymers, which we attribute to the combination of both the double-brush architecture as well as the presence of sulfated carbohydrate groups, as neither one of the nonmannose brush^2 polymers of the simple brush glycopolymers shows a similar behavior. Indeed, such highly extended chain conformations are typical features of natural mucins. Thus, in summary, we have succeeded in synthesizing double-brushed glycopolymers as new mucin mimetics with mucin-specific characteristics. Future studies will extend the synthetic strategy to include further features of natural mucins, such as hydrophobic regions. We will also study additional biophysical properties such as their ability to retain water and act as a lubricant, and will explore potential applications of brush^2 glycopolymers, e.g., in wound healing, mucosal barrier enhancement, and respiratory disease treatments, and to build increasingly complex glycocalyx models to study pathogen attachment.

■ ASSOCIATED CONTENT

Supporting Information

The Supporting Information is available free of charge at https://pubs.acs.org/doi/10.1021/jacs.5c08232.

Materials and methods; synthetic protocols; analysis of compounds via NMR; RP-HPLC; MALDI-Tof-MS; HR-ESI-MS; H_2O-SEC-MALS; THF-SEC; elemental analysis; SANS; DLS; and AFM (PDF)

■ AUTHOR INFORMATION

Corresponding Authors

Bizan N. Balzer − *Institute of Physical Chemistry, 79104 Freiburg, Germany; Cluster of Excellence livMatS @ FIT-Freiburg Center for Interactive Materials and Bioinspired Technologies, University of Freiburg, 79110 Freiburg, Germany; Freiburg Materials Research Center (FMF), University of Freiburg, 79104 Freiburg, Germany;* orcid.org/0000-0001-6886-0857; Email: bizan.balzer@physchem.uni-freiburg.de

Laura Hartmann − *Cluster of Excellence livMatS @ FIT-Freiburg Center for Interactive Materials and Bioinspired Technologies, University of Freiburg, 79110 Freiburg, Germany; Freiburg Materials Research Center (FMF), University of Freiburg, 79104 Freiburg, Germany; Institute for Macromolecular Chemistry, University of Freiburg, D-79104 Freiburg im Breisga., Germany;* orcid.org/0000-0003-0115-6405; Email: laura.hartmann@makro.uni-freiburg.de

Authors

Melina I. Feldhof − *Department of Organic Chemistry and Macromolecular Chemistry, Heinrich-Heine-University Düsseldorf, 40225 Düsseldorf, Germany*

Rebecca Schlatterer − *Institute of Physical Chemistry, 79104 Freiburg, Germany;* orcid.org/0000-0003-4983-2644

Friederike Strahl − *Institute of Physical Chemistry, 79104 Freiburg, Germany*

Jonathan Garthe − *Institute of Physical Chemistry I, Heinrich-Heine-University Düsseldorf, 40225 Düsseldorf, Germany*

Sylvain Prévost − *Instrument Responsible D11, Institut Max von Laue − Paul Langevin (ILL), 38042 Grenoble, France*

Stephan Schmidt − *Cluster of Excellence livMatS @ FIT-Freiburg Center for Interactive Materials and Bioinspired Technologies, University of Freiburg, 79110 Freiburg, Germany;* orcid.org/0000-0002-4357-304X

Matthias Karg − *Institute of Physical Chemistry I, Heinrich-Heine-University Düsseldorf, 40225 Düsseldorf, Germany; Physical Chemistry of Functional Polymers, Martin Luther University Halle-Wittenberg, 06120 Halle (Saale), Germany*

Complete contact information is available at: https://pubs.acs.org/10.1021/jacs.5c08232

Author Contributions

◆M.I.F. and R.S. contributed equally to this work. The manuscript was written through the contributions of all authors. All authors have given approval to the final version of the manuscript.

Funding

This project was supported by the Deutsche Forschungsgemeinschaft (DFG, German Research Foundation) under Germany's Excellence Strategy−EXC-2193/1−390951807 (livMatS) (B.N.B.) and DFG grant BA 7349/1−1 (R.S., F.S., B.N.B.).

Notes

The authors declare no competing financial interest.

■ ACKNOWLEDGMENTS

Thanks to the CeMSA@HHU (Center for Molecular and Structural Analytics @ Heinrich Heine University) for recording the mass-spectrometric and the NMR-spectroscopic data. The authors thank the Institut Laue-Langevin for allocation of SANS beamtime on D22; data are available on demand (DOI:10.5291/ILL-DATA.9-10-1845). We thank Thorsten Hugel (University of Freiburg) and Ralf Ludwig (University of Rostock) for fruitful discussions.

■ REFERENCES

(1) Purcell, S. C.; Godula, K. Synthetic glycoscapes: addressing the structural and functional complexity of the glycocalyx. *Interface Focus* **2019**, *9* (2), No. 20180080.

(2) Varki, A.; Cummings, R. D.; Esko, J. D.; Stanley, P.; Hart, G. W.; Aebi, M.; Darvill, A. G.; Kinoshita, T.; Packer, N. H.; Prestegard, J. H.et al. *Essentials of Glycobiology*; Cold Spring Harbor Laboratory Press, 2022.

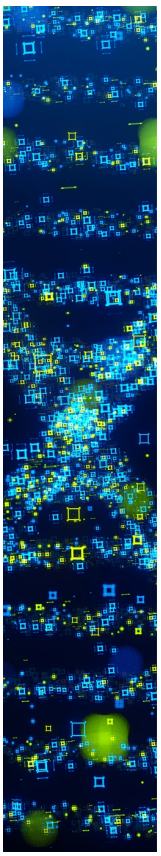
(3) Bafna, S.; Kaur, S.; Batra, S. K. Membrane-bound mucins: the mechanistic basis for alterations in the growth and survival of cancer cells. *Oncogene* **2010**, *29* (20), 2893−2904.

(4) Bansil, R.; Turner, B. S. Mucin structure, aggregation, physiological functions and biomedical applications. *Curr. Opin. Colloid Interface Sci.* **2006**, *11* (2−3), 164−170.
(5) Coles, J. M.; Chang, D. P.; Zauscher, S. Molecular mechanisms of aqueous boundary lubrication by mucinous glycoproteins. *Curr. Opin. Colloid Interface Sci.* **2010**, *15* (6), 406−416.
(6) Lai, S. K.; Wang, Y.-Y.; Wirtz, D.; Hanes, J. Micro-and macrorheology of mucus. *Adv. Drug Delivery Rev.* **2009**, *61* (2), 86−100.
(7) Linden, S. K.; Sutton, P.; Karlsson, N.; Korolik, V.; McGuckin, M. Mucins in the mucosal barrier to infection. *Mucosal immunol.* **2008**, *1* (3), 183−197.
(8) Yakubov, G. E.; McColl, J.; Bongaerts, J. H.; Ramsden, J. J. Viscous boundary lubrication of hydrophobic surfaces by mucin. *Langmuir* **2009**, *25* (4), 2313−2321.
(9) Käsdorf, B. T.; Weber, F.; Petrou, G.; Srivastava, V.; Crouzier, T.; Lieleg, O. Mucin-inspired lubrication on hydrophobic surfaces. *Biomacromolecules* **2017**, *18* (8), 2454−2462.
(10) Hsu, S. M. Boundary lubrication: current understanding. *Tribol. Lett.* **1997**, *3* (1), 1−11.
(11) Marczynski, M.; Balzer, B. N.; Jiang, K.; Lutz, T. M.; Crouzier, T.; Lieleg, O. Charged glycan residues critically contribute to the adsorption and lubricity of mucins. *Colloids Surf., B* **2020**, *187*, No. 110614.
(12) Schlatterer, R.; Marczynski, M.; Hermann, B.; Lieleg, O.; Balzer, B. N. Unfolding of von Willebrand Factor Type D Like Domains Promotes Mucin Adhesion. *Nano Lett.* **2025**, *25*, 1765−1774.
(13) Petrou, G.; Crouzier, T. Mucins as multifunctional building blocks of biomaterials. *Biomater. Sci.* **2018**, *6* (9), 2282−2297.
(14) Authimoolam, S. P.; Dziubla, T. D. Biopolymeric mucin and synthetic polymer analogs: Their structure, function and role in biomedical applications. *Polymers* **2016**, *8* (3), No. 71.
(15) Kwan, C. S.; Cerullo, A. R.; Braunschweig, A. B. Design and Synthesis of Mucin-Inspired Glycopolymers. *ChemPlusChem* **2020**, *85* (12), 2704−2721.
(16) Bej, R.; Stevens, C. A.; Nie, C.; Ludwig, K.; Degen, G. D.; Kerkhoff, Y.; Pigaleva, M.; Adler, J. M.; Bustos, N. A.; Page, T. M.; et al. Mucus-Inspired Self-Healing Hydrogels: A Protective Barrier for Cells against Viral Infection. *Adv. Mater.* **2024**, *36* (32), No. 2401745.
(17) Rabuka, D.; Parthasarathy, R.; Lee, G. S.; Chen, X.; Groves, J. T.; Bertozzi, C. R. Hierarchical assembly of model cell surfaces: synthesis of mucin mimetic polymers and their display on supported bilayers. *J. Am. Chem. Soc.* **2007**, *129* (17), 5462−5471.
(18) Bej, R.; Nie, C.; Ludwig, K.; Ahmadi, V.; Trimpert, J.; Adler, J. M.; Povolotsky, T. L.; Achazi, K.; Kagelmacher, M.; Vidal, R. M.; et al. Mucin-Inspired Single-Chain Polymer (MIP) Fibers as Potent SARS-CoV-2 Inhibitors. *Angew. Chem., Int. Ed.* **2023**, *62* (29), No. e202304010.
(19) Dubber, M.; Sperling, O.; Lindhorst, T. K. Oligomannoside mimetics by glycosylation of 'octopus glycosides' and their investigation as inhibitors of type 1 fimbriae-mediated adhesion of *Escherichia coli*. *Org. Biomol. Chem.* **2006**, *4* (21), 3901−3912.
(20) Luis, A. S.; Yates, E. A.; Cartmell, A. Functions and specificity of bacterial carbohydrate sulfatases targeting host glycans. *Essays Biochem.* **2023**, *67* (3), 429−442.
(21) Ribeiro, J. P. M.; Mendonça, P. V.; Coelho, J. F.; Matyjaszewski, K.; Serra, A. C. Glycopolymer brushes by reversible deactivation radical polymerization: Preparation, applications, and future challenges. *Polymers* **2020**, *12* (6), No. 1268.
(22) Wang, Y.; Gu, L.; Xu, F.; Xin, F.; Ma, J.; Jiang, M.; Fang, Y. Chemoenzymatic synthesis of branched glycopolymer brushes as the artificial glycocalyx for lectin specific binding. *Langmuir* **2019**, *35* (13), 4445−4452.
(23) Park, H.; Rosencrantz, R. R.; Elling, L.; Böker, A. Glycopolymer Brushes for Specific Lectin Binding by Controlled Multivalent Presentation of N-Acetyllactosamine Glycan Oligomers. *Macromol. Rapid Commun.* **2015**, *36* (1), 45−54.
(24) Martínez-Bailén, M.; Rojo, J.; Ramos-Soriano, J. Multivalent glycosystems for human lectins. *Chem. Soc. Rev.* **2023**, *52* (2), 536−572.
(25) Shamout, F.; Monaco, A.; Yilmaz, G.; Becer, C. R.; Hartmann, L. Synthesis of Brush-Like Glycopolymers with Monodisperse, Sequence-Defined Side Chains and Their Interactions with Plant and Animal Lectins. *Macromol. Rapid Commun.* **2020**, *41* (1), No. 1900459.
(26) Von der Ehe, C.; Weber, C.; Gottschaldt, M.; Schubert, U. S. Immobilized glycopolymers: Synthesis, methods and applications. *Prog. Polym. Sci.* **2016**, *57*, 64−102.
(27) Xie, G.; Martinez, M. R.; Olszewski, M.; Sheiko, S. S.; Matyjaszewski, K. Molecular bottlebrushes as novel materials. *Biomacromolecules* **2019**, *20* (1), 27−54.
(28) Miura, Y. Design and synthesis of well-defined glycopolymers for the control of biological functionalities. *Polym. J.* **2012**, *44* (7), 679−689.
(29) von der Ehe, C.; Weber, C.; Wagner, M.; Czaplewska, J. A.; Gottschaldt, M.; Schubert, U. S. Synthesis of Thermoresponsive Glycopolymers Combining RAFT Polymerization, Thiol-Ene Reaction, and Subsequent Immobilization onto Solid Supports. *Macromol. Chem. Phys.* **2014**, *215* (13), 1306−1318.
(30) Spain, S. G.; Gibson, M. I.; Cameron, N. R. Recent advances in the synthesis of well-defined glycopolymers. Journal of Polymer Science Part A. *Polym. Chem.* **2007**, *45* (11), 2059−2072.
(31) Ting, S. R. S.; Chen, G.; Stenzel, M. H. Synthesis of glycopolymers and their multivalent recognitions with lectins. *Polym. Chem.* **2010**, *1* (9), 1392−1412.
(32) Gauthier, M. A.; Gibson, M. I.; Klok, H. A. Synthesis of functional polymers by post-polymerization modification. *Angew. Chem., Int. Ed.* **2009**, *48* (1), 48−58.
(33) Theato, P.; Klok, H.-A. *Functional Polymers by Post-Polymerization Modification: Concepts, Guidelines and Applications*; John Wiley & Sons, 2013.
(34) Batz, H. G.; Franzmann, G.; Ringsdorf, H. Model reactions for synthesis of pharmacologically active polymers by way of monomeric and polymeric reactive esters. *Angew. Chem., Int. Ed.* **1972**, *11* (12), 1103−1104.
(35) Das, A.; Theato, P. Multifaceted synthetic route to functional polyacrylates by transesterification of poly (pentafluorophenyl acrylates). *Macromolecules* **2015**, *48* (24), 8695−8707.
(36) Crouzier, T.; Boettcher, K.; Geonnotti, A. R.; Kavanaugh, N. L.; Hirsch, J. B.; Ribbeck, K.; Lieleg, O. Modulating mucin hydration and lubrication by deglycosylation and polyethylene glycol binding. *Adv. Mater. Interfaces* **2015**, *2* (18), No. 1500308.
(37) Lieleg, O.; Lieleg, C.; Bloom, J.; Buck, C. B.; Ribbeck, K. Mucin biopolymers as broad-spectrum antiviral agents. *Biomacromolecules* **2012**, *13* (6), 1724−1732.
(38) Co, J. Y.; Crouzier, T.; Ribbeck, K. Probing the role of mucin-bound glycans in bacterial repulsion by mucin coatings. *Adv. Mater. Interfaces* **2015**, *2* (17), No. 1500179.
(39) Blawitzki, L.-C.; Bartels, N.; Bonda, L.; Schmidt, S.; Monzel, C.; Hartmann, L. Glycomacromolecules to Tailor Crowded and Heteromultivalent Glycocalyx Mimetics. *Biomacromolecules* **2024**, *25* (9), 5979−5994.
(40) Blawitzki, L. C.; Monzel, C.; Schmidt, S.; Hartmann, L. Selective Glycan Presentation in Liquid-Ordered or-Disordered Membrane Phases and its Effect on Lectin Binding. *Angew. Chem., Int. Ed.* **2025**, *64* (2), No. e202414847.
(41) Ebbesen, M. F.; Gerke, C.; Hartwig, P.; Hartmann, L. Biodegradable poly (amidoamine) s with uniform degradation fragments via sequence-controlled macromonomers. *Polym. Chem.* **2016**, *7* (46), 7086−7093.
(42) Ponader, D.; Wojcik, F.; Beceren-Braun, F.; Dernedde, J.; Hartmann, L. Sequence-defined glycopolymer segments presenting mannose: synthesis and lectin binding affinity. *Biomacromolecules* **2012**, *13* (6), 1845−1852.

https://doi.org/10.1021/jacs.5c08232
J. Am. Chem. Soc. 2025, 147, 32698−32709

(43) Zemplén, G.; Pacsu, E. Über die Verseifung acetylierter Zucker und verwandter Substanzen. *Ber. Dtsch. Chem. Ges.* **1929**, *62* (6), 1613−1614.
(44) Illmann, M. D.; Schäfl, L.; Drees, F.; Hartmann, L.; Schmidt, S. Glycan-Presenting Coacervates Derived from Charged Poly (active esters): Preparation, Phase Behavior, and Lectin Capture. *Biomacromolecules* **2023**, *24* (6), 2532−2540.
(45) Boyer, C.; Davis, T. P. One-pot synthesis and biofunctionalization of glycopolymers via RAFT polymerization and thiol−ene reactions. *Chem. Commun.* **2009**, No. 40, 6029−6031.
(46) Hoffmann, M.; Snyder, N. L.; Hartmann, L. Glycosaminoglycan Mimetic Precision Glycomacromolecules with Sequence-Defined Sulfation and Rigidity Patterns. *Biomacromolecules* **2022**, *23* (9), 4004−4014.
(47) Chen, Y.; Lord, M. S.; Piloni, A.; Stenzel, M. H. Correlation between molecular weight and branch structure of glycopolymers stars and their binding to lectins. *Macromolecules* **2015**, *48* (2), 346−357.
(48) Sletten, E. T.; Loka, R. S.; Yu, F.; Nguyen, H. M. Glycosidase inhibition by multivalent presentation of heparan sulfate saccharides on bottlebrush polymers. *Biomacromolecules* **2017**, *18* (10), 3387−3399.
(49) Zhang, C.; Peng, H.; Puttick, S.; Reid, J.; Bernardi, S.; Searles, D. J.; Whittaker, A. K. Conformation of hydrophobically modified thermoresponsive poly (OEGMA-co-TFEA) across the LCST revealed by NMR and molecular dynamics studies. *Macromolecules* **2015**, *48* (10), 3310−3317.
(50) Strzelczyk, A. K.; Paul, T. J.; Schmidt, S. Quantifying Thermoswitchable Carbohydrate-Mediated Interactions via Soft Colloidal Probe Adhesion Studies. *Macromol. Biosci.* **2020**, *20* (10), No. 2000186.
(51) Paul, T. J.; Strzelczyk, A. K.; Feldhof, M. I.; Schmidt, S. Temperature-Switchable Glycopolymers and Their Conformation-Dependent Binding to Receptor Targets. *Biomacromolecules* **2020**, *21* (7), 2913−2921.
(52) Hammouda, B.SANS from homogeneous polymer mixtures: A unified overview. In *Advances in Polymer Science*; Springer, 2005; pp 87−133.
(53) Flory, P. J. *Principles of Polymer Chemistry*; Cornell university press, 1953.
(54) Flory, P. J.; Volkenstein, M. *Statistical Mechanics of Chain Molecules*; Wiley Online Library, 1969.
(55) Hammouda, B.; Ho, D. L. Insight into chain dimensions in PEO/water solutions. *J. Polym. Sci., Part B:Polym. Phys.* **2007**, *45* (16), 2196−2200.
(56) Netopilík, M. Model analysis of the determination of the Mark—Houwink—Kuhn—Sakurada parameters and molecular weight distribution by means of size exclusion chromatography with dual detection. *Polymer* **1994**, *35* (22), 4799−4803.
(57) Carpenter, J.; Wang, Y.; Gupta, R.; Li, Y.; Haridass, P.; Subramani, D. B.; Reidel, B.; Morton, L.; Ridley, C.; O'Neal, W. K.; et al. Assembly and organization of the N-terminal region of mucin MUC5AC: Indications for structural and functional distinction from MUC5B. *Proc. Natl. Acad. Sci. U.S.A.* **2021**, *118* (39), No. e2104490118.
(58) Marczynski, M.; Lutz, T. M.; Schlatterer, R.; Henkel, M.; Balzer, B. N.; Lieleg, O. Contamination with black carbon nanoparticles alters the selective permeability of mucin hydrogels: implications for molecular transport across mucosal barriers. *ACS Appl. Nano Mater.* **2022**, *5* (11), 16955−16970.
(59) Wang, X.; Du, M.; Han, H.; Song, Y.; Zheng, Q. Boundary lubrication by associative mucin. *Langmuir* **2015**, *31* (16), 4733−4740.
(60) Claesson, P. M.; Christenson, H. K.; Berg, J. M.; Neuman, R. D. Interactions between mica surfaces in the presence of carbohydrates. *J. Colloid Interface Sci.* **1995**, *172* (2), 415−424.
(61) Janshoff, A.; Neitzert, M.; Oberdörfer, Y.; Fuchs, H. Force spectroscopy of molecular systems—single molecule spectroscopy of polymers and biomolecules. *Angew. Chem., Int. Ed.* **2000**, *39* (18), 3212−3237.
(62) Giannotti, M. I.; Vancso, G. J. Interrogation of single synthetic polymer chains and polysaccharides by AFM-based force spectroscopy. *ChemPhysChem* **2007**, *8* (16), 2290−2307.
(63) Balzer, B. N.; Gallei, M.; Hauf, M. V.; Stallhofer, M.; Wiegleb, L.; Holleitner, A.; Rehahn, M.; Hugel, T. Nanoscale friction mechanisms at solid-liquid interfaces. *Angew. Chem., Int. Ed.* **2013**, *52* (25), 6541−6544, DOI: 10.1002/anie.201301255.
(64) Horinek, D.; Serr, A.; Geisler, M.; Pirzer, T.; Slotta, U.; Lud, S. Q.; Garrido, J. A.; Scheibel, T.; Hugel, T.; Netz, R. R. Peptide adsorption on a hydrophobic surface results from an interplay of solvation, surface, and intrapeptide forces. *Proc. Natl. Acad. Sci. U.S.A.* **2008**, *105* (8), 2842−2847.
(65) Kienle, S.; Gallei, M.; Yu, H.; Zhang, B.; Krysiak, S.; Balzer, B. N.; Rehahn, M.; Schlüter, A. D.; Hugel, T. Effect of molecular architecture on single polymer adhesion. *Langmuir* **2014**, *30* (15), 4351−4357.
(66) Krysiak, S.; Wei, Q.; Rischka, K.; Hartwig, A.; Haag, R.; Hugel, T. Adsorption mechanism and valency of catechol-functionalized hyperbranched polyglycerols. *Beilstein J. Org. Chem.* **2015**, *11* (1), 828−836.
(67) Petrovskii, V. S.; Potemkin, I. I. Effect of Macromolecular Architecture on Adhesion. *Langmuir* **2025**, *41* (1), 371−377.
(68) Cai, W.; Jäger, M.; Bullerjahn, J. T.; Hugel, T.; Wolf, S.; Balzer, B. N. Anisotropic Friction in a Ligand-Protein Complex. *Nano Lett.* **2023**, *23* (10), 4111−4119.
(69) Cai, W.; Bullerjahn, J. T.; Lallemang, M.; Kroy, K.; Balzer, B. N.; Hugel, T. Angle-dependent strength of a single chemical bond by stereographic force spectroscopy. *Chem. Sci.* **2022**, *13* (19), 5734−5740.
(70) Kolberg, A.; Wenzel, C.; Hackenstrass, K.; Schwarzl, R.; Rüttiger, C.; Hugel, T.; Gallei, M.; Netz, R. R.; Balzer, B. N. Opposing Temperature Dependence of the Stretching Response of Single PEG and PNiPAM Polymers. *J. Am. Chem. Soc.* **2019**, *141* (29), 11603−11613.
(71) Walder, R.; LeBlanc, M.-A.; Van Patten, W. J.; Edwards, D. T.; Greenberg, J. A.; Adhikari, A.; Okoniewski, S. R.; Sullan, R. M. A.; Rabuka, D.; Sousa, M. C.; Perkins, T. T. Rapid Characterization of a Mechanically Labile α-Helical Protein Enabled by Efficient Site-Specific Bioconjugation. *J. Am. Chem. Soc.* **2017**, *139* (29), 9867−9875.
(72) Kolberg, A.; Wenzel, C.; Hugel, T.; Gallei, M.; Balzer, B. N. Covalent Attachment of Single Molecules for AFM-based Force Spectroscopy. *J. Vis. Exp.* **2020**, No. 157, No. e60934, DOI: 10.3791/60934.
(73) Ibrahim, M.; Wenzel, C.; Lallemang, M.; Balzer, B. N.; Schwierz, N. Adsorbing DNA to Mica by Cations: Influence of Valency and Ion Type. *Langmuir* **2023**, *39* (44), 15553−15562.
(74) Pirzer, T.; Hugel, T. Adsorption Mechanism of Polypeptides and Their Location at Hydrophobic Interfaces. *ChemPhysChem* **2009**, *10* (16), 2795−2799.
(75) Liese, S.; Gensler, M.; Krysiak, S.; Schwarzl, R.; Achazi, A.; Paulus, B.; Hugel, T.; Rabe, J. P.; Netz, R. R. Hydration Effects Turn a Highly Stretched Polymer from an Entropic into an Energetic Spring. *ACS Nano* **2017**, *11* (1), 702−712.
(76) Geisler, M.; Horinek, D.; Hugel, T. Single Molecule Adhesion Mechanics on Rough Surfaces. *Macromolecules* **2009**, *42* (23), 9338−9343.
(77) Friedsam, C.; Gaub, H. E.; Netz, R. R. Probing surfaces with single-polymer atomic force microscope experiments. *Biointerphases* **2006**, *1* (1), MR1−MR21.
(78) Lallemang, M.; Yu, L.; Cai, W.; Rischka, K.; Hartwig, A.; Haag, R.; Hugel, T.; Balzer, B. N. Multivalent non-covalent interactions lead to strongest polymer adhesion. *Nanoscale* **2022**, *14* (10), 3768−3776.
(79) Kanduč, M.; Netz, R. R. Hydration force fluctuations in hydrophilic planar systems. *Biointerphases* **2016**, *11*, No. 019004.
(80) Schwierz, N.; Horinek, D.; Liese, S.; Pirzer, T.; Balzer, B. N.; Hugel, T.; Netz, R. R. On the relationship between peptide

adsorption resistance and surface contact angle: a combined experimental and simulation single-molecule study. *Proc. Natl. Acad. Sci. U.S.A.* **2012**, *134* (48), 19628−19638.
(81) Fischer, L.; Strzelczyk, A. K.; Wedler, N.; Kropf, C.; Schmidt, S.; Hartmann, L. Sequence-defined positioning of amine and amide residues to control catechol driven wet adhesion. *Chem. Sci.* **2020**, *11* (36), 9919−9924.
(82) Boland, T.; Ratner, B. Direct measurement of hydrogen bonding in DNA nucleotide bases by atomic force microscopy. *Proc. Natl. Acad. Sci. U.S.A.* **1995**, *92* (12), 5297−5301.
(83) Shen, X.-C.; Bao, L.; Zhang, Z.-L.; Liu, X.; Pang, D.-W.; Xu, J. A simple and effective sample preparation method for atomic force microscopy visualization of individual DNA molecules in situ. *Mol. Biol. Rep.* **2011**, *38*, 965−969.
(84) Ibrahim, M.; Wenzel, C.; Lallemang, M.; Balzer, B. N.; Schwierz, N. Adsorbing DNA to mica by cations: influence of valency and ion type. *Langmuir* **2023**, *39* (44), 15553−15562.
(85) Kawanishi, N.; Christenson, H. K.; Ninham, B. W. Measurement of the interaction between adsorbed polyelectrolytes: gelatin on mica surfaces. *J. Phys. Chem. A* **1990**, *94* (11), 4611−4617.
(86) Stanley, C.; Rau, D. C. Evidence for water structuring forces between surfaces. *Curr. Opin. Colloid Interface Sci.* **2011**, *16* (6), 551−556.
(87) Gonella, G.; Backus, E. H.; Nagata, Y.; Bonthuis, D. J.; Loche, P.; Schlaich, A.; Netz, R. R.; Kühnle, A.; McCrum, I. T.; Koper, M. T.; et al. Water at charged interfaces. *Nat. Rev. Chem.* **2021**, *5* (7), 466−485.
(88) Kubincová, A.; Hünenberger, P. H.; Krishnan, M. Interfacial solvation can explain attraction between like-charged objects in aqueous solution. *J. Chem. Phys.* **2020**, *152* (10), No. 104713.
(89) Samanta, R.; Halabe, A.; Ganesan, V. Influence of charge regulation and charge heterogeneity on complexation between polyelectrolytes and proteins. *J. Phys. Chem. B* **2020**, *124* (22), 4421−4435.
(90) Cowman, M. K.; Li, M.; Balazs, E. A. Tapping mode atomic force microscopy of hyaluronan: extended and intramolecularly interacting chains. *Biophys. J.* **1998**, *75* (4), 2030−2037.
(91) Cowman, M. K.; Spagnoli, C.; Kudasheva, D.; Li, M.; Dyal, A.; Kanai, S.; Balazs, E. A. Extended, relaxed, and condensed conformations of hyaluronan observed by atomic force microscopy. *Biophys. J.* **2005**, *88* (1), 590−602.
(92) Spagnoli, C.; Korniakov, A.; Ulman, A.; Balazs, E. A.; Lyubchenko, Y. L.; Cowman, M. K. Hyaluronan conformations on surfaces: effect of surface charge and hydrophobicity. *Carbohydr. Res.* **2005**, *340* (5), 929−941.
(93) Spagnoli, C.; Loos, K.; Ulman, A.; Cowman, M. K. Imaging structured water and bound polysaccharide on mica surface at ambient temperature. *J. Am. Chem. Soc.* **2003**, *125* (23), 7124−7128.


CAS BIOFINDER DISCOVERY PLATFORM™
STOP DIGGING THROUGH DATA —START MAKING DISCOVERIES
CAS BioFinder helps you find the right biological insights in seconds
Start your search
CAS
A division of the American Chemical Society

https://doi.org/10.1021/jacs.5c08232
J. Am. Chem. Soc. 2025, 147, 32698−32709

3.4 Sequence-Defined Oligoamidoamines as Macroinitiator for Thiol-Induced, Light-Activated Controlled Radical Polymerization of Star-Shaped Glyco-block-copolymers

Authors: Melina I. Feldhof, Ben Raunitschke, Jolana Both, Susanne Boye and Laura Hartmann

Issue: under preparation

First author contribution:

Author contribution: Collaborative project development. Development of the synthetic methodology, collaborative synthesis and characterization of the star-shaped glycopolymers. Collaborative writing of the manuscript.

Sequence-Defined Oligoamidoamines as Macroinitiator for Thiol-Induced, Light-Activated Controlled Radical Polymerization of Star-Shaped Glyco-block-copolymers

Melina I. Feldhof,[a] Ben Raunitschke,[a] Jolana Both,[a] Susanne Boye[b] and Laura Hartmann[*c]*

a *M. I. Feldhof, Jolana Both, Ben Raunitschke, Department of Organic and Macromolecular Chemistry, Heinrich-Heine-University Düsseldorf, Universitätsstraße 1, 40225 Düsseldorf, Germany.*

b *S. Boye, Advanced Macromolecular Structure Analysis, Leibniz-Institut für Polymerforschung Dresden, Hohe Str. 6, 01069 Dresden, Germany*

c *Prof. Dr. Laura Hartmann, Institute for Macromolecular Chemistry, University of Freiburg, Stefan-Meier-Str. 31, D-79104 Freiburg i.Br., Germany, E-mail: laura.hartmann@makro.uni-freiburg.de.*

Keywords: thiol-induced light-activated controlled radical polymerization, star-shaped glycol-block-copolymers, macroinitiator, solid phase synthesis

We present the synthesis of homo- and hetero-star glycopolymers by combining sequence-defined macroinitators directly accessible through standard solid phase chemistry and thiol-induced, light-activated controlled radical polymerization (TIRP). This approach allows for high variability as well as control over structural parameters such as chemical composition of the core and arms as well as the number, density and length of arms.

Introduction

Star-shaped polymers are a class of branched macromolecules with unique properties due to their complex three-dimensional structure compared to linear analogues.[1, 2] From a structural point-of-view, a core links at least three linear polymers, the so-called arms, to form a star-shaped polymer.[3, 4] Identical arms form homo-star polymers, while hetero-star polymers comprise at least two different monomeric units e.g., classified as core-shell architecture for block-copolymers as arm or micto-arm star polymers with different polymers as arms.[3] In terms of their properties, star-shaped polymers have higher compactness and segmental density near the core resulting in reduced viscosities and greater solubility compared to linear structures with comparable molecular weights.[5] These unique properties have led to successful applications in materials science, medicine and pharmacy e.g., as drug delivery systems.[6, 7] Two main synthetic approaches have been established to derive star-shaped polymers: the arm-first and the core-first approach.[8] In the arm-first approach, the polymeric arms are synthesized first before connecting them via crosslinking reactions.[9] The individual arms can be well controlled due to independent synthesis, but limitations include varying arm quantity as stars often have a distribution in the total number of arms and persistent linear chains require removal.[3, 10-12] In the core-first approach, initiation of the polymerization to derive the polymeric arms occurs on the core that needs to carry multiple initiator units for this purpose. In order to ensure efficient initiation at all initiator units, typically, controlled polymerization processes are employed such as reversible addition−fragmentation chain-transfer polymerization (RAFT) or atom transfer radical polymerization (ATRP).[10, 13-15] The precise number of arms can be controlled by the number of initiating functionalities present on the multifunctional core, provided the initiating sites have equal reactivity and require no additional coupling or cross-linking reactions.[12] Recently, we introduced the thiol-induced, light-activated controlled radical polymerization (TIRP) method, using readily available thiol initiators, including simple organic thiols and high molecular weight proteins with free cysteine residues.[16-19] TIRP is also particularly suitable for hydrophilic monomers with larger side groups such as glycomonomers giving access to glycopolymers.[16-18] Here, we extend this approach to using oligomers with multiple thiol groups as macroinitiators for TIRP to generate star-shape polymers (Figure 1). Solid phase peptide and polymer synthesis are well-established methods using easily accessible and commercially available building blocks such as amino acids to derive monodisperse, sequence-defined macromolecules. Here we make use of such defined macromolecules to derive highly defined and customized core structures in the synthesis of star-shape polymers. From the site-selective introduction of multiple thiol groups the number and density of polymeric arms is controlled.

Using TIRP, these arms can also be synthesized as block-copolymer structures by re-initiating the chain end after polymerizing the first monomer and introducing a second monomer block. Thereby we obtain both homo- and block-copolymer star-shaped polymers, demonstrating the applicability to get access to functional polymers by using mannose-acrylamide monomer and deriving a library of mannose-block-copolymers that can selectively interact with model lectin Concanavalin A (ConA). First binding studies demonstrate that variation of structural parameters such as the number and length of glycopolymer arms affects the lectin binding capacity with the star glyco-block-copolymer with the highest number of carbohydrates showing the highest binding capacity. It is well established that many pathogens use carbohydrate-lectin interactions in their infection processes. In the future, such star-shape glycopolymers could thus be further investigated for their use as antibacterial or antiviral agents.[20]

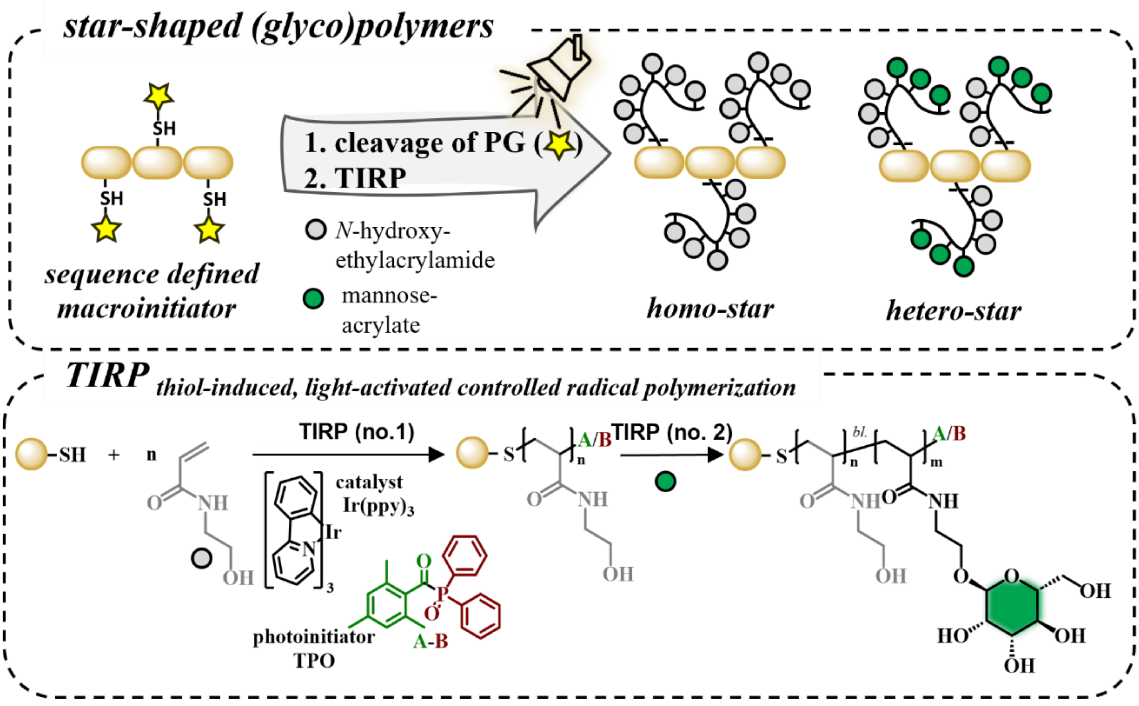


Figure 1. Schematic representation of star-shaped homo- and block-copolymers using macroinitiators synthesized via SPPoS and TIRP. Reaction conditions of 1. cleavage of the protecting group (PG) - DMF, 15 min, 365 nm, 576.4 mW/cm² and 2. TIRP - DMF, 120 min, 405 nm, 1.15 mW/cm², 1 eq. TPO, 0.05 mol% $Ir(ppy)_3$, 10 eq. tris(2-carboxyethyl)phosphine.

Results and Discussion

First, we synthesized a series of oligomers containing cysteine (Cys) for introducing thiol side chains to be used as macroinitiators in TIRP following previously established solid phase protocols (see SI for details). Cys was combined with ethylene glycol diamine succinic acid (EDS)[21] as well-established building block to vary the positioning of Cys within the oligomer

backbone and commercially available tyrosine to allow for later ^{1}H-NMR analysis. The number of Cys was varied from one to three to derive star-shape polymers with one or three arms, accordingly. Additionally, in the trivalent structure the spacing between the Cys was varied by introducing EDS building blocks. To maintain the same molar mass of the different macroinitiators as well as to ensure sufficient solubility, all oligomers contain three EDS building blocks in total (Figure 2). In order to avoid disulfide formation of the free thiols and thus formation of unwanted side products, thiol groups were protected during solid phase assembly using UV-cleavable 2-nitroveratryl (*o*NV) protecting group (Figure 2).[22] We chose the photolabile *o*NV protecting group as it can be efficiently cleaved at 365 nm,[22] which offers rapid, selective and gentle cleavage conditions and allows a one-pot deprotection-TIRP reaction using the same set-up for both, deprotection and polymerization. Two strategies were explored for efficient introduction of *o*NV protecting groups: synthesis of a *o*NV protected cysteine building block and exchange of the protecting groups on cysteine containing oligomers. Fluorenylmethoxycarbonyl-Cys(*o*Nv)-OH was successfully synthesized and used to derive oligomer **MI-2**, **MI-3** applying standard coupling conditions (see SI for detail information). The advantage of this route is the universal applicability of this building block to derive various oligomeric structures. An apparent disadvantage is the handling, as strict light exclusion had to be maintained during the entire synthesis to prevent thiol deprotection and unintended side reactions. For the second option, the oligomer is first built up using commercially available Fmoc-Cys(Trityl)-OH. While still attached to the resin, Trityl (Trt) protecting groups are cleaved and replaced with *o*Nv protecting groups (see SI for details on the synthetic procedure). All oligomers used in the following as macroinitiators for TIRP were synthesized by this second route and were fully characterized by ^{1}H-NMR, RP-HPLC-MS, MALDI and HR-ESI MS (see SI).

For the use as macroinitiators in a one-pot reaction, the *o*NV temporary protective groups of the oligomer must be removed quickly and quantitatively without causing unintended side reactions with other components, such as the acrylamide monomers. Cleavage of *o*NV protecting groups from the oligomers was investigated by irradiating the macroinitiators **MI-1** and **MI-3**, at 365 nm and 405 nm and following the reaction via RP-HPLC-MS (see SI). TIRP operates at a wavelength of 405 nm, which could potentially enable a single-step, one-pot process combining deprotection and polymerization reactions if efficient cleavage occurs under these conditions. Full deprotection of all tested macroinitiators was observed in 2 to 10 minutes at 365 nm. At 405 nm, the cleavage was slower, with full cleavage after 10 to 25 minutes. Thus, since activation of the radical initiator and initiation in TIRP is faster than 10 minutes, a one

step-one pot reaction is not possible using *o*Nv protected macroinitiators. Arm growth initiation at the core should also be faster than the chain growth/arm growth itself.[23, 24] This would not be feasible with a slow deprotection while initiation would already partially occur. Thus, a two step-one pot deprotection/polymerization procedure was explored further.

Previously, we have established the use of TIRP as a controlled radical polymerization method, particularly for the preparation of glycopolymers[16-18], and to provide access to protein-polymer conjugates with high molar masses and low dispersities.[17] Only the presentation of one easily accessible thiol as initiator is required for polymerization via TIRP, which can then be polymerized efficiently at an irradiation wavelength of 405 nm with the photoinitiator diphenyl(2,4,6-trimethylbenzoyl) phosphine oxide (TPO) and the catalyst tris(2-phenylpyridine)iridium ($Ir(ppy)_3$). Here we now explore oligomers presenting multiple thiol side chains as macroinitiators to derive star-shape polymers from a core-first approach. Consequently, the previously prepared oligomers were used as macroinitiators for the preparation of linear (**MI-1** – $f = 1$) and star-shaped (**MI-2**, **MI-3** – $f = 3$) polymers in a two-step, one-pot reaction (Figure 2).

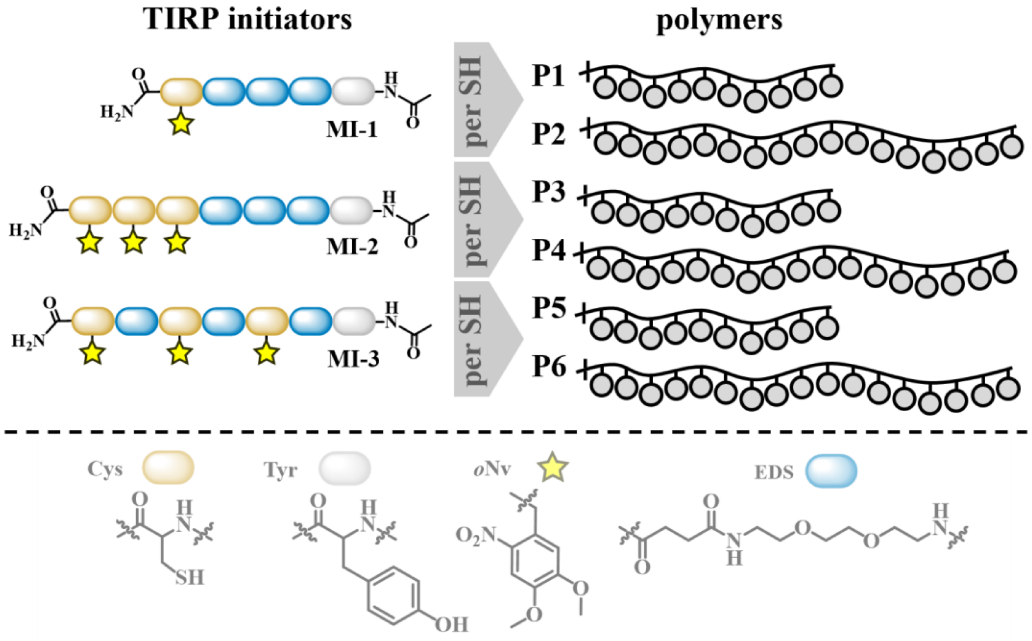


Figure 2. Summary of Macroinitiators **MI-1** – **MI-3** and the schematic representation of the synthesized (star-shaped) p(HEAA) polymers **P1** - **P6**.

Therefore, the corresponding macroinitiator was first deprotected for 15 min at a wavelength of 365 nm and an intensity of 576.4 mW/cm² and then mixed immediately with all other components required for TIRP, for 120 min, irradiation at 405 nm with an intensity of 1.15 mW/cm². The formed poly(*N*-hydroxyethyl acrylamide) (pHEAA) polymers **P1-P6** were isolated by precipitation in diethylether, dialyzed against water and analyzed via ^{1}H-NMR and

aqueous SEC with a quintuple detection (SEC-D5, see SI). The analytical results are summarized in Table 1.

Table 1. Summary of the synthesized (star-shaped) polymers and their characteristic results from SEC-D5.

sample	*f*	$M_{n,\,theor.}$ *1 [kDa]	M_n *2 [kDa]	Đ*2 [M_w/M_n]	Pn per SH	a_{KMHS} *2	$R_{h,h}$ *2 [nm]	$R_{h,DLS}$ *2 [nm]	normal elution
P1	1	18	28.5	1.34	239	0.736	6.0	4.4	✓
P2	1	104	49.2	1.40	416	0.739	8.6	7.0	✓
P3	3	19	12.9	1.15	34	0.635	3.4	-	×
P4	3	53	25.6	1.30	71	0.674	5.6	3.7	×
P5	3	19	14.5	1.15	38	0.643	3.6	1.8	×
P6	3	53	26.0	1.27	72	0.713	5.4	3.6	×

*[1]theoretically determined value; *[2]determined by SEC-D5 (more experimental information can be found in SI)

The characterization of star-shaped polymers is generally challenging due to their branched architecture and the resulting changes in their solution properties. Their compact structure causes them to elute later in GPC than linear polymers of the same molar mass, leading to inaccurate results with conventional calibration. Furthermore, universal calibration is less reliable due to their lower intrinsic viscosity, and interactions with the stationary phase can further distort the separation.[25] Nevertheless, the separation profiles obtained via SEC-D5 provide compelling evidence for the successful formation of star-shaped polymer topologies. All synthesized polymer architectures exhibit low dispersities, indicative of well-controlled polymerization processes. The experimentally determined molar masses–particularly for long-chain star-shaped polymers– are consistently lower than the corresponding theoretical values. This deviation might be attributed to increased steric hindrance at higher molar masses, which restricts the accessibility of active chain ends during chain extension. Furthermore, we have previously shown that TIRP requires optimized reaction conditions e.g., for different types of initiators. Here, the scope was to first establish the combination of sequence-defined thiol-presenting oligomers and TIRP to access star-shaped polymers rather than optimize reaction conditions. A subsequent project will involve optimizing synthesis conditions to refine parameters and enhance the approach's efficiency.

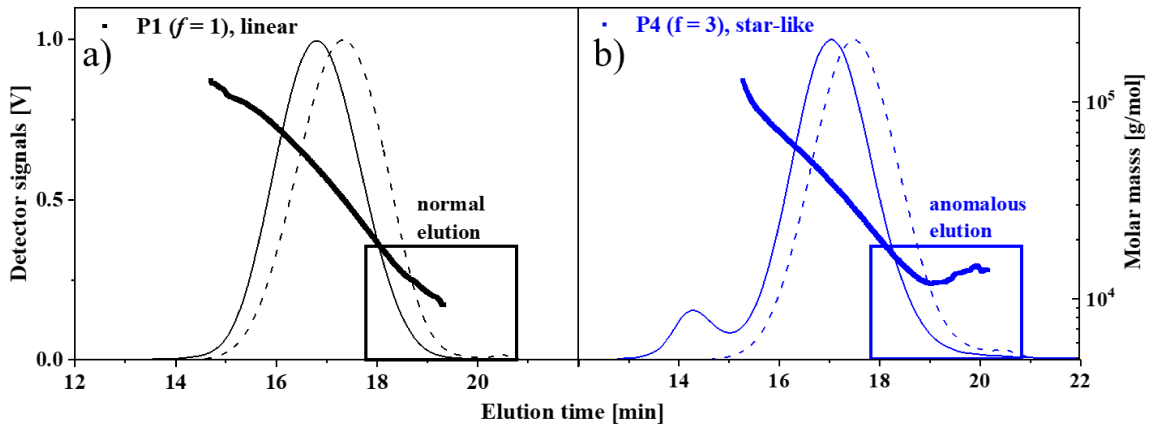


Figure 3. SEC-D5 studies: detector signals (solid line – LS; dashed line – dRI) and molar masses (symbols) vs. elution time of linear (**P1**, black, left side) and b) star-like polymer (**P4**, blue, right side) with indication of deviation in elution behavior.

Figure 3 presents exemplary molar mass curves for a linear **P1** and a star-shaped **P4** polymer of this series. While SEC separation is theoretically governed by hydrodynamic volume and entropic forces, branched polymers may exhibit restricted separation due to interactions with the stationary phase.

The observation of increasing molar masses at high elution times as monitored for all star-shaped polymers (**P2-P6**) –often referred to as the "smiley effect" or anomalous elution– can be attributed to anomalous elution, a long-known but still not fully understood phenomenon that has been discussed in the literature for decades.[26, 27] Anomalous elution effects intensify with an increase in polymer branches. As the chemical structure is comparable, interactions due to the functional units can be excluded. Additionally, the star-shaped polymers exhibit a marginal tendency to aggregate, as indicated by a high-molar-mass peak in the early elution region. However, this fraction is present at very low concentration and does not affect the determined molar masses.

Furthermore, analysis of the viscometry (VS) detector data in SEC-D5, particularly the exponent α from the Kuhn–Mark–Houwink–Sakurada (KMHS) equation (Eq.1, and SI), provides insights into the polymer's conformation and its interaction with the solvent. [28]

$$[\eta] = KM^{\alpha} \quad (1)$$

The α exponents derived from KMHS relation confirm the expected solution behavior of the synthesized polymers. Linear polymers **P1** and **P2** exhibit α values of approximately 0.73, characteristic of flexible, fully solvated coil conformations in a good solvent.[29] In contrast, the star polymers (**P3-P6**) show slightly reduced α values in the range of 0.63–0.71. This decrease reflects the more compact hydrodynamic structure due to branching and increased steric hindrance near the core.[30] The observed trend is consistent with literature data and supports the

successful formation of star-like topologies with distinct conformational characteristics in solution.[31] Additional structural insights can be obtained by analyzing the hydrodynamic radii (R_h) of polymers with comparable molar masses (**P1**, **P4**, **P6**), as determined by SEC-D5 using the DLS and VS data (Table 1). The R_h values reveal the largest size for the linear polymer **P1**, while the star-shaped polymers **P4** and **P6** exhibit slightly lower values. This observation is consistent with the more compact conformation of star-shaped polymers in solution.[32]

As we have previously demonstrated that TIRP provided features of controlled radical polymerization methods, this offers the opportunity to derive block-copolymer structures from simple re-initiation of polymers derived from a first monomer in the presence of a second monomer.[18] Therefore, we next explored the opportunity to also create star-shaped polymers with block-copolymer arms thus generating a core-shell architecture of the star glyco-block-copolymers. Specifically, we employed mannose-acrylamide now as second monomer presenting mannose ligands on the outer block (or shell) and HEAA as first monomer for the inner block (or core). Recent studies have shown that star-shaped glycopolymers might distinctly different properties in comparison to their linear counterparts.[2] For example Qui et al.[33] shows high drug-release time of star-shaped glycopolymers and Chen et al.[34] highlights that star-shaped glycopolymers exhibited superior lectin recognition compared to comparable linear glycopolymers. In a previous studies comparing the binding of differently branched mannose-presenting brush glycopolymers, we could show that branching not only affected affinity but also the selectivity in binding to lectins.[35]

Using the macroinitiator **MI-3**, which presents three thiol functionalities, we synthesized the p(HEAA) core **S4** under standard TIRP conditions (see SI for detailed information). The resulting star-shaped precursors were isolated by precipitation in diethyl ether and subsequently purified by dialysis against water. These p(HEAA) precursors were then employed for reinitiation in the presence of mannose-acrylamide monomers, again following standard TIRP procedures (Figure 4).

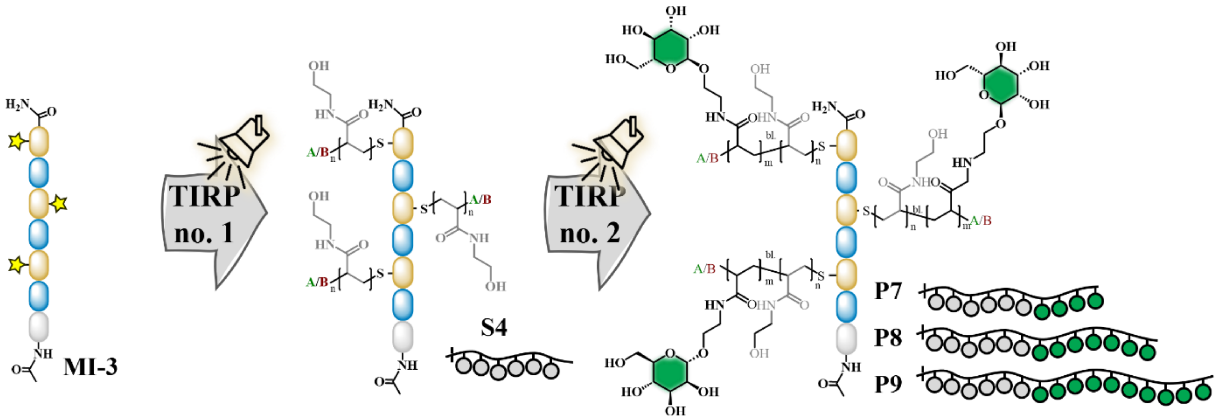


Figure 4. Schematic representation of the synthesis of core-shell star-shaped glyco-block polymers.

The final core-shell star-shaped glyco-block polymers were obtained by precipitation in diethyl ether and further purified via dialysis against water. All synthetic steps were characterized by ^{1}H NMR spectroscopy and SEC-D4 analysis (see Table 2 and Supporting Information).

Table 2. Summary of the synthesized star-shaped glyco-block-copolymers and their characteristic results from SEC-D4 and ^{1}H-NMR.

sample	$M_{n,\,theor.}$ *1 [kDa]	M_n *2 [kDa]	Pn HEEA/Man per SH*2	M_n *3 [kDa]	Đ *3 [M_w/M_n]	$R_{h,DLS}$ *3 [nm]	$Pn^{HEEA/Man}$ per SH*3
S4	12.1	8.8	22	3.0	1.73	2.2	5
P7	19.3	12.1	4	17.5	1.45	4.1	16
P8	26.0	14.6	7	19.4	1.41	4.2	18
P9	52.7	27.1	22	16.8	1.49	4.2	16

*1theoretically determined value; *2determined via ^{1}H-NMR; *3determined by SEC-D4 (more experimental information can be found in SI)

In total, three star-shaped block glycopolymers were synthesized from the precursor **S4**, differing in the number of incorporated mannose units per thiol (4, 7, and 22 units), thereby varying in both arm length and overall molar mass. All resulting polymers exhibited higher molar masses relative to the precursor. However, the molar masses determined by ^{1}H NMR and SEC-D4 were lower than the theoretical values, the discrepancy increasing with increasing molecular weights. This trend had already been observed for the star polymers **P1–P6** and can likely be attributed to increased steric hindrance with growing chains and the not yet optimized TIRP conditions.

Finally, to gain first insights into the lectin binding, we performed initial binding studies using model lectin ConA and quantify binding via a well-established turbidity assay.[17, 36] In short, Con A has four carbohydrate recognition domains that selectively bind mannose. Multivalent glycoligands, such as the star glyco-block-copolymers of this study, can interact with several ConA molecules forming clusters. Cluster formation is thus an indicator for the affinity of the

glycopolymer to ConA and can easily be followed by increasing turbidity with a UV spectrometer at 420 nm. At a specific polymer concentration, turbidity will reach a plateau as now clusters will start to precipitate from solution. As measure of the affinity, half-maximum turbidity is derived from the sigmoidal curves of plotting turbidity vs. concentration of polymer (SI for further details). The results indicate that increased mannose units in the shell correlate with decreased half-maximal turbidity and thus increased affinity (Figure 5).

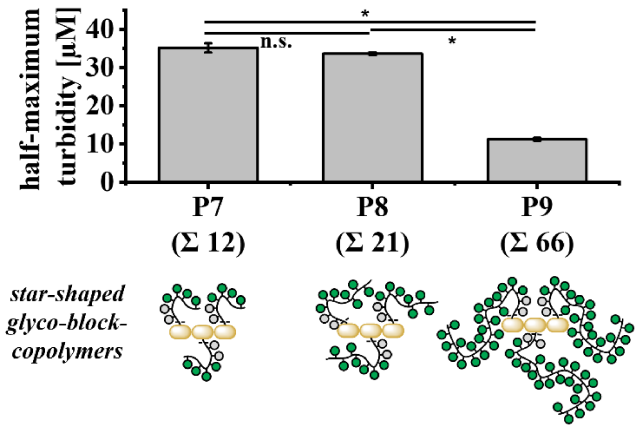


Figure 5. Half-maximum turbidity results of structures **P7**-**P9**.

P8 shows slightly increased concentration of the half-maximum turbidity of 33.6 ± 0.4 µM in comparison to **P7** (35.1 ± 1.2 µM), with increased content of three mannose units per polymer arm. Further increase in **P9** then shows a clear increase in the concentration of half-maximal turbidity to 11.2 ± 0.4 µM, with increasing up to 22 mannose units per polymer arm. This trend is in good agreement with previous studies correlating the carbohydrate valency of star-shape glycopolymers with an increase in cluster formation.[36] Comparing the cluster formation of star-shaped glyco-block-copolymers, particularly **P9**, with values reported in the literature, they exhibit considerably higher half-maximum opacity values (5.61 ± 0.38 µM)[17] in comparison to similar linear homo glycopolymer structures.[34] We hypothesize that for interaction with ConA, it is sufficient for the star glycopolymers to present the mannose units in the shell or outer part of the arms, as the inner segments will likely not be accessible for lectin binding and thus will not contribute to the overall binding affinity.[37]

Conclusion

In conclusion, we demonstrate the successful synthesis of star-shaped glyco-block-copolymers by combining solid phase synthesis and TIRP and enabling a one-pot/two-step core-first strategy that offers great variability in the controlled design of both, core and arm structures. Future research will explore the use of multifunctional cores including stimuli-responsive

linkers and use star-shaped glyco-block-copolymers for targeted drug delivery and as potentially antibacterial and antiviral therapeutics.

Conflicts of interest

There are no conflicts to declare.

Data Availability Statement

The data supporting this article has been included as part of the SI.

Received: ((will be filled in by the editorial staff))
Revised: ((will be filled in by the editorial staff))
Published online: ((will be filled in by the editorial staff))

References

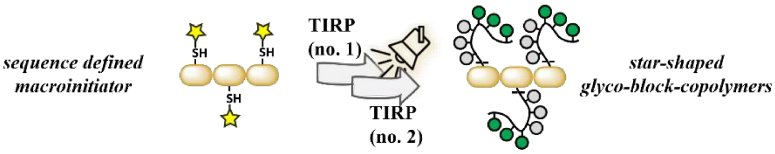
1. X. Liao, G. Walden, N. D. Falcon, S. Donell, M. J. Raxworthy, M. Wormstone, G. P. Riley and A. Saeed, *European Polymer Journal*, 2017, **87**, 458-467.
2. Y. Abdouni, G. Yilmaz and C. R. Becer, *Sequence‐Controlled Polymers*, 2018, 229-256.
3. R. A. Patil, N. Aloorkar, A. Kulkarni and D. Ingale, *International Journal of Pharmaceutical Sciences and Nanotechnology (IJPSN)*, 2012, **5**, 1675-1684.
4. Y. Abdouni, G. Yilmaz, A. Monaco, R. Aksakal and C. R. Becer, *Biomacromolecules*, 2020, **21**, 3756-3764.
5. M. B. Khajeheian and A. Rosling, *Journal of Applied Polymer Science*, 2016, **133**.
6. D. P. Yang, M. N. N. L. Oo, G. R. Deen, Z. Li and X. J. Loh, *Macromolecular rapid communications*, 2017, **38**, 1700410.
7. A. Duro-Castano, R. M. England, D. Razola, E. Romero, M. Oteo-Vives, M. A. Morcillo and M. J. Vicent, *Molecular Pharmaceutics*, 2015, **12**, 3639-3649.
8. J. M. Ren, Q. Fu, A. Blencowe and G. G. Qiao, *ACS Macro Letters*, 2012, **1**, 681-686.
9. J. Xia, X. Zhang and K. Matyjaszewski, *Macromolecules*, 1999, **32**, 4482-4484.
10. D. Boschmann, 2008.
11. C. Zhang, Y. Zhou, Q. Liu, S. Li, S. Perrier and Y. Zhao, *Macromolecules*, 2011, **44**, 2034-2049.
12. A. Blencowe, J. F. Tan, T. K. Goh and G. G. Qiao, *Polymer*, 2009, **50**, 5-32.
13. J. M. Ren, T. G. McKenzie, Q. Fu, E. H. Wong, J. Xu, Z. An, S. Shanmugam, T. P. Davis, C. Boyer and G. G. Qiao, *Chemical reviews*, 2016, **116**, 6743-6836.
14. A. W. Bosman, R. Vestberg, A. Heumann, J. M. Fréchet and C. J. Hawker, *Journal of the American Chemical Society*, 2003, **125**, 715-728.
15. R. A. Masud and T. Hasan.
16. L.-C. Blawitzki, N. Bartels, L. Bonda, S. Schmidt, C. Monzel and L. Hartmann, *Biomacromolecules*, 2024, **25**, 5979-5994.
17. M. Feldhof, S. Sperzel, L. Bonda, S. Boye, A. Braunschweig, U. I. Gerling-Driessen and L. Hartmann, *Chemical Science*, 2024.
18. L. Bonda, D. J. Valles, T. L. Wigger, J. Meisner, A. B. Braunschweig and L. Hartmann, *Macromolecules*, 2023, **56**, 5512-5523.

19. M. I. Feldhof, S. Walber, S. Sperzel, S. Boye, U. I. Gerling‐Driessen and L. Hartmann, *Small*, 2025, 2500531.
20. U. I. Gerling-Driessen, M. Hoffmann, S. Schmidt, N. L. Snyder and L. Hartmann, *Chemical Society Reviews*, 2023, **52**, 2617-2642.
21. S. Boden, F. Reise, J. Kania, T. K. Lindhorst and L. Hartmann, *Macromolecular bioscience*, 2019, **19**, 1800425.
22. J. A. Karas, D. B. Scanlon, B. E. Forbes, I. Vetter, R. J. Lewis, J. Gardiner, F. Separovic, J. D. Wade and M. A. Hossain, *Chemistry–A European Journal*, 2014, **20**, 9549-9552.
23. D. Baskaran and A. H. Müller, *Progress in Polymer Science*, 2007, **32**, 173-219.
24. K. Matyjaszewski, *Advanced Materials*, 2018, **30**, 1706441.
25. M. Gaborieau and P. Castignolles, *Analytical and bioanalytical chemistry*, 2011, **399**, 1413-1423.
26. S. Podzimek, T. Vlcek and C. Johann, *Journal of Applied Polymer Science*, 2001, **81**, 1588-1594.
27. M. Netopilik and S. Podzimek, *ACS omega*, 2020, **5**, 14254-14260.
28. W. Wang, S. Bo, S. Li and W. Qin, *International Journal of Biological Macromolecules*, 1991, **13**, 281-285.
29. W. Li, S. W. Cui and Q. Wang, *Biomacromolecules*, 2006, **7**, 446-452.
30. M. Zhang, H. Liu, W. Shao, K. Miao and Y. Zhao, *Macromolecules*, 2013, **46**, 1325-1336.
31. W. Burchard, *Branched polymers II*, 1999, 113-194.
32. K. Matyjaszewski and S. G. Gaynor, *Macromolecules*, 1997, **30**, 7042-7049.
33. S. Qiu, H. Huang, X. H. Dai, W. Zhou and C. M. Dong, *Journal of Polymer Science Part A: Polymer Chemistry*, 2009, **47**, 2009-2023.
34. Y. Chen, G. Chen and M. H. Stenzel, *Macromolecules*, 2010, **43**, 8109-8114.
35. F. Shamout, A. Monaco, G. Yilmaz, C. R. Becer and L. Hartmann, *Macromolecular rapid communications*, 2020, **41**, 1900459.
36. C. Gerke, M. F. Ebbesen, D. Jansen, S. Boden, T. Freichel and L. Hartmann, *Biomacromolecules*, 2017, **18**, 787-796.
37. G. Yilmaz and C. R. Becer, *Polymer Chemistry*, 2015, **6**, 5503-5514.

Supporting Information

Supporting Information is available from the authors.

ToC figure



Synthesis of star-shaped polymers with homo- and glyco-block-copolymer arms by combining sequence-defined macroinitators accessible through standard solid phase chemistry and TIRP.

4 Conclusion and Outlook

The results presented in this thesis focused on the synthesis of complex glycomimetics, inspired by naturally occurring glycoconjugates such as glycoproteins and were presented in three parts: 1) protein-glycopolymers conjugates extended by the formulation of protein-polymer based multi-shell nanoparticles, 2) mucin-inspired double-brush glycopolymers, 3) star-shaped glycopolymers as another class of branching topology.

In the first part, the goal was to synthesize protein-polymer conjugates using TIRP and native proteins such as BSA and the enzyme CRL without prior protein modification (Figure 16). This direct *grafting-from* initiation at accessible thiols from specific cysteine residues - BSA: Csy'34 and CRL: Cys'217 - gave straightforward access to various protein-polymer conjugates and was conducted at room temperature in an aqueous buffer, thereby preserving the native structure and activity of the proteins and enzymes. Advantages over current approaches are evident in achieving high yields, straightforward conjugation, maintaining precise site control, and allowing direct conjugation without the need of additional artificial initiators. The resulting protein-polymer conjugates exhibit high molecular weights and low dispersities. The versatility of this approach was established by introducing different types of polymers: a) hydrophilic pHEAA, a well-established biocompatible polymer with non-toxic, non-immunogenic and anti-fouling properties; b) temperature-responsive pNIPAM, a non-toxic polymer; c) glycopolymers derived from mannose (Man) and galactose (Gal) acrylamide monomers to mimic natural protein glycosylation and enable selective interactions. Conjugates were successfully characterized by a multitude of analytical methods. To demonstrate that polymer conjugation preserves protein structure and function, CRL-polymer conjugates activity was determined by photometric quantification of the enzymatically driven hydrolysis product of *p*-nitrophenol. Enzyme activity of CRL in glycopolymer conjugates remained unaffected, but the CRL-pNIPAM conjugate showed a 40% increase in activity. The activity assay at 30 °C was close to the lower critical solution temperature (LCST) of CRL-pNIPAM conjugate (32 °C), likely promote cluster formation and enhance activity at elevated temperatures. To verify aggregation-induced increase in CRL enzymatic activity, *Ricinus*

Communis Agglutinin I (RCA_{120}) was used to cluster CRL-pGalEAA conjugate, with CRL-pManEAA as negative control. Turbidity measurements confirmed cluster formation between CRL-pGalEAA and RCA_{120}, while no interaction was observed with CRL-pManEAA. Enzymatic activity of CRL-pGalEAA increased by approximately 20% upon clustering, whereas CRL-pManEAA activity remained unaffected. Effective protein and polymer combinations, such as temperature-induced aggregation boosting enzyme activity and artificial glycosylation were demonstrated, prompting specific protein-protein clustering. Selective binding and protein-protein complex formation were studied using turbidity measurements, which have shown specific cluster formation between BSA-pManEAA and ConA where conjugation did not affect carbohydrate ligands' binding affinity, and BSA-pGalEAA with RCA_{120}, respectively. BSA was utilized to immobilize protein-glycopolymer conjugates on glass surfaces, which create specific ligand-mediated receptor interactions on glycofunctionalized surfaces detected by fluorescence microscopy, commonly used in glycan arrays or for detection and isolation of pathogens and tumor cells. This established new methodology allows protein-polymer conjugation while preserves protein's native structure and function by conjugating various polymers including glycopolymers and gave access to introducing artificial glycosylation.

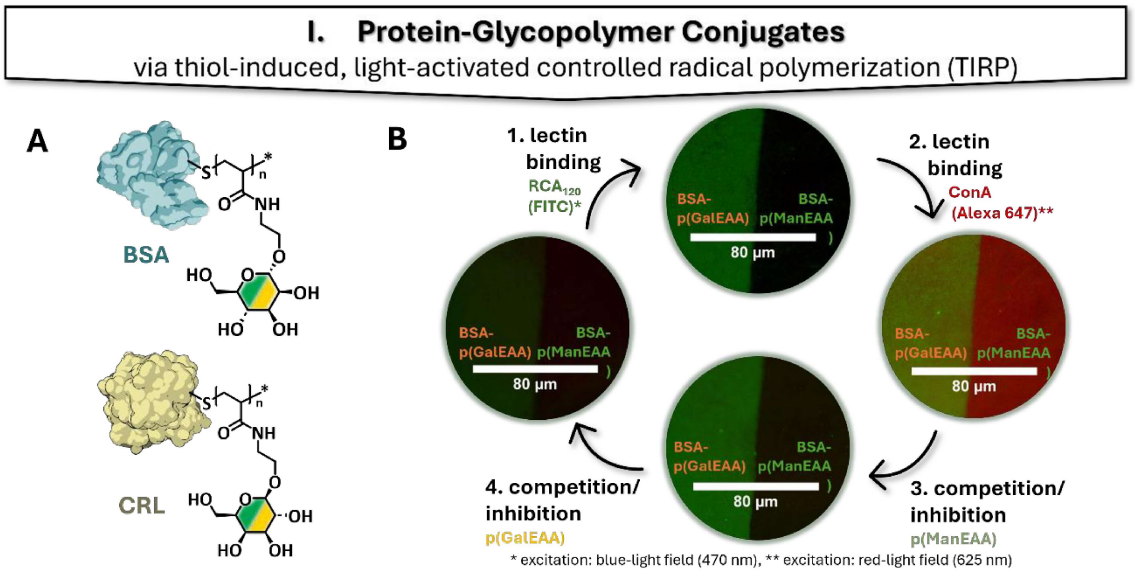


Figure 16: Highlighted results of glycoprotein mimetics, first publication.[I] ***A.*** *Synthesized glycoprotein mimetic.* ***B.*** *Specific ligand-mediated receptor interactions on glycofunctionalized surfaces via fluorescence microscopy.*

Further research will explore additional proteins, including membrane-spanning proteins for *de novo* glycocalyx engineering and antibodies for enhanced binding properties with reduced immunogenicity. Recombinant protein expression methods facilitate the modification of protein sequences, enabling the introduction of cysteine residues as natural amino acids. This would allow then also proteins without accessible cysteines to be adapted for the native side specific *grafting-from* approach presented here and could offer additional applications in material and bio-medical sciences.

Further exploring this new methodology, the now established protein-polymer conjugates were extended by the introduction of a second defined polymer on the BSA-pNIPAM conjugate using a newly symmetrically designed rebridging agent to enable access to additional free thiol that serves as a starting point for a *grafting-from* of a second glycopolymer via TIRP (Figure 17). UV/Vis and fluorescence measurements confirmed successful conjugation, as the newly synthesized rebridged protein exhibited UV activity and inherent fluorescence. Effective polymerization and formation of polymer-protein-polymer conjugates were confirmed by ^{1}H-NMR and AF4-LS, demonstrating that the conjugates with two different polymers had higher molecular weights than the initial BSA-polymer conjugate. CD-spectroscopy confirmed that the protein's conformation was retained after the rebridging and the second polymerization. These successfully synthesized multifunctional pNIPAM-BSA-glycopolymer conjugates without altered protein secondary structure, gave access to temperature self-assembled nanoparticles, which were characterized via DLS, fluorescence microscopy and SEM. In order to achieve a more comprehensive understanding of the dimensions and adaptability of foundational nanoparticles, distinct characteristics of pure BSA-pNIPAM formations were investigated. The nanoparticle size was tuned in the range from 130±0.32 to 363±0.21 nm with low PDIs (0.04±0.01 – 0.19±0.01) by varying the molecular weight of the conjugated pNIPAM, the heating ramp and the concentration of the BSA-pNIPAM conjugate. Temperatures above the LCST enabled dual responsive multilayer nanoparticles formation with a hydrophobic core and a hydrophilic BSA shell that presented carbohydrates (e.g., mannose or galactose) on the outer corona. These nanoparticles were suitable for binding studies with ConA, and enabled the formation of defined multilayers triggered by two distinct stimuli (temperature and carbohydrate interaction). The lectin corona also protected the

nanoparticles from disassembling due to temperature changes over several days. Further, the nanoparticles only disassembled to individual polymer-protein-polymer conjugates when exposed to high-affinity competing ligands. Distinct nanoparticles or large clusters were formed by adjusting the ratio of binding to non-binding glycopolymers in the outer corona of multilayer nanoparticles. Dual responsive multilayered polymer-protein-polymer nanoparticles with controllable properties like assembly and disassembly are now accessible while protein's native structure and function are maintained.

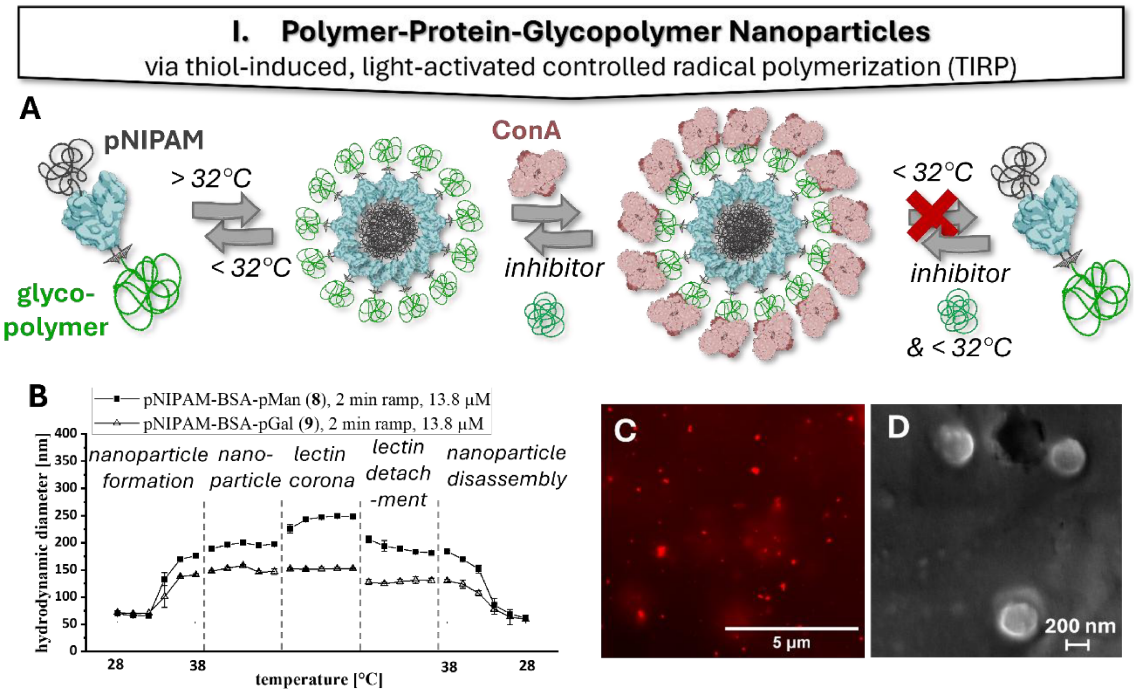


Figure 17: Highlighted research results of multilayered nanoparticles, second publication.[II] ***A.*** *Schematic drawing of dual responsive formation of multilayer (core-shell) nanoparticles.* ***B.*** *Comparison of DLS measurements of mannose- and galactose-based bivalent systems verify mannose specific interaction (D_h increase) and detachment (D_h decrease) with ConA.* ***C.*** *Fluorescence image (excitation: 641 nm, emission: 690 nm) of mannose-derivate below the LCST with addition of ConA$^{Alexa\ 647}$.* ***D.*** *SEM images of mannose-derivate fixed via ConA as nanoparticles in LBB below the LCST.*

Future research can explore the substitution of the thermo-responsive polymer by other stimuli-responsive polymers. Especially in the context of biomedical applications, polymers that can respond to pH variations are highly relevant, thereby activating particle disassembly exclusively in the acidic or alkaline environments, characteristic of tumors or inflammation sites. Subsequently, a systematic investigation into the encapsulation and release of drugs, such as chemotherapeutics, peptides, or antibodies, can be considered as next step. Moreover, the investigation of nanoclusters can be extended

beyond their role as drug carriers to include their potential as diagnostic markers, for instance, by incorporating fluorescent markers.

In the second part of this thesis, the goal was to synthesize highly brushed and sulfated glycopolymers that more closely resemble brushed topologies of natural mucins, an important biological lubricant e.g., found in human epithelial tissues. To accomplish this, SPPoS and polymer analogue reactions on pPFPA active ester polymer scaffolds were optimized to now access to globally sulfated derivatives of double brushed (brush^2), well-defined, high complex glycopolymer mimetics (Figure 18). This method is particularly advantageous as it allows to precisely control important structural features such as the carbohydrate content, side chain length and sulfation. In collaboration with the research group of Prof. Karg (HHU Düsseldorf) and Dr. Balzer (Uni Freiburg), polymer-based mucin mimetics were characterized regarding to mucin-specific properties, such as conformation, hydration and adhesion properties. A bottom-up approach was employed for the synthesis of these complex structures, beginning with the design of sequence-defined glycooligoamidoamines that were successfully synthesized via SPPoS. These glycooligoamidoamines carried one or three mannose units and a free amine at the *N*-terminus which served for the incorporation into RAFT-synthesized short (~30 units) and long (~60 units) pPFPA active ester polymers. The successfully synthesized brushed glycopolymers were subsequently end-functionalized, enabling their incorporation into high molecular weight pPFPA (~200 units) to build double bruched glycopolymers. The derived brush^2 glycopolymers were successfully isolated and sulfated to mimic the negative charges of natural mucin polymers. To analyze structure-property relationships, negative controls were synthesized and examined alongside comparisons between sulfated and non-sulfated samples. Subsequently, selected structures were analyzed, in cooperation with AG Karg and Balzer, which determined mucin-specific characteristics like conformation, hydration and adhesion properties and the associated influence of carbohydrates, side chain length and sulfation. The characterization via DLS, SANS, AFM-SMFS and AFM imaging confirmed that brush^2 glycopolymers successfully mimic key interaction parameters of mucins. Glycopolymer adhesion increased with branching, sugar content, and charge density, allowing for multivalent binding via hydrogen bonds. This is similar to the glycoprotein mucins, where multivalent interactions of the

polyanionic, glycosylated chain are observed. AFM imaging revealed a highly linear conformation of sulfated brush[2] glycopolymers, attributed to the combination of double-brushed architecture and carbohydrate groups, as neither non-mannose brush[2] polymers nor simple brushed glycopolymers showed similar behavior. Such highly extended chain conformations are a typical feature of natural mucins. These successful synthesized double-brushed glycopolymers imitate some mucin-specific characteristics and thus serve as new mucin mimetics.

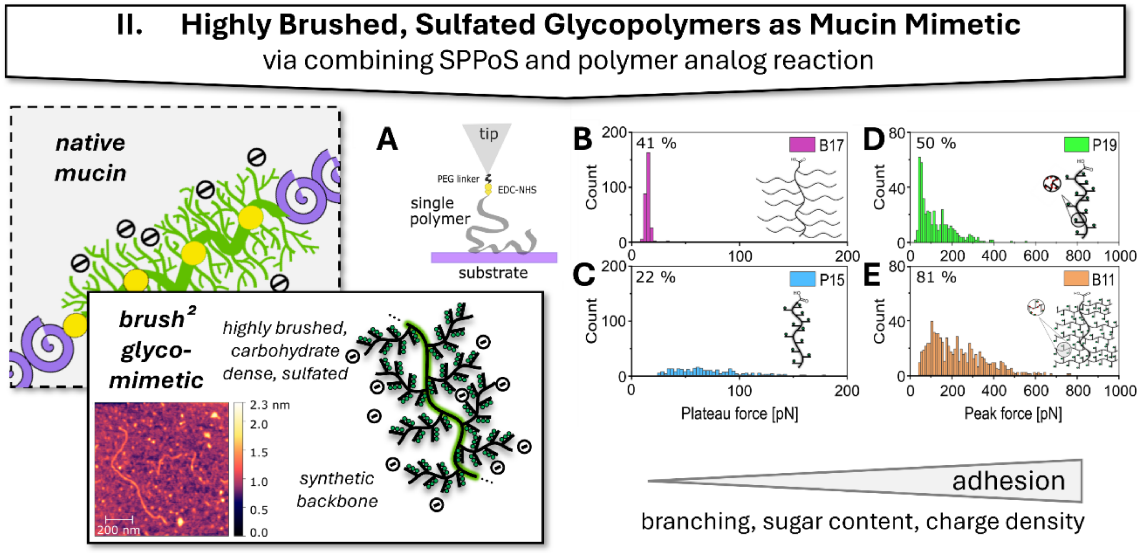


Figure 18: Highlighted research results of double-brushed mucin mimetic glycopolymers, third publication draft. ***A.*** *Scheme of the covalent attachment of a single polymer to an AFM cantilever.* ***B.*** *-* ***E.*** *Plateau forces of* ***B17***, ***P15***, ***P19*** *and* ***B11***.

Future research can now expand the synthetic strategy to incorporate additional features from natural mucins, such as hydrophobic domains or the integration of sialyl acid groups, to create a more complex biomimetic replica of mucins. Furthermore, the derived mucin mimetics can be studied for their potential applications e.g., in wound healing, the enhancement of mucosal barriers, and treatments for respiratory diseases.

The third part of this thesis focused on employing TIRP to derive star-shaped polymers by enabling polymerization at multiple initiating units of a well-defined macroinitiator synthesized using SPPoS. Star-shaped glycopolymers represent a further branched glycomimetic topology and are thus relevant in mimicking more closely natural branched glycan-conjugates such as oligosaccharides and proteoglycans (Figure 19). In order to develop suitable macroinitiators accessible through SPPoS, employing a photolabile

protecting group was necessary. Photocleavable protecting groups effectively prevented disulfide formation and undesirable side reactions prior to polymerization. This enabled a one-pot, two-step release of initiators, followed by simultaneous polymerization at three sites. These macroinitiators were employed in synthesizing star-shaped pHEAA-homopolymers and pHEAA-block-glycopolymers derived from mannose acrylate. Initial ConA binding studies utilizing pHEAA-block-glycopolymers with varying carbohydrate content have demonstrated enhanced binding to ConA with increased carbohydrate content. It is potentially sufficient for the star glycopolymers to present mannose units in the shell or outer part of the polymer chains, as inner segments are likely inaccessible for lectin binding and do not contribute to overall binding affinity.

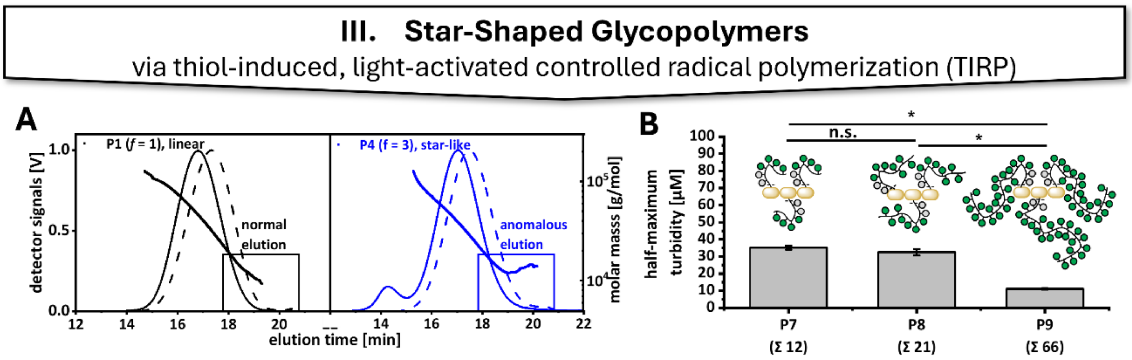


Figure 19: Highlighted research results of star-shaped glycopolymers, fourth publication draft. ***A.*** *Demonstration of the smiley effect of the star polymer vs. linear polymer.* ***B.*** *Graphical summary of binding studies via turbidity assay of glyco-block-copolymers with ConA.*

Future studies can now synthesize more complex star-shape glycopolymers e.g., investigating multifunctional cores, including stimuli-responsive linkers, and employ star-shaped glycopolymers for targeted drug delivery, antibacterial and antiviral treatments.

Overall, this thesis has provided new synthetic methodologies to further the studies and potential applications of glycomimetics in biomedicine. Many infectious diseases involve complex glycocalyx-mediated interactions. Glycomimetics enhance understanding of these processes, enabling novel therapeutic strategies. The advanced glycomimetics presented here provide now new tools to study infection processes and potentially derive new antipathogen strategies. Additionally, to address the glycocalyx's complexity, future work can now also combine these glycomimetics, e.g., in membrane-based vesicles or

on surfaces to derive 3D glycocalyx models. This is now possible based on the synthetic methods and glycomimetics derived in this thesis, as these systems provide both, high level of structural control and effective mimicking of key biological functions of the glycoconjugates.

5 References

(I) Feldhof, M. I., Sperzel, S., Bonda, L., Boye, S., Braunschweig, A. B., Gerling-Driessen, U. I., & Hartmann, L. **2024**, *Chemical Science* 15 (40), 16768-16777.
(II) Feldhof, M. I., Walber, S., Sperzel, S., Boye, S., Gerling-Driessen, U. I., & Hartmann, L. **2025**, *Small*, 2500531.

(1) Purcell, S. C.; Godula, K. Synthetic glycoscapes: addressing the structural and functional complexity of the glycocalyx. *Journal of the Royal Society Interface Focus* **2019**, *9* (2), 20180080.
(2) Varki, A.; Cummings, R. D.; Esko, J. D.; Stanley, P.; Hart, G. W.; Aebi, M.; Darvill, A. G.; Kinoshita, T.; Packer, N. H.; Prestegard, J. H. Essentials of Glycobiology **2015**.
(3) Bernardino de la Serna, J.; Schütz, G. J.; Eggeling, C.; Cebecauer, M. There is no simple model of the plasma membrane organization. *Frontiers in cell and developmental biology* **2016**, *4*, 106.
(4) Patterson, E. K.; Cepinskas, G.; Fraser, D. D. Endothelial glycocalyx degradation in critical illness and injury. *Frontiers in Medicine* **2022**, *9*, 898592.
(5) Sullivan, R. C.; Rockstrom, M. D.; Schmidt, E. P.; Hippensteel, J. A. Endothelial glycocalyx degradation during sepsis: Causes and consequences. *Matrix Biology Plus* **2021**, *12*, 100094.
(6) Möckl, L. The emerging role of the mammalian glycocalyx in functional membrane organization and immune system regulation. *Frontiers in cell and developmental biology* **2020**, *8*, 253.
(7) Tarbell, J. M.; Cancel, L. The glycocalyx and its significance in human medicine. *Journal of internal medicine* **2016**, *280* (1), 97-113.
(8) Villalba, N.; Baby, S.; Yuan, S. Y. The endothelial glycocalyx as a double-edged sword in microvascular homeostasis and pathogenesis. *Frontiers in Cell and Developmental Biology* **2021**, *9*, 711003.
(9) Imberty, A.; Varrot, A. Microbial recognition of human cell surface glycoconjugates. *Current opinion in structural biology* **2008**, *18* (5), 567-576.
(10) Werz, D. B.; Seeberger, P. H. Carbohydrates as the next frontier in pharmaceutical research. *Chemistry–A European Journal* **2005**, *11* (11), 3194-3206.
(11) Bertozzi, C. R.; Kiessling; L, L. Chemical glycobiology. *Science* **2001**, *291* (5512), 2357-2364.
(12) Soliman, C.; Yuriev, E.; Ramsland, P. A. Antibody recognition of aberrant glycosylation on the surface of cancer cells. *Current Opinion in Structural Biology* **2017**, *44*, 1-8.
(13) Tan, N. Y.; Bailey, U.-M.; Jamaluddin, M. F.; Mahmud, S. H. B.; Raman, S. C.; Schulz, B. L. Sequence-based protein stabilization in the absence of glycosylation. *Nature communications* **2014**, *5* (1), 3099.
(14) Zacchi, L. F.; Schulz, B. L. SWATH-MS glycoproteomics reveals consequences of defects in the glycosylation machinery. *Molecular & Cellular Proteomics* **2016**, *15* (7), 2435-2447.
(15) Ansori, A. N. M.; Kharisma, V. D.; Antonius, Y.; Tacharina, M. R.; Rantam, F. A. Immunobioinformatics analysis and phylogenetic tree construction of severe acute respiratory syndrome coronavirus 2 (SARS-CoV-2) in Indonesia: spike glycoprotein gene. *Jurnal Teknologi Laboratorium* **2020**, *9* (1), 13-20.

(16) Bartold, P. M.; Wiebkin, O. W.; Thonard, J. C. Proteoglycans of human gingival epithelium and connective tissue. *Biochemical Journal* **1983**, *211* (1), 119-127.
(17) Shi, D.; Sheng, A.; Chi, L. Glycosaminoglycan-protein interactions and their roles in human disease. *Frontiers in molecular biosciences* **2021**, *8*, 639666.
(18) Lin, B.; Qing, X.; Liao, J.; Zhuo, K. Role of protein glycosylation in host-pathogen interaction. *Cells* **2020**, *9* (4), 1022.
(19) Shriver, Z.; Capila, I.; Venkataraman, G.; Sasisekharan, R. Heparin and heparan sulfate: analyzing structure and microheterogeneity. *Heparin-A Century of Progress* **2012**, 159-176.
(20) Purushothaman, A.; Sugahara, K.; Faissner, A. Chondroitin sulfate "wobble motifs" modulate maintenance and differentiation of neural stem cells and their progeny. *Journal of Biological Chemistry* **2012**, *287* (5), 2935-2942.
(21) Yamada, S.; Sugahara, K. Potential therapeutic application of chondroitin sulfate/dermatan sulfate. *Current Drug Discovery Technologies* **2008**, *5* (4), 289-301.
(22) Pomin, V. H. Keratan sulfate: An up-to-date review. *International Journal of Biological Macromolecules* **2015**, *72*, 282-289.
(23) Spiro, R. G. Protein glycosylation: nature, distribution, enzymatic formation, and disease implications of glycopeptide bonds. *Glycobiology* **2002**, *12* (4), 43R-56R.
(24) North, S. J.; Hitchen, P. G.; Haslam, S. M.; Dell, A. Mass spectrometry in the analysis of N-linked and O-linked glycans. *Current opinion in structural biology* **2009**, *19* (5), 498-506.
(25) Ohtsubo, K.; Marth, J. D. Glycosylation in cellular mechanisms of health and disease. *cell* **2006**, *126* (5), 855-867.
(26) Smith, B. A.; Bertozzi, C. R. The clinical impact of glycobiology: targeting selectins, Siglecs and mammalian glycans. *Nature reviews Drug discovery* **2021**, *20* (3), 217-243.
(27) Varki, A.; Cummings, R. D.; Aebi, M.; Packer, N. H.; Seeberger, P. H.; Esko, J. D.; Stanley, P.; Hart, G.; Darvill, A.; Kinoshita, T. Symbol nomenclature for graphical representations of glycans. *Glycobiology* **2015**, *25* (12), 1323-1324.
(28) Neelamegham, S.; Aoki-Kinoshita, K.; Bolton, E.; Frank, M.; Lisacek, F.; Lütteke, T.; O'Boyle, N.; Packer, N. H.; Stanley, P.; Toukach, P. Updates to the symbol nomenclature for glycans guidelines. *Glycobiology* **2019**, *29* (9), 620-624.
(29) Lopes, N.; Correia, V. G.; Palma, A. S.; Brito, C. Cracking the breast cancer glyco-code through glycan-lectin interactions: targeting immunosuppressive macrophages. *International Journal of Molecular Sciences* **2021**, *22* (4), 1972.
(30) Bagdonaite, I.; Malaker, S. A.; Polasky, D. A.; Riley, N. M.; Schjoldager, K.; Vakhrushev, S. Y.; Halim, A.; Aoki-Kinoshita, K. F.; Nesvizhskii, A. I.; Bertozzi, C. R. Glycoproteomics. *Nature Reviews Methods Primers* **2022**, *2* (1), 48.
(31) Van Kooyk, Y.; Rabinovich, G. A. Protein-glycan interactions in the control of innate and adaptive immune responses. *Nature immunology* **2008**, *9* (6), 593-601.
(32) Cylwik, B.; Lipartowska, K.; Chrostek, L.; Gruszewska, E. Congenital disorders of glycosylation. Part II. Defects of protein O-glycosylation. *Acta Biochimica Polonica* **2013**, *60* (3), 361-368.
(33) Corfield, A. P. Mucins: a biologically relevant glycan barrier in mucosal protection. *Biochimica et Biophysica Acta (BBA)-General Subjects* **2015**, *1850* (1), 236-252.
(34) Bafna, S.; Kaur, S.; Batra, S. K. Membrane-bound mucins: the mechanistic basis for alterations in the growth and survival of cancer cells. *Oncogene* **2010**, *29* (20), 2893-2904.
(35) Bansil, R.; Turner, B. S. Mucin structure, aggregation, physiological functions and biomedical applications. *Current opinion in colloid & interface science* **2006**, *11* (2-3), 164-170.

(36) Coles, J. M.; Chang, D. P.; Zauscher, S. Molecular mechanisms of aqueous boundary lubrication by mucinous glycoproteins. *Current Opinion in Colloid & Interface Science* **2010**, *15* (6), 406-416.
(37) Lai, S. K.; Wang, Y.-Y.; Wirtz, D.; Hanes, J. Micro-and macrorheology of mucus. *Advanced drug delivery reviews* **2009**, *61* (2), 86-100.
(38) Linden, S.; Sutton, P.; Karlsson, N.; Korolik, V.; McGuckin, M. Mucins in the mucosal barrier to infection. *Mucosal immunology* **2008**, *1* (3), 183-197.
(39) Xia, B.; Royall, J. A.; Damera, G.; Sachdev, G. P.; Cummings, R. D. Altered O-glycosylation and sulfation of airway mucins associated with cystic fibrosis. *Glycobiology* **2005**, *15* (8), 747-775.
(40) Brockhausen, I. Mucin-type O-glycans in human colon and breast cancer: glycodynamics and functions. *EMBO reports* **2006**, *7* (6), 599-604.
(41) Jensen, P. H.; Kolarich, D.; Packer, N. H. Mucin-type O-glycosylation–putting the pieces together. *The FEBS journal* **2010**, *277* (1), 81-94.
(42) Crouzier, T.; Boettcher, K.; Geonnotti, A. R.; Kavanaugh, N. L.; Hirsch, J. B.; Ribbeck, K.; Lieleg, O. Modulating mucin hydration and lubrication by deglycosylation and polyethylene glycol binding. *Advanced Materials Interfaces* **2015**, *2* (18), 1500308.
(43) Caldara, M.; Friedlander, R. S.; Kavanaugh, N. L.; Aizenberg, J.; Foster, K. R.; Ribbeck, K. Mucin biopolymers prevent bacterial aggregation by retaining cells in the free-swimming state. *Current Biology* **2012**, *22* (24), 2325-2330.
(44) Co, J. Y.; Crouzier, T.; Ribbeck, K. Probing the role of mucin-bound glycans in bacterial repulsion by mucin coatings. *Advanced Materials Interfaces* **2015**, *2* (17), 1500179.
(45) Melo-Gonzalez, F.; Fenton, T. M.; Forss, C.; Smedley, C.; Goenka, A.; MacDonald, A. S.; Thornton, D. J.; Travis, M. A. Intestinal mucin activates human dendritic cells and IL-8 production in a glycan-specific manner. *Journal of Biological Chemistry* **2018**, *293* (22), 8543-8553.
(46) Porowska, H.; Paszkiewicz-Gadek, A.; Wosek, J.; Wnuczko, K.; Rusak, M.; Szczepański, M. Expression of MUC1 mucin in human umbilical vein endothelial cells (HUVEC). *Folia Histochemica et Cytobiologica* **2010**, *48* (3), 417-424.
(47) Weber, F.; Petrou, G.; Srivastava, V.; Crouzier, T.; Lieleg, O. Mucin-Inspired Lubrication on Hydrophobic Surfaces. *Biomacromolecules* **2017**.
(48) Marczynski, M.; Balzer, B. N.; Jiang, K.; Lutz, T. M.; Crouzier, T.; Lieleg, O. Charged glycan residues critically contribute to the adsorption and lubricity of mucins. *Colloids and Surfaces B: Biointerfaces* **2020**, *187*, 110614.
(49) Takeyama, K.; Jung, B.; Shim, J. J.; Burgel, P.-R.; Dao-Pick, T.; Ueki, I. F.; Protin, U.; Kroschel, P.; Nadel, J. A. Activation of epidermal growth factor receptors is responsible for mucin synthesis induced by cigarette smoke. *American Journal of Physiology-Lung Cellular and Molecular Physiology* **2001**, *280* (1), L165-L172.
(50) Yu, Q.; Chen, X.; Fang, X.; Chen, Q.; Hu, C. Caveolin-1 aggravates cigarette smoke extract-induced MUC5AC secretion in human airway epithelial cells. *International journal of molecular medicine* **2015**, *35* (5), 1435-1442.
(51) Hata, K.; Tsubouchi, K.; Suzuki, K.; Eto, D.; Ando, H.; Yanagihara, T.; Kan-o, K.; Okamoto, I. Surfactant protein D prevents mucin overproduction in airway goblet cells via SIRPα. *Scientific reports* **2024**, *14* (1), 1799.
(52) Mammen, M. J.; Ali, J.; Aurora, A.; Sharma, U. C.; Aalinkeel, R.; Mahajan, S. D.; Sands, M.; Schwartz, S. A. IL-17 Is a Key Regulator of Mucin-Galectin-3 Interactions in Asthma. *International Journal of Cell Biology* **2021**, *2021* (1), 9997625.

(53) Ali, M. M.; Zhu, S.; Amin, F. R.; Hussain, D.; Du, Z.; Hu, L. Molecular imprinting of glycoproteins: From preparation to cancer theranostics. *Theranostics* **2022**, *12* (5), 2406.
(54) Xu, D.; Prestegard, J. H.; Linhardt, R. J.; Esko, J. D. Proteins that bind sulfated glycosaminoglycans. **2022**.
(55) Taylor, M.; Drickamer, K.; Imberty, A.; van Kooyk, Y.; Schnaar, R.; Etzler, M.; Varki, A. Discovery and classification of glycan-binding proteins. *Essentials of Glycobiology, 4th edition* **2022**.
(56) Meneghetti, M. C.; Hughes, A. J.; Rudd, T. R.; Nader, H. B.; Powell, A. K.; Yates, E. A.; Lima, M. A. Heparan sulfate and heparin interactions with proteins. *Journal of the Royal Society Interface* **2015**, *12* (110), 20150589.
(57) Clausen, T. M.; Sandoval, D. R.; Spliid, C. B.; Pihl, J.; Perrett, H. R.; Painter, C. D.; Narayanan, A.; Majowicz, S. A.; Kwong, E. M.; McVicar, R. N. SARS-CoV-2 infection depends on cellular heparan sulfate and ACE2. *Cell* **2020**, *183* (4), 1043-1057. e1015.
(58) Drickamer, K.; Taylor, M. E. Recent insights into structures and functions of C-type lectins in the immune system. *Current opinion in structural biology* **2015**, *34*, 26-34.
(59) Osorio, F.; e Sousa, C. R. Myeloid C-type lectin receptors in pathogen recognition and host defense. *Immunity* **2011**, *34* (5), 651-664.
(60) Rao, X.-J.; Cao, X.; He, Y.; Hu, Y.; Zhang, X.; Chen, Y.-R.; Blissard, G.; Kanost, M. R.; Yu, X.-Q.; Jiang, H. Structural features, evolutionary relationships, and transcriptional regulation of C-type lectin-domain proteins in Manduca sexta. *Insect biochemistry and molecular biology* **2015**, *62*, 75-85.
(61) Aretz, J.; Wamhoff, E.-C.; Hanske, J.; Heymann, D.; Rademacher, C. Computational and experimental prediction of human C-type lectin receptor druggability. *Frontiers in immunology* **2014**, *5*, 323.
(62) Ting, S. S.; Chen, G.; Stenzel, M. H. Synthesis of glycopolymers and their multivalent recognitions with lectins. *Polymer Chemistry* **2010**, *1* (9), 1392-1412.
(63) Lee, R. T.; Lee, Y. C. Affinity enhancement by multivalent lectin–carbohydrate interaction. *Glycoconjugate journal* **2000**, *17*, 543-551.
(64) Liese, S.; Netz, R. R. Quantitative prediction of multivalent ligand–receptor binding affinities for influenza, cholera, and anthrax inhibition. *ACS nano* **2018**, *12* (5), 4140-4147.
(65) Pieters, R. J. Maximising multivalency effects in protein–carbohydrate interactions. *Organic & biomolecular chemistry* **2009**, *7* (10), 2013-2025.
(66) Lundquist, J. J.; Toone, E. J. The cluster glycoside effect. *Chemical reviews* **2002**, *102* (2), 555-578.
(67) Kiessling, L. L.; Gestwicki, J. E.; Strong, L. E. Synthetic multivalent ligands as probes of signal transduction. *Angewandte Chemie International Edition* **2006**, *45* (15), 2348-2368.
(68) Galan, M. C.; Dumy, P.; Renaudet, O. Multivalent glyco (cyclo) peptides. *Chemical Society Reviews* **2013**, *42* (11), 4599-4612.
(69) Schwarzenbach, v. G. Der chelateffekt. *Helvetica Chimica Acta* **1952**, *35* (7), 2344-2359.
(70) Wittmann, V. Structural investigation of multivalent carbohydrate–protein interactions using synthetic biomolecules. *Current opinion in chemical Biology* **2013**, *17* (6), 982-989.
(71) Marradi, M.; Chiodo, F.; García, I.; Penadés, S. Glyconanoparticles as multifunctional and multimodal carbohydrate systems. *Chemical Society Reviews* **2013**, *42* (11), 4728-4745.
(72) Rísquez-Cuadro, R.; Garcia Fernandez, J. M.; Nierengarten, J. F.; Ortiz Mellet, C. Fullerene-sp2-iminosugar balls as multimodal ligands for lectins and glycosidases: A mechanistic hypothesis for the inhibitory multivalent effect. *Chemistry–A European Journal* **2013**, *19* (49), 16791-16803.

(73) Pussak, D.; Ponader, D.; Mosca, S.; Pompe, T.; Hartmann, L.; Schmidt, S. Specific adhesion of carbohydrate hydrogel particles in competition with multivalent inhibitors evaluated by AFM. *Langmuir* **2014**, *30* (21), 6142-6150.
(74) Ponader, D.; Maffre, P.; Aretz, J.; Pussak, D.; Ninnemann, N. M.; Schmidt, S.; Seeberger, P. H.; Rademacher, C.; Nienhaus, G. U.; Hartmann, L. Carbohydrate-lectin recognition of sequence-defined heteromultivalent glycooligomers. *Journal of the American Chemical Society* **2014**, *136* (5), 2008-2016.
(75) Ernst, B.; Magnani, J. L. From carbohydrate leads to glycomimetic drugs. *Nature reviews Drug discovery* **2009**, *8* (8), 661-677.
(76) Hoffmann, M.; Snyder, N. L.; Hartmann, L. Glycosaminoglycan Mimetic Precision Glycomacromolecules with Sequence-Defined Sulfation and Rigidity Patterns. *Biomacromolecules* **2022**, *23* (9), 4004-4014.
(77) Leusmann, S.; Ménová, P.; Shanin, E.; Titz, A.; Rademacher, C. Glycomimetics for the inhibition and modulation of lectins. *Chemical Society Reviews* **2023**, *52* (11), 3663-3740.
(78) Tamburrini, A.; Colombo, C.; Bernardi, A. Design and synthesis of glycomimetics: Recent advances. *Medicinal research reviews* **2020**, *40* (2), 495-531.
(79) Cramer, J.; Lakkaichi, A.; Aliu, B.; Jakob, R. P.; Klein, S.; Cattaneo, I.; Jiang, X.; Rabbani, S.; Schwardt, O.; Zimmer, G. Sweet drugs for bad bugs: a glycomimetic strategy against the DC-SIGN-mediated dissemination of SARS-CoV-2. *Journal of the American Chemical Society* **2021**, *143* (42), 17465-17478.
(80) Magnani, J. L.; Ernst, B. Glycomimetic drugs-a new source of therapeutic opportunities. *Discovery medicine* **2009**, *8* (43), 247-252.
(81) Gerke, C.; Ebbesen, M. F.; Jansen, D.; Boden, S.; Freichel, T.; Hartmann, L. Sequence-controlled glycopolymers via step-growth polymerization of precision glycomacromolecules for lectin receptor clustering. *Biomacromolecules* **2017**, *18* (3), 787-796.
(82) Lete, M. G.; Hoffmann, M.; Schomann, N.; Martínez-Castillo, A.; Peccati, F.; Konietzny, P. B.; Delgado, S.; Snyder, N. L.; Jiménez-Oses, G.; Abrescia, N. G. Molecular recognition of glycan-bearing glycomacromolecules presented at membrane surfaces by lectins: an NMR view. *ACS omega* **2023**, *8* (19), 16883-16895.
(83) Freichel, T.; Heine, V.; Laaf, D.; Mackintosh, E. E.; Sarafova, S.; Elling, L.; Snyder, N. L.; Hartmann, L. Sequence-Defined Heteromultivalent Precision Glycomacromolecules Bearing Sulfonated/Sulfated Nonglycosidic Moieties Preferentially Bind Galectin-3 and Delay Wound Healing of a Galectin-3 Positive Tumor Cell Line in an In Vitro Wound Scratch Assay. *Macromolecular bioscience* **2020**, *20* (9), 2000163.
(84) Wojcik, F.; Mosca, S.; Hartmann, L. Solid-phase synthesis of asymmetrically branched sequence-defined poly/oligo (amidoamines). *The Journal of organic chemistry* **2012**, *77* (9), 4226-4234.
(85) Ponader, D.; Wojcik, F.; Beceren-Braun, F.; Dernedde, J.; Hartmann, L. Sequence-defined glycopolymer segments presenting mannose: synthesis and lectin binding affinity. *Biomacromolecules* **2012**, *13* (6), 1845-1852.
(86) Nagahori, N.; Nishimura, S.-I. Tailored Glycopolymers: Controlling the Carbohydrate–Protein Interaction Based on Template Effect. *Biomacromolecules* **2001**, *2* (1), 22-24.
(87) Muthukrishnan, S.; Jutz, G.; Andre, X.; Mori, H.; Müller, A. H. Synthesis of hyperbranched glycopolymers via self-condensing atom transfer radical copolymerization of a sugar-carrying acrylate. *Macromolecules* **2005**, *38* (1), 9-18.

(88) Aoi, K.; Tsutsumiuchi, K.; Aoki, E.; Okada, M. First synthesis of glycopeptide macromonomers and graft-type sugar-containing polymers with glycopeptide side chains. *Macromolecules* **1996**, *29* (12), 4456-4458.
(89) Loykulnant, S.; Hirao, A. Protection and polymerization of functional monomers. 30. Anionic living polymerization of 4-alkylstyrenes containing acetal-protected monosaccharide residues. *Macromolecules* **2000**, *33* (13), 4757-4764.
(90) Dai, X.-H.; Dong, C.-M.; Yan, D. Supramolecular and biomimetic polypseudorotaxane/glycopolymer biohybrids: Synthesis, glucose-surfaced nanoparticles, and recognition with lectin. *The Journal of Physical Chemistry B* **2008**, *112* (12), 3644-3652.
(91) Dong, C.-M.; Chaikof, E. L. Self-assembled nanostructures of a biomimetic glycopolymer–polypeptide triblock copolymer. *Colloid and Polymer Science* **2005**, *283*, 1366-1370.
(92) Miura, Y. Controlled polymerization for the development of bioconjugate polymers and materials. *Journal of Materials Chemistry B* **2020**, *8* (10), 2010-2019.
(93) Ahmed, M.; Wattanaarsakit, P.; Narain, R. Recent advances in the preparation of glycopolymer bioconjugates. *European polymer journal* **2013**, *49* (10), 3010-3033.
(94) Geng, J.; Mantovani, G.; Tao, L.; Nicolas, J.; Chen, G.; Wallis, R.; Mitchell, D. A.; Johnson, B. R.; Evans, S. D.; Haddleton, D. M. Site-directed conjugation of "clicked" glycopolymers to form glycoprotein mimics: binding to mammalian lectin and induction of immunological function. *Journal of the American Chemical Society* **2007**, *129* (49), 15156-15163.
(95) Banger, A.; Sindram, J.; Otten, M.; Kania, J.; Wilms, D.; Strzelczyk, A.; Miletic, S.; Marlovits, T. C.; Karg, M.; Hartmann, L. Synthesis and self-assembly of amphiphilic precision glycomacromolecules. *Polymer Chemistry* **2021**, *12* (33), 4795-4802.
(96) Ting, S. S.; Min, E. H.; Escale, P.; Save, M.; Billon, L.; Stenzel, M. H. Lectin recognizable biomaterials synthesized via nitroxide-mediated polymerization of a methacryloyl galactose monomer. *Macromolecules* **2009**, *42* (24), 9422-9434.
(97) Nemli, D. D.; Jiang, X.; Jakob, R. P.; Gloder, L. M.; Schwardt, O.; Rabbani, S.; Maier, T.; Ernst, B.; Cramer, J. Thermodynamics-Guided Design Reveals a Cooperative Hydrogen Bond in DC-SIGN-targeted Glycomimetics. *Journal of Medicinal Chemistry* **2024**.
(98) Porkolab, V.; Chabrol, E.; Varga, N.; Ordanini, S.; Sutkevičiūtė, I.; Thépaut, M.; García-Jiménez, M. J.; Girard, E.; Nieto, P. M.; Bernardi, A. Rational-differential design of highly specific glycomimetic ligands: targeting DC-SIGN and excluding langerin recognition. *ACS chemical biology* **2017**, *13* (3), 600-608.
(99) Camaleño de la Calle, A.; Gerke, C.; Chang, X. J.; Grafmüller, A.; Hartmann, L.; Schmidt, S. Multivalent interactions of polyamide based sequence-controlled glycomacromolecules with concanavalin A. *Macromolecular Bioscience* **2019**, *19* (6), 1900033.
(100) Merrifield, R. B. Solid phase peptide synthesis. I. The synthesis of a tetrapeptide. *Journal of the American Chemical Society* **1963**, *85* (14), 2149-2154.
(101) Jensen, K. J. Solid-phase peptide synthesis: an introduction. *Peptide synthesis and applications* **2013**, 1-21.
(102) Tanaka, H.; Moriwaki, M.; Takahashi, T. Efficient solid-phase synthesis of symmetric norbinaltorphimine derivatives. *Organic Letters* **2003**, *5* (21), 3807-3809.
(103) Pedersen, S. L.; Tofteng, A. P.; Malik, L.; Jensen, K. J. Microwave heating in solid-phase peptide synthesis. *Chemical Society Reviews* **2012**, *41* (5), 1826-1844.
(104) Blawitzki, L.-C.; Bartels, N.; Bonda, L.; Schmidt, S.; Monzel, C.; Hartmann, L. Glycomacromolecules to Tailor Crowded and Heteromultivalent Glycocalyx Mimetics. *Biomacromolecules* **2024**, *25* (9), 5979-5994.

(105) Blawitzki, L. C.; Monzel, C.; Schmidt, S.; Hartmann, L. Selective Glycan Presentation in Liquid-Ordered or-Disordered Membrane Phases and its Effect on Lectin Binding. *Angewandte Chemie International Edition* **2025**, *64* (2), e202414847.
(106) Jäck, N.; Hemming, A.; Hartmann, L. Synthesis of Dual-Responsive Amphiphilic Glycomacromolecules: Controlled Release of Glycan Ligands via pH and UV Stimuli. *Macromolecular Rapid Communications* **2024**, *45* (20), 2400439.
(107) Hill, S. A.; Gerke, C.; Hartmann, L. Recent Developments in Solid-Phase Strategies towards Synthetic, Sequence-Defined Macromolecules. *Chemistry–An Asian Journal* **2018**, *13* (23), 3611-3622.
(108) Stewart, J. M. [3] Cleavage methods following Boc-based solid-phase peptide synthesis. *Methods in enzymology* **1997**, *289*, 29-44.
(109) Grant, G. A. *Synthetic peptides: a user's guide*; Oxford University Press, USA, 2002.
(110) Chan, W.; White, P. *Fmoc solid phase peptide synthesis: a practical approach*; OUP Oxford, 1999.
(111) Carpino, L. A.; Han, G. Y. 9-Fluorenylmethoxycarbonyl Amino-Protecting Group. *J Org Chem* **1972**, *37* (22), 3404-&. DOI: DOI 10.1021/jo00795a005.
(112) Barany, G.; Albericio, F. A 3-Dimensional Orthogonal Protection Scheme for Solid-Phase Peptide-Synthesis under Mild Conditions. *Journal of the American Chemical Society* **1985**, *107* (17), 4936-4942. DOI: DOI 10.1021/ja00303a019.
(113) Neuhaus, K.; Wamhoff, E.-C.; Freichel, T.; Grafmüller, A.; Rademacher, C.; Hartmann, L. Asymmetrically branched precision glycooligomers targeting langerin. *Biomacromolecules* **2019**, *20* (11), 4088-4095.
(114) Mueller, L. K.; Baumruck, A. C.; Zhdanova, H.; Tietze, A. A. Challenges and perspectives in chemical synthesis of highly hydrophobic peptides. *Frontiers in Bioengineering and Biotechnology* **2020**, *8*, 162.
(115) Baier, M.; Giesler, M.; Hartmann, L. Split-and-Combine Approach Towards Branched Precision Glycomacromolecules and Their Lectin Binding Behavior. *Chemistry–A European Journal* **2018**, *24* (7), 1619-1630.
(116) Shamout, F.; Monaco, A.; Yilmaz, G.; Becer, C. R.; Hartmann, L. Synthesis of Brush-Like Glycopolymers with Monodisperse, Sequence-Defined Side Chains and Their Interactions with Plant and Animal Lectins. *Macromolecular rapid communications* **2020**, *41* (1), 1900459.
(117) Illmann, M. D.; Schäfl, L.; Drees, F.; Hartmann, L.; Schmidt, S. Glycan-presenting coacervates derived from charged poly (active esters): preparation, phase behavior, and lectin capture. *Biomacromolecules* **2023**, *24* (6), 2532-2540.
(118) Gerling-Driessen, U. I.; Hoffmann, M.; Schmidt, S.; Snyder, N. L.; Hartmann, L. Glycopolymers against pathogen infection. *Chemical Society Reviews* **2023**, *52* (8), 2617-2642.
(119) Voit, B.; Appelhans, D. Glycopolymers of various architectures—more than mimicking nature. *Macromolecular Chemistry and Physics* **2010**, *211* (7), 727-735.
(120) Miura, Y.; Hoshino, Y.; Seto, H. Glycopolymer nanobiotechnology. *Chemical reviews* **2016**, *116* (4), 1673-1692.
(121) Bhattacharya, K.; Kalita, U.; Singha, N. K. Tailor-made glycopolymers via reversible deactivation radical polymerization: design, properties and applications. *Polymer Chemistry* **2022**, *13* (11), 1458-1483.
(122) Ghadban, A.; Albertin, L. Synthesis of glycopolymer architectures by reversible-deactivation radical polymerization. *Polymers* **2013**, *5* (2), 431-526.

(123) Becer, C. R. The glycopolymer code: synthesis of glycopolymers and multivalent carbohydrate–lectin interactions. *Macromolecular rapid communications* **2012**, *33* (9), 742-752.
(124) Thalji, M. R.; Ibrahim, A. A.; Chong, K. F.; Soldatov, A. V.; Ali, G. A. Glycopolymer-based materials: synthesis, properties, and biosensing applications. *Topics in Current Chemistry* **2022**, *380* (5), 45.
(125) Hill, M. R.; Carmean, R. N.; Sumerlin, B. S. Expanding the Scope of RAFT Polymerization: Recent Advances and New Horizons. *Macromolecules* **2015**, *48* (16), 5459-5469. DOI: 10.1021/acs.macromol.5b00342.
(126) Allegrezza, M. L.; Konkolewicz, D. PET-RAFT polymerization: Mechanistic perspectives for future materials. *ACS Macro Letters* **2021**, *10* (4), 433-446.
(127) Zhang, Q.; Voorhaar, L.; De Geest, B. G.; Hoogenboom, R. One-Pot Preparation of Inert Well-Defined Polymers by RAFT Polymerization and In Situ End Group Transformation. *Macromolecular rapid communications* **2015**, *36* (12), 1177-1183.
(128) Alagi, P.; Hadjichristidis, N.; Gnanou, Y.; Feng, X. Fast and complete neutralization of thiocarbonylthio compounds using trialkylborane and oxygen: application to their removal from RAFT-synthesized polymers. *ACS Macro Letters* **2019**, *8* (6), 664-669.
(129) Imamura, Y.; Yamago, S. Role of Lewis Acids in preventing the degradation of dithioester-dormant species in the RAFT polymerization of acrylamides in methanol to enable the successful dual control of molecular weight and tacticity. *Polymer Chemistry* **2021**, *12* (37), 5336-5341.
(130) Liu, D.; Cai, W.; Zhang, L.; Boyer, C.; Tan, J. Efficient photoinitiated polymerization-induced self-assembly with oxygen tolerance through dual-wavelength type I photoinitiation and photoinduced deoxygenation. *Macromolecules* **2020**, *53* (4), 1212-1223.
(131) Chen, M.; Hao, J.; Zhang, W.; Shi, G.; Zhang, X.; Cui, Z.; Fu, P.; Liu, M.; Qiao, X.; He, Y. Highly Efficient Near-Infrared Photoinduced Electron/Energy Transfer-Reversible Addition–Fragmentation Chain Transfer Polymerization via the Energy Transfer Upconversion Mechanism. *Macromolecules* **2022**, *55* (24), 10788-10796.
(132) Zhao, M.; Zhu, S.; Yang, X.; Wang, Y.; Zhou, X.; Xie, X. A Porphyrinic Donor–Acceptor Conjugated Porous Polymer as Highly Efficient Photocatalyst for PET–RAFT Polymerization. *Macromolecular Rapid Communications* **2022**, *43* (18), 2200173.
(133) Nagao, M.; Kimoto, Y.; Hoshino, Y.; Miura, Y. Facile Preparation of a Glycopolymer Library by PET-RAFT Polymerization for Screening the Polymer Structures of GM1 Mimics. *ACS Omega* **2022**, *7* (15), 13254-13259. DOI: 10.1021/acsomega.2c00719.
(134) Wu, C.; Jung, K.; Ma, Y.; Liu, W.; Boyer, C. Unravelling an oxygen-mediated reductive quenching pathway for photopolymerisation under long wavelengths. *Nature Communications* **2021**, *12* (1), 478. DOI: 10.1038/s41467-020-20640-z.
(135) Poisson, J.; Polgar, A. M.; Fromel, M.; Pester, C. W.; Hudson, Z. M. Preparation of patterned and multilayer thin films for organic electronics via oxygen-tolerant SI-PET-RAFT. *Angewandte Chemie International Edition* **2021**, *60* (36), 19988-19996.
(136) Huang, Y.; Li, X.; Zhang, Y. C.; Shi, Z.; Zeng, L.; Xie, J.; Du, Y.; Lu, D.; Hu, Z.; Cai, T. Aqueous protein–polymer bioconjugation via photoinduced RAFT polymerization using high loading heterogeneous catalyst. *ACS Applied Materials & Interfaces* **2021**, *13* (37), 44488-44496.
(137) Li, Z.; Ganda, S.; Melodia, D.; Boyer, C.; Chapman, R. Well-Defined Polymers for Nonchemistry Laboratories using Oxygen Tolerant Controlled Radical Polymerization. *Journal of Chemical Education* **2020**, *97* (2), 549-556.

(138) Matyjaszewski, K. Advanced materials by atom transfer radical polymerization. *Advanced Materials* **2018**, *30* (23), 1706441.
(139) Lorandi, F.; Fantin, M.; Matyjaszewski, K. Atom transfer radical polymerization: a mechanistic perspective. *Journal of the American Chemical Society* **2022**, *144* (34), 15413-15430.
(140) Liu, X. h.; Wang, J.; Zhang, F. j.; An, S. l.; Ren, Y. l.; Yu, Y. h.; Chen, P.; Xie, S. Copper-mediated initiators for continuous activator regeneration atom transfer radical polymerization of acrylonitrile. *Journal of Polymer Science Part A: Polymer Chemistry* **2012**, *50* (20), 4358-4364.
(141) Herberg, A.; Yu, X.; Kuckling, D. End group stability of atom transfer radical polymerization (ATRP)-synthesized poly (N-isopropylacrylamide): Perspectives for diblock copolymer synthesis. *Polymers* **2019**, *11* (4), 678.
(142) Rabea, A. M.; Zhu, S. Ultrasonically enhanced bulk ATRP of methyl methacrylate at high conversion with good livingness and control. *AIChE Journal* **2016**, *62* (5), 1683-1687.
(143) Butcher, W. E.; Radzinski, S. C.; Tillman, E. S. Selective formation of diblock copolymers using radical trap-assisted atom transfer radical coupling. *Journal of Polymer Science Part A: Polymer Chemistry* **2013**, *51* (17), 3619-3626.
(144) Nedeljkovic, D. Polystyrene-b-Poly (2-(Methoxyethoxy) ethyl Methacrylate) Polymerization by Different Controlled Polymerization Mechanisms. *Polymers* **2021**, *13* (20), 3505.
(145) Kwak, Y.; Magenau, A. J.; Matyjaszewski, K. ARGET ATRP of methyl acrylate with inexpensive ligands and ppm concentrations of catalyst. *Macromolecules* **2011**, *44* (4), 811-819.
(146) Isse, A. A.; Gennaro, A. Electrochemistry for atom transfer radical polymerization. *The Chemical Record* **2021**, *21* (9), 2203-2222.
(147) Guerrero-Caicedo, A.; Pardo-Tamayo, J. S.; Romero, E. L.; Zuluaga, F.; Echegoyen, L.; Jaramillo-Gómez, L. M. α-Hydrogen spirocyclic alkoxyamines synthesis: ESR verified Nitroxides generation and their potential application in NMP polymerization. *ChemistrySelect* **2023**, *8* (33), e202301841.
(148) Sciannamea, V.; Catala, J. M.; Jerome, R.; Detrembleur, C. Fast controlled radical polymerization of styrene mediated by oligomeric nitroxides formed in situ. *Macromolecular rapid communications* **2007**, *28* (2), 147-151.
(149) Takamura, M.; Yamauchi, T.; Tsubokawa, N. Preparation and dispersibility of poly (L-lactide)-grafted silica nanoparticle. *Journal of applied polymer science* **2012**, *124* (5), 3854-3860.
(150) Tardy, A.; Nicolas, J.; Gigmes, D.; Lefay, C.; Guillaneuf, Y. Radical ring-opening polymerization: Scope, limitations, and application to (bio) degradable materials. *Chemical reviews* **2017**, *117* (3), 1319-1406.
(151) Nuyken, O.; Pask, S. D. Ring-opening polymerization—an introductory review. *Polymers* **2013**, *5* (2), 361-403.
(152) Cruz, P.; Pérez, Y.; del Hierro, I.; Fernández-Galán, R.; Fajardo, M. ε-Caprolactone polymerization using titanium complexes immobilized onto silica based materials functionalized with ionic liquids: insights into steric, electronic and support effects. *RSC advances* **2016**, *6* (24), 19723-19733.
(153) Zhang, X.; Cai, M.; Zhong, Z.; Zhuo, R. A water-soluble polycarbonate with dimethylamino pendant groups prepared by enzyme-catalyzed ring-opening polymerization. *Macromolecular rapid communications* **2012**, *33* (8), 693-697.

(154) Shi, Y.; Schmalz, H.; Agarwal, S. Designed enzymatically degradable amphiphilic conetworks by radical ring-opening polymerization. *Polymer Chemistry* **2015**, *6* (35), 6409-6415.
(155) Bonda, L.; Valles, D. J.; Wigger, T. L.; Meisner, J.; Braunschweig, A. B.; Hartmann, L. TIRP–Thiol-Induced, Light-Activated Controlled Radical Polymerization. *Macromolecules* **2023**, *56* (14), 5512-5523.
(156) Honigfort, D. J.; Altman, M. O.; Gagneux, P.; Godula, K. Glycocalyx crowding with mucin mimetics strengthens binding of soluble and virus-associated lectins to host cell glycan receptors. *Proceedings of the National Academy of Sciences* **2021**, *118* (40), e2107896118.
(157) Kim, K. H.; Lee, J. C.; Lee, J. Amphiphilic Comb-Like Polymers Based on Poly (oxyethylene) s as Drug-Delivery Carriers. *Macromolecular bioscience* **2008**, *8* (4), 339-346.
(158) Sieste, S.; Mack, T.; Synatschke, C. V.; Schilling, C.; Meyer zu Reckendorf, C.; Pendi, L.; Harvey, S.; Ruggeri, F. S.; Knowles, T. P.; Meier, C. Water-Dispersible Polydopamine-Coated Nanofibers for Stimulation of Neuronal Growth and Adhesion. *Advanced Healthcare Materials* **2018**, *7* (11), 1701485.
(159) Elias, H.-G. *Makromoleküle, Band 4: Anwendungen von Polymeren*; John Wiley & Sons, 2009.
(160) Gauthier, M. A.; Gibson, M. I.; Klok, H. A. Synthesis of functional polymers by post-polymerization modification. *Angewandte Chemie International Edition* **2009**, *48* (1), 48-58.
(161) Eissa, A. M.; Abdulkarim, A.; Sharples, G. J.; Cameron, N. R. Glycosylated nanoparticles as efficient antimicrobial delivery agents. *Biomacromolecules* **2016**, *17* (8), 2672-2679.
(162) Nagao, M.; Matsubara, T.; Hoshino, Y.; Sato, T.; Miura, Y. Topological design of star glycopolymers for controlling the interaction with the influenza virus. *Bioconjugate chemistry* **2019**, *30* (4), 1192-1198.
(163) Salvadó, M.; Reina, J. J.; Rojo, J.; Castillón, S.; Boutureira, O. Topological defects in hyperbranched glycopolymers enhance binding to lectins. *Chemistry–A European Journal* **2017**, *23* (62), 15790-15794.
(164) Wang, Y.; Gu, L.; Xu, F.; Xin, F.; Ma, J.; Jiang, M.; Fang, Y. Chemoenzymatic synthesis of branched glycopolymer brushes as the artificial glycocalyx for lectin specific binding. *Langmuir* **2019**, *35* (13), 4445-4452.
(165) Park, H.; Rosencrantz, R. R.; Elling, L.; Böker, A. Glycopolymer Brushes for Specific Lectin Binding by Controlled Multivalent Presentation of N-Acetyllactosamine Glycan Oligomers. *Macromolecular rapid communications* **2015**, *36* (1), 45-54.
(166) Ribeiro, J. P.; Mendonça, P. V.; Coelho, J. F.; Matyjaszewski, K.; Serra, A. C. Glycopolymer brushes by reversible deactivation radical polymerization: Preparation, applications, and future challenges. *Polymers* **2020**, *12* (6), 1268.
(167) Yu, K.; Kizhakkedathu, J. N. Synthesis of functional polymer brushes containing carbohydrate residues in the pyranose form and their specific and nonspecific interactions with proteins. *Biomacromolecules* **2010**, *11* (11), 3073-3085.
(168) Von der Ehe, C.; Weber, C.; Gottschaldt, M.; Schubert, U. S. Immobilized glycopolymers: Synthesis, methods and applications. *Progress in Polymer Science* **2016**, *57*, 64-102.
(169) Xie, G.; Martinez, M. R.; Olszewski, M.; Sheiko, S. S.; Matyjaszewski, K. Molecular bottlebrushes as novel materials. *Biomacromolecules* **2018**, *20* (1), 27-54.
(170) Ndugire, W.; Wu, B.; Yan, M. Synthesis of carbohydrate-grafted glycopolymers using a catalyst-free, perfluoroarylazide-mediated fast staudinger reaction. *Molecules* **2019**, *24* (1), 157.

(171) Chang, A. B.; Lin, T.-P.; Thompson, N. B.; Luo, S.-X. L.; Liberman-Martin, A. L.; Chen, H.-Y.; Lee, B.; Grubbs, R. H. Design, synthesis, and self-assembly of polymers with tailored graft distributions. *Journal of the American Chemical Society* **2017**, *139* (48), 17683-17693.
(172) Sumerlin, B. S.; Neugebauer, D.; Matyjaszewski, K. Initiation efficiency in the synthesis of molecular brushes by grafting from via atom transfer radical polymerization. *Macromolecules* **2005**, *38* (3), 702-708.
(173) Mitchell, D. A.; Zhang, Q.; Voorhaar, L.; Haddleton, D. M.; Herath, S.; Gleinich, A. S.; Randeva, H. S.; Crispin, M.; Lehnert, H.; Wallis, R. Manipulation of cytokine secretion in human dendritic cells using glycopolymers with picomolar affinity for DC-SIGN. *Chemical Science* **2017**, *8* (10), 6974-6980.
(174) Wang, J.; Zhou, J.; Ding, Y.; Hu, X.; Chen, Y. Glycopolymers based on carbohydrate or vinyl backbones and their biomedical applications. *Polymer Chemistry* **2023**, *14* (20), 2414-2434.
(175) Abdouni, Y.; Yilmaz, G.; Monaco, A.; Aksakal, R.; Becer, C. R. Effect of arm number and length of star-shaped glycopolymers on binding to dendritic and Langerhans cell lectins. *Biomacromolecules* **2020**, *21* (9), 3756-3764.
(176) Chen, Y.; Lord, M. S.; Piloni, A.; Stenzel, M. H. Correlation between molecular weight and branch structure of glycopolymers stars and their binding to lectins. *Macromolecules* **2015**, *48* (2), 346-357.
(177) Monaco, A.; Beyer, V. P.; Napier, R.; Becer, C. R. Multi-Arm Star-Shaped Glycopolymers with Precisely Controlled Core Size and Arm Length. *Biomacromolecules* **2020**, *21* (9), 3736-3744.
(178) Zhang, Q.; Su, L.; Collins, J.; Chen, G.; Wallis, R.; Mitchell, D. A.; Haddleton, D. M.; Becer, C. R. Dendritic cell lectin-targeting sentinel-like unimolecular glycoconjugates to release an anti-HIV drug. *Journal of the American Chemical Society* **2014**, *136* (11), 4325-4332.
(179) Gao, H.; Min, K.; Matyjaszewski, K. Synthesis of 3-arm star block copolymers by combination of "core-first" and "coupling-onto" methods using ATRP and click reactions. *Macromolecular Chemistry and Physics* **2007**, *208* (13), 1370-1378.
(180) Patil, R. A.; Aloorkar, N.; Kulkarni, A.; Ingale, D. Star polymers: An overview. *International Journal of Pharmaceutical Sciences and Nanotechnology (IJPSN)* **2012**, *5* (2), 1675-1684.
(181) Xia, J.; Zhang, X.; Matyjaszewski, K. Synthesis of star-shaped polystyrene by atom transfer radical polymerization using an "arm first" approach. *Macromolecules* **1999**, *32* (13), 4482-4484.
(182) Boschmann, D. Sternpolymere mittels RAFT-Polymerisation. **2008**.
(183) Zhang, C.; Zhou, Y.; Liu, Q.; Li, S.; Perrier, S.; Zhao, Y. Facile synthesis of hyperbranched and star-shaped polymers by RAFT polymerization based on a polymerizable trithiocarbonate. *Macromolecules* **2011**, *44* (7), 2034-2049.
(184) Ren, J. M.; McKenzie, T. G.; Fu, Q.; Wong, E. H.; Xu, J.; An, Z.; Shanmugam, S.; Davis, T. P.; Boyer, C.; Qiao, G. G. Star polymers. *Chemical reviews* **2016**, *116* (12), 6743-6836.
(185) Bosman, A. W.; Vestberg, R.; Heumann, A.; Fréchet, J. M.; Hawker, C. J. A modular approach toward functionalized three-dimensional macromolecules: from synthetic concepts to practical applications. *Journal of the American Chemical Society* **2003**, *125* (3), 715-728.
(186) Masud, R. A.; Hasan, T. Synthesis of Well-defined High Molecular Weight 3-Arm Star Poly (methyl methacrylate) Using the "Core-First" Method by Atom Transfer Radical Polymerization.
(187) Gao, H. Development of star polymers as unimolecular containers for nanomaterials. *Macromolecular Rapid Communications* **2012**, *33* (9), 722-734.
(188) Khajeheian, M. B.; Rosling, A. Preparation and characterization of linear and star-shaped poly l-lactide blends. *Journal of Applied Polymer Science* **2016**, *133* (2).

(189) Gao, H.; Matyjaszewski, K. Structural control in ATRP synthesis of star polymers using the arm-first method. *Macromolecules* **2006**, *39* (9), 3154-3160.
(190) Lisowska, E. The role of glycosylation in protein antigenic properties. *Cellular and Molecular Life Sciences CMLS* **2002**, *59*, 445-455.
(191) Baker, S. L.; Munasinghe, A.; Kaupbayeva, B.; Rebecca Kang, N.; Certiat, M.; Murata, H.; Matyjaszewski, K.; Lin, P.; Colina, C. M.; Russell, A. J. Transforming protein-polymer conjugate purification by tuning protein solubility. *Nature Communications* **2019**, *10* (1), 4718.
(192) DeBenedictis, E. P.; Hamed, E.; Keten, S. Mechanical reinforcement of proteins with polymer conjugation. *ACS nano* **2016**, *10* (2), 2259-2267.
(193) Cummings, C.; Murata, H.; Koepsel, R.; Russell, A. J. Dramatically increased pH and temperature stability of chymotrypsin using dual block polymer-based protein engineering. *Biomacromolecules* **2014**, *15* (3), 763-771.
(194) Mancini, R. J.; Lee, J.; Maynard, H. D. Trehalose glycopolymers for stabilization of protein conjugates to environmental stressors. *Journal of the American Chemical Society* **2012**, *134* (20), 8474-8479.
(195) Wang, Y.; Wu, C. Site-specific conjugation of polymers to proteins. *Biomacromolecules* **2018**, *19* (6), 1804-1825.
(196) Fu, C.; Wang, Z.; Gao, Y.; Zhao, J.; Liu, Y.; Zhou, X.; Qin, R.; Pang, Y.; Hu, B.; Zhang, Y. Sustainable polymer coating for stainproof fabrics. *Nature Sustainability* **2023**, *6* (8), 984-994.
(197) Lele, B. S.; Murata, H.; Matyjaszewski, K.; Russell, A. J. Synthesis of uniform protein–polymer conjugates. *Biomacromolecules* **2005**, *6* (6), 3380-3387.
(198) Wright, T. A.; Page, R. C.; Konkolewicz, D. Polymer conjugation of proteins as a synthetic post-translational modification to impact their stability and activity. *Polymer chemistry* **2019**, *10* (4), 434-454.
(199) Lin, K.; Kasko, A. M. Multivalent 3D Display of Glycopolymer Chains for Enhanced Lectin Interaction. *Bioconjugate Chemistry* **2015**, *26* (8), 1504-1512.
(200) Lee, S.-G.; Brown, J. M.; Rogers, C. J.; Matson, J. B.; Krishnamurthy, C.; Rawat, M.; Hsieh-Wilson, L. C. End-functionalized glycopolymers as mimetics of chondroitin sulfate proteoglycans. *Chemical science* **2010**, *1* (3), 322-325.
(201) Le Droumaguet, B.; Nicolas, J. Recent advances in the design of bioconjugates from controlled/living radical polymerization. *Polymer Chemistry* **2010**, *1* (5), 563-598.
(202) Zhao, W.; Liu, F.; Chen, Y.; Bai, J.; Gao, W. Synthesis of well-defined protein–polymer conjugates for biomedicine. *Polymer* **2015**, *66*, A1-A10.
(203) Messina, M. S.; Messina, K. M.; Bhattacharya, A.; Montgomery, H. R.; Maynard, H. D. Preparation of biomolecule-polymer conjugates by grafting-from using ATRP, RAFT, or ROMP. *Progress in polymer science* **2020**, *100*, 101186.
(204) Theodorou, A.; Liarou, E.; Haddleton, D. M.; Stavrakaki, I. G.; Skordalidis, P.; Whitfield, R.; Anastasaki, A.; Velonia, K. Protein-polymer bioconjugates via a versatile oxygen tolerant photoinduced controlled radical polymerization approach. *Nature communications* **2020**, *11* (1), 1486.
(205) Sumerlin, B. S. Proteins as initiators of controlled radical polymerization: grafting-from via ATRP and RAFT. ACS Publications: 2012; Vol. 1, pp 141-145.
(206) Mansfield, K. M.; Maynard, H. D. Site-specific insulin-trehalose glycopolymer conjugate by grafting from strategy improves bioactivity. *ACS macro letters* **2018**, *7* (3), 324-329.
(207) Zhang, Q.; Li, M.; Zhu, C.; Nurumbetov, G.; Li, Z.; Wilson, P.; Kempe, K.; Haddleton, D. M. Well-defined protein/peptide–polymer conjugates by aqueous Cu-LRP: synthesis and

controlled self-assembly. *Journal of the American Chemical Society* **2015**, *137* (29), 9344-9353.
(208) Averick, S.; Simakova, A.; Park, S.; Konkolewicz, D.; Magenau, A. J.; Mehl, R. A.; Matyjaszewski, K. ATRP under biologically relevant conditions: grafting from a protein. *ACS Macro Letters* **2012**, *1* (1), 6-10.
(209) Szczepaniak, G.; Łagodzińska, M.; Dadashi-Silab, S.; Gorczyński, A.; Matyjaszewski, K. Fully oxygen-tolerant atom transfer radical polymerization triggered by sodium pyruvate. *Chemical Science* **2020**, *11* (33), 8809-8816.
(210) Olson, R. A.; Levi, J. S.; Scheutz, G. M.; Lessard, J. J.; Figg, C. A.; Kamat, M. N.; Basso, K. B.; Sumerlin, B. S. Macromolecular photocatalyst for synthesis and purification of protein–polymer conjugates. *Macromolecules* **2021**, *54* (10), 4880-4888.
(211) Tucker, B. S.; Coughlin, M. L.; Figg, C. A.; Sumerlin, B. S. Grafting-from proteins using metal-free PET–RAFT polymerizations under mild visible-light irradiation. *ACS Macro Letters* **2017**, *6* (4), 452-457.
(212) Heredia, K. L.; Bontempo, D.; Ly, T.; Byers, J. T.; Halstenberg, S.; Maynard, H. D. In situ preparation of protein− "smart" polymer conjugates with retention of bioactivity. *Journal of the American Chemical Society* **2005**, *127* (48), 16955-16960.
(213) Ko, J. H.; Maynard, H. D. A guide to maximizing the therapeutic potential of protein–polymer conjugates by rational design. *Chemical Society Reviews* **2018**, *47* (24), 8998-9014.
(214) Liu, X.; Gao, W. Precision conjugation: An emerging tool for generating protein–polymer conjugates. *Angewandte Chemie International Edition* **2021**, *60* (20), 11024-11035.
(215) Braunecker, W. A.; Matyjaszewski, K. Controlled/living radical polymerization: Features, developments, and perspectives. *Progress in polymer science* **2007**, *32* (1), 93-146.
(216) Wei, H.; Pahang, J. A.; Pun, S. H. Optimization of brush-like cationic copolymers for nonviral gene delivery. *Biomacromolecules* **2013**, *14* (1), 275-284.
(217) Gerland, B.; Goudot, A.; Pourceau, G.; Meyer, A.; Vidal, S.; Souteyrand, E.; Vasseur, J.-J.; Chevolot, Y.; Morvan, F. o. Synthesis of homo-and heterofunctionalized glycoclusters and binding to Pseudomonas aeruginosa lectins PA-IL and PA-IIL. *The Journal of organic chemistry* **2012**, *77* (17), 7620-7626.
(218) Matyjaszewski, K. Atom transfer radical polymerization (ATRP): current status and future perspectives. *Macromolecules* **2012**, *45* (10), 4015-4039.
(219) Nicolas, J.; San Miguel, V.; Mantovani, G.; Haddleton, D. M. Fluorescently tagged polymer bioconjugates from protein derived macroinitiators. *Chemical Communications* **2006**, (45), 4697-4699.
(220) Theodorou, A.; Gounaris, D.; Voutyritsa, E.; Andrikopoulos, N.; Baltzaki, C. I. M.; Anastasaki, A.; Velonia, K. Rapid Oxygen-Tolerant Synthesis of Protein-Polymer Bioconjugates via Aqueous Copper-Mediated Polymerization. *Biomacromolecules* **2022**, *23* (10), 4241-4253.
(221) Barner, L.; Barner-Kowollik, C.; Davis, T. P.; Stenzel, M. H. Complex molecular architecture polymers via RAFT. *Australian journal of chemistry* **2004**, *57* (1), 19-24.
(222) De, P.; Li, M.; Gondi, S. R.; Sumerlin, B. S. Temperature-regulated activity of responsive polymer− protein conjugates prepared by grafting-from via RAFT polymerization. *Journal of the American Chemical Society* **2008**, *130* (34), 11288-11289.
(223) Boyer, C.; Bulmus, V.; Liu, J.; Davis, T. P.; Stenzel, M. H.; Barner-Kowollik, C. Well-defined protein− polymer conjugates via in situ RAFT polymerization. *Journal of the American Chemical Society* **2007**, *129* (22), 7145-7154.

(224) Pelegri-O'Day, E. M.; Lin, E.-W.; Maynard, H. D. Therapeutic protein–polymer conjugates: advancing beyond PEGylation. *Journal of the American Chemical Society* **2014**, *136* (41), 14323-14332.
(225) Ciepluch, K.; Radulescu, A.; Hoffmann, I.; Raba, A.; Allgaier, J. r.; Richter, D.; Biehl, R. Influence of PEGylation on domain dynamics of phosphoglycerate kinase: PEG acts like entropic spring for the protein. *Bioconjugate chemistry* **2018**, *29* (6), 1950-1960.
(226) Pang, Y.; Liu, J.; Qi, Y.; Li, X.; Chilkoti, A. A Modular Method for the High-Yield Synthesis of Site-Specific Protein–Polymer Therapeutics. *Angewandte Chemie International Edition* **2016**, *55* (35), 10296-10300.
(227) Azevedo, H. S.; Braunschweig, A. B.; Chiechi, R. C.; Fernandez, Y. D.; Gildersleeve, J. C.; Godula, K.; Hartmann, L.; Miura, Y.; Schmidt, S.; Turnbull, W. B. Glycan interactions on glycocalyx mimetic surfaces: general discussion. *Faraday Discussions* **2019**, *219*, 183-188.
(228) Wiederschain, G. Y. Essentials of glycobiology. Springer Nature BV: 2009.
(229) Lopez Aguilar, A.; Briard, J. G.; Yang, L.; Ovryn, B.; Macauley, M. S.; Wu, P. Tools for studying glycans: recent advances in chemoenzymatic glycan labeling. *ACS chemical biology* **2017**, *12* (3), 611-621.
(230) Griffin, M. E.; Hsieh-Wilson, L. C. Glycan engineering for cell and developmental biology. *Cell chemical biology* **2016**, *23* (1), 108-121.
(231) Dube, D. H.; Bertozzi, C. R. Metabolic oligosaccharide engineering as a tool for glycobiology. *Current opinion in chemical biology* **2003**, *7* (5), 616-625.
(232) Saxon, E.; Bertozzi, C. R. Chemical and biological strategies for engineering cell surface glycosylation. *Annual review of cell and developmental biology* **2001**, *17* (1), 1-23.
(233) Hudak, J. E.; Canham, S. M.; Bertozzi, C. R. Glycocalyx engineering reveals a Siglec-based mechanism for NK cell immunoevasion. *Nature chemical biology* **2014**, *10* (1), 69-75.
(234) Cohen, M.; Senaati, H. P.; Fisher, C. J.; Huang, M. L.; Gagneux, P.; Godula, K. Synthetic mucus nanobarriers for identification of glycan-dependent primary influenza A infection inhibitors. *ACS Central science* **2016**, *2* (10), 710-714.
(235) Honigfort, D. J.; Zhang, M. H.; Verespy, S.; Godula, K. Engineering of spectator glycocalyx structures to evaluate molecular interactions at crowded cellular boundaries. *Faraday discussions* **2019**, *219*, 138-153.
(236) Omidvar, R.; Römer, W. Glycan-decorated protocells: novel features for rebuilding cellular processes. *Interface Focus* **2019**, *9* (2), 20180084.

6 Supporting Information

6.1 Methodical section

This thesis was prepared using only the technical analytic methods outlined in the supporting informations, sections 0 - 6.5. Furthermore, the following programs were utilized in the completion of this work, along with their intended purposes: *Word* (version Office 16) as writing program of this dissertation, *PowerPoint* (version Office 16) to create and edit the figures, *OneNote* (version 21, Word add-in) as a citation program and for literature management, *ChemDraw* (version 22.2.0 64-bit) to draw and edit the chemical cultures, *Origin* (version 2021b) for creating and editing data sets and diagrams, *MestReNova* (version x64) for analyzing and interpreting NMR spectra, *Paperpal* (version 3.272.3, april 2025, Word add-in) was editorial used for linguistic revision and optimization to improve the text's comprehensibility and coherence. The focus was exclusively on stylistic and grammatical improvements, without changing the core content. All content-related and scientific aspects were developed independently and originated from my own considerations and research.

6.2 Supporting Information - Thiol-selective native grafting from polymerization for the generation of protein-polymer conjugates

Authors:	Melina I. Feldhof, Sandro Sperzel, Lorand Bonda, Susanne Boye, Adam B. Braunschweig, Ulla I. M. Gerling-Driessen and Laura Hartmann
Journal:	Royal Society of Chemistry
Issue:	**2024**, *15*, 16768-16777
Type of Paper:	Edge Article
Impact Factor:	7.6 (2023)
DOI:	10.1039/D4SC04818K

Reprinted with permission from Royal Society of Chemistry.

Copyright © 2024 Royal Society of Chemistry.

Supplementary Information (SI) for Chemical Science.
This journal is © The Royal Society of Chemistry 2024

Supporting Information

Thiol-selective *native grafting-from* polymerization for the generation of protein-polymer conjugates

Melina I. Feldhof,[a] Sandro Sperzel,[a] Lorand Bonda,[a] Susanne Boye,[b] Adam B. Braunschweig,[c] Ulla I.M. Gerling-Driessen,*[d] and Laura Hartmann*[d]

[a] Department of Organic and Macromolecular Chemistry, Heinrich-Heine-University Düsseldorf, Universitätsstraße 1, 40225 Düsseldorf, Germany
[b] Zentrum Makromolekulare Strukturanalyse, Leibniz-Institut für Polymerforschung Dresden, Hohe Str. 6, 01069 Dresden, Germany
[c] Advanced Science Research Center, Graduate Center, City University of New York, 85 St. Nicholas Terrace, New York, NY 10031, USA; PhD Programs in Chemistry and Biochemistry, Graduate Center, City University of New York, 365 5th Avenue, New York, NY 10016, USA; Department of Chemistry, Hunter College, 695 Park Avenue, New York, NY 10065, USA
[d] Institute for Macromolecular Chemistry, University of Freiburg, Stefan-Meier-Str. 31, D-79104 Freiburg i.Br., Germany, E-mail: laura.hartmann@hhu.de, ulla.gerling-driessen@makro.uni-freiburg.de

*Corresponding author

Table of Contents

1. Experimental Parts 2
1.1 Materials 2
1.2 Instrumentation 2
1.3 General Methods 4
2. Synthesis and analytical data 6
2.1 Synthesis of carbohydrate monomers ***S1*-*S4*** 6
2.2 Synthesis and measurements of BSA-polymer conjugates **1**-**4** 16
2.3 Synthesis and measurements of CRL-polymer conjugates **5**-**7** 40
2.4 Synthesis of inhibitor polymers ***S7*** and ***S8*** 46
2.5 Carbohydrate-lectin binding studies on glass surfaces 49

1. Experimental Parts

1.1 Materials

All chemicals and solvents were used without further purification and were purchased from commercial sources. Type I water, purified by Barnstead™ MicroPure™ ThermoFisher SCIENTIFIC ultrapure water system, was used unless otherwise mentioned. *Bio-Rad:* 10xtris-glycin/SDS-running buffer, pH 8.6, coomassie brilliant blue, precision plus protein™ kaleidoscope™; *Acros Organics:* 4-nitrophenyl acetate ≥ 97%, N-isopropylacrylamide ≥ 99%, para- toluene sulfonic acid ≥ 99%; *Alfa Aesar*: boron trifluoride dietherate ≥ 98%, sodium methanolate ≥ 98%; *BIOZOL*: RCA_{120}, RCA_{120} (FITC); *BLDpharm*: β-D-galactose pentaacetate ≥ 98%; *Carl Roth*: guanidine hydrochloride ≥ 99.5%; *Eurisotope*: chloroform-d ≥ 99.8%; *Fisher BioReagents*™: 2-(4-(2-hydroxyethyl)-1-piperazinyl)-ethane sulfonic acid (HEPES) ≥ 99%; *Fisher scientific*: Concanavalin A Alexa 647; *Fluka*: α-D-mannose ≥ 99; *Grüssing*: sodium dihydrogen phosphates ≥ 99%, sodium bicarbonate ≥ 99.5%; *Honeywell*: sodium sulphate ≥ 99%, acetonitrile ≥ 99.9%; *J&K*: tris(2-phenylpyridine)iridium(III) ≥ 99%; *Merck*: calcium chloride ≥ 90%, deuterated water ≥ 99.9%, dichloromethane ≥ 99.8%, acetic anhydride ≥ 99.5%, methanol ≥ 99.8%, sodium carbonate ≥ 99.7%, sodium chloride 100%; *PanReac AppliChem*: phosphate buffered saline tablet (PBS), dimethyl sulfoxide (DMSO) ≥ 99.9%; *Sigma Aldrich*: Concanavalin A (ConA), N-hydroxyethyl acrylamide ≥ 97.4%, 5,5′-Dithiobis(2-nitrobenzoic acid) ≥ 98%, Amberlite®IR120, *bovine serum albumin* (BSA) ≥ 96%, *candida rugosa lipase* ≥ 2U/mg, DMSO-d_6 ≥ 99.9%, ethylenediaminetetraacetic acid 99%, manganese(II) chloride tetrahydrate ≥ 99%; *TCI*: diphenyl(2,4,6-trimethylbenzoyl)phosphine oxide (TPO) ≥ 98%, tris(2-carboxyethyl)phosphine (TCEP) ≥ 98%; *Thermo-Fisher*: pierce BCA protein assay kit; *VWRChemicals*: acetone 100%.

1.2 Instrumentation

Nuclear magnetic Resonance Spectroscopy (NMR):

^{1}H-NMR spectra were measured with a Bruker Avance III 600 (600 MHz) at room temperature. Chemical shifts were reported in delta (δ) expressed in parts per million (ppm) for all ^{1}H-NMR spectrum. D_2O serves as the deuterated solvents for all ^{1}H-NMR spectrum. Parts of non-deuterated solvent were used as an internal standard with δ = 4.79 for HDO. Multiplicities were abbreviated as the following: singlet (s), doublet (d), triplet (t), quartet (q), multiplet (m). The assignment of carbohydrate signals on NMR followed the chronological enumeration of protons/carbon atoms within a monosaccharide starting from the reducing end.

Reversed Phase High Pressure Liquid Chromatography Mass Spectrometry (RP-HPLC-MS): RP-HPLC-MS measurements were performed on Agilent Technologies 1260 Infinity series coupled with Agilent quadrupole mass spectrometer with an Electrospray Ionization (ESI) source operating in a m/z range of 200 to 2000. All spectra were measured with A: 95% H_2O, 5% ACN, 0.1% formic acid and B: 5% H_2O, 95% ACN, 0.1% formic acid. Separation was performed at 25 °C using an Agilent MZ-Aqua Perfect C_{18} 3 µm (50 x 3.0 mm) column with a linear solvent gradient starting at 100% A, ending at 50% B in 17 min at a flow rate of 0.4 mL/min. Indicated purities were determined by integration of the UV-signal detected by a wavelength detector set to 214 nm with the OpenLab ChemStation software for LC/MS from Agilent Technologies.

UV/Vis spectroscopy: UV/Vis spectroscopy was performed with a dual-trace spectrometer Specord® 210 Plus from Analytik Jena AG. The measurements were conducted in quartz glass cuvettes (Starna GmbH d = 1 cm) at 20 °C. The instrument was operated with Win ASPECT PLUS software.

UV-Irradiation: UV irradiation of the polymerization was conducted with a UV-LED spot with a wavelength of 405 nm and a maximal irradiance of 114-5700 mW/cm^2 operated by a LEDControl both purchased from Opsytec Dr. Gröbel.

Microplate Reader: Absorption measurements were conducted on CLARIOstar® from BMG LABTECH. Measurements were performed at room temperature and analyzed by using BMG Mars software. 96 F-bottom corrugated plates from Greiner BIO-ONE were used for all measurements.

Sodium Dodecyl Sulfate – PolyAcrylamid Gel Electrophoresis (SDS-PAGE): Separations were performed with a 10% acrylamide gel at a voltage of 200 mV and current of 200 mA for about 36 min. 10xTris glycine/SDS buffer, which was diluted down to 1x, serves as the running buffer. Coomassie Brilliant Blue was used to stain the protein bands.

Asymmetrical flow field-flow fractionation with light scattering detection (AF4-LS): AF4-LS measurements were conducted on Eclipse Neon (Wyatt Technologies Europe) equipped with a Dilution Control Module™ (DCM) using an Agilent pump system (1260, Infinity Series) at 25 °C in PBS buffer (1 mM, pH 7.4). A short channel with fixed height (350 µm) and regenerated cellulose (cut-off: 10 kDa) as ultrafiltration membrane for all measurements. Detection was performed using the LS detector (DAWN Neon, Wyatt λ = 660 nm) with QELS option, RI detector (Optilab T-rEX, Wyatt) and UV detectors of various wavelengths (λ = 280, 300, 310, 330 nm).

Circular dichroism (CD): CD measurements were conducted on a Jasco J-710 CD spectrometer from Jasco Deutschland GmbH with quartz glass cuvettes (Starna GmbH d = 1 cm) at 20 °C in PBS buffer (pH 7.4).

Infrared spectroscopy (IR): IR spectroscopic measurements were conducted on a Nicolet iS50 FT-IR from Thermo Scientific with. The analysis was carried out with the OMNIC spectroscopy software from thermoscientific.

Fluorescence microscopy: All fluorescence microscopy images were conducted on Olympus IX73 with 60x oil-lenses. For the appropriate excitation we used Thorlabs LED-lamps (M625L4 – 625 nm, 700 mW, 1000 mA and M470L5 - 470 nm, 809 mW, 1000 mA).

Aqueous SEC-MALS-RI: SEC-MALS-RI measurements of the polymeric inhibitors ***S7*** and ***S8*** were conducted using Wyatt systems, isocratic pump, degasser, AS of 1260 Infinity series, LS detector: DAWN Heleos-II (Wyatt), λ = 660 nm RI detector: Optilab T-rEX (Wyatt), λ = 660 nm UV detector: UV detector SPD-M20 (Shimadzu): With variable wavelengths Channel (1) λ = 220 nm, Channel (2) λ = 230 nm Channel (3) λ = 250 nm, Channel (4) λ = 290 nm, Flow rate: 1 mL/min, temperature: 25 °C, Concentration: 3-4 mg/mL, Injection volume: 100 µL. Precolumn (50 mm, 2 x 160 Å of 300 mm and 1000 Å of 300 mm), two main columns (GE Healthcare GPC column Superdex 75 10/300, 8 mm diameter and 5 µm particle size), eluent: MilliQ water:acetonitrile 7:3 (v/v), 50 mM, NaH_2PO_4, 150 mM NaCl and 250 ppm NaN_3, pH = 7.0.

Differential Scanning Calorimetry (DSC): DSC measurements were performed using a Mettler Toledo DSC3 instrument calibrated with indium and zinc. Samples were weighed in 40 µL aluminum crucibles with perforated lids and experiments were performed under nitrogen atmosphere. Three measurements (heating, cooling, heating) were measured in the range of 20 °C - 200 °C with a heating or cooling rate of 10 K/min. DSC measurements were evaluated using STARe software.

1.3 General Methods

SDS-PAGE: Molecular weights of the protein polymer conjugates were determined using 10% acrylamide gels and 1X-Tris/glycine/SDS running buffer. 1 mg/mL stock solutions (in 1x PBS, pH 7.4) were prepared for each sample and 15 µL of each was mixed with 5 µL of Laemmli buffer followed by denaturation in a thermal shaker at 95 °C for 15 min. After cooling to room temperature, 8 µL of each sample mixture was applied to the gel. Precision Plus Protein™ Dual

Xtra Prestained Protein Standard (3µL) was used as reference for molecular weights. Separation was performed over a period of 36 min at 200 mV and 200 mA. Coomassie Brilliant Blue was used to stain the proteins. Stained gels were imaged using a ChemiDoc™ MP Imaging System gel from BioRad.

CD Measurements: CD measurements were conducted in quartz cuvettes (d = 1 cm). The measurement volume was 200 µL and the wavelength range was 190 nm – 260 nm. Measurements were performed as triplicates at a scanning speed of 100 nm/min. For thermal denaturation experiments temperature-dependent measurements at 222 nm were performed in a temperature range from 20 °C to 95 °C with an increase of 2 °C/min.

AF4-LS measurements: The samples were dissolved in a 1 – 2 mg/mL stock solution. 10 mM PBS buffer at pH 7.4, containing 200 mg/L NaN_3 to prevent bacteria or algae contamination was used as eluent and solvent. Triplicate measurements were performed for each sample and 50 µL were injected for each measurement. The optimized flow profile for the separation of all samples is shown in Figure 1 of the manuscript. The following protocol was applied in order to separate the different populations of BSA: channel flow was set to 1.0 mL/min with a detector of 0.4 mL/min, focusing was performed with a focus flow of 3.0 mL/min for 6 min followed by an isocratic elution step with a cross flow (F_x) of 3 mL/min for 15 min. The last step proceeds without F_x (0 mL/min) for 20 min. Molar masses were calculated from the LS data applying a Zimm fit. Refractive index increments (dn/dc) were determined by manual injection of varied sample concentrations into above mentioned RI detector.

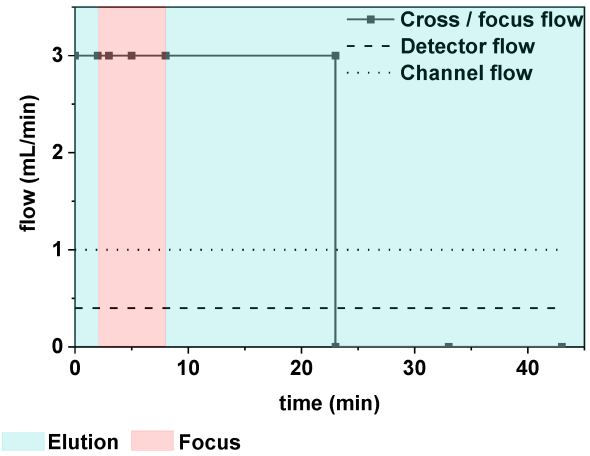


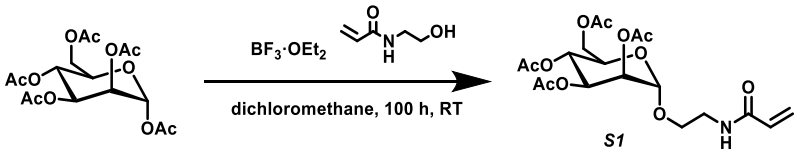
Fig. S1: Optimized AF4-LS separation flow profile.

2. Synthesis and analytical data

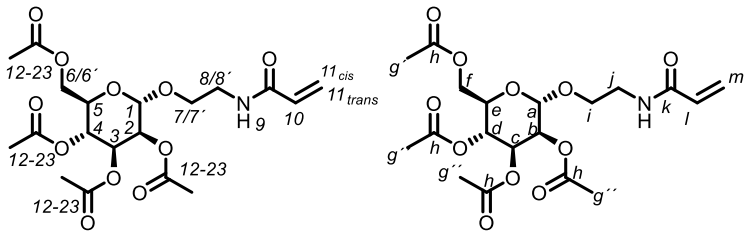
2.1 Synthesis of carbohydrate monomers *S1-S4*

The syntheses of the carbohydrate monomer are adapted from F. Schröer et al.[4]

S1 - 2,3,4,6-tetra-O-acetyl-α-D-mannopyranosyl-ethylacrylamide (AcManEAA)



67.3 g (172.4 mmol) of α-D-mannosepentaacetate, was dissolved with 500 mL dichloromethane, 27.6 mL (266 mmol) of *N*-hydroxyethyl acrylamide was added, and the reaction solution was cooled to 0 °C for 10 min using an ice bath. Then 105 mL (828.6 mmol) of boron trifluoride diethyl etherate was added over a period of 30 min, and the reaction was stirred for 100 h at room temperature (20 °C) in the absence of light. The reaction progress was checked by DC (ethyl acetate/hexane, 1:1, *v/v*). The reaction solution was added to 1 L of ice water and stirred until the ice was completely melted. Then, the organic phase was washed four times with 400 mL of saturated sodium hydrogen carbonate solution and three times with 400 mL of water and then dried using sodium sulfate. The solvent was removed under reduced pressure. An amber viscous product was obtained with a yield of 64.55 g (84%).



^{1}H-NMR (600 MHz, $CDCl_3$, 297.9 K) δ (ppm) 6.33 – 6.28 (dd, ^3J = 17.0, 1.4 Hz, 1H, *H10*), 6.18 – 6.13 (dd, ^3J = 17.0, 10.3 Hz, 1H, $H11_{cis}$), 6.11 (s, 1H, *H9*), 5.70 – 5.66 (dd, ^3J = 10.3, 1.4 Hz, 1H, $H11_{trans}$), 5.35 – 5.31 (m, 1H, *H4*), 5.27 – 5.23 (m, 2H, *H2 – H3*), 4.83 – 4.8 (d, ^3J = 1.7 Hz, 1H, *H1*), 4.26 – 4.22 (dd, ^3J = 12.2, 5.8 Hz, 1H, *H6a – H6b*), 4.13 – 4.10 (dd, ^3J = 12.2, 2.5 Hz, 1H, *H6a – H6b*), 3.99 – 3.95 (ddd, ^3J = 10.1, 5.7, 2.5 Hz, 1H, *H5*), 3.84 – 3.79 (m, 1H, *H7a - H7b*), 3.65 – 3.58 (m, 2H, *H7a, H7b, H8a, H8b*), 3.53 – 3.49 (m, 1H, *H8a - H8b*), 2.15 (s, 3H, *H12 - H23*), 2.09 (s, 3H, *H12 - H23*), 2.04 (s, 3H, *H12 - H23*), 2.00 (s, 3H, *H12 - H23*).

^{13}C-NMR (600 MHz, $CDCl_3$, 297.9 K) δ (ppm) 170.78 (4C, *Ch*), 165.73 (1C, *Ck*), 130.66 (1C, *Cl*), 127.11 (1C, *Cm*), 97.91 (1C, *Ca*), 69.49 (1C, *Ce*), 69.10, 68.91, 67.72 (3C, *Cb – Cd*), 66.29 (1C, *Ci*), 62.64 (1C, *Cf*), 39.27 (1C, *Cj*), 21.00 (3C, *C7g´´*), 20.83 (1C, *Cg´*).

LC-MS: m/z calculated for $C_{19}H_{27}NO_{11}$ $[M+H]^+$ 446.16, found 446.20 und $[M+Na]^+$ 468.16, found 468.20 determined relative purity: > 95%.

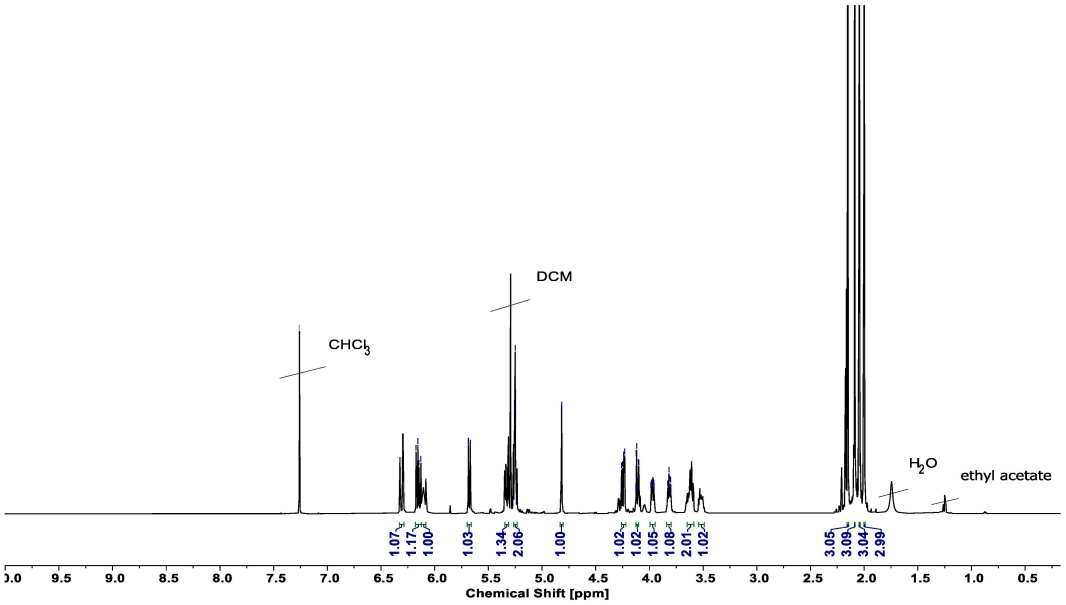


*Fig. S2: [1]H-NMR spectrum (600 MHz, CHCl3, 297.9 K) of α-D-ManAcEAA (**S1**).*

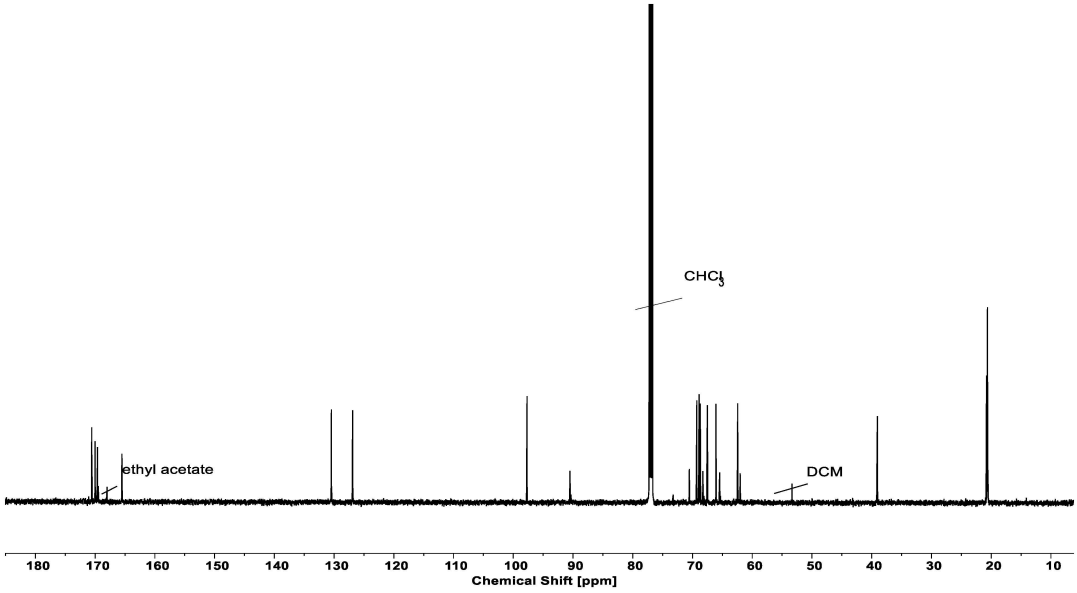


*Fig. S3: 13C-NMR spectrum (600 MHz, CHCl3, 297.9 K) of α-D-ManAcEAA (**S1**).*

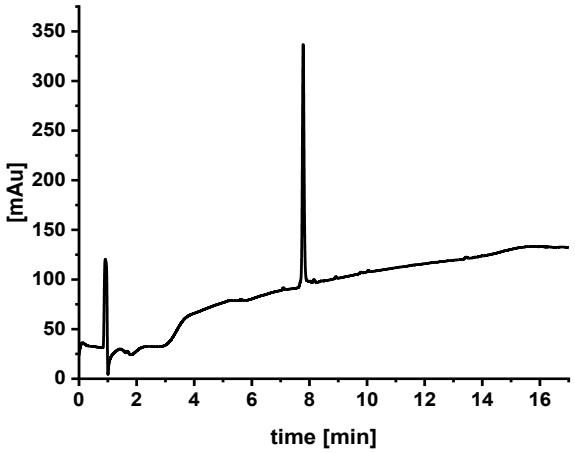


*Fig. S4: RP-HPCL chromatogram of α-D-ManAcEAA (**S1**) at t = 8.46 min (gradient of 5 to 95 vol% acetonitrile/water with 0.1 vol% formic acid, run time: 17 min).*

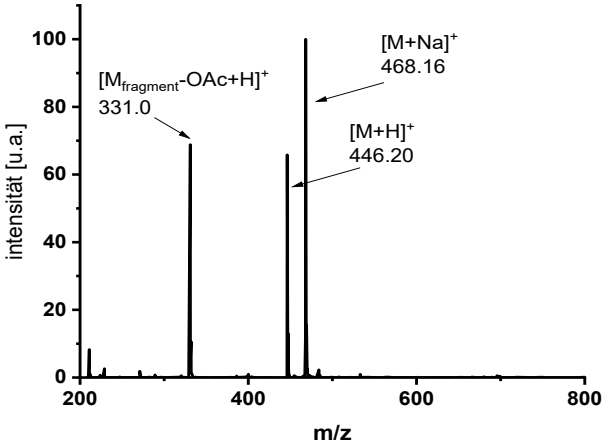
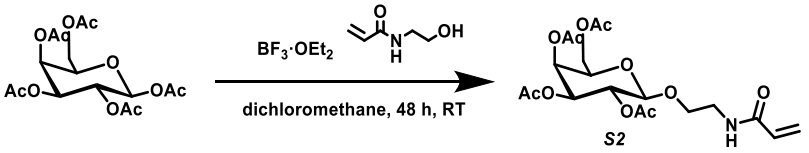
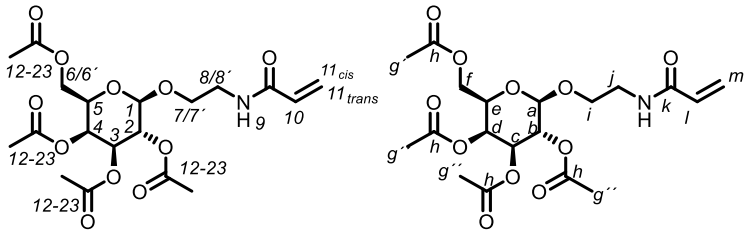


*Fig. S5: Mass spectrum of α-D-ManAcEAA (**S1**) at t = 8.46 min (gradient of 5 to 95 vol.% acetonitrile/water with 0.1 vol.% formic acid, run time: 17 min) by ESI-MS. The fragment at 331.0 m/z occurs during the ESI-MS measurement and corresponds to the product, where the acetyl group at the anomeric center was cleaved off.*

S2 - 2,3,4,6-Tetra-O-acetyl-β-D-Galactopyranosyl-ethylacrylamid (AcGalEAA)



20 g (51.2 mmol) of β-D-galactose pentaacetate was dissolved with 200 mL of dichloromethane to which 8 mL (76.4 mmol) of *N*-hydroxyethyl acrylamide was added, and the reaction solution was cooled to 0°°C in an ice bath for 10 min. Subsequently, 31 mL (244.6 mmol) of boron trifluoride diethyl etherate was added over a period of 30 min and the reaction was stirred for 48 h at room temperature (20°°C) in the absence of light. The reaction progress was checked by DC (ethyl acetate/hexane 1:1, *v/v*). The reaction solution was added to 500 mL of ice water and stirred until the ice was completely melted. The organic phase was washed three times with 300 mL of each, saturated sodium bicarbonate solution and water and was subsequently dried using sodium sulfate. The solvent was removed under reduced pressure. A viscous semi-crystalline yellowish product was obtained with a yield of 27.49 g (> 95%).



^{1}H-NMR (600 MHz, $CDCl_3$, 297.9 K) δ (ppm) 6.32 – 6.27 (dd, ^{3}J = 17.0, ^{2}J = 1.4 Hz, 1H, *H11$_{cis}$*), 6.13 – 6.08 (dd, ^{3}J = 17.0, 10.3 Hz, 1H, *H10*), 6.06 (s_{br}, 1H, *H9*), 5.67 – 5.64 (dd, ^{3}J = 10.3, ^{2}J = 1.4 Hz, 1H, *H11$_{trans}$*), 5.40 – 5.38 (dd, ^{3}J = 3.5, 1.1 Hz, 1H, *H4*), 5.20 – 5.16 (dd, ^{3}J = 10.5, 7.9 Hz, 1H, *H2 – H3*), 5.03 – 5.00 (dd, ^{3}J = 10.5, 3.4 Hz, 1H, *H2 – H3*), 4.48 – 4.45 (d, ^{3}J = 7.9 Hz, 1H, *H1*), 4.16 – 4.11 (m, 2H, *H6a – H6b*), 3.94 – 3.89 (m, 2H, *H7a – H7b*), 3.94 – 3.88 (ddd, ^{3}J = 10.3, 7.3, 3.4 Hz, 1H, *H5*), 3.64 – 3.58 (m, 1H, *H8a – H8b*), 3.52 – 3.46 (m, 1H, *H8a – H8b*), 2.16 (s, 3H, *H12 – H23*), 2.05 (s, 3H, *H12 – H23*), 2.04 (s, 3H, *H12 – H23*), 1.99 (s, 3H, *H12 – H23*).

^{13}C-NMR (600 MHz, $CDCl_3$, 297.9 K) δ (ppm) 170.53, 170.30, 170.20, 169.92 (4C*, Ch*), 165.59 (1C*, Ck*), 130.81 (1C, *Cl*), 126.86 (1C*, Cm*), 101.62 (1C, *Ca*), 71.02 (1C, *Ce*), 70.81*,* 69.27, 69.09 (3C, *Cb – Cd*), 67.10 (1C, *Ci*), 61.52 (1C, *Cf*)*,* 39.31 (1C, *Cj*)*,* 20.99*,* 20.81*,* 20.79 (3C, *Cg´´*)*,* 20.70 (1C, *Cg´*).

LC-MS: m/z calculated for $C_{19}H_{27}NO_{11}$ $[M+H]^+$ 446.16, found 446.20, determined relative purity: 93%.

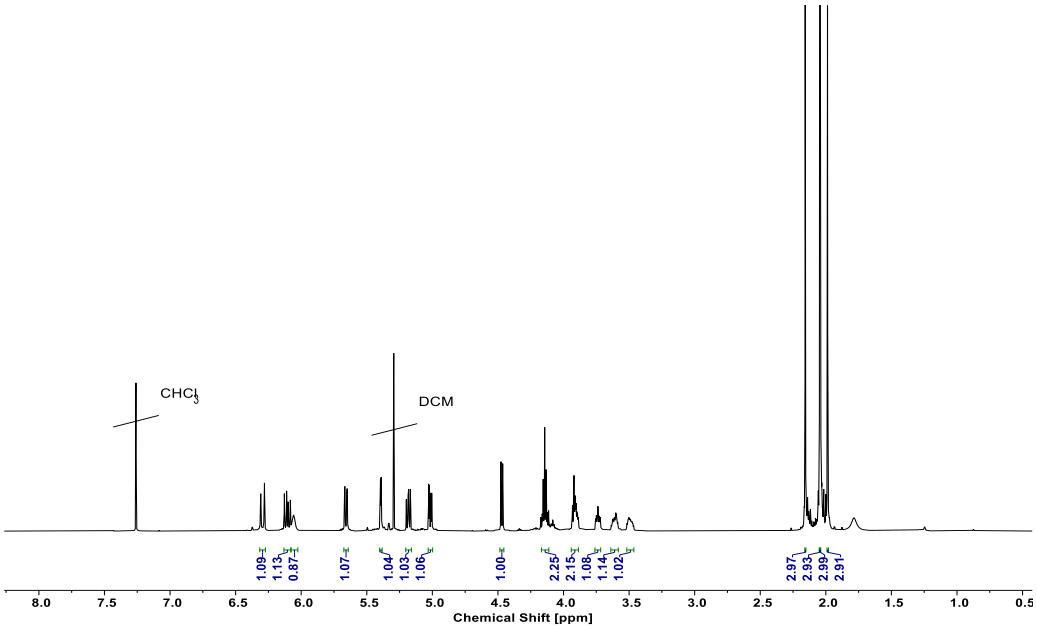


*Fig. S6: [1]H-NMR spectrum (600 MHz, CHCl3, 297.9 K) of β-D-GalAcEAA (**S2**).*

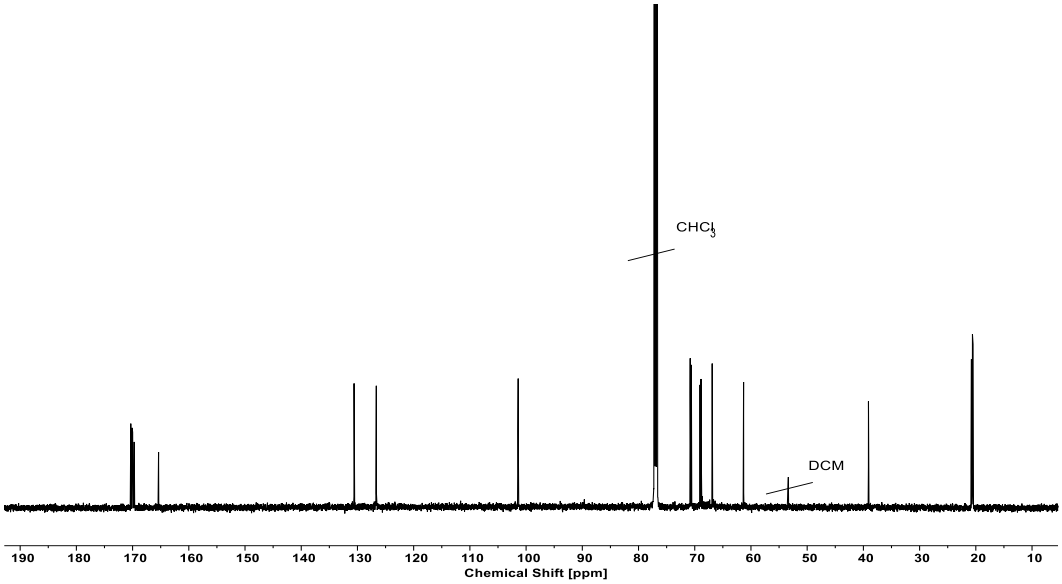


*Fig. S7: [13]C-NMR spectrum (600 MHz, $CHCl_3$, 297.9 K) of β-D-GalAcEAA (**S2**).*

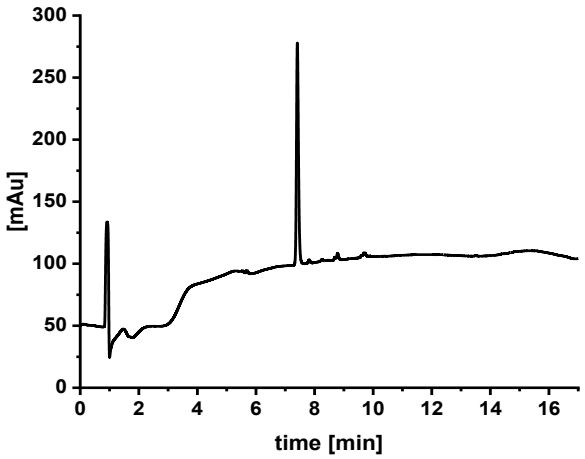


*Fig. S8: RP-HPCL chromatogram of β-D-GalAcEAA (**S2**) at t = 7.53 min (gradient of 5 to 95 vol% acetonitrile/water with 0.1 vol% formic acid, run time: 17 min).*

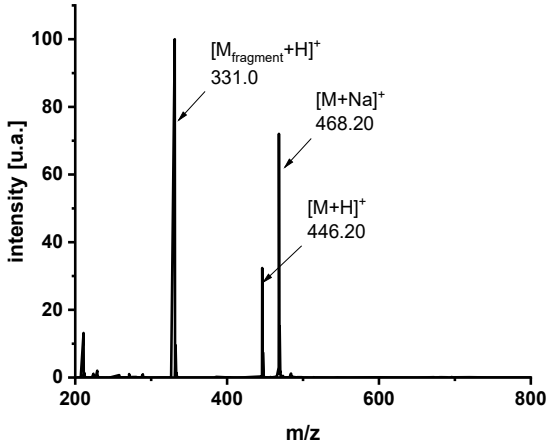
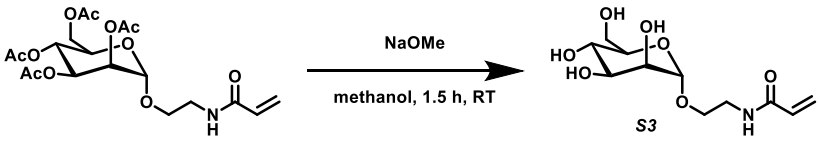


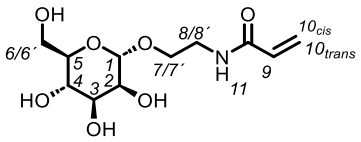
*Fig.S9: Mass spectrum of β-D-GalAcEAA (**S2**) at t = 7.53 min (gradient of 5 to 95 vol.% acetonitrile/water with 0.1 vol.% formic acid, run time: 17 min) by ESI-MS. The fragment at 331.0 m/z occurs during the ESI-MS measurement and corresponds to the product, where the acetyl group at the anomeric center was cleaved off.*

S3 – α-D-Mannopyranosyl-ethylacrylamid (ManEAA)



6.05 g (13.6 mmol) AcManEAA ***S1*** was dissolved in 50 mL methanol, mixed with 180 mL 0.2 M sodium methanolate/methanol solution and stirred for 90 min. The organic solvent was removed under reduced pressure and the residue dissolved in water. Amberlite®IR-120 was subsequently added as ion exchange resin until pH 7 was reached. The exchange resin was filtered off and the product lyophilized.

S3 was isolated as a yellowish oil with a yield of 4.62 g (> 95%).



^{1}H-NMR (600 MHz, D_2O, 297.9 K) δ (ppm) 8.37 (s, 1H, *H11*), 6.24 – 6.15 (dd, ^3J = 17.1, 10.3 Hz, 1H, *H9*), 6.15 – 6.08 (dd, ^3J = 17.2, ^2J = 1.3 Hz, 1H, *H10$_{cis}$*), 5.71 – 5.66 (dd, ^3J = 10.3, ^2J = 1.3 Hz, 1H, *H10$_{trans}$*), 4.80 – 4.77 (s, 1H, *H1*), 4.92 – 3.27 (m, H11, *H2 – H5, H6a – H6b*, *H7a – H7b*, *H8a – H8b*).

LC-MS: m/z calculated for $C_{11}H_{19}NO_7$ $[M+Na]^+$ 300.12 found 300.00 in injection peak.

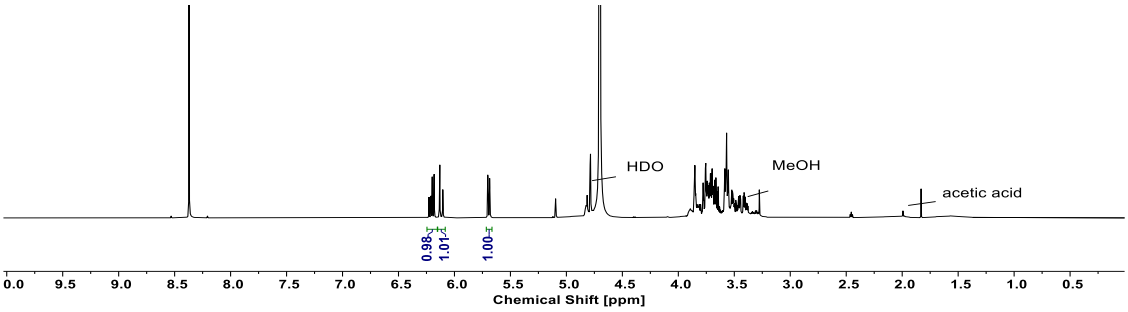


*Fig. S10: ^{1}H-NMR spectrum (600 MHz, D_2O, 297.9 K) of α-D-ManEAA (**S3**).*

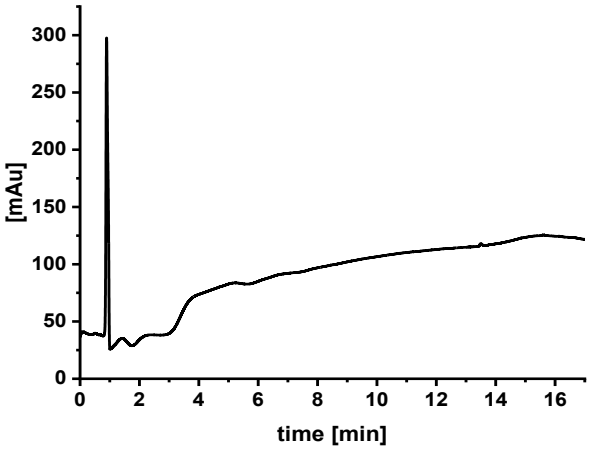


*Fig. S11: RP-HPCL chromatogram of α-D-ManEAA (**S3**) (gradient of 5 to 95 vol% acetonitrile/water with 0.1 vol% formic acid, run time: 17 min). The corresponding mass could be detected in the injection peak.*

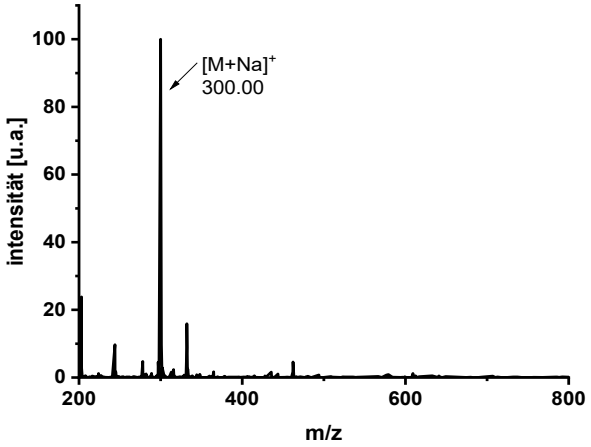
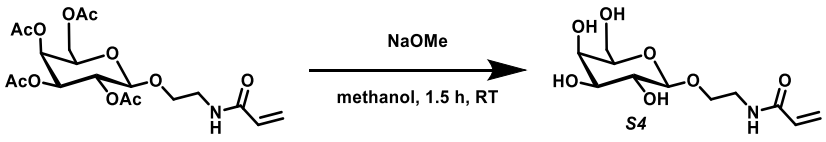


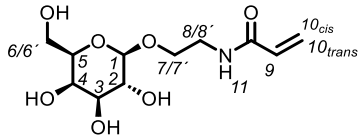
*Fig. S12: Mass spectrum of α-D-ManEAA (**S3**) at t = 1.00 min (gradient of 5 to 95 vol.% acetonitrile/water with 0.1 vol.% formic acid, run time: 17 min) by ESI-MS.*

S4 – β-D-Galactopyranosyl-ethylacrylamid (GalEAA)



6.22 g (14.0 mmol) AcGalEAA ***S2*** was dissolved in 100 mL methanol, mixed with 190 mL 0.2 M sodium methanolate/methanol solution and stirred for 90 min. The organic solvent was removed under reduced pressure and the residue dissolved in water. Amberlite®IR-120 was subsequently added as ion exchange resin until pH 7 was reached. The exchange resin was filtered off and the product was lyophilized.

S4 was isolated as a whitish oil with a yield of 5.1 g (> 95%).



^{1}H-NMR (600 MHz, D_2O, 297.9 K) δ (ppm) 8.46 (s, 1H, *H11*), 6.35 – 6.26 (dd, ^3J = 17.2, 10.3 Hz, 1H, *H9*), 6.24 – 6.18 (dd, ^3J = 17.2, ^2J = 1.3 Hz, 1H, $H10_{cis}$), 5.80 – 5.75 (dd, ^3J = 10.3, ^2J = 1.3 Hz, 1H, $H10_{trans}$), 4.44 – 4.38 (d, ^3J = 7.9 Hz, 1H, *H1*), 4.05 – 3.46 (m, H11, *H2 – H5, H6a – H6b*, *H7a – H7b*, *H8a – H8b*).

LC-MS: m/z calculated for $C_{11}H_{19}NO_7$ $[M+Na]^+$ 300.12 found 300.00 in injection peak.

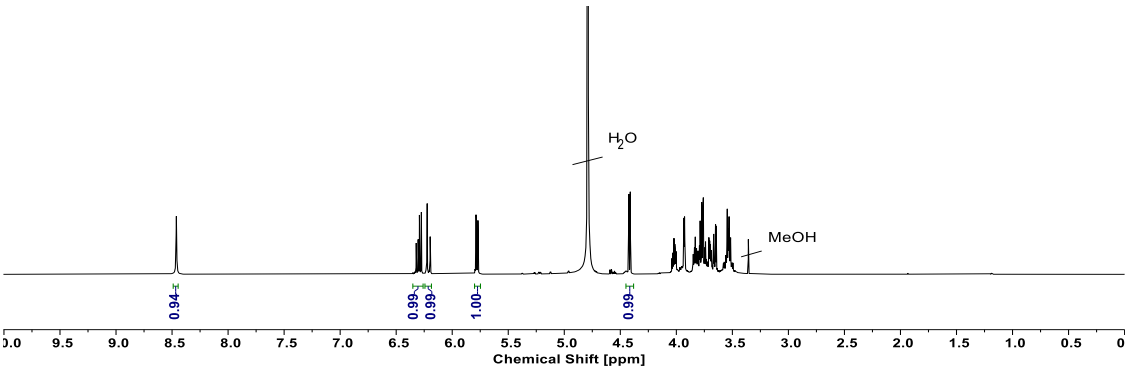


*Fig. S13: ^{1}H-NMR spectrum (600 MHz, D_2O, 297.9 K) of β-D-GalEAA (**S4**).*

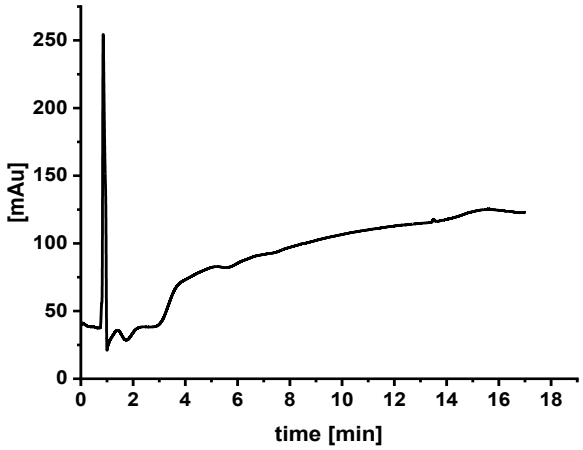


*Fig. S14: RP-HPCL chromatogram of β-D-GalEAA (**S4**) (gradient of 5 to 95 vol% acetonitrile/water with 0.1 vol% formic acid, run time: 17 min). The corresponding mass could be detected in the injection peak.*

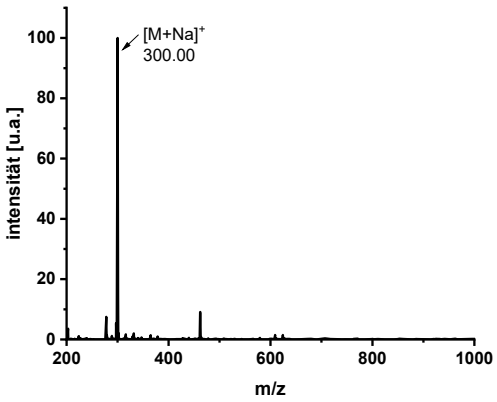
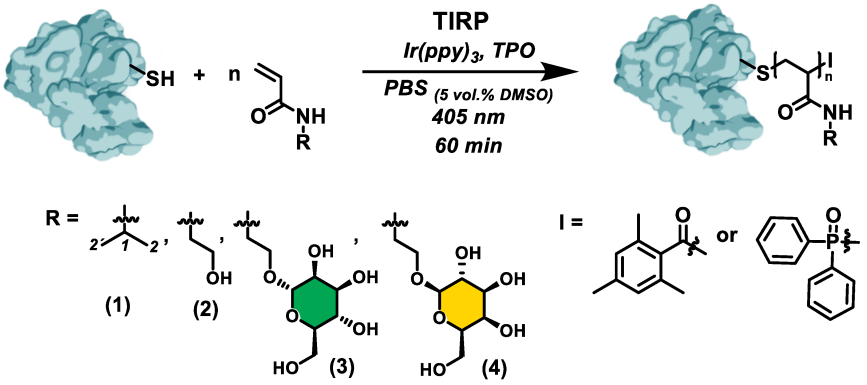


*Fig. S15: Mass spectrum of β-D-GalEAA (**S4**) at t = 1.00 min (gradient of 5 to 95 vol.% acetonitrile/water with 0.1 vol.% formic acid, run time: 17 min) by ESI-MS.*

2.2 Synthesis and measurements of BSA-polymer conjugates 1-4



500 mg (7.5 µmol) of *bovine serum albumin* were dissolved in 5 mL of deoxygenated phosphate buffered saline (PBS buffer). Separate solutions *I*-*III* were prepared. *I*: **A** mg (375 µmol) of monomer in **B** µL of PBS buffer (50 mg/mL), *II*: 0.12 mg (0.18 µmol) of catalyst tris(2 phenylpyridine)iridium (Ir-Cat.) in 0.1 mL of dimethyl sulfoxide, *III*: 1.3 mg (3.75 µmol) of diphenyl(2,4,6-trimethylbenzoyl)phosphine oxide (TPO) in 0.1 mL of dimethyl sulfoxide. Ir-Cat. solution *II* was added to monomer solution *I* and deoxygenated with nitrogen for 10 min. In parallel, the TPO solution *III* was slowly drop-wise added to the protein solution and also deoxygenated with nitrogen for 10 min before it was irradiated in the focus of the UV lamp (λ = 405 nm) for 3 min at an intensity of 1.15 mW/cm^2. Subsequently, the mixture of monomer *I* and catalyst solution *II* was added to the protein and the entire mixture was irradiated for another 60 min at 5.22 mW/cm^2 intensity. The reaction mixture was purified by dialysis (exclusion volume 50 kDa) and then lyophilized. A white, fluffy powder was obtained.

Table 1: Formulation values of the monomers and buffer volumes of polymerizations.

structure	monomer functionality	mass of monomer A [mg]	PBS buffer volume B [µL]	yields [mg]
1	*N*-Hydroxyethyl acrylamide	43.2	864	518.9
2	*N*-Isopropyl acrylamide	42.4	849	523.6
3	ManEAA ***S3***	104.0	2080	539.2
4	GalEAA ***S4***	104.0	2080	547.8

S5 – BSA$_{native}$

^{1}H-NMR (600 MHz, D_2O, 297.9 K) δ (ppm) 9.17 – 6.29 (m, H_{BSA}), 4.56 – 0.00 (m, H_{BSA}).

AF4-LS (10 mM PBS, pH = 7.4, 298,15 K, whole fraction): Mn = 69.4 kDa, Mw = 74.2 kDa, Đ = 1.07, R_h = 3.5 nm.

IR (ATR) $\tilde{\nu}$ = 3281.68 cm^{-1} (broad O-H), 1644.11 cm^{-1} (stretch C=C), 1531.53 cm^{-1} (amide II), 1392.76 cm^{-1} (deformation C-H), 1242.77 cm^{-1} (deformation O-H).

CD: area 215 nm – 245 nm: 218.5 nm, -25.9 mdeg, area 198 nm – 215 nm: 209.0 nm, -27.9 mdeg

DSC: Enthalpy: 439 mJ, Enthalpy referenced to sample weight: 264 mJ/mg, Onset: 25 °C, Endset: 112 °C, Midpoint of thermal transition: 66 °C.

Ellman's Assay (amount of free thiols): 54%

SDS PAGE see Fig. S41.

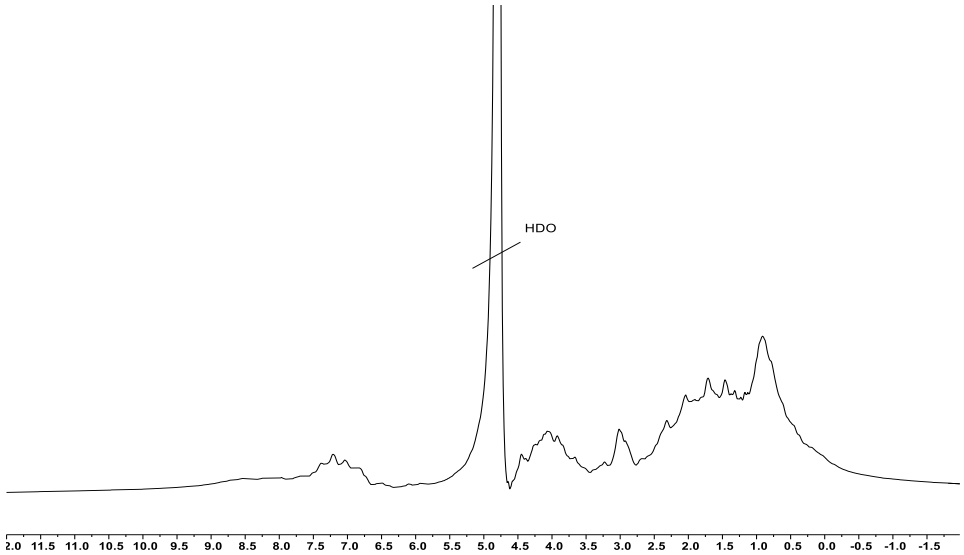


Fig. S16: ^{1}H-NMR spectrum (600 MHz, D_2O, 297.9 K) of BSA$_{native}$.

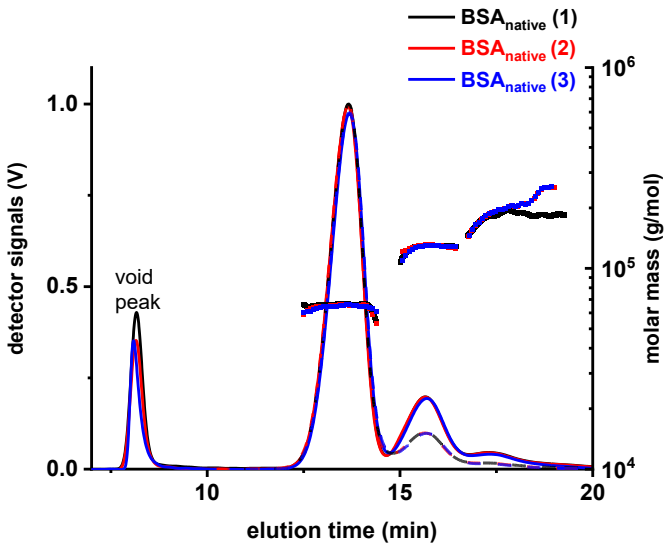


Fig. S17: Triplicate measurements and presentation of AF4-LS elugrams of BSA_{native} opt. separation, RI and LS signal, molar masses vs. elution time.

Table 2:Results of the triplicate AF4-LS measurements.

Measurement	M_n*1 (kg/mol)	M_w*1 (kg/mol)	Đ (M_w/M_n)	R_g (nm)	R_h (nm)
1. (50 µL)	69.4	74.5	1.07		3.5
2. (50 µL)	68.7	73.4	1.07		3.5
3. (50 µL)	70.1	74.6	1.06		3.5
Average (whole Peak)	**69.4**	**74.2**	**1.07**		**3.5**

*1 dn/dc = 0.185 mL/g

Table 3: Analysis of the individual fractions / populations of conjugates by AF4-LS. The values shown are average values from the triplicate measurements.

Fraction / population	M_n*1 (kg/mol)	M_w*1 (kg/mol)	Đ (M_w/M_n)	R_h (nm)	Mass fraction (%)	Mol fraction (%)
1 - Monomer	65.1	65.2	1.00	3.3	86.7	92.9
2 – Dimer	119	123	1.04	6.3	11.2	6.5
3- Trimer / Multimer	196	201	1.02	6.7	2.1	0.6

*1 dn/dc = 0.185 mL/g

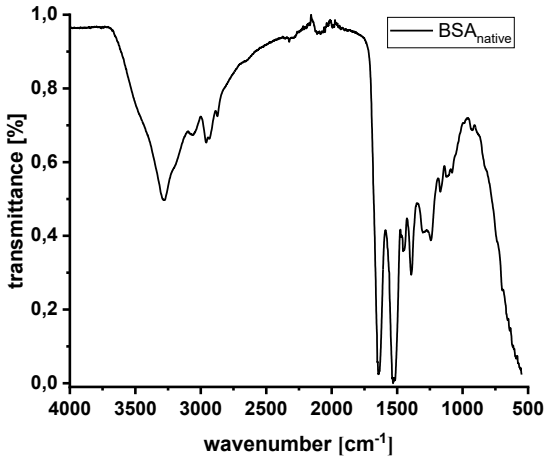


Fig. S18: IR spectrum of BSA_{native}.

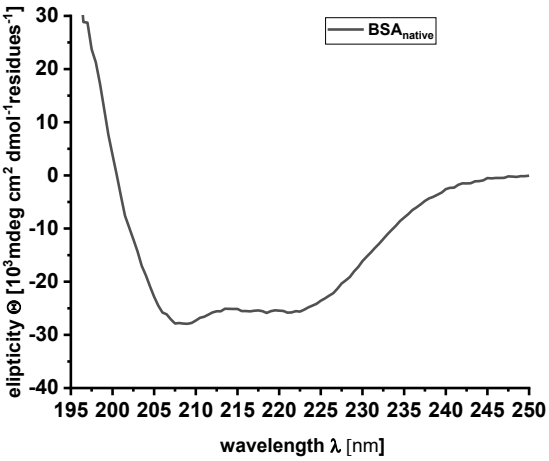


Fig. S19: CD spectrum of BSA_{native}.

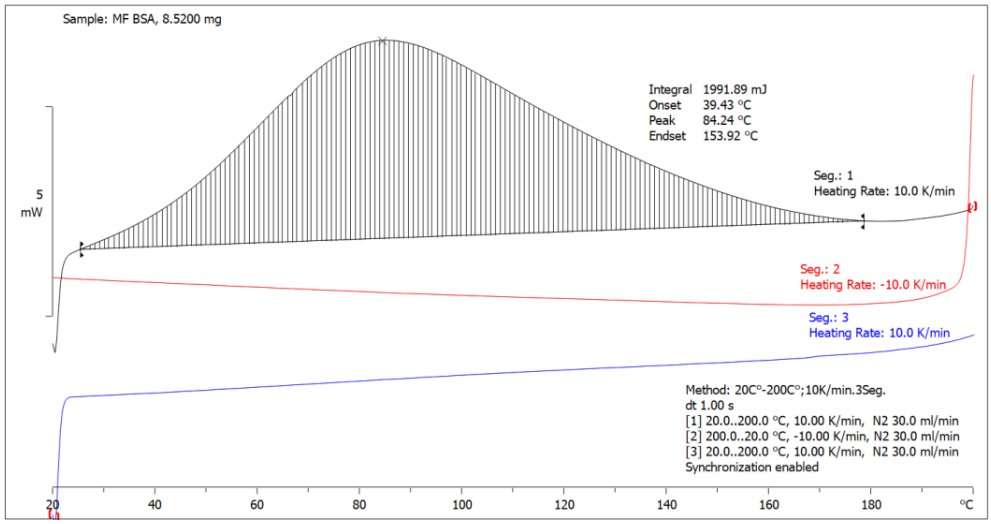


Fig. S20: DCS curves of BSA$_{native}$.

(1) – BSA-p(NIPAM) conjugate

^{1}H-NMR (600 MHz, D_2O, 297.9 K) δ (ppm) 9.17 – 6.40 (m, H_{BSA}), 4.57 – 0.00 (m, H_{BSA}, $H_{NIPAM\text{-}side\ chain}$, $H_{NIPAM\text{-}backbone}$ overlap with HDO peak), 3.91 (s_{br}, *H1*), 1.16 (s_{br}, *H2, H´2*).

AF4-LS (10 mM PBS, pH = 7.4, 298,15 K, whole fraction): Mn = 74.2 kDa, Mw = 80.2 kDa, Đ = 1.08, R_h = 3.2 nm.

IR (ATR) $\tilde{\nu}$ = 1077.24 cm^{-1} (deformation C-OH). All other wavelengths identical to BSA.

CD: area 215 nm – 245 nm: 220.0 nm, -28.6 mdeg, area 198 nm – 215 nm: 208.0 nm, -30.7 mdeg.

DSC: Enthalpy: 362 mJ, Enthalpy referenced to sample weight: 212 mJ/mg, Onset: 27 °C, Endset: 106 °C, Midpoint of thermal transition: 64 °C.

SDS PAGE see Fig. S41.

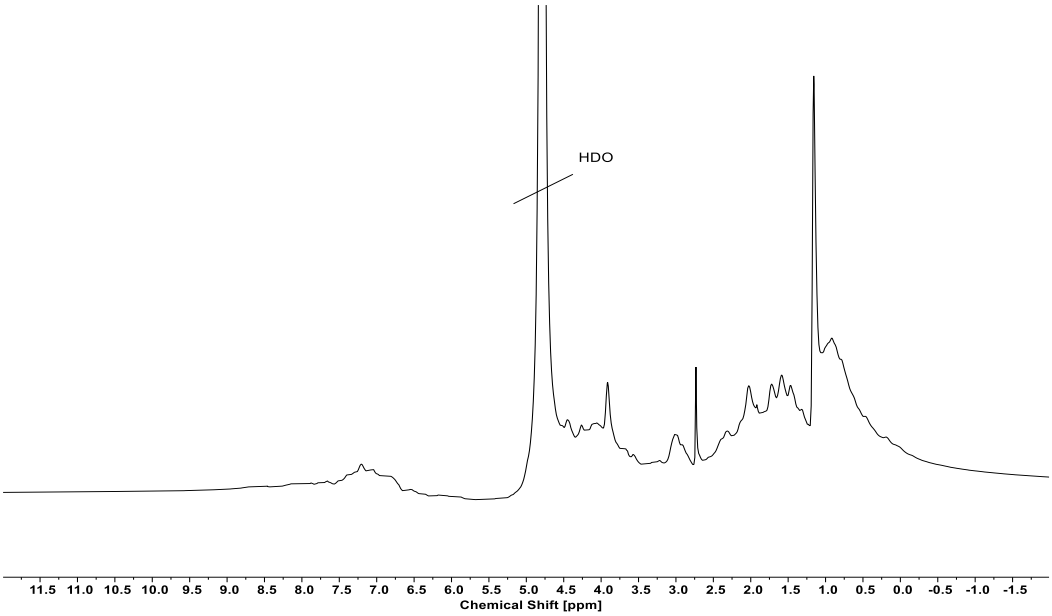


*Fig. S21: ^{1}H-NMR spectrum (600 MHz, D_2O, 297.9 K) of BSA-p(NIPAM) conjugate (**1**).*

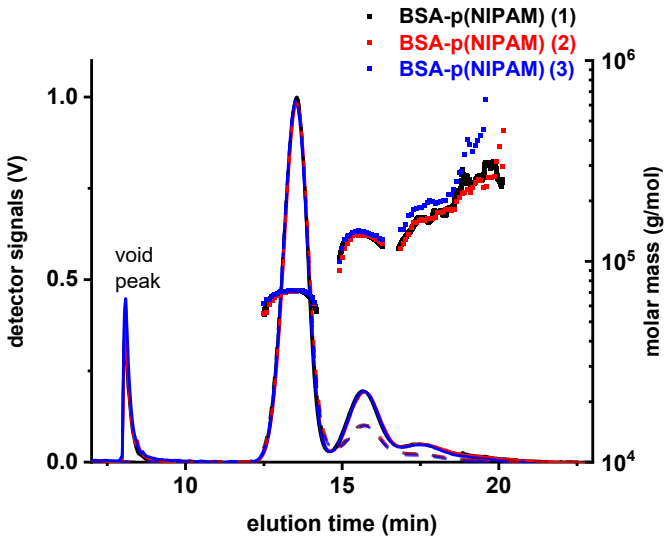


*Fig. S22: Triplicate measurements and presentation of AF4-LS elugrams of BSA-p(NIPAM) conjugate (**1**) opt. separation, RI and LS signal, molar masses vs. elution time.*

Table 4: Results of the triplicate AF4-LS measurements.

Measurement	**M_n**[*1] (kg/mol)	**M_w**[*1] (kg/mol)	**Đ** (M_w/M_n)	**R_g** (nm)	**R_h** (nm)
1. (50 µL)	74.2	79.9	1.08	*6.4*	3.2
2. (50 µL)	73.7	79.3	1.08		3.3
3. (50 µL)	74.9	81.3	1.09	*6.3*	3.1
Average (whole Peak)	**74.2**	**80.2**	**1.08**		**3.2**

*1 dn/dc = 0.172 mL/g

Table 5: Analysis of the individual fractions / populations of conjugates by AF4-LS. The values shown are average values from the triplicate measurements.

Fraction / population	**M_n**[*1] (kg/mol)	**M_w**[*1] (kg/mol)	**Đ** (M_w/M_n)	**R_h** (nm)	**Mass fraction** (%)	**Mol fraction** (%)
1 - Monomer	70.5	70.6	1.00	3.1	93.1	91.5
2 – Dimer	134	134	1.00		5.7	7.0
3- Trimer / Multimer	167	167	1.00	7.4	1.2	1.5

*1 dn/dc = 0.172 mL/g

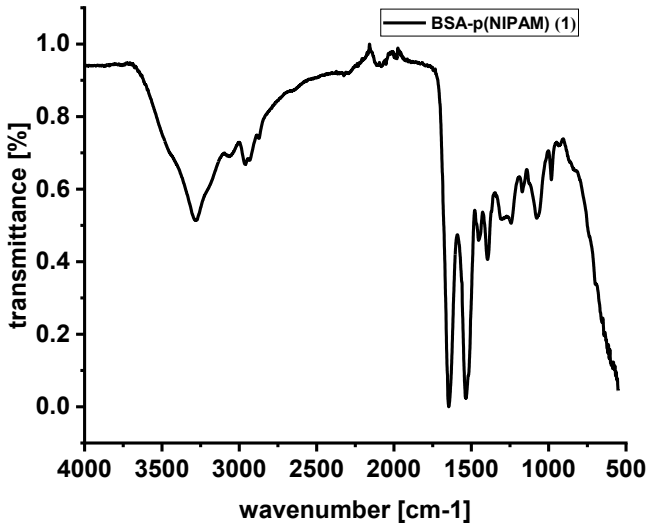


*Fig. S23: IR spectrum BSA-p(NIPAM) conjugate (**1**).*

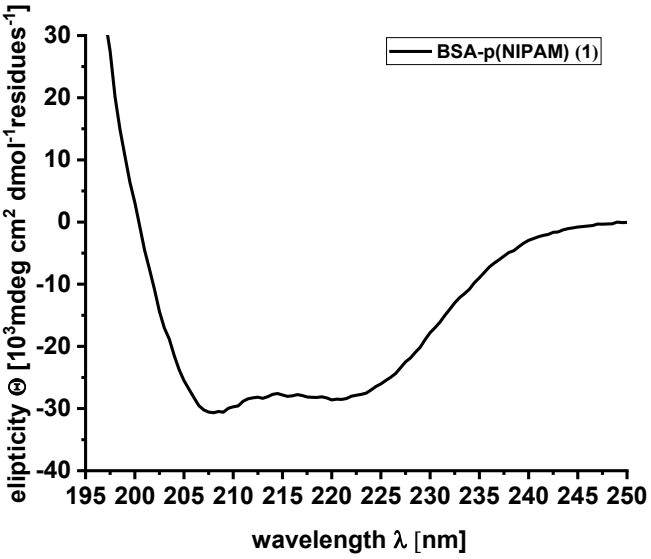


*Fig. S24: CD spectrum of BSA-p(NIPAM) conjugate (**1**).*

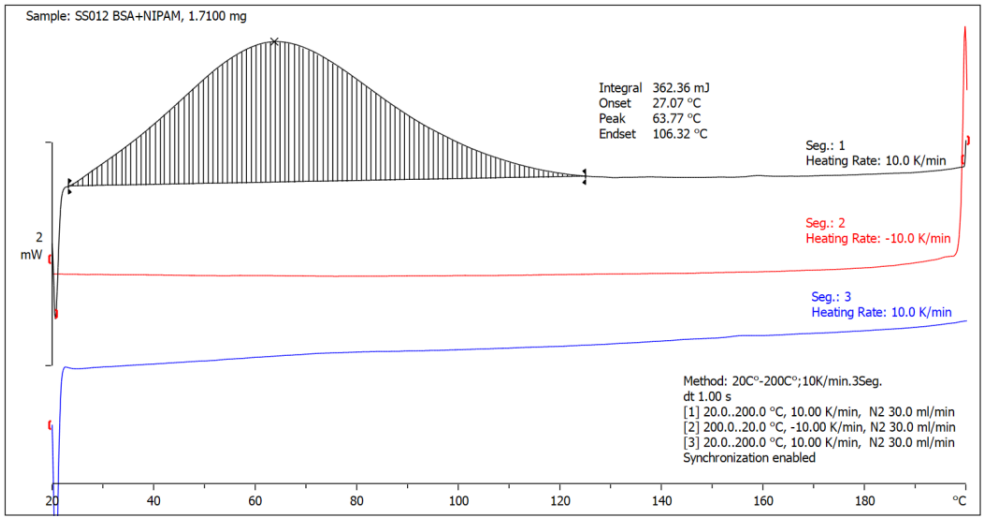


*Fig. S25: DSC curve of BSA-p(NIPAM) conjugate (**1**).*

(2) – BSA-p(HEAA) conjugate

^{1}H-NMR (600 MHz, D_2O, 297.9 K) δ (ppm) 9.17 – 6.46 (m,H_{BSA}), 4.57 – 0.00 (m, H_{BSA}, $H_{HEAA\text{-}side\ chain}$, $H_{HEAA\text{-}backbone}$ overlap with HDO peak), 4.35 – 3.13 (m, $H_{HEAA\text{-}side\ chain}$).

AF4-LS (10 mM PBS, pH = 7.4, 298,15 K, whole fraction): Mn = 71.5 kDa, Mw = 77.0 kDa, Đ = 1.08, R_h = 4.1 nm.

IR (ATR) $\tilde{\nu}$ = 1066.41 cm^{-1} (deformation C-OH). All other wavelengths identical to BSA.

CD: area 215 nm – 245 nm: 219.5 nm, -30.7 mdeg, area 198 nm – 215 nm: 209.0 nm, -32.7 mdeg.

DSC: Enthalpy: 522 mJ, Enthalpy referenced to sample weight: 211 mJ/mg, Onset: 30 °C, Endset: 116 °C, Midpoint of thermal transition: 70 °C.

SDS PAGE see Fig. S41.

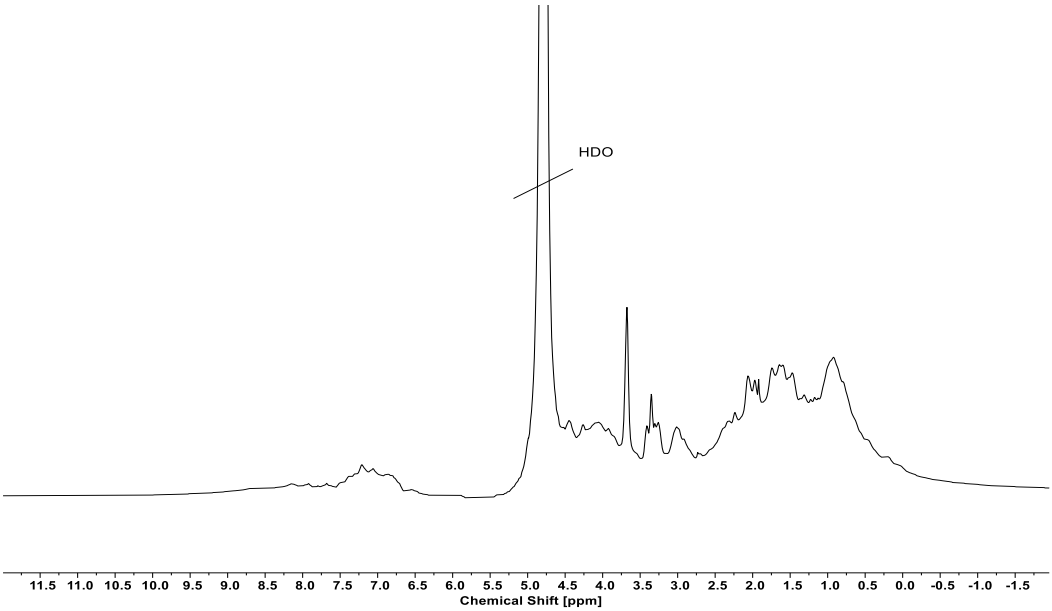


*Fig. S26: ^{1}H-NMR spectrum (600 MHz, D_2O, 297.9 K) of BSA-p(HEAA) conjugate (**2**).*

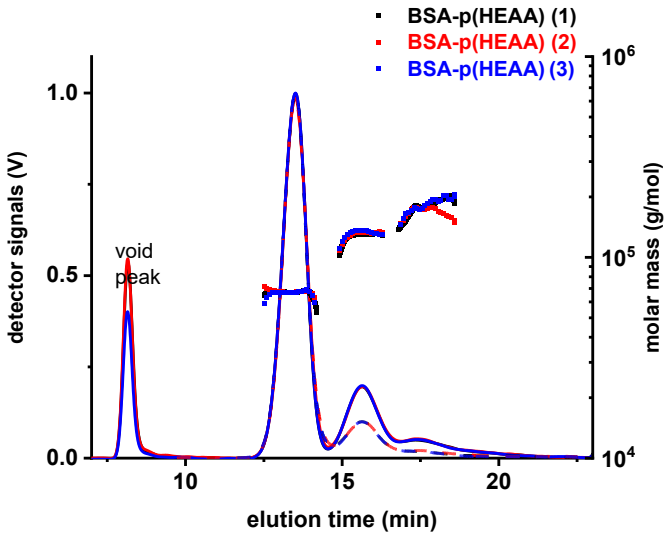


*Fig. S27: Triplicate measurements and presentation of AF4-LS elugrams of BSA-p(HEAA) conjugate (**2**) opt. separation, RI and LS signal, molar masses vs. elution time.*

Table 6: Results of the triplicate AF4-LS measurements.

Measurement	**M_n**[*1] (kg/mol)	**M_w**[*1] (kg/mol)	**Đ** (M_w/M_n)	**R_g** (nm)	**R_h** (nm)
1. (50 µL)	71.5	77.0	1.08	*6.8*	4.0
2. (50 µL)	71.4	76.7	1.07	*9.2*	5.0
3. (50 µL)	71.5	77.4	1.08	*5.8*	3.4
Average (whole Peak)	**71.5**	**77.0**	**1.08**	***7.3***	**4.1**

*1 dn/dc = 0.181 mL/g

Table 7: Analysis of the individual fractions / populations of conjugates by AF4-LS. The values shown are average values from the triplicate measurements.

Fraction / population	**M_n**[*1] (kg/mol)	**M_w**[*1] (kg/mol)	**Đ** (M_w/M_n)	**R_h** (nm)	**Mass fraction** (%)	**Mol fraction** (%)
1 - Monomer	66.1	66.3	1.00	3.0	84.9	92.2
2 – Dimer	126	128	1.01	6.1	11.8	6.6
3- Trimer / Multimer	171	174	1.01	8.8	3.3	1.2

*1 dn/dc = 0.181 mL/g

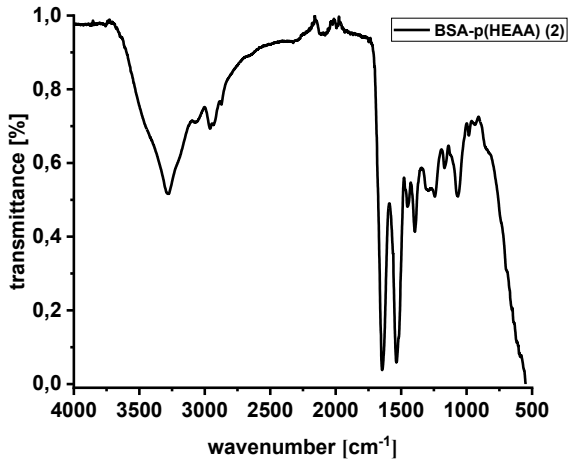


*Fig. S28: IR spectrum of BSA-p(HEAA) conjugate (**2**).*

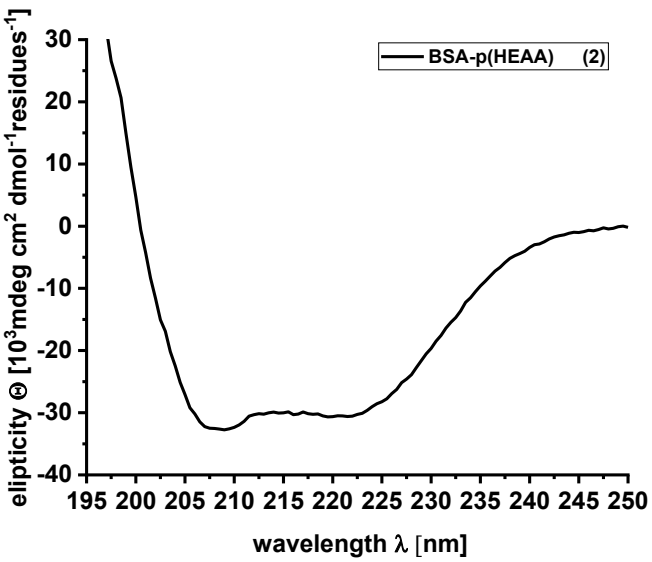


*Fig. S29: CD spectrum of BSA-p(HEAA) conjugate (**2**).*

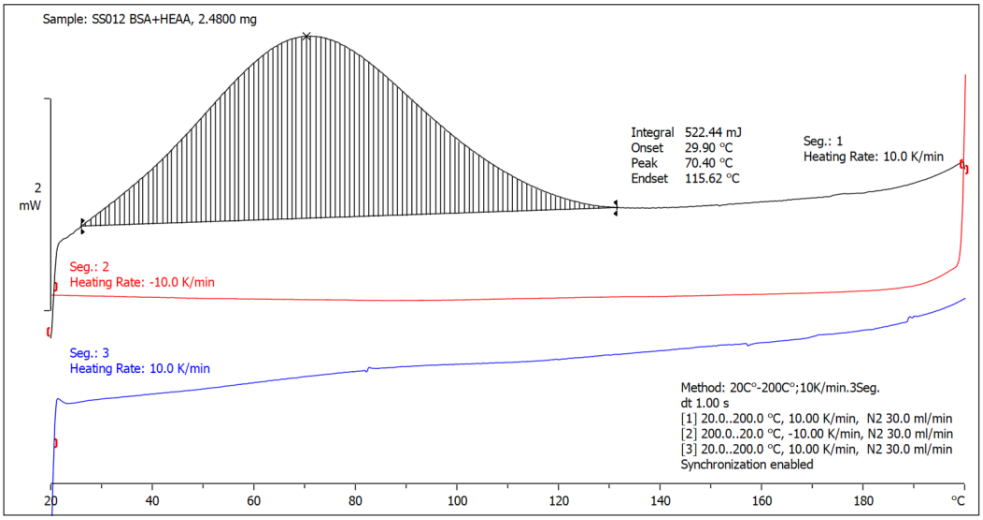


*Fig. S30: DSC curve of BSA-p(HEAA) conjugate (**2**).*

(3) – BSA-p(ManEAA) conjugate

^{1}H-NMR (600 MHz, D_2O, 297.9 K) δ (ppm) 9.17 – 6.46 (m, H_{BSA}), 4.57 – 0.00 (m, H_{BSA}, $H_{ManEAA\text{-}side\ chain}$, $H_{ManEAA\text{-}backbone}$ overlap with HDO peak), 4.50 – 3.40 (m, $H_{ManEAA\text{-}side\ chaine}$).

AF4-LS (10 mM PBS, pH = 7.4, 298,15 K, whole fraction): Mn = 81.9 kDa, Mw = 88.2 kDa, Đ = 1.08, R_h = 3.1 nm.

IR (ATR) $\tilde{\nu}$ = 1065.87 cm^{-1} (deformation C-OH). All other wavelengths identical to BSA.

CD: area 215 nm – 245 nm: 221.5 nm, -26.6 mdeg, area 198 nm – 215 nm: 208.5 nm, -28.9 mdeg.

DSC: Enthalpy: 534 mJ, Enthalpy referenced to sample weight: 243 mJ/mg, Onset: 28 °C, Endset: 117 °C, Midpoint of thermal transition: 67 °C.

SDS PAGE see Fig. S41.

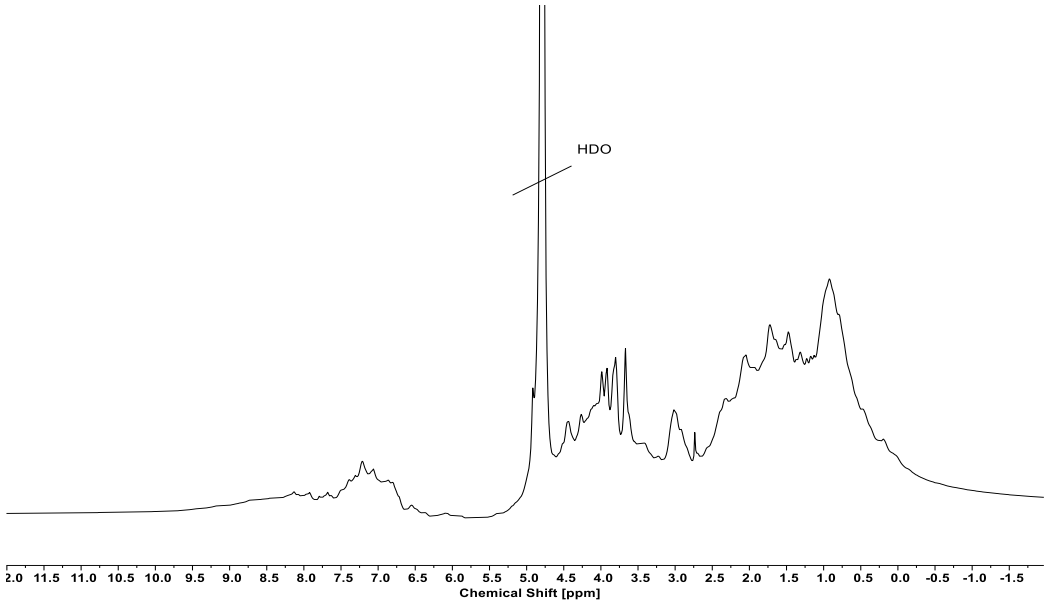


*Fig. S31: ^{1}H-NMR spectrum (600 MHz, D_2O, 297.9 K) of BSA-p(ManEAA) conjugate (**3**).*

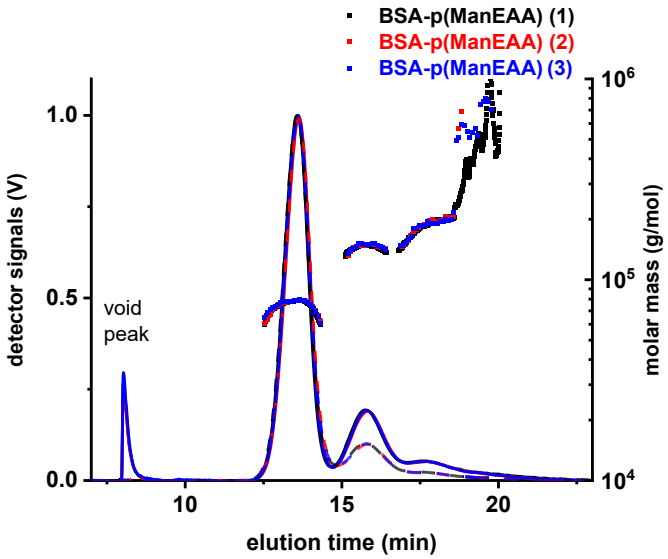


*Fig. S32: Triplicate measurements and presentation of AF4-LS elugrams of BSA-p(ManEAA) conjugate (**3**) opt. separation, RI and LS signal, molar masses vs. elution time.*

Table 8: Results of the triplicate AF4-LS measurements.

Measurement	**M_n**[*1] (kg/mol)	**M_w**[*1] (kg/mol)	**Đ** (M_w/M_n)	**R_g** (nm)	**R_h** (nm)
1. (50 µL)	81.7	88.2	1.08	*6.4*	3.1
2. (50 µL)	81.6	87.8	1.08	*3.3*	3.1
3. (50 µL)	82.4	88.8	1.08	*9.3*	3.0
Average (whole Peak)	**81.9**	**88.2**	**1.08**	***6.3***	**3.1**

*1 dn/dc = 0.158 mL/g

Table 9: Analysis of the individual fractions / populations of conjugates by AF4-LS. The values shown are average values from the triplicate measurements.

Fraction / population	**M_n**[*1] (kg/mol)	**M_w**[*1] (kg/mol)	**Đ** (M_w/M_n)	**R_h** (nm)	**Mass fraction** (%)	**Mol fraction** (%)
1 - Monomer	78.1	78.2	1.00	3.2	83.7	91.2
2 – Dimer	148	148	1.00	4.5	12.7	7.3
3- Trimer / Multimer	198	198	1.00		3.6	1.5

*1 dn/dc = 0.158 mL/g

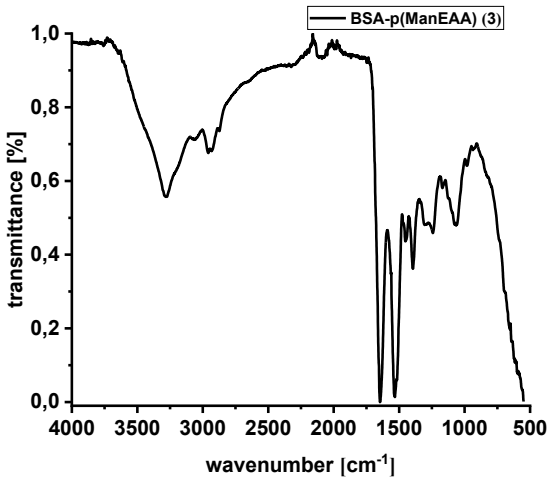


*Fig. S33: IR spectrum of BSA-p(ManEAA) conjugate (**3**).*

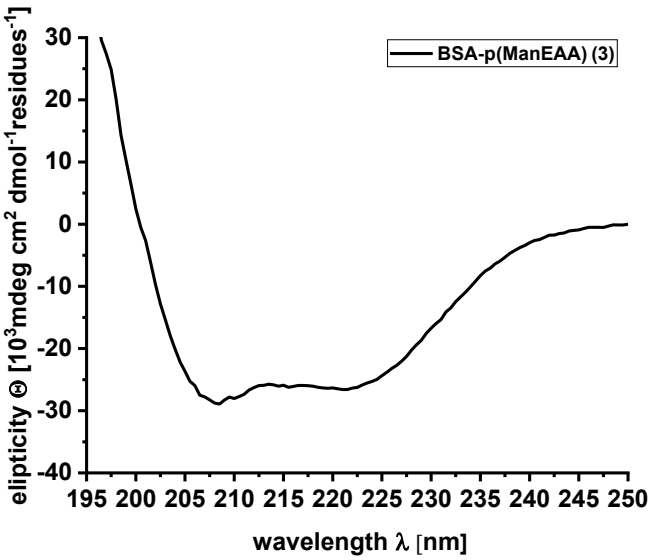


*Fig. S34: CD spectrum of BSA-p(ManEAA) conjugate (**3**).*

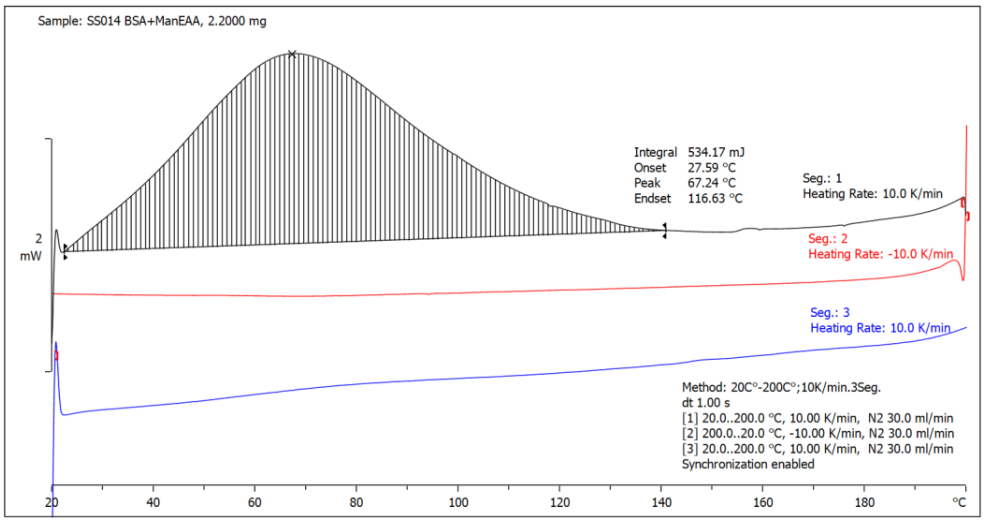


*Fig. S35: DSC curve of BSA-p(ManEAA) conjugate (**3**).*

(4) – BSA-p(GalEAA) conjugate

^{1}H-NMR (600 MHz, D_2O, 297.9 K) δ (ppm) 9.17 – 6.46 (m, H_{BSA}), 4.57 – 0.00 (m, H_{BSA}, $H_{GalEAA\text{-}side\ chain}$, $H_{GalEAA\text{-}backbone}$ overlap with HDO peak), 4.53 – 3.37 (m, $H_{GalEAA\text{-}side\ chain}$).

AF4-LS (10 mM PBS, pH = 7.4, 298,15 K, whole fraction): Mn = 81.9 kDa, Mw = 88.3 kDa, Đ = 1.08, R_h = 3.2 nm.

IR (ATR) $\tilde{\nu}$ = 1017.00 cm^{-1} (deformation C-OH). All other wavelengths identical to BSA.

CD: area 215 nm – 245 nm: 220.5 nm, -26.3 mdeg, area 198 nm – 215 nm: 208.0 nm, -28.5 mdeg.

DSC: Enthalpy: 460 mJ, Enthalpy referenced to sample weight: 171 mJ/mg, Onset: 30 °C, Endset: 104 °C, Midpoint of thermal transition: 69 °C.

SDS PAGE see Fig. S41.

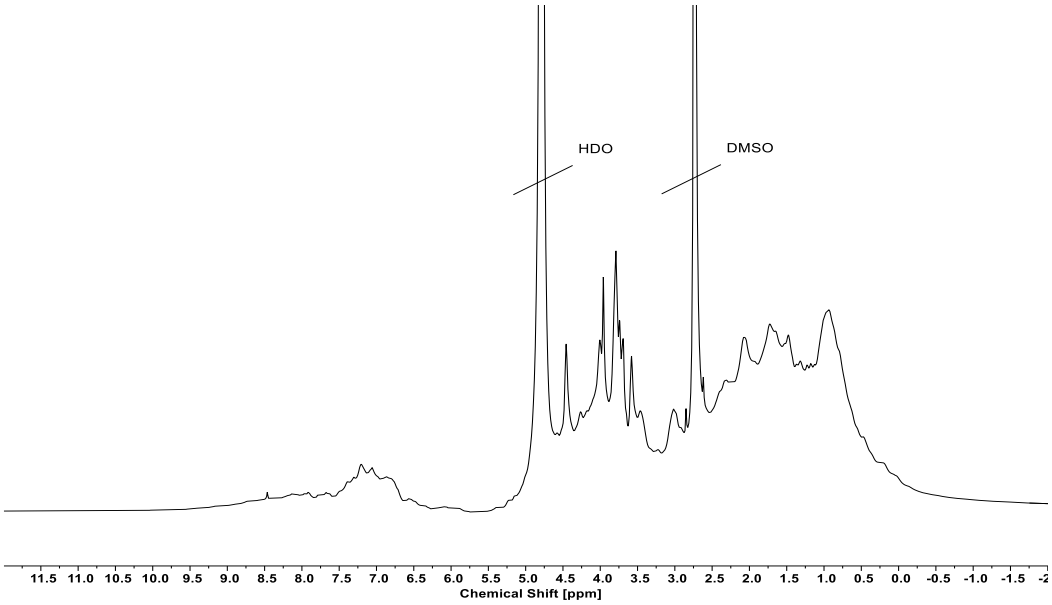


*Fig. S36: ^{1}H-NMR spectrum (600 MHz, D_2O, 297.9 K) of BSA-p(GalEAA) conjugate (**4**).*

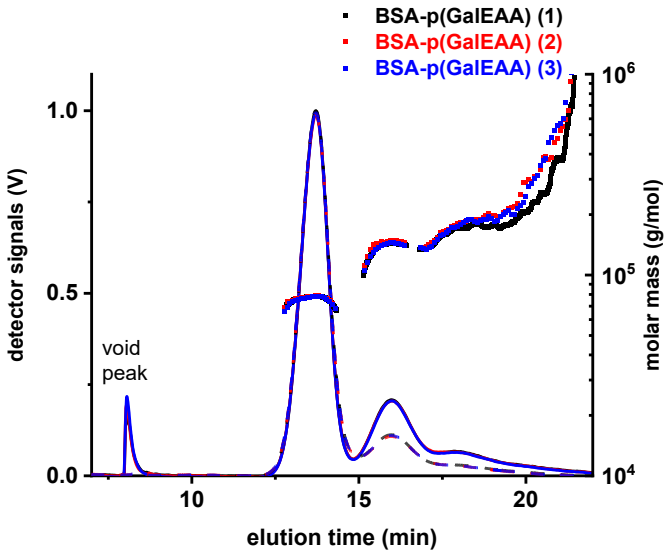


*Fig. S37: Triplicate measurements and presentation of AF4-LS elugrams of BSA-p(GalEAA) conjugate (**4**) opt. separation, RI and LS signal, molar masses vs. elution time.*

Table 10: Results of the triplicate AF4-LS measurements.

Measurement	**M_n**[*1] (kg/mol)	**M_w**[*1] (kg/mol)	**Đ** (M_w/M_n)	**R_g** (nm)	**R_h** (nm)
1. (50 µL)	82.6	88.1	1.07		3.2
2. (50 µL)	82.4	89.1	1.08		3.3
3. (50 µL)	81.1	87.6	1.08		3.2
Average (whole Peak)	**81.9**	**88.3**	**1.08**		**3.2**

*1 dn/dc = 0.158 mL/g

Table 11: Analysis of the individual fractions / populations of conjugates by AF4-LS. The values shown are average values from the triplicate measurements.

Fraction / population	**M_n**[*1] (kg/mol)	**M_w**[*1] (kg/mol)	**Đ** (M_w/M_n)	**R_h** (nm)	**Mass fraction** (%)	**Mol fraction** (%)
1 - Monomer	77.1	77.1	1.00	3.2	81.1	89.6
2 – Dimer	144	144	1.00	3.9	14.3	8.4
3- Trimer / Multimer	186	186	1.00	5.6	4.6	2.0

*1 dn/dc = 0.158 mL/g

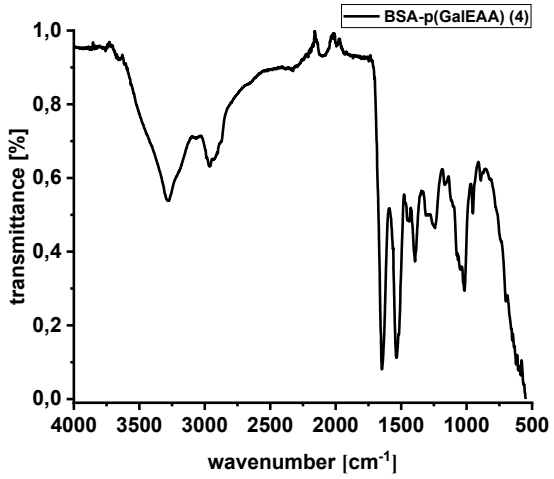


*Fig. S38: IR spectrum of BSA-p(GalEAA) conjugate (**4**).*

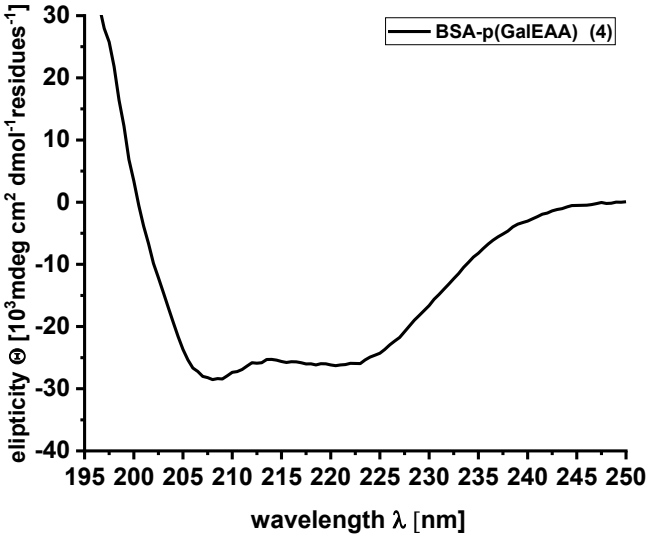


*Fig. S39: CD spectrum of BSA-p(GalEAA) conjugate (**4**).*

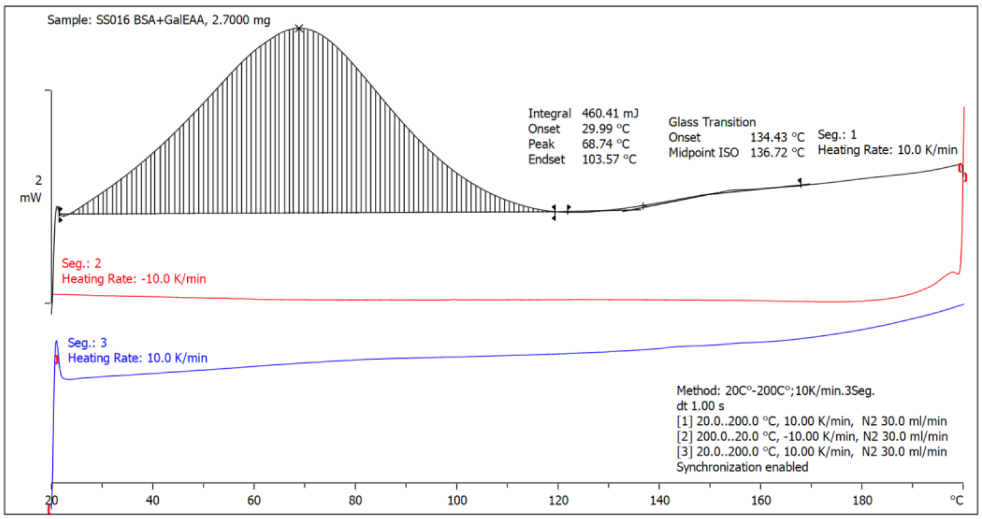
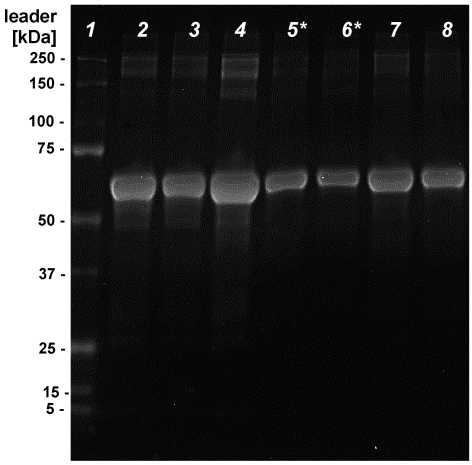


*Fig. S40: DSC curve of BSA-p(GalEAA) conjugate (**4**).*

SDS-PAGE



lane	*loading*
1	protein leader
2	BSA_{native}
3	BSA-p(HEAA)
4	BSA-p(NIPAM)
5	$BSA\text{-}p(NIPAM)_{100}$*
6	$BSA\text{-}p(NIPAM)_{200}$*
7	BSA-p(ManEAA)
8	BSA-p(GalEAA)

*Fig. S41: SDS PAGE of BSA_{native} (**S5**), BSA-p(NIPAM) (**1**), BSA-p(HEAA) (**2**), BSA-p(ManEAA) (**3**), BSA-p(GalEAA) (**4**). *These structures were loaded as references of higher MW conjugate samples but are not discussed in this paper.*

Summary of CD measurements

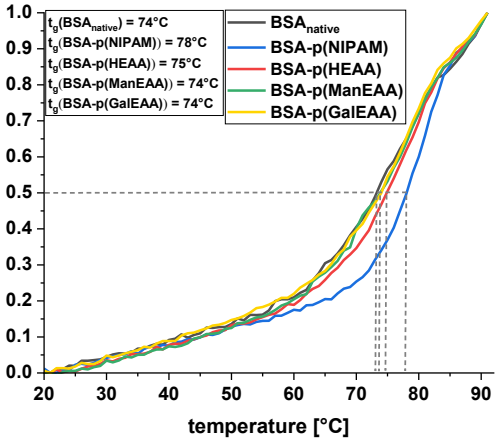


*Fig. S42: Denaturation studies measuring the temperature-dependent ellipticity at 222 nm of BSA$_{native}$ (**S6**), BSA-p(NIPAM) (**1**), BSA-p(HEAA) (**2**), BSA-p(ManEAA) (**3**), BSA-p(GalEAA) (**4**). Temperature steps from 20 – 90 °C in PBS buffer at pH 7.4.*

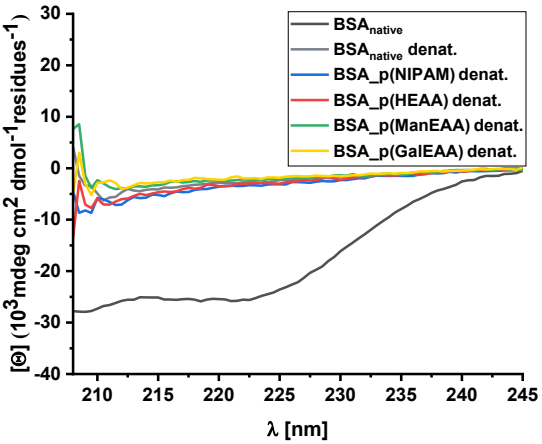


*Fig. S43: Denaturation studies in 6 M Guanidinium chloride and under influence of temperature (30 °C for 120 min) of BSA$_{native}$ (**S6**), BSA-p(NIPAM) (**1**), BSA-p(HEAA) (**2**), BSA-p(ManEAA) (**3**), BSA-p(GalEAA) (**4**). CD spectra were recorded between 208 nm and 245 nm in PBS buffer at pH 7.4.*

Determination of the half-maximum turbidity

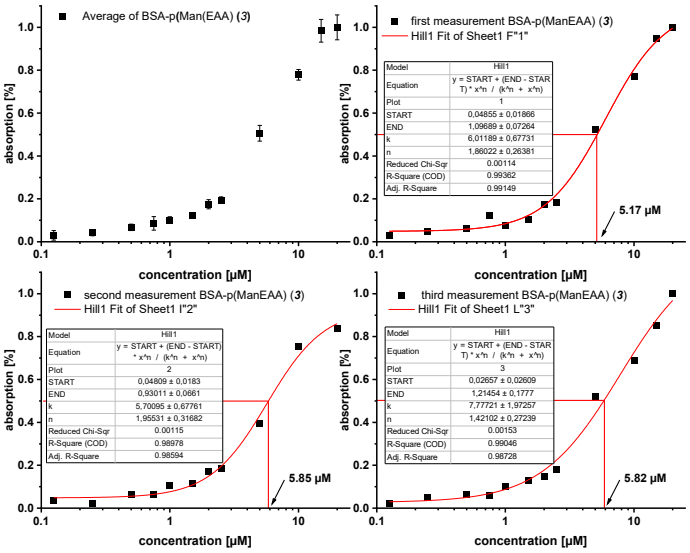


*Fig. S44: Compilation of the individual measurements of BSA-p(ManEAA) (**3**) with corresponding values of the half-maximum turbidity. The mean value of the individual measurements is 5.61 ± 0.38 µM.*

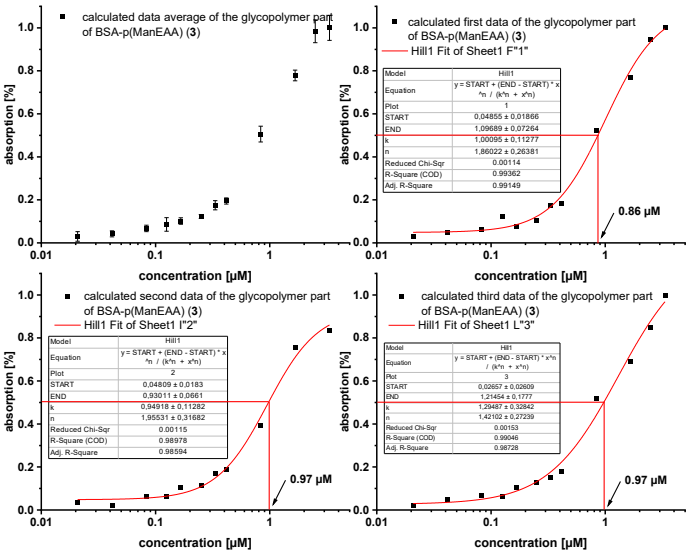


*Fig. S45: Calculated data of the glycopolymer part of BSA-p(ManEAA) (**3**) conjugate with corresponding values of the half-maximum turbidity. The purpose of the calculations was to determine the value of the half-maximum turbidity independent of the molecular weight of the protein, by solely considering the quantity of sugar present. The mean value of the individual measurements is 0.94 ± 0.06 µM.*

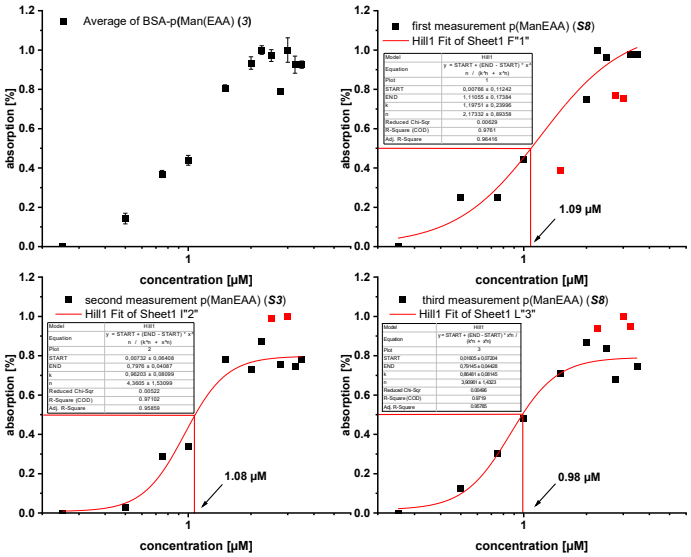


*Fig. S46: Compilation of the individual measurements of p(ManEAA) (**S7**) with corresponding values of the half-maximum turbidity. The mean value of the individual measurements is 1.05 ± 0.06 µM.*

Ellman's Assay

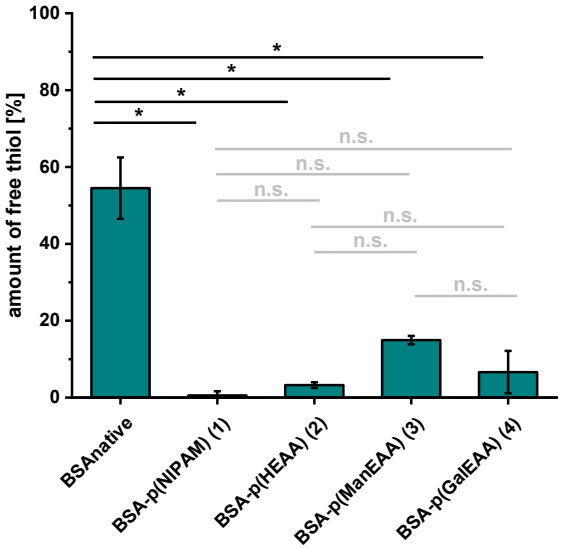
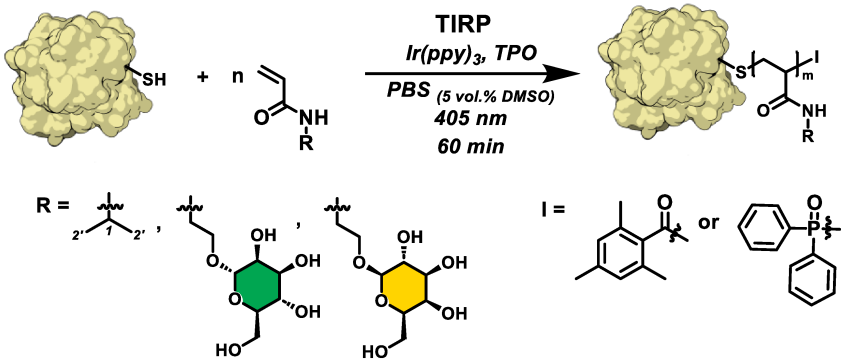


*Fig. S47: Results of the Ellman's assay of native BSA in comparison to conjugates **1**-**4**. 196 µL of Ellman's buffer was mixed with 20 µL of the protein stock solution (0.75 mM in Ellman's buffer) followed by 4 µL of the Ellman's stock solution (1 mg/mL in Ellman's buffer) and incubated for 15 min. The absorbance was measured at 412 nm and the amount of accessible thiols was determined based on a previously established calibration curve. Data were evaluated using one-way ANOVA analysis followed by Bonferroni correction (*<0.05, not significant (n.s.)). The reduced amount of free thiol is indicative of a polymer conjugation via the free thiol of the BSA.*

2.3 Synthesis and measurements of CRL-polymer conjugates 5-7



200 mg (3.47 µmol) of *Candida Rugose Lipase* was dissolved in 4 mL of deoxygenated phosphate buffered saline (PBS buffer). Separate solutions *I*-*III* were prepared. *I*: **A** mg (**B** µmol) of monomer in **C** µL of PBS buffer (50 mg/mL), *II*: **D** mg (**E** µmol) of catalyst tris(2 phenylpyridine)iridium (Ir-Cat.) in 0.1 mL of dimethyl sulfoxide, *III*: 0.6 mg (1.73 µmol) of diphenyl(2,4,6-trimethylbenzoyl)phosphine oxide (TPO) in 0.1 mL of dimethyl sulfoxide. Ir-Cat. solution *II* was added to monomer solution *I* and deoxygenated with nitrogen for 10 min. In parallel, the TPO solution *III* was slowly dropped to the protein solution and also deoxygenated with nitrogen for 10 min before it was irradiated in the focus of the UV lamp (λ = 405 nm) for 10 min at an intensity of 1.15 mW/cm^2. Subsequently, the mixture of monomer *I* and catalyst solution *II* was added to the protein and the entire mixture was irradiated for another 60 min at 5.22 mW/cm^2 intensity. The reaction mixture was purified by dialysis (exclusion volume 50 kDa) and then lyophilized. A white, fluffy powder was obtained.

Table 12: Formulation values of the monomers and buffer volumes of polymerizations.

structure	monomer functionality	mass of monomer A [mg]	amount of monomer A [µmol]	PBS buffer volume B [µL]	mass of Ir-Cat. D [mg]	amount of Ir-Cat. E [µmol]	yields [mg]
5	*N*-Isopropyl acrylamide	78.6	694.6	1572	0.22	0.35	254
6	ManEAA ***S4***	48.7	173.7	974	0.06	0.09	197
7	GalEAA ***S5***	48.7	173.7	974	0.06	0.09	216

S6 – CRL$_{native}$

^{1}H-NMR (600 MHz, D_2O, 297.9 K) δ (ppm) 8.56 – 6.62 (m, H_{CRL}), 4.43 – 0.43 (m, H_{BSA} overlaps with HDO peak).

DLS: 345.1 ± 80.4 nm

Ellman's Assay (amount of free thiols): 95%

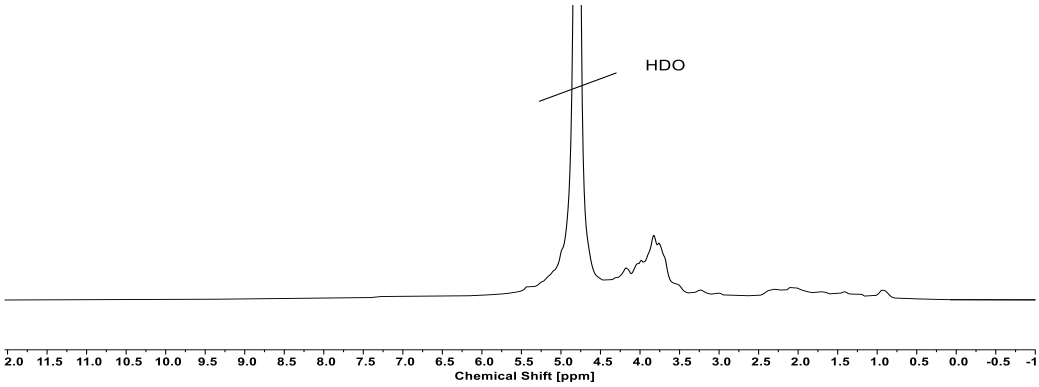


Fig. S48: ^{1}H-NMR spectrum (600 MHz, D2O, 297.9 K) of CRL$_{native}$.

(5) – CRL-p(NIPAM)

^{1}H-NMR (600 MHz, D_2O, 297.9 K) δ (ppm) 8.16 – 6.06 (m, H_{CRL}), 4.42 – 0.49 (m, H_{CRL}, $H_{NIPAM\text{-}side\ chain}$, $H_{NIPAM\text{-}backbone}$ overlap with HDO peak), 2.22 – 1.36 (m, $H_{NIPAM\text{-}backbone}$ overlaps with H_{CRL} peak), 3.92 (s_{br}, *H1* overlap with H_{CRL} peak), 1.18 (s_{br}, *H2, H´2*).

DLS: 121.2 ± 17.3 nm

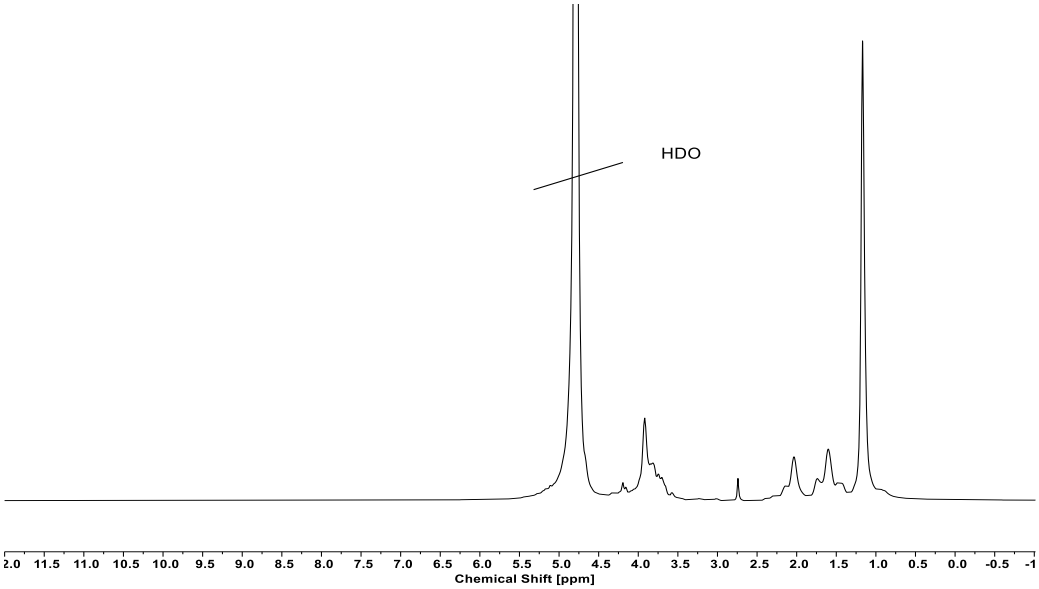


*Fig. S49: ^{1}H-NMR spectrum (600 MHz, D_2O, 297.9 K) of CRL-p(NIPAM) (**5**).*

(6) – CRL-p(ManEAA)

^{1}H-NMR (600 MHz, D_2O, 297.9 K) δ (ppm) 8.24 – 6.16 (m, H_{CRL}), 4.39 – 0.63 (m, H_{CRL}, $H_{ManEAA\text{-}side\ chain}$, $H_{ManEAA\text{-}backbone}$ overlap with HDO peak).

DLS: 129.7 ± 8.6 nm

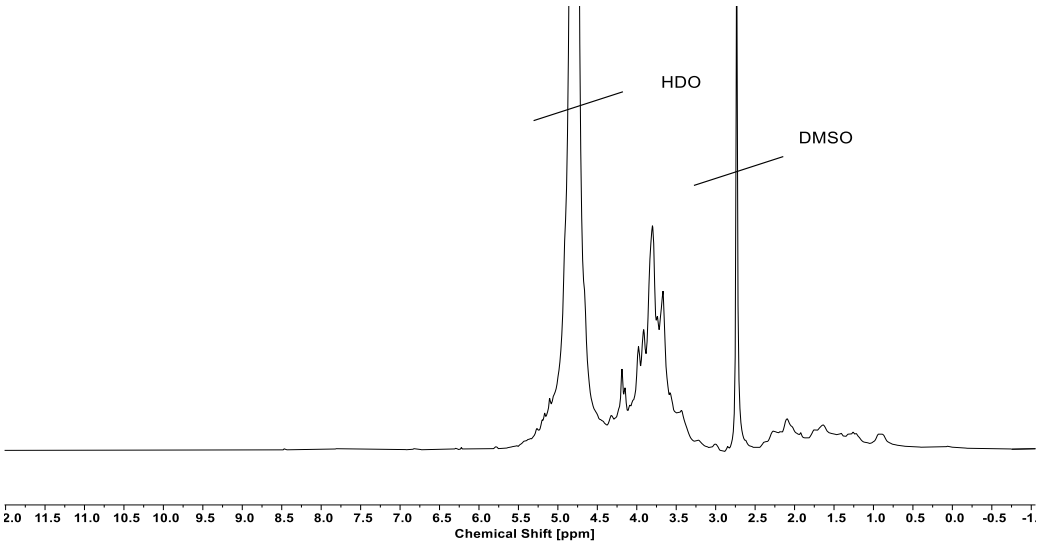


*Fig. S50: ^{1}H-NMR spectrum (600 MHz, D2O, 297.9 K) of CRL-p(ManEAA) (**6**).*

(7) – CRL-p(GalEAA)

^{1}H-NMR (600 MHz, D_2O, 297.9 K) δ (ppm) 8.47 – 6.17 (m, H_{CRL}), 4.46 (s, $H_{GalEAA\text{-}anomeric\ center}$) 4.36 – 0.47 (m, H_{CRL}, $H_{ManEAA\text{-}side\ chain}$, $H_{ManEAA\text{-}backbone}$).

DLS: 125.6 ± 13.2 nm

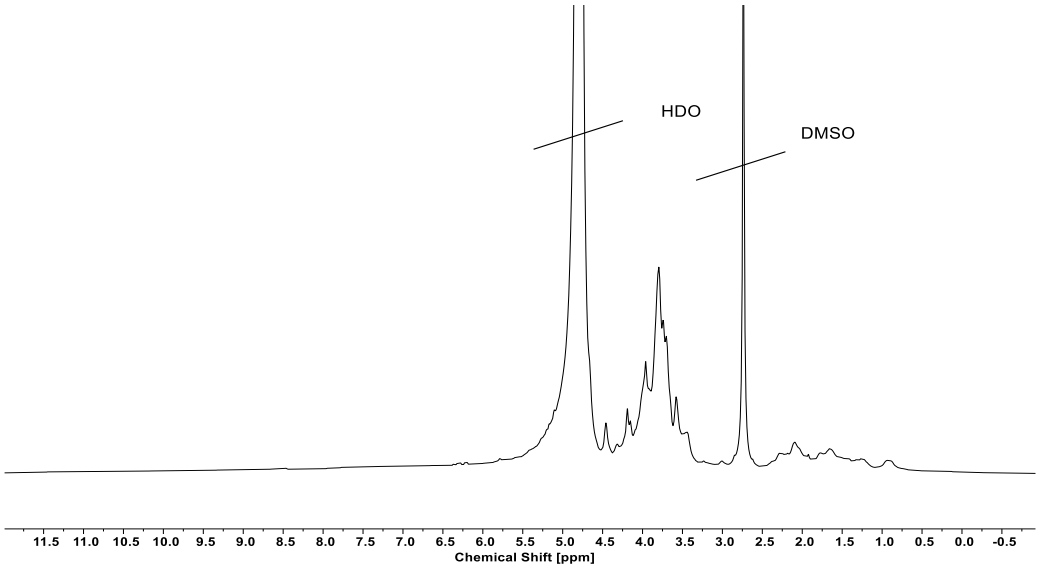
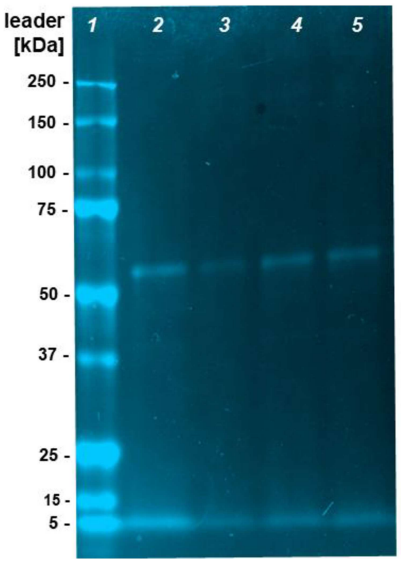


*Fig. S51: ^{1}H-NMR spectrum (600 MHz, D_2O, 297.9 K) of CRL-p(GalEAA) (**7**).*

SDS-PAGE



lane	*loading*
1	protein leader
2	CRL_{native}
3	CRL_p(NIPAM)
4	CRL_p(ManEAA)
5	CRL_p(GalEAA)

*Fig. S52: SDS PAGE with 2 mg/mL of CRLnative (**S6**), CRL-p(NIPAM) (**5**), CRL-p(ManEAA) (**6**), CRL-p(GalEAA) (**7**).*

Turbidity measurements

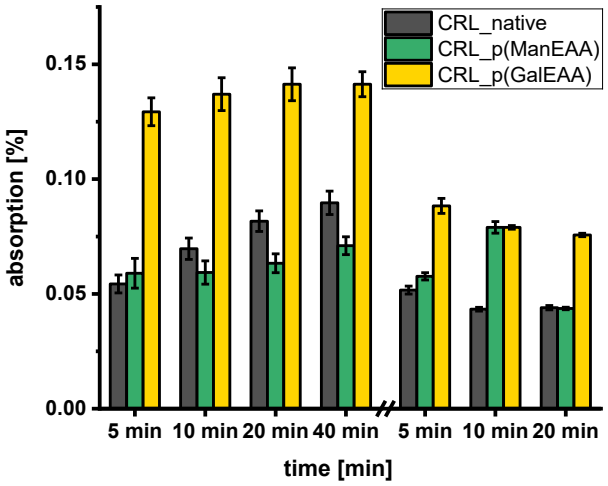


*Fig. S53: Turbidity measurements were performed at 420 nm at room temperature (20 °C). A. Competition-Inhibition of native CRL (**S6**) and CRL-conjugates **6** and **7** (5 µM). 120 µL of each structures were mixed with RCA_{120} (50 µM) and measured after 5, 10, 20, and 40 min, respectively. Inhibitor p(GalEAA) **S8** (30 mM) was then added and measured for another 5, 10, and 20 min.*

Activity measurements

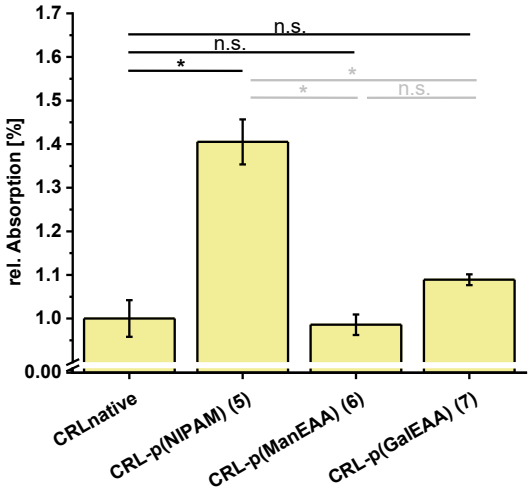


*Fig. S54: Illustration of the activity/ester cleavage of the enzyme CRL. All thiol detections were performed in reactions buffer: 0.1 M sodium phosphate, pH 8.0, containing 1 mM EDTA. Ellman's stock solution of 4 mg/mL Ellman's reagent and a 0.75 mM protein stock solution were prepared in reactions buffer. The assay was performed in triplicate measurements with an incubation time of 15 min and absorbance was measured at 412 nm. Comparison of the activity of the native enzyme CRL and the conjugates **5**-**7**. Data were evaluated using one-way ANOVA analysis followed by Bonferroni correction (*<0.05, not significant (n.s.)).*

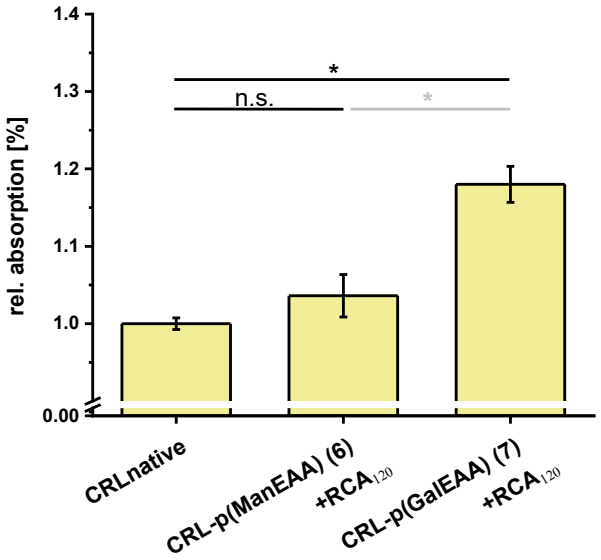


*Fig. S55: Illustration of the activity/ester cleavage of the enzyme CRL. All thiol detections were performed in reactions buffer: 0.1 M sodium phosphate, pH 8.0, containing 1 mM EDTA. Ellman's stock solution of 4 mg/mL Ellman's reagent and a 0.75 mM protein stock solution were prepared in reactions buffer. The assay was performed in triplicate measurements with an incubation time of 15 min and absorbance was measured at 412 nm. Comparison of native CRL with CRL-polymer conjugates **6** and **7** incubated with lectin RCA_{120}. Data were evaluated using one-way ANOVA analysis followed by Bonferroni correction (*<0.05 not significant (n.s.)).*

LCST measurement of CRL-p(NIPAM) conjugate 5

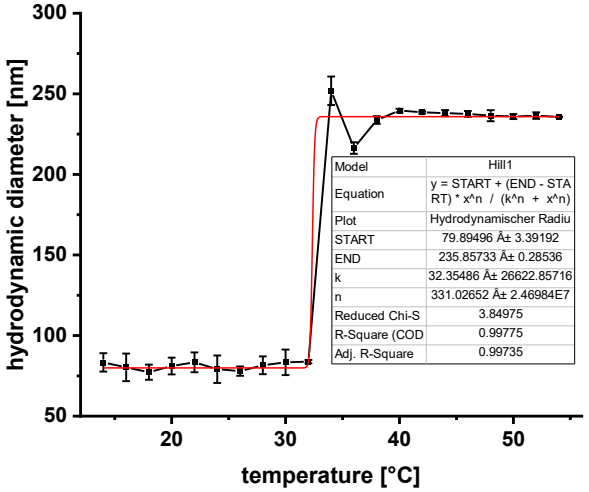
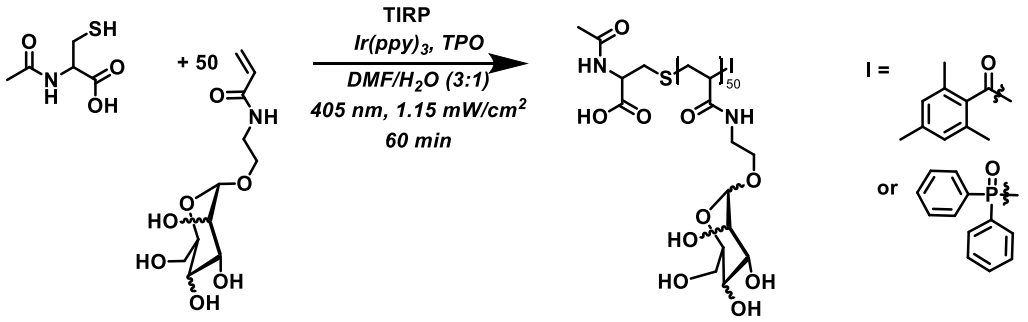


*Fig. S56: DLS measurement to analyze the LSCT of the CRL-p(NIPAM) conjugate **5**. The measurements were performed at a concentration of 0.5 mg/mL in PBS buffer (pH 7.4) in triplicates. The resulting LCST temperature is 32.4 °C.*

2.4 Synthesis of inhibitor polymers *S7* and *S8*

Synthesis of p(ManEAA) (S7) and p(GalEAA) (S8)



Solution I: 2.5 mg acetylcysteine (15.3 µmol) was dissolved in 2 mL DMF and both pre-dissolved TPO (5.43 mg, 15.3 µmol) in 100 µL DMF and 8.5 eq (35 mg, 130 µmol) TCEP in 0.5 mL DMF/H_2O (*v/v*) were added and deoxygenated for 20 min in a nitrogen stream. **Solution II:** Separately, 211.6 mg (766 µmol) of monomer ***S3*** and ***S4***, respectively, were dissolved in 2 mL of DMF and mixed with 0.25 mg $Ir(ppy)_3$ (0.38 µmol) in 100 µL of DMF and deoxygenated for 20 min under nitrogen flow. Solution I was irradiated at 1.15 mW/cm^2 for 2 min, then solution II was added to I and the entire mixture was irradiated at 1.15 mW/cm^2 for one hour. The resulting polymer was precipitated in cold acetone and purified via dialysis (cut-off: 1 kDa) and dried via freeze-drying. The products were isolated as white solids with yields of 83.4 mg (***S7***) and 101.8 mg (***S8***), respectively.

p(ManEAA) (S7):

^{1}H-NMR (600 MHz, D_2O, 297.9 K) δ (ppm) 9.99 – 7.58 (m, $H_{initiator}$), 4.97 – 4.84 (m, $H_{\alpha anomer}$), 4.05 – 3.22 (m, $H_{carbohydrates\ and\ side\ chain}$), 2.70 – 1.37 (m, $H_{backbone}$).

Aqueous SEC: (SEC buffer, pH = 7.0, 293,15 K, whole fraction, dn/dc = 0.153): Mn = 9.1 kDa, corresponds to 43 repeat units, Đ = 4.14, R_h = 7.5 nm.

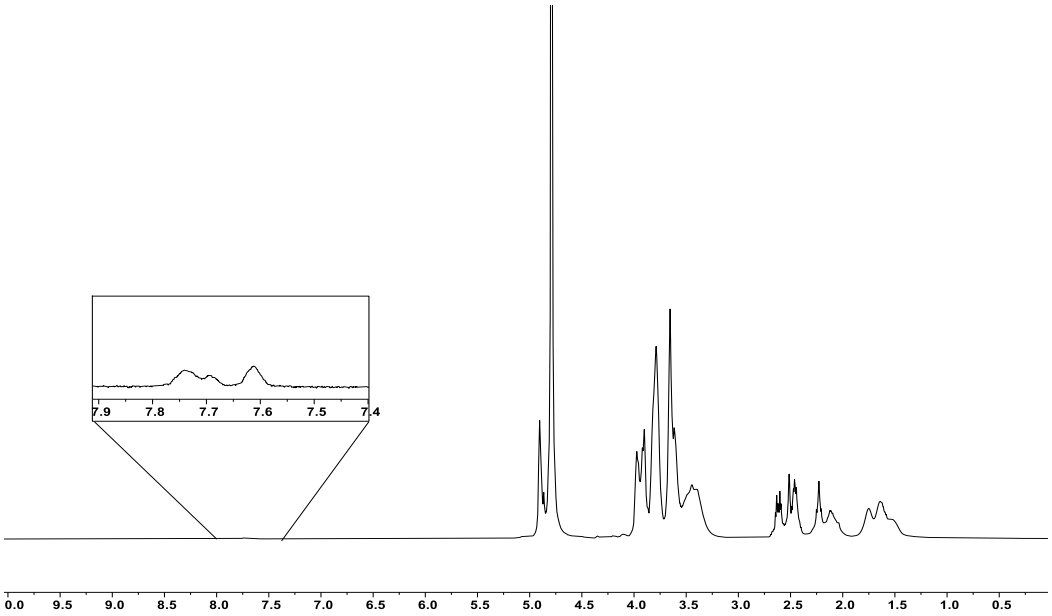


*Fig. S57: ^{1}H-NMR spectrum of p(ManEAA) (**S7**).*

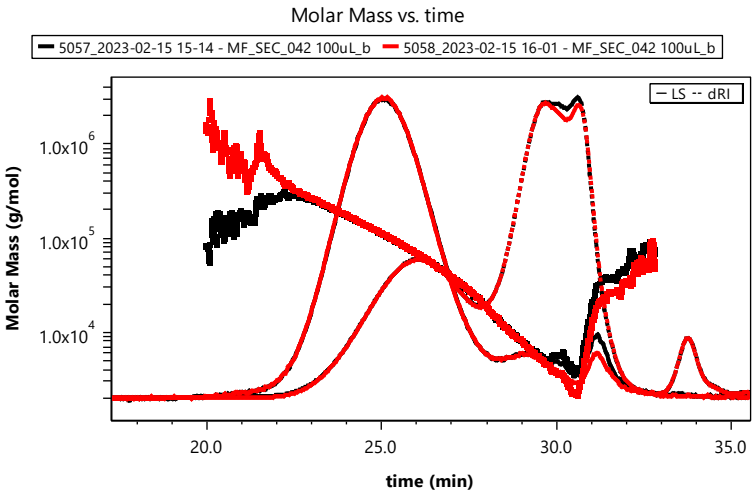


*Fig.S58: Aqueous SEC curve of p(ManEAA) (**S7**), LS and RI detector signal and molar masses, upswing of molar masses in late elution range is due to sample-column interaction.*

p(GalEAA) (S8):

^{1}H-NMR (600 MHz, D_2O, 297.9 K) δ (ppm) 8.14 – 7.55 (m, $H_{initiator}$), 4.51 – 4.35 (m, $H_{\beta anomer}$), 4.12 – 3.26 (m, $H_{carbohydrates\ and\ side\ chain}$), 2.72 – 1.39 (m, $H_{backbone}$).

Aqueous SEC: (SEC buffer, pH = 7.0, 293,15 K, whole fraction, dn/dc = 0.153): Mn = 7.8 kDa, corresponds to 37 repeat units, Đ = 5.08, R_h = 12.9 nm.

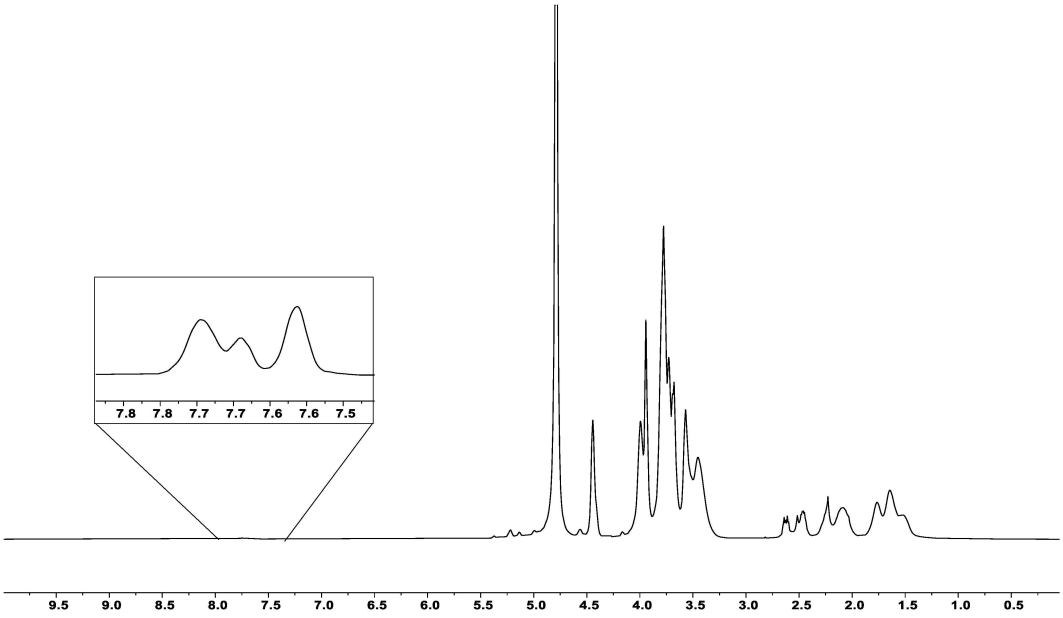


*Fig. S59: ^{1}H-NMR spectrum of p(GalEAA) (**S8**).*

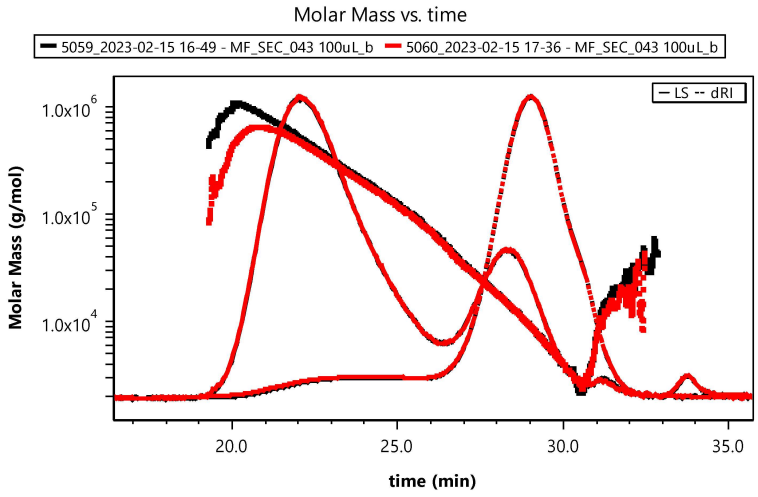


*Fig. S60: Aqueous SEC curves of p(GalEAA) (**S8**), LS and RI detector signal and molar masses, upswing of molar masses in late elution range is due to sample-column interaction.*

2.5 Carbohydrate-lectin binding studies on glass surfaces

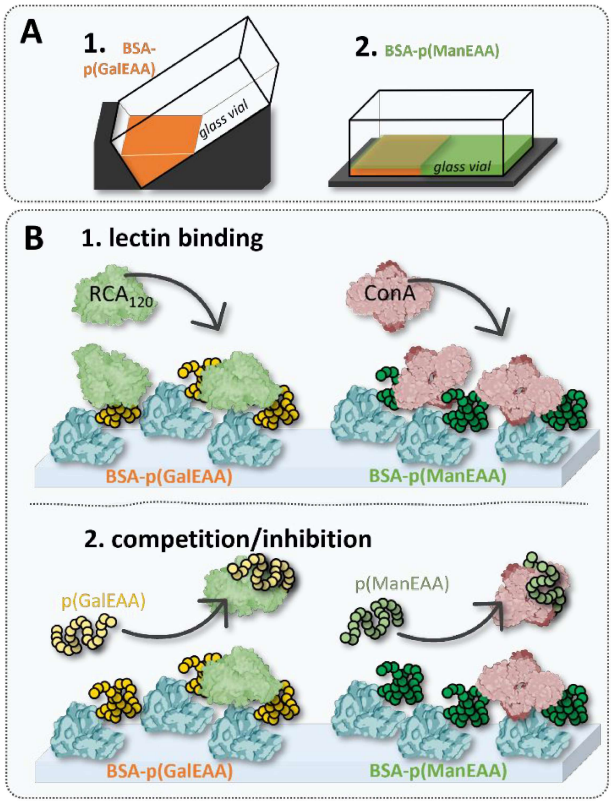


Fig. S61: ***A.*** *Schematic representation of the sample preparation.* ***B.*** *Schematic representation of lectin binding followed by competition/inhibition on the glass surface.*

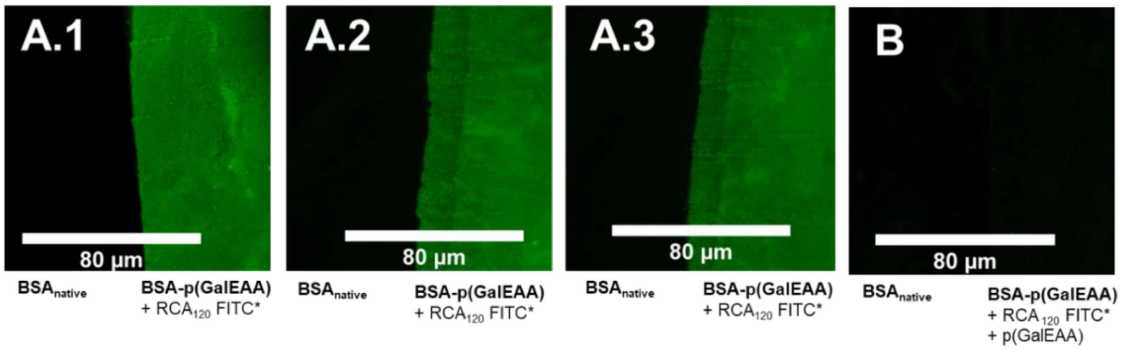


Fig. S62: Surface assay via half-side coating of glass. ***A.1-3*** *Presentation of native BSA (left) and galactose functionalized conjugate* ***4*** *(right) with bound fluorescently labeled (FITC) RCA$_{120}$.* ***B.*** *Imaging of inhibition of the sugar-lectin interaction on glass surface by using p(GalEAA)* ***S8****. (*Excitation: blue-light field 470 nm, contrast was adjusted for better visibility).*

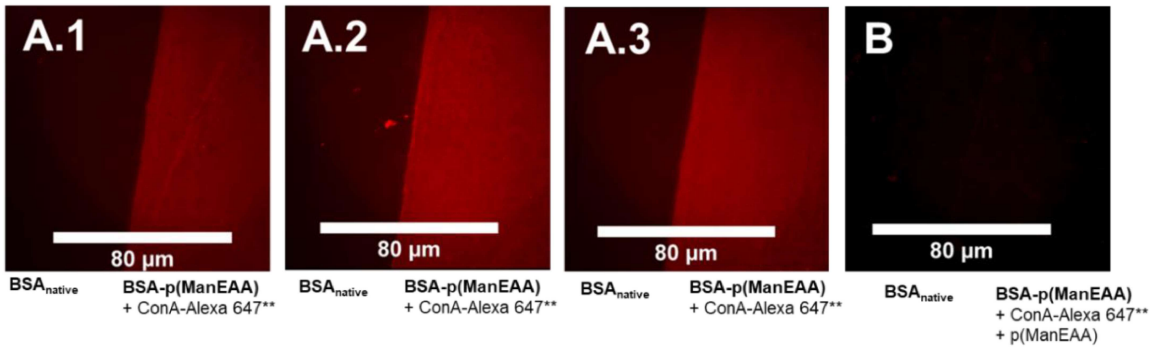


Fig. S63: Surface assay via half-side coating of glass. ***A.1-3*** *Presentation of native BSA (left) and mannose functionalized conjugate* ***3*** *(right) with bound fluorescently labeled (Alexa 647) ConA.* ***B.*** *Imaging of inhibition of the sugar-lectin interaction on glass surface by using p(ManEAA)* ***S7****. (**Excitation: red-light field 625 nm, contrast was adjusted for better visibility).*

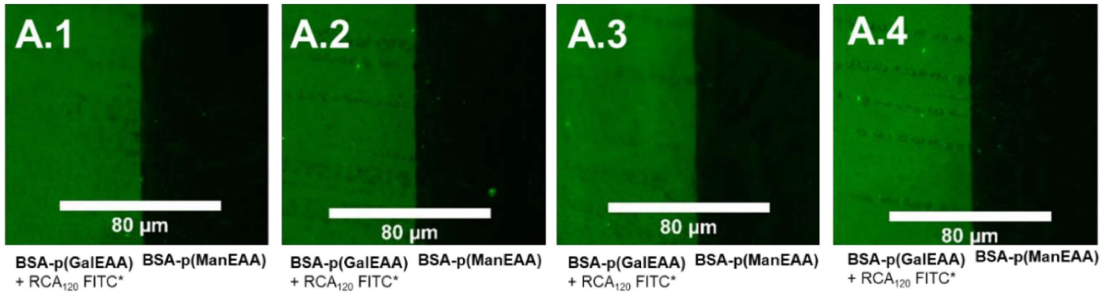


Fig. S64: Surface assay via half-side coating of glass. ***A.1-4*** *Presentation of galactose functionalized conjugate* ***4*** *(left) and mannose functionalized conjugate* ***3*** *(right) with bound fluorescently labeled (FITC) RCA$_{120}$.* ***B.*** *(*Excitation: blue-light field 470 nm, contrast was adjusted for better visibility).*

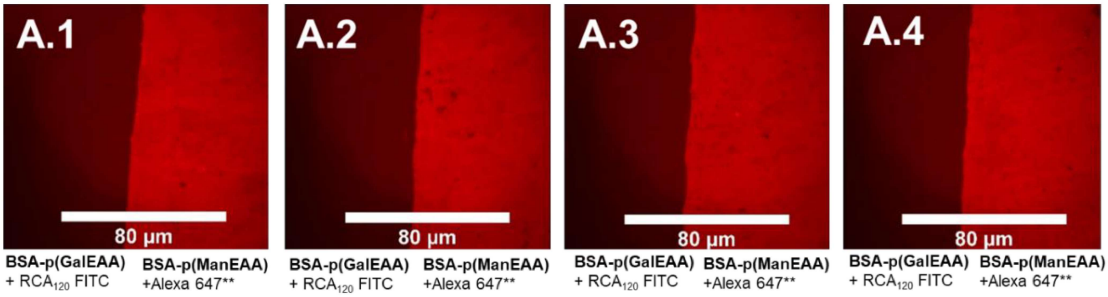


Fig. S65: Surface assay via half-side coating of glass. ***A.1-4*** *Presentation of galactose functionalized conjugate* ***4*** *(left) and mannose functionalized conjugate* ***3*** *(right) with bound fluorescently labeled (FITC) RCA$_{120}$ and bound fluorescently labeled (Alexa 647) ConA. Both fluorescence-labeled lectins were detected on the surface, with only red light used for excitation, resulting in only the Alexa 647 dye of ConA emitting a fluorescent signal. (**Excitation: red-light field 625 nm, contrast was adjusted for better visibility).*

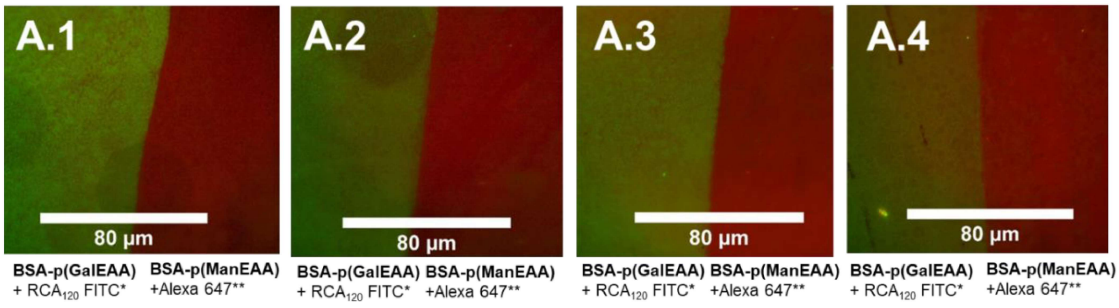


*Fig. S66: Surface assay via half-side coating of glass. **A.1-4** Presentation of galactose functionalized conjugate **4** (left) and mannose functionalized conjugate **3** (right) with bound fluorescently labeled (FITC) RCA_{120} and bound fluorescently labeled (Alexa 647) ConA. Both fluorescently labeled lectins were detected on the surface, and the images show an overlay of the fluorescence signals of both dyes. (*Excitation: blue-light field 470 nm, **Excitation: red-light field 625 nm, contrast was adjusted for better visibility).*

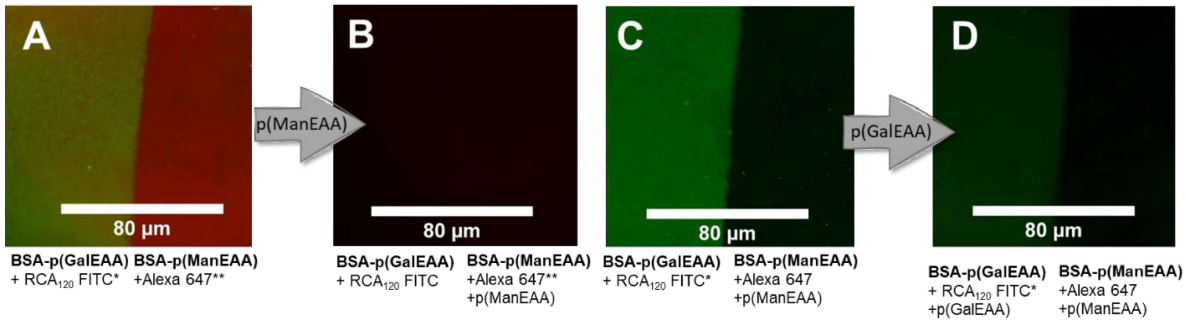


*Fig. S67: **A.** corresponds to figure **A.3** in Fig. S66. Due to the addition of the ConA-specific inhibitor **S7**, no significant fluorescence signal was detected on image **B** via the excitation in the red field. However, the fluorescence signal of the galactose-recognizing lectin RCA_{120}-FITC can still be detected in image **C** by excitation in the blue field. Image **D** shows the detachment of the galactose-recognizing lectin with the inhibitor **S8**, which was not detected by a significant fluorescence signal in the blue field. (*Excitation: blue-light field 470 nm, **Excitation: red-light field 625 nm, contrast was adjusted for better visibility).*

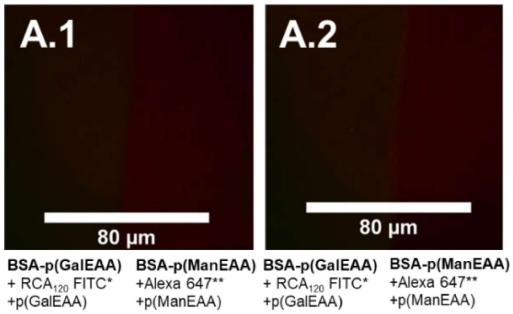


*Fig. S68: Both images **A.1** and **A.2** show the superimposed signals of the surfaces after inhibition with **S7** and **S8**. No significant fluorescence signal is visible on either side of the semi-coated surfaces. (*Excitation: blue-light field 470 nm, **Excitation: red-light field 625 nm, contrast was adjusted for better visibility).*

2.6 Thermal amino acid degradation

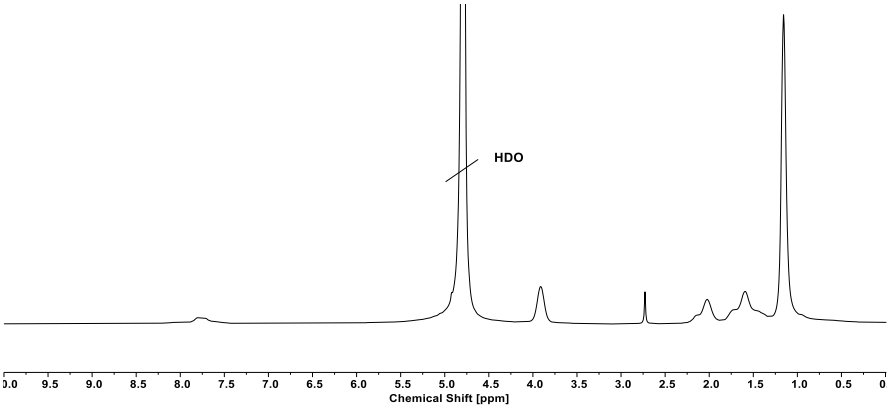


*Fig. S69: ^{1}H-NMR spectrum of thermal amino acid degradation of BSA-p(NIPAM) (**1**).*

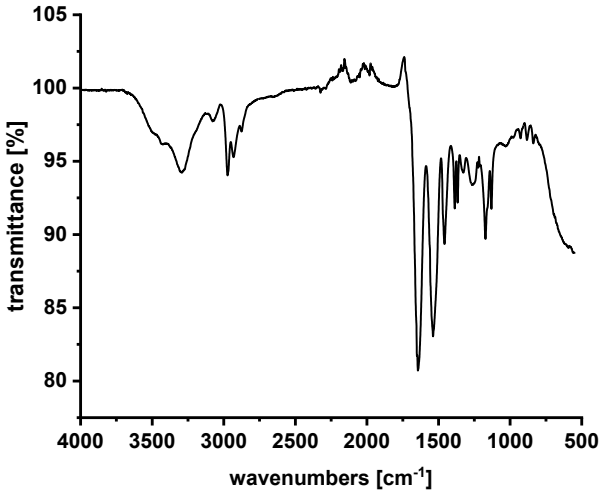


*Fig. S70: IR spectrum of thermal amino acid degradation of BSA-p(NIPAM) (**1**).*

References

[1] J. Janatova, J. K. Fuller, M. J. Hunter, *J Biol Chem* **1968**, *243*, 3612-3622.

[2] K. L. Heredia, D. Bontempo, T. Ly, J. T. Byers, S. Halstenberg, H. D. Maynard, *J Am Chem Soc* **2005**, *127*, 16955-16960.

[3] R. Margesin, G. Feller, M. Hammerle, U. Stegner, F. Schinner, *Biotechnol Lett* **2002**, *24*, 27-33.

[4] F. Schroer, T. J. Paul, D. Wilms, T. H. Saatkamp, N. Jack, J. Muller, A. K. Strzelczyk, S. Schmidt, *Molecules* **2021**, *26*.

6.3 Supporting Information - Site-Specific Polymer-Protein-Polymer Conjugates for the Preparation of Dual Responsive Multilayer Nanoparticles

Authors:	M. I. Feldhof, S. Walber, S. Sperzel, S. Boye, U. I.M. Gerling-Driessen, L. Hartmann
Journal:	Small
Issue:	**2025**, 2500531
Type of Paper:	Research Article
Impact Factor:	13 (2023)
DOI:	10.1002/smll.202500531

Reprinted with permission from Small.

Copyright © 2025 Small.

NANO · MICRO small

Supporting Information

for *Small*, DOI 10.1002/smll.202500531

Site-Specific Polymer-Protein-Polymer Conjugates for the Preparation of Dual Responsive Multilayer Nanoparticles

*Melina I. Feldhof, Simon Walber, Sandro Sperzel, Susanne Boye, Ulla I.M. Gerling-Driessen and Laura Hartmann**

Supporting Information

Site-Specific Polymer-Protein-Polymer Conjugates for the Preparation of Dual Responsive Multilayer Nanoparticles

Melina I. Feldhof, Simon Walber, Sandro Sperzel, Susanne Boye, Ulla I.M. Gerling-Driessen, and Laura Hartmann*

M. I. Feldhof, S. Sperzel, Department of Organic and Macromolecular Chemistry, Heinrich-Heine-University Düsseldorf, Universitätsstraße 1, 40225 Düsseldorf, Germany, E-mail: laura.hartmann@hhu.de
Dr. S. Boye, Macromolecular Structure Analysis, Polymer Separation, Leibniz-Institut für Polymerforschung Dresden, Hohe Str. 6, 01069 Dresden, Germany
Simon Walber, Dr. U.I.M. Gerling-Driessen, Prof. Dr. L. Hartmann, Institute for Macromolecular Chemistry, University of Freiburg, Stefan-Meier-Str. 31, D-79104 Freiburg i.Br., Germany
*corresponding author

Table of Contents

1. Experimental Parts 2
1.1 Materials 2
1.2 Instrumentation 2
1.3 General Methods 7
2. Synthesis and analytical data 11
2.1 Synthesis of carbohydrate monomers **S1**-**S2** 11
2.2 Synthesis of protein-polymer conjugates **1**-**4** 11
2.2 Synthsis of rebridging agent 19
2.3 Conjugation of the rebridging agent to precursor conjugates **1** and **4** 27
2.4 DLS Particle Experiments 39
2.5 Inhibition-Competition experiment of double switchable systems 45
2.6 DLS inhibition Competition Man mix Gal 51
2.7 Synthesis of inhibitor polymers **S3** and **S4** 65

1. Experimental Parts

1.1 Materials

All used chemicals and solvents were used without further purification and were purchased from commercial sources. Type I water, purified by Barnstead™ MicroPure™ ThermoFisher SCIENTIFIC ultrapure water system, was used unless otherwise mentioned.

Acros Organics: N-isopropylacrylamide ≥ 99%; *Alfa Aesar*: cystamine dihydrochloride ≥ 98%; *Bio-Rad:* 10xtris-glycin/SDS-running buffer, pH 8.6, coomassie brilliant blue, precision plus protein™ kaleidoscope™; *BLDpharm*: 3,4-Dibromo-1h-pyrrole-2,5-dione ≥ 99.4%; *Chemsolute*: sodium hydroxide ≥ 99%; *Eurisotope*: chloroform-d ≥ 99.8%; *Fisher Chemicals: potassium carbonate* ≥ 99%; *Fisher BioReagents*™: 2-(4-(2-hydroxyethyl)-1-piperazinyl)-ethane sulfonic acid (HEPES) ≥ 99%; *Fisher scientific*: Concanavalin A Alexa 647, chloroform ≥ 99.8%; *Honeywell*: sodium sulphate ≥ 99%, acetonitrile ≥ 99.9%, diethyl ether ≥ 99.8%; *J&K*: tris(2-phenylpyridine)iridium(III) ≥ 99%; *Merck*: calcium chloride ≥ 90%, deuterated water ≥ 99.9%, sodium carbonate ≥ 99.7%, sodium chloride 100%, tetrahydrofuran ≥ 99.9%; *PanReac AppliChem*: phosphate buffered saline tablet (PBS), dimethyl sulfoxide (DMSO) ≥ 99.9%; *Sigma Aldrich*: Concanavalin A (ConA), *N*-hydroxyethyl acrylamide ≥ 97.4%, *bovine serum albumin* (BSA) ≥ 96%, DMSO-d_6 ≥ 99.9%, manganese(II) chloride tetrahydrate ≥ 99%; *TCI*: bromoacetyl bromide ≥ 98%,diphenyl(2,4,6-trimethylbenzoyl)phosphine oxide (TPO) ≥ 98%, tris(2-carboxyethyl)phosphine (TCEP) ≥ 98%; *Thermo-Fisher*: pierce BCA protein assay kit; *VWRChemicals*: magnesium sulfate 100%, acetone 100%.

1.2 Instrumentation

Nuclear magnetic Resonance Spectroscopy (NMR):

^{1}H-NMR and ^{13}C-NMR spectrum were measured with a Bruker Avance III 600 (600 MHz) at room temperature. The magnetic field has a strength of 14.10 Tesla. This corresponds to an absorption frequency in the ^{1}H-NMR of 600 MHz and in the ^{13}C-NMR of 150 MHz. Chemical shifts were reported in delta (δ) expressed in oarts per million (ppm) for all ^{1}H-NMR spectrum. D_2O serves as the deuterated solvents for all ^{1}H-NMR spectrum. Parts of non-deuterated solvent was used as an internal standard with δ = 4.79 for HDO. Multiplicities were abbreviated as the following: singlet (s), dublet (d), triplet (t), quartet (q), multiplet (m). The abbreviations CH_3-

primary carbon, CH_2-secondary carbon, CH-tertiary carbon and Cquart-quartary carbon were used for the ^{13}C-NMR and spectrum. The assignment of carbohydrate signals on NMR followed the chronological enumeration of protons/carbon atoms within a monosaccharide starting from the reducing end.

Reversed Phase High Pressure Liquid Chromotography Mass Spectrometry (RP-HPLC-MS): RP-HPLC-MS measurements were performed on Agilent Technologies 1260 Infinity series coupled with Agilent quadrupole mass spectrometer with an Electrospray Ionization (ESI) source operating in a m/z range of 200 to 2000. All spectrum were measured with A: 95% H_2O, 5% ACN, 0.1% formic acid and B: 5% H_2O, 95% ACN, 0.1% formic acid. Separation is performed at 25 °C using an Agilent MZ-Aqua Perfect C_{18} 3 µm (50 x 3.0 mm) column with a linear solvent gradient starting at 100% A, ending at 50% B in 17 minutes at a flow rate of 0.4 mL/minute. Indicated purities were determined by integration of the UV-signal detected by a wavelength detector set to 214 nm with the OpenLab ChemStation software for LC/MS from Agilent Technologies.

Matrix-assisted laser desorption/ionization with time-of-flight mass spectrometer (MALDI-TOF-MS): MALDI-TOF-MS spectrum was performed using a Bruker Daltonics UltfelXtreme device. The matrix used was 2,5 dihydroxybenzoic acid (DHB).

High-resolution-electrospray-ionisation mass-spectrometry (HR-ESI): HR-ESI-MS were performed on UHR-QTOF maXis 4G from Bruker Daltonics.

Dynamic light scattering (DLS): DLS measurements were performed at a Malvern HPPS 3.3 instrument (Malvern Panalytical, Kassel, Germany) equipped with a 633 nm He/Ne-laser with the detector set in backscattering configuration (171°). Protein-polymer conjugates (1-0.25 mg/mL) in 1 cm polystyrene cuvettes were analyzed in a temperature range of 14-54 °C or 28-38 °C with a temperature increment of 2°C and a 2, 10, 20 min equilibration time lag between the temperature steps. For evaluation the autocorrection function, the decay constant and first cumulant were determined by exponential fits the and the hydrodynamic radii were calculated by the Stokes-Einstein relation.

UV/Vis spectroscopy: UV/Vis spectroscopy was performed with a dual-trace spectrometer Specord® 210 Plus from Analytik Jena AG. The measurements were conducted in quartz glass

cuvettes (Starna GmbH d = 1 cm) at 20°C. The instrument was operated with Win ASPECT PLUS software.

UV-Irradiation: UV irradiation of the polymerization was conducted with a UV-LED spot with a wavelength of 405 nm and a maximal irradiance of 114-5700 mW/cm^2 operated by a LEDControl both purchased from Opsytec Dr. Gröbel.

Microplate Reader: Absorption measurements were conducted on CLARIOstar® from BMG LABTECH. Measurements were performed at room temperature and analysed by using BMG Mars software. 96 F-bottom corrugated plates from Greiner BIO-ONE were used for all measurements.

Sodium Dodecyl Sulfate – PolyAcrylamid Gel Electrophoresis (SDS-PAGE): Separations were performed with a 10% acrylamide Page at a voltage of 200 mV and current of 200 mA for about 36 min. 10xTris glycine/SDS buffer, which was diluted down to 1x, serves as the running buffer. Coomassie Brilliant Blue is used to stain the protein bands.

Asymmetrical flow field-flow fractionation with light scattering detection (AF4-LS): AF4-LS measurements were conducted on Eclipse Neon (Waters/Wyatt Technologies) with Agilent pump system (1260, Infinity Series) at 25°C in PBS buffer (1 mM, pH 7.4) according Ref. 2. A short channel with fixed height and regenerated cellulose (cut-off: 10 kDa) was used for all measurements. Detection was performed using the LS detector (DAWN Neon, Waters/Wyatt Technologies λ = 660 nm), RI detector (Optilab T rEX, Wyatt) and UV detectors of various wavelengths (λ = 280, 300, 310, 330 nm). Triplicate measurements with 50 µl injection volume were performed. The following protocol was applied in order to separate the different populations of BSA: channel flow was set to 1.0 mL/min with a detector flow of 0.4 mL/min, focusing was performed with a focus flow of 3.0 mL/min for 6 min followed by an isocratic elution step with a cross flow (Fx) of 3 mL/min for 15 min. The last step proceeds without Fx (0 mL/min) for 20 min. Molar masses were calculated from the LS data applying a Berry fit. Refractive index increments (dn/dc) were determined by manual injection of varied sample concentrations into above mentioned RI detector.

Circular dichroism (CD): CD measurements were conducted on a Jasco J-710 CD spectrometer from Jasco Deutschland GmbH with quartz glass cuvettes (Starna GmbH d = 1 cm) at 20 °C in PBS buffer (pH 7.4). University of Duisburg-Essen, Center for Medical Biotechnology and Structural and Medical Biochemistry, AG Bayer.

Fluorescence microscopy: The microscopic fluorescence images were generated by Epifluorescence IX83 microscope from Olympus (Olympus Corporation, Tokyo, JPN) equipped with a 60x, NA 1.25 objective (Olympus Corporation, 60x Planfluor PH3 UPLFLN60XOIPH/1.25, Tokyo, JPN). The temperature was set using Tempcontroller 2000-2 (PeCon GmbH, Erbach, GER). F49-641 640/30 ET Bandpass Excitation Filter, F47-690 690/50 ET Bandpass Emission Filter and F48-660 Beam Splitter T660 LPXR were used as beam splitters. Heinrich-Heine Universität Düsseldorf, Institute of Experimental Medical Physics AG Monzel.

SEM: SEM Images were generated by ZEISS SUPRA 55V high-resolution scanning electron microscope has a field emission cathode (FEG: Field Emission Gun) with VP (variable pressure) mode from 2 - 133 Pascal, adjustable in 1 Pascal steps with an SE2 detector. We would like to acknowledge the Center for Advanced Imaging (CAi) at Heinrich Heine University and especially Steffen Köhler for performing the sample preparation and the imaging at the transmission electron microscope.

Infrared spectroscopy (IR): IR spectroscopic measurements were conducted on a Nicolet iS50 FT-IR from Thermo Scientific with. The analysis is carried out with the OMNIC spectroscopy software from thermoscientific.

Aqueous gel permeation chromatography (GPC): GPC measurements of the protein-polymer conjugates were conducted using an Agilent 1200 series HPLC system equipped with a GE Healthcare GPC column (Superdex 75 10/300). The eluent used was MilliQ water containing 50 mM NaH_2PO_4, 150 mM NaCl, 250 ppm NaN_3 and pH 7 with 30 vol% acetonitrile. was used. This was passed through an inline membrane filter of 0.1 um, with filtered at a flow rate of 0.8 mL/min. The average molecular weights were determined by multi-angle light scattering. determined. A miniDAWN TREOS from Wyatt was used for this purpose. The detection was performed with an Optilab rEX from Wyatt.

Aqueous SEC-MALS-RI: SEC-MALS-RI measurements of the polymeric Inhibitors *S7* and *S8* were conduted using Wyatt systems, isocratic pump, degasser, AS of 1260 Infinity series, LS detector: DAWN Heleos-II (Wyatt), λ = 660 nm RI detector: Optilab T-rEX (Wyatt), λ = 660 nm UV detector: UV detector SPD-M20 (Shimadzu): With variable wavelengths Channel (1) λ = 220 nm, Channel (2) λ = 230 nm Channel (3) λ = 250 nm, Channel (4) λ = 290 nm, Flow rate: 1 mL/min, temperature: 25 °C, Concentration: 3-4 mg/mL, Injection volume: 100 µL. Precolumn (50 mm, 2 x 160 Å of 300 mm and 1000 Å of 300 mm), two main columns (GE Healthcare GPC column Superdex 75 10/300, 8 mm diameter and 5 µm particle size), eluent: MilliQ water:acetonitrile 7:3 (v/v), 50 mM, NaH_2PO_4, 150 mM NaCl and 250 ppm NaN_3, pH = 7.0.

1.3 General Methods

Standard protocols for a) preparation of BSA-polymer conjugates via TIRP, b) Pierce-Protein-Assay, c) SDS-PAGE, d) CD measurements and e) AF4-LS measurements have already been published by Feldhof et.al.[1]

Ellman's Assay: The measurements were carried out in triplicates, for each measurement: 196 µL of Ellman's buffer (0.1M sodium phosphate, pH 8.0, containing 1mM EDTA) was mixed with 20 µL of the protein stock solution or the reduced form with 10eq. TCEP (0.75 mM in Ellman's buffer) followed by 4 µL of the Ellman's stock solution (1 mg/mL in Ellman's buffer) and incubated for 15 min. The absorbance was measured at 412 nm and the amount of accessible thiols was determined based on a previously established calibration curve. For unmodified BSA, the measured value of 54 ± 8% aligns with previously values in the literature.[1, 2] When BSA is reduced with TCEP, the value increases to 257 ± 8%, representing a 200% rise compared to the untreated sample. This observation indicates that using 10 eq. of TCEP results in the exposure of only one disulfide bond, making two additional thiol groups available. This value is also supported by the literature.[2] Data were evaluated using one-way ANOVA analysis followed by Bonferroni correction and shows a significant difference (*<0.05).

Standard protocol for introducing the rebridging agent on previous synthesized BSA-polymer conjugates and reduction of the disulfide bridge from the rebridging agent: 40 mg (0.6 µmol) of BSA-p(HEAA) (**4**) or BSA-pNIPAM (**1**) conjugate was dissolved in 1.5 mL PBS buffer. To this, 100 µL of a 60 mM (10 eq.) tris(2-carboxyethyl)phosphine (TCEP) stock solution in PBS buffer was added and stirred for 10 min at room temperature. The solution was briefly purified via dialysis (exclusion volume 50 kDa, refilled to 1.5 mL with PBS), followed by a second addition of 100 µL of TCEP stock solution (60 mM in PBS) and further stirring for 10 min at room temperature. Remaining TCEP residues were completely removed by repeated purification with deoxygenated PBS buffer via dialysis (exclusion volume 50 kDa, refilled to 1.5 mL with PBS). Ten equivalents of TCEP were used based on Heredia et al.'s demonstration that one disulfide bridge is opened under these conditions.[2] To the reduced protein, 50 µL (1 eq.) of the rebridging stock solution (12 mM in DMSO) was added and stirred for 10 min, producing a yellow coloration upon successful conjugation. The protein was then purified again via dialysis (exclusion volume 50 kDa, refilled to 1.5 mL with PBS) to remove unconjugated rebridging agent. To reduce the

rebridging agent's disulfide bridge, the following steps were repeated three times: the protein conjugate was adjusted to 1.5 mL with PBS buffer, mixed with 100 µL of TCEP stock solution (60 mM in PBS), stirred for 10 min, and rapidly purified via dialysis (exclusion volume 50 kDa, refilled to 1.5 mL with PBS). The protein conjugate was subsequently dialyzed three more times with PBS buffer only and lyophilized.

Standard protocol for preparation of functionalized BSA-polymer conjugates via TIRP: 50 mg (0.77 µmol) BSA-pNIPAM-r.b. (**8**) was dissolved in 2 mL PBS buffer and deoxygenated with nitrogen for 20 minutes. Subsequently, 0.13 mg (0.38 µmol) TPO in 20 µL DMSO was added to the protein solution and deoxygenated for another 20 minutes. Separately, 25 eq. (18.8 µmol) of the vinyl monomer were dissolved in PBS (50 mg/mL), and 0.05 mol% (0.0095 µmol) Ir-Cat. in 20 µL DMSO was added before deoxygenation for 20 minutes. The protein/TPO solution was irradiated for 3 minutes under a UV lamp ($\lambda = 405$ nm) at 114 mW/cm². Then, the monomer/Ir-Cat. mixture was added and irradiated for 60 minutes at 5700 mW/cm². The reaction mixture was purified by dialysis (exclusion volume 50 kDa) and lyophilized.

DLS Experiments for particle formation: Hydrodynamic diameters of thermally induced particles were measured for homovalent conjugates BSA-pNIPAM (**1**-**3**) in polystyrene cuvettes from SARSTEDT at concentrations of 1 mg/mL, 0.5 mg/mL, and 0.25 mg/mL in PBS buffer. Measurements were conducted cyclically, with a forward run (14-54 °C) followed by a return run (54-14 °C). Samples were tested at different heating rates, with a temperature increment of 2 °C and equilibration times of 2, 10, and 20 minutes between steps.

DLS experiments for particle formation in combination with competition-inhibition assay in solution of heterovalent BSA-polymer conjugates and the mannose and galactose mixed particle: The double-switchable systems for "I ConA inhibition before particle dissociation" were evaluated using hydrodynamic diameters via DLS measurements in four phases. First, 400 µL (13.8 µM in LBB: 50 mM sodium chloride, 1 mM manganese (II) chloride tetrahydrate, 1 mM calcium chloride, and 10 mM HEPES in ultrapure water, pH 7.4) of the conjugate was placed in a SARSTEDT polystyrene cuvette and heated above the LCST from 28-38 °C, with a 2-minute equilibration between temperature steps. Subsequently, five measurements were taken at 38 °C with the same equilibration time. In the second phase, 30 µL of ConA solution (5 µM in LBB),

preheated to 38 °C, was added, followed by five measurements at 38 °C. In phase three, 100 µL (15 mM) of the pMan (**S3**) inhibitor solution was added at 38 °C, and five more measurements were taken at 38 °C. In the final phase, the temperature was reduced from 38 °C to 28 °C with a 2-minute equilibration between steps.

For the second experiment, "II Lectin stabilized particle below LCST followed by inhibition," phases one and two were identical to the first experiment. However, in phase three, the temperature was reduced from 38 °C to 28 °C with five measurements taken with a 2-minute equilibration, stabilizing the ConA particle below LCST. In phase four, 100 µL (15 mM) of the pMan (**S3**) inhibitor was added at 28 °C to dissolve the specific binding and the particle.

For the mixed systems, the measurement approach was similar to the four phases of "I ConA inhibition before particle dissociation," except that phase one included mixtures of conjugates **8** and **9**. Additionally, a measurement was conducted with 11% mannose in an acetate buffer (100 mM sodium acetate, 100 mM sodium chloride, 5 mM calcium chloride, and 5 mM manganese (II) chloride tetrahydrate, pH 5.2). The ratios are provided in the following table:

Table S1: Summary of the volumes for the mixed measurements.

mannose content	**mannose conjugate (8) (13.8 µM) [µL]**	**galactose conjugate (9) (13.8 µM) [µL]**
50%	200	200
30%	133.3	266.7
20%	80	320
11%	44.4	355.6
6%	23.5	376.5
3%	12.1	387.9

UV/Vis and fluorescence measurements of BSA-pNIPAM-r.b. (*8*): UV/Vis and fluorescence measurements were conducted to verify the conjugation of the rebridging agent to the conjugates. UV/Vis was measured in quartz cuvettes from 200-800 nm. Fluorescence was measured using a microplate reader with an excitation of 396.5 ± 25 nm and an emission range of 480 ± 10 nm to 605 ± 10 nm. As references, absorbance and fluorescence were independently measured from the conjugate (14 µM in PBS with 10 µL DMSO, deoxygenated with N_2) and the pure rebridging agent (**6**) (14 µM in PBS). Next, 1 mg of the BSA-polymer conjugate was dissolved in 1 mL of 140 µM (10 eq.) tris(2-carboxyethyl)phosphine hydrochloride (TCEP) solution, deoxygenated for 10 min, and its absorbance and fluorescence were measured. Then, 10 µL of the rebridging agent stock

solution (1.4 mM in DMSO) was added, and absorbance was measured. As the highest absorbance occurred at approximately 20 min, fluorescence was also measured at this time.

Fluorescence microscope: Fluorescence images were taken in µ-Slides 8 Well with glass bottom from ibidi, after 30 min of ozone cleaning. The glass surface was blocked with 1 mg/mL BSA for 15 min to prevent unspecific interactions, followed by washing five times with LBB. The chamber was then filled with 100 µL pNIPAM-BSA-pMan (**8**) (4.6 µM in LBB), heated at 1 °C/min, and equilibrated for 20 min at 38 °C. Subsequently, 5 µL of a 5 µM ConA stock solution in LBB was added and equilibrated for another 20 min. The temperature was reduced to 28 °C at 1 °C/min, and after 20 min of equilibration, 20 µL of the pMan (**S3**) inhibitor stock solution (15 mM in LBB) was added and equilibrated for another 20 min. To test particle formation with ConA added below the LCST, 5 µL ConA (5 µM in LBB) was added to 100 µL pNIPAM-BSA-pMan (**8**) (4.6 µM in LBB) at 28 °C, then the temperature was raised to 38 °C at 1 °C/min.

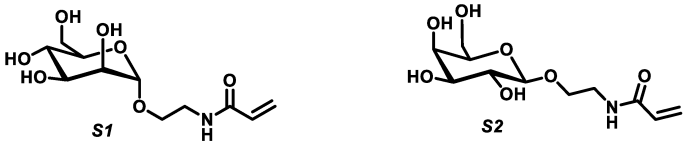
SEM imaging: Samples for SEM were prepared similarly to DLS experiments, but after adding lectin to fix the particles, the solution was removed and diluted from 4.6 µM to 0.46 µM with LBB buffer at 38 °C. The solutions were then dried on 10-well coverslips, sputtered with gold, and measured.

2. Synthesis and analytical data

2.1 Synthesis of carbohydrate monomers S1-S2

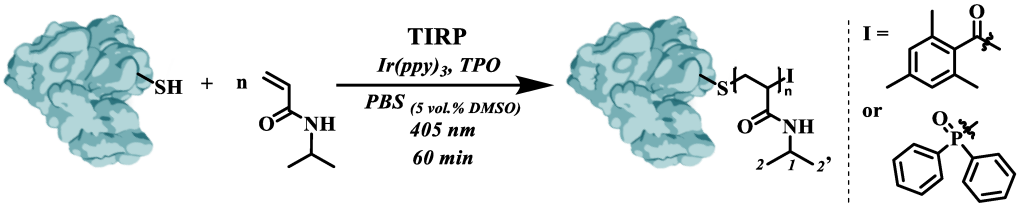
S1 α-D-Mannopyranosyl-ethylacrylamid (Man) and

S2 β-D-Galaktopyranosyl-ethylacrylamid (Gal)



The syntheses of structures S1 and S2 have already been published by Feldhof et.al.[1]

2.2 Synthesis of protein-polymer conjugates 1-4



200 mg (3 µmol) of *bovine serum albumin* was dissolved in 5 mL of deoxygenated phosphate buffered saline (PBS buffer). Separate solutions *I-III* were prepared. *I*: **A** mg **B** µmol) of *N*-isopropylacrylaminde (NIPAM) in **C** µL of PBS buffer (50 mg/mL), *II*: **D** mg (**E** µmol) of catalyst tris(2 phenylpyridine)iridium (Ir-Cat.) in 0.1 mL of dimethyl sulfoxide, *III*: 0.54 mg (1.5 µmol) of diphenyl(2,4,6-trimethylbenzoyl)phosphine oxide (TPO) in 0.1 mL of dimethyl sulfoxide. Ir-Cat. solution *II* is then added to monomer solution *I* and deoxygenated with nitrogen for 10 minutes. In parallel, the TPO solution *III* is slowly dropped to the protein solution and also deoxygenated with nitrogen for 10 minutes before it was irradiated in the focus of the UV lamp (405 nm) for 3 minutes at an intensity of 1.15 mW/cm^2. Subsequently, the mixture of monomer *I* and catalyst solution *II* was also added to the protein and the entire mixture was irradiated for another 60 minutes at 5.22 mW/cm^2 intensity. The reaction mixture was purified by dialysis (exclusion volume 50 kDa) and then lyophilized. A white, fluffy powder was obtained.

Table S2: Formulation values of the monomers and buffer volumes of polymerizations.

structure	mass of monomer A [mg]	amount of monomer B [µmol]	PBS buffer volume C [µL]	mass of Ir-Kat D [mg]	amount of monomer E [µmol]	yields [mg]
1	17.0	150	340	0.05	0.075	209.44
2	34.2	300	680	0.10	0.15	211.31
3	68.3	600	1360	0.20	0.30	243.50

1 – BSA-pNIPAM$_{50}$ conjugate

The characterization of this structure was carried out completely in Feldhof et al.[1]

2 – BSA-pNIPAM$_{100}$ conjugate

^{1}H-NMR (600 MHz, D_2O, 297.9 K) δ (ppm) 9.36 – 5.69 (m, H_{BSA}), 4.59 – 0.00 (m, H_{BSA}, $H_{NIPAM\text{-}side\ chain}$, $H_{NIPAM\text{-}backbone}$, overlap with water peak), 3.91 (m_{br}, *H1*), 1.67 (s_{br}, *H2, H´2*).

AF4-LS (1 mM PBS, pH = 7.4, 298,15 K, monomer fraction): Mn = 75.8 kDa, Mw = 81.6 kDa, Đ = 1.08, Rh = 2.6 nm.

IR (ATR) $\tilde{\nu}$ = 1066.66 cm^{-1} (deformation C-OH). All other wavelengths identical to BSA.

CD: area 215 nm – 245 nm: 221 nm, -18.84 mdeg, area 198 nm – 215 nm: 210.0 nm, -18.94 mdeg.

SDS PAGE see Fig. S10.

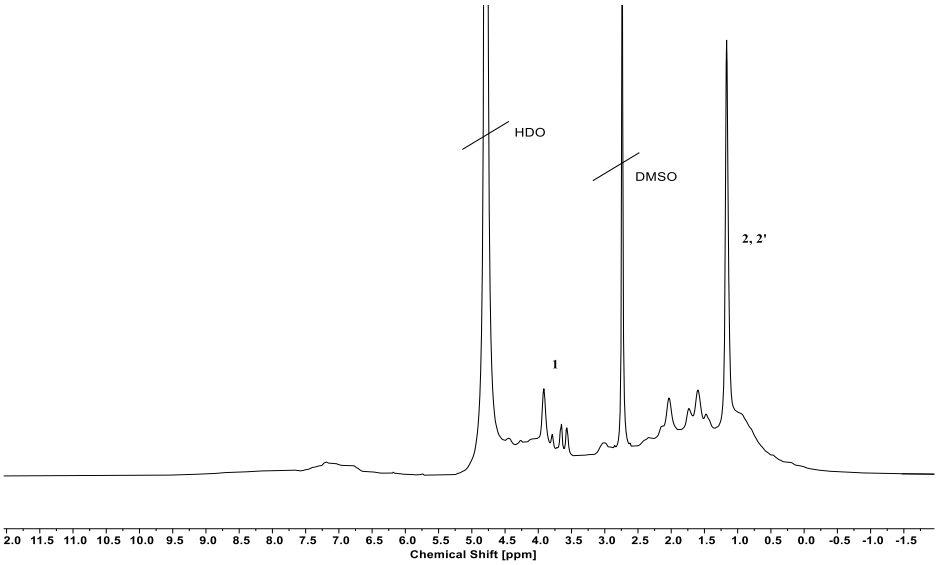


*Fig. S1: ^{1}H-NMR spectrum (600 MHz, D_2O, 297.9 K) of BSA-pNIPAM$_{100}$ conjugate (**2**).*

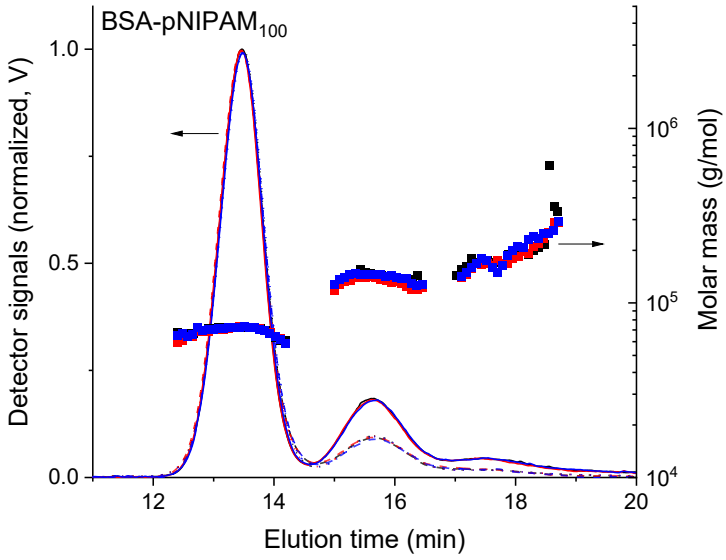


*Fig. S2: Triplicate measurements and presentation of fractograms of BSA-pNIPAM$_{100}$ conjugate (**2**) opt. separation, RI (dashed line), UV (dotted line) and LS signal (solid line), molar masses (symbols) vs. elution time.*

Table S3: Results of the triplicate AF4-LS measurements.

measurement	**M_n**[*1] (kg/mol)	**M_w**[*1] (kg/mol)	**Đ** (M_w/M_n)
1. (50 µl)	76.4	82.8	1.08
2. (50 µl)	75.5	80.8	1.07
3. (50 µl)	75.5	81.3	1.08
average (whole peak)	**75.8**	**81.6**	**1.08**

*1 dn/dc = 0.172 ml/g

Table S4: Analysis of the individual fractions of AF4-LS. The values shown are average values from the triplicate measurements.

fraction	**M_n**[*1] (kg/mol)	**M_w**[*1] (kg/mol)	**Đ** (M_w/M_n)	**mass fraction** (%)	**mol fraction** (%)
1 - monomer	72.1	72.1	1.00	85.5	92.5
2 – dimer	143	143	1.00	11.8	6.3
3- trimer / multimer	176	177	1.01	2.7	1.2

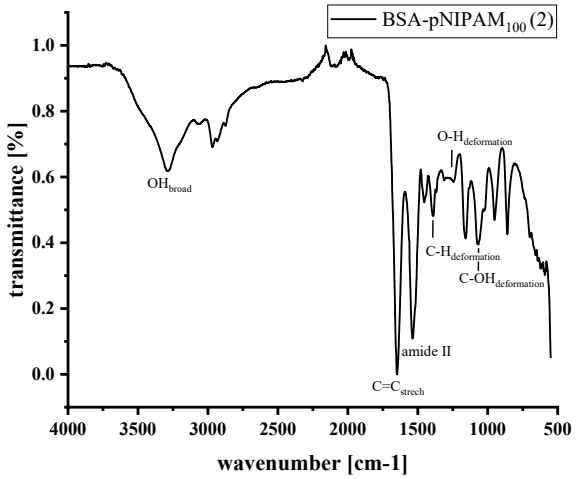


*Fig. S3: IR spectrum BSA-pNIPAM$_{100}$ conjugate (**2**).*

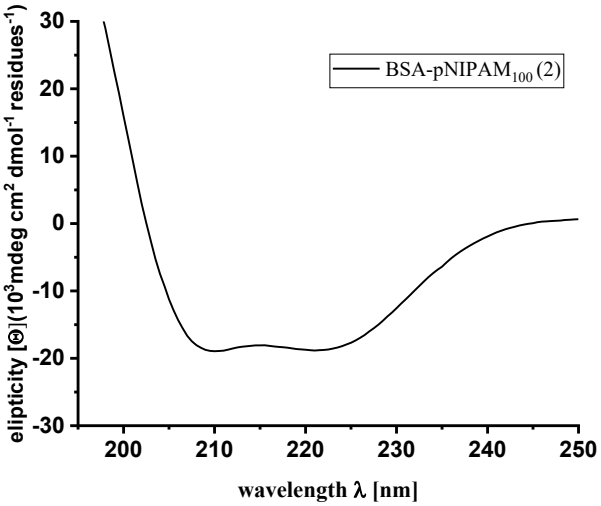


Fig. S4: CD spectrum of BSA-pNIPAM conjugate (2).

3 – BSA-pNIPAM$_{200}$ conjugate

^{1}H-NMR (600 MHz, D_2O, 297.9 K) δ (ppm) 9.18 – 6.20 (m, H_{BSA}), 4.48 – 0.00 (m, H_{BSA}, $H_{NIPAM\text{-}side\ chain}$, $H_{NIPAM\text{-}backbone}$, overlap with water peak), 3.92 (m_{br}, *H1*), 1.67 (m_{br}, *H2, H´2*).

AF4-LS (1 mM PBS, pH = 7.4, 298,15 K, monomer fraction): Mn = 74.8 kDa, Mw = 80.9 kDa, Đ = 1.08, Rh = 2.6 nm.

Aqueous SEC: M_n: 96 kDa with 1,045 Đ.

IR (ATR) $\tilde{\nu}$ = 1077.21 cm^{-1} (deformation C-OH). All other wavelengths identical to BSA.

CD: area 215 nm – 245 nm: 218.5 nm, -28.05 mdeg, area 198 nm – 215 nm: 208.0 nm, -30.4 mdeg.

SDS PAGE see Fig. S10.

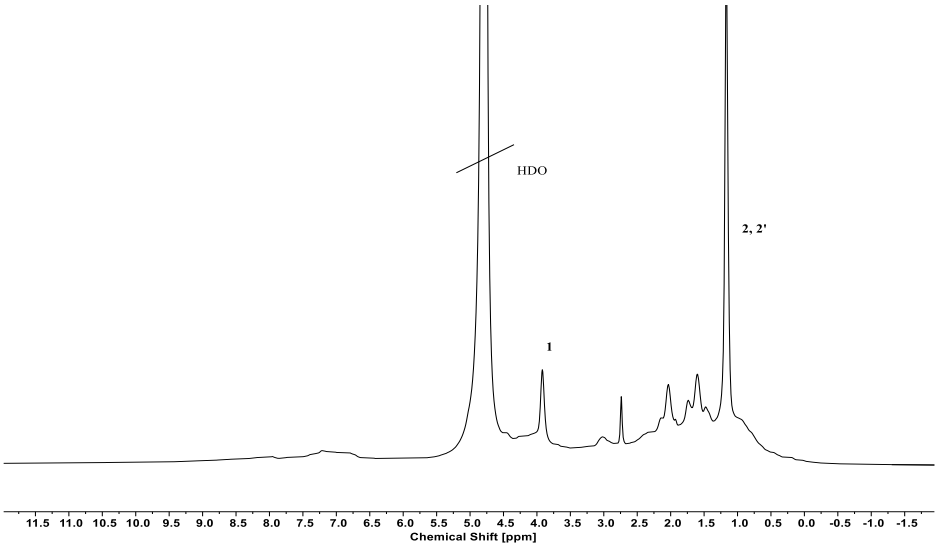


*Fig. S5: ^{1}H-NMR spectrum (600 MHz, D_2O, 297.9 K) of BSA-pNIPAM$_{200}$ conjugate (**3**).*

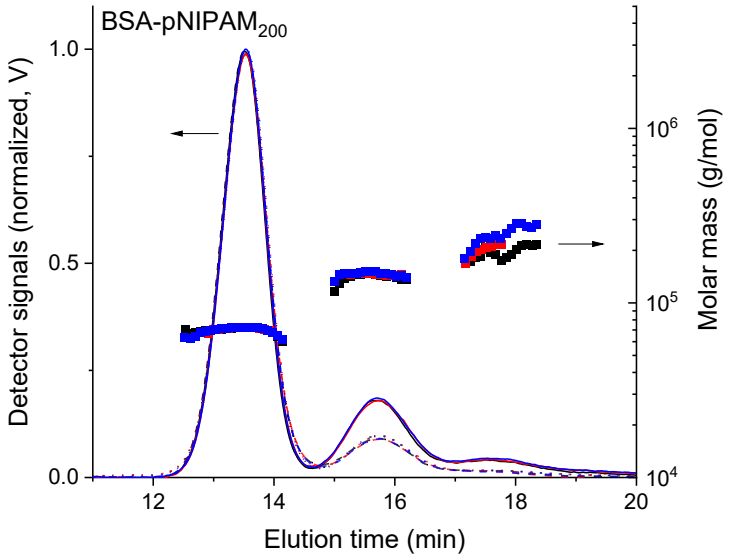


*Fig. S6: Triplicate measurements and presentation of fractograms of BSA-pNIPAM$_{100}$ conjugate (**2**) opt. separation, RI (dashed line), UV (dotted line) and LS signal (solid line), molar masses (symbols) vs. elution time.*

Table S5: Results of the triplicate AF4-LS measurements.

Measurement	**M_n**[*1] (kg/mol)	**M_w**[*1] (kg/mol)	**Đ** (M_w/M_n)
1. (50 µl)	74.5	80.0	1.07
2. (50 µl)	74.7	80.7	1.08
3. (50 µl)	75.2	81.9	1.09
average (whole peak)	**74.8**	**80.9**	**1.08**

*1 dn/dc = 0.172 ml/g

Table S6: Analysis of the individual fractions of AF4-LS. The values shown are average values from the triplicate measurements.

fraction	**M_n**[*1] (kg/mol)	**M_w**[*1] (kg/mol)	**Đ** (M_w/M_n)	**mass fraction** (%)	**mol fraction** (%)
1 - monomer	71.6	71.6	1.00	86.6	93.5
2 – dimer	146	146	1.00	10.8	5.9
3- trimer / multimer	209	211	1.01	2.6	0.6

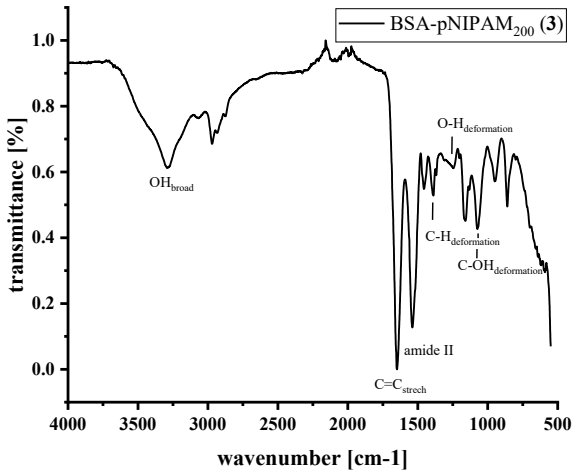


*Fig. S7: IR spectrum BSA-pNIPAM$_{200}$ conjugate (**3**).*

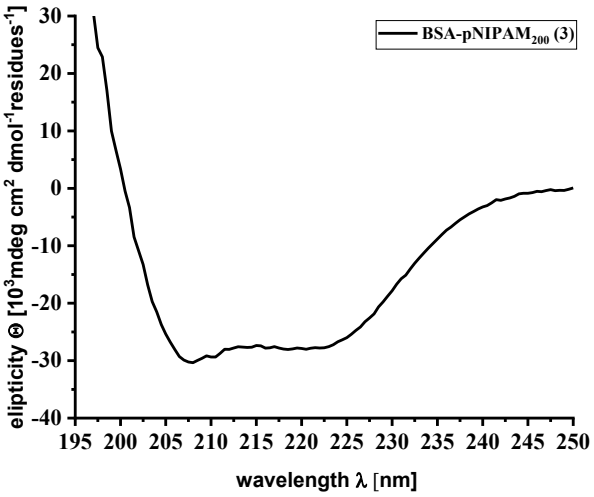


*Fig. S8: CD spectrum of BSA-pNIPAM$_{200}$ conjugate (**3**).*

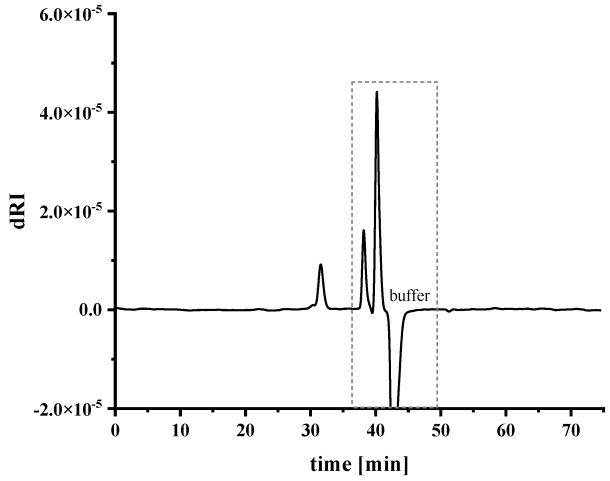
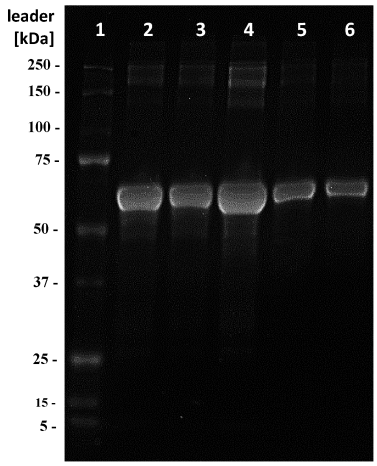


*Fig. S9: Aqueous SEC-MALS measurement of BSA-pNIPAM$_{200}$ (**3**).*



lane	*loading*
1	protein leader
2	BSA_{native}
3	BSA-pHEAA (4)
4	BSA-pNIPAM (1)
5	BSA-pNIPAM (2)
6	BSA-pNIPAM (3)

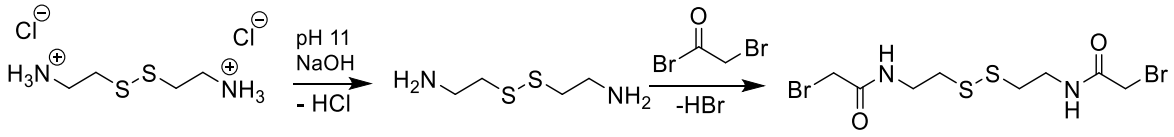
*Fig. S10: SDS-PAGE of BSA_{native} BSA-pNIPAM$_{50}$ (**1**), BSA-pNIPAM$_{100}$ (**2**), BSA-pNIPAM$_{200}$ (**3**). Since SDS-PAGE estimates the molecular weight of denatured proteins, the observed differences in the molecular weights of individual protein-polymer conjugates were marginal and did not reflect the actual molecular weights. This is expected, as polymers behave differently from proteins under denaturing conditions. The polymers likely remain highly coiled, not significantly influencing the denatured protein's behavior in SDS-PAGE.*

4 – BSA-pHEAA$_{50}$ conjugate

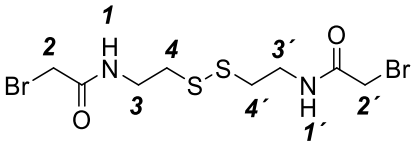
The characterization of this structure was carried out completely in Feldhof et al.[1]

2.2 Synthsis of rebridging agent

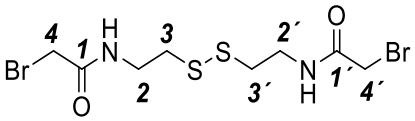
5 – Synthesis of N,N' (disulfanediylbis(ethan2,1diyl))-bis(2bromo-acetamide)



1 g (4.44 mmol) of cystamine dihydrochloride was added to 10 mL of water and adjusted to a pH value of 10 with sodium hydroxide. The cystamine was extracted four times with 40 mL chloroform each time. Then 0.81 mL (9.3 mmol) bromoacetyl bromide was slowly added and the reaction solution was stirred for 2 h at room temperature (21 °C). The product mixture was washed three times with water and the organic phase was dried using magnesium sulfate. Finally, the solvent was removed under reduced pressure. A colorless powder with a yield of 0.7 g (40%) was obtained.



^{1}H-NMR (600 MHz, $CDCl_3$, 297.9 K) δ (ppm) 7.03 (s_{br}, 2H, *H1, H1´*), 3.90 (s, 4H, *H2, H2´*), 3.69 – 3.57 (q, ^{3}J = 6.3 Hz, 4H, *H3, H3´*), 2.91 – 2:77 (t, ^{3}J = 6.4 Hz, 4H, *H4, H4´*).



^{13}C-NMR (600 MHz, $CDCl_3$, 297.9 K) δ (ppm) 166.18 (2C, *C1, C1´*), 39.14 (2C, *C2, C2´*), 37.41 (2C, *C3, C3´*), 29.17 (2C, *C4, C4´*).

LC-MS: m/z calculated for $C_8H_{14}Br_2N_2O_2S_2$ $[M+H]^+$ 394.88, found 394.80 und $[M+Na]^+$ 416.88, found 416.80 certain relative purity: >95%.

HR-ESI-MS: m/z calculated for $C_8H_{14}Br_2N_2O_2S_2$ $[M+H]^+$ 394.88 found 394.89.

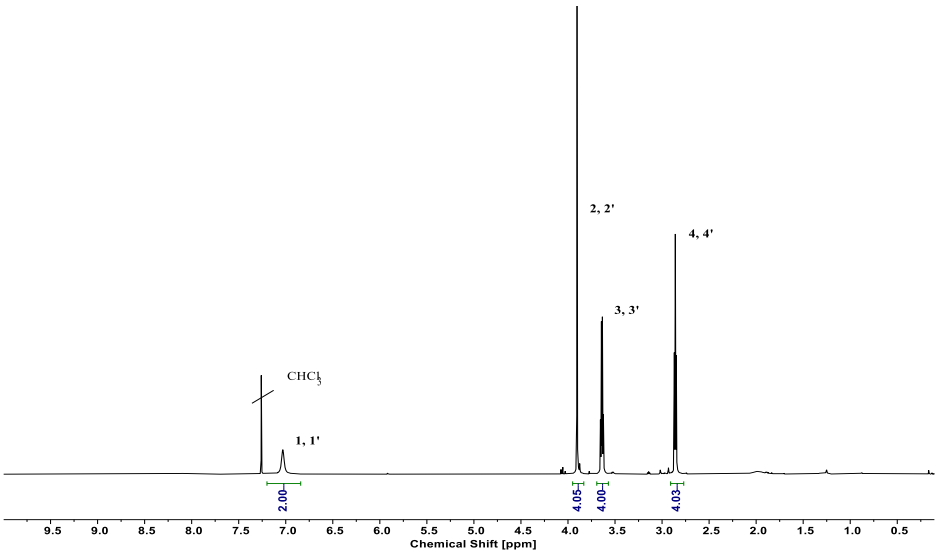


*Fig. S11. [1]H-NMR spectrum (600 MHz, $CDCl_3$, 297.9 K) of N,N' (disulfanediylbis(ethan2,1diyl))-bis(2bromo-acetamide) (**5**).*

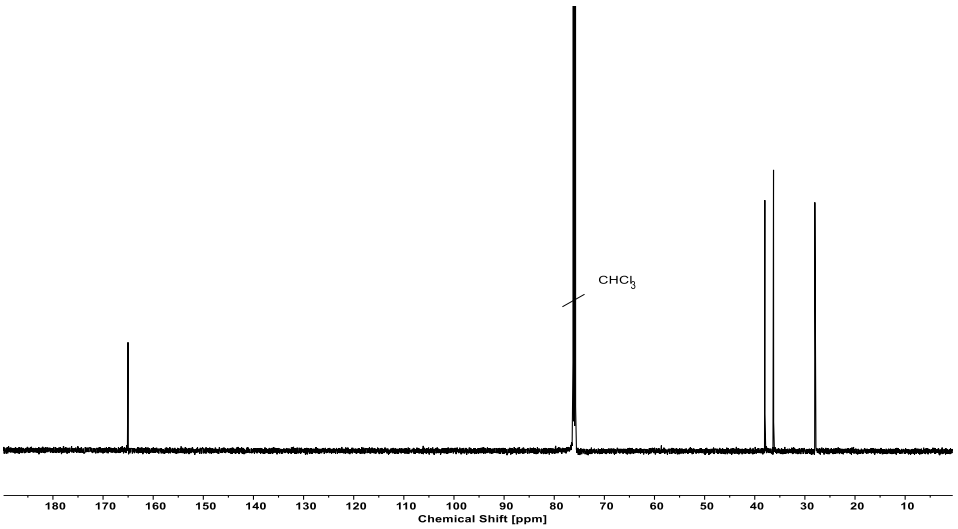


*Fig. S12: [13]C-NMR spectrum (150 MHz, $CDCl_3$, 297.9 K) of N,N' (disulfanediylbis(ethan2,1diyl))-bis(2bromo-acetamide) (**5**).*

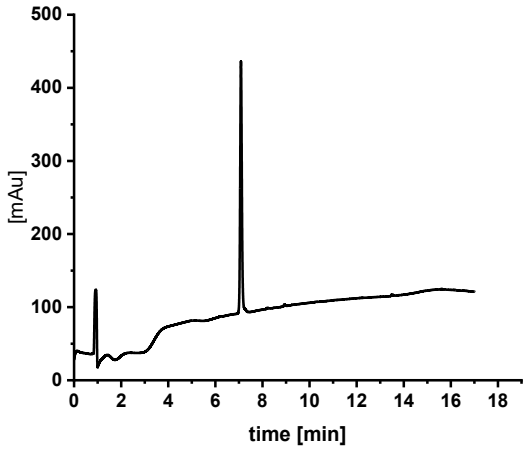


*Fig. S13: RP-HPCL chromatogram of the N,N' (disulfanediylbis(ethane2,1diyl))-bis(2bromoacetamide) (**5**) (gradient from 5 to 95vol.% acetonitrile/water with 0.1vol.% formic acid, run time: 17 min).*

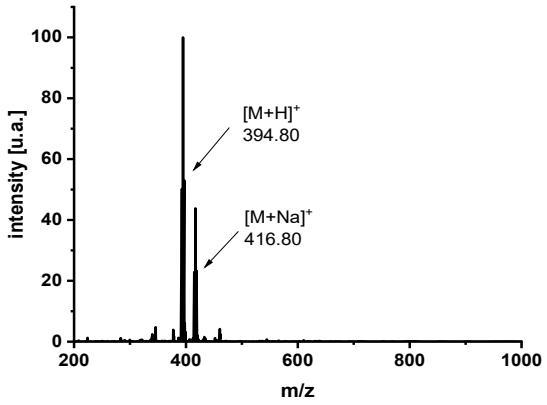


*Fig. S14. ESI mass spectrum of N,N' (disulfanediylbis(ethane2,1diyl))-bis(2bromoacetamide)(**5**) at t = 7.2 min (gradient from 5 to 95 vol.% acetonitrile/water with 0.1 vol.% formic acid, run time: 17 min).*

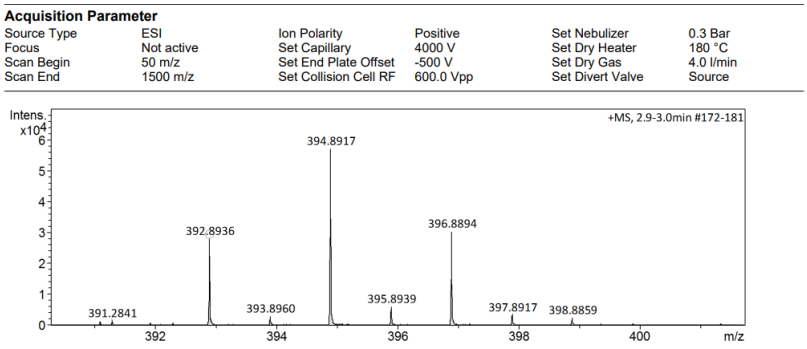
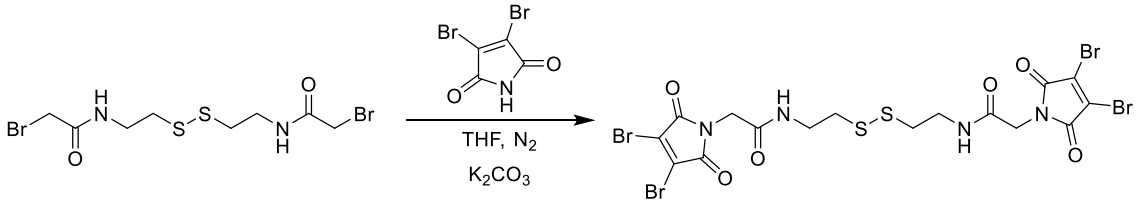
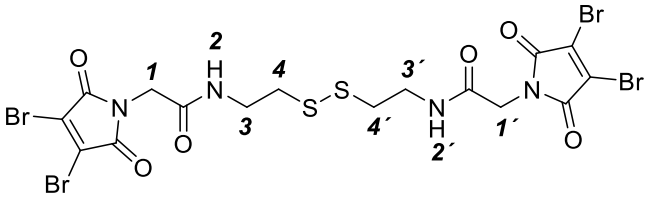


*Fig. S15: HR-ESI-MS spectrum of N,N' (disulfanediylbis(ethane2,1diyl))-bis(2bromoacetamide) (**5**).*

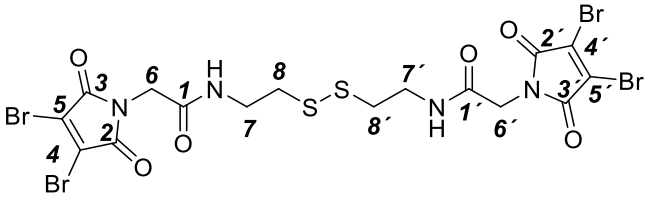
6 – N,N'-(disulfanediylbis(ethan-2,1-diyl))bis(2-(3,4-dibromo-2,5-dioxo-2,5-dihydro-1H-pyrrol-1-yl)acetamide (rebridging agent)



3 g (11.77 mmol) of 3,4-dibromopyrrole-2,5-dione and 8.04 g (58.2 mmol) of potassium carbonate were placed in 30 mL of dry tetrahydrofuran and purged with nitrogen for 15 min. 1.53 g (3.99 mmol) of N,N'-(disulfanediylbis(ethane-2,1-diyl))bis(2-bromoacetamide) was suspended in 15 mL of tetrahydrofuran and slowly added to the reaction solution. The reaction mixture was purged with nitrogen for a further 2 h and stirred overnight at room temperature (21 °C). The solvent was removed under reduced pressure, the oily residue was taken up with 50 mL chloroform, washed three times with 30 mL water each time, the organic phase was dried over magnesium sulfate and the solvent was removed under reduced pressure. The product mixture was recrystallized in ethyl acetate and a white powder with a yield of 0.21 g (7%) was obtained.



^{1}H-NMR (600 MHz, DMSO-d_6, 297.9 K) δ (ppm) 8.54 – 8.3 (t, ^{3}J = 5.7 Hz, 2H, *H2, H2´*), 4.10 (s, 4H, *H1, H1´),* 3.48 – 3.21 (q, ^{3}J = 6.5 Hz, 4H, *H3, H3´*), 2.89 – 2.66 (t, ^{3}J = 6.8 Hz, 4H, *H4, H4´*).



^{13}C-NMR (600 MHz, DMSO-d_6, 297.9 K) δ (ppm) 165.76 (2C, *C1, C1´*), 163.93 (4C, *C2, C2´,C3, C3´),* 129.56 (4C, *C4, C4´, C5, C5´*), 41.39 (2C, *C6, C6´*), 38.09 (2C, *C7, C7´*), 36.75 (2C, *C8, C8´*).

LC-MS: m/z calculated for $C_{16}H_{14}Br_4N_4O_6S_2$ $[M+H]^+$ 742.70, found 742.70, certain relative purity: 94%.

HR-ESI-MS: m/z calculated for $C_{16}H_{14}Br_4N_4O_6S_2$ $[M+H]^+$ 742.70 found 742.71.

MALDI-TOF: m/z calculated mass $[M+H]^+$ 742.70 found 742.71, m/z calculated mass $[M+Na]^+$ 762.70 found 762.63.

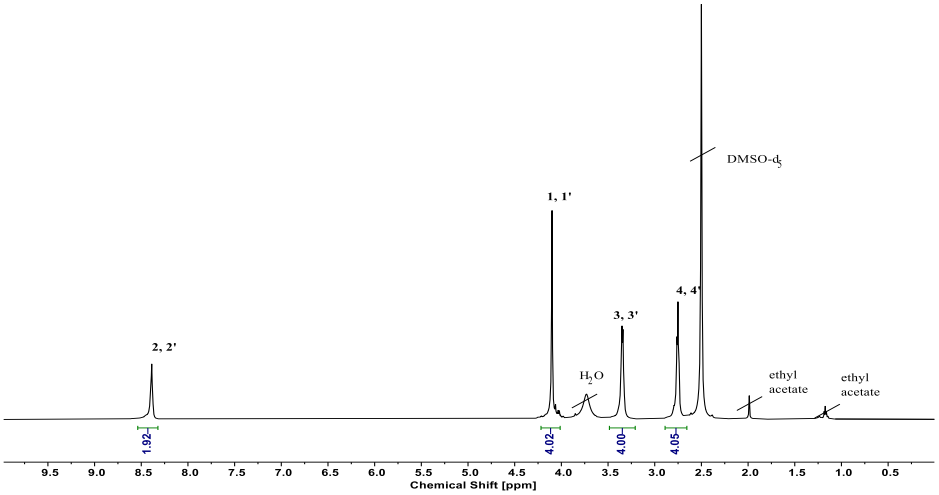


*Fig. S16: [1]H-NMR spectrum (600 MHz, DMSO-d_6, 297.9 K) of N,N'-(disulfanediylbis(ethan-2,1-diyl))bis(2-(3,4-dibromo-2,5-dioxo-2,5-dihydro-1H-pyrrol-1-yl)acetamide (rebridging agent) (**6**).*

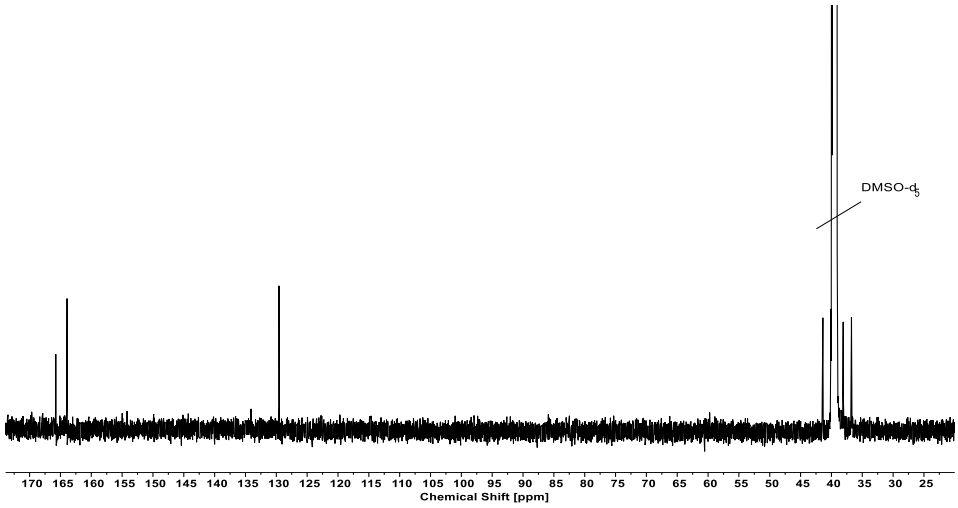


*Fig. S17: [13]C-NMR spectrum (150 MHz, $CDCl_3$, 297.9 K) of N,N'-(disulfanediylbis(ethan-2,1-diyl))bis(2-(3,4-dibromo-2,5-dioxo-2,5-dihydro-1H-pyrrol-1-yl)acetamide (rebridging agent) (**6**).*

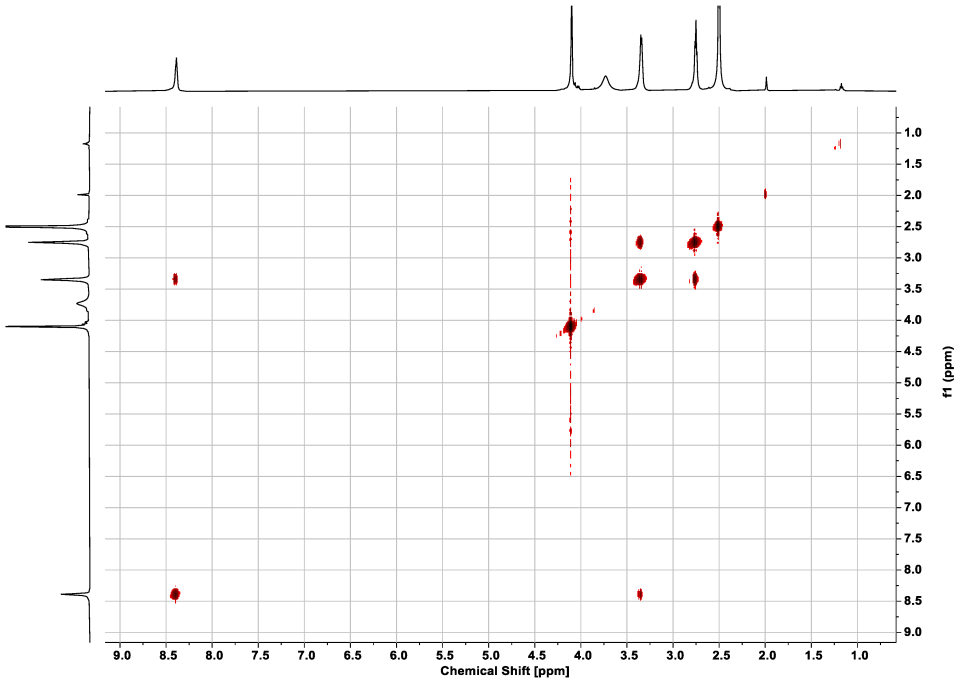


*Fig. S18: COSY-NMR spectrum (600 MHz, DMSO-d_6, 297.9 K) of N,N'-(disulfanediylbis(ethan-2,1-diyl))bis(2-(3,4-dibromo-2,5-dioxo-2,5-dihydro-1H-pyrrol-1-yl)acetamide (rebridging agent) (**6**).*

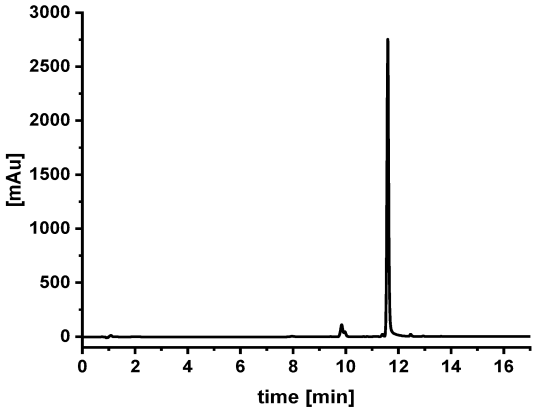


*Fig. S19: RP-HPLC chromatogram of N,N'-(disulfanediylbis(ethan-2,1-diyl))bis(2-(3,4-dibromo-2,5-dioxo-2,5-dihydro-1H-pyrrol-1-yl)acetamide (rebridging agent) (**6**) (gradient from 5 to 95vol.% acetonitrile/water with 0.1vol.% formic acid, run time: 17 min).*

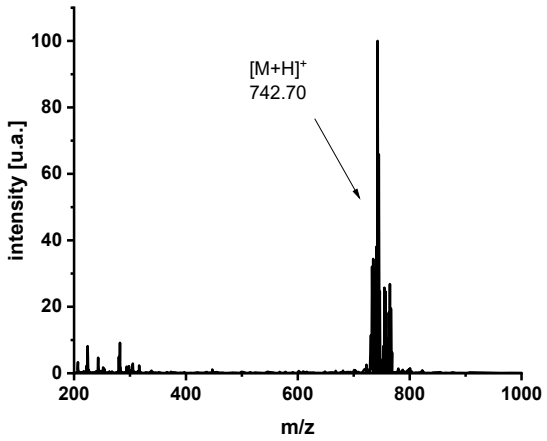


*Fig. S20: ESI mass spectrum of N,N'-(disulfanediylbis(ethan-2,1-diyl))bis(2-(3,4-dibromo-2,5-dioxo-2,5-dihydro-1H-pyrrol-1-yl)acetamide (rebridging agent) (**6**) at t = 11.86 min (gradient from 5 to 95 vol.% acetonitrile/water with 0.1 vol.% formic acid, run time: 17 min).*

Acquisition Parameter

Source Type	ESI	Ion Polarity	Positive	Set Nebulizer	0.3 Bar
Focus	Not active	Set Capillary	4000 V	Set Dry Heater	180 °C
Scan Begin	50 m/z	Set End Plate Offset	-500 V	Set Dry Gas	4.0 l/min
Scan End	1500 m/z	Set Collision Cell RF	600.0 Vpp	Set Divert Valve	Source

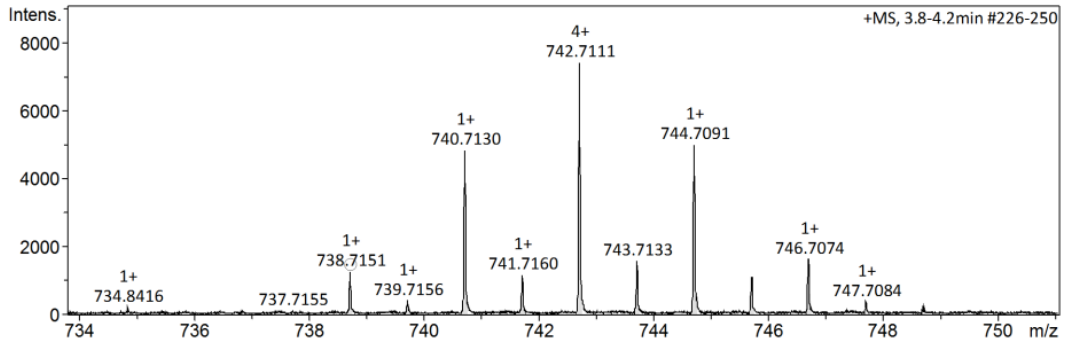


*Fig. S21: HR-ESI-MS spectrum of N,N'-(disulfanediylbis(ethan-2,1-diyl))bis(2-(3,4-dibromo-2,5-dioxo-2,5-dihydro-1H-pyrrol-1-yl)acetamide (rebridging agent) (**6**).*

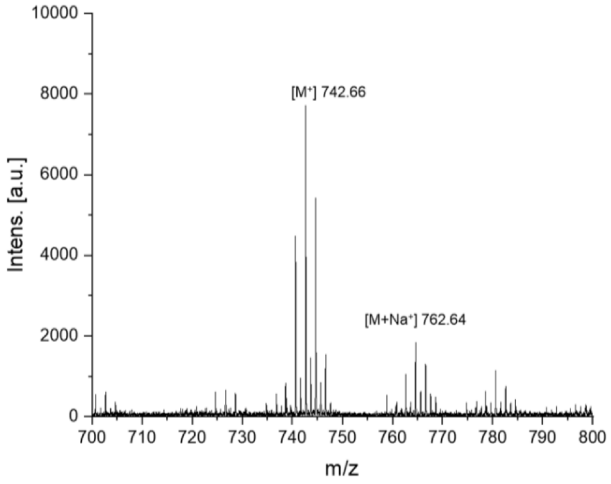
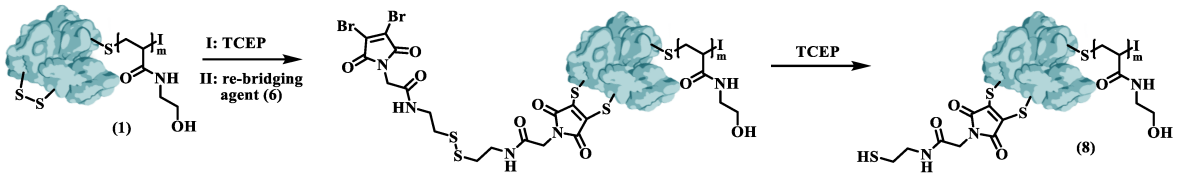


*Fig. S22: MALDI-TOF-MS of N,N'-(disulfanediylbis(ethan-2,1-diyl))bis(2-(3,4-dibromo-2,5-dioxo-2,5-dihydro-1H-pyrrol-1-yl)acetamide (rebridging agent) (**6**).*

2.3 Conjugation of the rebridging agent to precursor conjugates 1 and 4

Based on the analytical methods currently available to our group and collaboration partners, at this time, we cannot yet quantify the conjugation efficiency and determine how much BSA might remain unfunctionalized.

S4 – Synthesis of BSA-pHEAA conjugated with rebridging agent (BSA-pHEAA-r.b.)



The synthesis was carried out as described in the standard protocol and a yellowish solid was obtained.

CD: area 215 nm – 245 nm: 219 nm, -25.93 mdeg, area 198 nm – 215 nm: 208.0 nm, -29.08 mdeg.

UV/Vis: maximum 382 nm.

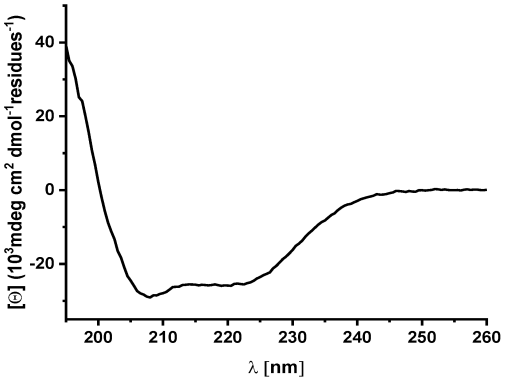


*Fig. S23: CD spectrum of BSA-p(HEAA)-rebridging agent (**S4**).*

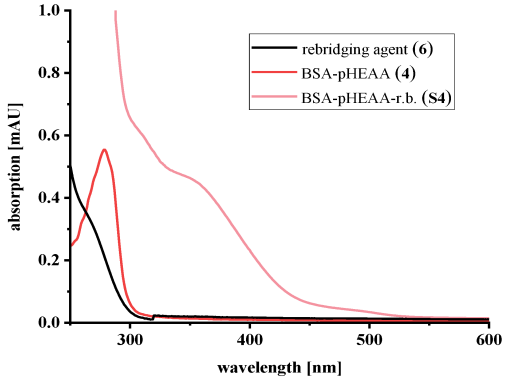
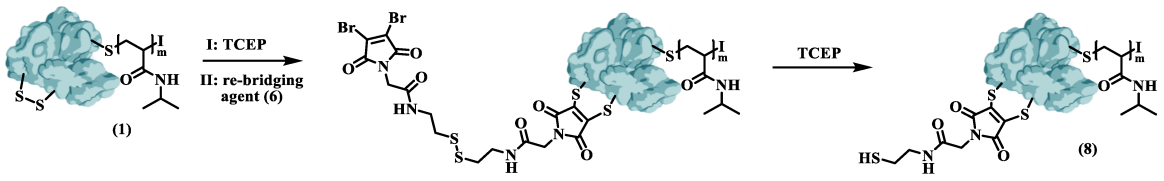


*Fig. S24: Presentation of the absorption spectra of the conjugated rebridging agent on BSA-pHEAA (**4**) and BSA-pHEAA)-r.b. (**S4**). The maximum absorption after four minutes is at 382 nm.*

S5 – Synthesis of BSA-pNIPAM conjugated with rebridging agent (BSA-pNIPAM-r.b.)



The synthesis was carried out as described in the standard protocol and a yellowish solid was obtained.

CD: area 215 nm – 245 nm: 220 nm, -26.59 mdeg, area 198 nm – 215 nm: 208.0 nm, -29.21 mdeg.

UV/Vis: maximum 382 nm.

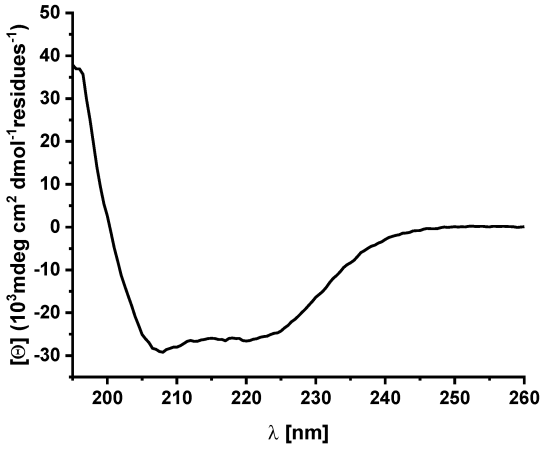


*Fig. S25: CD spectrum of BSA-pNIPAM-rebridging agent (**S5**).*

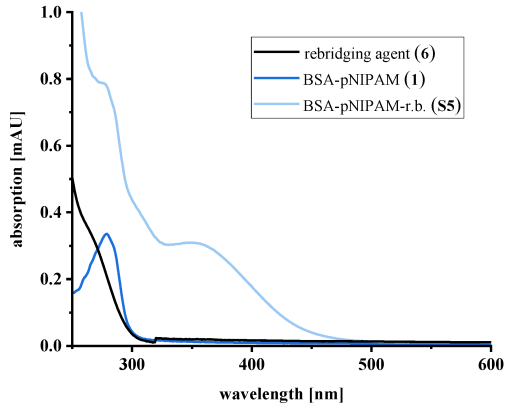


*Fig. S26: Presentation of the absorption spectra of the conjugated rebridging agent on BSA-pNIPAM (**1**) and BSA-pNIPAM-r.b. (**S5**). The maximum absorption after four minutes is at 382 nm.*

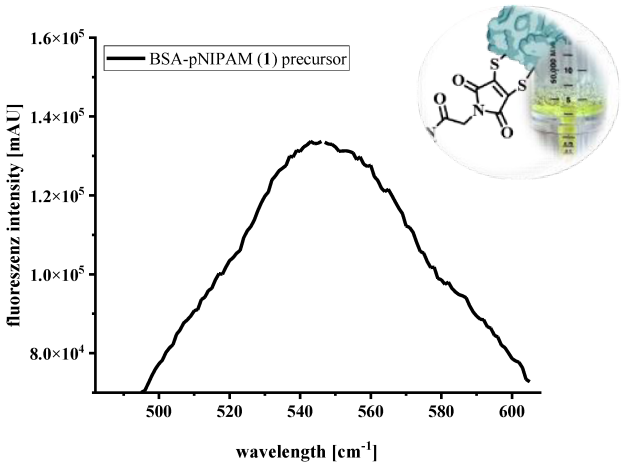


*Fig. S27: Exemplary presentation of the fluorescence spectrum of the conjugated rebridging agent on BSA-pNIPAM (**1**) precursor*

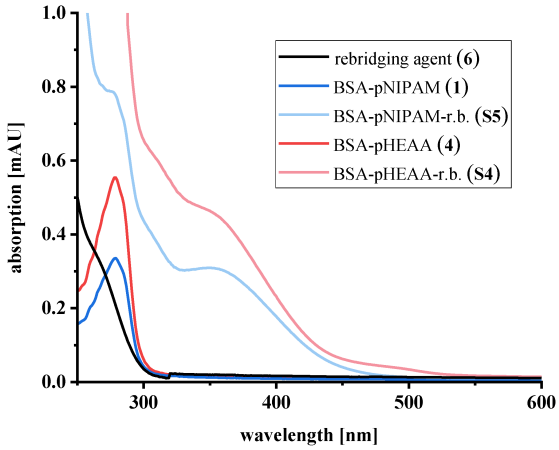
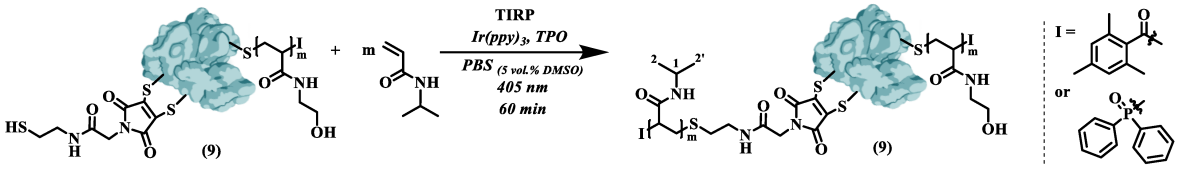


*Fig. S28: Comparison of the absorption spectra of the conjugated rebridging agent on BSA-pNIPAM (**1**) and BSA-pHEAA (**4**). The maximum absorption after four minutes is at 382 nm.*

7 – Synthesis of pHEAA-BSA-pNIPAM



The synthesis was carried out as described in the standard protocol and a yellowish solid was obtained.

^{1}H-NMR (600 MHz, D_2O, 297.9 K) δ (ppm) 8.43 – 6.25 (m, H_{BSA}), 4.53 – 0.00 (m, H_{BSA}, $H_{HEAA\text{-}side\ chain}$, $H_{NIPAM\text{-}side\ chain}$ $H_{HEAA\text{-}backbone}$, $H_{NIPAM\text{-}backbone}$, overlap with water peak), 3.78 – 3.19 (m, $H_{HEAA\text{-}Seitenkette}$), 3.93 (sbr, *H1*), 1.18 (sbr, *H2, H´2*).

AF4-LS (1 mM PBS, pH = 7.4, 298,15 K, monomer fraction): Mn = 71.3 kDa, Mw = 71.3 kDa, Đ = 1.00, mol fraction: 58.4% compared to the monomer fraction of BSA-p(HEAA) (***4***) with 66.1 kDa, the re-bridged derivative ***9*** is about 5.2 kDa larger than the mono functional derivate ***4***.

CD: area 215 nm – 245 nm: 219.5 nm, -27.05 mdeg, area 198 nm – 215 nm: 208.0 nm, -30.29 mdeg.

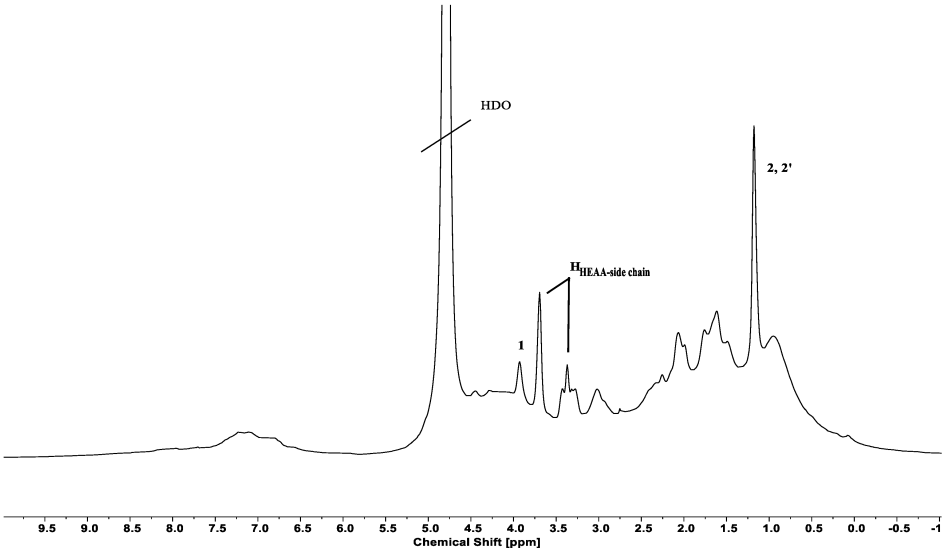


Fig. S29: ^{1}H-NMR spectrum (600 MHz, DMSO-d_6, 297.9 K) of Synthesis of BSA-pHEAA-r.b.-pNIPAM (7).

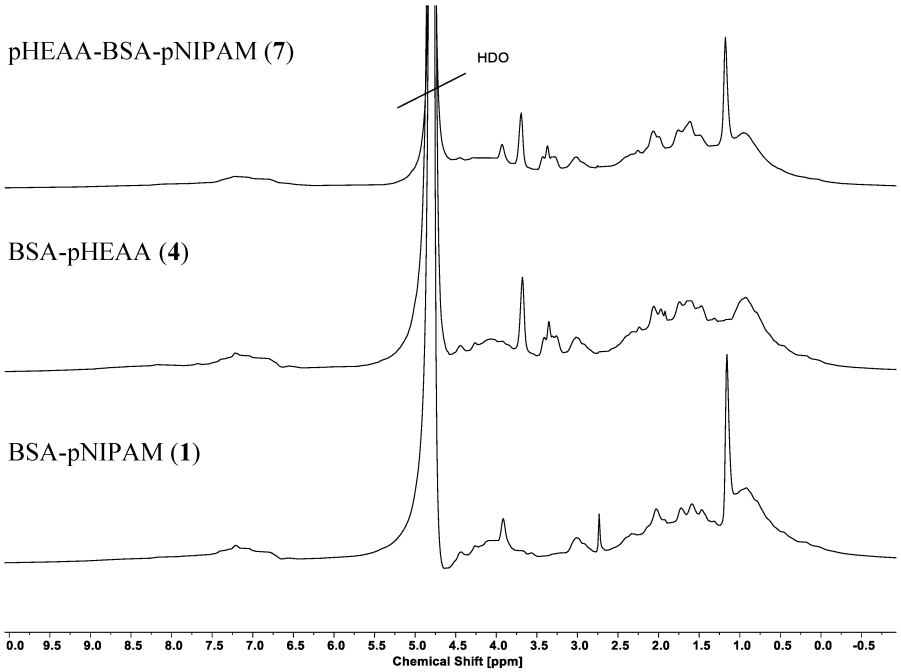


*Fig. S30: Comparison of ^{1}H-NMR spectrum (600 MHz, DMSO-d_6, 297.9 K) of pHEAA-BSA-pNIPAM (**7**), BSA-pHEAA (**4**), BSA-pNIPAM (**1**).*

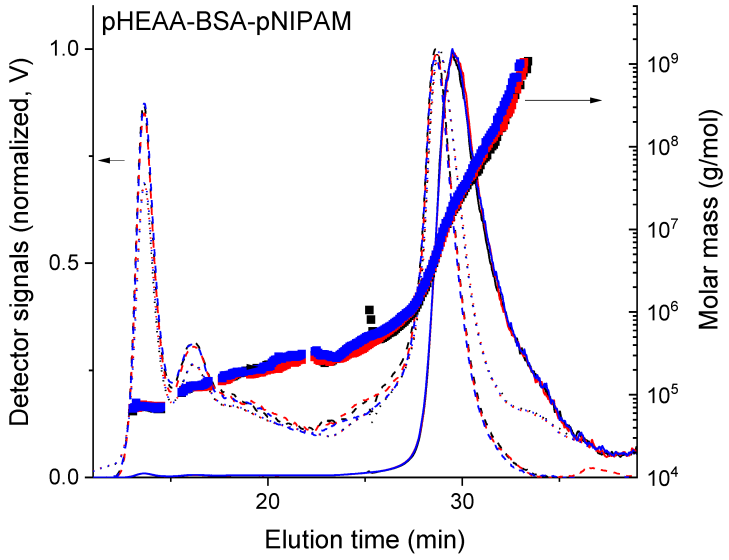


*Fig. S31: Triplicate measurements and presentation of fractograms of pHEAA-BSA-pNIPAM (**7**) opt. separation, RI (dashed line), UV (dotted line) and LS signal (solid line), molar masses (symbols) vs. elution time.*

Table S7: Results of the triplicate AF4-LS measurements.

Measurement	M_n*1 (kg/mol)	M_w*1 (kg/mol)	Đ (M_w/M_n)	R_g (nm)	R_h (nm)
1. (50 µl)	205	10,500	51.4	89.6	91.7
2. (50 µl)	209	11,500	55.4	92.0	88.8
3. (50 µl)	207	13,200	63.8	93.9	87.1
average (whole peak)	**207**	**11,800**	**56.8**	**91.8**	**89.2**

*1 dn/dc = 0.172 ml/g, average of all components

Table S8: Analysis of the individual fractions of AF4-LS. The values shown are average values from the triplicate measurements.

fraction	M_n*1 (kg/mol)	M_w*1 (kg/mol)	Đ (M_w/M_n)	mass fraction (%)	mol fraction (%)
1 - monomer	71.3	71.3	1.00	19.8	58.4
2 – dimer	125	125	1.00	12.0	20.8
3- trimer / multimer	211	212	1.01	12.1	12.1
4 - aggregates	1,280	23,800	18.5	56.1	8.7

**1 dn/dc = 0.172 ml/g, average of all components*

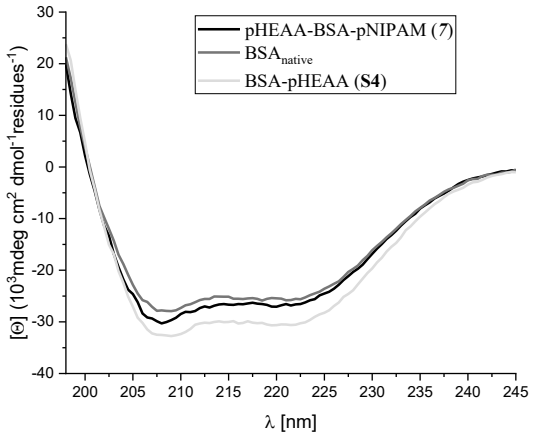
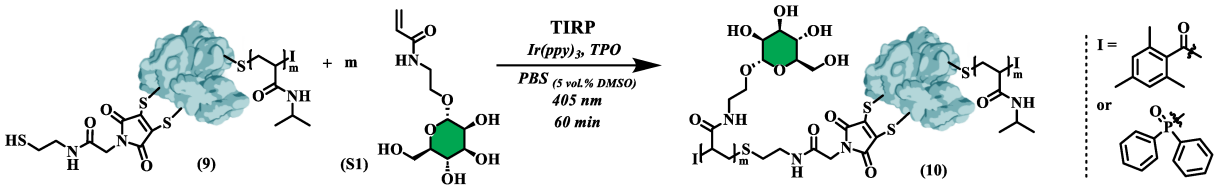


*Fig. S32: Comparison of the CD spectra of the BSA_{native}, BSA-pHEAA (**4**), BSA-pHEAA-r.-b. (**S4**) und pHEAA-BSA-pNIPAM (**7**).*

8 – Synthesis of pNIPAM-BSA-pMan



The synthesis was carried out as described in the standard protocol and a yellowish solid was obtained.

^{1}H-NMR (600 MHz, D_2O, 297.9 K) δ (ppm) 8.37 – 6.43 (m, H_{BSA}), 4.47 – 0.00 (m, H_{BSA}, $H_{NIPAM\text{-}side\ chain}$, $H_{Man\text{-}side\ chain}$, $H_{NIPAM\text{-}backbone}$, $H_{Man\text{-}backbone}$, overlap with water peak), 4.06 – 3.55 (s_{br}, $H_{Man\text{-}side\ chain}$), 3.92 ($s_{br}$, *H1*), 1.17 ($s_{br}$, *H2, H´2*).

AF4-LS (1 mM PBS, pH = 7.4, 298,15 K, monomer fraction): Mn = 73.4 kDa, Mw = 73.4 kDa, Đ = 1.00, mol fraction: 57.5% compared to the monomer fraction of BSA-pNIPAM (**1**) with 70.5 kDa, the re-bridged derivative **8** is about 2.9 kDa larger than the mono functional derivate ***1***.

CD: area 215 nm – 245 nm: 220.0 nm, -27.47 mdeg, area 198 nm – 215 nm: 209.0 nm, -30.24 mdeg.

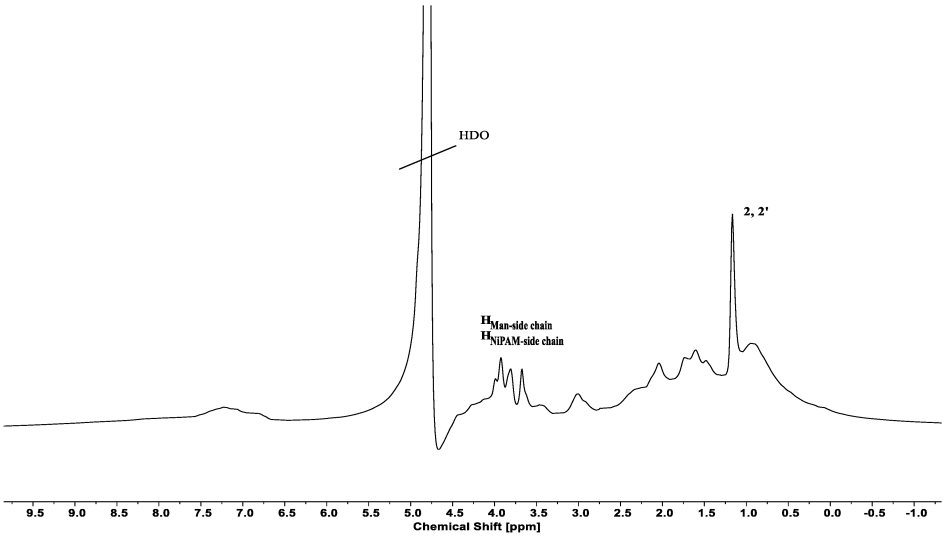


*Fig. S33: ^{1}H-NMR spectrum (600 MHz, DMSO-d_6, 297.9 K) of Synthesis of pNIPAM-BSA-pMan (**8**).*

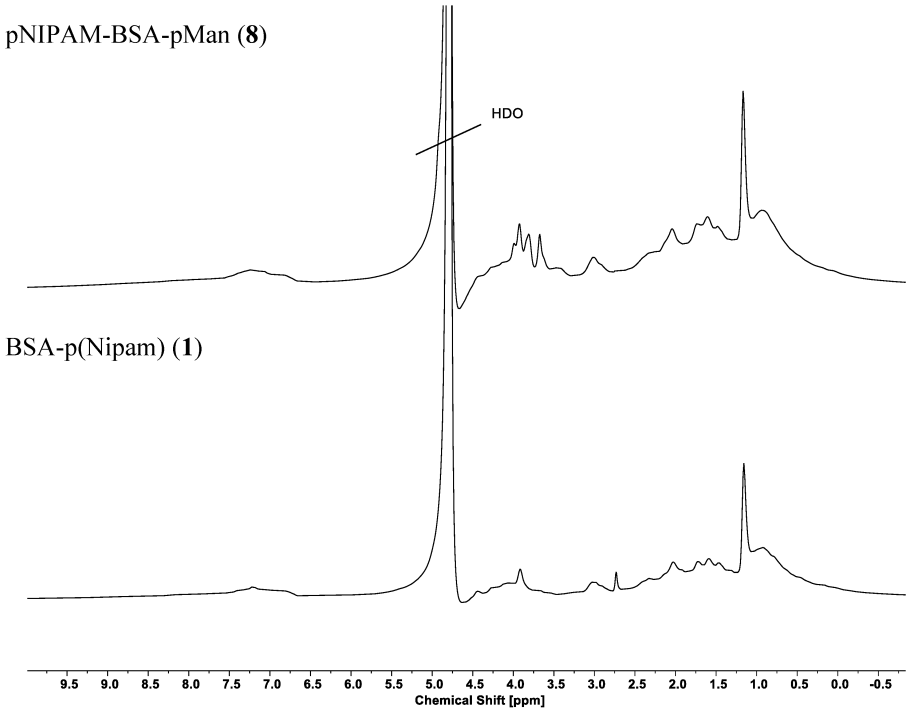


*Fig. S34: Comparison of ^{1}H-NMR spectrum (600 MHz, DMSO-d_6, 297.9 K) of pNIPAM-BSA-pMan (**8**), BSA-pNIPAM (**1**).*

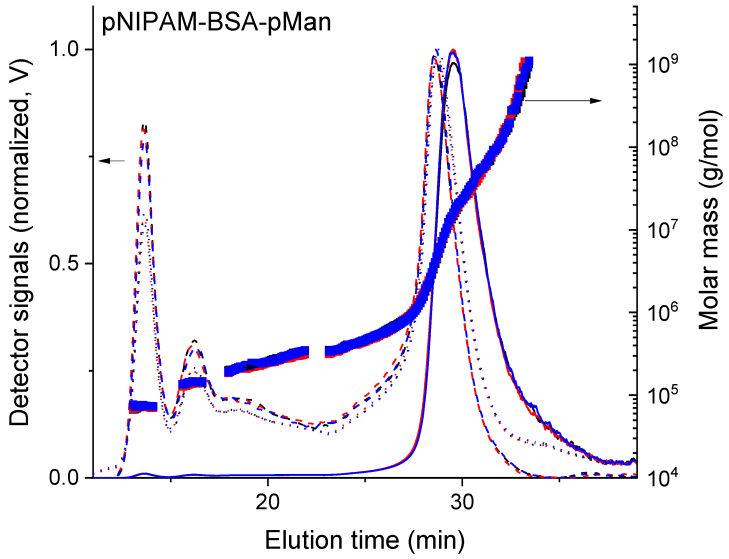


*Fig. S35: Triplicate measurements and presentation of fractograms of pNIPAM-BSA-pMan (**8**) opt. separation, RI (dashed line), UV (dotted line) and LS signal (solid line), molar masses (symbols) vs. elution time.RI, UV and LS signal, molar masses vs. elution time.*

Table S9: Results of the triplicate AF4-LS measurements.

measurement	M_n*1 (kg/mol)	M_w*1 (kg/mol)	Đ (M_w/M_n)	R_g (nm)	R_h (nm)
1. (50 µl)	232	7,930	34.2	81.3	74.1
2. (50 µl)	229	7,740	33.8	75.4	72.1
3. (50 µl)	244	8,960	36.8	80.0	79.1
Average (whole Peak)	235	**8,210**	**34.9**	**78.9**	**75.1**

*1 dn/dc = 0.172 ml/g, average of all components

Table S10: Analysis of the individual fractions of AF4-LS. The values shown are average values from the triplicate measurements.

fraction	M_n*1 (kg/mol)	M_w*1 (kg/mol)	Đ (M_w/M_n)	mass fraction (%)	mol fraction (%)
1 - monomer	73.4	73.4	1.00	17.9	57.5
2 – dimer	141	141	1.00	11.1	18.7
3- trimer / multimer	264	271	1.03	13.3	13.9
4 - aggregates	1,310	14,300	10.9	57.7	9.9

*1 dn/dc = 0.172 ml/g, average of all components

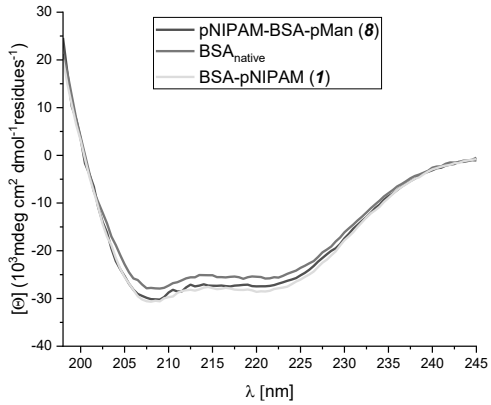
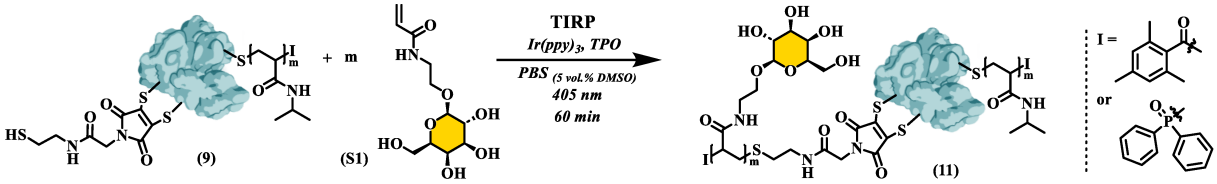


*Fig. S36: Comparison of the CD spectra of the BSA_{native}, BSA-pNIPAM (**1**), BSA-pNIPAM-r.b. (**S5**) und pNIPAM-BSA-pMan (**8**).*

9 – Synthesis of pNIPAM-BSA-pGal



The synthesis was carried out as described in the standard protocol and a yellowish solid was obtained.

^{1}H-NMR (600 MHz, D_2O, 297.9 K) δ (ppm) 8.36 – 6.45 (m, H_{BSA}), 4507 – 0.00 (m, H_{BSA}, $H_{NIPAM\text{-}side\ chain}$, $H_{Gal\text{-}side\ chain}$, $H_{NIPAM\text{-}backbone}$, $H_{Gal\text{-}backbone}$, overlap with water peak), 4.46 (s_{br}, $H_{anomer\ of\ galactose}$) 4.51 – 3.33 ($s_{br}$, $H_{Gal\text{-}side\ chain}$), 1.17 ($s_{br}$, *H2, H´2*).

AF4-LS (1 mM PBS, pH = 7.4, 298,15 K, monomer fraction): Mn = 74.8 kDa, Mw = 74.8 kDa, Đ = 1.00, mol fraction: 54.6% compared to the monomer fraction of BSA-pNIPAM (***1***) with 70.5 kDa, the re-bridged derivative **9** is about 4.3 kDa larger than the mono functional derivate ***1***.

CD: area 215 nm – 245 nm: 219.0 nm, -27.97 mdeg, area 198 nm – 215 nm: 208.5 nm, -30.53 mdeg.

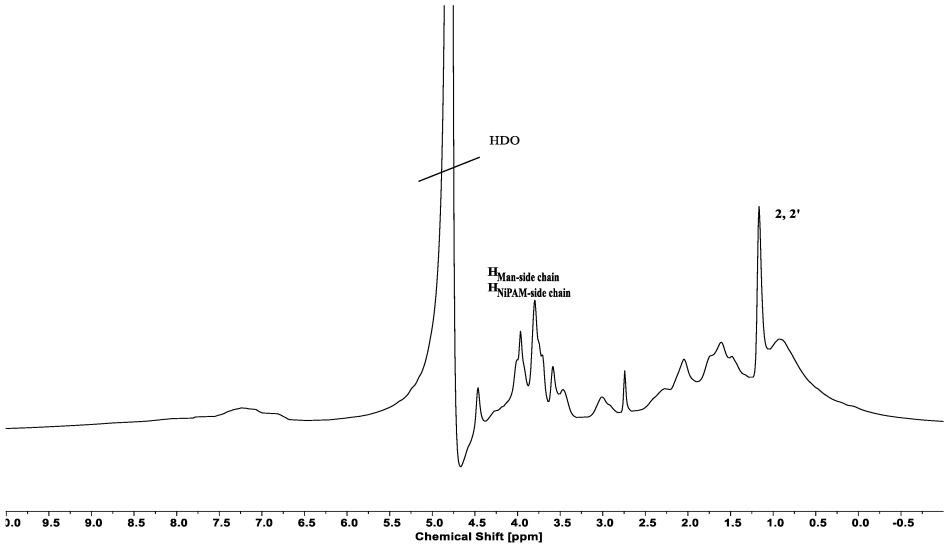


*Fig. S37: ^{1}H-NMR spectrum (600 MHz, DMSO-d_6, 297.9 K) of Synthesis of pNIPAM-BSA-pGal (**9**).*

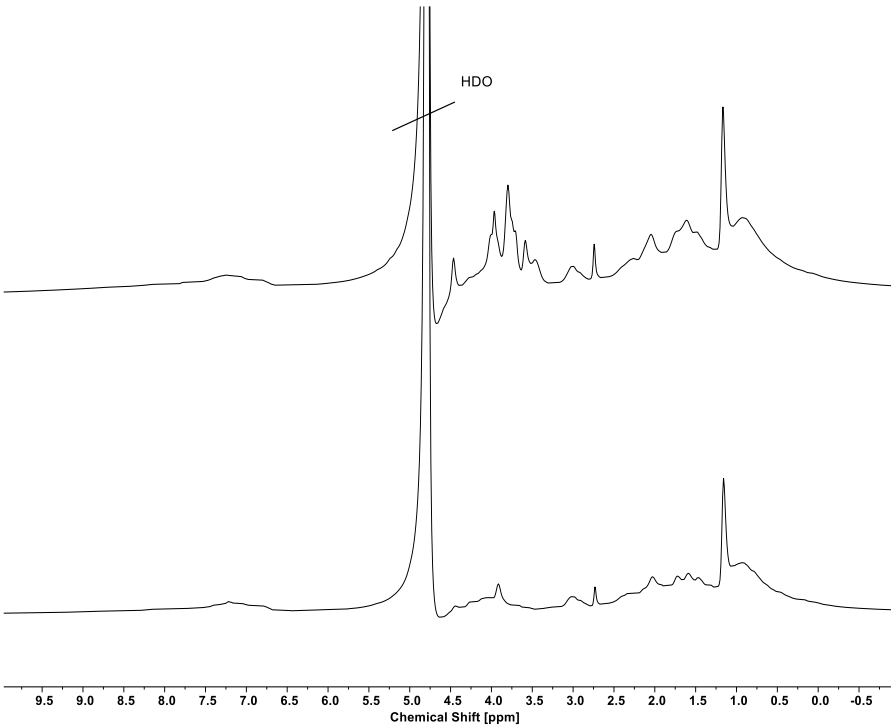


*Fig. S38: Comparison of ^{1}H-NMR spectrum (600 MHz, DMSO-d_6, 297.9 K) of pNIPAM-BSA-pGal (**9**), BSA-pNIPAM (**1**).*

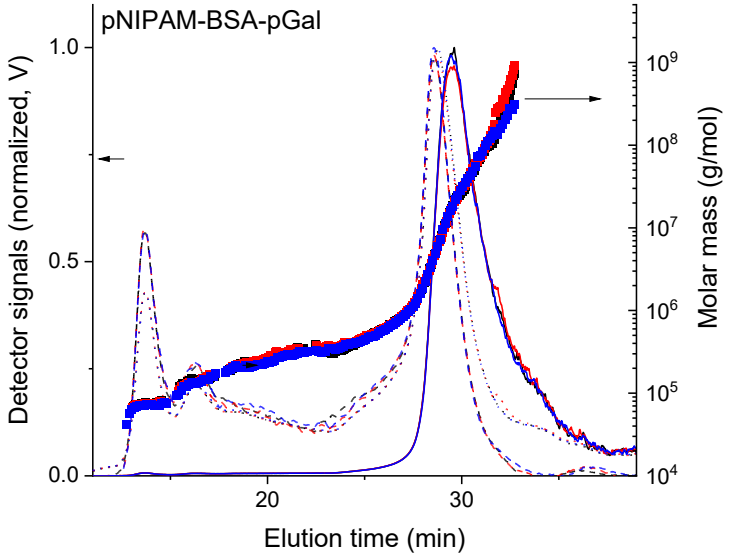


*Fig. S39: Triplicate measurements and presentation of fractograms of pNIPAM-BSA-pGal (**9**) opt. separation, RI (dashed line), UV (dotted line) and LS signal (solid line), molar masses (symbols) vs. elution time.*

Table S11: Results of the triplicate AF4-LS measurements.

measurement	M_n*1 (kg/mol)	M_w*1 (kg/mol)	Đ (M_w/M_n)	R_g (nm)	R_h (nm)
1. (50 µl)	272	9,000	33.1	108	78.7
2. (50 µl)	266	12,500	47.0	131	78.5
3. (50 µl)	256	10,100	39.5	119	86.8
average (whole peak)	265	**10,500**	**39.9**	**117**	**81.3**

*1 dn/dc = 0.172 ml/g, average of all components

Table S12: Analysis of the individual fractions of AF4-LS. The values shown are average values from the triplicate measurements.

fraction	M_n*1 (kg/mol)	M_w*1 (kg/mol)	Đ (M_w/M_n)	mass fraction (%)	mol fraction (%)
1 - monomer	74.8	74.8	1.00	15.3	54.6
2 – dimer	143	144	1.01	11.0	18.1
3- trimer / multimer	252	253	1.01	12.7	14.6
4 - aggregates	1,260	14,500	11.5	61.0	12.7

*1 dn/dc = 0.172 ml/g, average of all components

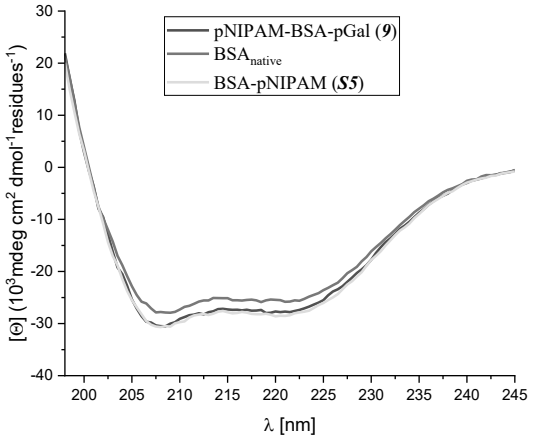


*Fig. S40: Comparison of the CD spectra of the BSAnative, BSA-pNIPAM (**1**), BSA-pNIPAM-r.b. (**S5**) und pNIPAM-BSA-pGal (**9**).*

2.4 DLS Particle Experiments

Particle properties of BSA-pNIPAM samples 1, 2 and 3 by using a 2 min temperature ramp (1°C/min)

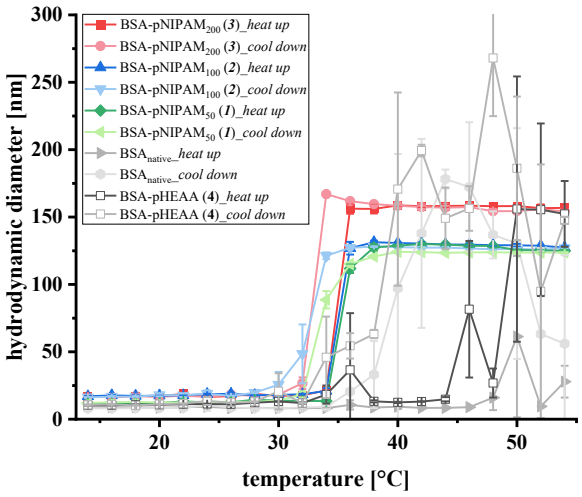


*Fig. S41: Hydrodynamic diameter profiles of temperature-dependent particle formation and dissociation of the BSA-pNIPAM conjugates **1-4** and native BSA at a concentration of 0.5 mg/mL in PBS buffer with a heating rate of 1 °C/min.*

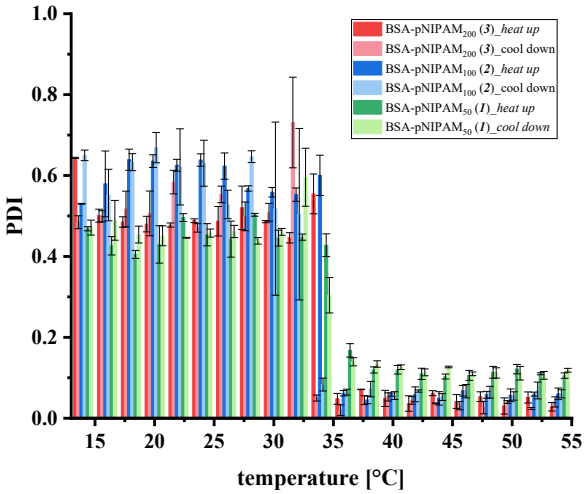


*Fig. S42: Polydispersities of the DLS measurements (PDI) of temperature-dependent particle formation and dissociation of the BSA-pNIPAM conjugates **1**, **2** and **3** at a concentration of 0.5 mg/mL in PBS buffer with a heating rate of 1 °C/min.*

Particle properties of BSA-pNIPAM samples 1, 2 and 3 by using a 10 min temperature ramp (0.2 °C/min)

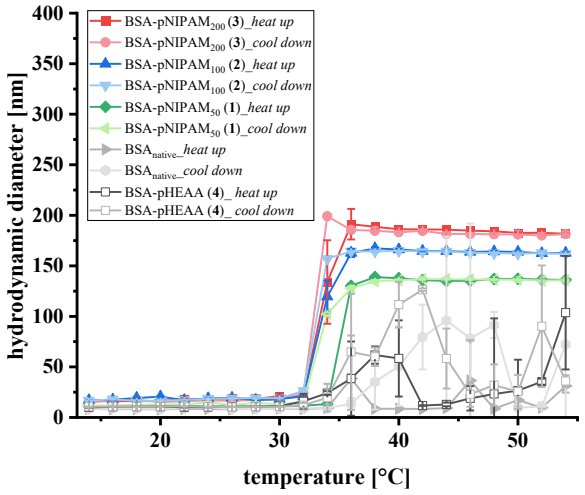


*Fig. S43: Hydrodynamic diameter profiles of temperature-dependent particle formation and dissociation of the BSA-pNIPAM conjugates **1** - **4** and native BSA at a concentration of 0.5 mg/mL in PBS buffer with a heating rate of 0.2 °C/min.*

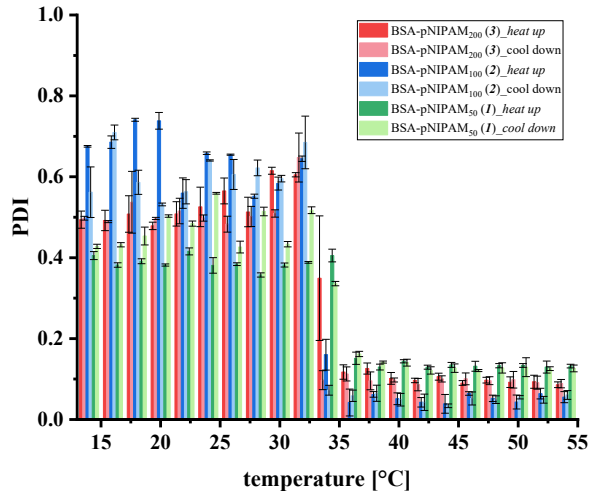


*Fig. S44: Polydispersities of the DLS measurements (PDI) of temperature-dependent particle formation and dissociation of the BSA-pNIPAM conjugates **1**, **2** and **3** at a concentration of 0.5 mg/mL in PBS buffer with a heating rate of 0.2 °C/min.*

Particle properties of BSA-pNIPAM samples 1, 2 and 3 by using a 20 min temperature ramp (0.1 °C/min)

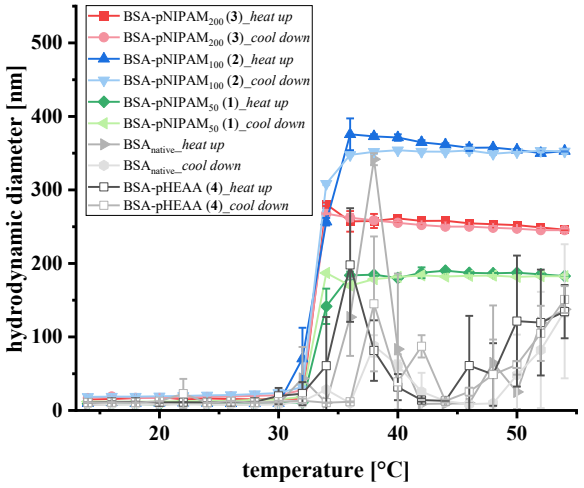


*Fig. S45: Hydrodynamic diameter profiles of temperature-dependent particle formation and dissociation of the BSA-pNIPAM conjugates **1-4** and native BSA at a concentration of 0.5 mg/mL in PBS buffer with a heating rate of 0.1 °C/min.*

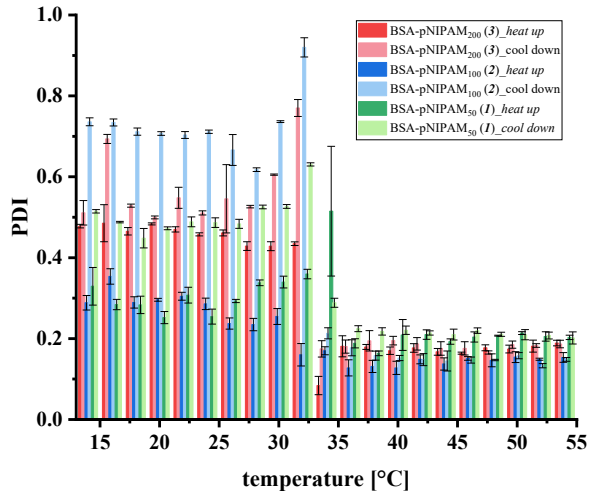


*Fig. S46: Polydispersities of the DLS measurements (PDI) of temperature-dependent particle formation and dissociation of the BSA-pNIPAM conjugates **1**, **2** and **3** at a concentration of 0.5 mg/mL in PBS buffer with a heating rate of 0.2 °C/min.*

Particle properties of BSA-pNIPAM samples 1, 2 and 3 depending on the heating rate

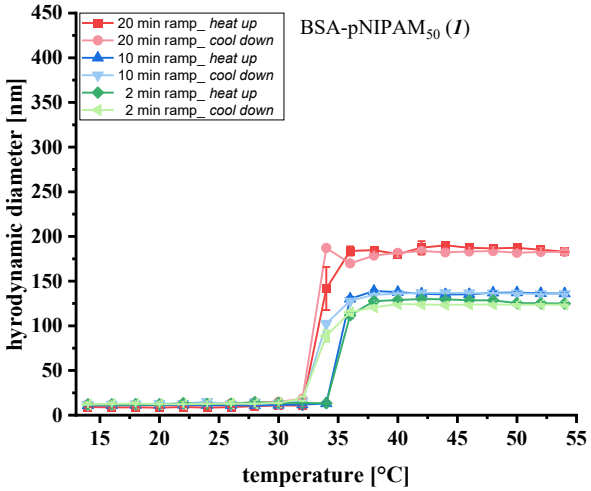


*Fig. S47: Hydrodynamic diameters profile of temperature-dependent particle formation and dissociation of the BSA-pNIPAM conjugates **1** at a concentration of 0.5 mg/mL in PBS buffer with different heating rates from 1°C/min, 0.2°C/min and 0.1 °C/min.*

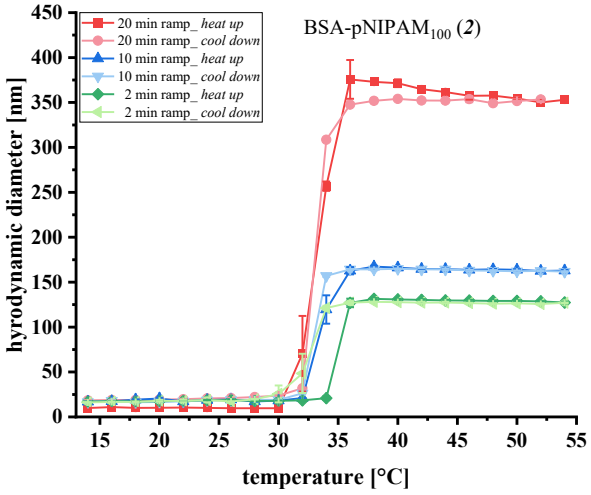


*Fig. S48: Hydrodynamic diameters profile of temperature-dependent particle formation and dissociation of the BSA-pNIPAM conjugates **2** at a concentration of 0.5 mg/mL in PBS buffer with different heating rates from 1°C/min, 0.2°C/min and 0.1 °C/min.*

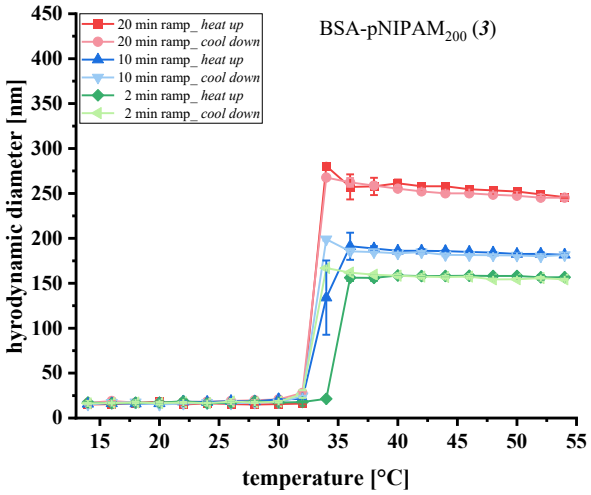


*Fig. S49: Hydrodynamic diameters profile of temperature-dependent particle formation and dissociation of the BSA-pNIPAM conjugates **3** at a concentration of 0.5 mg/mL in PBS buffer with different heating rates from 1°C/min, 0.2°C/min and 0.1 °C/min.*

Particle properties of BSA-pNIPAM samples 1, 2 and 3 depending on the concentration

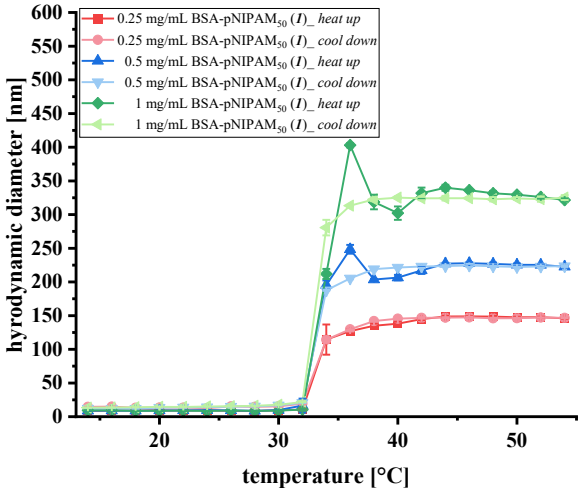


*Fig. SS50: Hydrodynamic diameters profile of temperature-dependent particle formation and dissociation of the BSA-pNIPAM conjugates **1** at different concentration of 0.25 mg/mL, 0.5 mg/mL and 1 mg/mL in PBS buffer with a heating rate of 0.1 °C/min.*

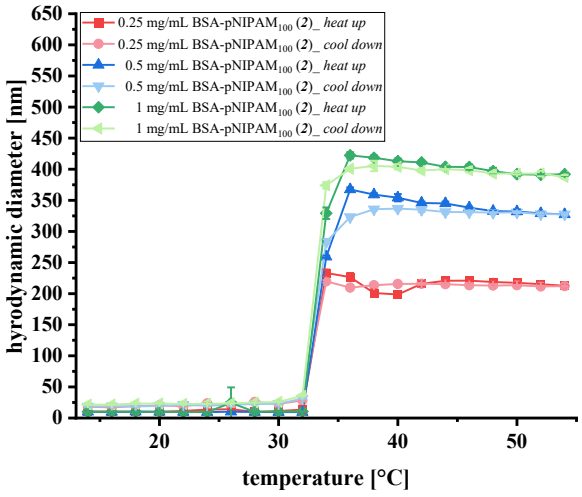


*Fig. S51: Hydrodynamic diameters profile of temperature-dependent particle formation and dissociation of the BSA-pNIPAM conjugates **2** at different concentration of 0.25 mg/mL, 0.5 mg/mL and 1 mg/mL in PBS buffer with a heating rate of 0.1 °C/min.*

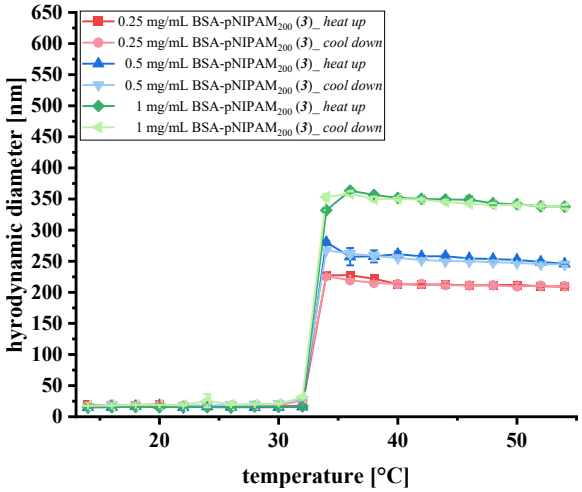
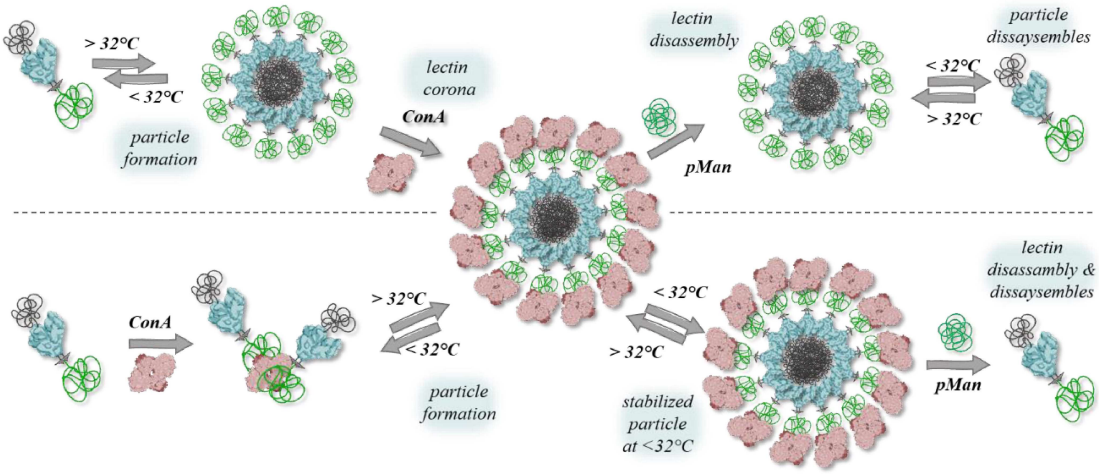


*Fig. S52: Hydrodynamic diameters profile of temperature-dependent particle formation and dissociation of the BSA-pNIPAM conjugates **3** at different concentration of 0.25 mg/mL, 0.5 mg/mL and 1 mg/mL in PBS buffer with a heating rate of 0.1 °C/min.*

2.5 Inhibition-Competition experiment of double switchable systems



Experiments based on pNIPAM-BSA-pMan (8)

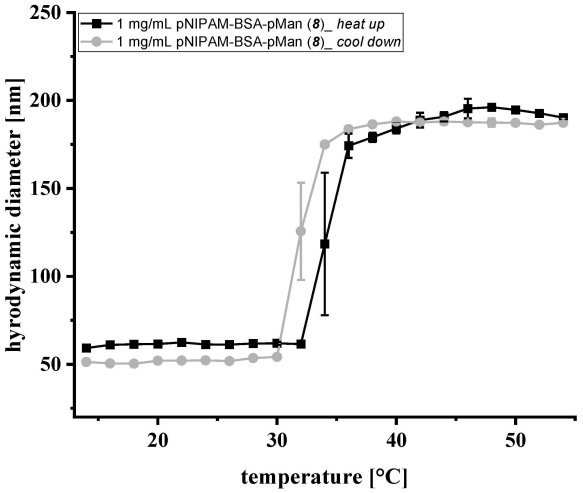


*Fig. S53: Hydrodynamic diameter profile of temperature-dependent particle formation and dissociation of the pNIPAM-BSA-pMan conjugates **8** at a concentration of 1 mg/mL in PBS buffer with a heating rate of 1 °C/min.*

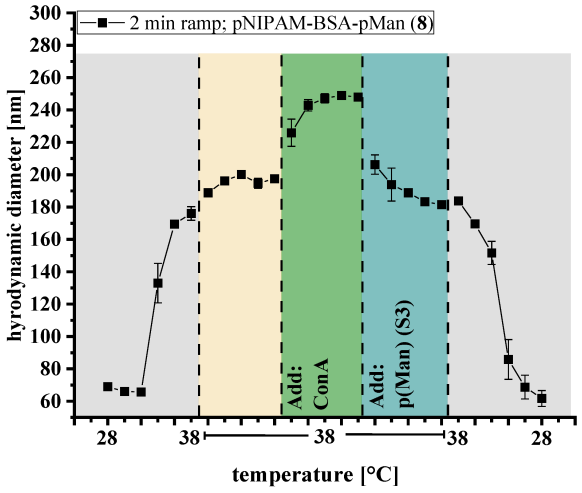


*Fig. S54: Hydrodynamic diameter profil of temperature-dependent particle formation and dissociation with the polymeric inhibitor pMan (**S3**) (15 mM in LBB) of the PNIPAM-BSA-pMan conjugates **8** at a concentration of 13.8 µM in LBB buffer with a heating rate of 1 °C/min.*

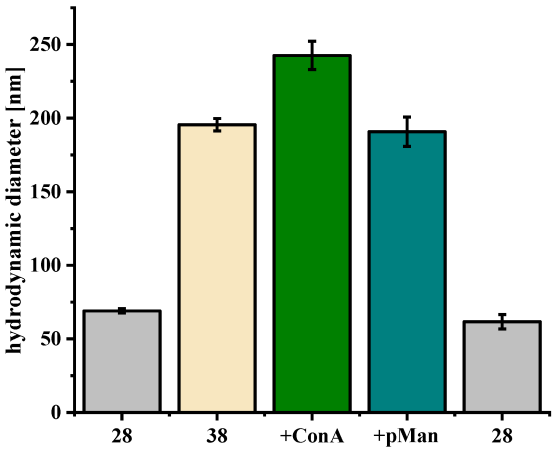


*Fig. S55: The mean values of the hydrodynamic diameter of temperature-dependent particle formation and dissociation from pNIPAM-BSA-pMan conjugates **8** at a concentration of 13.8 µM in LBB buffer with a heating rate of 1 °C/min and with the polymeric inhibitor pMan (**S3**) (15 mM in LBB).*

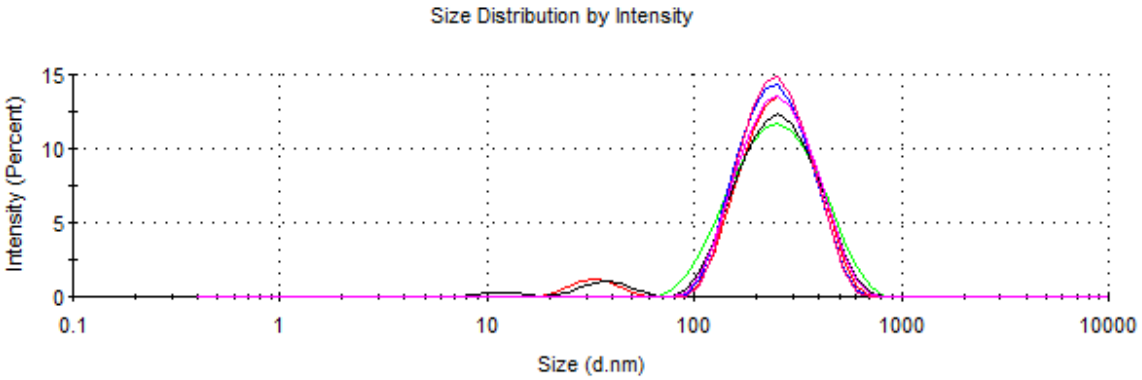


*Fig. S56: Hydrodynamic diameter distribution of pNIPAM-BSA-pMan conjugates **8** at a concentration of 13.8 µM in LBB buffer with a heating rate of 1 °C/min after particle formation (38°C).*

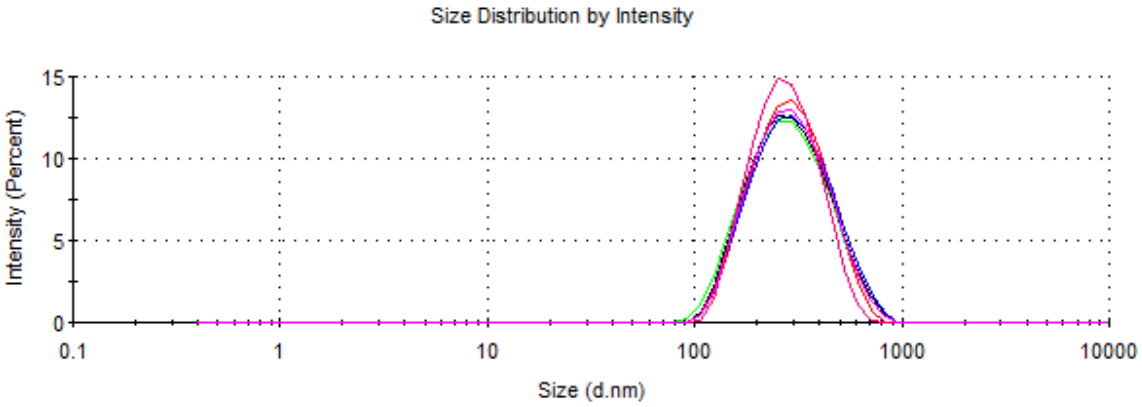


*Fig. S57: Hydrodynamic diameter distribution of pNIPAM-BSA-pMan conjugates **8** at a concentration of 13.8 µM in LBB buffer with a heating rate of 1 °C/min with lectin (ConA) corona at 38°C.*

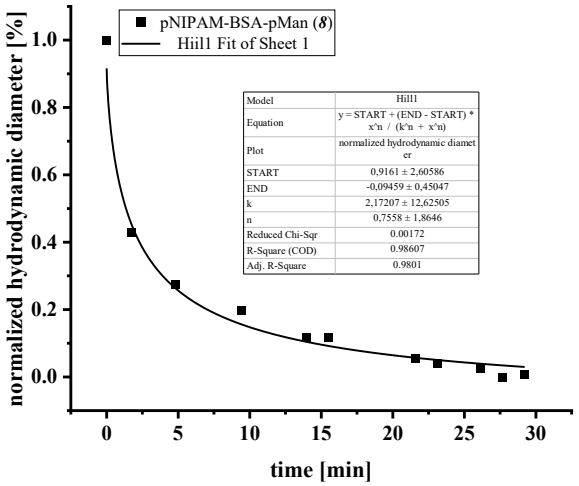


*Fig. S58: Kinetics of pNIPAM-BSA-pMan (**8**) inhibition after pMan addition (Hill 1 Fit).*

Experiments based on pNIPAM-BSA-pGal (*9*)

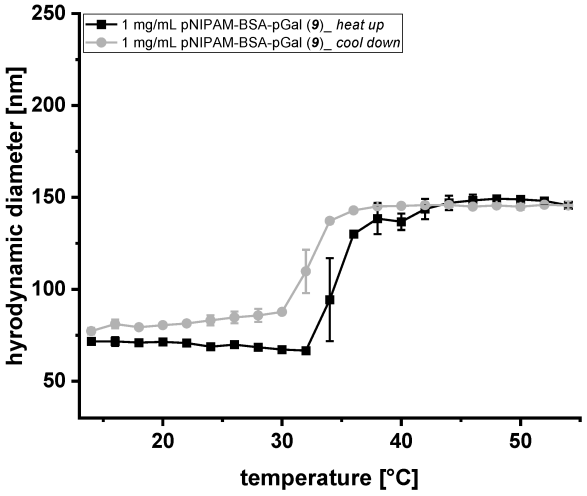


Fig. S59: Hydrodynamic diameter profile of temperature-dependent particle formation and dissociation of the pNIPAM-BSA-pGal conjugates ***9*** *at a concentration of 1 mg/mL in PBS buffer with a heating rate of 1 °C/min.*

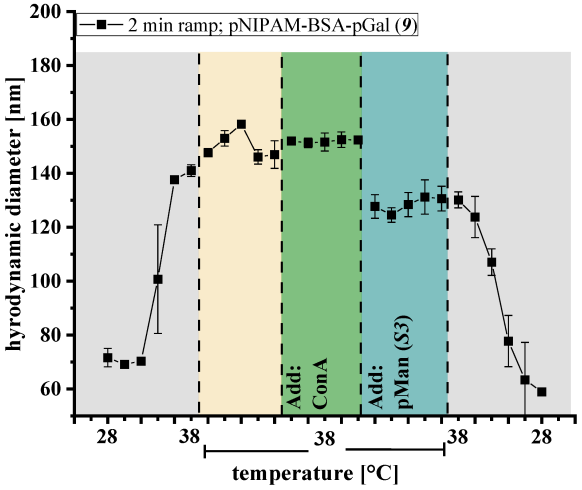


*Fig. S60: Hydrodynamic diameter profile of temperature-dependent particle formation and dissociation with the polymeric inhibitor pMan (****S3****) (15 mM in LBB) of the pNIPAM-BSA-pGal conjugates* ***9*** *at a concentration of 13.8 µM in LBB buffer with a heating rate of 1 °C/min.*

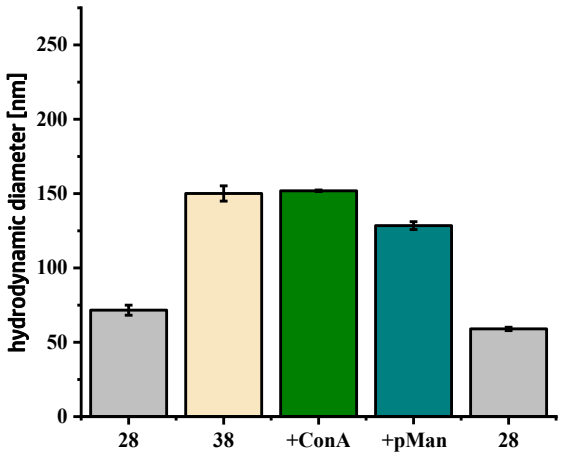


*Fig. S61: The mean values of the hydrodynamic diameter of temperature-dependent particle formation and dissociation from pNIPAM-BSA-pGal conjugates **9** at a concentration of 13.8 µM in LBB buffer with a heating rate of 1 °C/min and with the polymeric inhibitor pMan (**S3**) (15 mM in LBB).*

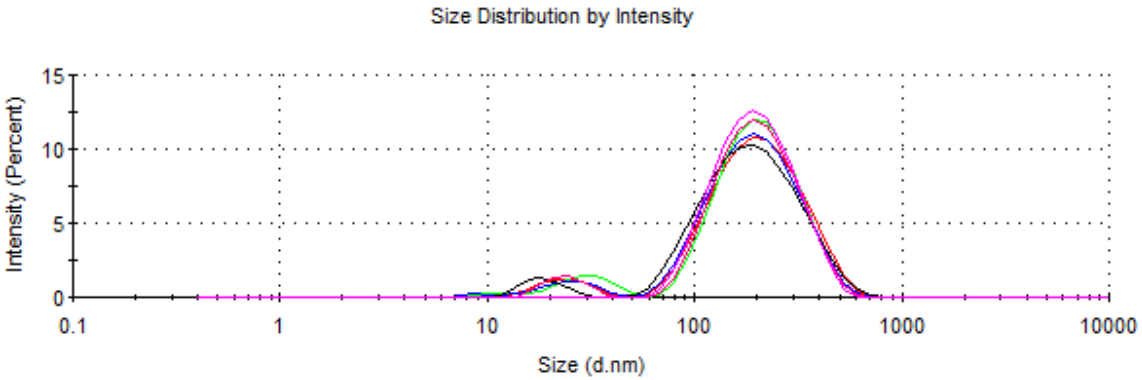


*Fig. S62: Hydrodynamic diameter distribution of pNIPAM-BSA-pGal conjugates **9** at a concentration of 13.8 µM in LBB buffer with a heating rate of 1 °C/min after particle formation (38°C).*

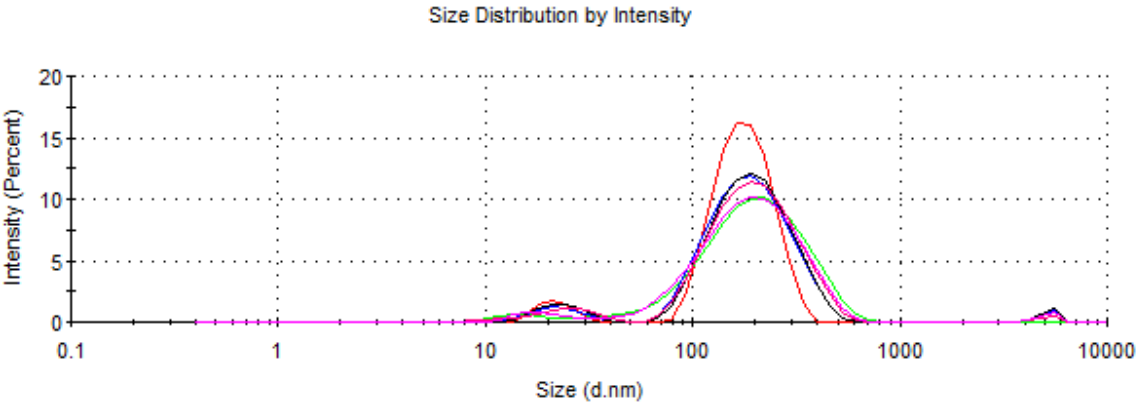


*Fig. S63: Hydrodynamic diameter distribution of pNIPAM-BSA-pGal conjugates **9** at a concentration of 13.8 µM in LBB buffer with a heating rate of 1 °C/min with lectin (ConA) corona at 38°C.*

Lectin stabilized particle below LCST followed by inhibition

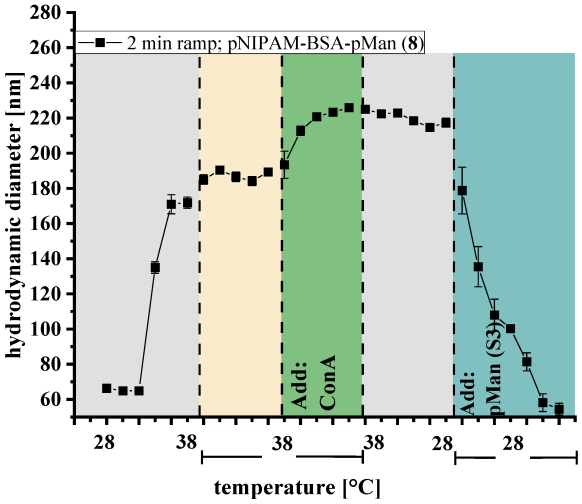


*Fig. S64: Hydrodynamic diameter profile of temperature-dependent particle formation and dissociation with the polymeric inhibitor pMan (**S3**) (15 mM in LBB) of the pNIPAM-BSA-pMan conjugates **8** at a concentration of 13.8 µM in LBB buffer with a heating rate of 1 °C/min. The ConA fixed particle is also stable below the LCST.*

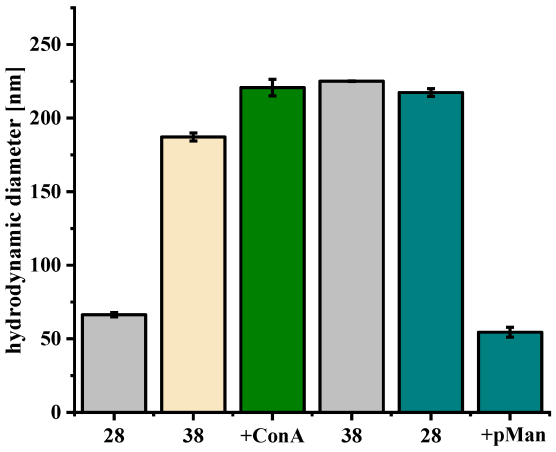


*Fig. S65: The mean values of the hydrodynamic diameter of temperature-dependent particle formation and dissociation from PNIPAM-BSA-pMan conjugates **8** at a concentration of 13.8 µM in LBB buffer with a heating rate of 1 °C/min and with the polymeric inhibitor pMan (**S3**) (15 mM in LBB).*

2.6 DLS inhibition Competition Man mix Gal

50% pNIPAM-BSA-pMan (**8**)/ 50% of pNIPAM-BSA-pGal (**9**)

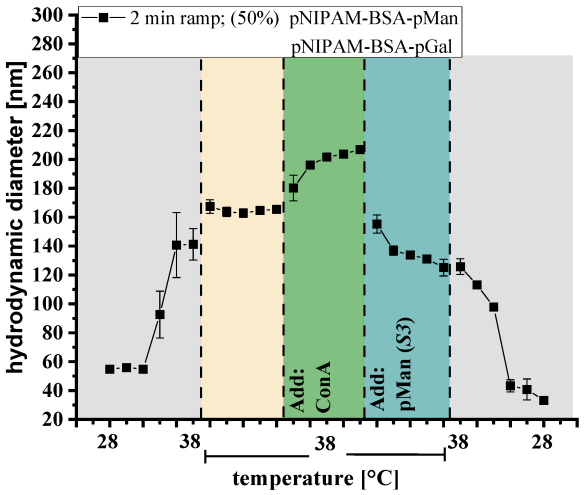


*Fig. S66: Hydrodynamic diameter profile of temperature-dependent particle formation and dissociation with the polymeric inhibitor pMan (**S3**) (15 mM in LBB) of a mixture of 50% pNIPAM-BSA-pMan (**8**) and the other50% of pNIPAM-BSA-pGal (**9**) conjugates at a concentration of 13.8 µM in LBB buffer each with a heating rate of 1 °C/min.*

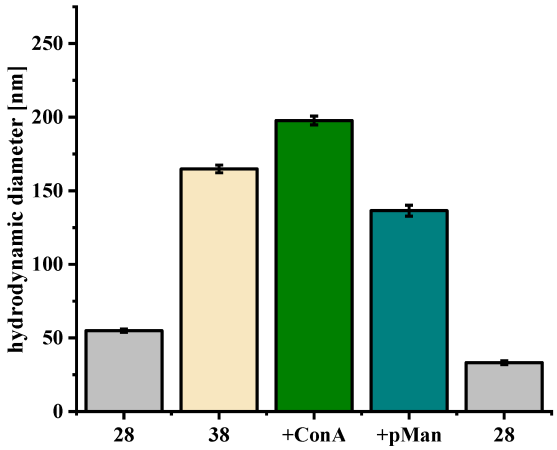


*Fig. S67: The mean values of the hydrodynamic diameter of temperature-dependent particle formation and dissociation from the mixture of 50% pNIPAM-BSA-pMan (**8**) and the other 50% of pNIPAM-BSA-pGal (**9**) at a concentration of 13.8 µM in LBB buffer with a heating rate of 1 °C/min and with the polymeric inhibitor pMan (**S3**) (15 mM in LBB).*

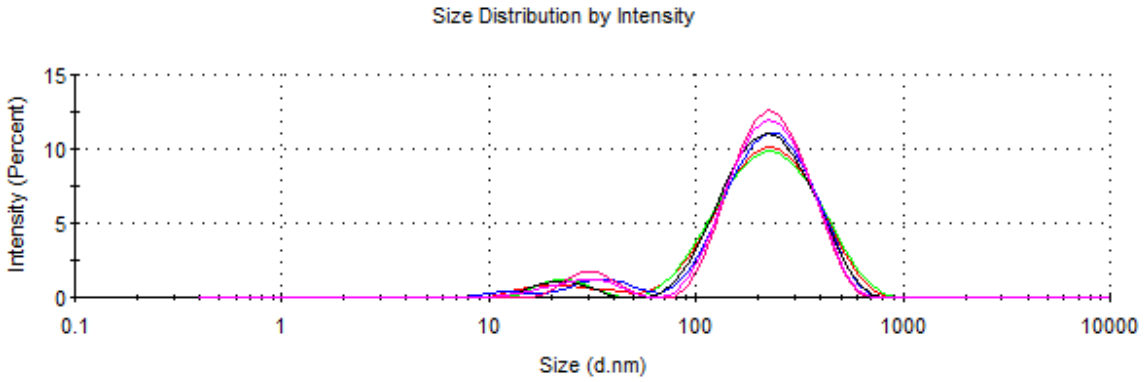


*Fig. S68: Hydrodynamic diameter distribution from the mixture of 50% pNIPAM-BSA-pMan (**8**) and the other 50% of pNIPAM-BSA-pGal (**9**) at a concentration of 13.8 µM in LBB buffer with a heating rate of 1 °C/min after particle formation (38°C).*

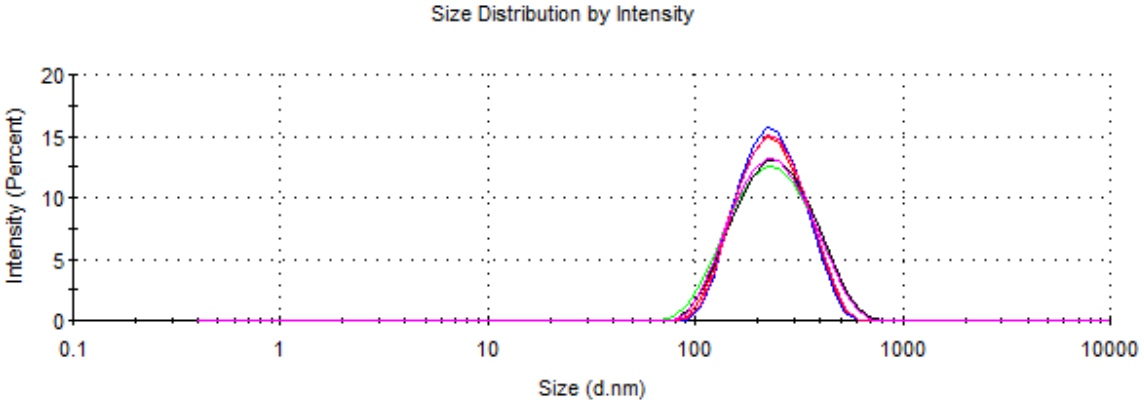


*Fig. S69: Hydrodynamic diameter distribution from the mixture of 50% pNIPAM-BSA-pMan (**8**) and the other 50% of pNIPAM-BSA-pGal (**9**) at a concentration of 13.8 µM in LBB buffer with a heating rate of 1 °C/min with lectin (ConA) corona at 38°C.*

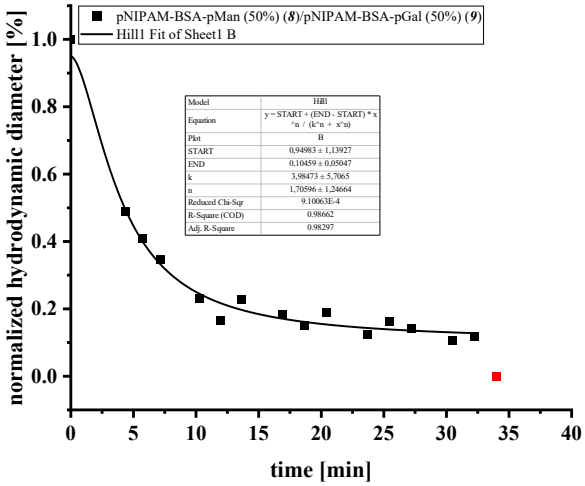


*Fig. S70: Kinetics of 50% pNIPAM-BSA-pMan (**8**) inhibition after pMan addition (Hill 1 Fit).*

30% pNIPAM-BSA-pMan (**8**)/ 70% pNIPAM-BSA-pGal (**9**)

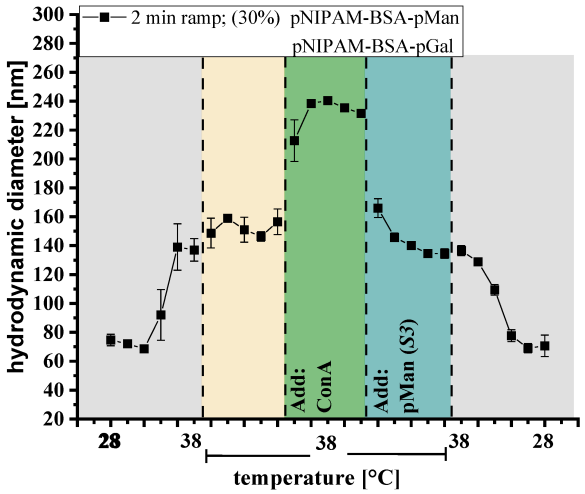


*Fig. S71: Hydrodynamic diameter profile of temperature-dependent particle formation and dissociation with the polymeric inhibitor pMan (**S3**) (15 mM in LBB) of a mixture of 30% pNIPAM-BSA-pMan (**8**) and the other70% of pNIPAM-BSA-pGal (**9**) conjugates at a concentration of 13.8 µM in LBB buffer each with a heating rate of 1 °C/min.*

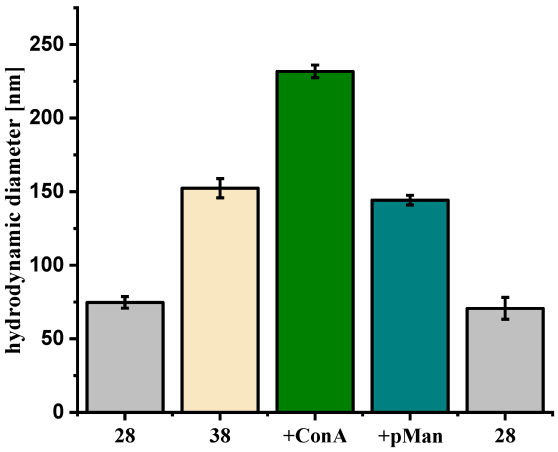


*Fig. S72: The mean values of the hydrodynamic diameter of temperature-dependent particle formation and dissociation from the mixture of 30% pNIPAM-BSA-pMan (**8**) and the other 70% of pNIPAM-BSA-pGal (**9**) at a concentration of 13.8 µM in LBB buffer with a heating rate of 1 °C/min and with the polymeric inhibitor pMan (**S3**) (15 mM in LBB).*

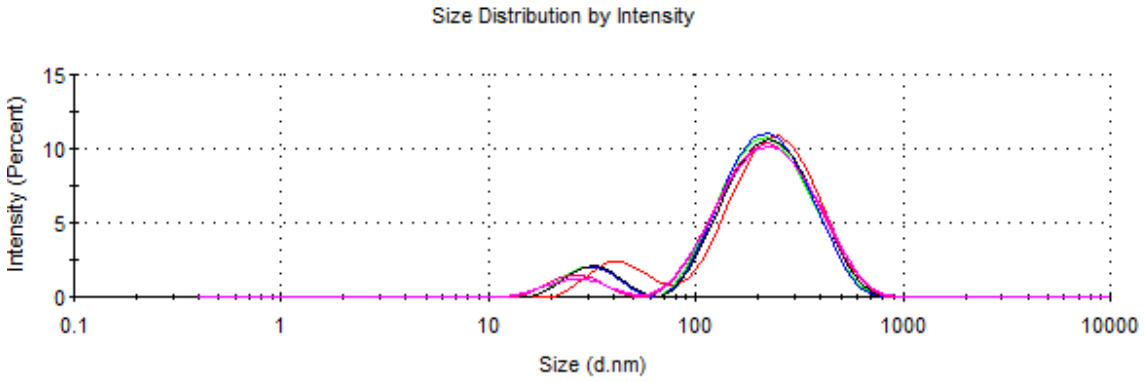


*Fig. S73: Hydrodynamic diameter distribution from the mixture of 30% pNIPAM-BSA-pMan (**8**) and the other 70% of pNIPAM-BSA-pGal (**9**) at a concentration of 13.8 µM in LBB buffer with a heating rate of 1 °C/min after particle formation (38°C).*

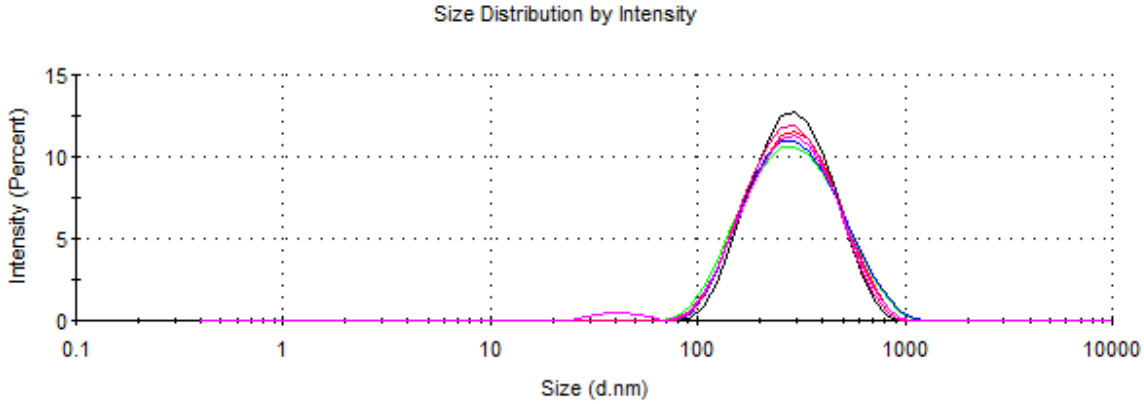


*Fig. S74: Hydrodynamic diameter distribution from the mixture of 30% pNIPAM-BSA-pMan (**8**) and the other 70% of pNIPAM-BSA-pGal (**9**) at a concentration of 13.8 µM in LBB buffer with a heating rate of 1 °C/min with lectin (ConA) corona at 38°C.*

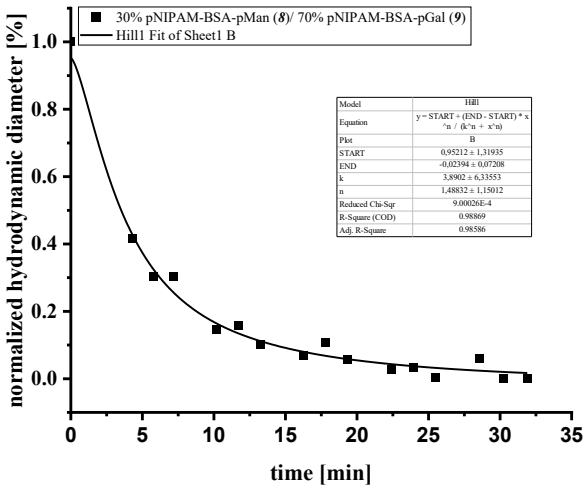


*Fig. S75: Kinetics of 30% pNIPAM-BSA-pMan (**8**) inhibition after pMan addition (Hill 1 Fit).*

20% pNIPAM-BSA-pMan (**8**)/ 80% pNIPAM-BSA-pGal (**9**)

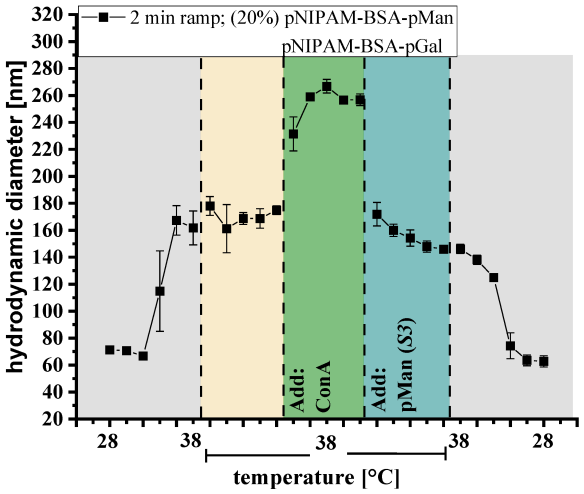


*Fig. S76: Hydrodynamic diameter profile of temperature-dependent particle formation and dissociation with the polymeric inhibitor pMan (**S3**) (15 mM in LBB) of a mixture of 20% pNIPAM-BSA-pMan (**8**) and the other 80% of pNIPAM-BSA-pGal (**9**) conjugates at a concentration of 13.8 µM in LBB buffer each with a heating rate of 1 °C/min.*

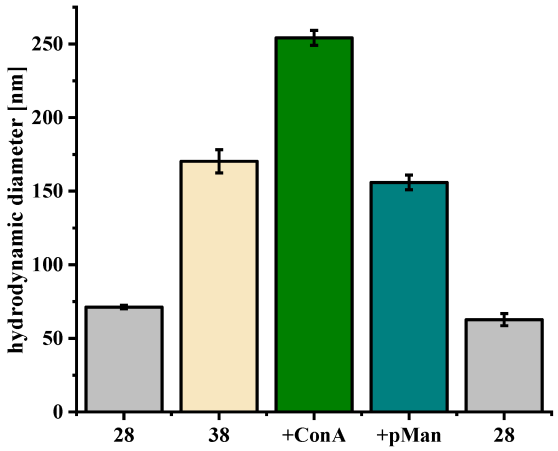


*Fig. S77: The mean values of the hydrodynamic diameter of temperature-dependent particle formation and dissociation from the mixture of 20% pNIPAM-BSA-pMan (**8**) and the other 80% of pNIPAM-BSA-pGal (**9**) at a concentration of 13.8 µM in LBB buffer with a heating rate of 1 °C/min and with the polymeric inhibitor pMan (**S3**) (15 mM in LBB).*

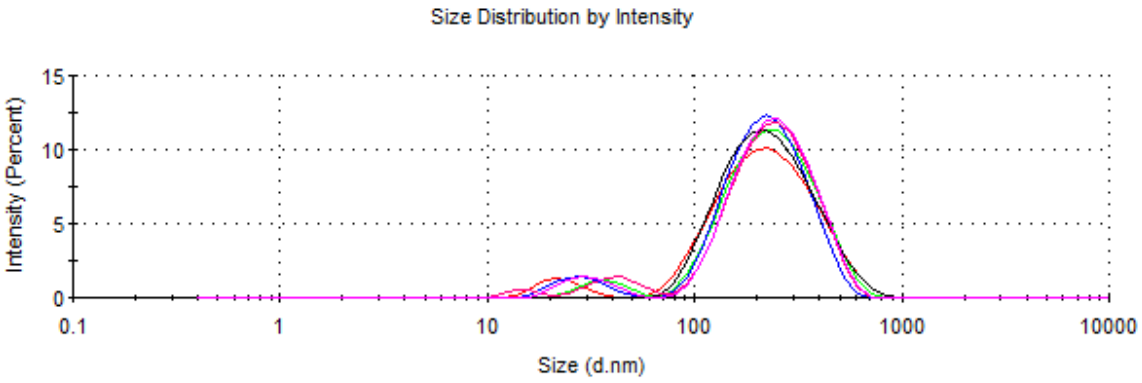


*Fig. S78: Hydrodynamic diameter distribution from the mixture of 20% pNIPAM-BSA-pMan (**8**) and the other 80% of pNIPAM-BSA-pGal (**9**) at a concentration of 13.8 µM in LBB buffer with a heating rate of 1 °C/min after particle formation (38°C).*

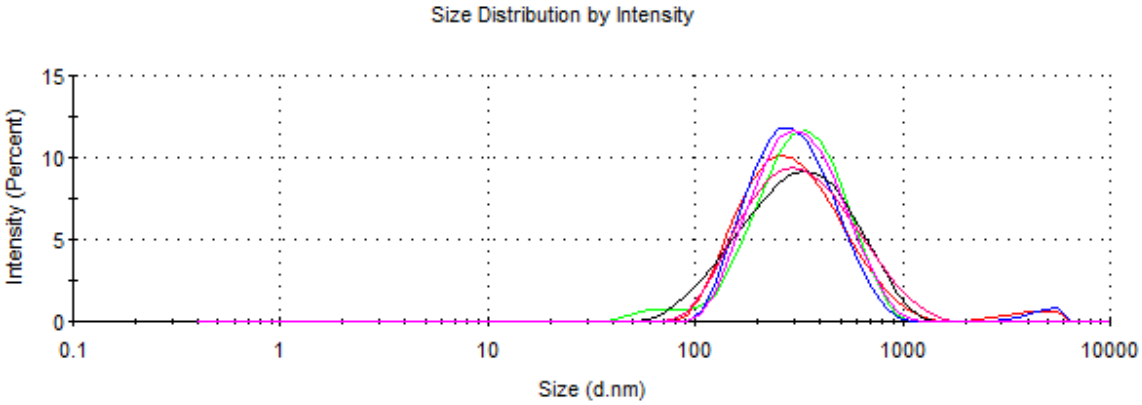


*Fig. S79: Hydrodynamic diameter distribution from the mixture of 30% pNIPAM-BSA-pMan (**8**) and the other 70% of pNIPAM-BSA-pGal (**9**) at a concentration of 13.8 µM in LBB buffer with a heating rate of 1 °C/min with lectin (ConA) corona at 38°C.*

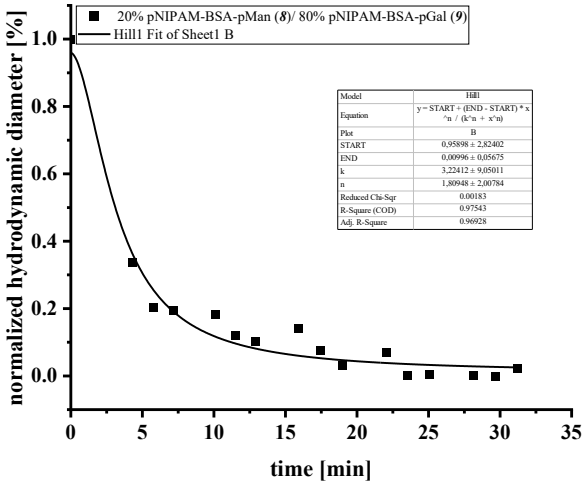


*Fig. S80: Kinetics of 20% pNIPAM-BSA-pMan (**8**) inhibition after pMan addition (Hill 1 Fit).*

11% pNIPAM-BSA-pMan (**8**)/ 89% pNIPAM-BSA-pGal (**9**)

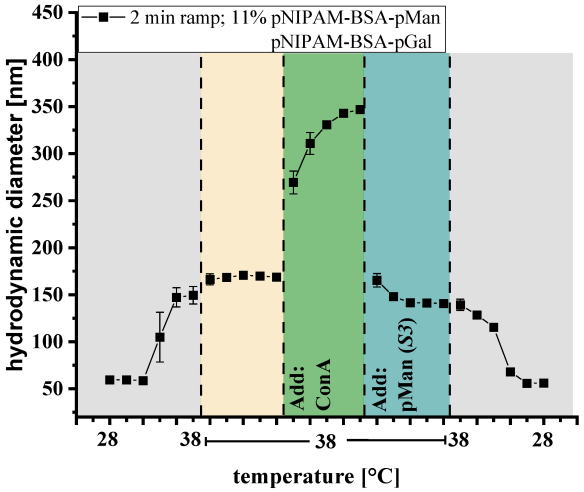


*Fig. S81: Hydrodynamic diameter profile of temperature-dependent particle formation and dissociation with the polymeric inhibitor pMan (**S3**) (15 mM in LBB) of a mixture of 11% pNIPAM-BSA-pMan (**8**) and the other 89% of pNIPAM-BSA-pGal (**9**) conjugates at a concentration of 13.8 µM in LBB buffer each with a heating rate of 1 °C/min.*

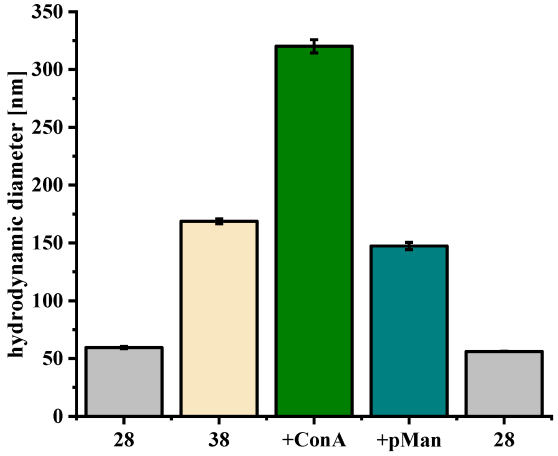


*Fig. S82: The mean values of the hydrodynamic diameter of temperature-dependent particle formation and dissociation from the mixture of 11% pNIPAM-BSA-pMan (**8**) and the other 89% of pNIPAM-BSA-pGal (**9**) at a concentration of 13.8 µM in LBB buffer with a heating rate of 1 °C/min and with the polymeric inhibitor pMan (**S3**) (15 mM in LBB).*

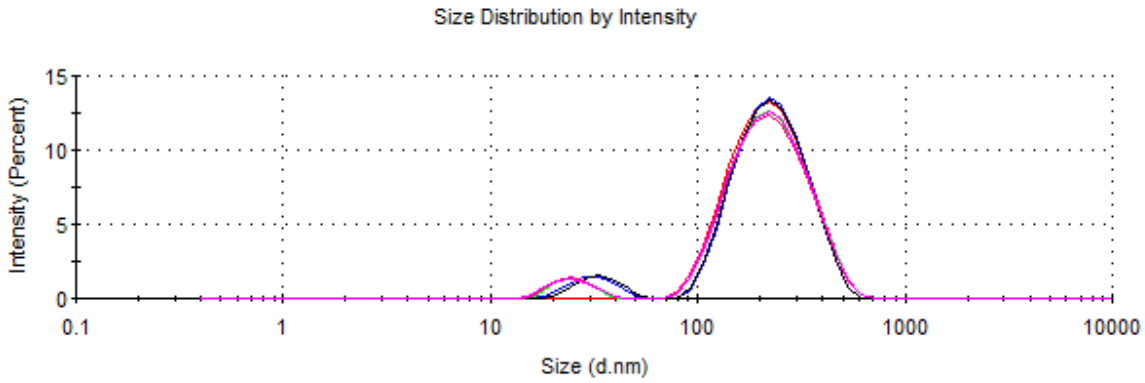


*Fig. S83: Hydrodynamic diameter distribution from the mixture of 11% pNIPAM-BSA-pMan (**8**) and the other 89% of pNIPAM-BSA-pGal (**9**) at a concentration of 13.8 µM in LBB buffer with a heating rate of 1 °C/min after particle formation (38°C).*

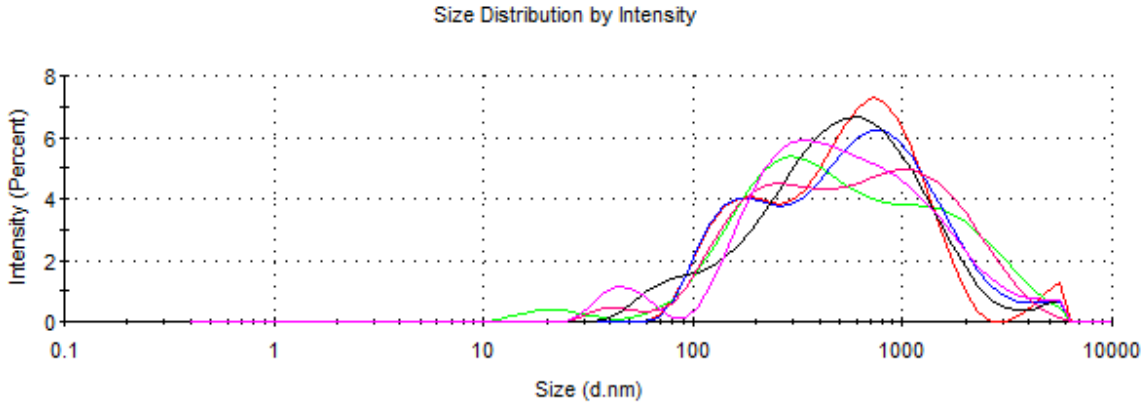


*Fig. S84: Hydrodynamic diameter distribution from the mixture of 11% pNIPAM-BSA-pMan (**8**) and the other 89% of pNIPAM-BSA-pGal (**9**) at a concentration of 13.8 µM in LBB buffer with a heating rate of 1 °C/min with lectin (ConA) corona at 38°C.*

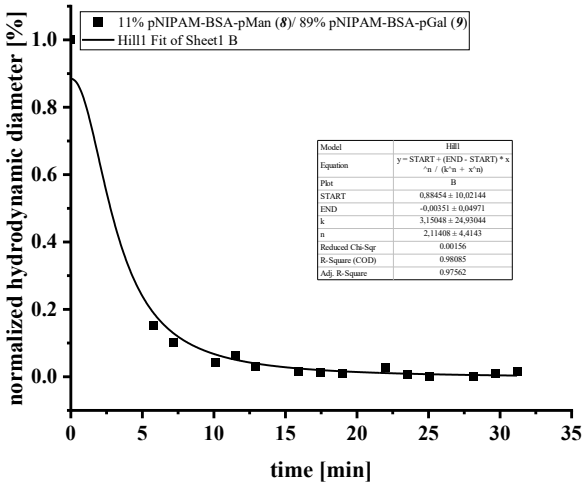


*Fig. S85: Kinetics of 11% pNIPAM-BSA-pMan (**8**) inhibition after pMan addition (Hill 1 Fit).*

6% pNIPAM-BSA-pMan (**8**)/ 94% pNIPAM-BSA-pGal (**9**)

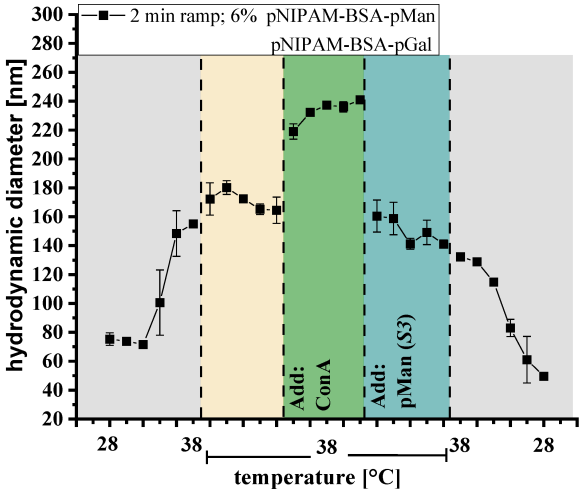


*Fig. S86: Hydrodynamic diameter profile of temperature-dependent particle formation and dissociation with the polymeric inhibitor pMan (**S3**) (15 mM in LBB) of a mixture of 6% pNIPAM-BSA-pMan (**8**) and the other 94% of pNIPAM-BSA-pGal (**9**) conjugates at a concentration of 13.8 µM in LBB buffer each with a heating rate of 1 °C/min.*

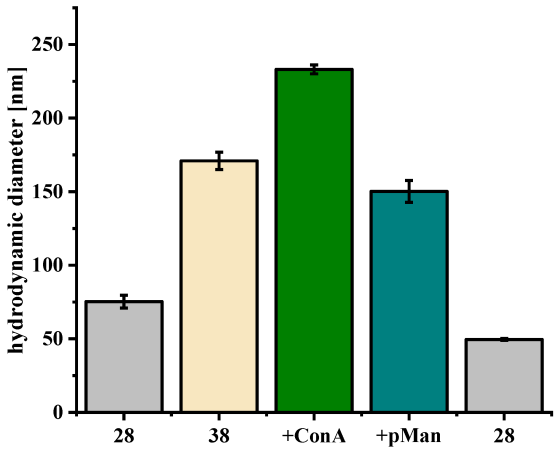


*Fig. S87: The mean values of the hydrodynamic diameter of temperature-dependent particle formation and dissociation from the mixture of 6% pNIPAM-BSA-pMan (**8**) and the other 94% of pNIPAM-BSA-pGal (**9**) at a concentration of 13.8 µM in LBB buffer with a heating rate of 1 °C/min and with the polymeric inhibitor pMan (**S3**) (15 mM in LBB).*

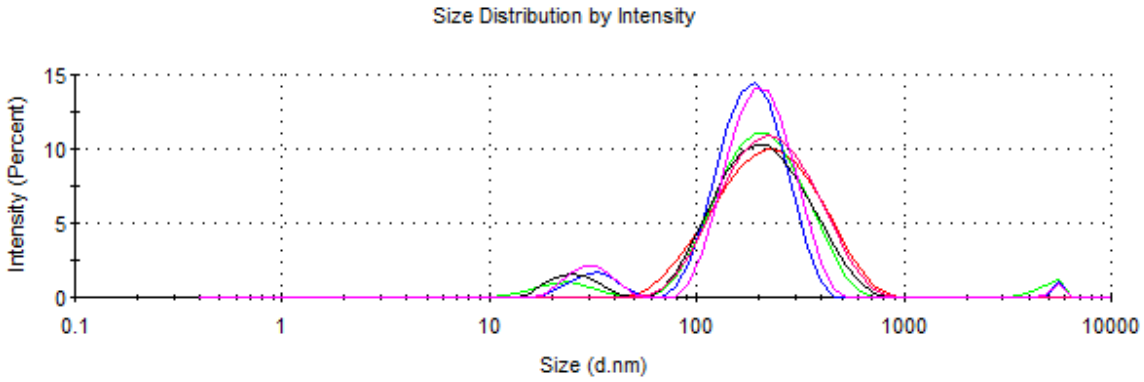


*Fig. S88: Hydrodynamic diameter distribution from the mixture of 6% pNIPAM-BSA-pMan (**8**) and the other 94% of pNIPAM-BSA-pGal (**9**) at a concentration of 13.8 µM in LBB buffer with a heating rate of 1 °C/min after particle formation (38°C).*

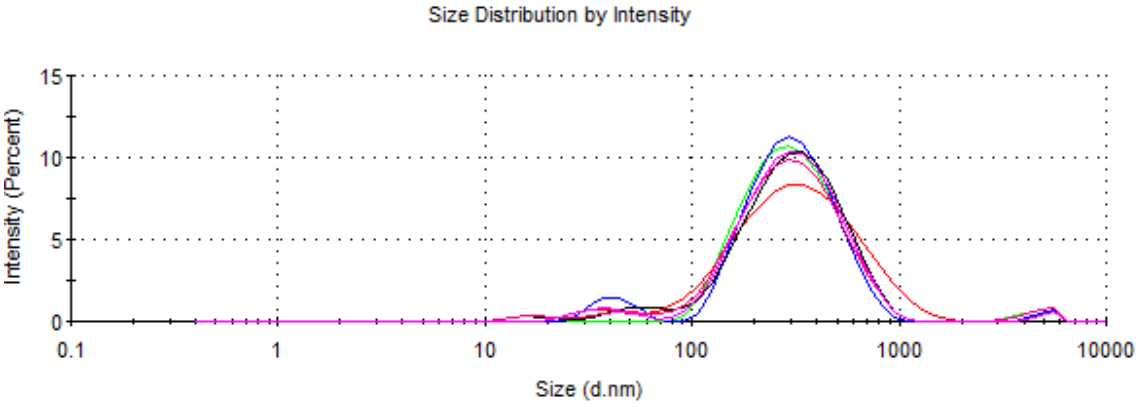


*Fig. S89: Hydrodynamic diameter distribution from the mixture of 6% pNIPAM-BSA-pMan (**8**) and the other 94% of pNIPAM-BSA-pGal (**9**) at a concentration of 13.8 µM in LBB buffer with a heating rate of 1 °C/min with lectin (ConA) corona at 38°C.*

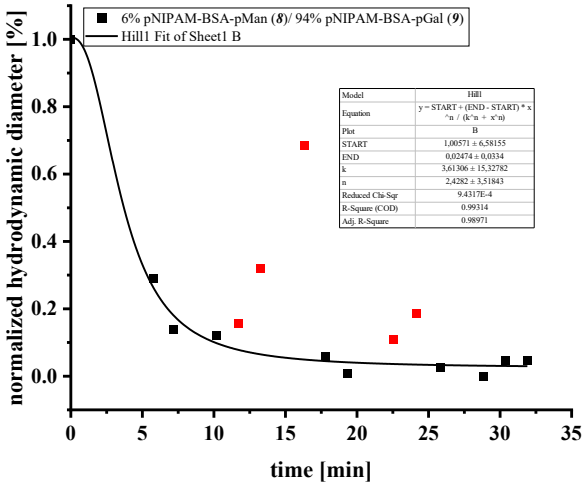


*Fig. S90: Kinetics of 6% pNIPAM-BSA-pMan (**8**) inhibition after pMan addition (Hill 1 Fit).*

3% pNIPAM-BSA-pMan (**8**)/ 97% pNIPAM-BSA-pGal (**9**)

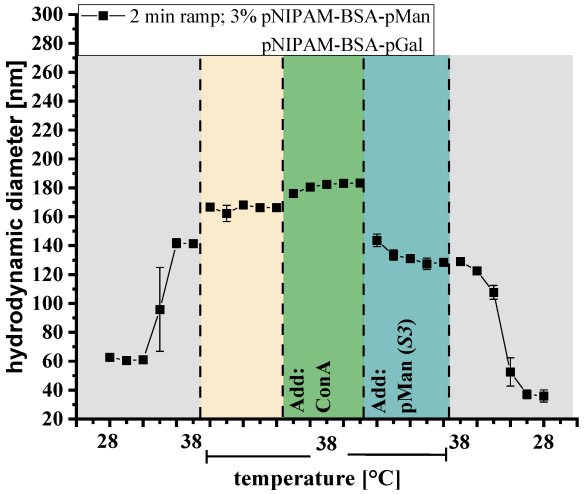


*Fig. S91: Hydrodynamic diameter profile of temperature-dependent particle formation and dissociation with the polymeric inhibitor pMan (**S3**) (15 mM in LBB) of a mixture of 3% pNIPAM-BSA-pMan (**8**) and the other 97% of pNIPAM-BSA-pGal (**9**) conjugates at a concentration of 13.8 µM in LBB buffer each with a heating rate of 1 °C/min.*

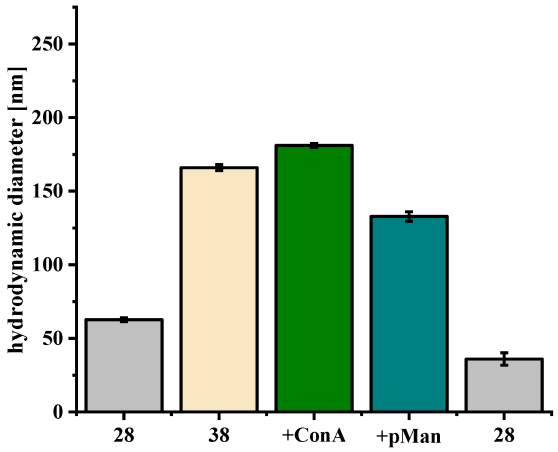


*Fig. S92: The mean values of the hydrodynamic diameter of temperature-dependent particle formation and dissociation from the mixture of 3% pNIPAM-BSA-pMan (**8**) and the other 97% of pNIPAM-BSA-pGal (**9**) at a concentration of 13.8 µM in LBB buffer with a heating rate of 1 °C/min and with the polymeric inhibitor pMan (**S3**) (15 mM in LBB).*

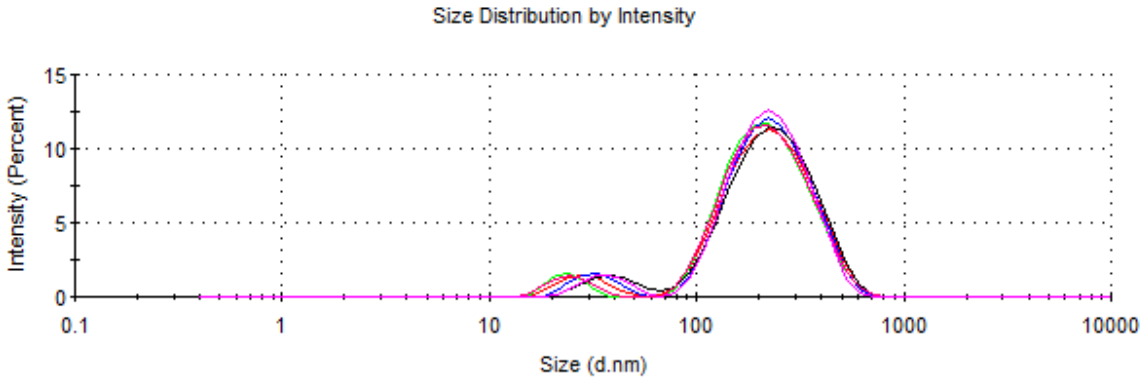


*Fig. S93: Hydrodynamic diameter distribution from the mixture of 3% pNIPAM-BSA-pMan (**8**) and the other 97% of pNIPAM-BSA-pGal (**9**) at a concentration of 13.8 µM in LBB buffer with a heating rate of 1 °C/min after particle formation (38°C).*

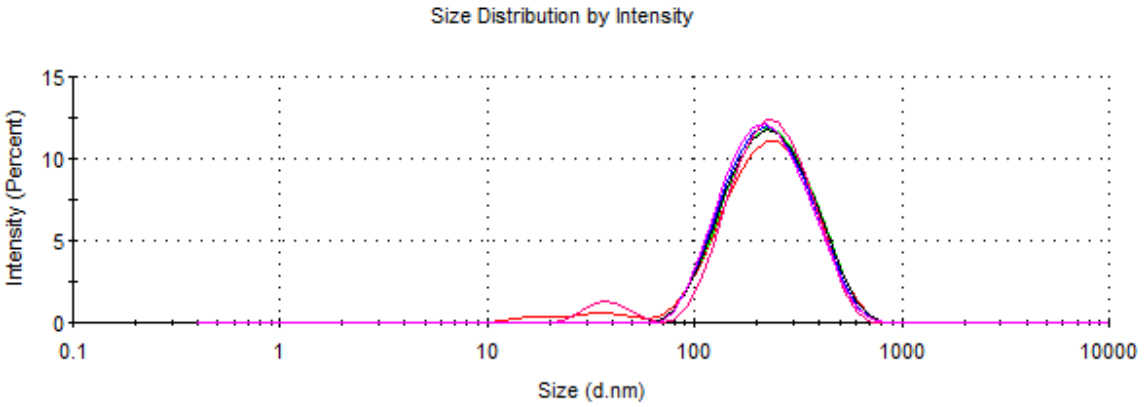


*Fig. S94: Hydrodynamic diameter distribution from the mixture of 3% pNIPAM-BSA-pMan (**8**) and the other 97% of pNIPAM-BSA-pGal (**9**) at a concentration of 13.8 µM in LBB buffer with a heating rate of 1 °C/min with lectin (ConA) corona at 38°C.*

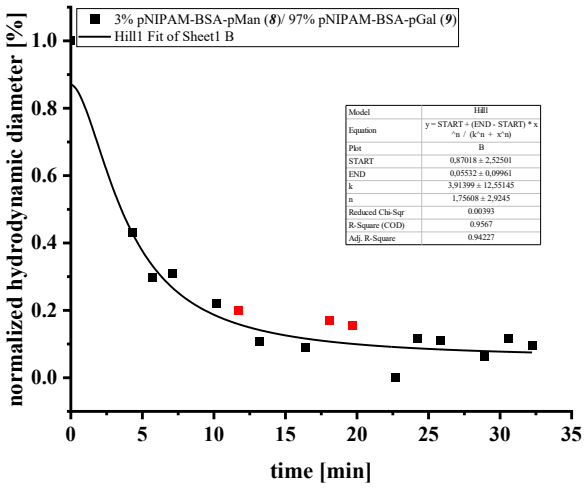


*Fig. S95: Kinetics of 3% pNIPAM-BSA-pMan (**8**) inhibition after pMan addition (Hill 1 Fit).*

pNIPAM-BSA-pMan (**8**) long-term experiment

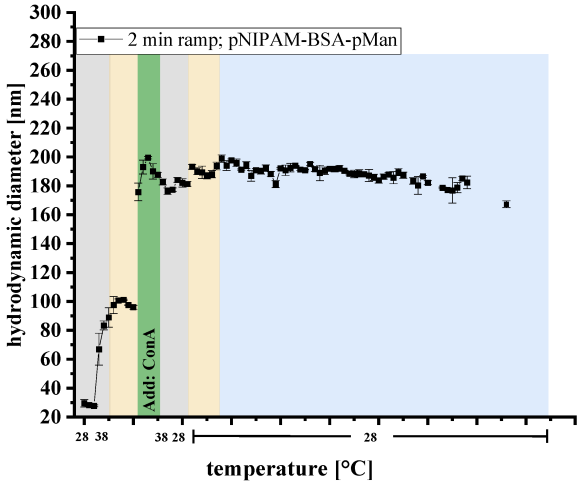


*Fig. S96: Hydrodynamic diameter profile of temperature-dependent particle formation and dissociation with the polymeric inhibitor pMan (**S3**) (15 mM in LBB) of pNIPAM-BSA-pMan (**8**) conjugate at a concentration of 13.8 µM in LBB buffer each with a heating rate of 1 °C/min. The last measurement point took place after approx. 4 days.*

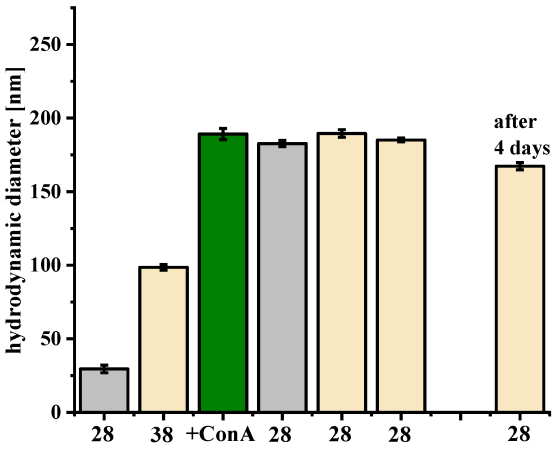


*Fig. S97: The mean values of the hydrodynamic diameter of temperature-dependent particle formation and dissociation from pNIPAM-BSA-pMan conjugates **8** at a concentration of 13.8 µM in LBB buffer with a heating rate of 1 °C/min and with the polymeric inhibitor pMan (**S3**) (15 mM in LBB). The last measurement point took place after approx. 4 days.*

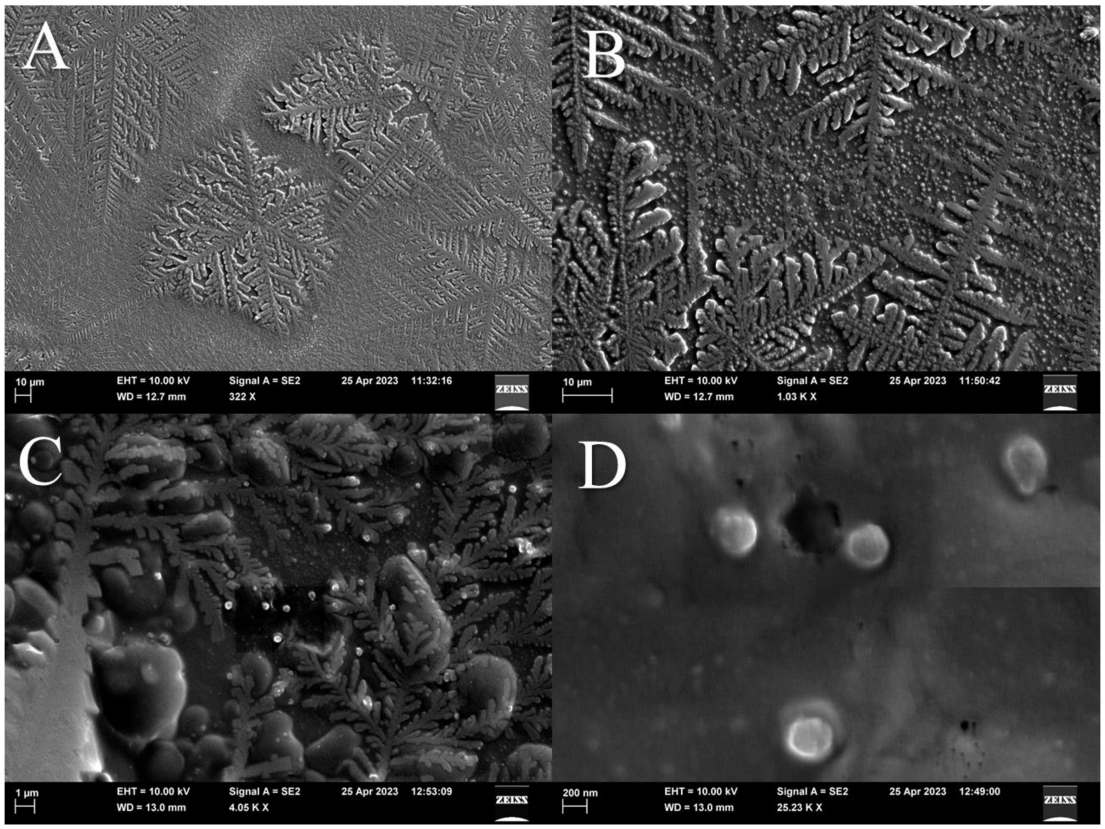


*Fig. S98: SEM images of pNIPAM-BSA-pMan conjugate (**8**) fixed via ConA as nanoparticles in LBB below the LCST. **A** and **B** show concentrations at 4.6µM and **C** and **D** at 0.46µM.*

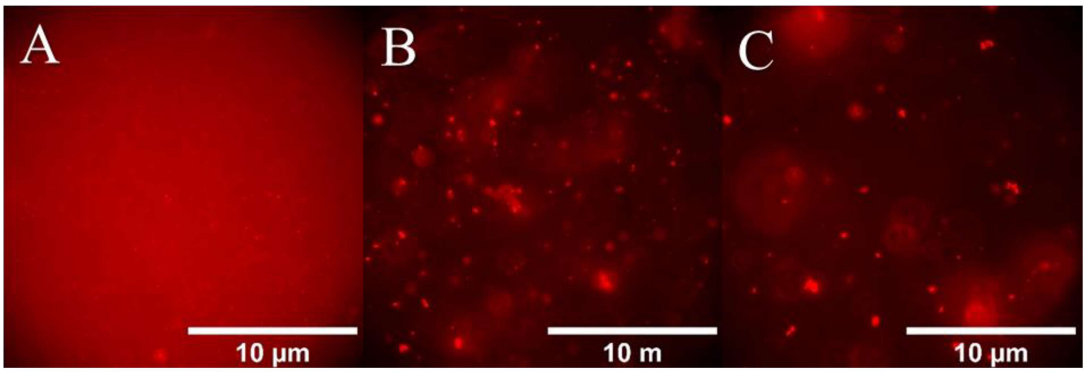
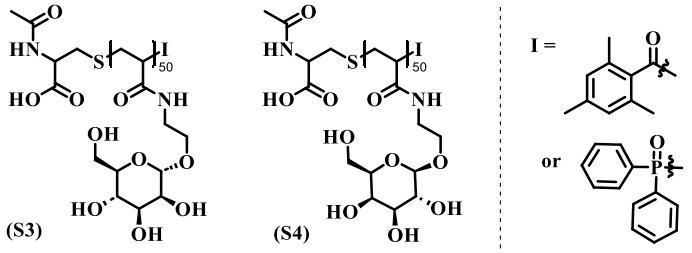


*Fig. S99: Microscopic images of the pNIPAM-BSA-pMan conjugate (**8**) below and above the LCST with the addition of the lectine ConA$^{Alexa\ 647}$: **A**: Fluorescence image (excitation: 641 nm, emission: 690 nm) of conjugate **8** after addition of ConA below the LCST (28°C) - entire solution fluoresces and no local enrichments, **B**: Fluorescence image (excitation: 641 nm, emission: 690 nm) of conjugate **8** after addition of ConA above the LCST (38°C) - local concentration of ConA at formed particles, **C**: Fluorescence image (excitation: 641 nm, emission: 690 nm) of conjugate **8** after addition of ConA above the LCST (10 min, 38°C) - formation of the nanoparticles with binding of the lectin to the mannose-presenting micelles.*

2.7 Synthesis of inhibitor polymers S3 and S4

Synthesis of pMan (S3) and pGal (S4)



The syntheses of structures **S3** and **S4** have already been published by Feldhof et.al.[2]

References

[1] K. L. Heredia, D. Bontempo, T. Ly, J. T. Byers, S. Halstenberg, H. D. Maynard, *J. Am. Chem. Soc.* **2005**, *127*, 16955-16960.

[2] M. Feldhof, S. Sperzel, L. Bonda, S. Boye, A. Braunschweig, U. I. Gerling-Driessen, L. Hartmann, *Chem. Sci.* **2024**, *15*, 16768-16777.

6.4 Supporting Information - Highly Branched Sulfated Glycopolymers as Mucin Mimetics

Authors:	Melina I. Feldhof,‡ Rebecca Schlatterer,‡ Friederiek Strahl, Jonathan Garthe, Stephan Schmidt, Matthias Karg, Bizan N. Balzer, Laura Hartmann
	‡authors contributed equally
Journal:	Journal of the American Chemical Society
Issue:	**2025**, 47, 36, 32698–32709.
Type of Paper:	Research Article
Impact Factor:	15.7 (2024)
DOI:	10.1021/jacs.5c08232

Reprinted with permission from J. Am. Chem. Soc. **2025**, 147, 36, 32698–32709. Copyright © 2025 American Chemical Society.

Supporting Information

Highly branched sulfated glycopolymers as mucin mimetics

Melina I. Feldhof,†[a] Rebecca Schlatterer,†[b] Friederike Strahl,[b] Jonathan Garthe,[c] Sylvain Prévost,[d] Stephan Schmidt,[e] Matthias Karg,[c, f] Bizan N. Balzer,[b,e,g] Laura Hartmann*[g,h]*

[a] Department of Organic Chemistry and Macromolecular Chemistry, Heinrich-Heine-University Düsseldorf, Universitätsstraße 1, 40225 Düsseldorf, Germany
[b] Institute of Physical Chemistry, Albertstr. 21, 79104 Freiburg, Germany
[c] Institute of Physical Chemistry I, Heinrich-Heine-University Düsseldorf, Universitätsstraße 1, 40225 Düsseldorf, Germany
[d] Instrument responsible D11, Institute Max von Laue – Paul Langevin (ILL), 71, avenue des Martyrs – CS 20156, 38042 Grenoble cedex 9, France
[e] Cluster of Excellence livMatS @ FIT-Freiburg Center for Interactive Materials and Bioinspired Technologies, University of Freiburg, Georges-Köhler-Allee 105, 79110 Freiburg, Germany
[f] Physical Chemistry of Functional Polymers, Martin Luther University Halle-Wittenberg, Von-Danckelmann-Platz 4, 06120 Halle (Saale), Germany
[g] Freiburg Materials Research Center (FMF), University of Freiburg, Stefan-Meier-Str. 21, 79104 Freiburg, Germany
[h] Institute for Macromolecular Chemistry, University of Freiburg, Stefan-Meier-Str. 31, D-79104 Freiburg i.Br., Germany

†First authorship contributed equally
*Corresponding authors: Dr. Bizan N. Balzer, E-Mail: bizan.balzer@physchem.uni-freiburg.de; Prof. Dr. Laura Hartmann, E-mail: laura.hartmann@makro.uni-freiburg.de

Table of Contents

1. Experimental Parts S2
1.1 Materials S2
1.2 Instrumentation S2
1.3 General Methods S4
2. Synthesis and analytical data S9
2.1 Synthesis of PFPA (***S1***) and the bridge structure (***S2***) S9
2.2 Synthesis of p(PFPA) and p(HEAA) for analytics S14
2.3 Oligoamidoamide synthesis of **O1** and **O2** S25
2.4 Synthesis of side chain glycopolymers **P7**-**P14** S33
2.5 Synthesis of brush²-glycopolymers **B1**-**B16** S41
2.6 Synthesis of reference structures **P15**–**P24** and **B17** S57
2.7 DLS measurement S68
2.8 SANS measurement S69
2.9 AFM measurement S70
3. Literature S74

1. Experimental Parts

1.1 Materials

All chemicals and solvents were used without further purification and were purchased from commercial sources. Type I water, purified by Barnstead™ MicroPure™ ThermoFisher SCIENTIFIC ultrapure water system, was used unless otherwise mentioned.

Acros Organics: piperidine 99%, copper(II) sulfate 98%; *Biosolve Chemicals*: *N*,*N*-dimethylformamide (DMF) > 99.8%, for peptide synthesis; *Carbosynth*: benzotriazol-1-yloxytripyrrolidinophosphonium hexafluorophosphate (PyBOP); *Carl Roth*: *N*,*N*-diisopropylethylamine (DIPEA) ≥ 99%, *N*,*N*-dimethylformamide (DMF) > 99.8%, chloroform ≥ 99.9%, hexane ≥ 95%, for synthesis, triethylamine ≥ 99.5%; *Fisher Scientific*: 2,2′-(ethylenedioxy)bis(ethylamine) 97 +%, trifluoroacetic acid ≥ 99.5%, acetonitrile ≥ 99.9%, diethyl ether ≥ 99.8%, with BHT, acetone ≥ 99.8%, toluene ≥ 99.8%; *Merck*: acryloyl chloride 97%, benzene ≥ 99.8%, deuterium oxide ≥ 99.9%, sodium diethyldithiocarbamate ≥ 97%; *Nanocs*: triethoxysilane-polyethylene glycole (PEG)-methoxy 5 kDa; *RAPP Polymere*: TentaGel® S RAM resin (loading: 0.26 mmol/g); *Sigma Aldrich*: 2-(2-carboxyethylsulfanylthiocarbonylsulfanyl)propionic acid 95%, azobisisobutyronitrile 98%, dichloromethane ≥ 99.9%, ethanolamine ≥ 99%, sodium sulfate ≥ 99.0%, triisopropyl silane (TIPS) 98%, *TCIchemicals*: pentafluorophenol > 98%, trityl chloride > 98%; *VWR*: ethanol ≥ 99.9%.

1.2 Instrumentation

Nuclear Magnetic Resonance Spectroscopy (NMR):

^{1}H-NMR and ^{19}F-NMR spectra were measured with a Bruker Avance III 600 (600 MHz) at room temperature. ^{13}C-NMR spectra were measured with a Bruker Avance III 300 (300 MHz) at room temperature. Chemical shifts were reported in delta (δ) expressed in parts per million (ppm) for all NMR spectra. D_2O and $CDCl_3$ serve as the deuterated solvents for the spectra. Multiplicities were abbreviated as the following: singlet (s), doublet (d), triplet (t), quartet (q), multiplet (m). The assignment of carbohydrate signals on NMR followed the chronological enumeration of protons atoms within a monosaccharide starting from the reducing end.

Reversed Phase High Pressure Liquid Chromatography Mass Spectrometry (RP-HPLC-MS): RP-HPLC-MS measurements were performed on Agilent Technologies 1260 Infinity series coupled with Agilent quadrupole mass spectrometer with an Electrospray Ionization (ESI) source operating in a m/z range of 200 to 2000. Spectra were measured with A: 95% H_2O, 5% ACN, 0.1% formic acid and B: 5% H_2O, 95% ACN, 0.1% formic acid. Separation was performed at 25 °C using an Agilent MZ-Aqua Perfect C_{18} 3 µm (50 x 3.0 mm) column with a linear solvent gradient starting at 100% A, ending at 50% B in 17 min at a flow rate of 0.4 mL/min. Indicated purities were determined by integration of

the UV-signal detected by a wavelength detector set to 214 nm with the OpenLab ChemStation software for LC/MS from Agilent Technologies.

Matrix-assisted laser desorption/ionization with time-of-flight mass spectrometer (MALDI-TOF-MS): MALDI-TOF-MS spectra was performed using a Bruker Daltonics UltfelXtreme device. 2,5 dihydroxybenzoic acid (DHB) was the used matrix.

High-resolution-electrospray-ionisation mass-spectrometry (HR-ESI): HR-ESI-MS were performed on UHR-QTOF maXis 4G from Bruker Daltonics.

Dynamic light scattering (DLS): DLS measurements were performed at a Malvern HPPS 3.3 instrument (Malvern Panalytical, Kassel, Germany) equipped with a 633 nm He/Ne-laser with the detector set in backscattering configuration (171°). Protein-polymer conjugates (1-0.25 mg/mL) in 1 cm polystyrene cuvettes were analyzed at temperatures of 20°C or 40°C. For evaluation the autocorrection function, the decay constant and first cumulant were determined by exponential fits the and the hydrodynamic radii were calculated by the Stokes-Einstein relation.

Size Exclusion Chromatography—Multi-Angle Light Scattering (H_2O-SEC-MALS): SEC analysis was measured on an Agilent 1200 series HPLC system and three aqueous SEC columns provided by Polymer Standards Service (PSS). The columns were two Suprema Lux analytical columns (8 mm diameter and 5 µm particle size) and one precolumn (50 mm, 2 × 160 Å of 300 mm and 1000 Å of 300 mm). The eluents were buffer systems: (I) MilliQ water mixed with 30% acetonitrile, 50 mM, NaH_2PO_4, 150 mM NaCl, and 250 ppm NaN_3 with a pH = 7.0 (via addition of 50 mL of 3 molar aqueous sodium hydroxide solution) filtered with an inline 0.1 µm membrane and running at 0.8 mL per min, (II) PBS buffer, 5% NaN_3 at pH 7.4 with filtered with an inline 0.1 µm membrane and running at 1.0 mL per min. Multi-angle light scattering is recorded via miniDAWN TREOS and differential refractive index spectra with Optilab rEX both supplied by Wyatt Technologies EU. Data analysis was committed with Astra 5 software and a d*n*/d*c* value of 0.156 for each polymer.

Tetrahydrofuran-Size Exclusion Chromatography (THF-SEC): THF-SEC measurements were carried out with a Viscotek VE 3580 RI detector and a SYKAM S 3250 UV/Vis detector equipped with a polystyrene column (300 × 8.0 mm, 5 µm) and a polyacryl column (300 × 8.0 mm, 5 µm). A S5200 (SYKAM) sample injector as an auto sampler was utilized. THF was used as a solvent and toluene as a reference. The measurements were carried out with an injection volume of 100 µL and a flow rate of 1 mL/min. The molecular weights were determined with the Chromatographica (hs GmbH) software.

Elementar analysis: The ratios of carbon, hydrogen, nitrogen, and sulfur were determined using a Vario Micro Cube provided by Analysensysteme GmbH.

Small-Angle Neutron Scattering (SANS): SANS data were measured on D22 [DOI:10.5291/ILL-DATA.9-10-1845] at the Institut Laue-Langevin – The European Neutron Source, Grenoble, France. The front detector was positioned at 1.4 m from the sample at an angle of 20°, the rear detector was at 17.6 m, the beam was collimated at 17.6 m and the sample aperture was 7×10 (h×v) mm^2. One wavelength λ (relative full width at half maximum 10 %) was used: selecting λ =6.0 Å with a source aperture of 40×55 mm^2 (direct beam standard-deviation on detector 0.90 mrad) allowed covering a continuous q-range of 0.0024–0.66 $Å^{-1}$, where q is the magnitude of the wavevector ($q = (4\pi/\lambda) \times \sin(\Theta/2)$, Θ being the scattering angle) (flux of 1.67 MHz). Samples were kept in quartz cuvettes (type 100-QS and 110-QS, Hellma GmbH, Müllheim, Germany) of 1 mm pathway, on a thermalized rack with recorded temperature. Data were reduced with the program Grasp V.10.26h[1] normalizing with monitor, subtracting the contribution from the empty cell, taking into account noise from the measurement with a sintered $^{10}B_4C$ piece at the sample position, and using for transmission the intensity transmitted by a semi-transparent beam stop. Parallax from the detector and from the sample attenuation were corrected for, and a flat field was used. Absolute scale was obtained from the measurement of the direct beam with a calibrated attenuator.

1.3 General Methods

Standard protocols for solid phase synthesis: TentaGel resin was utilized in the synthesis process of both oligoamidoamines and the building block assembly, which involved iterative repetition of deprotection and conjugation steps. The backbone sequences were finished by Fmoc deprotection of the terminal amine enabling the conjugation to the active ester polymers. The required methods are described in the following section and can performed either by manual or automated synthesis (CS136XT, CS Bio). The given equivalents are related to 0.1 mmol scale.

> ***Swelling protocol:*** Before the first cleavage of the N-Fmoc protecting group, the resin was swollen twice with approx. 5 mL DCM and then reconditioned 10 times to DMF.
>
> ***Fmoc-Deprotection:*** *N*-Fmoc protecting groups of the functionalized TentaGel resin or the immobilized building blocks were removed by incubating approx. 5 ml 25% piperidine solution in DMF, shaken for 15 minutes and washed five times with DMF. The deprotection step was repeated and the resin was then washed with ten times with DMF.
>
> ***Building block assembly:*** The two *N*-Fmoc-protected building blocks used here, **EDS** and **TDS**, were assembled on the solid support of the sequence-defined oligoamidoamines. After the respective Fmoc deprotection of the N-terminus, the next building block was conjugated using amide coupling methods. For this purpose, a solution of the **TDS** or **EDS** building block (5.0 eq.), PyBOP (4.9 eq.) and DIPEA (10 eq.) was dissolved in 2 mL DMF and added to the reaction vessel. The reaction mixture was shaken for 60 minutes at room temperature (20 °C) and then the resin was washed 10 times with 5 mL DMF each time.

Copper(I)-mediated azide-alkyne cycloaddition (CuAAC): After complete assembly of the sequence, the azide-functionalized mannose was conjugated to the alkyne-functional groups of the **TDS** building block of the macromolecule. For this purpose, copper(I)-mediated azide-alkyne cycloaddition (CuAAC) was performed by subsequent addition of N-methyloxyamine solution (2.5 eq. per alkyne group, solution in 100 µl DMF), copper(II) sulfate (2.5 eq. per alkyne group, solution in 100 µl water) and sodium ascorbate (2.0 eq. per alkyne group, solution in 100 µl water). The reaction vessel was covered with aluminum foil to protect it from light and shaken at room temperature for 18 h. The resin was then washed with the following wash cycle and repeated until it had regained its original yellow color: 5 ml of solution was used each time, 3 x 23 mM DDC solution (in DMF/water, *v/v*, 1:1, sodium diethyldithiocarbamate), 5 x DMF, 3 x water, 2 x DMF, 3 x DCM, 2 x DMF.

Deacetylation: The glycooligomers underwent deacetylation using Zemplén conditions.[2] Initially, the resin was washed five times with methanol. Subsequently, 5 mL of a 0.2 M NaOMe solution in MeOH was drawn into the reactor. The resin was agitated for 30 minutes before discarding the solution. Following this, the resin was washed twice with MeOH. Then, an additional 5 mL of the 0.2 M NaOMe was pulled into the reactor. After another 30 minutes, the solution was again discarded, and the resin was washed five times with MeOH.

***Cleavage reaction*:** The synthesized macromolecules were cleaved from the resin by adding 2 ml of TFA/TIPS/DCM (95/2.5/2.5) solution to the reaction vessel and shaking for 30 minutes, precipitated in cold diethyl ether and freeze-dried.

Synthesis of brush glycopolymers and linear reference structures:The corresponding p(PFPA) (***P1-3***) was dissolved in DMF (50 mg/mL). The amount of the corresponding oligoamidoamine was dissolved in 500 µL DMF and added to the active ester polymer solution. Then 20 eq. triethylamine (based on the amine) was added and the reaction and stirred at 40 °C for approx. 18 h, before 20 eq. ethanolamine or isopropylamine (based on the active ester repeating unit) was added and stirred at 40 °C for a further 18 h. The fully quenched polymer was then precipitated in cold acetone (for ethanolamine conversion) or cold diethyl ether (for isopropylamine conversion) for 2 h at -20 °C, centrifuged, purified by dialysis (cut off: 1 kDa) and lyophilized. In the reference samples, the functionalization with **O1** or **O2** was not required, whereby the active ester polymer was reacted directly with the 20 eq. ethanolamine or isoproplamine over 18 h at 40 °C.

Attachment of the bridge molecule to glycopolymers: The bridge molecule was attached via EDC-NHS chemistry. The corresponding arm polymer (***P7-P14***) was dissolved in 700 µL DMF and pre-activated with 10 eq. EDC*HCL (dissolved in 100 µL DMF/water (*v/v* 1:1, 15 minutes at room temperature) before 10 eq. NHS (dissolved in 100 µL DMF, 15 minutes at room temperature, 20 °C) forms the corresponding active ester. Subsequently, 10 eq. of the bridging molecule (dissolved in

100 µL DMF) were added and the mixture was stirred for 18 h at room temperature before the polymer was purified and lyophilized by dialysis (cut off: 1 kDa).

Cleavage of the protecting group of the conjugated bridge molecule: In order to cleave off the triphenylmethyl protecting group, the corresponding polymer was dissolved in 200 µL DMF and suspended with 1 mL DCM. This was followed by 10 eq. triisopropylsilane and 2 mL trifluoroacetic acid were added and the suspension was stirred for one hour at room temperature (20 °C), whereby the suspension dissolved after ten minutes. The polymer was precipitated in diethyl ether, centrifuged and lyophilized.

Attachment of the amine-activated glycopolymers to polymer scaffold to gain brush² structures: The corresponding amount of p(PFPA) ***P3*** was dissolved in 200 µL DMF. The appropriate amine preactivated arm polymer was dissolved in 800 µL DMF and set to alkaline (pH~10) with 200 eq. triethylamine and allowed to swell for one hour before it was added to the active ester polymer and the reaction was stirred for 18 h at 40 °C. Subsequently, 80 eq. ethanolamine was added and stirred for another 18 h at 40 °C before the brush² polymer was precipitated in cold acetone, centrifuged off and purified and lyophilized via dialysis (cut off: 50 kDa).

Standard protocol for global sulfation: The corresponding brush-like glycopolymer were dissolved in 5-7 mL dry DMF before 40 Eq. TMA*SO_3 per OH-group were added. The mixture was stirred for 24h at 70 °C. After cooling to room temperature, the mixture was added in an aqueous sodium acetate solution (10wt.%) at 0 °C. The DMF/water mixture was evaporated under reduced pressure before dialysis (cut off: 50 kDa) and followed by lyophilization.

Cantilever functionalization for AFM-Based Single Molecule Force Spectroscopy: The corresponding structures were covalently attached to Si_3N_4 AFM cantilevers tips (MLCT-BIO-DC, Bruker Nano). After removal from the gel pad box, the cantilever chips were stored in toluene (≥ 99,8 %, Thermo Fisher Scientific,) for 15 min to dissolve any remaining contaminants. Then, they were dried and placed in the evacuated reaction chamber of a plasma system (Tetra 30 LF PC, Diener electronic) at 0.1 mbar. There, they were exposed to oxygen plasma for 4 min at a power of 20 % (120 W) and then quickly transferred from the plasma chamber and directly incubated in a 50:1 solution of 1.25 mg mL^{-1} triethoxysilane-PEG-methoxy (5 kDa, Nanocs) solved in dry toluene (≥ 99,5 %, ≤ 30 ppm water, Th. Geyer) and 1.25 mg mL^{-1} triethoxysilane-PEG-amine dissolved in dry chloroform (≥ 99,9 %, Carl Roth) at 60°C for 1 hour. Afterwards, they were rinsed twice in toluene twice in ethanol (≥ 99,9 %, VWR), and once in N,N-Dimethylmethanamid (DMF, ≥ 99,8 %, Carl Roth). Then, the cantilever chips were incubated in the respective polymer solution at 4°C over night.

Solutions of polymers were prepared by dissolving the polymers in 100 µL DMF and 100 µL ultrapure water if they contained charges, otherwise they were dissolved in 200 µL DMF. As they all

contain a unique terminal carboxylic end group, coupling to the amine-functionalized cantilever tip was carried out by EDC/NHS coupling. Thus, N-(3-Dimethylaminopropyl)-N′-ethyl-carbodiimid-hydrochlorid was dissolved in 50 µL DMF and 50 µL ultrapure water and then added to the polymer solution and stirred for 10 min. Next, N-Hydroxysuccinimide was dissolved in 50 µL DMF and then added to the polymer solution, already containing EDC*HCL, and stirred for another 10 min. Then, the polymer solution was diluted to obtain a concentration of 0.05-0.20 mg mL^{-1}, depending on the respective structure (see Table 2). The next day, the functionalized cantilever chips were rinsed in ultrapure water and mounted to the AFM for measurements in ultrapure water.

AFM-Based Force Spectroscopy: Force spectroscopy measurements were performed with a MFP3D (Asylum Research, an Oxford Instruments company) using a closed fluid cell at approx. 22°C. All measurements were performed on freshly cleaved mica (muscovite, diameter 10–12 mm, Plano). Mica was glued onto the AFM fluid cell using the high-resolution replicating compound 101RF (Microset Products). After immersing a functionalized AFM cantilever chip into solution, an equilibration time of 20 to 30 mins was used, after which the cantilever deflection remained stable. For calibration, the inverse optical lever sensitivity (invOLS) was determined by indentation into the underlying hard surface and averaging of five values at the beginning of any experiment. The force constant was obtained by the thermal noise method,[3] see Table 1.

A trigger point of up to 1.8 nN (50 nm deflection) was used and the dwell time was set to 1.0 s. Approach and retraction velocities were usually kept constant at 1.0 µm s^{-1} with a sampling rate of 5 kHz. Force curves were obtained by contacting the underlying surface in a grid-like fashion (force map). Therefore, force maps with 10 by 10 points on an area of 10 µm by 10 µm were taken, resulting in 100 force curves per force map. Thus, the AFM cantilever tip contacted the surface once within a square-like area of 1 μm^2.

Table 1. Inverse optical lever sensitivity (invOLS) and force constant k obtained from the cantilever calibration using thermal noise method.[3] c_m indicates the mass concentration used for the cantilever functionalization described in the experimental section.

Sample	c_m / mg mL^{-1}	invOLS / nm V^{-1}	k / pN nm^{-1}
2	0.20	420	8
3	0.10	140	66
4	0.05	253	12
6	0.05	434	26

Control experiments with PEG: A trigger force of up to 1.8 nN (50 nm deflection) and a dwell time of 1.0 s were applied. The approach and retraction velocities were usually kept constant at 1.0 μm s^{-1} with a sampling rate of 5 kHz, taking force maps (10 by 10 points, 10 μm by 10 μm).

AFM Data Evaluation: Self-programmed procedures based on Igor Pro (Version 8, Wavemetric) were used to evaluate the force-extension curves with respect to desorption peaks. The desorption forces and extensions of plateaus of constant force were determined by fitting a sigmoidal function to the end of the plateaus.

The desorption peak evaluation was done by selecting the force and position of every last peak, wherein each peak corresponded to the breakage of an interaction of a single molecule or a portion thereof with the underlying surface. Absolute force values were subject to the uncertainty of cantilever spring constant calibration. The absolute force error amounted to around 10 %, while the relative uncertainties are about 2 %, when one and the same cantilever is used, as argued previously by *Pirzer et al.*[4] The desorption position error resulted from the standard deviation of the respective desorption position distribution.

AFM-Based Imaging: AFM images were acquired by a Cypher ES (Asylum Research, an Oxford Instruments company) at ca. 22°C on mica (muscovite, diameter 10–12 mm, Plano). The images were obtained using Scout 70 RAu (NuNano) cantilevers (nominal cantilever tip radius: 5 nm) with a resonance frequency of 70 kHz. AC mode imaging in air was performed with the blueDrive (photothermal excitation). A scan rate of 2.44 Hz and a scan angle of 0° (i.e., parallel to cantilever axis) were chosen. The mica surface was cleaved with a transparent adhesive tape until a flat surface was obtained; then, 100 μL of a solution containing the respective polymer in ultrapure water with a concentration of 0.1 μg mL^{-1} was applied and immediately placed in a desiccator to dry under vacuum for at least 2.5 h at ca. 22°C.

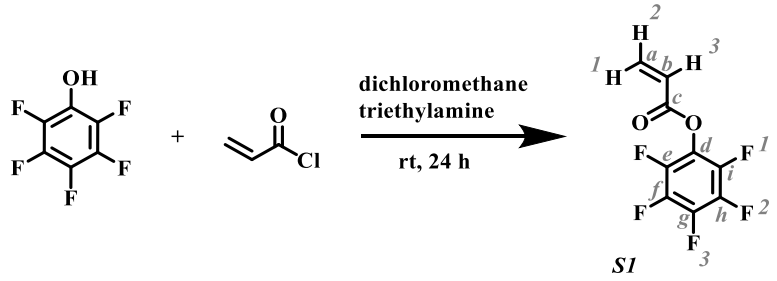
The acquired height images were analyzed with the Gwyddion Free SPM analysis software (ver. 2.59).[5] AFM topography images were evaluated by applying a mean plane subtraction, row alignment (medium of difference) and a correction of horizontal scars. The minimum values were shifted to zero. Wherever useful (e.g., for particularly large globules), masking was used prior to image correction to prevent correction artifacts. Note that each AFM images provide local information about the respective sample.

2. Synthesis and analytical data

Building blocks **EDS** (**e**thylene glycol **d**iamine **s**uccinyl, 1-(9H-fluoren-9-yl)-3,14-dioxo-2,7,10-trioxa-4,13-diazaheptadecan-17-oic acid), **TDS** (**t**riple **b**ond diethylenetriamine **s**uccinyl, 1-(fluorenyl)-3,11-dioxo-7-(pent-4-ynoyl)-2-oxa-4,7,10-triazatetra-decan-14-oic acid) and **α-D-mannose azid** were synthesized as previously reported.[6-8] p(PFPA) with Pn ~ 98 and Đ = 1.28 were synthesized as previously reported.[9]

2.1 Synthesis of PFPA (*S1*) and the bridge structure (*S2*)

S1 – PFPA



The synthesis of pentafluorophenyl acrylate was carried out based on Graisuwan et al.[10] 10.38 g (56.40 mmol) pentafluorophenol was dissolved in 70 mL DCM, mixed with 9 mL triethylamine and cooled to 0 °C. Then 5.7 mL (70.53 mmol) acryloyl chloride was slowly added and kept for 24 h at room temperature. The reaction suspension was filtered, and the filtrate was washed twice with aqueous hydrochloric acid solution (pH 2). The organic phase was then washed twice with saturated sodium bicarbonate solution and twice more with distilled water. The organic phase was dried over sodium sulfate, filtered and the solvent removed on a rotary evaporator. A clear, light yellow, liquid product was obtained, which was purified by flash chromatography using a 120 g silica column and hexane as running agent. The product is a colorless solution.

Yield: 9.9 g (41.58 mmol; 74%)

^{1}H-NMR (600 MHz, Chloroform-*d*) δ (ppm) 6.75 – 6.69 (dt, *J* = 17.32, 0.91 Hz, 1H, *H1*), 6.41 – 6.31 (ddd, *J* = 17.32, 10.62, 0.97 Hz, 1H, *H3*), 6.21 – 6.15 (dt, *J* = 10.59, 0.92 Hz, 1H, *H2*).

^{13}C-NMR (300 MHz, Chloroform-*d*) δ (ppm) 161.83 (s, *Cc*), 143.00 (m, *Ci*), 141.37 (m, *Ce*), 139.75 (m, *Cg*), 138.01 (m, *Cf*), 136.37 (m, *Ch*), 135.64 (s, *Cb*), 125.50 (s, *Ca*), 125.09 (m, *Cd*).

^{19}F-NMR (564 MHz, Chloroform-*d*) δ (ppm) -152.50 – -152.63 (m, *F1*), -157.9 – -1157.99 (m, *F3*), -162.27 – -162.40 (m, *F2*).

LC-MS m/z calculated for $C_9H_3F_5O_2$ $[M + ACN + H]^+$ 280.03, found 280.00, $[M + 2ACN + H]^+$ 321.06 found 320.0, determined relative purity: > 95%

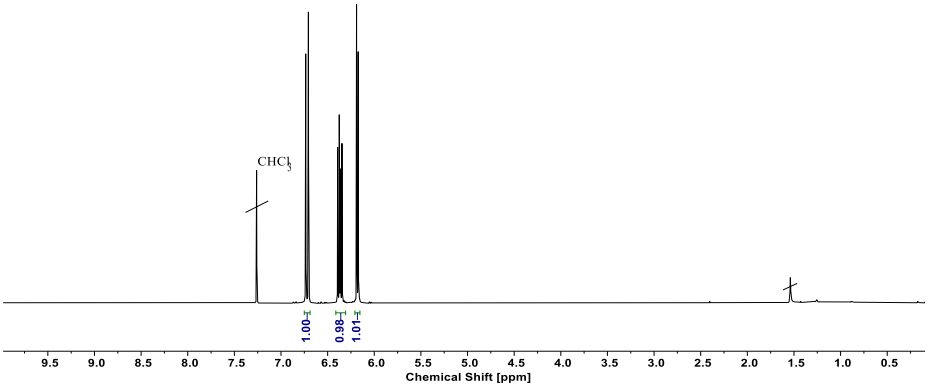


*Figure S1: ^{1}H-NMR spectra of PFPA (**S1**) (600 MHz, $CDCl_3$).*

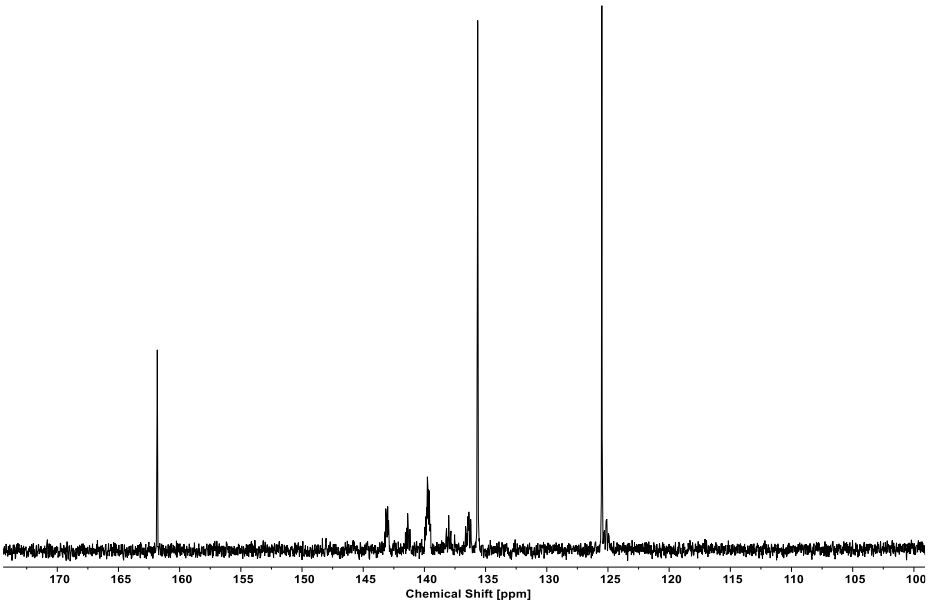


*Figure S2: ^{13}C-NMR spectra of PFPA (**S1**) (300 MHz, $CDCl_3$).*

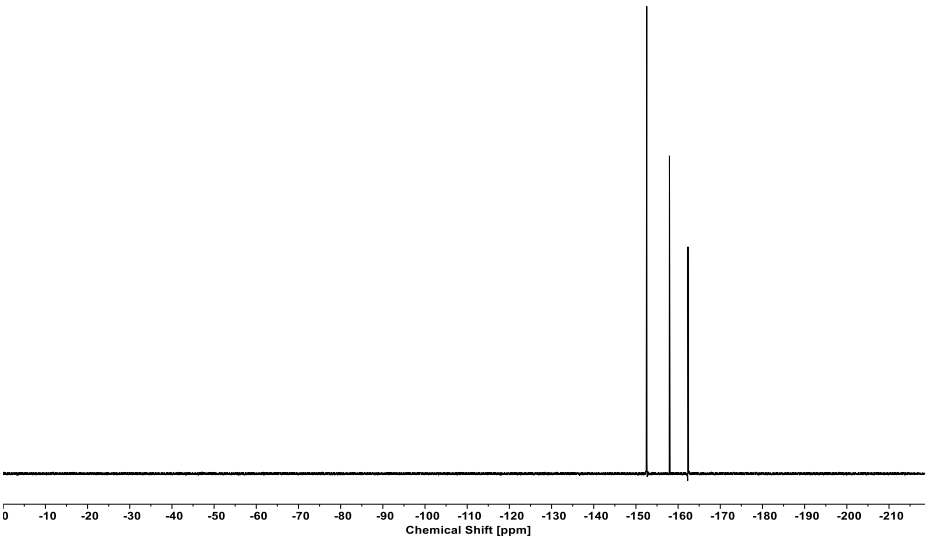


*Figure S3: ^{19}F-NMR spectra of PFPA (**S1**) (600 MHz,$CDCl_3$).*

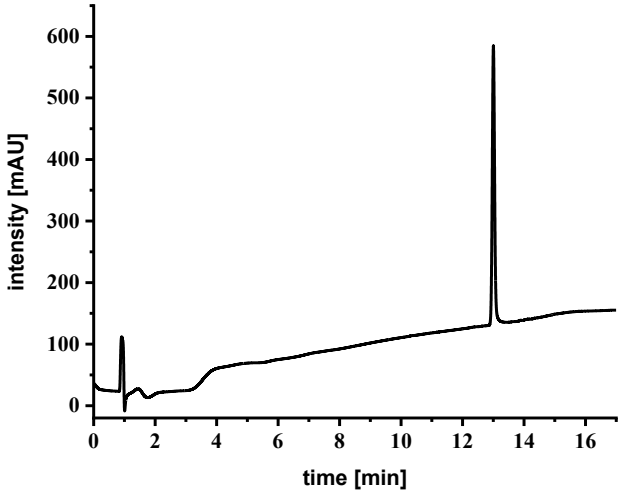


*Figure S4:RP-HPLC- chromatogram of PFPA (**S1**) (gradient of 5 to 95 vol% acetonitrile/water with 0.1 vol% formic acid, run time: 17 min).*

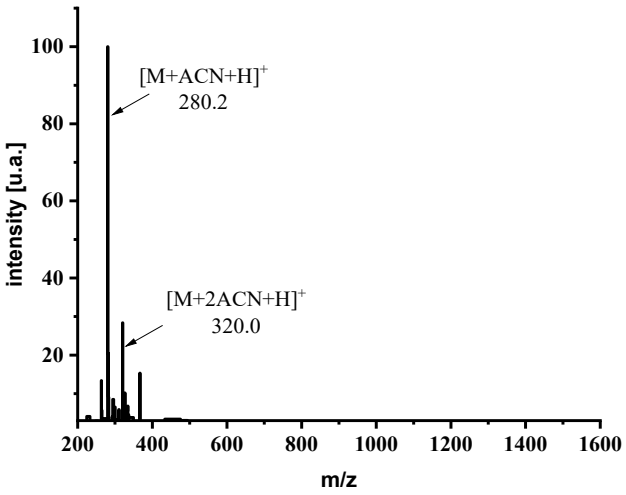
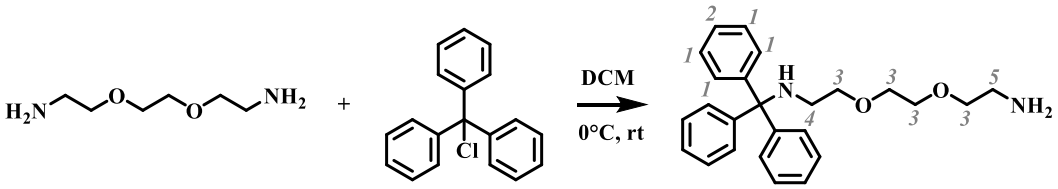


*Figure S5: ESI-MS chromatogram of PFPA (**S1**) at t = 13.00 min (gradient of 5 to 95 vol.% acetonitrile/water with 0.1 vol.% formic acid, run time: 17 min).*

S2 – bridge molecule



29.2 g (200.00 mmol) of 2,2′-(ethylenedioxy)bis(ethylamine) was dissolved in 500 mL of DCM and the solution was cooled to 0 °C in an ice bath. 13.94 g (50 mmol) of trityl chloride was dissolved in 300 mL of DCM and added over a period of about one hour and allowed to warm to room temperature overnight with stirring. The volume of solvent was halved on the rotary evaporator and washed three times with 300 mL of saturated sodium hydrogen carbonate solution each time. The organic phase was dried over magnesium sulphate and the solvent was removed under reduced pressure, leaving the product as a colorless syrup.

Yield: 18.18 g (46.55 mmol; 93%)

^{1}H-NMR (600 MHz, Chloroform-*d*): δ (ppm) 7.50 - 7.45 (dt, ^3J = 8.62 Hz, ^4J = 1.50 Hz, 6H, *H1*), 7.28 – 7.23 (m, 6H, *H1*), 7.19 – 7.15 (tt, ^3J= 7.34 Hz, ^4J= 1.30 Hz, 3H, *H2*), 3.62-3.46 (m, 8H, *H3*), 2.87 – 2.77 (t, ^3J = 5.20 Hz, 2H, *H4*), 2.38 – 2.33 (t, ^3J= 5.40 Hz, 2H, *H5*).

LC-MS m/z calculated for $C_{25}H_{30}N_2O_2$ $[M + Na]^+$ 413.23, found 413.2, $[M +Na]^+$, determined relative purity: 94%

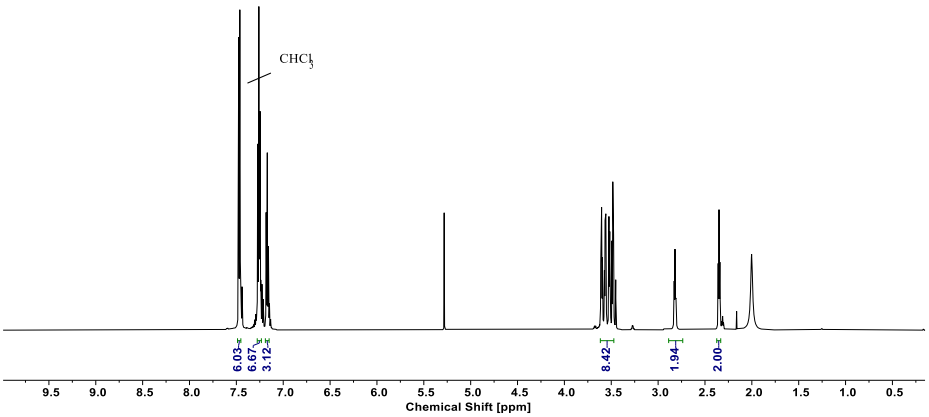


*Figure S6: ^{1}H-NMR spectra of bridge (**S2**) (600 MHz, $CDCl_3$).*

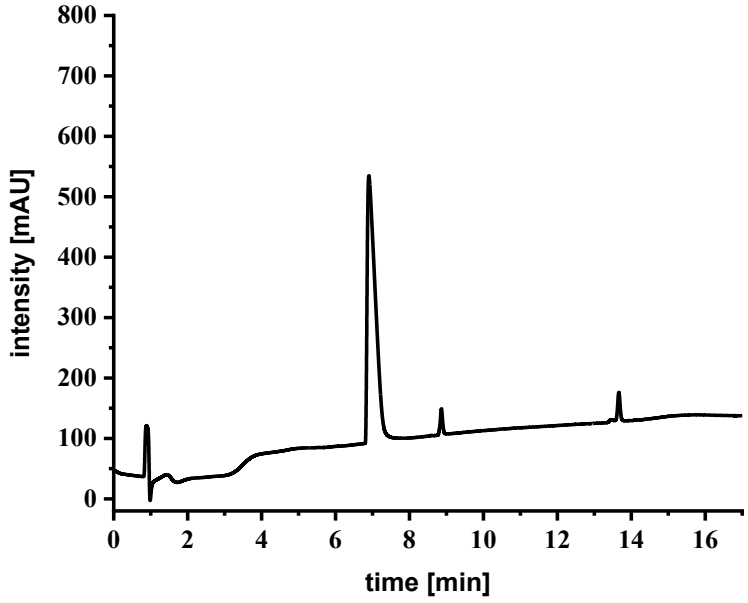


*Figure S7: RP-HPLC- chromatogram of bridge structure (**S2**) (gradient of 5 to 95 vol% acetonitrile/water with 0.1 vol% formic acid, run time: 17 min).*

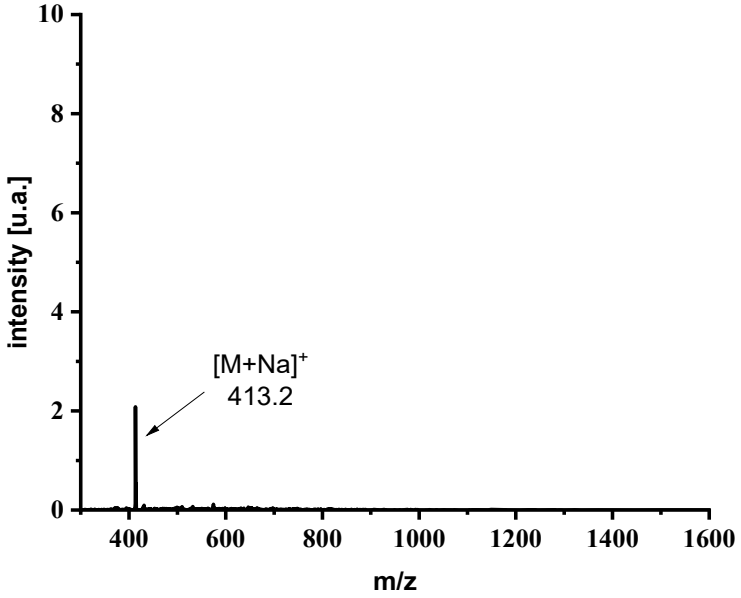
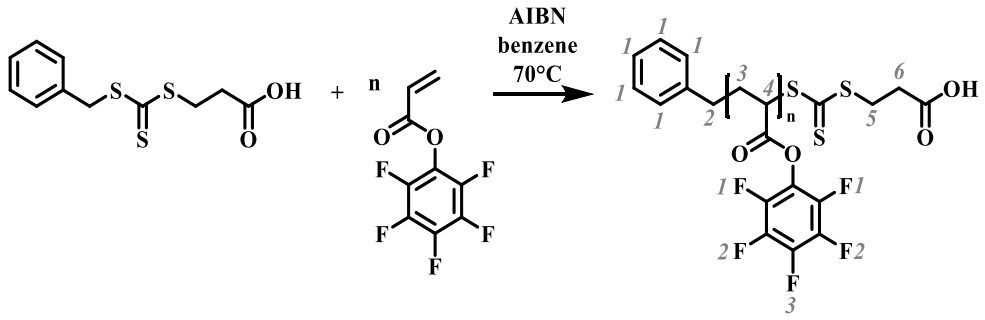


*Figure S8: ESI-MS chromatogram of PFPA (**S1**) at t = 6.89 min (gradient of 5 to 95 vol.% acetonitrile/water with 0.1 vol.% formic acid, run time: 17 min).*

2.2 Synthesis of p(PFPA) and p(HEAA) for analytics

P1-3 – p(PFPA)



According to Fadi Shamout[11] synthesis procedure, **A** mg (**B** mmol) of azobisisobutyronitrile (AIBN) and **C** mg (**D** mmol) of 2-(2-carboxyethylsulfanylthiocarbonylsulfanyl)propionic acid (RAFT reagent) were dissolved in 8 mL of benzene and cooled in an ice bath. **E** mL of the monomer pentafluorophenyl acrylate (***S1***) (**F** mmol) was added and everything was rinsed under argon for 30 min. The reaction solution was heated to 70 °C for 24 hours. The polymerization was stopped by cooling with liquid nitrogen and under the influence of oxygen. The product was precipitated in 30 mL cold hexane and was centrifuged. The yellowish solid obtained was dissolved again with 2 mL benzene, precipitated a second time in cold hexane, washed twice more with 30 mL hexane, centrifuged and the polymer was dried under nitrogen.

Table 1: Summary of RAFT polymerization parameters for the synthesis of p(PFPA) P1-3.

polymer (*P*)	AIBN		RAFT reagent		monomer		Yield	
	A [mg]	B [mmol]	C [mg]	D [mmol]	E [mL]	F [mmol]	[mg]	[%]
P1	32.8	0.2	272.4	1	5.1	35	7.45	89
P2	23.0	0.14	190.7	0.7	5.1	35	7.61	91
P3	5.8	0.04	47.7	0.2	5.1	35	7.05	85

P1 – p(PFPA)

^{1}H-NMR (600 MHz, Chloroform-*d*) δ (ppm) 7.24 – 7.12 (d_{br}, J = 7.2 Hz, 5H, *H1*), 3.63 (s_{br}, 2H, *H5*), 3.23 – 0.58 (*H2 - H4, H6*). Pn ~ 46

^{19}F-NMR (564 MHz, Chloroform-*d*) δ (ppm) -153.15 (s, *F1*), -156.73 (s, *F3*), -162.20 (s, *F2*).

GPC (THF, toluene standard) *UV detector:* M_n = 6033 g/mol, M_w = 7602 g/mol, Đ = 1.26, *RI detector:* M_n = 5722 g/mol, M_w = 7185 g/mol, Đ = 1.26.

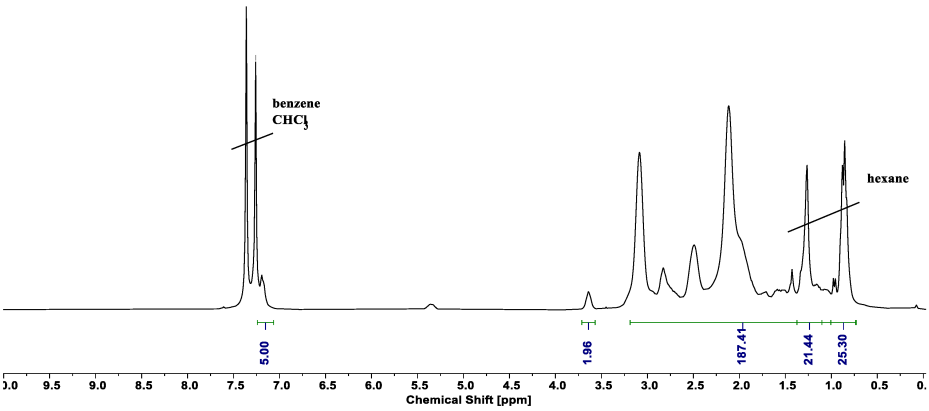


*Figure S9: ^{1}H-NMR spectra of p(PFPA) (**P1**) (600 MHz, $CDCl_3$).*

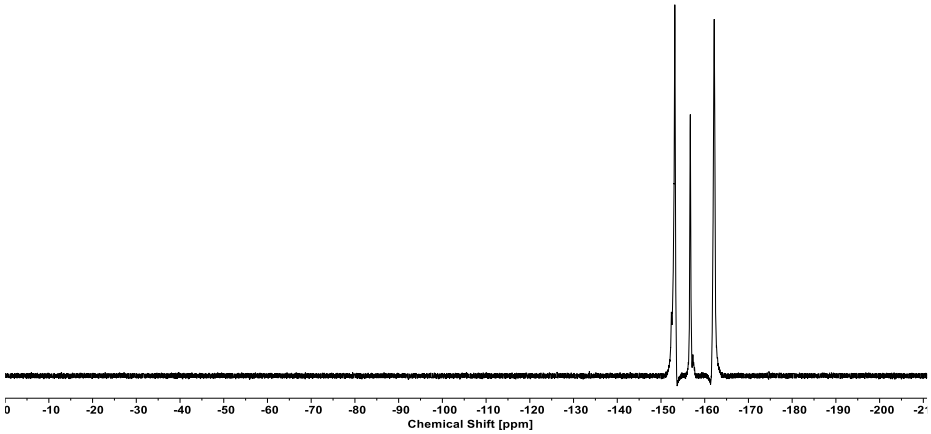


*Figure S10. ^{19}F-NMR spectra of p(PFPA) (**P1**) (600 MHz, $CDCl_3$).*

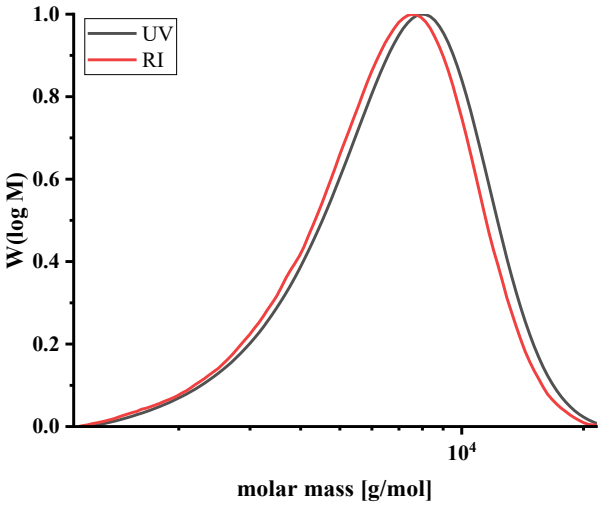


*Figure S11: GPC measurement of p(PFPA) **P1**, eluent: THF.*

P2 – p(PFPA)

^{1}H-NMR (600 MHz, Chloroform-*d*) δ (ppm) 7.20 – 7.11 (d_{br}, J = 7.7 Hz, 5H, *H1*), 3.24 – 1.20 (*H2 – H6*). Pn ~ 63

^{19}F-NMR (564 MHz, Chloroform-*d*) δ (ppm) -153.18 (s, *F1*), -156.70 (s, *F3*), -162.16 (s, *F2*).

GPC (THF, toluene standard) *UV detector:* M_n = 7372 g/mol, M_w = 9537 g/mol, Đ = 1.29, *RI detector:* M_n = 7079 g/mol, M_w = 9071 g/mol, Đ = 1.28.

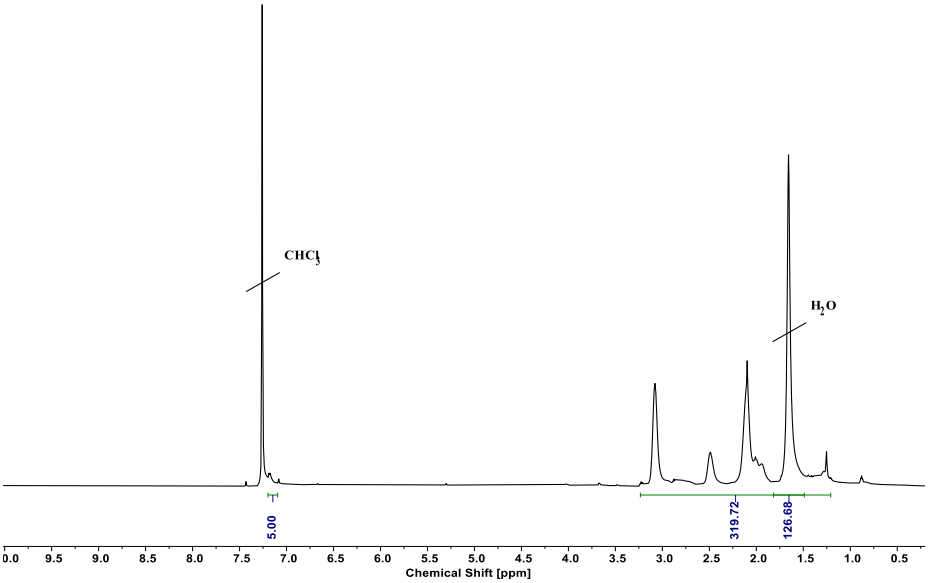


*Figure S12: [1]H-NMR spectra of p(PFPA) (**P2**) (600 MHz, $CDCl_3$).*

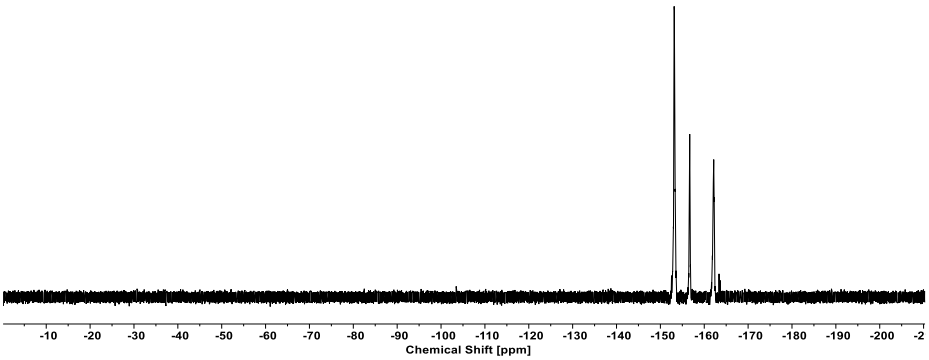


*Figure S13: [19]F-NMR spectra of p(PFPA) (**P2**) (600 MHz, $CDCl_3$).*

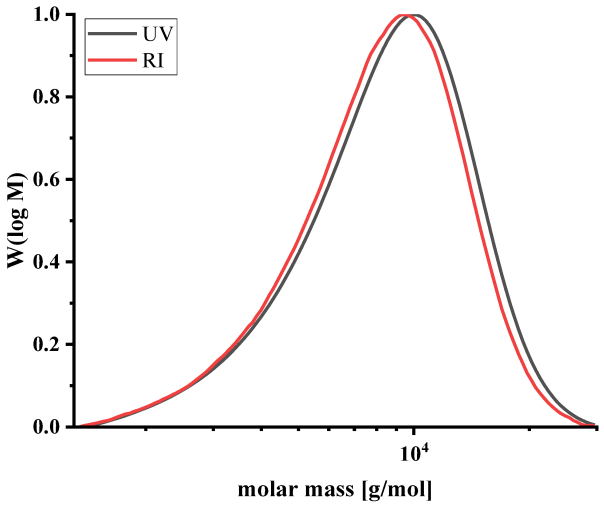


Figure S14: GPC measurement of p(PFPA) ***P2****, eluent: THF.*

P3 – p(PFPA)

^{1}H-NMR (600 MHz, Chloroform-*d*) δ (ppm) 7.21 – 7.13 (d_{br}, J = 6.9 Hz, 5H, *H1*), 3.31 – 0.78 (*H2 – H6*). Pn ~ 202

^{19}F-NMR (564 MHz, Chloroform-*d*) δ (ppm) -153.18 (s, *F1*), -156.70 (s, *F3*), -162.16 (s, *F2*).

GPC (THF, toluene standard) *UV detector:* M_n = 23488 g/mol, M_w = 32464 g/mol, Đ = 1.38, *RI detector:* M_n = 22542 g/mol, M_w = 30793 g/mol, Đ = 1.37.

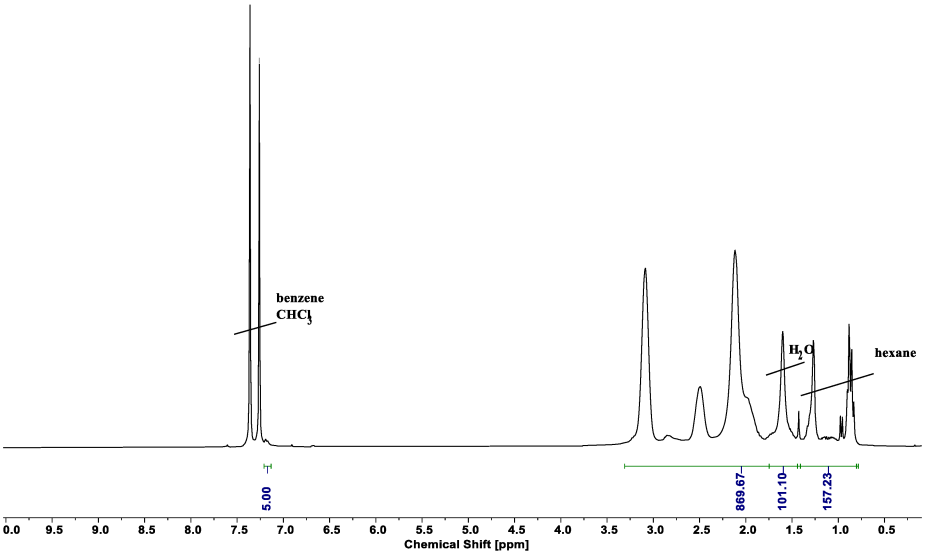


*Figure S15: ^{1}H-NMR spectra of p(PFPA) (****P3****) (600 MHz, $CDCl_3$).*

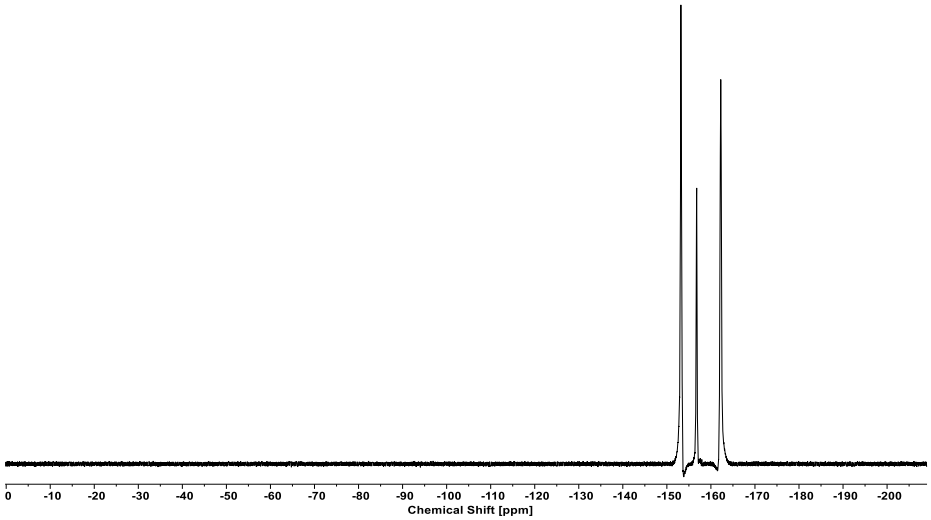


*Figure S16: ^{19}F-NMR spectra of p(PFPA) (**P3**) (600 MHz, $CDCl_3$).*

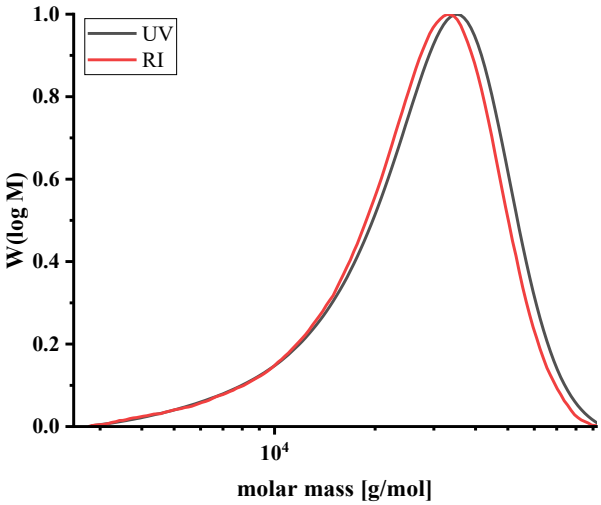
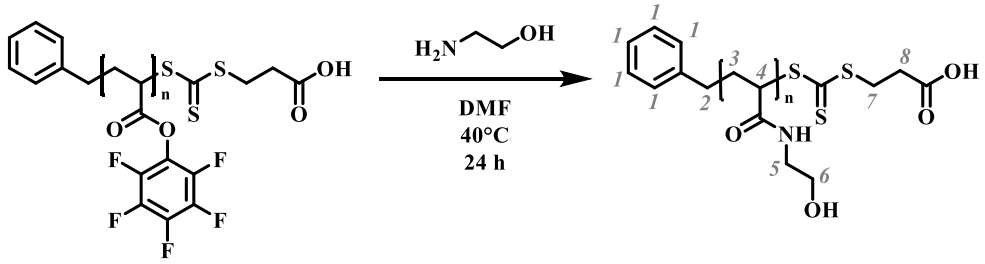


*Figure S17: GPC measurement of p(PFPA) **P3**, eluent: THF.*

P4-6 – p(HEAA)



100 mg (0.42 mmol) of p(PFPA) (***P4-6***) was dissolved in 1 mL DMF, 291 µL (2.1 mmol, 5 eq. relative to the amine) triethylamine was added and mixed with 507 µL (8.4 mmol, 20 eq. relative to the repeating unit) ethanolamine and the reaction solution was stirred for 24 h at 40 °C in a sand bath. The product was then removed in cold acetone, centrifuged and purified by dialysis (cut off: 1 kDa) over three days and dried by lyophilization.

Yield: ***P4***: 31.18 mg, ***P5:*** 29.47 mg, **P6:** 36.67 mg

P4 – p(HEAA)

^{1}H-NMR (600 MHz, D_2O) δ (ppm) 7.32 – 6.99 (m, 5H, *H1*), 3.86 – 2.92 (m, *H5*, *H6*), 2.55 – 2.41 (m, 2H, *H7*), 2.26 – 1.16 (m, *H2*, *H3*, *H4*, *H8*). Pn ~ 29

^{19}F-NMR (564 MHz, D_2O) δ (ppm) No signals determined.

GPC (10 mM PBS, pH = 7.4, 298,15 K) *RI detector:* M_n = 4472 g/mol, M_w = 7256 g/mol, Đ = 1.48, *UV detector:* M_n = 4875 g/mol, M_w = 7196 g/mol, Đ = 1.62.

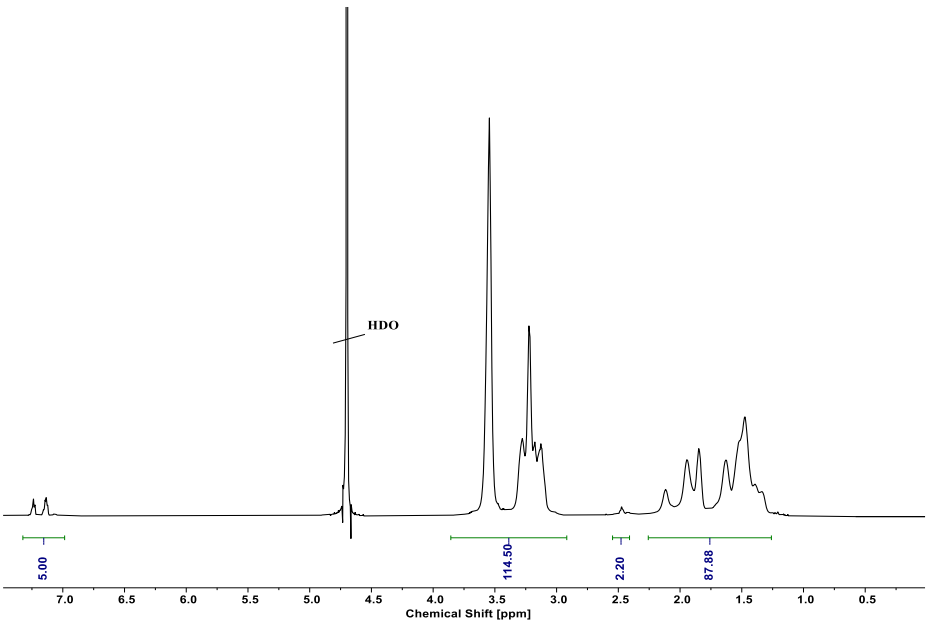


*Figure S18: ^{1}H-NMR spectra of p(HEAA) (**P4**) (600 MHz, D_2O).*

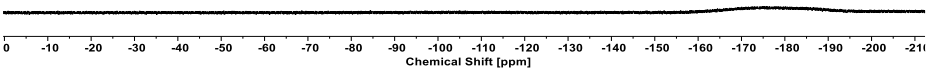


*Figure S19: ^{19}F-NMR spectra of p(HEAA) (**P4**) (600 MHz, D_2O).*

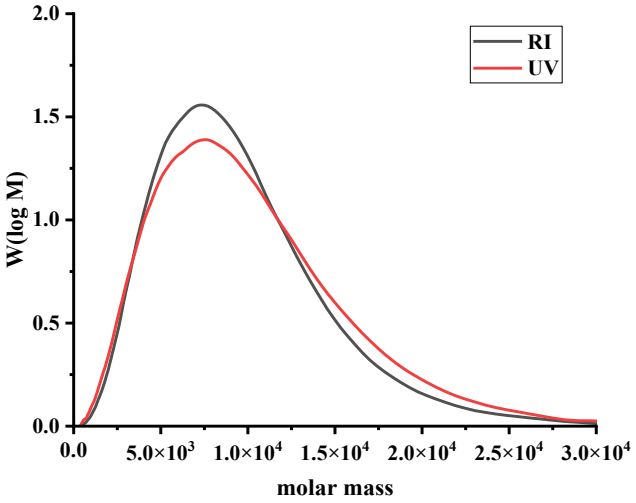


*Figure S20: Aqueous GPC measurement of p(HEAA) **P4**, eluent: PBS. RI Calculation.*

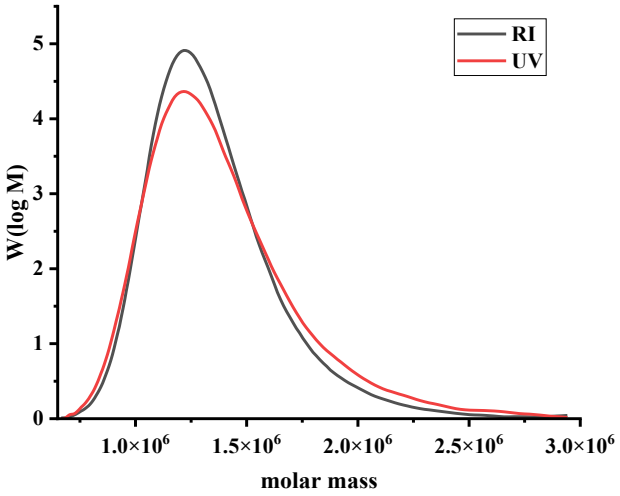


*Figure S21: Aqueous GPC measurement of p(HEAA) **P4**, eluent: PBS. LS Calculation.*

P5 – p(HEAA)

^{1}H-NMR (600 MHz, D_2O) δ (ppm) 7.35 – 6.99 (m, 5H, *H1*), 3.74 – 2.97 (m, *H5*, *H6*), 2.57 – 2.37 (m, 2H, *H7*), 2.21 – 1.22 (m, *H2*, *H3*, *H4*, *H8*). Pn ~ 57

^{19}F-NMR (564 MHz, D_2O) δ (ppm) No signals determined.

GPC (10 mM PBS, pH = 7.4, 298,15 K) *RI detector:* M_n = 7311.3 g/mol, M_w = 1003.2 g/mol, Đ = 1.37, *UV detector:* M_n = 6881 g/mol, M_w = 9984 g/mol, Đ = 1.45.

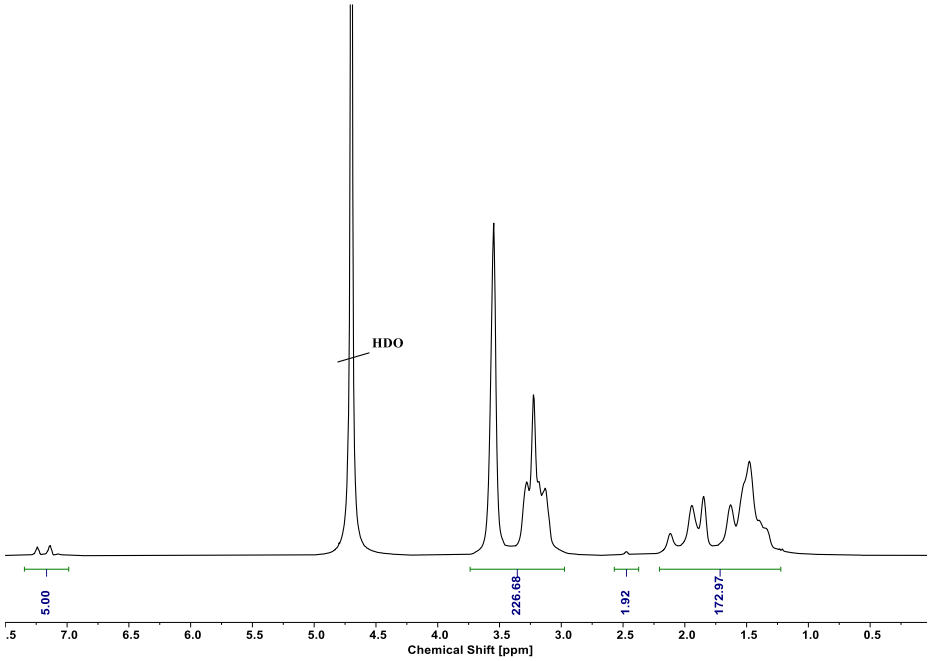


*Figure S22: ^{1}H-NMR spectra of p(HEAA) (**P5**) (600 MHz, D_2O).*

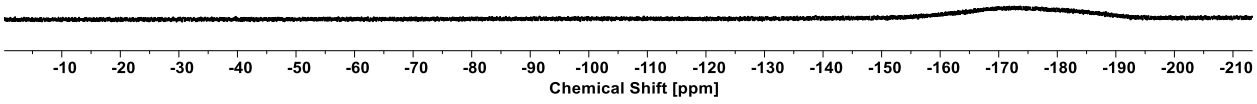


*Figure S23: ^{19}F-NMR spectra of p(HEAA) (**P5**) (600 MHz, D_2O).*

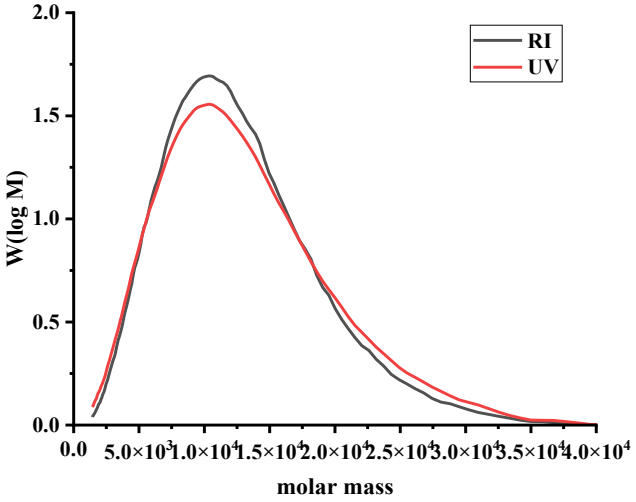


*Figure S24: Aqueous GPC measurement of p(HEAA) **P5**, eluent: PBS. RI Calculation.*

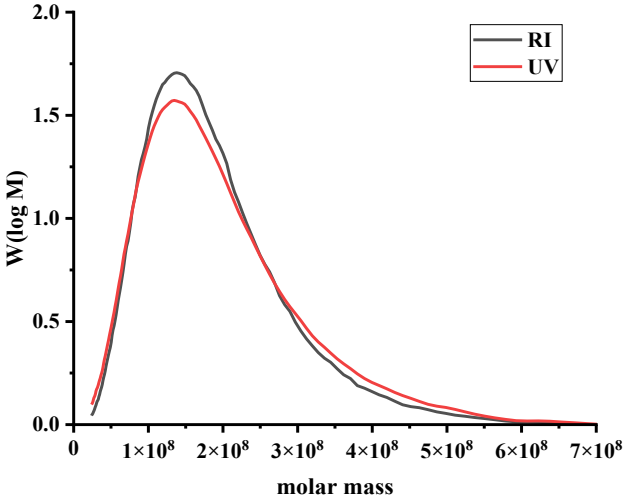


Figure S25: Aqueous GPC measurement of p(HEAA) ***P5****, eluent: PBS. LS Calculation.*

P6 – p(HEAA)

^{1}H-NMR (600 MHz, D_2O) δ (ppm) 7.27 – 7.05 (m, 5H, *H1*), 3.71 – 2.97 (m, *H5*, *H6*), 2.16 – 1.19 (m, *H2*, *H3*, *H4*, *H7*, *H8*). Pn ~ 235

^{19}F-NMR (564 MHz, D_2O) δ (ppm) No signals determined.

GPC (10 mM PBS, pH = 7.4, 298,15 K) *RI detector:* M_n = 21320 g/mol, M_w = 32360 g/mol, Đ = 1.52, *UV detector:* M_n = 16570 g/mol, M_w = 28120 g/mol, Đ = 1.70.

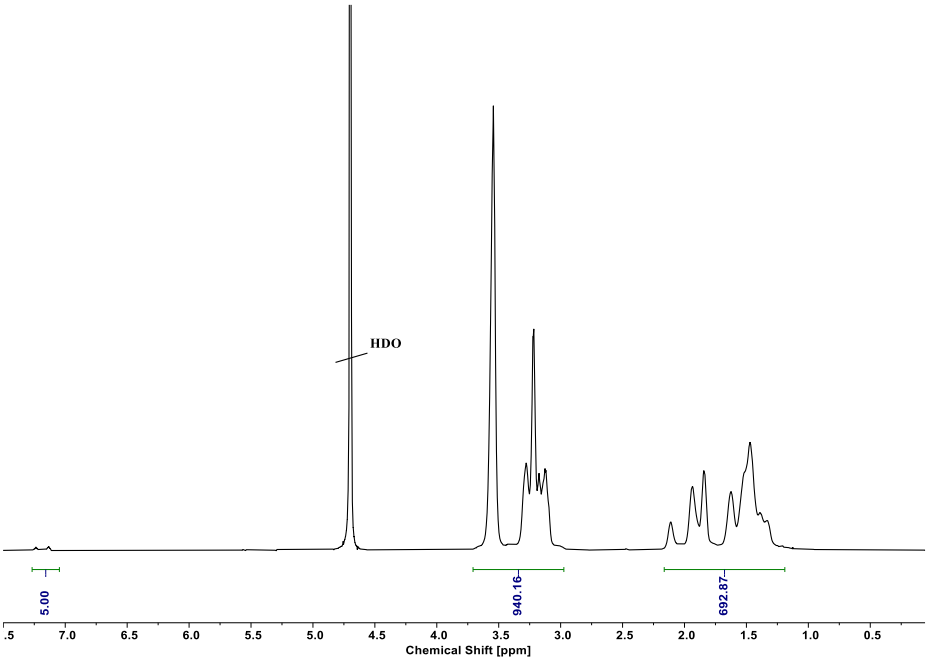


*Figure S26: ^{1}H-NMR spectra of p(HEAA) (****P6****) (600 MHz, D_2O).*

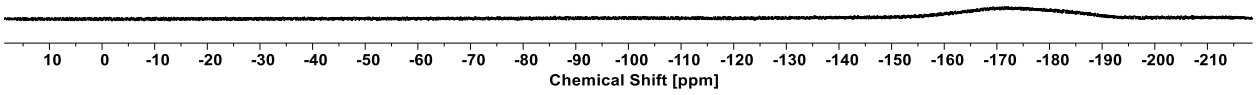


*Figure S27: ^{19}F-NMR spectra of p(HEAA) (**P6**) (600 MHz, D_2O).*

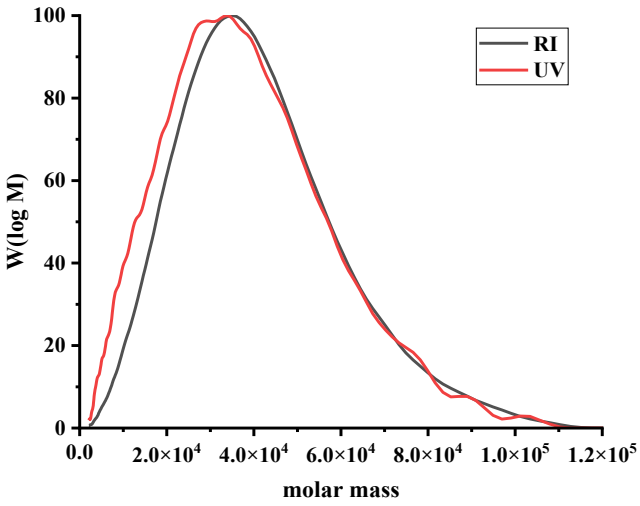


*Figure S28: Aqueous GPC measurement of p(HEAA) **P6**, eluent: PBS. RI Calculation.*

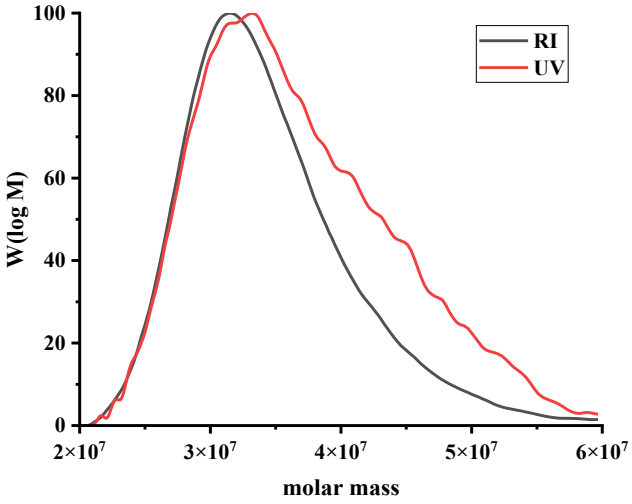
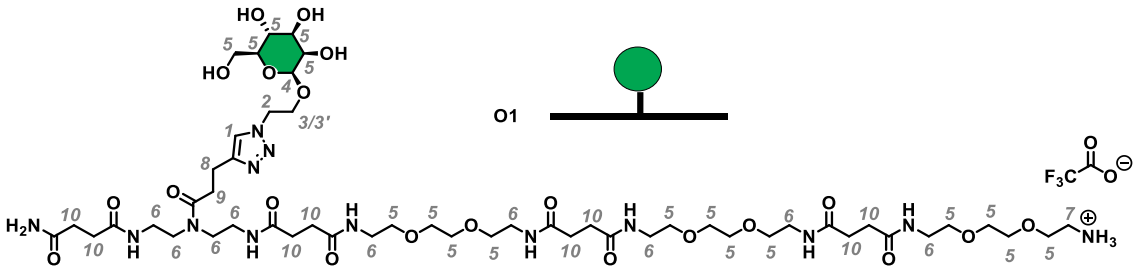


*Figure S29: Aqueous GPC measurement of p(HEAA) **P6**, eluent: PBS. LS Calculation.*

2.3 Oligoamidoamide synthesis of O1 and O2

Both mannose functionalized oligoamidoamides (O1, O2) were obtained by the application of solid phase synthesis, described in "1.3 General Methods". The structures were synthesized in 0.2 mmol scale, were received as a white powder (***O1***: 249.56 mg, 1.9 mmol, 94% yield, ***O2***: 351.76 mg, 0.2 mmol, 92% yield) and were used without further purification.

O1 – monovalent N-functional oligoamidoamide



^{1}H NMR (300 MHz, D_2O) *δ (ppm)* 7.94 (s, 1H, *H1*), 4.68 – 4.64 (m, 2H, *H2*), 4.14 – 4.04 (m, 1H, *H3*), 3.97 – 3.89 (m, 1H, *H3'*), 3.88 – 3.84 (dd, ^3J = 3.3, 1.8 Hz, 1H, *H4*), 3.78 – 3.56 (m, 30H, *H5*), 3.50 – 3.32 (m, 18H, *H6*), 3.24 – 3.19 (t, ^3J = 5.1 Hz, 2H, *H7*), 3.07 – 3.01 (m, 2H, *H8*), 2.84 – 2.78 (m, 2H, *H9*), 2.56 – 2.46 (m, 16H, *H10*).

For a more definite analysis, the oligoamidoamine was analyzed once with protective groups via PR-HPLC-MS and once without protective groups.

LC-MS m/z calculated for $C_{74}H_{109}N_{13}O_{27}$ (with protecting groups) $[M + H]^+$ 1612.8, found 1613.6, $[M + H]^{2+}$ 806.9 found 807.0, $[M + H]^{3+}$ 538.3 found 538.3, determined relative purity: > 95%

LC-MS m/z calculated for $C_{66}H_{100}N_{13}O_{23}$ $[M + H]^{2+}$ 611.8 found 611.9, $[M + H]^{3+}$ 408.2 found 408.0

HR-ESI-MS m/z calculated for $C_{66}H_{100}N_{13}O_{23}$ $[M + H]^{3+}$ 611.8298 found 611.8322

MALDI m/z calculated for $C_{66}H_{100}N_{13}O_{23}$ $[M + H]^+$ 1222.66 found 1222.78, $[M + Na]^+$ 1244.64 found 1244.76, $[M + K]^+$ 1260.61 found 1260.74

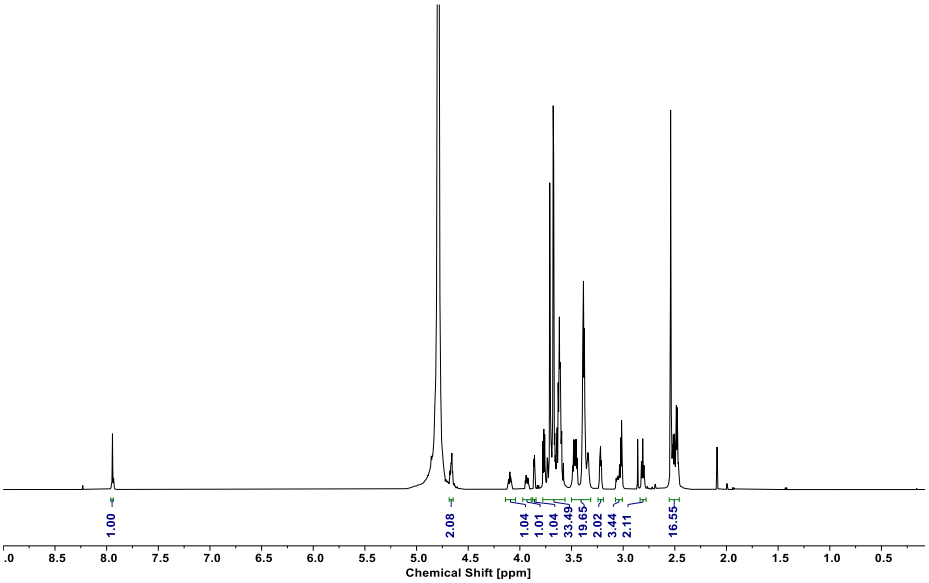


*Figure S30: [1]H-NMR spectra of monovalent oligoamidoamine (**O1**) (300 MHz, D_2O).*

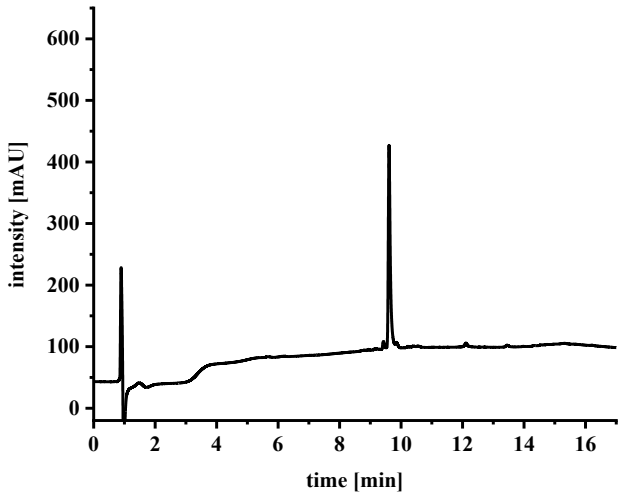


*Figure S31: RP-HPLC- chromatogram of monovalent oligoamidoamine (**O1**) with protecting groups (gradient of 5 to 95 vol% acetonitrile/water with 0.1 vol% formic acid, run time: 17 min).*

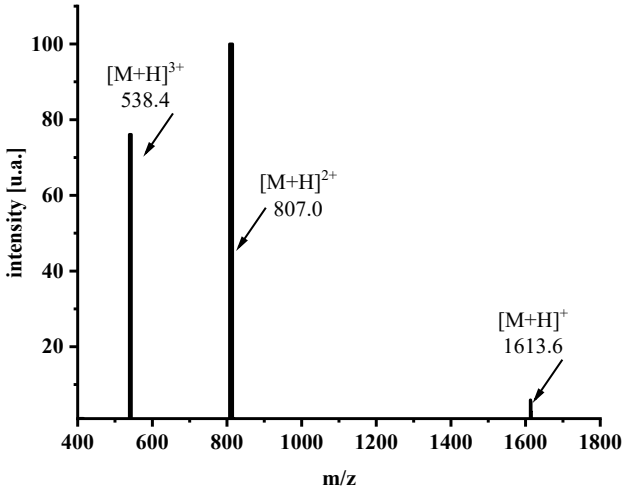


*Figure S32:ESI-MS spectra of monovalent oligoamidoamine (**O1**) with protecting groups at t = 9.61 min (gradient of 5 to 95 vol.% acetonitrile/water with 0.1 vol.% formic acid, run time: 17 min).*

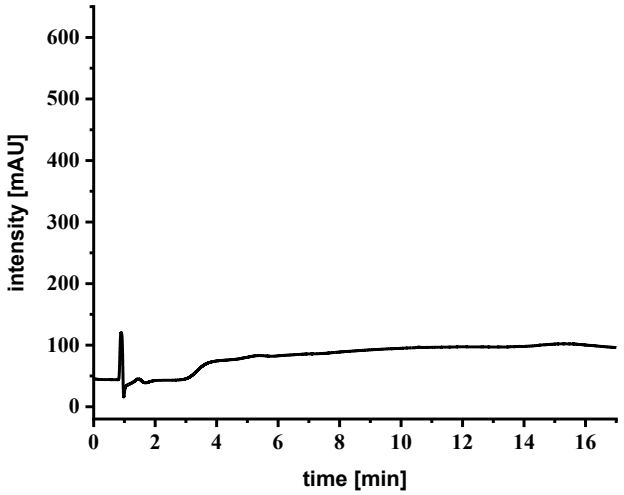


*Figure S33. RP-HPLC- chromatogram of monovalent oligoamidoamine (**O1**) (gradient of 5 to 95 vol% acetonitrile/water with 0.1 vol% formic acid, run time: 17 min). The product signal is detected in the injection peak.*

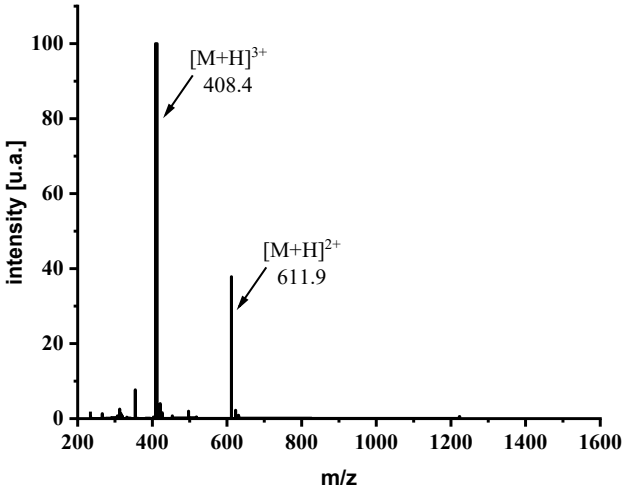


*Figure S34: ESI-MS spectra of monovalent oligoamidoamine (**O1**) at t = 0.89 min (gradient of 5 to 95 vol.% acetonitrile/water with 0.1 vol.% formic acid, run time: 17 min).*

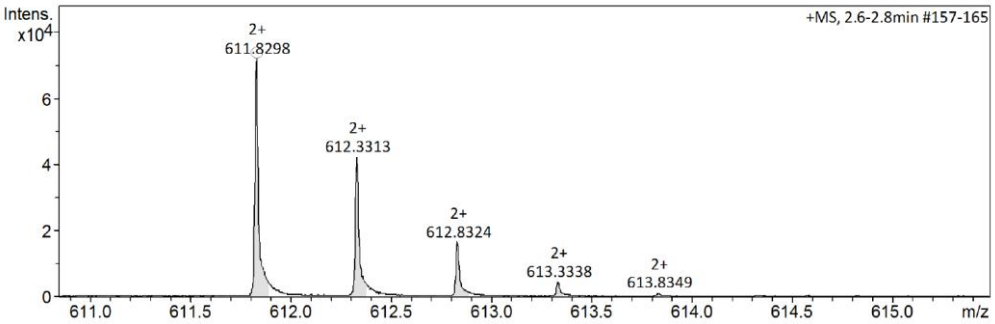


*Figure S35: HR-ESI-MS spectra of monovalent oligoamidoamine (**O1**).*

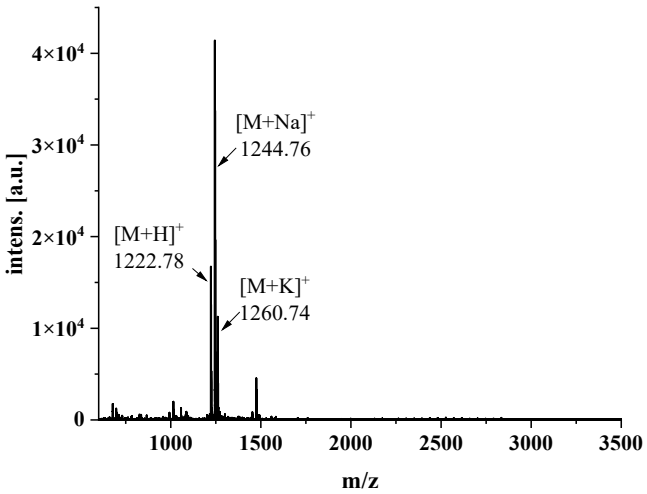
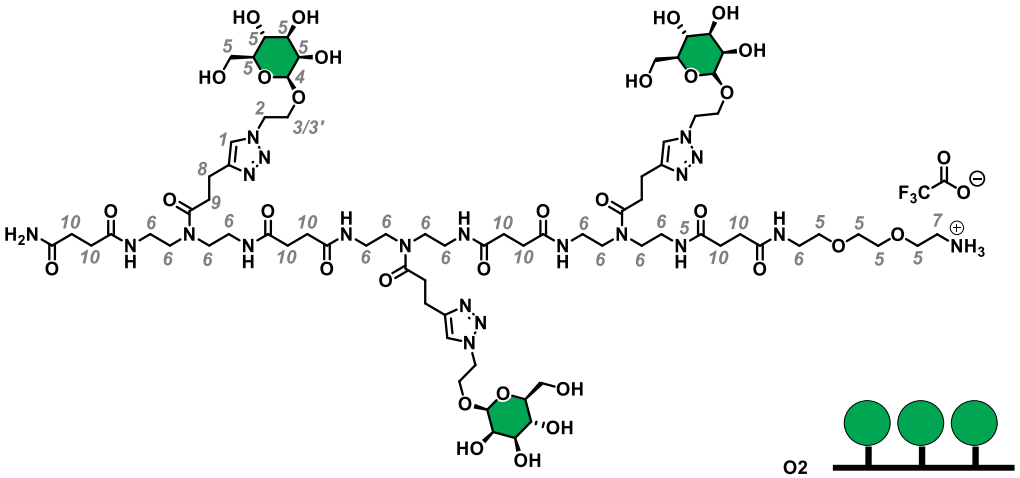


*Figure S36: MALDI spectra of chromatogram ofmonovalent oligoamidoamine (**O1**).*

O2 – trivalent N-functional oligoamidoamide



^{1}H NMR (300 MHz, D_2O) *δ (ppm)* 7.96 (s, 3H, *H1*), 4.70 – 4.659 (m, 6H, *H2*), 4.15 – 4.05 (m, 3H, *H3*), 3.99 – 3.88 (m, 3H, *H3'*), 3.88 – 3.83 (m, 3H, *H4*), 3.80 – 3. 53 (m, 26H, *H5*), 3.53 – 3.26 (m, 26H, *H6*), 3.25 – 3.18 (t, ^3J = 5.3 – 2.98 (m, 6H overlap with DMF peak, *H8*), 2.88 – 2.74 (m, 6H overlap with DMF peak, *H9*), 2.57 – 2.38 (m, 16H, *H10*).

For a more definite analysis, the oligoamidoamine was analyzed once with protective groups via PR-HPLC-MS and once without protective groups.

LC-MS m/z calculated for $C_{112}H_{157}N_{21}O_{45}$ (with protecting groups) $[M + H]^{2+}$ 1259.0, found 1259.4, $[M + H]^{3+}$ 839.7 found 840.0, $[M + H]^{4+}$ 630.0 found 630.2, determined relative purity: > 91%

LC-MS m/z calculated for $C_{73}H_{123}N_{21}O_{31}$ $[M + H]^{2+}$ 896.4 found 896.5, $[M + H]^{3+}$ 598.0 found 597.8, $[M + H]^{4+}$ 448.7 found 448.6

HR-ESI-MS m/z calculated for $C_{73}H_{123}N_{21}O_{31}$ $[M + H]^{3+}$ 597.6306 found 597.6308

MALDI m/z calculated for $C_{73}H_{123}N_{21}O_{31}$ $[M + H]^{+}$ 1790.88 found 1791.06, $[M + Na]^{+}$ 1812.86 found 1813.03, $[M + K]^{+}$ 1828.83 found 1829.02

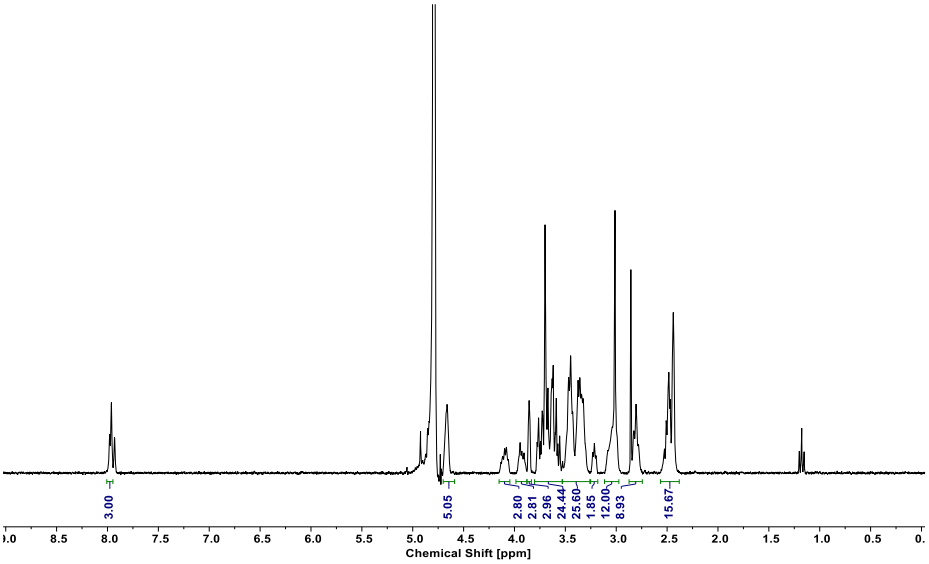


*Figure S37: [1]H-NMR spectra of trivalent oligoamidoamine (**O2**) (300 MHz, D_2O).*

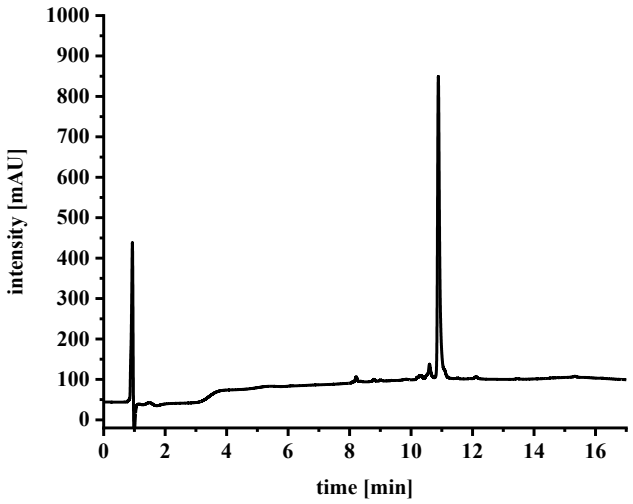


*Figure S38: RP-HPLC- chromatogram of trivalent oligoamidoamine (**O2**) with protecting groups (gradient of 5 to 95 vol% acetonitrile/water with 0.1 vol% formic acid, run time: 17 min).*

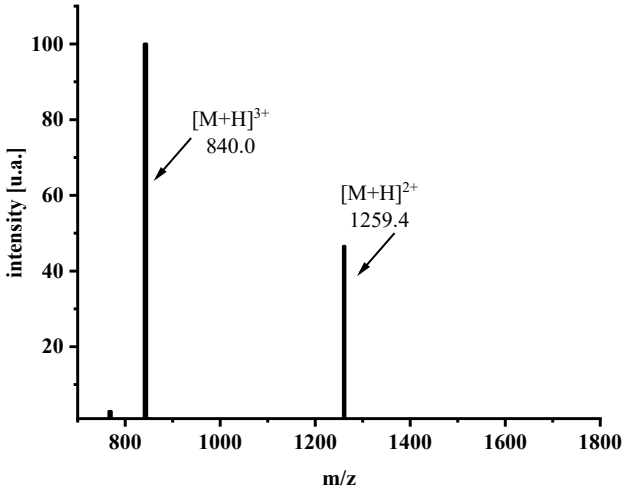


*Figure S39: ESI-MS spectra of trivalent oligoamidoamine (**O2**) with protecting groups at t = 10.88 min (gradient of 5 to 95 vol.% acetonitrile/water with 0.1 vol.% formic acid, run time: 17 min).*

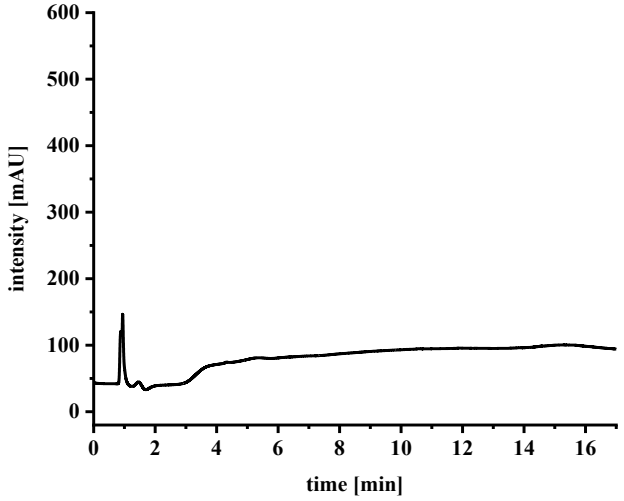


*Figure S40: RP-HPLC- chromatogram of trivalent oligoamidoamine (**O2**) (gradient of 5 to 95 vol% acetonitrile/water with 0.1 vol% formic acid, run time: 17 min). The product signal is detected in the injection peak.*

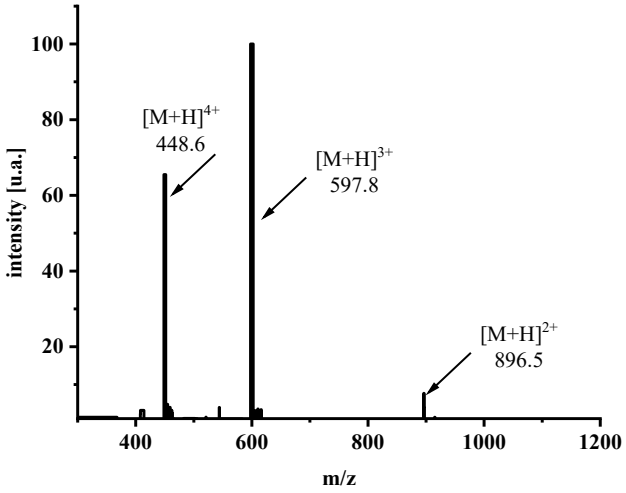


*Figure S41: ESI-MS spectra of trivalent oligoamidoamine (**O2**) at t = 0.94 min (gradient of 5 to 95 vol.% acetonitrile/water with 0.1 vol.% formic acid, run time: 17 min).*

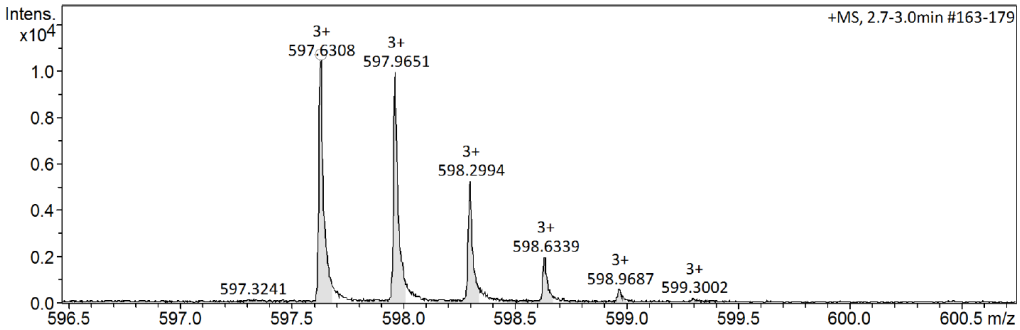


*Figure S42: HR-ESI-MS spectra of trivalent oligoamidoamine (**O2**).*

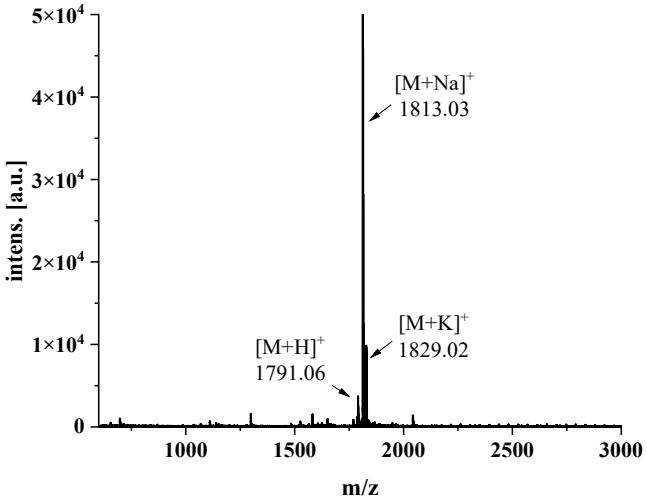
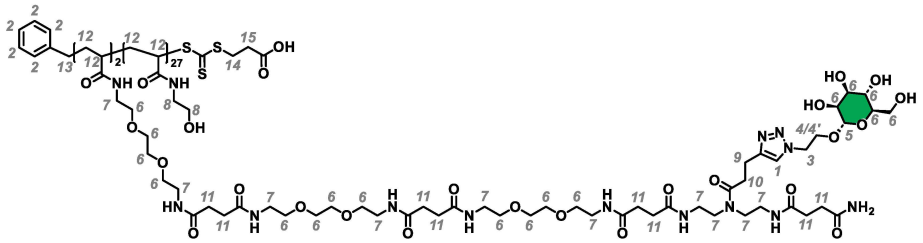


*Figure S43: MALDI spectra of trivalent oligoamidoamine (**O2**).*

2.4 Synthesis of side chain glycopolymers P7-P14

As all incorporation values brush and brush² structures are determined using ^{1}H-NMR spectroscopy in the following, the used molecular weights refer to the repeating units of polymers ***P4-6*** determined using ^{1}H-NMR.

P7 – ($_{2}E_{29}$)



The synthesized polymer ***P7*** were obtained by the application of *synthesis of brush-like glycopolymers (arm-structures) and linear reference structures*, described in "1.3 General Methods". 50 mg (7 µmol, 210.1 µmol related to the repetition unit) of p(PFPA) ***P1*** were functionalized with oligoamidoamine ***O1*** (5%, 13.85 mg, 10.5 µmol) quenched with ethanolamine and were received after dialysis as a white powder (17.59 mg, 7% incorporation, 2.9 µmol, 42% yield).

^{1}H-NMR (600 MHz, D_2O) δ (ppm) 7.87 (s, 2H, *H1*), 7.35 – 7.05 (m, 5H, *H2*), 4.67 – 4.59 (m, *H3,* overlap with water peak), 4.12 – 4.04 (m, *H4*), 3.95 – 3.88 (m, *H4'*), 3.88 – 3.84 (m, *H5*), 3.83 – 3.09 (m, *H6* - *H8*), 3.04 – 0.86 (m, *H9- H 15*).

^{19}F-NMR (564 MHz, D_2O) δ (ppm) No signals determined.

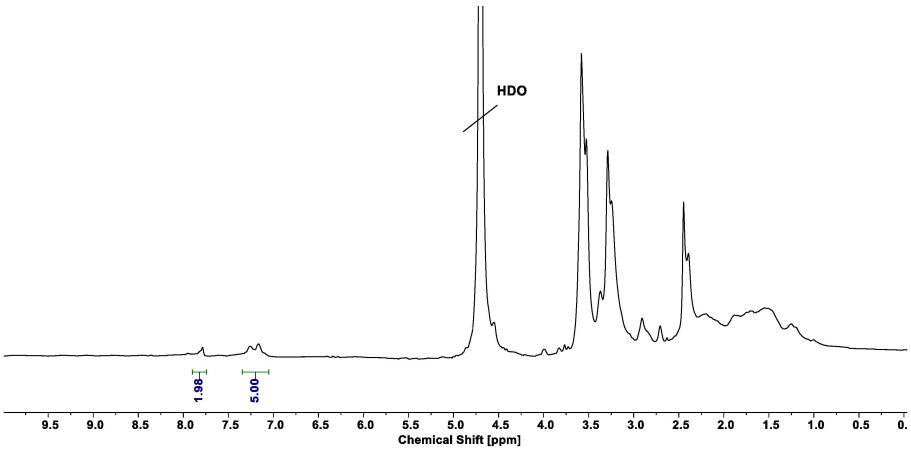


*Figure S44: ^{1}H-NMR spectra of $_{2}E_{29}$ (**P7**) (600 MHz, D_2O).*

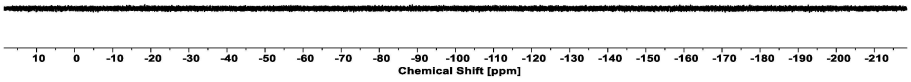
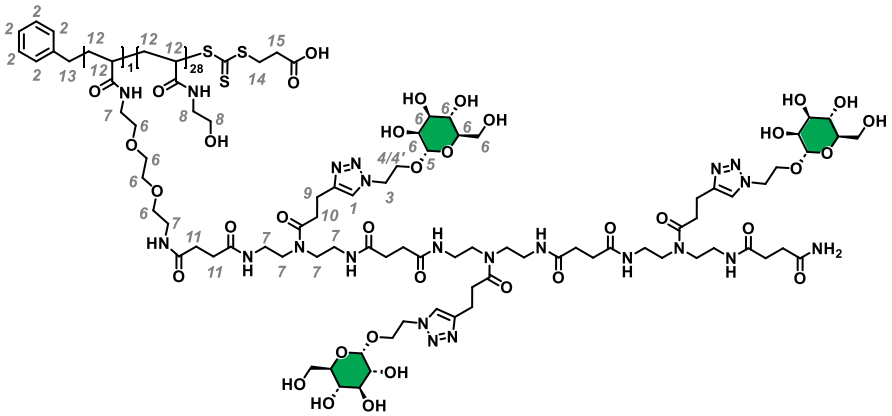


*Figure S45: ^{19}F-NMR spectra of $_{2}E_{29}$ (**P7**) (564 MHz, D_2O).*

P8 – ($_6E_{29}$)



The synthesized polymer ***P8*** were obtained by the application of *synthesis of brush-like glycopolymers (arm-structures) and linear reference structures*, described in "1.3 General Methods". 50 mg (7 µmol, 210.1 µmol related to the repetition unit) of p(PFPA) ***P1*** were functionalized with oligoamidoamine ***O2*** (5%, 19.84 mg, 10.5 µmol) quenched with ethanolamine and were received after dialysis as a white powder (17.8 mg, 3% incorporation, 5.22 µmol, 75% yield).

^{1}H-NMR (300 MHz, D_2O) δ (ppm) 7.87 (s, 3H, *H1*), 7.47 – 7.16 (m, 5H, *H2*), 4.72 – 4.54 (m, *H3*), 4.14 – 4.02 (m, *H4*), 3.97 – 3.83 (m, *H4', H5*), 3.83 – 3.53 (m, *H6*, *H8*), 3.53 – 3.14 (m, *H7*, *H8*), 3.06 – 2.87 (m, *H9*), 2.87 – 2.72 (m, *H10*), 2.58 – 2.38 (m, *H11*), 3.08 – 0.99 (m, *H12 – H15*).

^{19}F-NMR (282 MHz, D_2O) δ (ppm) No signals determined.

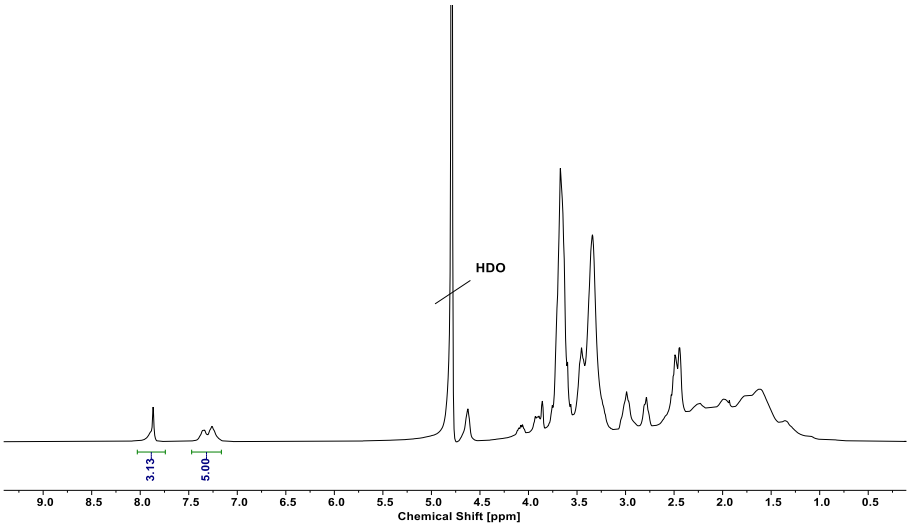


*Figure S46: ^{1}H-NMR spectra of $_6E_{29}$ (**P8**) (300 MHz, D_2O).*

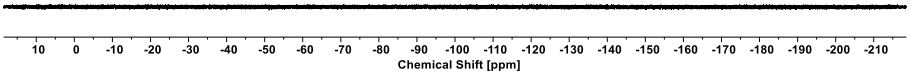
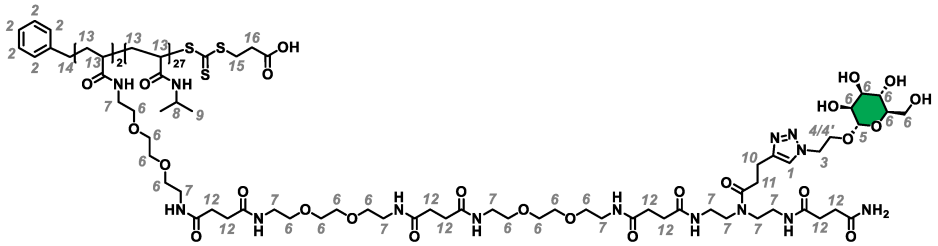


*Figure S47: ^{19}F-NMR spectra of $_6E_{29}$ (**P8**) (282 MHz, D_2O).*

P9 – ($_2I_{29}$)



The synthesized polymer ***P9*** were obtained by the application of *synthesis of brush-like glycopolymers (arm-structures) and linear reference structures*, described in "1.3 General Methods". 50 mg (7 µmol, 210.1 µmol related to the repetition unit) of p(PFPA) ***P1*** were functionalized with oligoamidoamine ***O1*** (5%, 13.85 mg, 10.5 µmol) quenched with isopropylamine and were received after dialysis as a white powder (20.10 mg, 7% incorporation, 3.43 µmol, 49% yield).

^{1}H-NMR (600 MHz, D_2O) δ (ppm) 7.87 (s, 2H, *H1*), 7.44 – 7.06 (m, 5H, *H2*), 4.67 – 4.57 (m, *H3,* overlap with water peak), 4.22 – 3.79 (m, *H4, H4', H5, H8*), 3.75 – 3.53 (m, *H6*) 3.53 – 3.20 (m, *H7*), 3.08 – 2.96 (m, *H10*), 2.86 – 2.74 (m, *H11)*, 2.70 – 2.40 (m, *H12*), 1.26 – 0.96 (m, *H9*), 3.14 – 0.48 (m, *H13- H16*).

^{19}F-NMR (282 MHz, D_2O) δ (ppm) No signals determined.

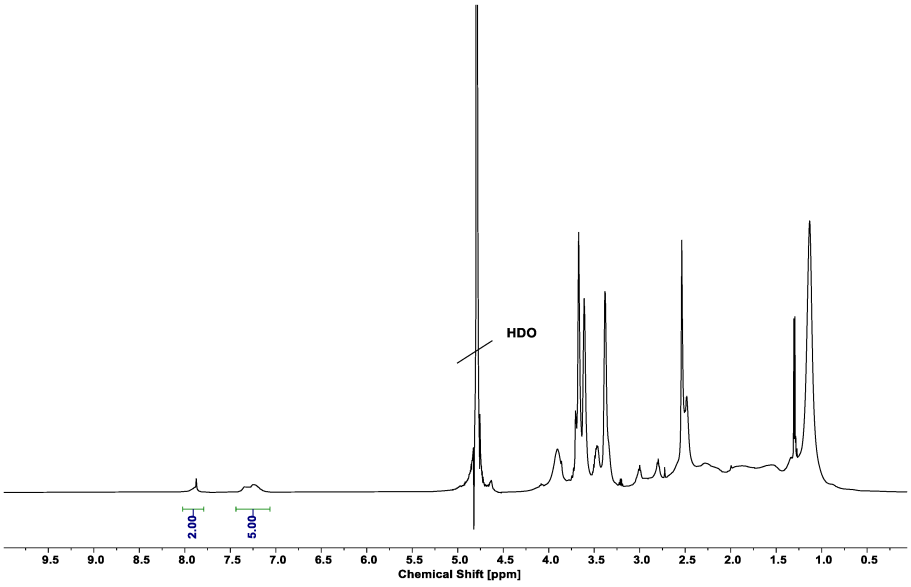


*Figure S48: ^{1}H-NMR spectra of $_2I_{29}$ (**P9**) (600 MHz, D_2O).*

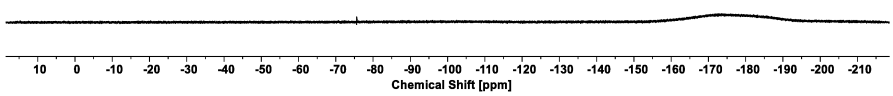
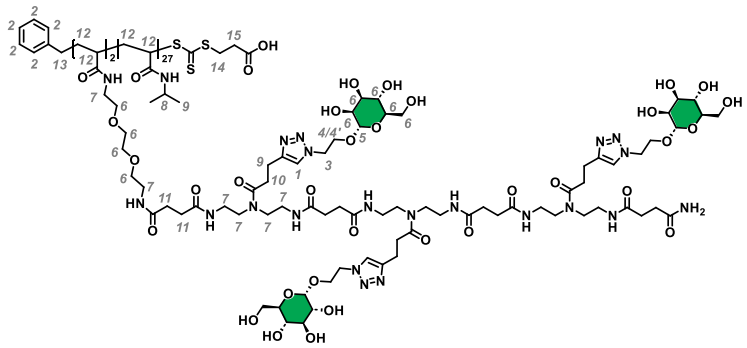


*Figure S49: ^{19}F-NMR spectra of $_2I_{29}$ (**P9**) (564 MHz, D_2O).*

P10 – ($_6I_{29}$)



The synthesized polymer ***P10*** were obtained by the application of *synthesis of brush-like glycopolymers (arm-structures) and linear reference structures*, described in "1.3 General Methods". 50 mg (7 µmol, 210.1 µmol related to the repetition unit) of p(PFPA) ***P1*** were functionalized with oligoamidoamine ***O2*** (5%, 19.84 mg, 10.5 µmol) quenched with isopropylamine and were received after dialysis as a white powder (28.06 mg, 7% incorporation, 4.0 µmol, 57% yield).

^{1}H-NMR (300 MHz, D_2O) δ (ppm) 7.87 (s, 5H, *H1*), 7.39 – 7.17 (m, 5H, *H2*), 4.70 – 4.55 (m, *H3*), 4.16 – 3.79 (m, *H4, H4', H5, H8*), 3.80 – 3.54 (m, *H6*), 3.54 – 3.17 (m, *H7*), 3.08 – 2.89 (m, *H9*), 2.89 – 2.71 (m, *H10*), 2.57 – 2.36 (m, *H11*), 1.25 – 0.93 (m, *H9*), 3.15 – 0.46 (m, *H12 – H15*).

^{19}F-NMR (282 MHz, D_2O) δ (ppm) No signals determined.

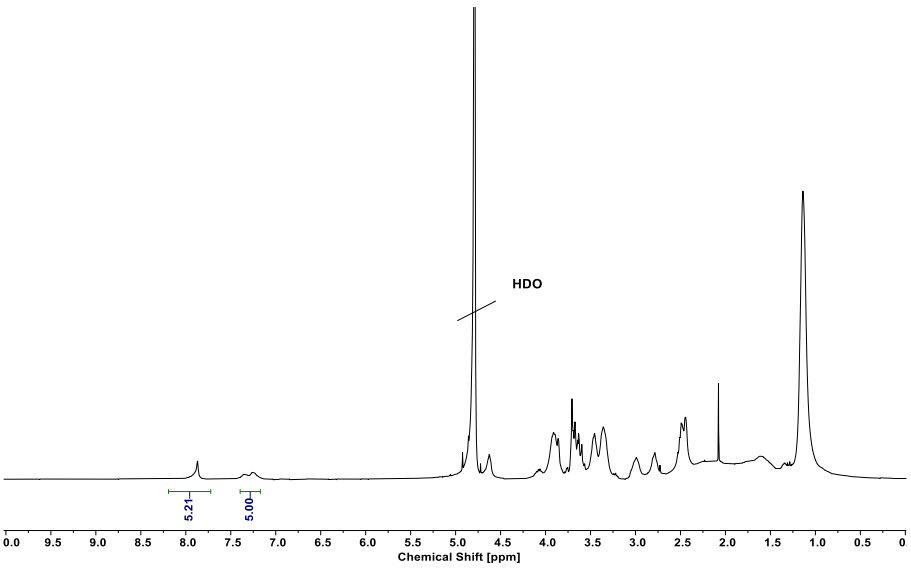


*Figure S50: ^{1}H-NMR spectra of $_6I_{29}$ (**P10**) (300 MHz, D_2O).*

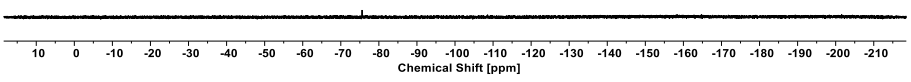
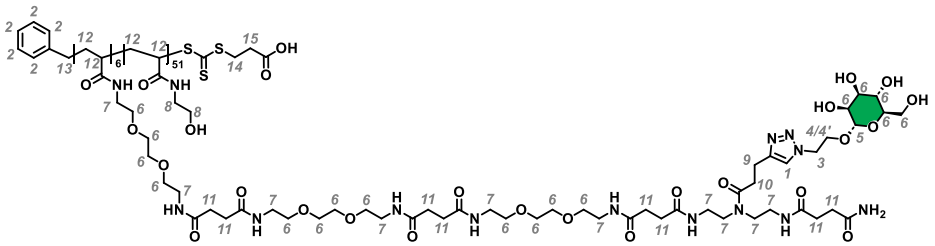


*Figure S51: ^{19}F-NMR spectra of $_6I_{29}$ (**P10**) (282 MHz, D_2O).*

P11 – ($_6E_{57}$)



The synthesized polymer ***P11*** were obtained by the application of *synthesis of brush-like glycopolymers (arm-structures) and linear reference structures*, described in "1.3 General Methods". 50 mg (3.6 µmol, 210.1 µmol related to the repetition unit) of p(PFPA) ***P2*** were functionalized with oligoamidoamine ***O1*** (15%, 41.55 mg, 31.51 µmol) quenched with ethanolamine and were received after dialysis as a white powder (38.18 mg, 11% incorporation, 2.77 µmol, 77% yield).

^{1}H-NMR (600 MHz, D_2O) δ (ppm) 7.88 (s, 6H, *H1*), 7.38 – 7.10 (m, 5H, *H2*), 4.66 – 4.61 (m, *H3,* overlap with water peak), 4.11 – 4.06 (m, *H4*), 3.94 – 3.89 (m, *H4'*), 3.87 – 3.85 (m, *H5*), 3.79 – 3.17 (m, *H6* - *H8*), 3.06 – 1.03 (m, *H9* – *H15*).

^{19}F-NMR (282 MHz, D_2O) δ (ppm) No signals determined.

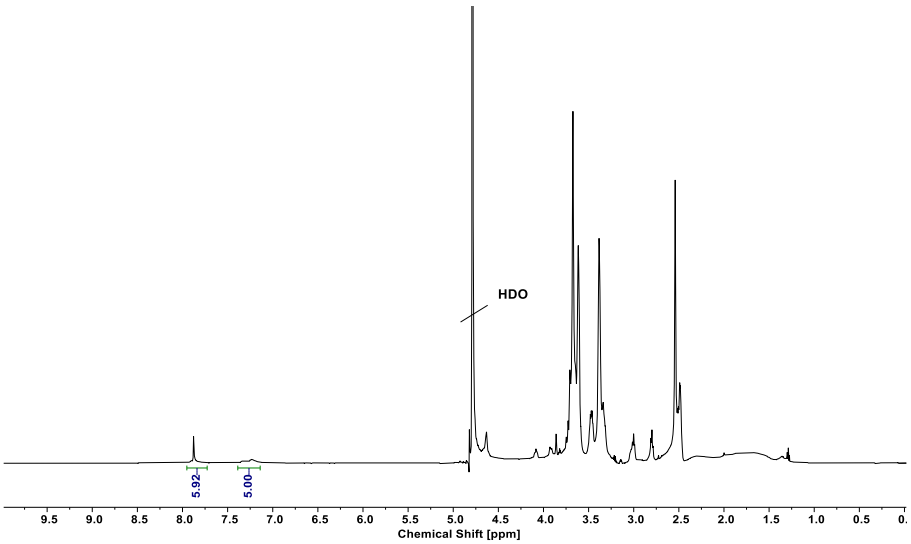


*Figure S52: ^{1}H-NMR spectra of $_6E_{57}$ (**P11**) (600 MHz, D_2O).*

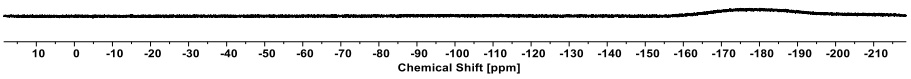
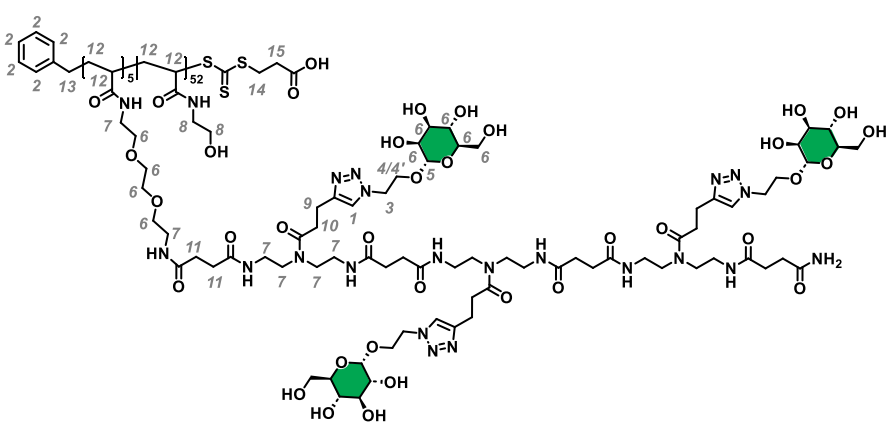


*Figure S53: ^{19}F-NMR spectra of $_6E_{57}$ (**P11**) (564 MHz, D_2O).*

P12 – ($_{18}E_{57}$)



The synthesized polymer ***P12*** were obtained by the application of *synthesis of brush-like glycopolymers (arm-structures) and linear reference structures*, described in "1.3 General Methods". 50 mg (3.6 µmol, 210.1 µmol related to the repetition unit) of p(PFPA) ***P2*** were functionalized with oligoamidoamine ***O2*** (15%, 59.52 mg, 31.51 µmol) quenched with ethanolamine and were received after dialysis as a white powder (40.49 mg, 9% incorporation, 2.62 µmol, 73% yield).

^{1}H-NMR (300 MHz, D_2O) δ (ppm) 7.87 (s, 3H, *H1*), 7.47 – 7.10 (m, 5H, *H2*), 4.72 – 4.55 (m, *H3*), 4.13 – 4.02 (m, *H4*), 3.96 – 3.82 (m, *H4', H5*), 3.80 – 3.54 (m, *H6*, *H8*), 3.54 – 3.14 (m, *H7*, *H8*), 3.08 – 2.88 (m, *H9*), 2.88 – 2.71 (m, *H10*), 2.57 – 2.35 (m, *H11*), 3.12 – 0.57 (m, *H12 – H15*).

^{19}F-NMR (282 MHz, D_2O) δ (ppm) No signals determined.

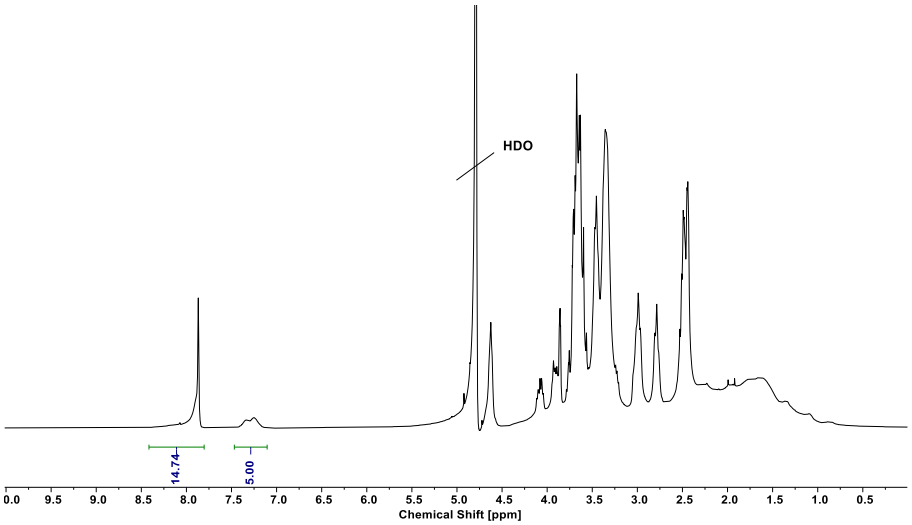


*Figure S54: ^{1}H-NMR spectra of $_{18}E_{57}$ (**P12**) (300 MHz, D_2O).*

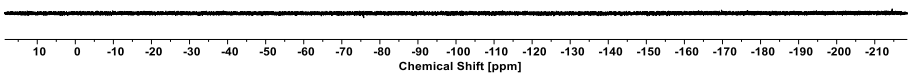
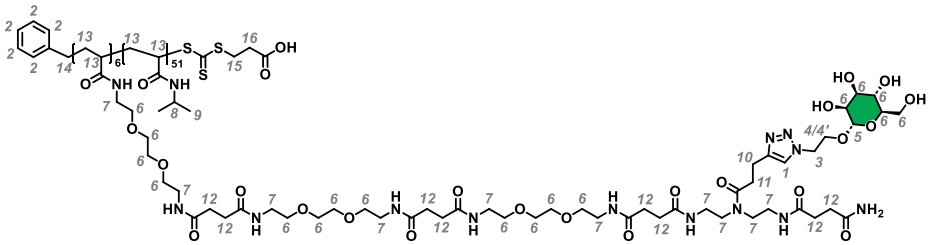


*Figure S55: ^{19}F-NMR spectra of $_{18}E_{57}$ (**P12**) (282 MHz, D_2O).*

P13 – ($_6I_{57}$)



The synthesized polymer ***P13*** were obtained by the application of *synthesis of brush-like glycopolymers (arm-structures) and linear reference structures*, described in "1.3 General Methods". 50 mg (3.6 µmol, 210.1 µmol related to the repetition unit) of p(PFPA) ***P2*** were functionalized with oligoamidoamine ***O1*** (15%, 41.55 mg, 31.51 µmol) quenched with isopropylamine and were received after dialysis as a white powder (39.57 mg, 11% incorporation, 2.89 µmol, 80% yield).

^{1}H-NMR (300 MHz, D_2O) δ (ppm) 7.87 (s, 6H, *H1*), 7.41 – 7.11 (m, 5H, *H2*), 4.69– 4.57 (m, *H3,* overlap with water peak), 4.11 – 4.05 (m, *H4*), 3.99 – 3.84 (m, *H4', H5, H8*), 3.75 – 3.52 (m, *H6*) 3.52 – 3.28 (m, *H7, H8*), 3.05 – 2.96 (m, *H10*), 2.85 – 2.74 (m, *H11)*, 2.67 – 2.41 (m, *H12*), 1.24– 0.95 (m, *H9*), 3.14 – 0.74 (m, *H13- H16*).

^{19}F-NMR (282 MHz, D_2O) δ (ppm) No signals determined.

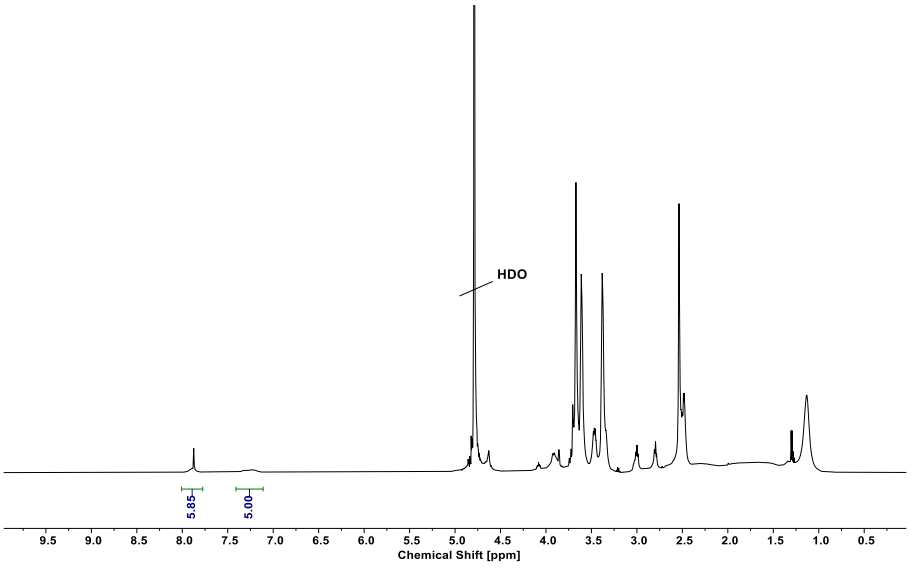


*Figure S56: ^{1}H-NMR spectra of $_6I_{57}$ (**P13**) (600 MHz, D_2O).*

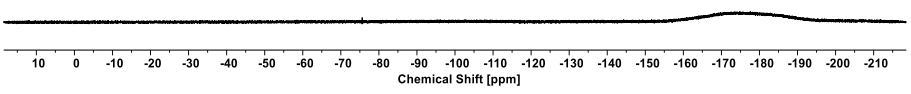
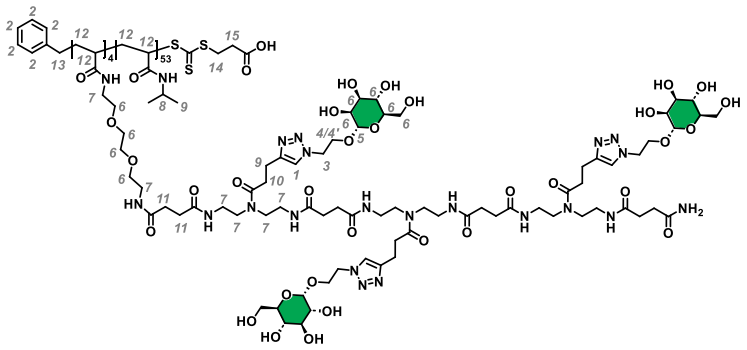


*Figure S57: ^{19}F-NMR spectra of $_6I_{57}$ (**P13**) (564 MHz, D_2O).*

P14 – ($_{18}I_{57}$)



The synthesized polymer ***P14*** were obtained by the application of *synthesis of brush-like glycopolymers (arm-structures) and linear reference structures*, described in "1.3 General Methods". 50 mg (3.6 µmol, 210.1 µmol related to the repetition unit) of p(PFPA) ***P2*** were functionalized with oligoamidoamine ***O2*** (15%, 59.52 mg, 31.51 µmol) quenched with isopropylamine and were received after dialysis as a white powder (34.5 mg, 7% incorporation, 2.53 µmol, 70% yield).

^{1}H-NMR (300 MHz, D_2O) δ (ppm) 7.87 (s, 12H, *H1*), 7.43 – 7.05 (m, 5H, *H2*), 4.71 – 4.54 (m, *H3*), 4.12 – 4.01 (m, *H4*), 4.01 – 3.80 (m, *H4', H5, H8*), 3.80 – 3.55 (m, *H6*), 3.55 – 3.16 (m, *H7*), 3.07 – 2.89 (m, *H9*), 2.89 – 2.72 (m, *H10*), 2.58 – 2.34 (m, *H11*), 1.27 – 0.95 (m, *H9*), 3.14 – 0.56 (m, *H12 – H15*).

^{19}F-NMR (282 MHz, D_2O) δ (ppm) No signals determined.

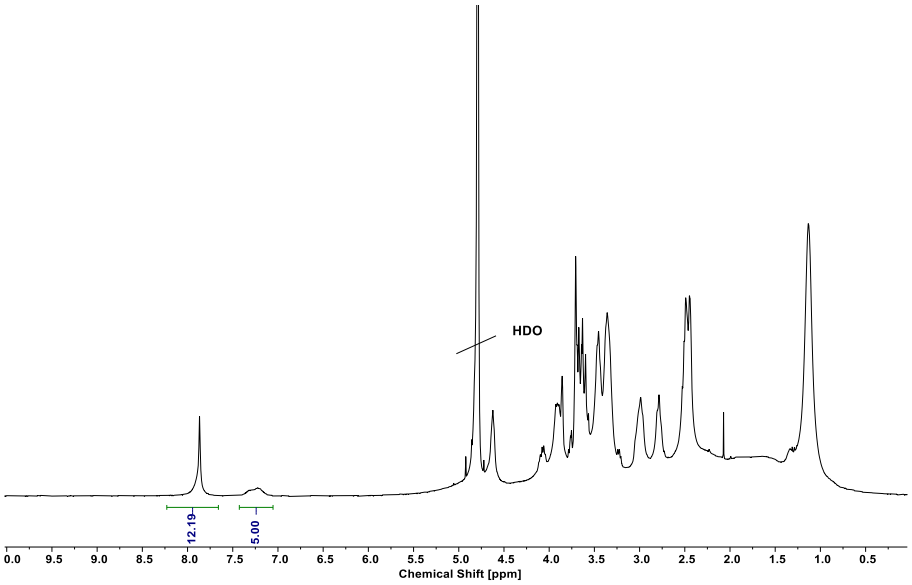


*Figure S58: ^{1}H-NMR spectra of $_{18}I_{57}$ (**P14**) (300 MHz, D_2O).*

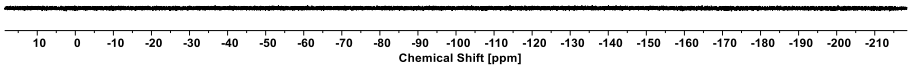
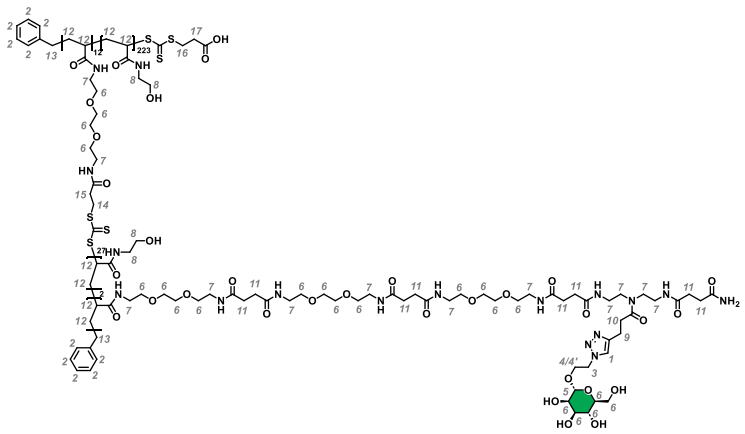


*Figure S59: ^{19}F-NMR spectra of $_{18}I_{57}$ (**P14**) (282 MHz, D_2O).*

2.5 Synthesis of brush²-glycopolymers B1-B16

B1 – ($_{22}E^{2}_{29}$)



The synthesized brush² glycopolymer ***B1*** were obtained by the application of two steps: (1) *Attachment of the bridge molecule to arm polymers,* followed by *Cleavage of the protecting group of the conjugated bridge molecule* (2) *Attachment of the amine-activated arm polymers to the long polymer to gain brush² structures* described in "1.3 General Methods". 13 mg (0.23 µmol, 54.62 µmol related to the repetition unit) of p(PFPA) ***P3*** were functionalized with amine-preactivated arm polymer with comes from ***P7*** (5%, 16.79 mg, 2.73 µmol) quenched with ethanolamine and were received after dialysis as a white powder (13.77 mg, 5% incorporation, 0.14 µmol, 61% yield).

^{1}H-NMR (600 MHz, D_2O) δ (ppm) 7.88 (s, 24H, *H1*), 7.43 – 6.94 (m, 65H, *H2*), 4.66 – 4.59 (m, *H3,* overlap with water peak), 4.12 – 4.05 (m, *H4*), 3.96 – 3.12 (m, *H4', H5 - H8*), 3.05 – 2.97 (m, *H9*), 2.97 – 2.87 (m, *H15*), 2.87 – 2.76 (m, *H10*), 2.64 – 2.42 (m, *H11*), 3.11 – 0.79 (m, *H12- H 14, H16, H17*).

^{19}F-NMR (282 MHz, D_2O) δ (ppm) No signals determined.

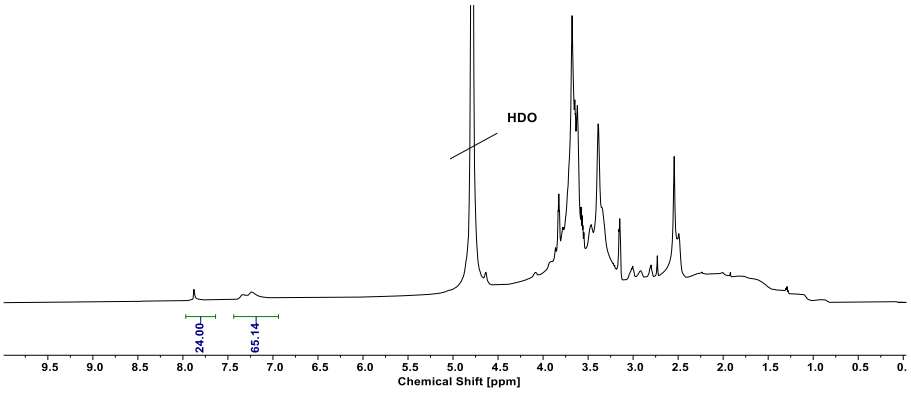


*Figure S60: ^{1}H-NMR spectra of $_{22}B^{2}_{29}$ (**B1**) (600 MHz, D_2O).*

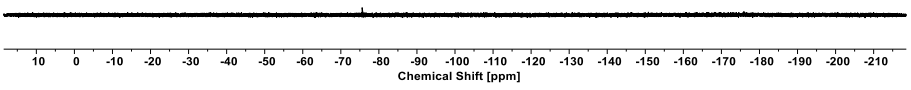
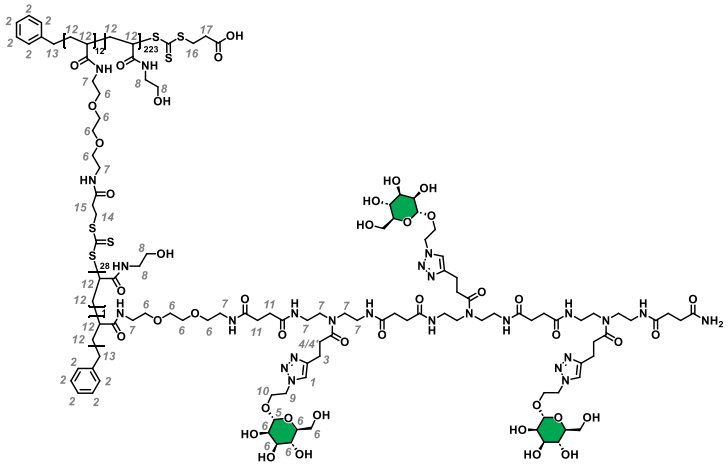


*Figure S61: ^{19}F-NMR spectra of $_{22}B^{2}_{29}$ (**B1**) (564 MHz, D_2O).*

B2 – ($_{66}E^{2}_{29}$)



The synthesized brush² glycopolymer ***B2*** were obtained by the application of two steps: (1) *Attachment of the bridge molecule to arm polymers,* followed by *Cleavage of the protecting group of the conjugated bridge molecule* (2) *Attachment of the amine-activated arm polymers to the long polymer to gain brush² structures* described in "1.3 General Methods". 18 mg (0.32 µmol, 75.7 µmol related to the repetition unit) of p(PFPA) ***P3*** were functionalized with amine-preactivated arm polymer with comes from ***P8*** (5%, 23.6 mg, 3.8 µmol) quenched with ethanolamine and were received after dialysis as a white powder (15.79 mg, 5% incorporation, 0.17 µmol, 53% yield).

^{1}H-NMR (300 MHz, D_2O) δ (ppm) 7.89 (s, 36H, *H1*), 7.49 – 7.18 (m, 66H, *H2*), 4.67 – 4.55 (m, *H3*, overlap with water), 4.16 – 4.01 (m, *H4*), 4.01 – 0.00 (m, H4'-H17).

^{19}F-NMR (282 MHz, D_2O) δ (ppm) No signals determined.

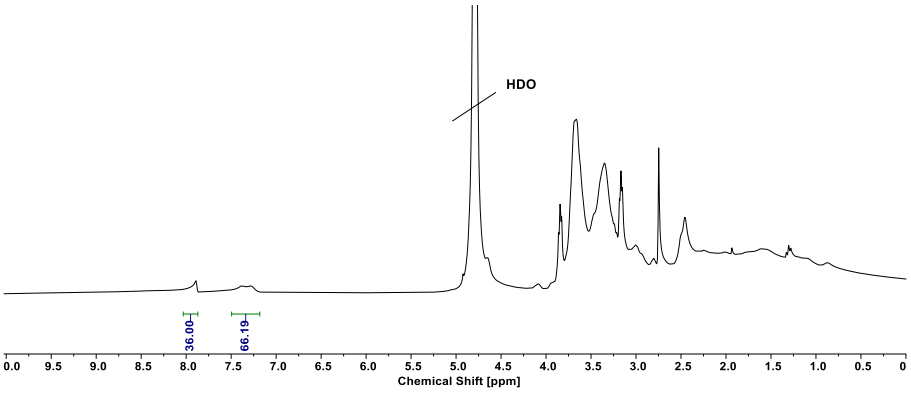


*Figure S62: ^{1}H-NMR spectra of $_{66}\boldsymbol{B^{2}_{29}}$ (**B2**) (300 MHz, D_2O).*

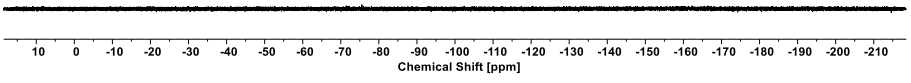
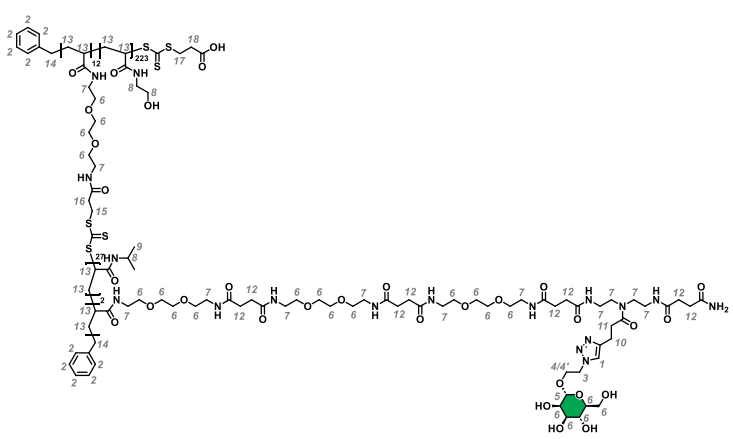


*Figure S63: ^{19}F-NMR spectra of $_{66}\boldsymbol{B^{2}_{29}}$ (**B2**) (282 MHz, D_2O).*

B3 – ($_{22}I^{2}_{29}$)



The synthesized brush² glycopolymer ***B3*** were obtained by the application of two steps: (1) *Attachment of the bridge molecule to arm polymers,* followed by *Cleavage of the protecting group of the conjugated bridge molecule* (2) *Attachment of the amine-activated arm polymers to the long polymer to gain brush² structures* described in "1.3 General Methods". 20 mg (0.36 µmol, 84.03 µmol related to the repetition unit) of p(PFPA) ***P3*** were functionalized with amine-preactivated arm polymer with comes from ***P9*** (5%, 25.60 mg, 4.20 µmol) quenched with ethanolamine and were received after dialysis as a white powder (26.75 mg, 5% incorporation, 0.27 µmol, 75% yield, slight impurities with ethanolamine).

^{1}H-NMR (300 MHz, D_2O) δ (ppm) 7.87 (s, 24H, *H1*), 7.60 – 7.07 (m, 65H, *H2*), 4.65 – 4.58 (m, *H3,* overlap with water peak), 4.11 – 3.76 (m, *H4, H4', H5, H8*), 3.76 – 3.51 (m, *H6*) 3.51 – 3.06 (m, *H7*), 3.06 – 2.96 (m, *H10*), 2.96- 2.84 (m, *H16*), 2.85 – 2.75 (m, *H11)*, 2.65 – 2.34 (m, *H12*), 1.26 – 0.95 (m, *H9*), 3.14 – 0.48 (m, *H13 - H15, H17, H18*).

^{19}F-NMR (282 MHz, D_2O) δ (ppm) No signals determined.

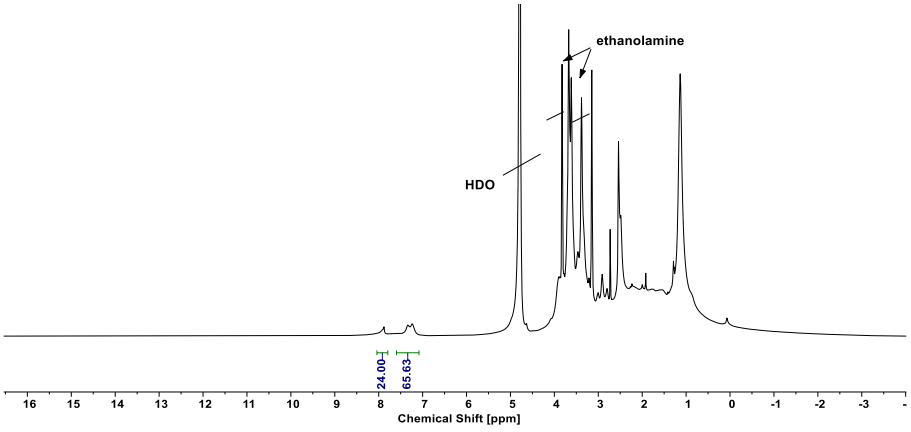


*Figure S64: ^{1}H-NMR spectra of $_{22}I^{2}_{29}$ (**B3**) (600 MHz, D_2O).*

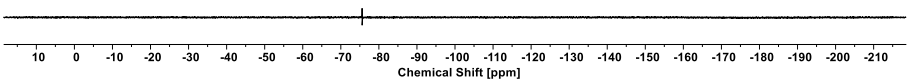
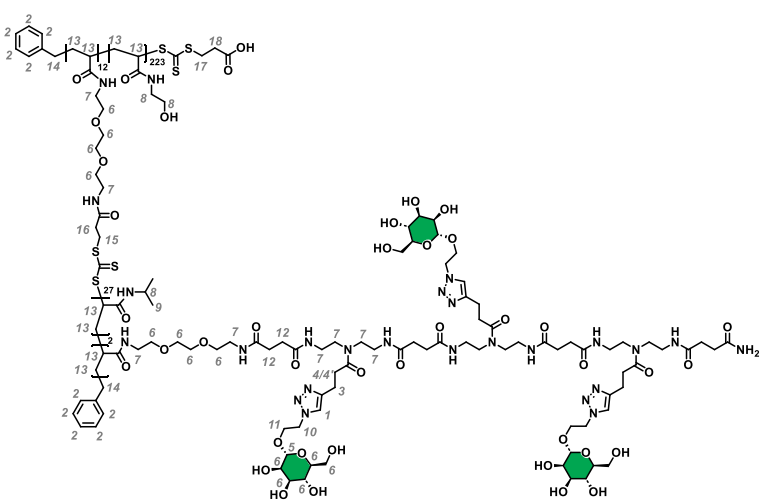


*Figure S65: ^{19}F-NMR spectra of $_{22}I^{2}_{29}$ (**B3**) (564 MHz, D_2O).*

B4 – ($_{66}I^{2}_{29}$)



The synthesized brush² glycopolymer ***B4*** were obtained by the application of two steps: (1) *Attachment of the bridge molecule to arm polymers,* followed by *Cleavage of the protecting group of the conjugated bridge molecule* (2) *Attachment of the amine-activated arm polymers to the long polymer to gain brush² structures* described in "1.3 General Methods". 16 mg (0.28 µmol, 67.22 µmol related to the repetition unit) of p(PFPA) ***P3*** were functionalized with amine-preactivated arm polymer with comes from ***P10*** (5%, 24.30 mg, 3.36 µmol) quenched with ethanolamine and were received after dialysis as a white powder (20.10 mg, 5% incorporation, 0.18 µmol, 64% yield, slight impurities with ethanolamine).

^{1}H-NMR (300 MHz, D_2O) δ (ppm) 7.89 (s, 72H, *H1*), 7.48 – 7.17 (m, 67H, *H2*), 4.68 – 4.58 (m, *H3,* overlap with water peak), 4.32 – 3.10 (m, *H4, H4', H5 – H8)*, 3.09 – 2.87 (m, *H10, H16*), 2.87 – 2.71 (m, *H11*), 2.58 – 2.35 (m, *H12*), 1.28 – 0.83 (m, *H9*), 3.11 – 0.46 (m, *H13 – H15, H17, H18*).

^{19}F-NMR (282 MHz, D_2O) δ (ppm) No signals determined.

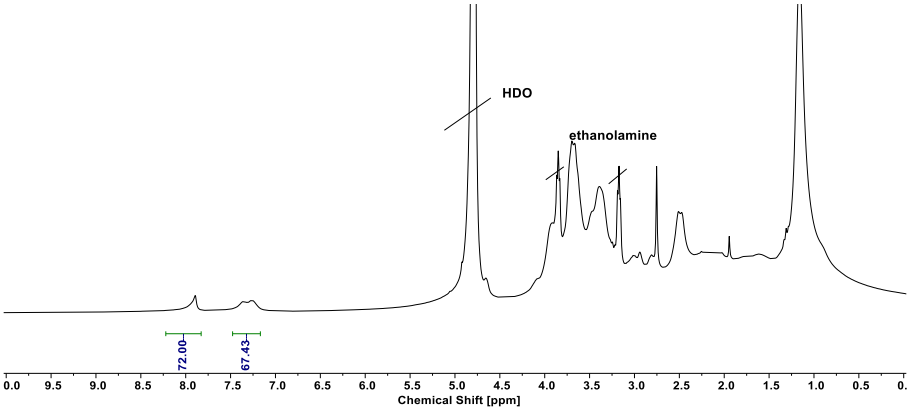


*Figure S66: ^{1}H-NMR spectra of $_{66}I^{2}_{29}$ (**B4**) (300 MHz, D_2O).*

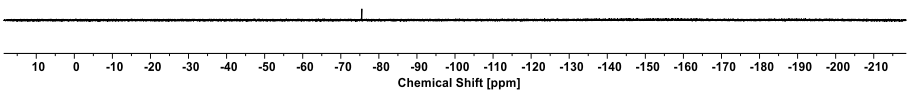
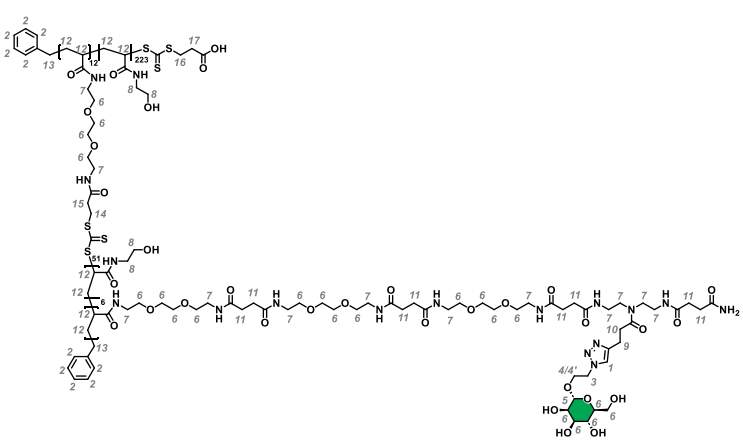


*Figure S67: ^{19}F-NMR spectra of $_{66}I^{2}_{29}$ (**B4**) (282 MHz, D_2O).*

B5 – ($_{66}E^{2}_{57}$)



The synthesized brush² glycopolymer ***B5*** were obtained by the application of two steps: (1) *Attachment of the bridge molecule to arm polymers,* followed by *Cleavage of the protecting group of the conjugated bridge molecule* (2) *Attachment of the amine-activated arm polymers to the long polymer to gain brush² structures* described in "1.3 General Methods". 10 mg (0.18 µmol, 42.02 µmol related to the repetition unit) of p(PFPA) ***P3*** were functionalized with amine-preactivated arm polymer with comes from ***P11*** (5%, 29.44 mg, 2.10 µmol) quenched with ethanolamine and were received after dialysis as a white powder (26.11 mg, 5% incorporation, 0.13 µmol, 74% yield).

^{1}H-NMR (300 MHz, D_2O) δ (ppm) 7.88 (s, 72H, *H1*), 7.46 – 6.97 (m, 65H, *H2*), 4.65 – 4.58 (m, *H3,* overlap with water peak), 4.12 – 4.05 (m, *H4*), 3.95 – 3.10 (m, *H4', H5 - H8*), 3.07 – 2.95 (m, *H9*), 2.95 – 2.85 (m, *H15*), 2.85 – 2.75 (m, *H10*), 2.70 – 2.38 (m, *H11*), 3.18 – 0.44 (m, *H12- H 14, H16, H17*).

^{19}F-NMR (282 MHz, D_2O) δ (ppm) No signals determined.

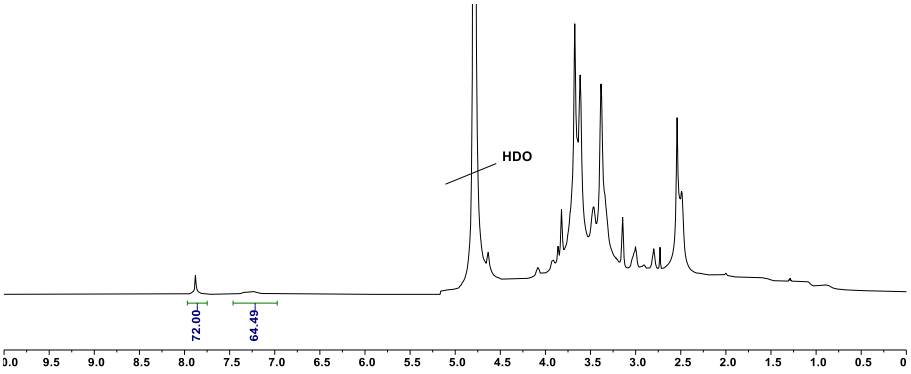


*Figure S68: ^{1}H-NMR spectra of $_{66}E^{2}_{57}$ (**B5**) (600 MHz, D_2O).*

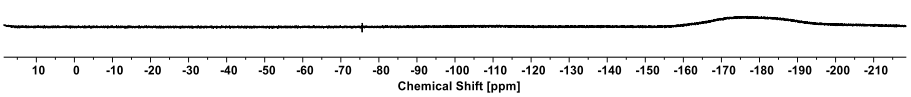
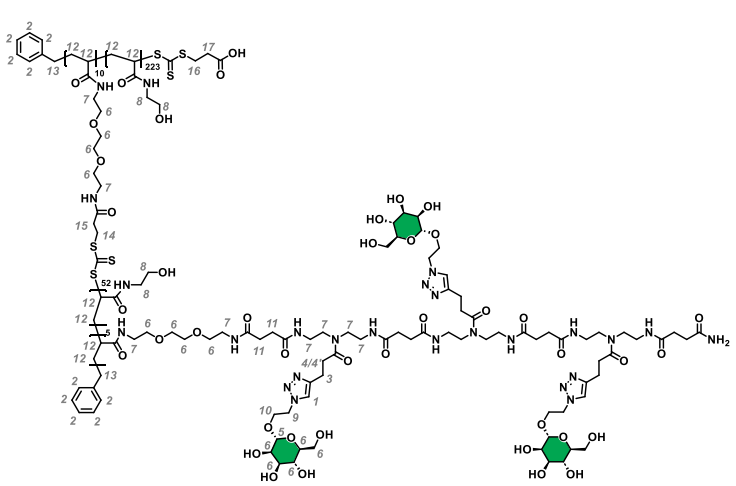


*Figure S69: ^{19}F-NMR spectra of $_{66}E^{2}_{57}$ (**B5**) (564 MHz, D_2O).*

B6 – ($_{198}E^2_{57}$)



The synthesized brush² glycopolymer ***B6*** were obtained by the application of two steps: (1) *Attachment of the bridge molecule to arm polymers,* followed by *Cleavage of the protecting group of the conjugated bridge molecule* (2) *Attachment of the amine-activated arm polymers to the long polymer to gain brush² structures* described in "1.3 General Methods". 10 mg (0.18 µmol, 42.02 µmol related to the repetition unit) of p(PFPA) ***P3*** were functionalized with amine-preactivated arm polymer with comes from ***P12*** (5%, 32.98 mg, 2.10 µmol) quenched with ethanolamine and were received after dialysis as a white powder (26.15 mg, 4% incorporation, 0.14 µmol, 79% yield).

^{1}H-NMR (300 MHz, D_2O) δ (ppm) 7.88 (s, 3H, *H1*), 7.40 – 7.11 (m, 5H, *H2*), 4.68 – 4.53 (m, *H3,* overlap with water), 4.15 – 4.04 (m, *H4*), 3.99 – 3.81 (m, *H4', H5*), 3.81 – 3.12 (m, *H6 – H8*), 3.12 – 2.89 (m, *H9*), 2.88 – 2.72 (m, *H10*), 2.65 – 2.39 (m, *H11*), 3.12 – 0.68 (m, *H12 – H15*).

^{19}F-NMR (282 MHz, D_2O) δ (ppm) No signals determined.

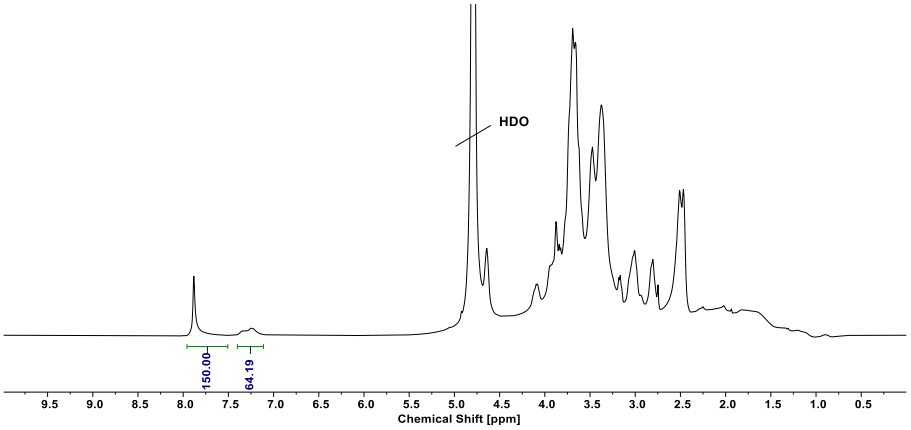


*Figure S70: ^{1}H-NMR spectra of $_{198}E^2_{57}$ (**B6**) (300 MHz, D_2O).*

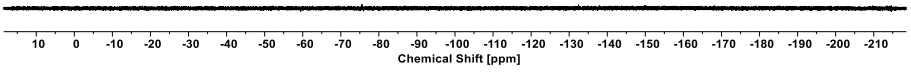
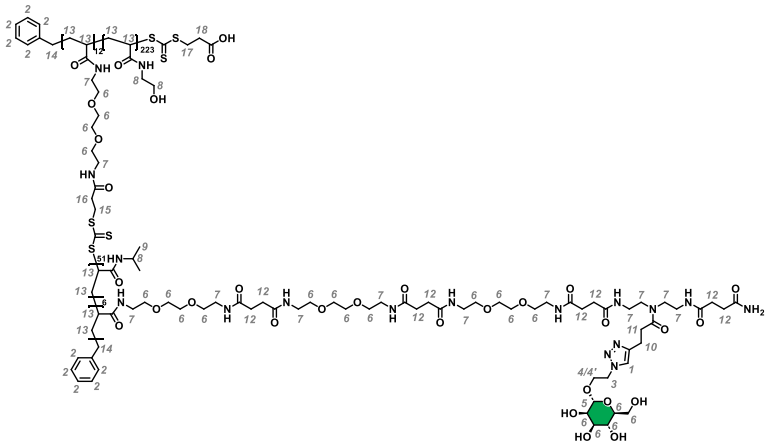


*Figure S71: ^{19}F-NMR spectra of $_{198}E^2_{57}$ (**B6**) (282 MHz, D_2O).*

B7 – ($_{66}I^{2}_{57}$)



The synthesized brush² glycopolymer ***B7*** were obtained by the application of two steps: (1) *Attachment of the bridge molecule to arm polymers,* followed by *Cleavage of the protecting group of the conjugated bridge molecule* (2) *Attachment of the amine-activated arm polymers to the long polymer to gain brush² structures* described in "1.3 General Methods". 16 mg (0.28 µmol, 67.22 µmol related to the repetition unit) of p(PFPA) ***P3*** were functionalized with amine-preactivated arm polymer with comes from ***P13*** (5%, 46.77 mg, 3.36 µmol) quenched with ethanolamine and were received after dialysis as a white powder (32.35 mg, 5% incorporation, 0.17 µmol, 61% yield).

^{1}H-NMR (300 MHz, D_2O) δ (ppm) 7.88 (s, 72H, *H1*), 7.42 – 6.99 (m, 65H, *H2*), 4.66 – 4.57 (m, *H3,* overlap with water peak), 4.12 – 3.75 (m, *H4, H4', H5, H8*), 3.75 – 3.52 (m, *H6*) 3.52 – 3.08 (m, *H7*), 3.07 – 2.95 (m, *H10*), 2.95- 2.85 (m, *H16*), 2.85 – 2.76 (m, *H11)*, 2.64 – 2.32 (m, *H12*), 1.25 – 0.94 (m, *H9*), 3.18 – 0.23 (m, *H13 - H15, H17, H18*).

^{19}F-NMR (282 MHz, D_2O) δ (ppm) No signals determined.

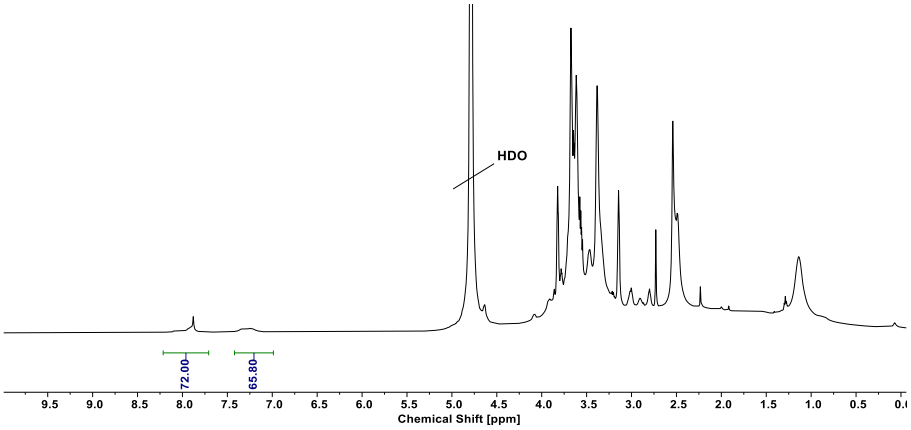


*Figure S72: ^{1}H-NMR spectra of $_{66}I^{2}_{57}$ (**B7**) (600 MHz, D_2O).*

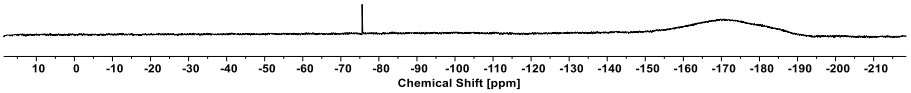
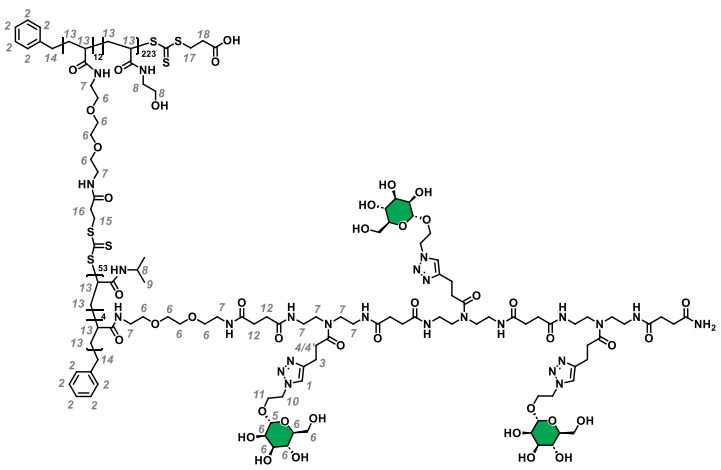


*Figure S73: ^{19}F-NMR spectra of $_{66}I^{2}_{57}$ (**B7**) (564 MHz, D_2O).*

B8 – ($_{198}I^{2}_{57}$)



The synthesized brush² glycopolymer ***B7*** were obtained by the application of two steps: (1) *Attachment of the bridge molecule to arm polymers,* followed by *Cleavage of the protecting group of the conjugated bridge molecule* (2) *Attachment of the amine-activated arm polymers to the long polymer to gain brush² structures* described in "1.3 General Methods". 14 mg (0.25 µmol, 58.82 µmol related to the repetition unit) of p(PFPA) ***P3*** were functionalized with amine-preactivated arm polymer with comes from ***P14*** (5%, 40.77 mg, 2.94 µmol) quenched with ethanolamine and were received after dialysis as a white powder (31.76 mg, 5% incorporation, 0.17 µmol, 68% yield).

^{1}H-NMR (300 MHz, D_2O) δ (ppm) 7.88 (s, 114H, *H1*), 7.44 – 7.11 (m, 64H, *H2*), 4.66 – 4.54 (m, *H3,* overlap with water peak), 4.14 – 3.09 (m, *H4, H4', H5 – H8)*, 3.09 – 2.86 (m, *H10, H16*), 2.86 – 2.71 (m, *H11*), 2.59 – 2.36 (m, *H12*), 1.25 – 0.97 (m, *H9*), 3.10 – 0.00 (m, *H13 – H15, H17, H18*).

^{19}F-NMR (282 MHz, D_2O) δ (ppm) No signals determined.

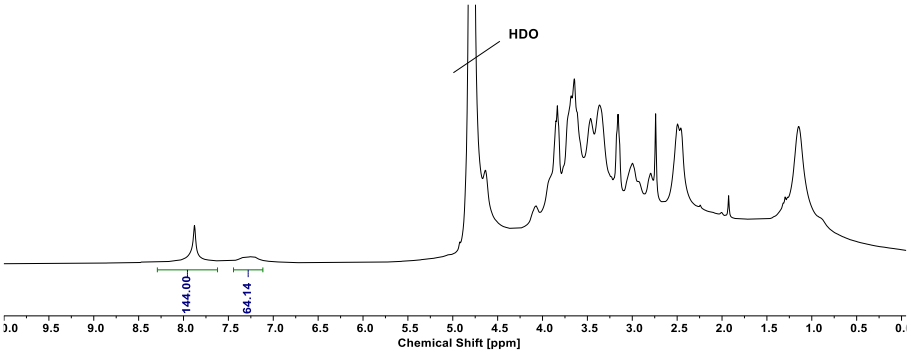


*Figure S74: ^{1}H-NMR spectra of $_{198}I^{2}_{57}$ (**B8**) (300 MHz, D_2O).*

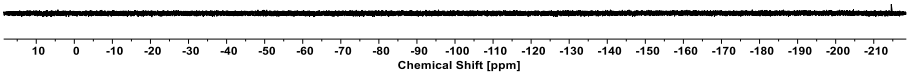
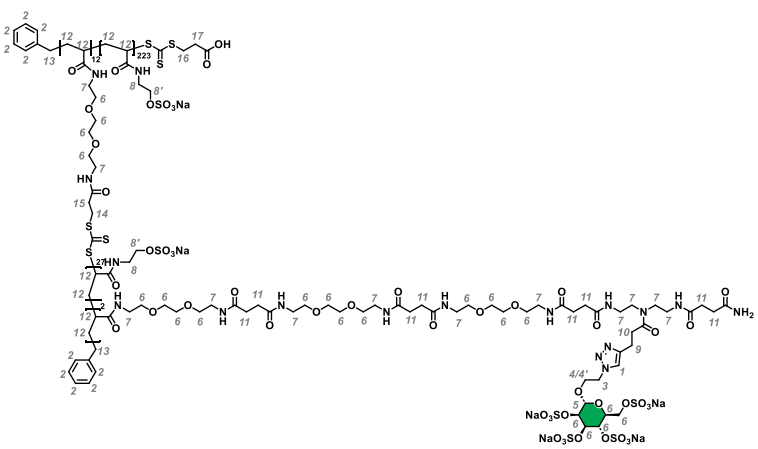


*Figure S75: ^{19}F-NMR spectra of $_{198}I^{2}_{57}$ (**B8**) (282 MHz, D_2O).*

B9 – ($_{22}^{*}E_{29}^{2}$)



The synthesized polymer ***B9*** were obtained by the application of *standard protocol for global sulfation*, described in "1.3 General Methods". 9.65 mg (0.097 µmol) of reference structure ***B1*** were sulfated and received after dialysis as a white powder (8.85 mg, 0.054 µmol assuming complete sulfation, 55% yield, degree of sulfation: ^{1}H-NMR - complete low field shift of e.g. the triazole peak by 0.05 ppm.

^{1}H-NMR (300 MHz, D_2O) δ (ppm) 7.93 (s, *H1*), 7.48 – 7.07 (m, *H2*), 5.19 – 5.11 (m, *H5,* overlap with water peak), 4.26 – 3.90 (m, *H8'*), 3.89 – 3.10 (m, *H6 - H8)*, 3.09 – 2.97 (m, *H9*), 2.97 – 2.88 (m, *H15*), 2.88 – 2.77 (m, *H10*), 2.63 – 2.39 (m, *H11*), 4.51 – 0.59 (m, *H3, H4, H4', H12- H14, H16, H17*).

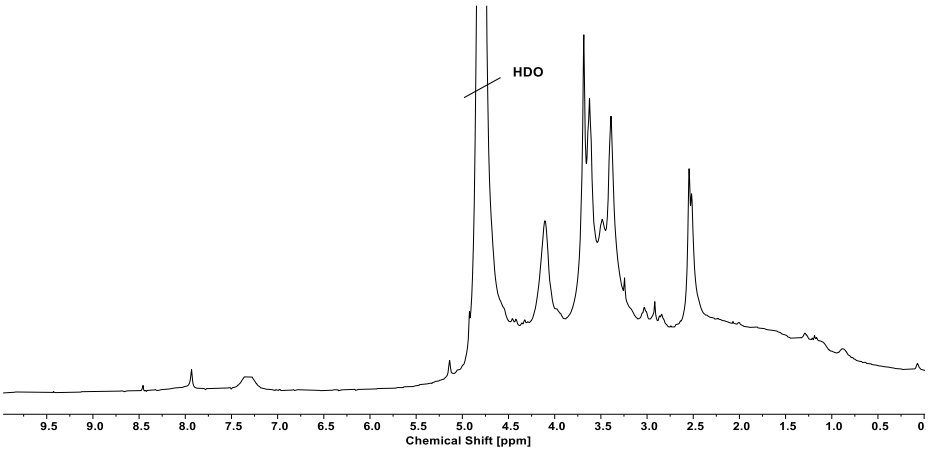


*Figure S76: ^{1}H-NMR spectra of sulfated $_{22}^{*}E_{29}^{2}$ (**B9**) (300 MHz, D_2O).*

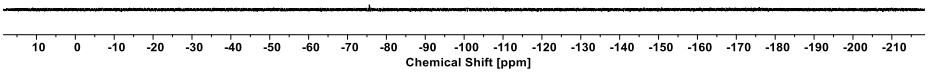
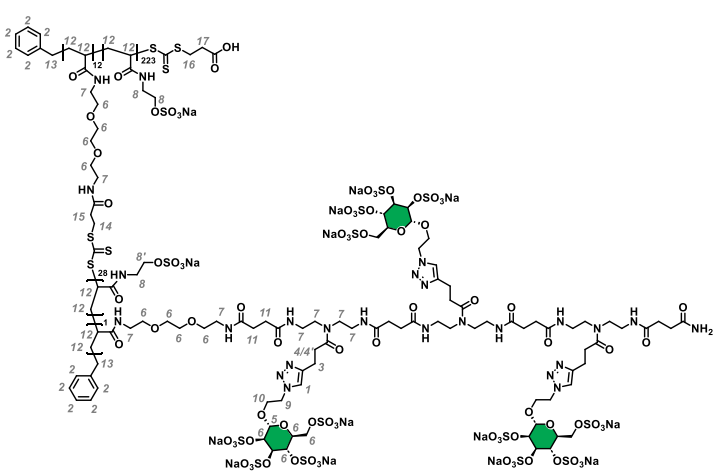


*Figure S77: ^{19}F-NMR spectra of sulfated $_{22}^{*}E_{29}^{2}$ (**B9**) (282 MHz, D_2O).*

B10 – ($_{66}^{*}E_{29}^{2}$)



The synthesized polymer ***B10*** were obtained by the application of *standard protocol for global sulfation*, described in "1.3 General Methods". 8.0 mg (0.087 µmol) of reference structure ***B2*** were sulfated and received after dialysis as a white powder (10.44 mg, 0.064 µmol assuming complete sulfation, 74% yield, degree of sulfation: ^{1}H-NMR - complete low field shift of e.g. the triazole peak by 0.03 ppm.

^{1}H-NMR (300 MHz, D_2O) δ (ppm) 7.90 (s, *H1*), 7.41 – 7.12 (m, *H2*), 5.16 – 5.10 (m, *H5,* overlap with water peak), 4.26 – 3.02 (m, *H8'*), 3.08 – 2.97 (m, *H9*), 2.97 – 2.89 (m, *H15*), 2.89 – 2.79 (m, *H10*), 2.63 – 2.39 (m, *H11*), 4.63 – 0.79 (m. *H3, H4, H4', H12- H14, H16, H17*).

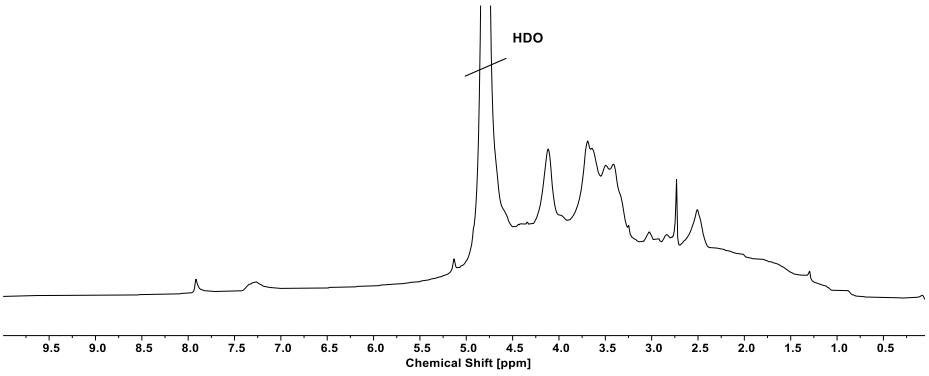


*Figure S78: ^{1}H-NMR spectra of sulfated $_{66}^{*}E_{29}^{2}$ (**B10**) (300 MHz, D_2O).*

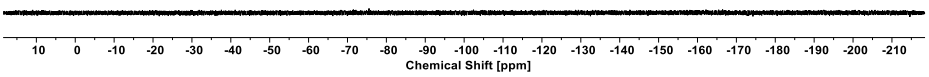
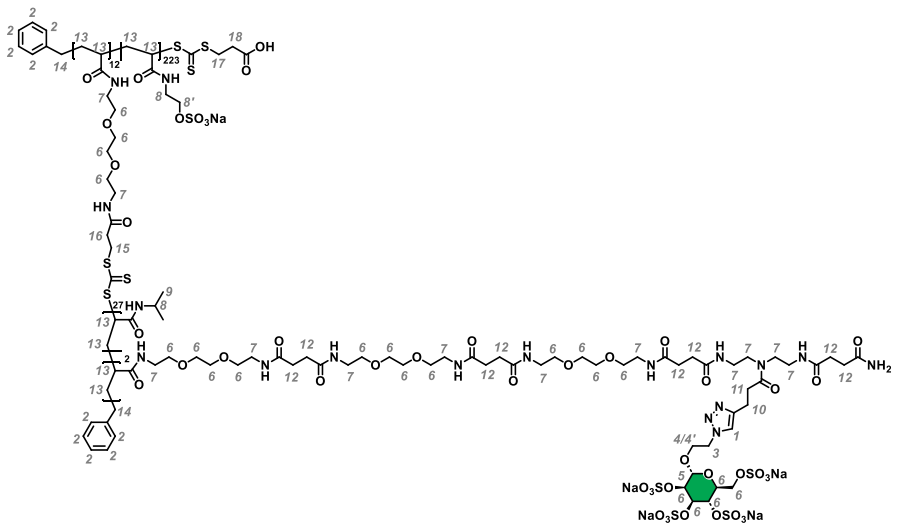


*Figure S79: ^{19}F-NMR spectra of sulfated $_{66}^{*}E_{29}^{2}$ (**B10**) (282 MHz, D_2O).*

B11 – ($_{22}^{*}I_{29}^{2}$)



The synthesized polymer ***B11*** were obtained by the application of *standard protocol for global sulfation*, described in "1.3 General Methods". 12.9 mg (0.131 µmol) of reference structure ***B3*** were sulfated and received after dialysis as a white powder (11.17 mg, 0.085 µmol assuming complete sulfation, 65% yield, degree of sulfation: ^{1}H-NMR - complete low field shift of e.g. the triazole peak by 0.06 ppm.

^{1}H-NMR (300 MHz, D_2O) δ (ppm) 7.94 (s, *H1*), 7.49 – 7.09 (m, *H2*), 4.51 – 0.14 (m *H3-H18,* overlap with water peak).

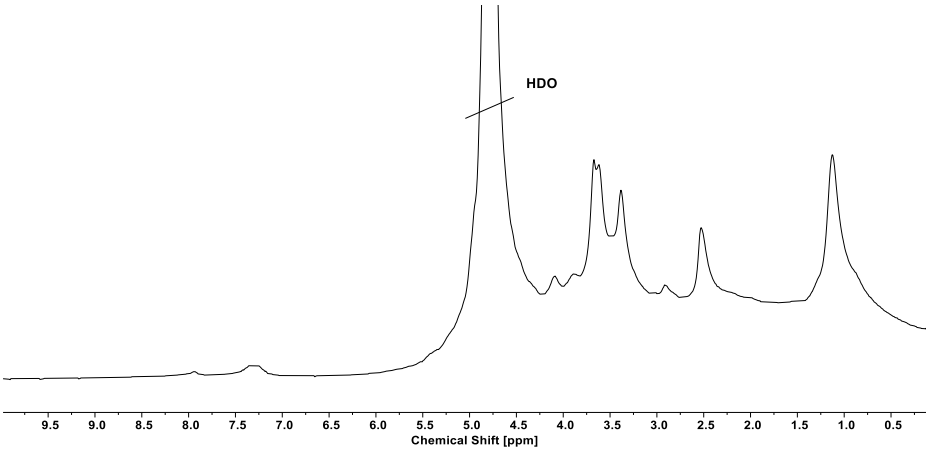


*Figure S80: ^{1}H-NMR spectra of sulfated $_{22}^{*}I_{29}^{2}$ (**B11**) (300 MHz, D_2O).*

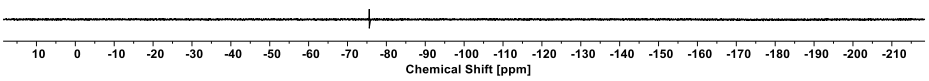
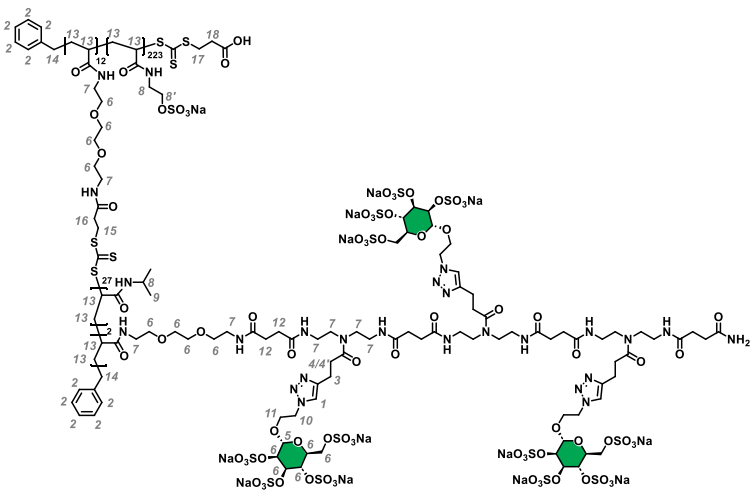


*Figure S81: ^{19}F-NMR spectra of sulfated $_{22}^{*}I_{29}^{2}$ (**B11**) (282 MHz, D_2O).*

B12 – ($_{66}^{*}I_{29}^{2}$)



The synthesized polymer ***B12*** were obtained by the application of *standard protocol for global sulfation*, described in "1.3 General Methods". 10 mg (0.089 µmol) of reference structure ***B4*** were sulfated and received after dialysis as a white powder (12.4 mg, 0.075 µmol assuming complete sulfation, 84% yield, degree of sulfation: ^{1}H-NMR - complete low field shift of e.g. the triazole peak by 0.03 ppm.

^{1}H-NMR (300 MHz, D_2O) δ (ppm) 7.92 (s, *H1*), 7.43 – 7.13 (m, *H2*), 5.15 – 5.01 (m, *H5, overlap with water peak*), 4.68 – 3.12 (m, *H3, H4, H4', H5 – H8,* overlap with water peak), 3.07 – 2.98 (m, *H10*), 2.98 – 2.88 (m*, H16*), 2.88 – 2.79 (m, *H11*), 2.61 – 2.36 (m, *H12*), 1.28 – 0.95 (m, *H9*), 3.09 – 0.00 (m, *H13 – H15, H17, H18*).

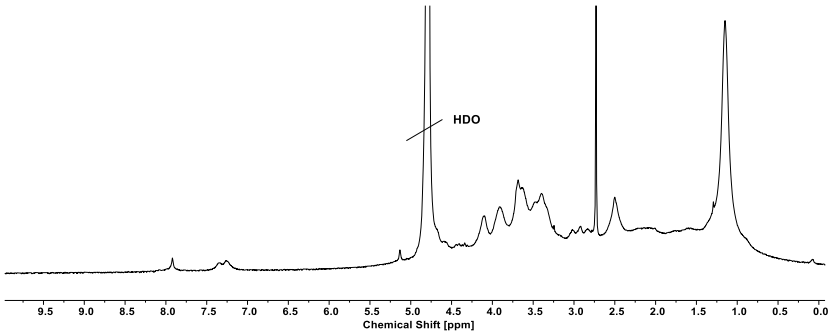


*Figure S82: ^{1}H-NMR spectra of sulfated $_{66}^{*}I_{29}^{2}$ (**B12**) (300 MHz, D_2O).*

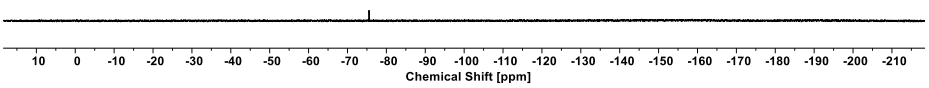
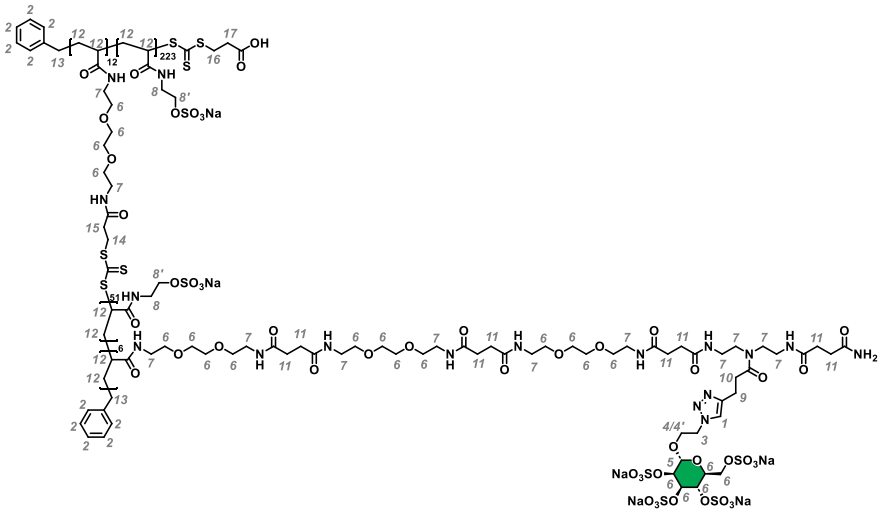


*Figure S83: ^{19}F-NMR spectra of sulfated $_{66}^{*}I_{29}^{2}$ (**B12**) (282 MHz, D_2O).*

B13 – ($_{66}^{*}E_{57}^{2}$)



The synthesized polymer ***B13*** were obtained by the application of *standard protocol for global sulfation*, described in "1.3 General Methods". 13 mg (0.067 µmol) of reference structure ***B5*** were sulfated and received after dialysis as a white powder (13.36 mg, 0.043 µmol assuming complete sulfation, 64% yield, degree of sulfation: EA – 52% ^{1}H-NMR - complete low field shift of e.g. the triazole peak by 0.06 ppm.

^{1}H-NMR (300 MHz, D_2O) δ (ppm) 7.93 (s, *H1*), 7.42 – 7.09 (m, *H2*), 5.27 – 5.08 (m, *H5,* overlap with water peak), 4.24 – 4.00 (m, *H8'*), 3.88 – 3.11 (m, *H6 - H8)*, 3.09 – 2.97 (m, *H9*), 2.97 – 2.88 (m, *H15*), 2.88 – 2.77 (m, *H10*), 2.65 – 2.40 (m, *H11*), 4.18 – 0.52 (m, *H3, H4, H4', H12- H14, H16, H17*).

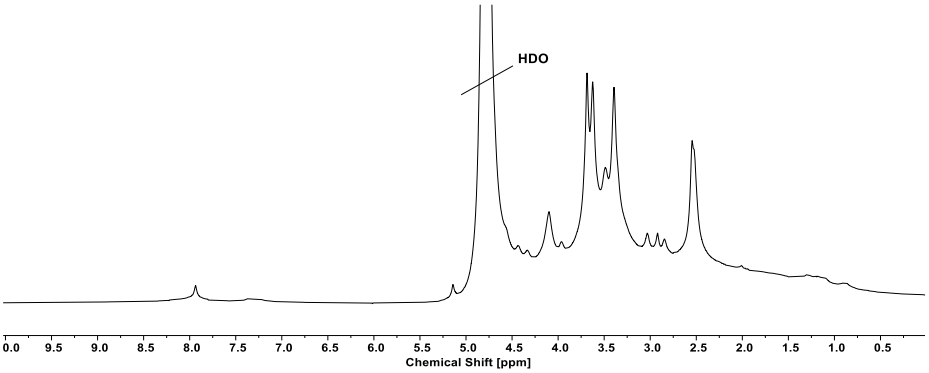


*Figure S84: ^{1}H-NMR spectra of sulfated $_{66}^{*}E_{57}^{2}$ (**B13**) (300 MHz, D_2O).*

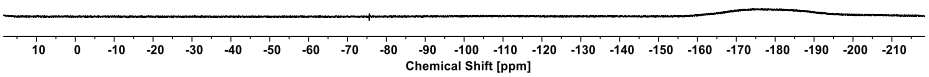
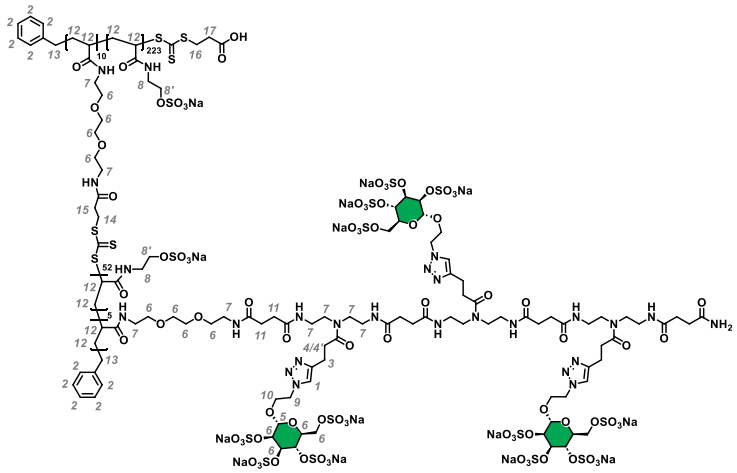


*Figure S85: ^{19}F-NMR spectra of sulfated $_{66}^{*}E_{57}^{2}$ (**B13**) (282 MHz, D_2O).*

B14 – ($_{198}^{*}E_{57}^{2}$)



The synthesized polymer ***B14*** were obtained by the application of *standard protocol for global sulfation*, described in "1.3 General Methods". 13 mg (0.071 µmol) of reference structure ***B6*** were sulfated and received after dialysis as a white powder (18.97 mg, 0.059 µmol assuming complete sulfation, 83% yield, degree of sulfation: ^{1}H-NMR - complete low field shift of e.g. the triazole peak by 0.04 ppm.

^{1}H-NMR (300 MHz, D_2O) δ (ppm) 7.92 (s, *H1*), 7.42 – 7.18 (m, *H2*), 5.17 – 5.10 (m, *H5,* overlap with water peak), 4.70 – 4.61 (m, *H3*, overlap with water), 4.21 – 4.02 (m, *H8'*), 4.62 – 0.00 (m, *H4, H4' – H7, H8 - H17*).

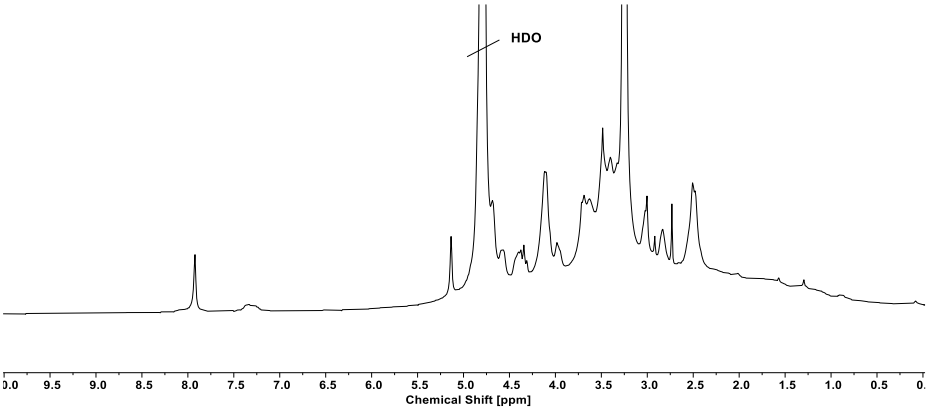


*Figure S86: ^{1}H-NMR spectra of sulfated $_{198}^{*}E_{57}^{2}$ (**B14**) (300 MHz, D_2O).*

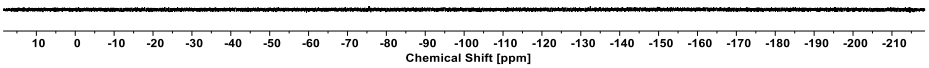
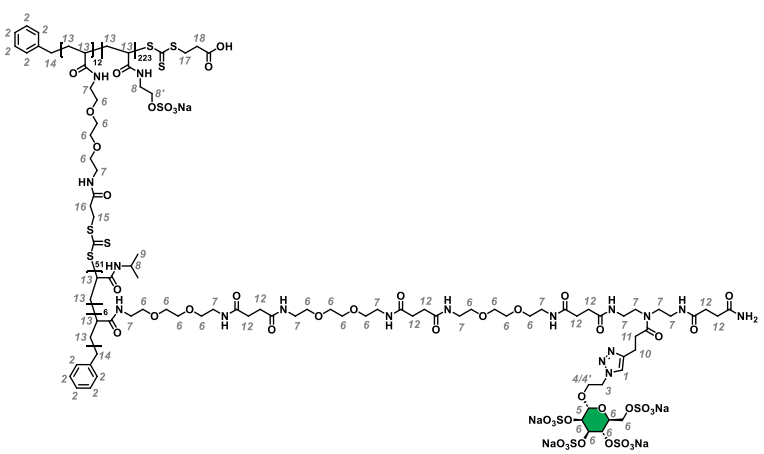


*Figure S87: ^{19}F-NMR spectra of sulfated $_{198}^{*}E_{57}^{2}$ (**B14**) (282 MHz, D_2O).*

B15 – ($_{66}^{*}I_{57}^{2}$)



The synthesized polymer ***B15*** were obtained by the application of *standard protocol for global sulfation*, described in "1.3 General Methods". 14.86 mg (0.077 µmol) of reference structure ***B7*** were sulfated and received after dialysis as a white powder (12.75 mg, 0.052 µmol assuming complete sulfation, 68% yield, degree of sulfation: ^{1}H-NMR - complete low field shift of e.g. the triazole peak by 0.06 ppm.

^{1}H-NMR (300 MHz, D_2O) δ (ppm) 7.93 (s, *H1*), 7.47 – 7.12 (m, *H2*), 4.36 – 0.19 (m *H3-H18,* overlap with water peak).

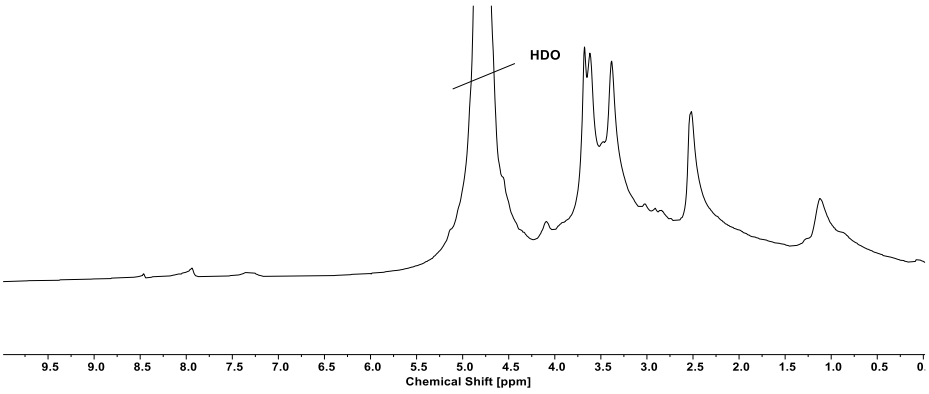


*Figure S88: ^{1}H-NMR spectra of sulfated $_{66}^{*}I_{57}^{2}$ (**B15**) (300 MHz, D_2O).*

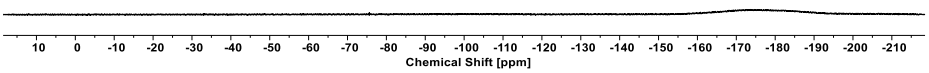
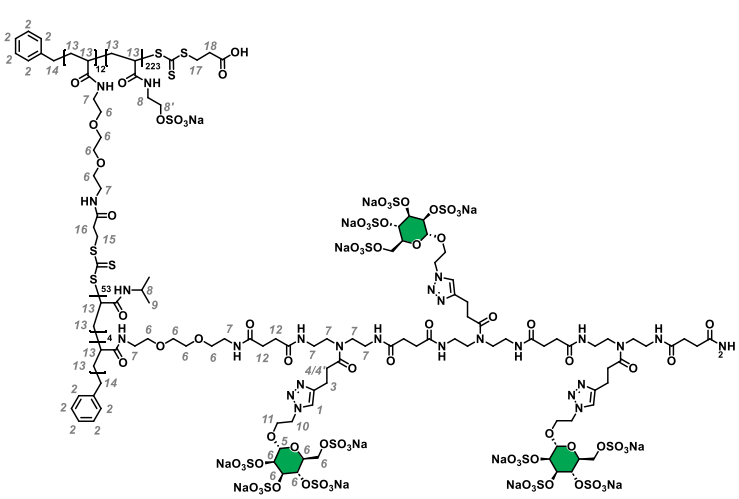


*Figure S89: ^{19}F-NMR spectra of sulfated $_{66}^{*}I_{57}^{2}$ (**B15**) (282 MHz, D_2O).*

B16 – ($_{198}^{*}I_{57}^{2}$)



The synthesized polymer ***B16*** were obtained by the application of *standard protocol for global sulfation*, described in "1.3 General Methods". 15 mg (0.078 µmol) of reference structure ***B8*** were sulfated and received after dialysis as a white powder (19.54 mg, 0.072 µmol assuming complete sulfation, 92% yield, degree of sulfation: ^{1}H-NMR - complete low field shift of e.g. the triazole peak by 0.05 ppm.

^{1}H-NMR (300 MHz, D_2O) δ (ppm) 7.92 (s, *H1*), 7.47 – 7.11 (m, *H2*), 5.16 – 5.10 (m, *H5, overlap with water*), 4.48 – 0.00 (m *H3-H18,* overlap with water peak).

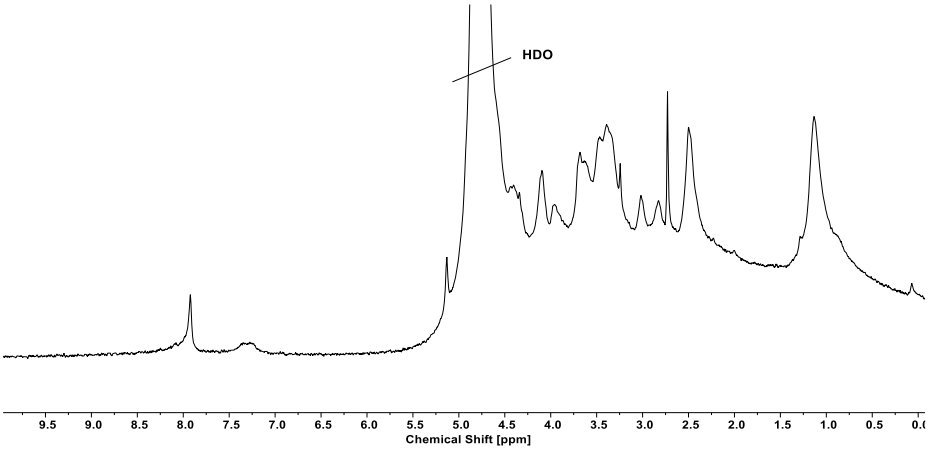


*Figure S90: ^{1}H-NMR spectra of sulfated $_{198}^{*}I_{57}^{2}$ (**B15**) (300 MHz, D_2O).*

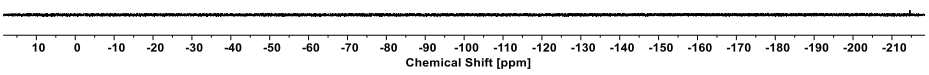
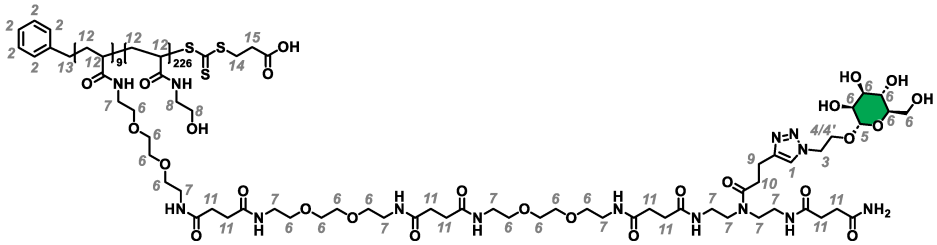


*Figure S91: ^{19}F-NMR spectra of sulfated $_{198}^{*}I_{57}^{2}$ (**B15**) (282 MHz, D_2O).*

2.6 Synthesis of reference structures P15–P24 and B17

P15 – ($_{11}E_{235}$)



The synthesized polymer ***P15*** were obtained by the application of *synthesis of brush-like glycopolymers (arm-structures) and linear reference structures*, described in "1.3 General Methods". 50 mg (0.89 µmol, 210.1 µmol related to the repetition unit) of p(PFPA) ***P3*** were functionalized with oligoamidoamine ***O1*** (5%, 13.85 mg, 10.5 µmol) quenched with ethanolamine and were received after dialysis as a white powder (31.52 mg, 4% incorporation, 0.84 µmol, 94% yield).

^{1}H-NMR (300 MHz, D_2O) δ (ppm) 7.88 (s, 9H, *H1*), 7.44 – 7.14 (m, 5H, *H2*), 4.67 – 4.59 (m, *H3,* overlap with water peak), 4.14 – 3.08 (m, *H4, H4', H5* - *H8*), 3.08 – 0.77 (m, *H9 – H15*).

^{19}F-NMR (282 MHz, D_2O) δ (ppm) No signals determined.

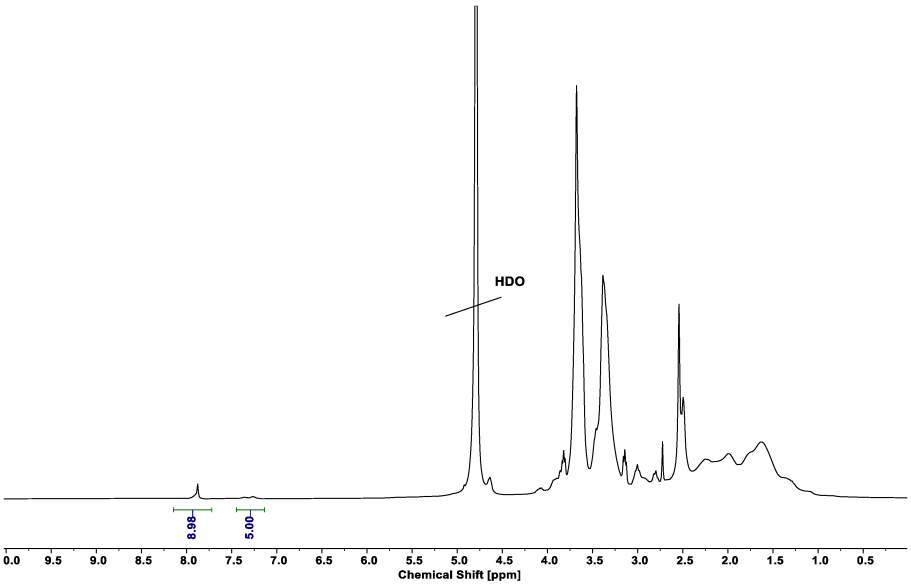


*Figure S92: ^{1}H-NMR spectra of $_{11}E_{235}$ (**P15**) (300 MHz, D_2O).*

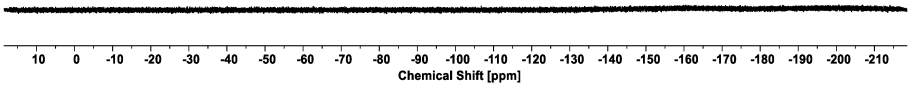
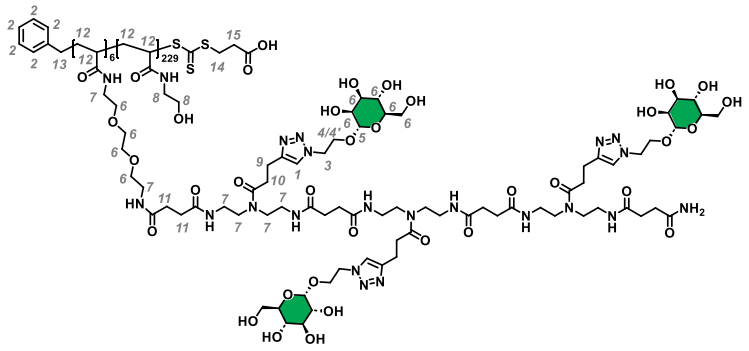


*Figure S93: ^{19}F-NMR spectra of $_{11}E_{235}$ (**P15**) (282 MHz, D_2O).*

P16 – ($_{33}E_{235}$)



The synthesized polymer ***P16*** were obtained by the application of *synthesis of brush-like glycopolymers (arm-structures) and linear reference structures*, described in "1.3 General Methods". 50 mg (0.89 µmol, 210.1 µmol related to the repetition unit) of p(PFPA) ***P3*** were functionalized with oligoamidoamine ***O2*** (5%, 19.84 mg, 10.5 µmol) quenched with ethanolamine and were received after dialysis as a white powder (27.25 mg, 3% incorporation, 0.72 µmol, 81% yield).

^{1}H-NMR (300 MHz, D_2O) δ (ppm) 7.87 (s, 3H, *H1*), 7.43 – 7.16 (m, 5H, *H2*), 4.68 – 4.52 (m, *H3,* overlap with water peak), 4.15 – 4.01 (m, *H4*), 4.01 – 3.09 (m, *H4', H5 - H8*), 3.07 – 2.86 (m, *H9*), 2.86 – 2.70 (m, *H10*), 2.58 – 2.37 (m, *H11*), 3.08 – 0.70 (m, *H12 – H15*).

^{19}F-NMR (282 MHz, D_2O) δ (ppm) No signals determined.

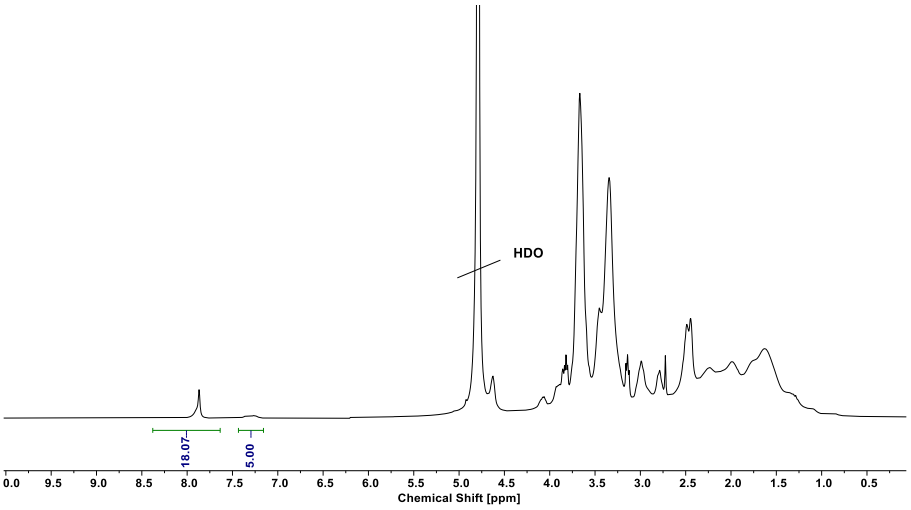


*Figure S94: ^{1}H-NMR spectra of $_{33}E_{235}$ (**P16**) (300 MHz, D_2O).*

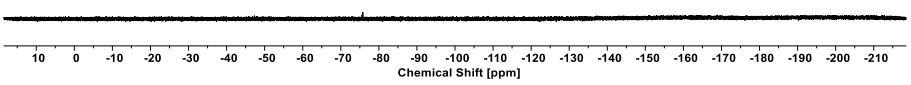
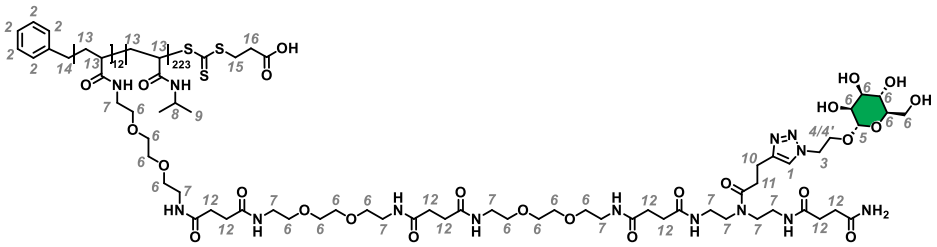


*Figure S95: ^{19}F-NMR spectra of $_{33}E_{235}$ (**P16**) (282 MHz, D_2O).*

P17 – ($_{11}I_{235}$)



The synthesized polymer ***P17*** were obtained by the application of *synthesis of brush-like glycopolymers (arm-structures) and linear reference structures*, described in "1.3 General Methods". 50 mg (0.89 µmol, 210.1 µmol related to the repetition unit) of p(PFPA) ***P3*** were functionalized with oligoamidoamine ***O1*** (5%, 13.84 mg, 10.5µmol) quenched with isopropylamine and were received after dialysis as a white powder (26.62 mg, 5% incorporation, 0.65 µmol, 73% yield).

^{1}H-NMR (300 MHz, D_2O) δ (ppm) 7.88 (s, 2H, *H1*), 7.44 – 7.11 (m, 5H, *H2*), 4.68 – 4.57 (m, *H3,* overlap with water peak), 4.20 – 3.79 (m, *H4, H4', H5, H8*), 3.78 – 3.54 (m, *H6*) 3.54 – 3.28 (m, *H7, H8*), 3.08 – 2.95 (m, *H10*), 2.88 – 2.74 (m, *H11)*, 2.62 – 2.41 (m, *H12*), 1.25 – 0.95 (m, *H9*), 3.12– 0.49 (m, *H13- H16*).

^{19}F-NMR (282 MHz, D_2O) δ (ppm) No signals determined.

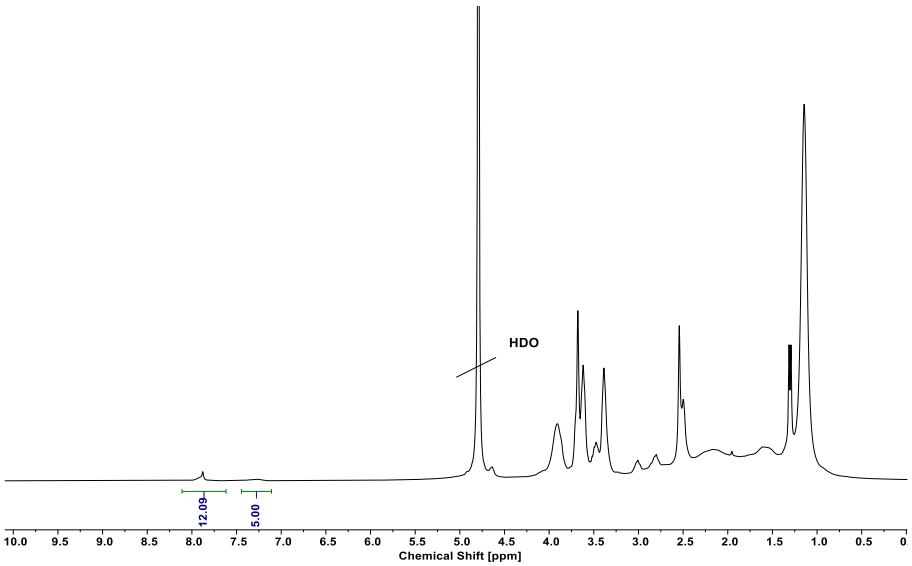


*Figure S96: ^{1}H-NMR spectra of $_{11}I_{235}$ (**P17**) (300 MHz, D_2O).*

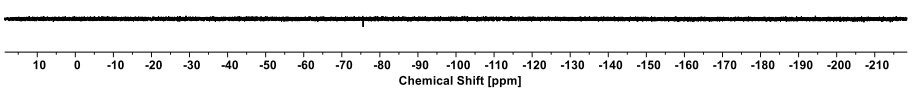
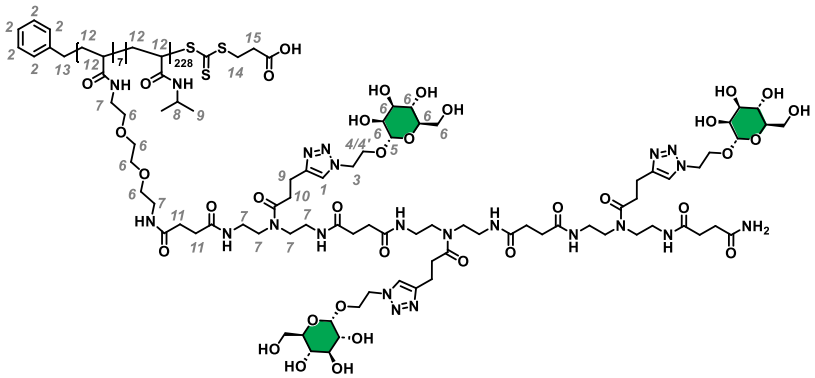


*Figure S97: ^{19}F-NMR spectra of $_{11}I_{235}$ (**P17**) (282 MHz, D_2O).*

P18 – ($_{33}I_{235}$)



The synthesized polymer ***P18*** were obtained by the application of *synthesis of brush-like glycopolymers (arm-structures) and linear reference structures*, described in "1.3 General Methods". 50 mg (0.89 µmol, 210.1 µmol related to the repetition unit) of p(PFPA) ***P3*** were functionalized with oligoamidoamine ***O2*** (5%, 19.84 mg, 10.5 µmol) quenched with isopropylamine and were received after dialysis as a white powder (28.75 mg, 3% incorporation, 0.74 µmol, 83% yield).

^{1}H-NMR (300 MHz, D_2O) δ (ppm) 7.87 (s, 21H, *H1*), 7.43 – 7.16 (m, 5H, *H2*), 4.68 – 4.55 (m, *H3,* overlap with water peak), 4.13 – 3.79 (m, *H4, H4', H5, H8*), 3.79 – 3.55 (m, *H6*), 3.55 – 3.17 (m, *H7*), 3.06 – 2.90 (m, *H9*), 2.90 – 2.70 (m, *H10*), 2.56 – 2.35 (m, *H11*), 1.25 – 0.99 (m, *H9*), 3.14 – 0.55 (m, *H12 – H15*).

^{19}F-NMR (282 MHz, D_2O) δ (ppm) No signals determined.

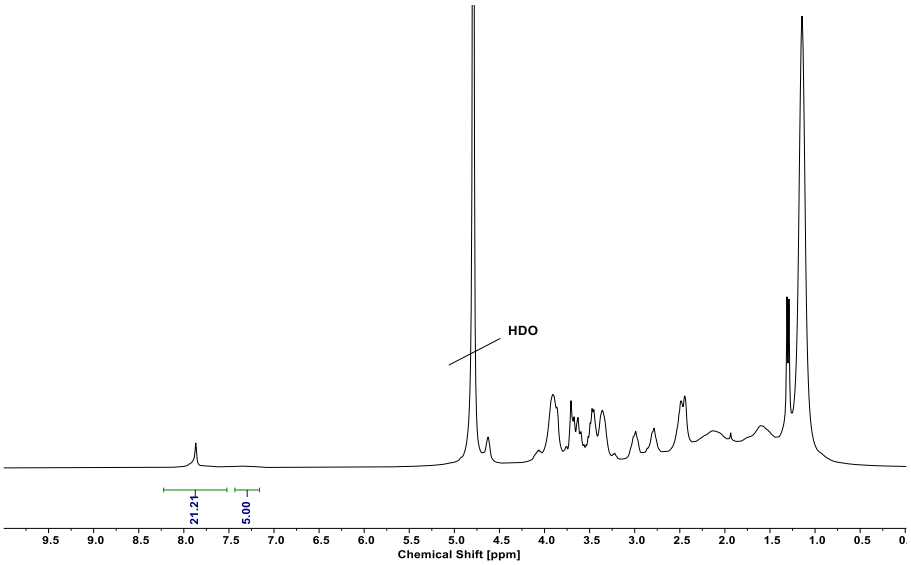


*Figure S98: ^{1}H-NMR spectra of $_{33}I_{235}$ (**P18**) (300 MHz, D_2O).*

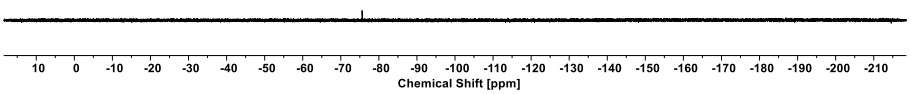
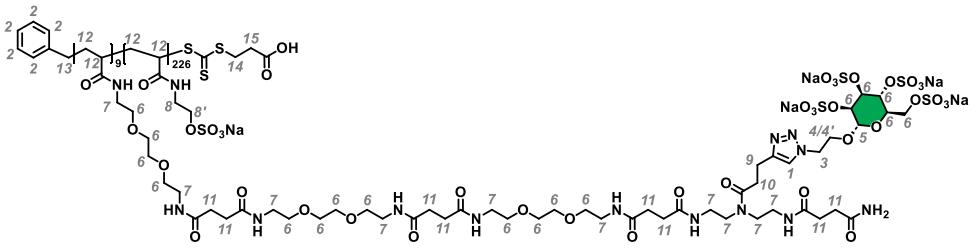


*Figure S99: ^{19}F-NMR spectra of $_{33}I_{235}$ (**P18**) (282 MHz, D_2O).*

P19 – ($_{11}^{*}E_{235}$)



The synthesized polymer ***P19*** were obtained by the application of *standard protocol for global sulfation*, described in "1.3 General Methods". 13.04 mg (0.35 µmol) of reference structure ***P15*** were sulfated and received after dialysis as a white powder (11.36 mg, 0.18 µmol assuming complete sulfation, 51% yield, degree of sulfation: ^{1}H-NMR - complete low field shift of e.g. the triazole peak (**1**) by 0.06 ppm or the ethanolamine side chain signals **8'** by 0.45 ppm and **8** by 0.13 ppm).

^{1}H-NMR (300 MHz, D_2O) δ (ppm) 7.93 (s, *H1*), 7.41 – 7.14 (m, *H2*), 5.16 – 5.11 (m, *H5*), 4.71 – 3.17 (m, H3, *H4, H4', H6 – H8,* overlap with water peak), 4.27 – 4.01 (m, *H8'*), 3.11 – 2.96 (m, *H9*), 2.89 – 2.78 (m, *H10*), 3.19 – 0.80 (m, *H11 – H15*).

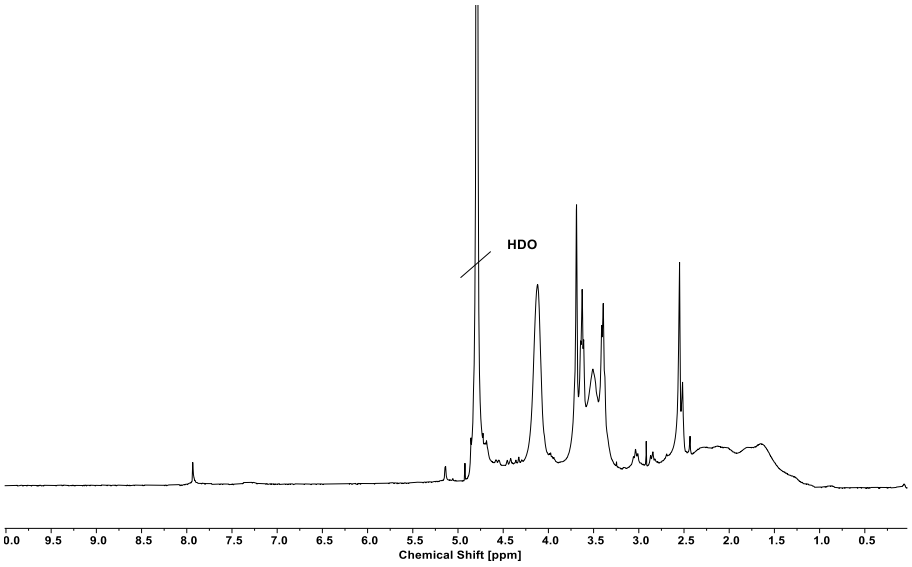
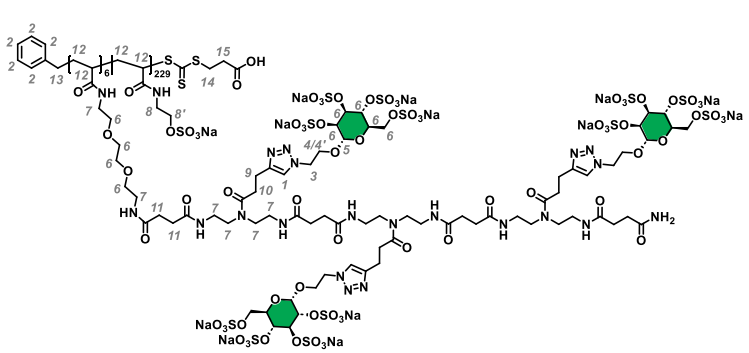


*Figure S100: ^{1}H-NMR spectra of sulfated $_{11}^{*}E_{235}$ (**P19**) (300 MHz, D_2O).*

P20 – ($_{33}^{*}E_{235}$)



The synthesized polymer ***P20*** were obtained by the application of *standard protocol for global sulfation*, described in "1.3 General Methods". 9.55 mg (0.25 µmol) of reference structure ***P19*** were sulfated and received after dialysis as a white powder (10.0 mg, 0.15 µmol assuming complete sulfation, 56% yield, degree of sulfation: ^{1}H-NMR - complete low field shift of e.g. the triazole peak by 0.05 ppm. **^{1}H-NMR** (300 MHz, D_2O) δ (ppm) 7.92 (s, *H1*), 7.41 – 7.18 (m, *H2*), 5.16 – 5.11 (m, *H5*), 4.71 – 3.22 (m, *H3, H4, H4', H6 – H8,* overlap with water peak), 4.27 – 4.01 (m, *H8'*), 3.08 – 2.94 (m, *H9*), 2.94 – 2.79 (m, *H10*), 3.19 – 0.77 (m, *H11 – H15*).

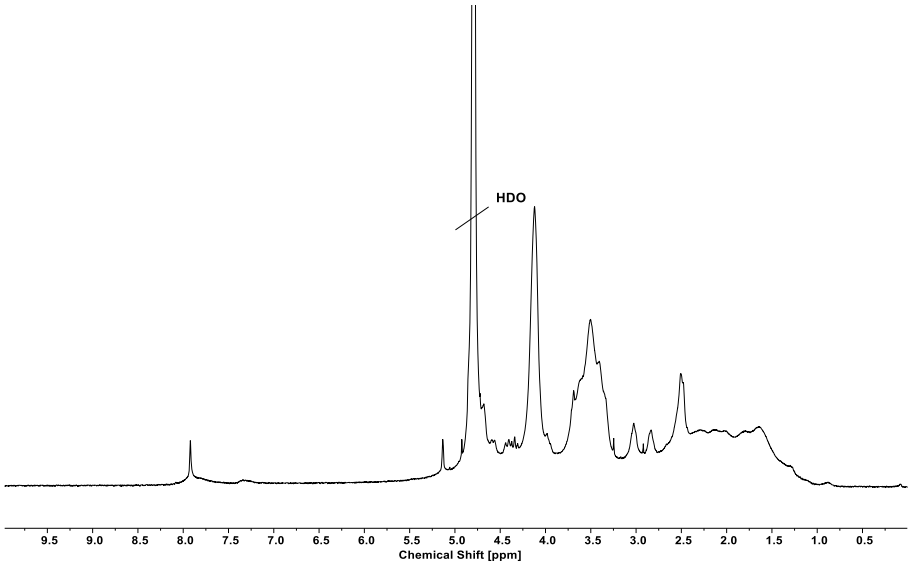
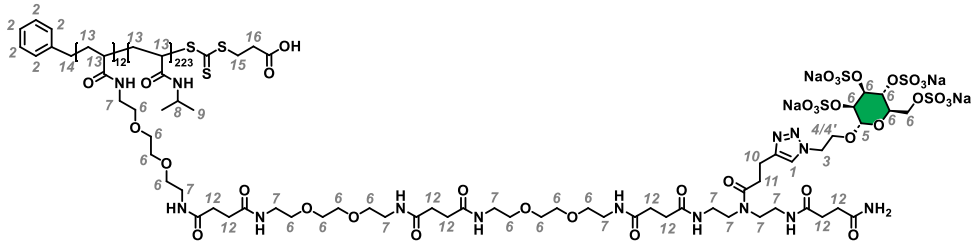


*Figure S101: ^{1}H-NMR spectra of sulfated $_{33}^{*}E_{235}$ (**P20**) (300 MHz, D_2O).*

P21 – ($_{11}^{*}I_{235}$)



The synthesized polymer ***P21*** were obtained by the application of *standard protocol for global sulfation*, described in "1.3 General Methods". 13.04 mg (0.32 µmol) of reference structure ***P17*** were sulfated and received after dialysis as a white powder (11.07 mg, 0.24 µmol assuming complete sulfation, 75% yield, degree of sulfation: ^{1}H-NMR - complete low field shift of e.g. the triazole peak by 0.06 ppm.

^{1}H-NMR (300 MHz, D_2O) δ (ppm) 7.93 (s, *H1*), 7.44 – 7.12 (m, *H2*), 5.18 – 5.10 (m, *H5*), 4.72 – 3.77 (m, *H3, H4, H4' H6,* overlap with water peak), 4.04 – 3.76 (m, *H8*), 3.77 – 3.54 (m, *H6*), 3.54 – 3.23 (m, *H7*), 3.09 – 2.98 (m, *H10*), 2.89 – 2.76 (m, *H11)*, 2.62 – 2.42 (m, *H12*), 1.26 – 0.85 (m, *H9*), 3.16– 0.55 (m, *H13- H16*).

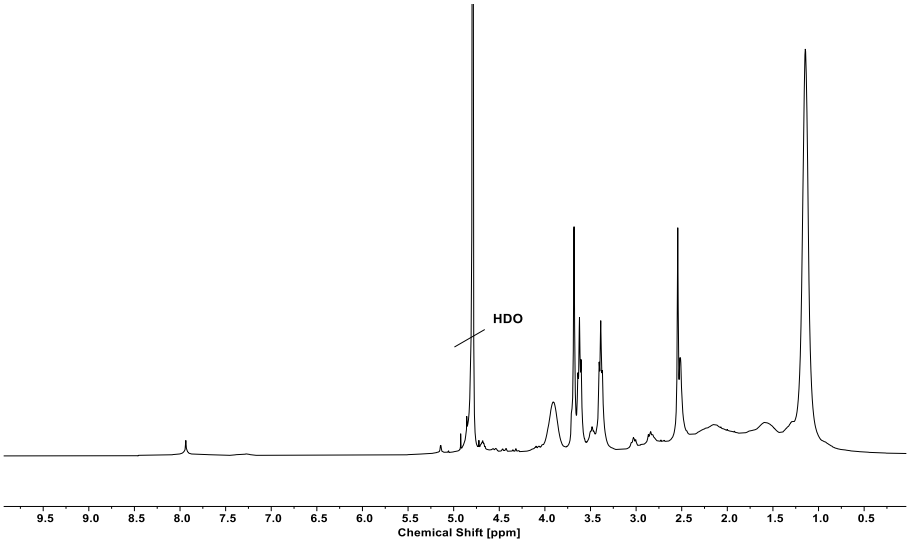
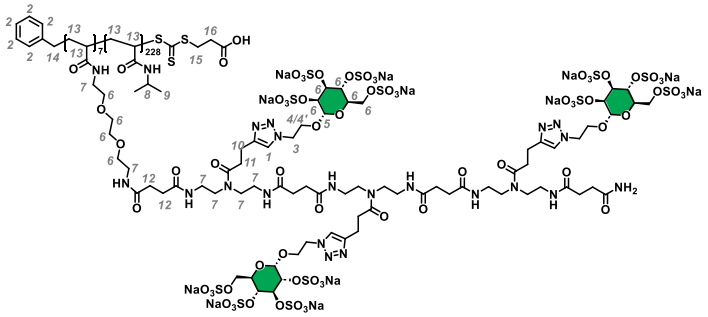


*Figure S102: ^{1}H-NMR spectra of sulfated $_{11}^{*}I_{235}$ (**P21**) (300 MHz, D_2O).*

P22 – ($_{33}^{*}I_{235}$)



The synthesized polymer ***P22*** were obtained by the application of *standard protocol for global sulfation*, described in "1.3 General Methods". 13.08 mg (0.34 µmol) of reference structure ***P21*** were sulfated and received after dialysis as a white powder (12.16 mg, 0.27 µmol assuming complete sulfation, 79% yield, degree of sulfation: ^{1}H-NMR - complete low field shift of e.g. the triazole peak by 0.05 ppm.

^{1}H-NMR (300 MHz, D_2O) δ (ppm) 7.92 (s, *H1*), 7.43 – 7.16 (m, *H2*), 5.18 – 5.09 (m, *H5*), 4.72 – 3.76 (m, *H3, H4, H4', H6)*, 4.03 – 3.76 (m, *H8*), 3.76 – 3.57 (m, *H6*), 3.57 – 3.20 (m, *H7*), 3.07 – 2.94 (m, *H10*), 2.95 – 2.72 (m, *H11)*, 2.56 – 2.38 (m, *H12*), 1.26 – 0.83 (m, *H9*), 3.12– 0.00 (m, *H13- H16*).

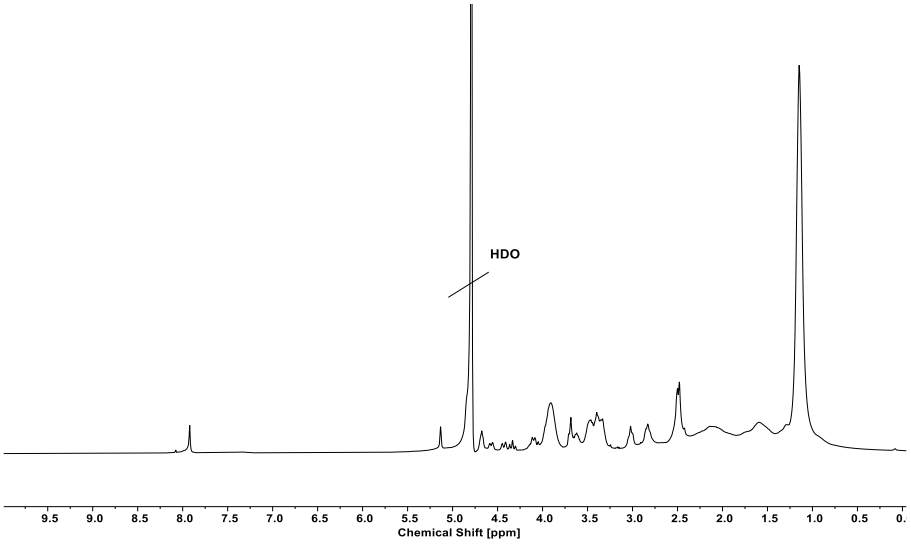
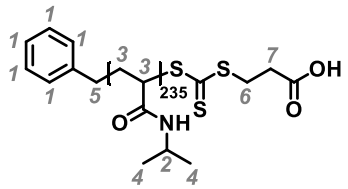


*Figure S103: ^{1}H-NMR spectra of sulfated $_{33}^{*}I_{235}$ (**P22**) (300 MHz, D_2O).*

P23 – ($_0I_{235}$)



The synthesized polymer ***P23*** were obtained by the application of *synthesis of brush-like glycopolymers (arm-structures) and linear reference structures*, described in "1.3 General Methods". 33 mg (138.65 µmol, 0.59 µmol related to the repetition unit) of p(PFPA) ***P3*** were non functionalized with carbohydrates, only quenched with isopropylamine and were received after dialysis as a white powder (15.37 mg, 0.57 µmol, 97% yield).

^{1}H-NMR (300 MHz, D_2O) δ (ppm) 7.10 – 6.82 (m, *H1*), 3.74 – 3.44 (m, *H2*), 2.07 – 0.36 (m, *H3 – H*).

^{19}F-NMR (282 MHz, D_2O) δ (ppm) No signals of PFP-side chain determined.

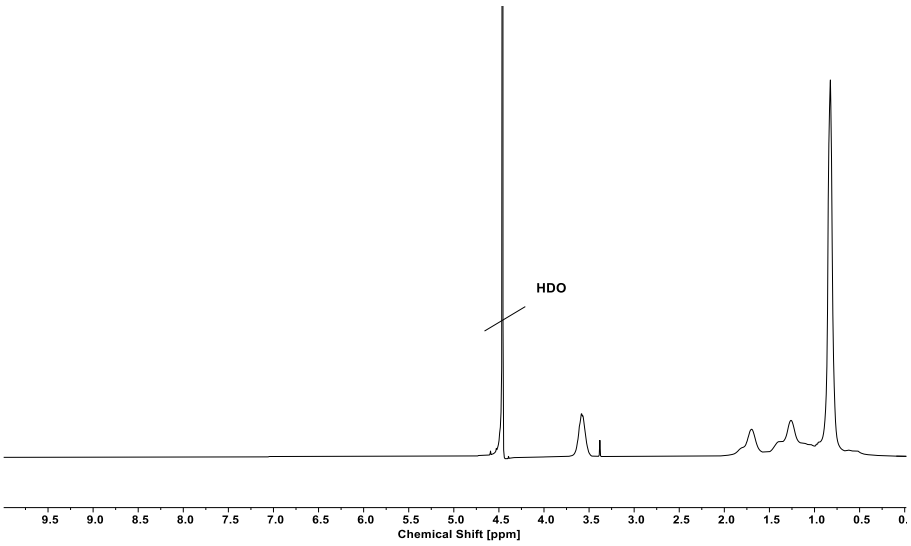


Figure S104: ^{1}H-NMR spectra of ***I_{235}*** *(**P23**) (300 MHz, D_2O).*

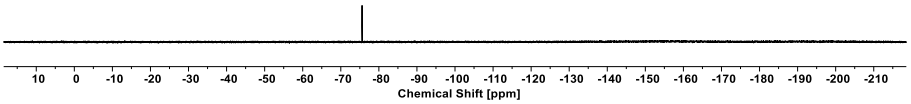
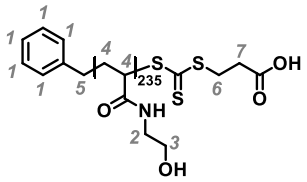


Figure S105: ^{19}F-NMR spectra of ***I_{235}*** (**P23**) (282 MHz, D_2O).

P24 – ($_0E_{235}$)



The synthesized polymer ***P24*** were obtained by the application of *synthesis of brush-like glycopolymers (arm-structures) and linear reference structures*, described in "1.3 General Methods". 38 mg (0.68 µmol, 159.66 µmol related to the repetition unit) of p(PFPA) ***P3*** were non functionalized with carbohydrates, only quenched with ethanolamine and were received after dialysis as a white powder (16.36 mg, 0.6 µmol, 88% yield).

^{1}H-NMR (300 MHz, D_2O) δ (ppm) 7.41 – 7.15 (m, *H1*), 4.00 – 2.82 (m, *H3*), 2.66 – 0.71 (m, *H7*), 2.26 – 1.16 (m, *H4 – H7*).

^{19}F-NMR (282 MHz, D_2O) δ (ppm) No signals determined.

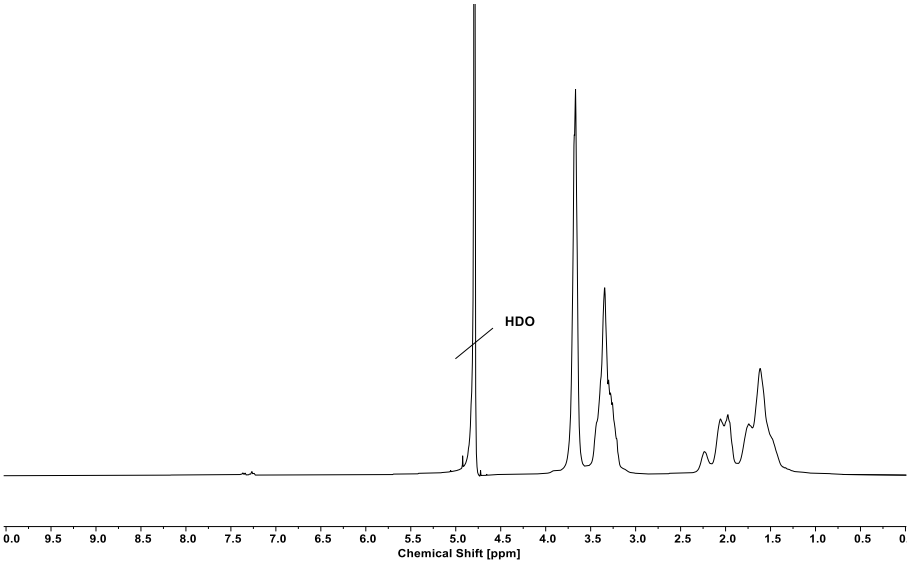


Figure S106: ^{1}H-NMR spectra of $\boldsymbol{E_{235}}$ ***(P24)*** *(300 MHz, D_2O).*

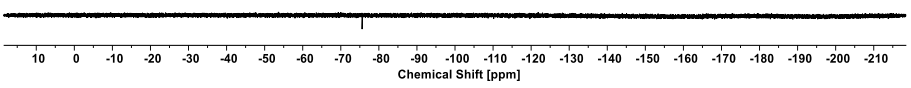
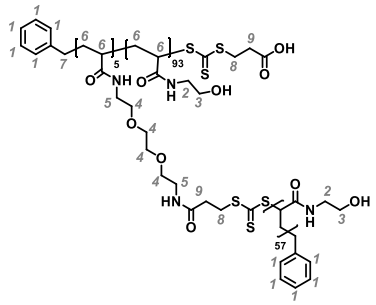


Figure S107: ^{19}F-NMR spectra of $\boldsymbol{E_{235}}$ ***(P24)*** *(282 MHz, D_2O).*

B17 – ($_0E^2_{57}$)



The synthesized brush² glycopolymer ***B17*** were obtained by the application of two steps: (1) *Attachment of the bridge molecule to arm polymers,* followed by *Cleavage of the protecting group of the conjugated bridge molecule* (2) *Attachment of the amine-activated arm polymers to the long polymer to gain brush² structures* described in "1.3 General Methods". 10 mg (0.18 µmol, 42.02 µmol related to the repetition unit) of p(PFPA) Pn ~ 98 were functionalized with amine-preactivated arm polymer with comes from **P5** (5%, 14.83 mg, 2.10 µmol) quenched with ethanolamine and were received after dialysis as a white powder (12.06 mg, only theoretically 5% incorporation, 0.11 µmol, 61% yield).

^{1}H-NMR (600 MHz, D_2O) δ (ppm) 7.45 – 7.10 (m, *H1*), 3.99 – 3.05 (m, *H2*, *H3*), 2.98 – 2.85 (m, *H4*), 2.84 – 0.76 (m, *H5 – H9*).

^{19}F-NMR (564 MHz, D_2O) δ (ppm) No signals determined.

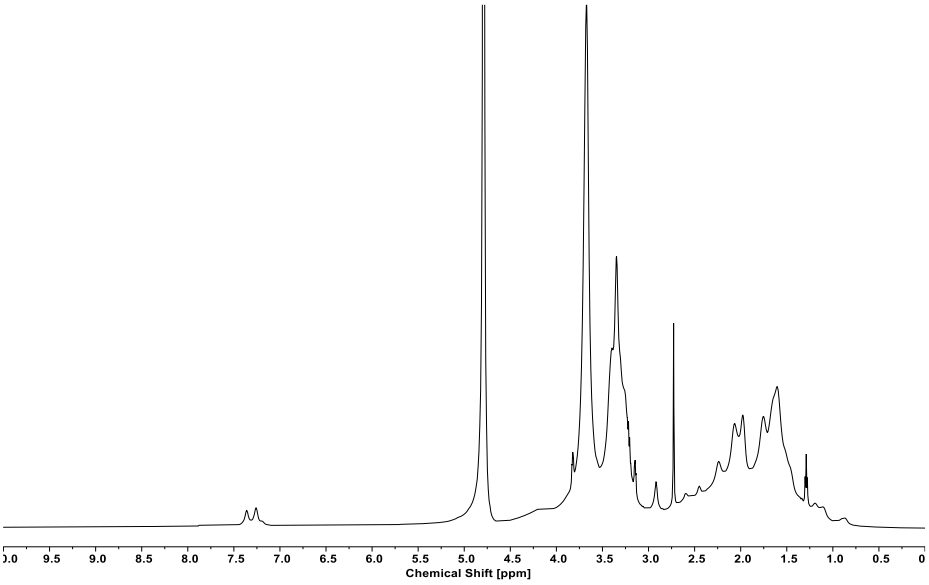


Figure S108: ^{1}H-NMR spectra of **($_0E^2_{57}$) (*B17*)** *(600 MHz, D_2O).*

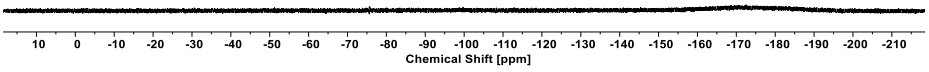
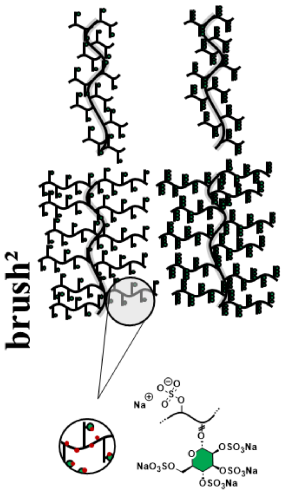
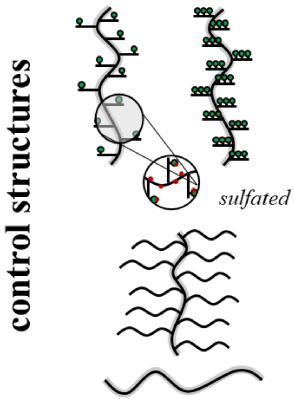


Figure S109: ^{19}F-NMR spectra of **($_0E^2_{57}$) (*B17*)** *(564 MHz, D_2O).*

2.7 DLS measurement

Table 2: Summary of the DLS results with a respective concentration of 0.5 mg/mL water. The limited reliability of the particle sizer in complex distributions (bi- or multimodal) - as partly observed in our AFM measurements - probably explains the deviations of individual DLS measurements from the trend.

structue type	label		temp. [°C]#	d_h [nm] #
brush² 	${}_{22}E^{2}_{29}$	B1	20	80.0
	${}_{66}E^{2}_{29}$	B2	20	65.6
	${}_{22}I^{2}_{29}$	B3	20	92.0
	${}_{66}I^{2}_{29}$	B4	20/40	102.6/99.8
	${}_{66}E^{2}_{57}$	B5	20	113.0
	${}_{198}E^{2}_{57}$	B6	20	73.0
	${}_{66}I^{2}_{57}$	B7	20/40	184.2/320.4
	${}_{198}I^{2}_{57}$	B8	20/40	123.0/445.3
	${}_{22}{}^{*}E^{2}_{29}$	B9	20	149.6
	${}_{66}{}^{*}E^{2}_{29}$	B10	20	77.1
	${}_{66}{}^{*}E^{2}_{57}$	B11	20	67.4
	${}_{198}{}^{*}E^{2}_{57}$	B12	20	67.1
	${}_{22}{}^{*}I^{2}_{29}$	B13	20/40	179.8/118.5
	${}_{66}{}^{*}I^{2}_{29}$	B14	20/40	73.6/61.5
	${}_{66}{}^{*}I^{2}_{57}$	B15	20/40	108.7/498.7
	${}_{198}{}^{*}I^{2}_{57}$	B16	20/40	118.7/96.7
control structures 	${}_{11}E_{235}$	P15	20	65.6
	${}_{33}E_{235}$	P16	20	118.3
	${}_{11}I_{235}$	P17	20/40	50.8/69.9
	${}_{33}I_{235}$	P18	20/40	71.4
	${}_{11}{}^{*}E_{235}$	P19	20	98.4
	${}_{33}{}^{*}E_{235}$	P20	20	107.1/16.4
	${}_{11}{}^{*}I_{235}$	P21	20/40	87.5/61.5
	${}_{33}{}^{*}I_{235}$	P22	20/40	97.2/83.0
	${}_{0}E^{2}_{57}$	B17	20	87.9
	${}_{0}E_{235}$	P23	20	107.8
	${}_{0}I_{235}$	P24	20/40	137.2/208.5

determined via DLS

2.8 SANS measurement

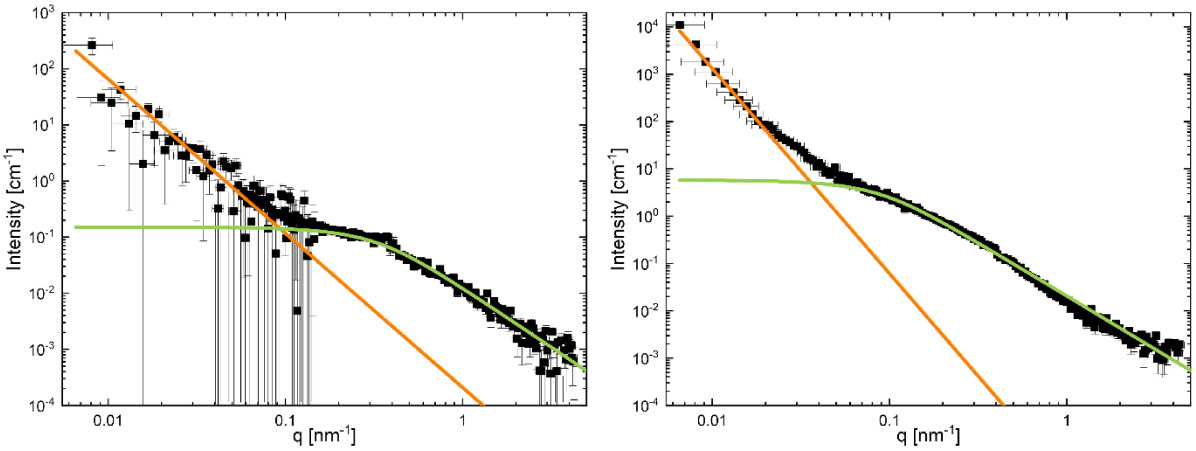


*Figure S110: Results from SANS measurements. The measurements were performed at 25 °C. Both samples were measured in D_2O with concentrations of 5 mg/ml. The Data of sample **B6** is shown on the left and of sample **P15** on the right. The measured data is shown as dots and the contributions to the fits are shown as a solid line. The power law at low q is shown in orange and the Gaussian coil fit is shown in green. The incoherent background scattering was subtracted.*

2.9 AFM measurement

Desorption by AFM-Based Single Molecule Force Spectroscopy

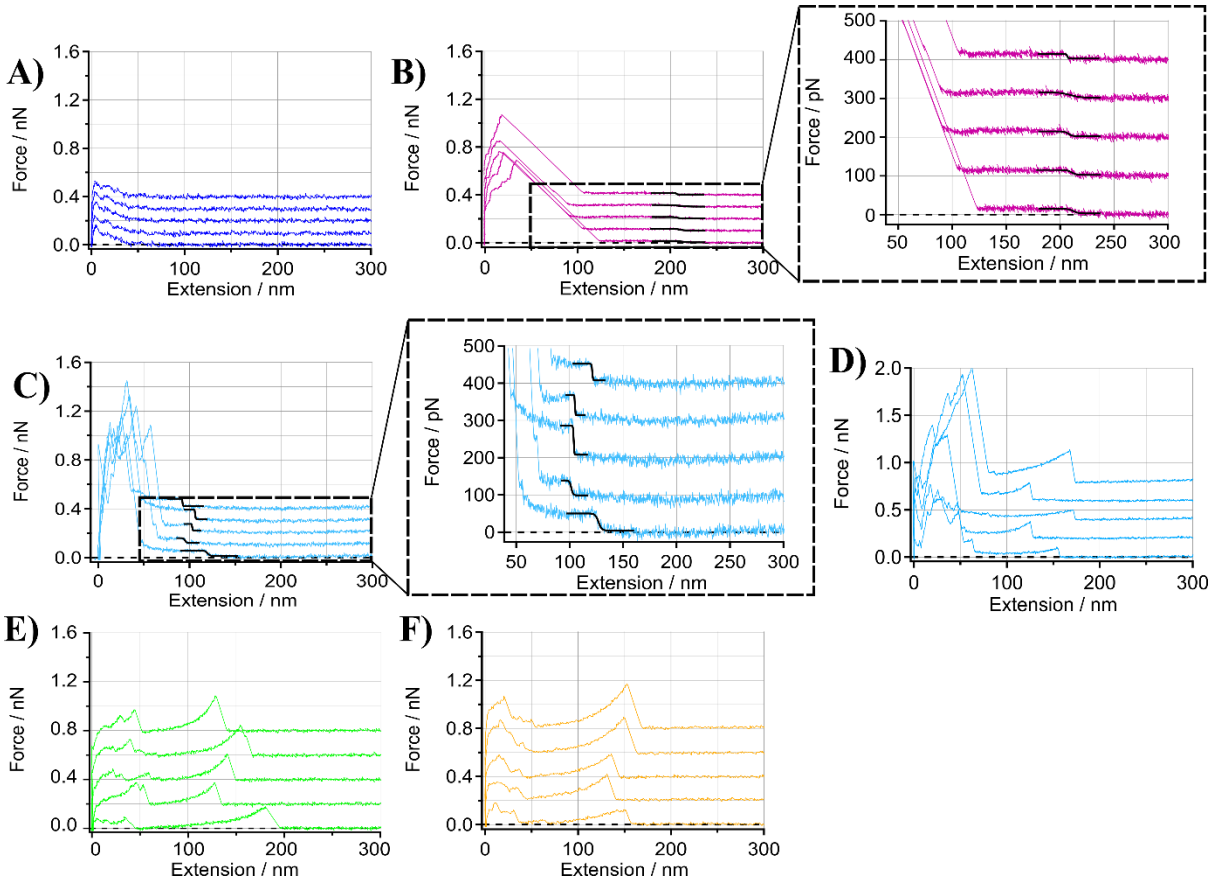


*Figure S111. Exemplary single molecule desorption force-extension curves for A) triethoxysilane-PEG-methoxy (5 kDa) and triethoxysilane-PEG-amine (5 kDa) in a 50:1 ratio on mica in water (control measurements) and B-F) polymers **B17**, **P15**, **P19** and **B11** on mica in water. The extensions range between 100-200 nm, which are consistent with the lengths of the synthesized polymers, which are expected to have a backbone of around 72 nm (based on the C-C length of 1.53 Å[12] for the repeating unit of 235 monomers), plus the PEG linker (ca. 41 nm).[13] The polydispersity index (PDI) of the polymer (1.37) leads to variability in the observed extensions, allowing for some molecules to extend beyond the sum of the backbone and linker lengths, reaching up to 200 nm. The curves either exhibit different desorption motifs, such as plateaus of constant force, as observed for B, C) polymers **B17** and **P15**, or a single desorption peak, as for D-F) polymers **P15**, **P19** and **B11**. We show the whole force-extension curve with a zoom into the relevant plateau portions in (B, C). Plateaus of constant force are indicated with a sigmoidal fit, used for the plateau force and extension evaluation. To improve the presentation, we have vertically offset the curves for (A-C) 100 or (D-F) 200 pN.*

We performed our AFM force spectroscopy experiments in pure water to specifically investigate hydrogen-bond-driven interactions between the glycopolymers and the mica substrate. While buffer conditions would better mimic physiological environments, water was chosen as a clean and suitable medium to investigate the desorption behavior. To further assign the interactions to hydrogen bonds, we performed experiments with **P15** and **B11** on mica using HEPES (10 mM, 50 mM NaCl, pH 7.0 adjusted with NaOH), which can align with the hexagonal lattice of mica and effectively block hydrogen bonding sites.[14] Furthermore, this formation of the hydrogen bonds might be reduced by water molecules aligning to the OH groups of the HEPES molecules. Altogether, this resulted in a loss of detectable interaction events, supporting our claim, that the interactions observed in water are primarily due to hydrogen bonds.

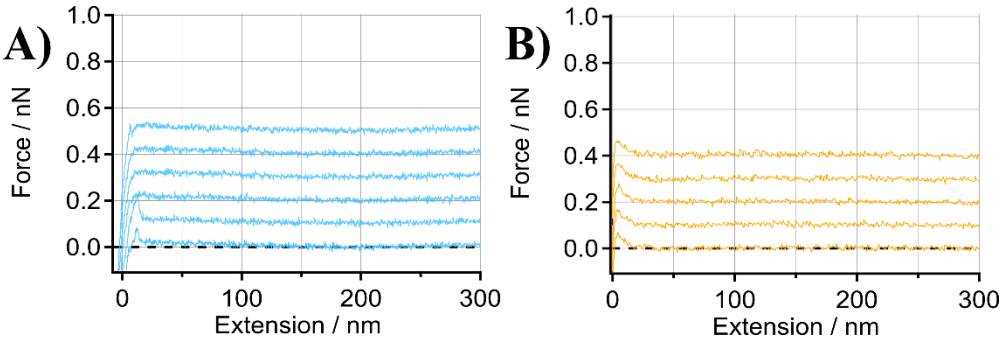


*Figure S112. Exemplary single molecule desorption force-extension curves for A) polymer **P15** and B) polymer **B11** on mica in HEPES (10 mM, 50 mM NaCl, pH 7.0 adjusted with NaOH). In contrast to measurements in pure water (S111) no single molecule desorption motifs are visible, most likely due to HEPES blocking hydrogen bonding sites by aligning with the hexagonal lattice of mica.*

Calculation hydrogen bond density (normalized for based on the backbone length)

One monomer unit contributes two C-C bonds to the backbone length. With 1.53 Å per C-C bond[12] and N= 235, this leads to a backbone length of L_b=$2 \cdot 0.153\ nm \cdot 235$=$72\ nm$. The structure **B17** has no mannose. **P15** and **P19** both have 11 side arms, each containing one mannose group, with each mannose contributing four free groups (hydroxyl for **P15,** hydroxyl and sulfate for **P19**) for hydrogen bonds. Compared to **B17**, this leads to an increase of the potential density of hydrogen bonds per nm of $\rho_{P15,\,P19}$= $\frac{11 \cdot 4}{72\ nm}$= 0.6 $\frac{H\text{-}bonds}{nm}$. **B11** has 11 side arms, each containing six mannose group, with each mannose contributing four free groups (hydroxyl and sulfate) for hydrogen bonds. Compared to **B17**, this leads to an increase of the potential density of hydrogen bonds per nm of ρ_{B11}= $\frac{66 \cdot 4}{72\ nm}$= 3.6 $\frac{H\text{-}bonds}{nm}$.

Conformations by AFM-Based Imaging

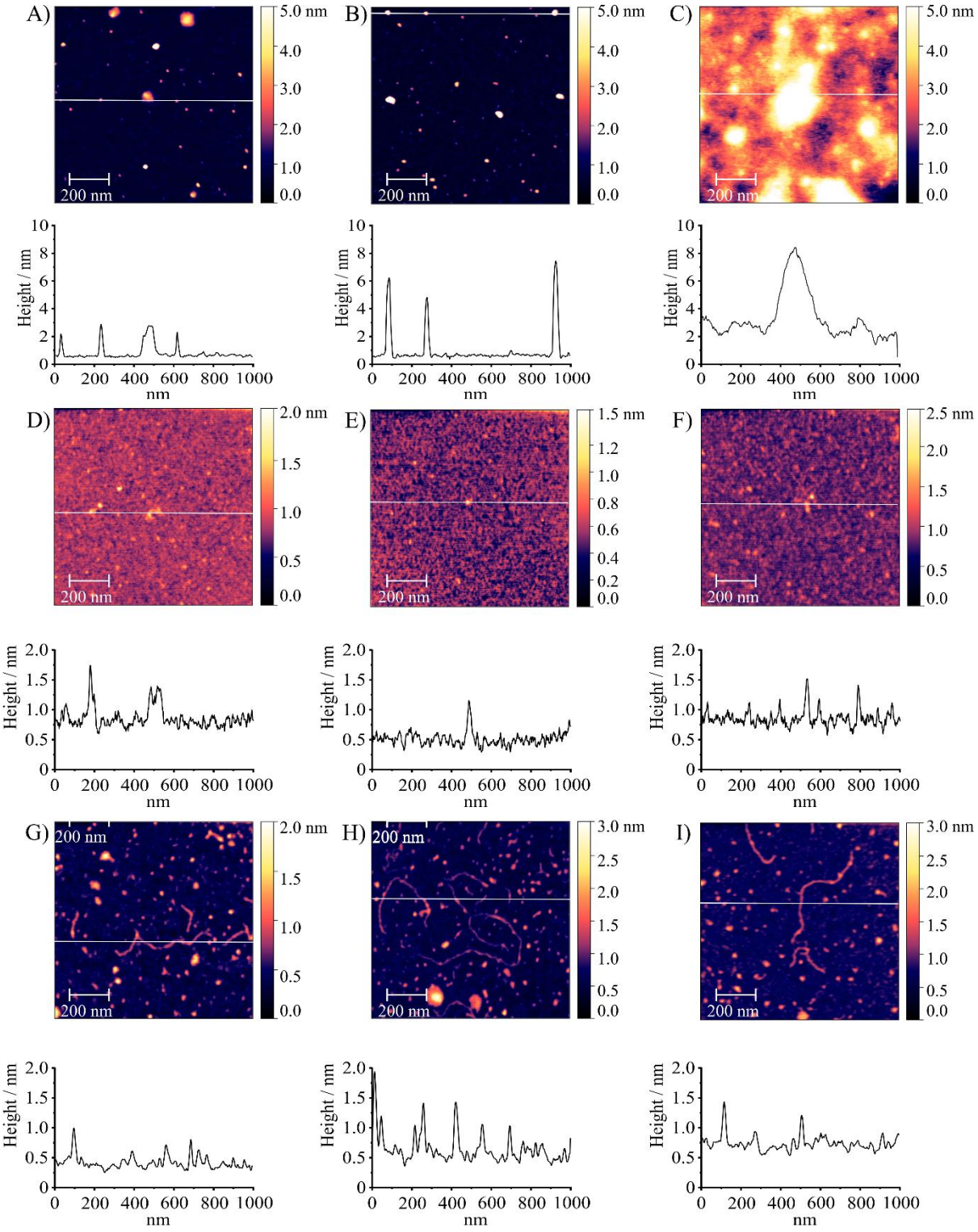


*Figure S*113*: AFM topography images (size: 1 µm²) revealing different conformations of A-C) polymer **B17** (brush²), D-F) polymer **P19** (linear) and G-I) polymer **B11** (brush²), in analogy to the AFM topography images in Figure 6 (main text), all taken on different mica surface positions. All polymers were deposited from a 0.1 µg mL^{-1} polymer solution in water and then dried under vacuum. Images were obtained in air. Line scans are given below the topography images, their positions are indicated by white lines in the topography images.*

B17 (Figure S113 A-C), without any mannose, shows a high degree of aggregation, whereas the glycopolymers **P19** and **B11** (Figure S113 D-I), containing mannose, form smaller aggregates, or in the case of **B11** even linear aggregates. The compact aggregates for brush glycopolymer **B17** (Figure S113 A-C) are clearly observed in the line profiles, where the surface itself is rather clean and flat, interrupted by features reaching heights of up to 9 nm. They might represent a larger aggregate or collapsed bundle. This is different for both, **P19** and **B11** (Figure S113 D-I), where the surface is uneven, showing small aggregates with collapsed conformations all over the line profile, reaching heights of up to 2 nm. This might be a sign of the polymers interacting with the substrate surface, likely mediated by multivalent interactions involving the mannose moieties. For **B11** (Figure S113 G-I), extended, linear conformations are visible with heights up to 1 nm. The width of all the structures observed in the AFM images ranges from 20 nm to 50 nm, except for the large aggregates in the case of **B17** (Figure S113 A-C). Please note that these width values are prone to tip convolution as the cantilever has a tip radius of 5 nm.

3. Literature

(1) Dewhurst, C. Graphical reduction and analysis small-angle neutron scattering program: GRASP. *J. App. Crystallogr.* **2023**, *56* (5), 1595.
(2) Zemplén, G.; Pacsu, E. Über die Verseifung acetylierter Zucker und verwandter Substanzen. *Berichte der deutschen chemischen Gesellschaft (A and B Series)* **1929**, *62* (6), 1613-1614.
(3) Hutter, J. L.; Bechhoefer, J. Calibration of atomic-force microscope tips. *Rev.Sci. Instrum.* **1993**, *64* (7), 1868-1873.
(4) Pirzer, T.; Geisler, M.; Scheibel, T.; Hugel, T. Single molecule force measurements delineate salt, pH and surface effects on biopolymer adhesion. *Phys. Biol.* **2009**, *6* (2), 025004.
(5) Nečas, D.; Klapetek, P. Gwyddion: an open-source software for SPM data analysis. *Open Phys.* **2012**, *10* (1), 181-188.
(6) Ponader, D.; Wojcik, F.; Beceren-Braun, F.; Dernedde, J.; Hartmann, L. Sequence-defined glycopolymer segments presenting mannose: synthesis and lectin binding affinity. *Biomacromolecules* **2012**, *13* (6), 1845-1852.
(7) Ebbesen, M.; Gerke, C.; Hartwig, P.; Hartmann, L. Biodegradable poly (amidoamine) s with uniform degradation fragments via sequence-controlled macromonomers. *Polym. Chem.* **2016**, *7* (46), 7086-7093.
(8) Hill, S. A.; Gerke, C.; Hartmann, L. Recent Developments in Solid-Phase Strategies towards Synthetic, Sequence-Defined Macromolecules. *Chem. Asian J.* **2018**, *13* (23), 3611-3622.
(9) Illmann, M. D.; Schäfl, L.; Drees, F.; Hartmann, L.; Schmidt, S. Glycan-Presenting Coacervates Derived from Charged Poly (active esters): Preparation, Phase Behavior, and Lectin Capture. *Biomacromolecules* **2023**, *24* (6), 2532-2540.
(10) Graisuwan, W.; Zhao, H.; Kiatkamjornwong, S.; Theato, P.; Hoven, V. P. Formation of thermo-sensitive and cross-linkable micelles by self-assembly of poly (pentafluorophenyl acrylate)-containing block copolymer. *J. Polym. Sci. A Polym. Chem.* **2015**, *53* (9), 1103-1113.
(11) Shamout, F.; Monaco, A.; Yilmaz, G.; Becer, C. R.; Hartmann, L. Synthesis of Brush-Like Glycopolymers with Monodisperse, Sequence-Defined Side Chains and Their Interactions with Plant and Animal Lectins. *Macromol. Rapid. Commun.* **2020**, *41* (1), 1900459.
(12) Haynes, W. M. *CRC Handbook of Chemistry and Physics*; CRC press, 2016.
(13) Kolberg, A.; Wenzel, C.; Hackenstrass, K.; Schwarzl, R.; Rüttiger, C.; Hugel, T.; Gallei, M.; Netz, R. R.; Balzer, B. N. Opposing temperature dependence of the stretching response of single PEG and PNiPAM polymers. *J. Am. Chem. Soc.* **2019**, *141* (29), 11603-11613.
(14) Trewby, W.; Livesey, D.; Voïtchovsky, K. Buffering agents modify the hydration landscape at charged interfaces. *Soft Matter* **2016**, *12* (9), 2642-2651.

6.5 Supporting Information - Sequence-Defined Oligoamidoamines as Macroinitiator for Thiol-Induced, Light-Activated Controlled Radical Polymerization of Star-Shaped Glyco-block-copolymers

Authors: Melina I. Feldhof, Ben Raunitschke, Jolana Both, Susanne Boye and Laura Hartmann

Issue: under preparation

Supporting Information

Sequence-Defined Oligoamidoamines as Macroinitiator for Thiol-Induced, Light-Activated Controlled Radical Polymerization of Star-Shaped Glyco-block-copolymers

Melina I. Feldhof,[a] Ben Raunitschke,[a] Jolana Both,[a] Susanne Boye[b] and Laura Hartmann[c]*

a M. I. Feldhof, Jolana Both, Ben Raunitschke, Department of Organic and Macromolecular Chemistry, Heinrich-Heine-University Düsseldorf, Universitätsstraße 1, 40225 Düsseldorf, Germany
b S. Boye, Advanced Macromolecular Structure Analysis, Leibniz-Institut für Polymerforschung Dresden, Hohe Str. 6, 01069 Dresden, Germany
c Prof. Dr. Laura Hartmann, Institute for Macromolecular Chemistry, University of Freiburg, Stefan-Meier-Str. 31, D- 79104 Freiburg i.Br., Germany, E-mail: laura.hartmann@makro.uni-freiburg.de
*Corresponding author

Table of Contents

1. Experimental Parts S2
1.1 Materials S2
1.2 Instrumentation S2
1.3 General Methods S4
2. Synthesis and analytical data S7
2.1 Synthesis of mannose monomer ***S1*** and building blocks ***S2***, ***S3*** for SPPoS S7
2.2 Synthesis macroinitiators (oligoamidoamine) **MI-1** - **MI-3** S10
2.3 TIRP homo-polymerization conditions and analytics **P1**-**P6** S19
2.4 TIRP block-polymerization conditions and analytics ***S4***, **P7**-**P9** S32
3. Deprotection kinetics S41
4. Ligand lectin binding studies S45
5. Literature S46

1. Experimental Parts

1.1 Materials

All chemicals and solvents were used without further purification and were purchased from commercial sources. Type I water, purified by Barnstead™ MicroPure™ ThermoFisher SCIENTIFIC ultrapure water system, was used unless otherwise mentioned.

Acros Organics: piperidine 99%, Magnesium sulphate 97% und copper(II) sulfate 98%; *Biosolve Chemicals*: *N*,*N*-dimethylformamide (DMF) >99.8%, for peptide synthesis; *BLD Pharmatech GmbH*: Fmoc-Cys(Trt)-OH (95%); *Carbosynth*: benzotriazol-1-yloxytripyrrolidinophosphonium hexafluorophosphate (PyBOP); *Carl Roth*: *N*,*N*-Diisopropylethylamine (DIPEA) ≥ 99%, triethylamine ≥ 99.5%, sodium chloride ≥ 99.5%; *ChemSolute*: Ethanol (absolut); *Fisher BioReagents*™: 2-(4-(2-hydroxyethyl)-1-piperazinyl)-ethane sulfonic acid (HEPES) ≥ 99%; *Fisher Scientific*: potassium carbonate water free, ≥ 99.5%, toluene (analytical reagent grade), trifluoroacetic acid ≥ 99.5%, concentrated hydrochloric acid (analytical reagent grade), 1,4-dioxane (analytical reagent grade), acetonitrile ≥ 99.9%, diethyl ether ≥ 99.8%, with BHT, acetone ≥ 99.8%; *J&K*: tris(2-phenylpyridine)iridium(III) ≥ 99%; *Merck*: calcium chloride ≥ 90%, 4,5-Dimethoxy-2-nitrobenzyl bromide 97%, deuterated water ≥ 99.9%, acetic anhydride ≥ 99.5%, methanol ≥ 99.8%, sodium carbonate ≥ 99.7%; *RAPP Polymere*: TentaGel® S RAM Resin (loading: 0.26 mmol/g); *Sigma Aldrich*: Concanavalin A (ConA), *N*-hydroxyethyl acrylamide ≥ 97.4%, DMSO-d_6 ≥ 99.9%, methanol ≥ 99.8%, ethyl acetate ≥ 99.5%, dichloromethane ≥ 99.9% tetrahydrofurane (THF) ≥ 99.9%, ethanolamine ≥ 99%, triisopropyl silane (TIPS) 98%, dimethyl sulfoxide (DMSO) ≥ 99.9%; manganese(II) chloride tetrahydrate ≥ 99%; *TCI*: diphenyl(2,4,6-trimethylbenzoyl)phosphine oxide (TPO) ≥ 98%, tris(2-carboxyethyl)phosphine (TCEP) ≥ 98%.

1.2 Instrumentation

Nuclear Magnetic Resonance Spectroscopy (NMR):

^{1}H-NMR were measured with a Bruker Avance III 600 (600 MHz) or Bruker Avance III 300 (300 MHz) at room temperature. Chemical shifts were reported in delta (δ) expressed in parts per million (ppm) for all NMR spectra. D_2O and $CDCl_3$ serve as the deuterated solvents for the spectra. Multiplicities were abbreviated as the following: singlet (s), doublet (d), triplet (t), quartet (q), multiplet (m). The assignment of carbohydrate signals on NMR followed the chronological enumeration of protons atoms within a monosaccharide starting from the reducing end.

Reversed Phase High Pressure Liquid Chromatography Mass Spectrometry (RP-HPLC-MS): RP-HPLC-MS measurements were performed on Agilent Technologies 1260 Infinity series coupled with Agilent quadrupole mass spectrometer with an Electrospray Ionization (ESI) source operating in a m/z range of 200 to 2000. Spectra were measured with A: 95% H_2O, 5% ACN, 0.1% formic acid and

B: 5% H_2O, 95% ACN, 0.1% formic acid. Separation was performed at 25 °C using an Agilent MZ-Aqua Perfect C_{18} 3 µm (50 x 3.0 mm) column with a linear solvent gradient starting at 100% A, ending at 50% B in 17 min at a flow rate of 0.4 mL/min. Indicated purities were determined by integration of the UV-signal detected by a wavelength detector set to 214 nm with the OpenLab ChemStation software for LC/MS from Agilent Technologies.

Matrix-assisted laser desorption/ionization with time-of-flight mass spectrometer (MALDI-TOF-MS): MALDI-TOF-MS spectra was performed using a Bruker Daltonics UltfelXtreme device. 2,5 dihydroxybenzoic acid (DHB) was the used matrix.

High-resolution-electrospray-ionisation mass-spectrometry (HR-ESI): HR-ESI-MS were performed on UHR-QTOF maXis 4G from Bruker Daltonics.

Size Exclusion Chromatography─Multi-Angle Light Scattering (H_2O-SEC-MALS): ***System 1:*** Additional SEC study with quadrupole (SEC-D4) was performed on an Agilent 1260 infinity series including isocratic pump, degasser, and autosampler. The columns were three Suprema Lux analytical columns (8 mm diameter and 5 µm particle size) and one precolumn (50 mm, 2 × 160 Å of 300 mm and 1000 Å of 300 mm). The eluent was 10 mM PBS buffer and 0.02 % NaN_3 (pH 7.4). The detector system also consisted of DAWN HELEOS-II (including QELS option) and Optilab T-rEX (Waters | Wyatt Technologies) and a variable wavelength detector SPD-M20 (Shimadzu). The flow rate was set to 1 mL per min. Data analysis was performed by Astra 8.1 software (Waters | Wyatt Technologies). The sample concentration was 3 -5 mg per mL and the injection volume was 100 µL. Each sample was analyzed in duplicate. ***System 2:*** Advanced SEC characterization with quintuple detection (SEC-D5) was done using an Agilent 1260 infinity II series including isocratic pump, degasser, autosampler and variable wavelength detector; one pre-column and two GE Healthcare Superdex (75/10/300) columns. The eluent was 10 mM PBS buffer and 0.02 % NaN_3 (pH 7.4). The detector system also consisted of DAWN NEON (including QELS option), ViscoStar, and Optilab T-rEX (Waters | Wyatt Technologies). The flow rate was set to 1 mL per min. Data analysis was performed by Astra 8.1 software (Waters | Wyatt Technologies). The sample concentration was 3.5 - 4.5 mg per mL and the injection volume was 75 µL, each sample was analyzed in triplicate.

d*n*/d*c* determination: The d*n*/d*c* values for the absolute molar mass calculation were determined by manually injecting a concentration series (0.25; 0.5; 1.0; 1.5and 2.0 mg per mL) in 10 mM PBs of selected samples into an Optilab T-rEX (Waters | Wyatt Technologies) RI detector.

Conformation analysis: The viscosity data obtained from SEC-D5 was used to consider conformational properties by Kuhn-Mark-Houwink-Sakurada (KMHS) plot.[1] The slope of the

intrinsic viscosity [η] plotted against molar mass provides insight into the shape and compactness of macromolecules in a given solvent. This relationship is described by the Mark–Houwink–Sakurada equation:

$$[\eta] = KM^{\alpha} \quad (1)$$

For compact, spherical macromolecules, the exponent α is theoretically expected to be close to 0. In contrast, for expanded, linear random coils in a good solvent, α typically ranges between 0.5 and 1.0.

1.3 General Methods

Standard protocols for solid phase synthesis

TentaGel™ resin was utilized in the synthesis process of both oligoamidoamines and the building block assembly, which involved iterative repetition of deprotection and conjugation steps. The backbone sequences were finished by Fmoc deprotection of the terminal amine enabling the conjugation to the active ester polymers. The required methods are described in the following section and can performed either by manual or automated synthesis (CS136XT, CS Bio). The given equivalents are related to 0.1 mmol scale.

Swelling protocol: Before the first cleavage of the *N*-Fmoc protecting group, the resin was swollen twice with approx. 5 mL DCM and then reconditioned 10 times to DMF.

Fmoc-Deprotection: *N*-Fmoc protecting groups of the functionalized TentaGel™ resin or the immobilized building blocks was removed by incubating approx. 5 ml 25% piperidine solution in DMF, shaken for 15 minutes and washed five times with DMF. The deprotection step was repeated and the resin was then washed with ten times with DMF.

Building block assembly: The two *N*-Fmoc-protected building blocks used here, **EDS** are assembled on the solid support of the sequence-defined oligoamidoamines. After the respective Fmoc deprotection of the *N*-terminus, the next building block was conjugated using amide coupling methods. For this purpose, a solution of the **EDS** building block (5.0 eq.), PyBOP (4.9 eq.) and DIPEA (10 eq.) was dissolved in 2 mL DMF and added to the reaction vessel. The reaction mixture was shaken for 60 minutes at room temperature and then the resin was washed 10 times with 5 mL DMF each time.

Switching the protecting group from Trt to oNv on thiol functionalities: First, the Trt protecting group is dissolved by 1 eq iodine in 2.5 mL or 5 mL MeOH. The reaction solution is then drawn up into the syringe reactor and deprotected for one hour at room temperature. Next, carefully draw up a 1 N sodium thiosulfate solution and expel it with the deprotection solution. Wash three more times with 2.5 mL of the sodium thiosulfate solution to reduce residual iodine. Then wash five times with 4 mL MeOH each, twice with 2.5 mL DMF each,

once with 4 mL DCM each, twice with 2.5 mL DMF each, five times with 2.5 mL MeOH each and finally five times with 2.5 mL DMF each. To break up and prevent any disulfide bridges that may have formed, the syringe reactor is then shaken with 5 eq TCEP in 2.5 mL or 5 mL DMF for one hour at room temperature. After ejection of the solution, a solution containing 5 eq oNv in 2.5 mL or 5 mL DMF and 20 eq DIPEA is immediately drawn into the syringe reactor. This is then wrapped in aluminum foil and allowed to shake for 18 hours at room temperature. Finally, wash five times with 2.5 mL DMF each and twice with 2.5 mL DCM each.

Cleavage of the tBu/Boc protecting group: Like the Fmoc cleavage, the removal of the Boc protecting group was also carried out in a different fume hood than the solid phase coupling. For this purpose, a 4 M HCl in dioxane solution was drawn up to half the syringe volume and allowed to shake for 30 min. It was then washed ten times with DMF and the pH value of the wash solution was measured. If this was slightly basic, washing with DMF could be stopped. Finally, wash again five times with 2.5 mL DMF in the regular fume hood.

***N-terminal capping*:** To prevent side reactions of primary amines (*N*-terminal), they are acetylated. For this purpose, after the final Fmoc deprotection, acetic anhydride is drawn into the syringe reactor and shaken for 15 minutes. Subsequently, the mixture is washed three times with 2.5 mL of DMF each. The reaction is then repeated. Finally, the product is washed ten times with 2.5 mL of DMF each.

***Cleavage reaction*:** The synthesized macromolecules were cleaved from the resin by adding 2 ml of TFA/TIPS/DCM (95/2.5/2.5) solution to the reaction vessel and shaking for 30 minutes, precipitated in cold diethyl ether and freeze-dried.

Standard protocols for TIRP: First, the macroinitiator **MI-1** - **MI-3** and 5 eq TCEP*HCl per thiol were dissolved in 10 wt% DMF (solution no. 1). 1 eq TPO per thiol was dissolved with 10 wt% DMF (solution no. 2). 0.05mol% $Ir(ppy)_3$ cat. and corresponding eq. monomer per thiol was dissolved in 10 wt% DMF (solution no. 3). All three solutions were then deoxygenated with nitrogen for 20 minutes. Solution no. 1 was then irradiated for 15 minutes at 365 nm with an intensity of 576.4 mW/cm^2. Polymerization was started by adding solution no. 2 and 3 in solution no. 1 for 120 minutes at 405 nm with a radiation intensity of 1.15 mW/cm^2. The reaction mixture was purified using dialysis (exclusion volume 10 kDa) and lyophilized. The polymers were obtained in a white, flaky powder.

Standard protocol for block-copolymers via TIRP: The core-shell polymers were synthesized through a two-step process. Initially, the core polymer was polymerized see “Standard protocols for TIRP“. The resulting precursor was then used as the initiator for the second polymerization via “Standard protocols for TIRP“. Finally, the acetyl protecting groups were cleaved off from the finished

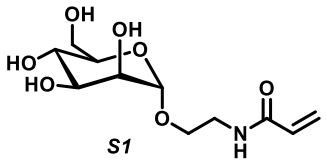
mannose-containing block copolymers under Zemplén conditions with 0.2 M NaOMe solution in MeOH for 1 h with stirring and the polymer was purified by dialysis against water.

Ligand lectin binding studies: For the measurement of star-glyco-block-copolymer and ConA clustering by specific ligand-receptor interactions in solution, absorbance spectra were measured as triplicates on a microplate reader. Specific ligand-receptor interactions in the clusters were determined based on quantifying the turbidity of the solution. Absorbance spectra (λ = 420 nm) were measured in lectin binding buffer (LBB, 50 mM sodium chloride, 1 mM manganese (II) chloride tetrahydrate, 1 mM calcium chloride and 10 mM HEPES dissolved in ultrapure water at a pH of 7.4). Initially, 198µL of the lectin ConA (5µM in LBB) were provided at the beginning. Then 2µL of the corresponding concentration series (with stock solution concentrations of **P7**: 80mM, **P8**: 53µM and **P9**: 18µM) were added and absorbance were measured after 20 min incubation.

2. Synthesis and analytical data

2.1 Synthesis of mannose monomer *S1* and building blocks *S2*, *S3* for SPPoS

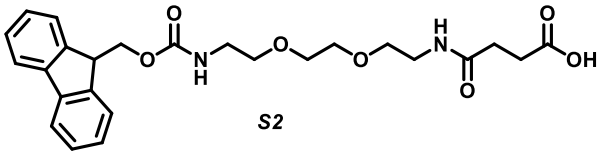
S1 a-D-Mannopyranosyl-ethylacrylamid (ManEAA)



S1

The syntheses of structures S1 and S2 have already been published by Schröer et. al.[2]

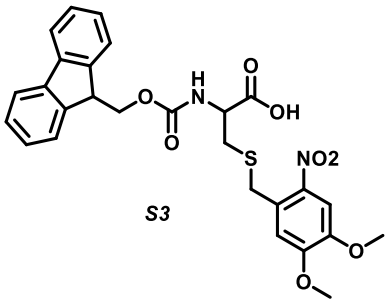
S2 ethylene glycol diamine succinyl, 1-(9H-fluoren-9-yl)-3,14-dioxo-2,7,10-trioxa-4,13-diazaheptadecan-17-oic acid (EDS)



S2

Building blocks EDS were synthesized as previously reported.[3]

S3 Fmoc-Cys(oNv)-OH



S3

The thiol function of the solid-phase compatible cysteine building block was rearranged by combining two synthesis routes known from the literature. 1 eq. (1 mmol) Fmoc-Cys(Trt)-OH was introduced into 0.2 mL DCM. Subsequently, 4.8 mL TFA and 0.2 mL TIPS were added. The solution was stirred at room temperature for one hour. The solvent and TFA were then removed under reduced pressure and the intermediate in the form of a white solid was used in the next step without further purification.

In the second step, 1 eq. (1 mmol) of 4,5-dimethyl-2-nitrobenzyl bromide was dissolved in 10 mL DCM and 5 eq. (5 mmol) of DIPEA was added dropwise. Slowly add the previously synthesized intermediate of deprotected cysteine to the resulting solution and stirred at room temperature for 18 hours. All subsequent steps are carried out in the absence of light. The

solvent is removed under reduced pressure and then dissolved again in 5 mL DMF. The reaction solution is added to a vigorously stirred cold 200 mL (0.5 M) HCl solution. The resulting precipitate is filtered off and washed three times with 10 mL of water. The crude product in the form of an orange oil is then dried on a rotary evaporator. Further purification is carried out by column chromatographic purification (0 - 10 vol.% MeOH in DCM). 296 mg were obtained in the form of a yellowish powder, which corresponds to a yield of 55% (Lit: 69%[4]).

^{1}H-NMR (600 MHz, DMSO-d$_6$): δ (ppm) 7.89 (d, ^3J = 7.56 Hz, 2H, Ar(Fmoc)-**H**), 7.71 (d, ^3J = 6,83 Hz, 3H, Ar(Fmoc)-**H**), 7.64 (s, 1H, Ar(*o*Nv)-**H**), 7.41 (t, ^3J = 7.42 Hz, 2H, Ar(Fmoc)-**H**), 7.31 (t, ^3J = 7.42 Hz, 2H, Ar(Fmoc)-**H**), 7.15 (s, 1H, Ar(*o*Nv)-**H**), 4.33-4,18 (m, 3H, -C(O)-O-CH$_2$-C**H**- overlap with -C(O)-O-C**H**$_2$-), 4.16-4.03 (m, 3H, -NH-C**H**-COOH H-8 overlap with Ar(*o*Nv)-C**H**$_2$-S-), 3.87 (s, 3H, -O-C**H**$_3$), 3.83 (s, 3H, -O-C**H**$_3$), 2.86 (dd, ^2J = 13.74, ^3J = 4.41 Hz, 1H, -S-C**H**$_2$-CH-COOH), 2.71 (dd, ^2J = 13.96, ^3J = 9.68 Hz, 1H, -S-C**H**$_2$-CH-COOH).

RP-HPLC-MS: t$_r$ = 13.25 min, relative purity: > 95%, m/z calculated for $C_{27}H_{26}N_2O_8S$ 539.1 $[M+H]^+$, 561.1 $[M+Na]^+$, 281.1 $[M+H+Na]^{2+}$, found 539.2 $[M+H]^+$, 561.6 $[M+Na]^+$, 281.3 $[M+H+Na]^{2+}$.

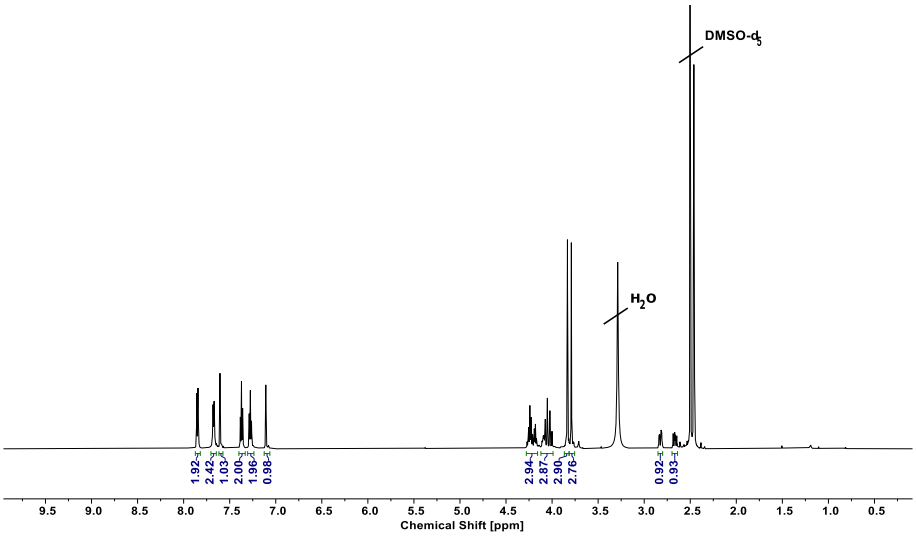


*Figure S1: ^{1}H-NMR spectrum (300 MHz, DMSO-d$_6$) of Fmoc-Cys(oNv)-OH (**S3**).*

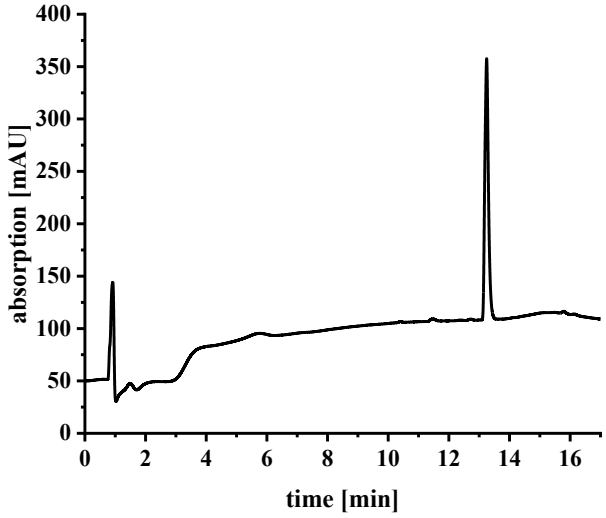


*Figure S2: RP-HPLC chromatogram of Fmoc-Cys(oNv)-OH (**S3**).*

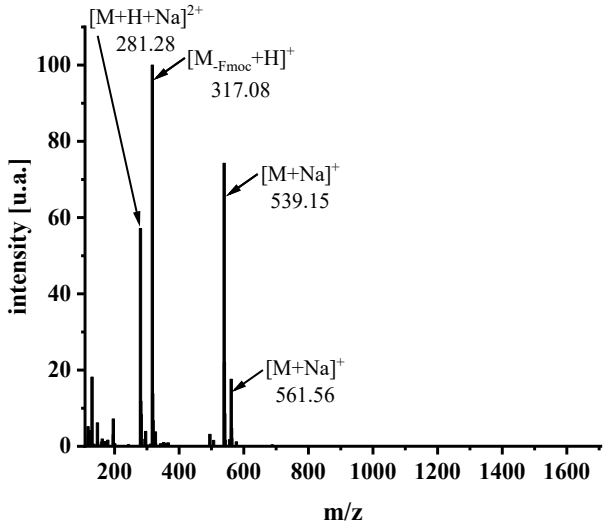
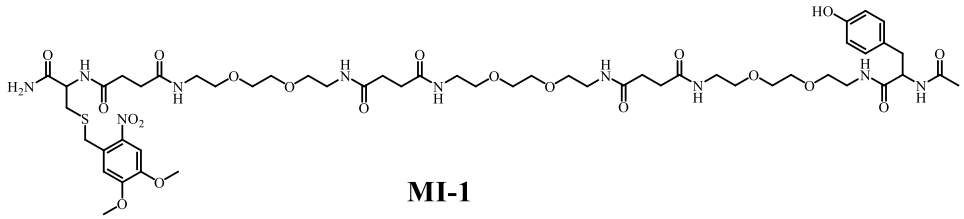


*Figure S3: Mass spectrum of Fmoc-Cys(oNv)-OH (**S3**) at t = 13.25 min (gradient of 5 to 95 vol.% acetonitrile/water with 0.1 vol.% formic acid, run time: 17 min) by ESI-MS.*

2.2 Synthesis macroinitiators (oligoamidoamine) MI-1 - MI-3

All following oligoamidoamides were synthesized via "Standard protocols for solid phase synthesis" (1.3 General Methods).

Synthesis of Cys(oNv)-(EDS)$_3$-Tyr (MI-1)



MI-1

Initially, the building block Fmoc-Cys(Trt)-OH was coupled, followed by three coupling steps of EDS building block, and finally, the Fmoc-Tyr(tBu)-OH building block was attached. Subsequently, a protective group exchange reaction was performed on the thiol functionalities, converting Trt to *o*Nv. After lyophilization, a yield of 79% and a purity of 71% were achieved.

^{1}H-NMR (600 MHz, DMSO-d$_6$): δ (ppm) 8.13-8.09 (m, 1H, -N**H**-, overlap with DMF), 8.02 (d, ^3J = 8.42 Hz, -N**H**-), 7.96 (t, ^3J = 5.47 Hz, -N**H**-, overlap with DMF), 7.90-7.84 (m, -N**H**-), 7.65 (s, Ar(*o*Nv)-**H**), 7.50 (s, -N**H$_2$**), 7.17 (s, -N**H$_2$**), 7.16-7.13 (m Ar(*o*Nv)-**H**), 6.99 (br. d, ^3J = 8.40 Hz, Ar(Tyr)-**H**), 6.62 (br. d, ^3J = 8.44 Hz, Ar(Tyr)-**H**), 4.41-4.34 (m, -NH-C(O)-C**H**-NH-C(O)-), 4.11-3.99 (m, Ar-CH$_2$-S-C**H$_2$**-), 3.92 (m, -O-C**H$_3$**), 3.84 (s, -O-C**H$_3$**), 3.51-3.47 (m, -C(O)-C**H$_2$**-C**H$_2$**-C(O)-), 3.40-3.36 (m, -NH-CH$_2$-C**H$_2$**-O-), 3.21-3.15 (m, -NH-C**H$_2$**-CH$_2$-O-), 2.85-2.74 (m, Ar-C**H$_2$**-S-), 2.58-2.51 (m, Ar-C**H$_2$**-S-), 1.76 (s, -C(O)-C**H$_3$**).

RP-HPLC-MS: t_r = 7.33 min, relative purity: 71 %, m/z calculated for $C_{53}H_{82}N_{10}O_{20}S$ 404.5 $[M+3H]^{3+}$, 606.3 $[M+2H]^{2+}$, 1211.5 $[M+H]^+$, found 404.6 $[M+3H]^{3+}$, 606.3 $[M+2H]^{2+}$, 1213.4 $[M+H]^+$.

MALDI-TOF-MS: m/z calculated for $C_{53}H_{82}N_{10}O_{20}S$: 1233.53 $[M+Na]^+$, 1249.50 $[M+K]^+$, found 1233.79 $[M+Na]^+$, 1249.77 $[M+K]^+$.

HR-ESI-MS: m/z calculated for $C_{53}H_{82}N_{10}O_{20}S$: 606.28 $[M+2H]^+$, found 606.28 $[M+2H]^+$.

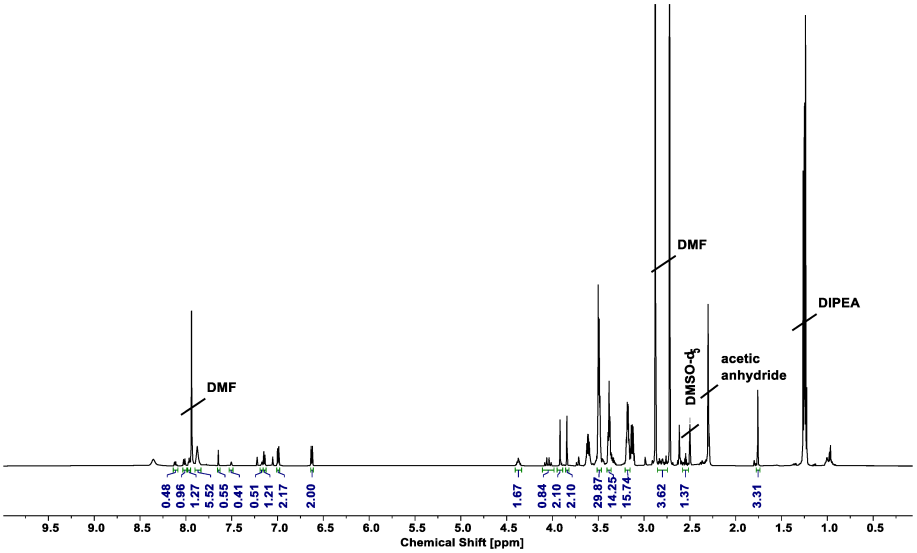


Figure S4: ^{1}*H-NMR spectrum (600 MHz, DMSO-d*$_6$*) of* ***MI-1****.*

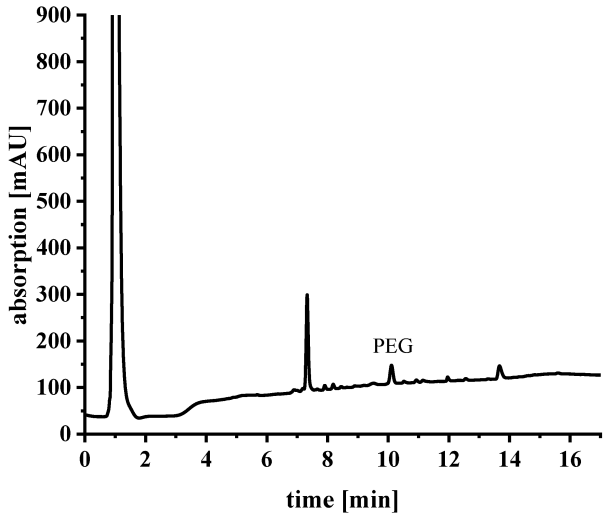


Figure S5: RP-HPLC chromatogram of ***MI-1****.*

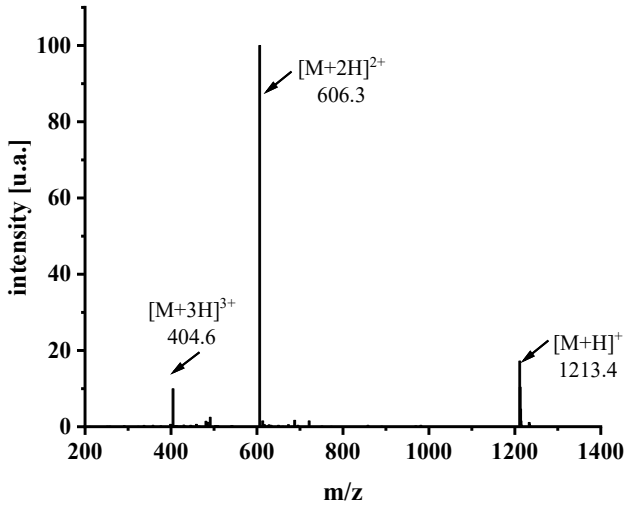


*Figure S6: Mass spectrum of **MI-1** at t = 7.33 min (gradient of 5 to 95 vol.% acetonitrile/water with 0.1 vol.% formic acid, run time: 17 min) by ESI-MS.*

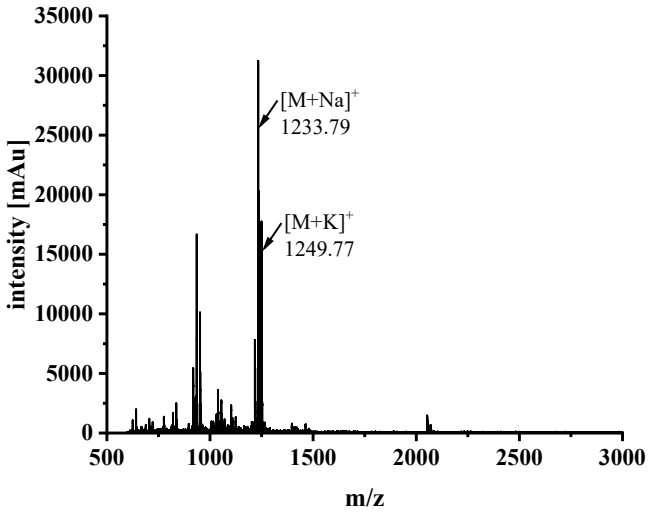


*Figure S7: MALDI-TOF-MS spectrum of **MI-1**.*

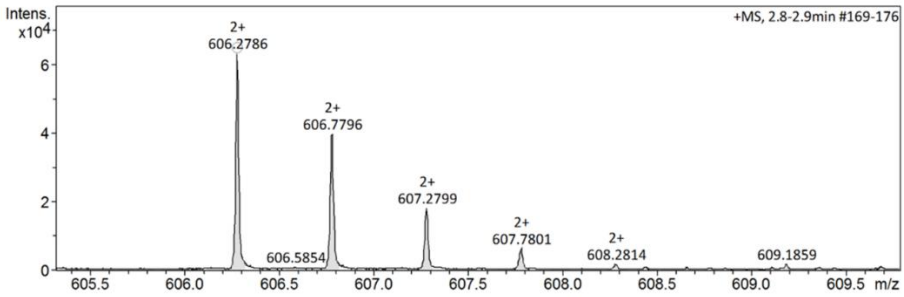
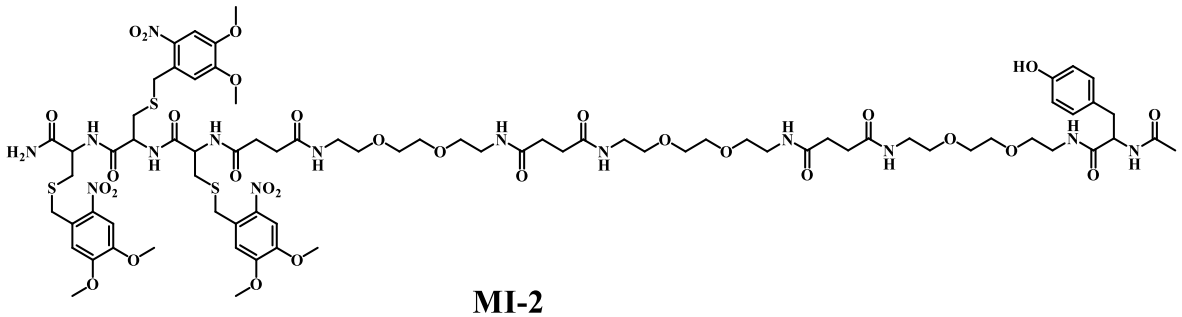


*Figure S8: HR-ESI-MS spectrum of **MI-1**.*

Synthesis of (Cys(oNv))$_3$-(EDS)$_3$-Tyr (MI-2)



MI-2

Initially, the building block Fmoc-Cys(Trt)-OH was coupled three times, followed by three coupling steps of EDS building block, and finally, the Fmoc-Tyr(tBu)-OH building block was attached. Subsequently, a protective group exchange reaction was performed on the thiol functionalities, converting Trt to *o*Nv. After lyophilization, a yield of 66% and a purity of 77% were achieved.

^{1}H-NMR (600 MHz, DMSO-d$_6$): δ (ppm) 8.40 (d, ^3J = 7.73 Hz, 1H, -N**H**-), 8.28 (d, ^3J = 7.60 Hz, 1H, -N**H**-), 8.12 (d, ^3J = 7.93 Hz, 1H, -N**H**-), 8.01-7.93 (m, 2H, -N**H**-, overlap with DMF), 7.90-7.81 (m, 5H, -N**H**-), 7.67-7.60 (m, 3H, Ar(*o*Nv)-**H**, overlap with already cleaved Ar(*o*Nv)-**H**), 7.33 (s, 1H, -N**H**$_2$), 7.28 (s, 1H, -N**H**$_2$), 7.16-7.08 (m, 3H, Ar(*o*Nv)-**H**, overlap with already cleaved Ar(*o*Nv)-**H**), 6.99 (d, ^3J = 8.42 Hz, 2H, Ar(Tyr)-**H**), 6.62 (br. d, ^3J = 8.40 Hz, 2H, Ar(Tyr)-**H**), 4.55-4.47 (m, 2H, -NH-C(O)-C**H**-NH-C(O)-, overlap with water peak), 4.39-4.33 (m, 2H, -NH-C(O)-C**H**-NH-C(O)-, overlap with water peak), 4.10-3.94 (m, 6H, Ar-CH$_2$-S-C**H**$_2$- overlap with ethyl acetate), 3.91-3.88 (m, 9H, -O-C**H**$_3$, overlap with already cleaved -O-C**H**$_3$), 3.83 (s, 9H, -O-C**H**$_3$, overlap with already cleaved -O-C**H**$_3$), 3.52-3.42 (m, 24H, -C(O)-C**H**$_2$-C**H**$_2$-C(O)), 3.40-3.29 (m, 12H, -NH-CH$_2$-C**H**$_2$-O-), 3.20-3.10 (m, 12H, -NH-C**H**$_2$-CH$_2$-O-), 2.82-2.73 (m, 4H, Ar-C**H**$_2$-S-, overlap with DMF), 2.63-2.52 (m, 4H, Ar-C**H**$_2$-S-, overlap with DMF), 1.75 (s, 3H, -C(O)-C**H**$_3$).

RP-HPLC-MS: t_r = 10.08 min, relative purity: 77 %, m/z calculated for $C_{77}H_{110}N_{14}O_{30}S_3$ 603.2 $[M+3H]^{3+}$, 904.3 $[M+2H]^{2+}$, 1807.7 $[M+H]^+$, found 603.4 $[M+3H]^{3+}$, 904.4 $[M+2H]^{2+}$, 1807.6 $[M+H]^+$.

MALDI-TOF-MS: m/z calculated for $C_{77}H_{110}N_{14}O_{30}S_3$ 1829.66 $[M+Na]^+$, 1845.63 $[M+K]^+$, found 1829.95 $[M+Na]^+$, 1845.93 $[M+K]^+$.

HR-ESI-MS: m/z calculated for $C_{77}H_{110}N_{14}O_{30}S_3$ 904.34 $[M+2H]^{2+}$, found 904.34 $[M+2H]^{2+}$.

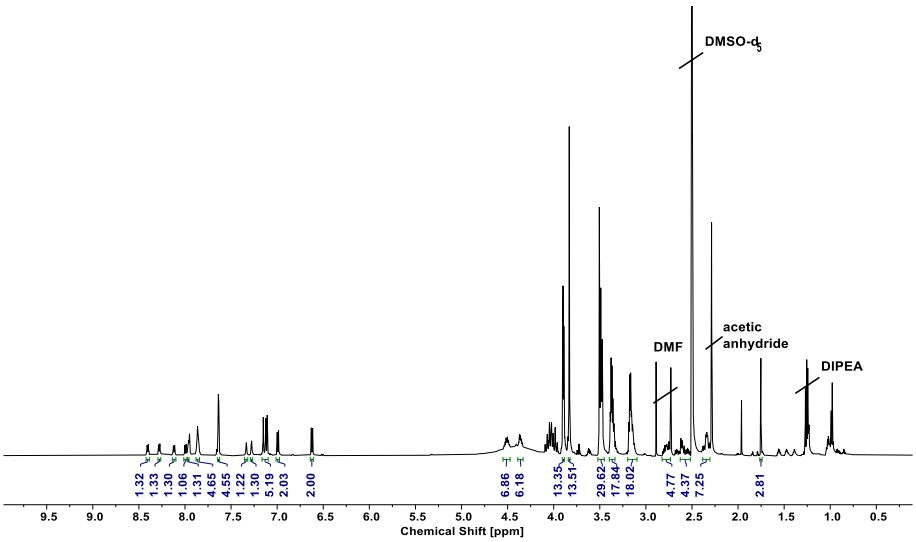


*Figure S9: [1]H-NMR spectrum (600 MHz, DMSO-d6) of **MI-2**.*

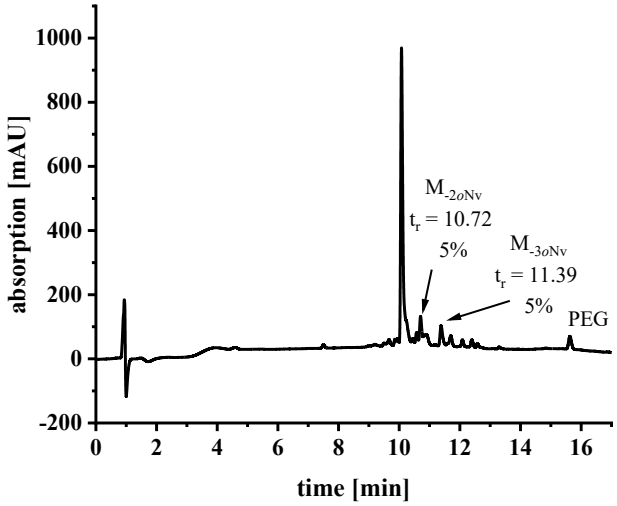


*Figure S10: RP-HPLC chromatogram of **MI-2**.*

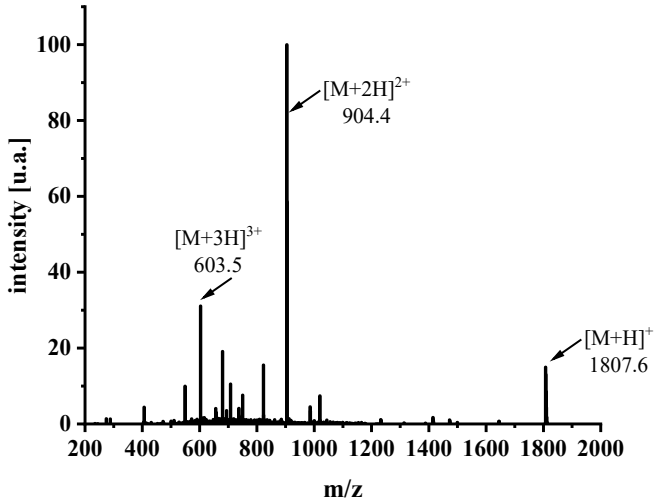


*Figure S11: Mass spectrum of **MI-2** at t = 10.08 min (gradient of 5 to 95 vol.% acetonitrile/water with 0.1 vol.% formic acid, run time: 17 min) by ESI-MS.*

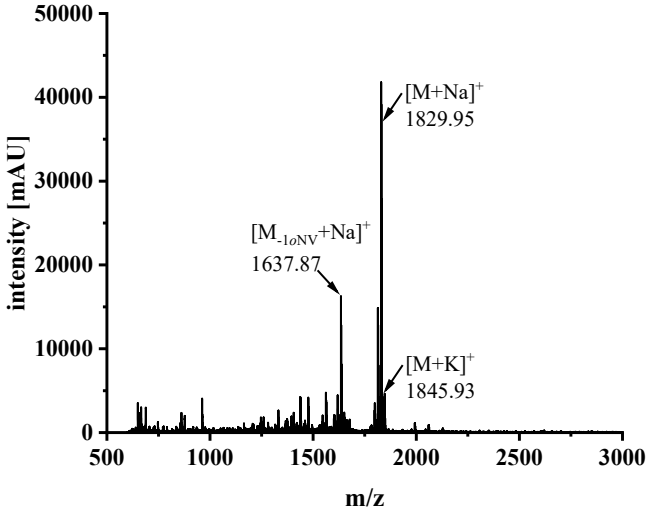


*Figure S12: MALDI-TOF-MS spectrum of **MI-2**.*

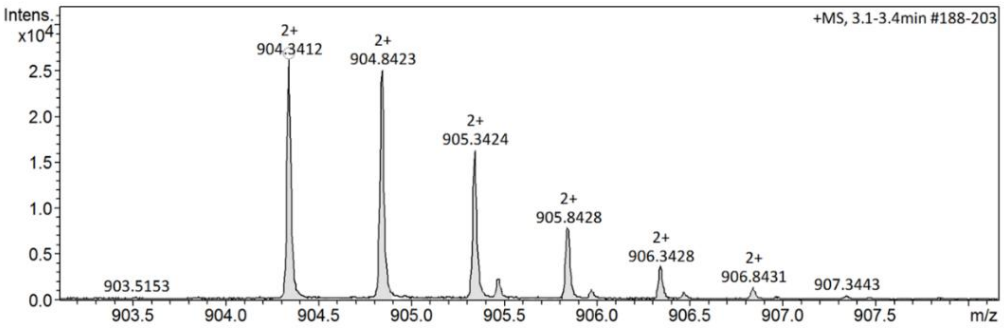
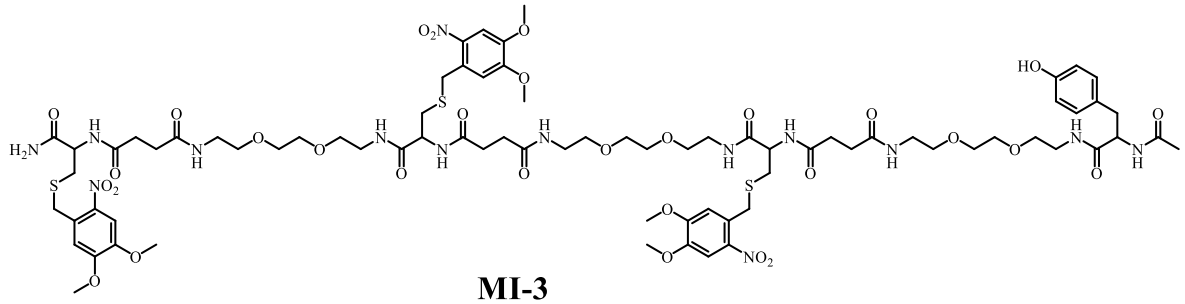


*Figure S13: HR-ESI-M spectrum of **MI-2**.*

Synthesis of (Cys(oNv)-EDS)$_3$-Tyr (MI-3)



MI-3

Initially, the building block Fmoc-Cys(Trt)-OH was coupled followed by coupling of one EDS building block, this was carried out further two times, and finally, the Fmoc-Tyr(tBu)-OH building block was attached. Subsequently, a protective group exchange reaction was performed on the thiol functionalities, converting Trt to *o*Nv. After lyophilization, a yield of 69% and a purity of 82% were achieved.

^{1}H-NMR (600 MHz, DMSO-d$_6$): δ (ppm) 9.14 (s, 1H, -O**H**), 8.18-8.07 (m, 5H, -N**H**-), 8.02-7.89 (m, 5H, -N**H**-), 7.67-7.63 (m, 3H, Ar(*o*Nv)-**H**, overlap with already cleaved Ar(*o*Nv)-**H**), 7.49 (s, 1H, -N**H$_2$**), 7.17 (s, 1H, -N**H$_2$**), 7.15 (s, 3H, Ar(*o*Nv)-**H**, overlap with already cleaved Ar(*o*Nv)-**H**), 6.99 (br. d, ^3J = 8.48 Hz, 2H, Ar(Tyr)-**H**), 6.62 (br. d, ^3J = 8.47 Hz, 2H, Ar(Tyr)-**H**), 4.48-4.41 (m, 2H, -NH-C(O)-C**H**-NH-C(O)-), 4.40-4.32 (m, 2H, -NH-C(O)-C**H**-NH-C(O)-), 4.09-4.00 (m, 6H, Ar-CH$_2$-S-C**H$_2$**- overlap with ethyl acetate), 3.93-3.30 (4 m, 54H, -O-C**H$_3$**, overlap with already cleaved -O-C**H$_3$**, -C(O)-C**H$_2$**-C**H$_2$**-C(O)-, -NH-CH$_2$-C**H$_2$**-O-), 3.25-3.10 (m, 12H, -NH-C**H$_2$**-CH$_2$-O-), 2.83-2.52 (2 m, 8H, Ar-C**H$_2$**-S-, overlap with DMF and DMSO), 1.75 (s, 3H, -C(O)-C**H$_3$**).

RP-HPLC-MS: t_r = 9.77 min, relative purity: 82 %, m/z calculated for $C_{77}H_{110}N_{14}O_{30}S_3$ 603.2 $[M+3H]^{3+}$, 904.3 $[M+2H]^{2+}$, 1807.7 $[M+H]^+$, found 603.4 $[M+3H]^{3+}$, 904.4 $[M+2H]^{2+}$, 1807.5 $[M+H]^+$.

MALDI-TOF-MS: m/z calculated for $C_{77}H_{110}N_{14}O_{30}S_3$ 1829.66 $[M+Na]^+$, 1845.63 $[M+K]^+$, found 1829.97 $[M+Na]^+$, 1845.96 $[M+K]^+$.

HR-ESI-MS: m/z calculated for $C_{77}H_{110}N_{14}O_{30}S_3$ 904.34 $[M+2H]^{2+}$, found 904.34 $[M+2H]^{2+}$.

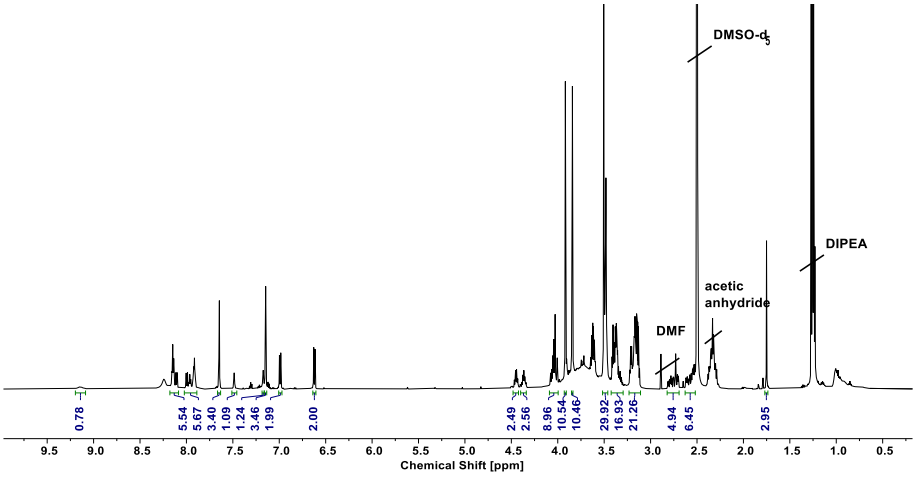


*Figure S14: [1]H-NMR spectrum (600 MHz, DMSO-d_6) of **MI-3**.*

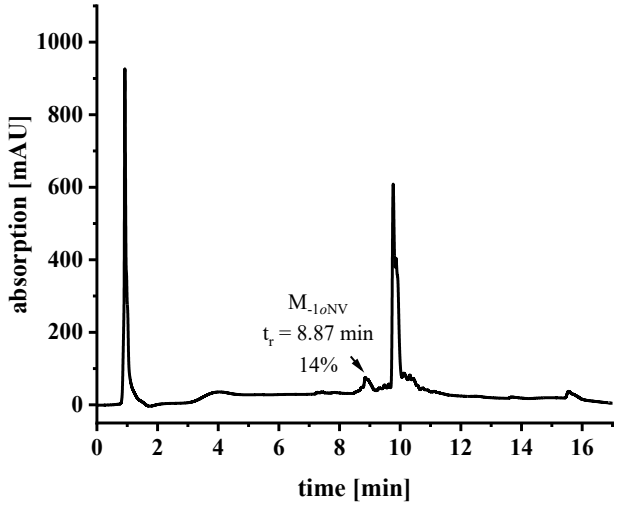


*Figure S15: RP-HPLC chromatogram of **MI-3**.*

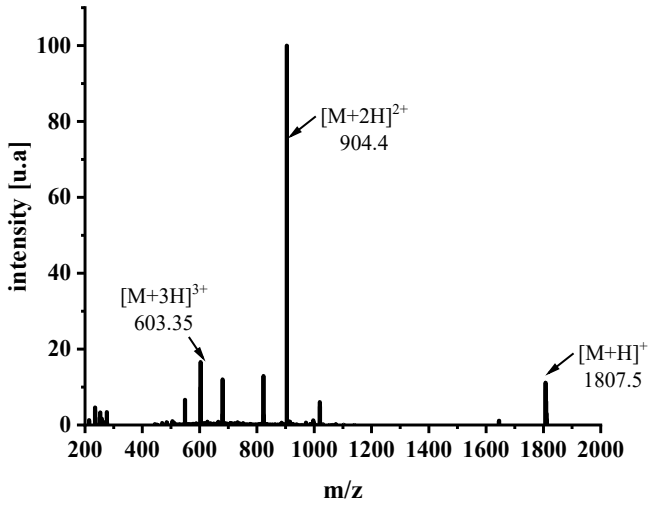


*Figure S16: Mass spectrum of **MI-3** at t = 9.69 min (gradient of 5 to 95 vol.% acetonitrile/water with 0.1 vol.% formic acid, run time: 17 min) by ESI-MS.*

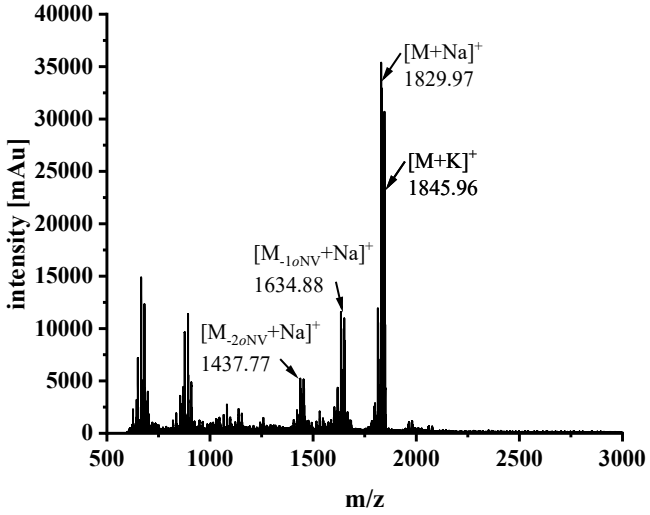


*Figure S17: MALDI-TOF-MS spectrum of **MI-3**.*

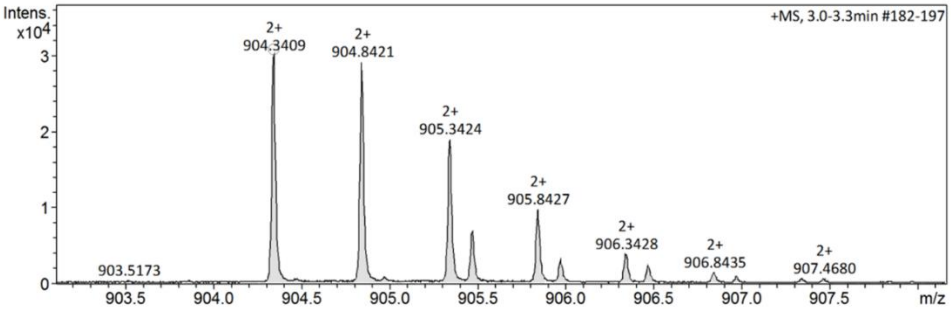


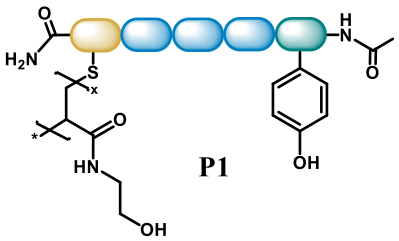
Figure S18: HR-ESI-MS spectrum of MI-3.

2.3 TIRP homo-polymerization conditions and analytics P1-P6

*Table S1: Sample values of the used TIRP components and yields of polymers **P1** – **P6**.*

No.	macroinitiator [mg]	TCEP [mg]	TPO [mg]	Ir(ppy)$_3$-cat. [mg]	HEAA [mg]	yield [mg]	yield [%]
P1	MI-1  8.04	9.63	1.14	0.34	113.36		54
P2	MI-1  2.82	1.88	0.18	0.34	118.85	51	43
P3	MI-2  5.85	14.38	1.70	0.16	55.95	16	32
P4	MI-2  4.07	9.80	1.18	0.35	117.28	56	47
P5	MI-3  5.85	14.30	1.70	0.17	56.10	20	33
P6	MI-3  4.13	9.99	1.17	0.35	117.28	67	56

P1 – HEAA TIRP from macroinitiator MI-1



The polymerization is conducted as described in section 1.3 general methods "Standard protocols for TIRP" and sample sizes and yields are summarized in Table S1, see p. 19.

^{1}H-NMR (600 MHz, D_2O): δ (ppm) 8.24-8.00 (m, NH), 7.77-7.55 (m, H_{TPO}), 7.15-7.12 (m, H_{Tyr}), 6.97 (s, H_{TPO}), 6.86-6.81 (m, H_{Tyr}), 3.82-3.15 (m, $H_{HEAA\text{-side chain}}$), 3.06-2.48 (m, $H_{MI\text{-}1}$), 2.30-1.37 (m, $H_{HEAA\text{-backbone}}$).

GPC: $\overline{M_n}$ = 28.5 ± 0.1 kDa, Đ = 1.34.

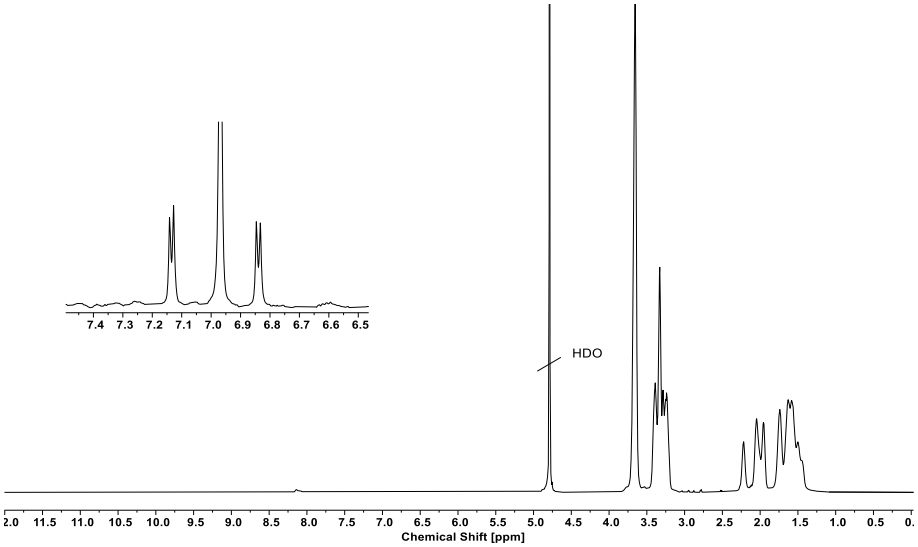


*Figure S19: ^{1}H-NMR spectrum (600 MHz, D_2O) of **P1**. The zoom shows the tyrosine signals of the macroinitiator.*

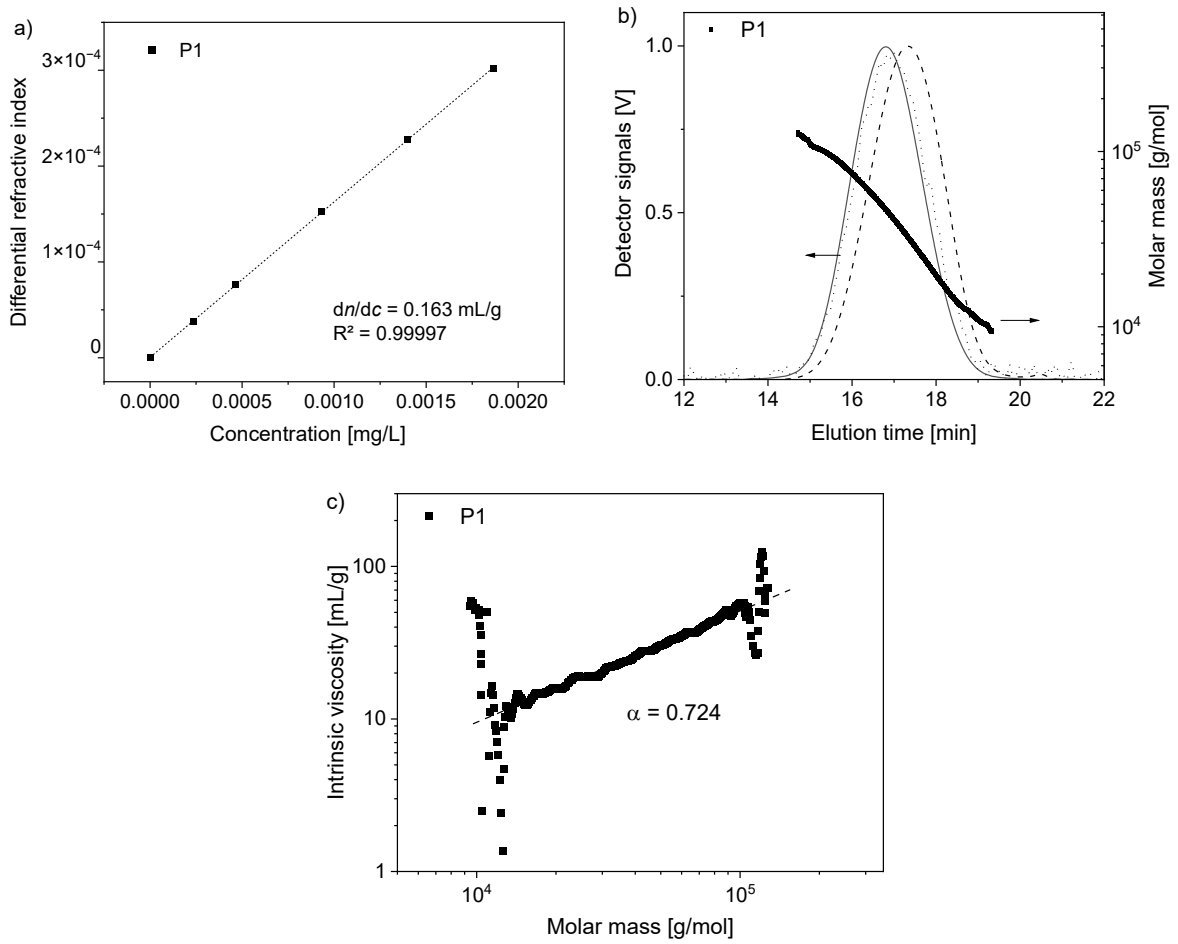


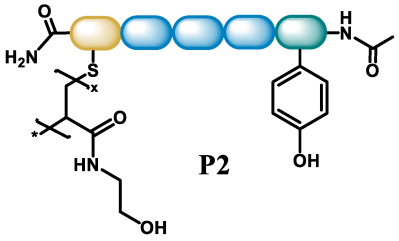
*Figure S20: SEC-D5 studies: a) results of dn/dc determination, dRI vs. concentration, b) detector signals (solid line – LS; dashed line – dRI, dotted line – specific viscosity) and molar masses (symbols)vs. elution time; and c) Kuhn-Mark-Houwink-Sakurada plot (intrinsic viscosity vs. molar masses) of **P1**.*

*Table S2: Results of SEC-D5 studies of **P1.***

Measurement	M_n *1 [kg/mol]	M_w *1 [kg/mol]	Đ (M_w/M_n)	R_g [nm]	$R_{h,DLS}$ [nm]	$R_{h,h}$ [nm]
1	28.6	38.2	1.34	*n.d.*	4.4	6.0
2	28.5	38.1	1.34	*n.d.*	4.5	6.1
3	28.5	38.0	1.33	*n.d.*	4.6	6.0
average	**28.5 ± 0.1**	**38.1 ± 0.1**	**1.34**	**n.d.**	**4.5 ± 0.1**	**6.0 ± 0.1**

*1 calculated by dn/dc = 0.163 ml, experimentally determined, SEC-D5 performed by System 2

P2 – HEAA TIRP from macroinitiator MI-1



P2

The polymerization is conducted as described in section 1.3 general methods "Standard protocols for TIRP" and sample sizes and yields are summarized in Table S1, see p. 19.

^{1}H-NMR (600 MHz, D_2O): *δ (ppm)* 8.26-8.01 (m, NH), 7.77-7.55 (m, H_{TPO}), 7.17-7.11 (m, H_{Try}), 6.97 (s, H_{TPO}), 6.87-6.82 (m, H_{Tyr}), 3.90-3.12 (m, $H_{HEAA\text{-side chain}}$), 3.06-2.45 (m, $H_{MI\text{-}1}$), 2.30-1.27 (m, $H_{HEAA\text{-backbone}}$).

GPC: $\overline{M_n}$ = 49.2 ± 0.5 kDa, Đ = 1.40.

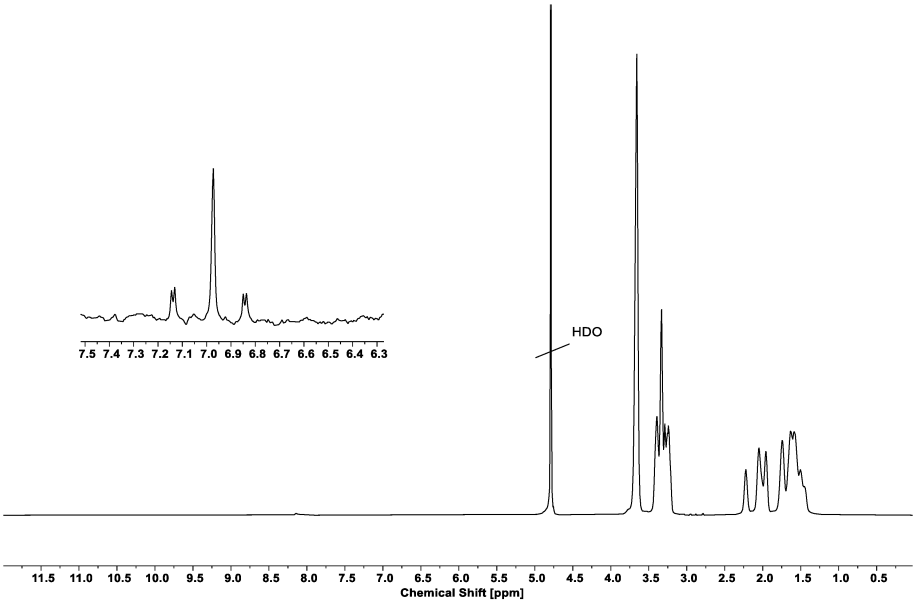


*Figure S21: ^{1}H-NMR spectrum (600 MHz, D_2O) of **P2**. The zoom shows the tyrosine signals of the macroinitiator.*

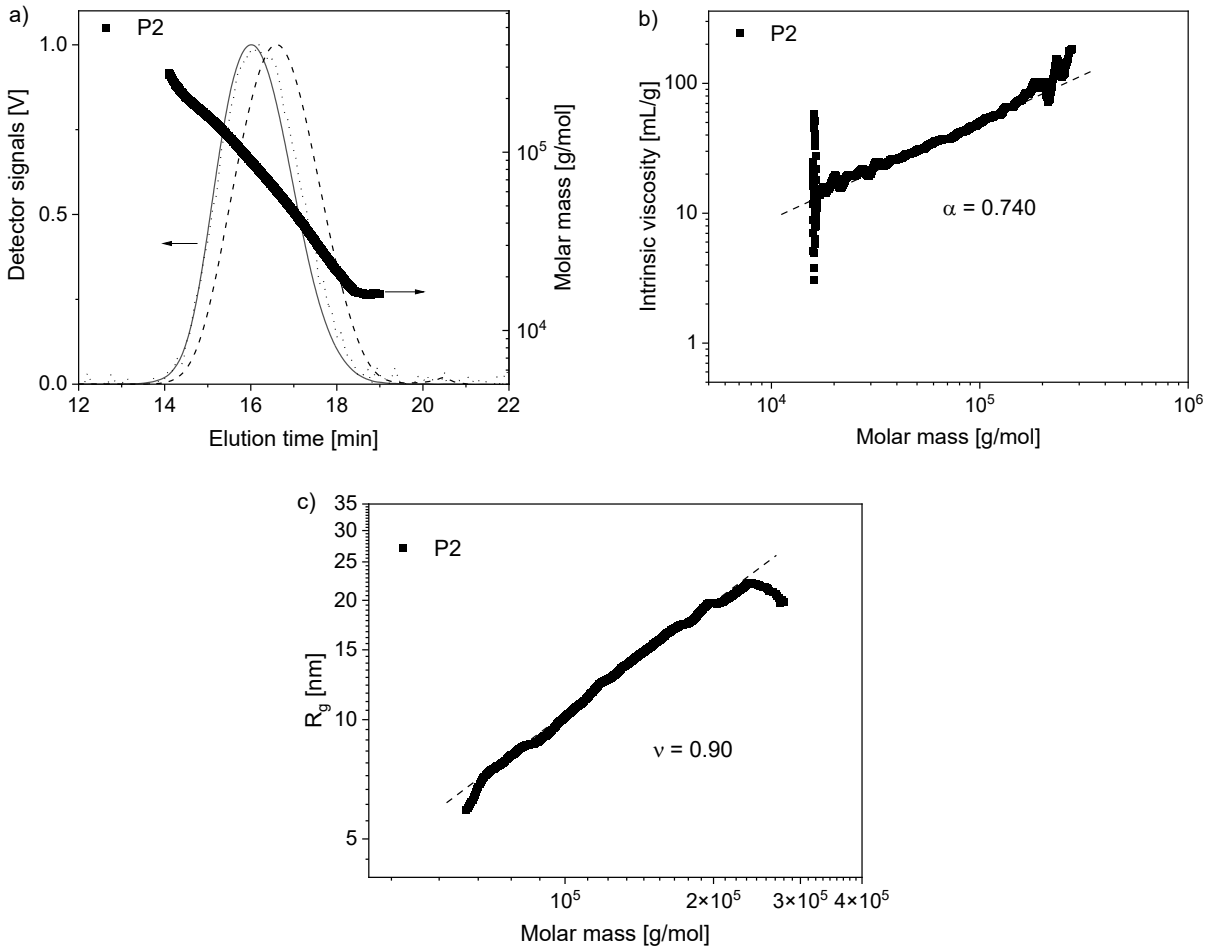


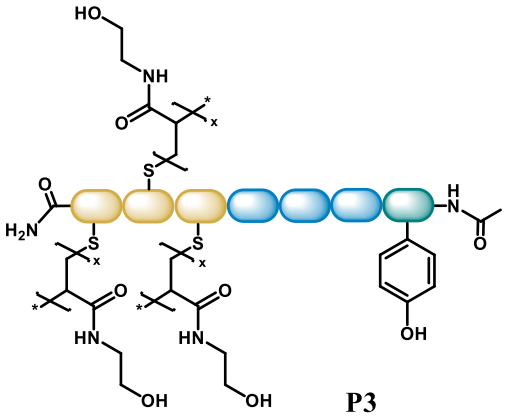
*Figure S22: SEC-D5 studies: a) detector signals (solid line – LS; dashed line – dRI, dotted line – specific viscosity) and molar masses (symbols)vs. elution time; b) Kuhn-Mark-Houwink-Sakurada plot (intrinsic viscosity vs. molar masses) and c) scaling plot (R_g vs molar mass; only elution range from 13 - 18 min) of **P2**.*

*Table S3: Results of SEC-D5 studies of **P2.***

Measurement	M_n [*1] [kg/mol]	M_w [*1] [kg/mol]	Đ (M_w/M_n)	R_g [*2] [nm]	$R_{h,DLS}$ [nm]	$R_{h,h}$ [nm]
1	48.7	68.2	1.40	9.6	7.0	8.5
2	49.4	69.8	1.41	10.8	7.1	8.6
3	49.5	69.2	1.40	10.8	7.0	8.6
average	**49.2 ± 0.5**	**69.1 ± 0.8**	**1.40**	**10.4 ± 0.7**	**7.0 ± 0.1**	**8.6 ± 0.1**

[*1] calculated by dn/dc = 0.163 ml, experimentally determined, SEC-D5 performed by System 2, [*2] only elution range from 13 - 18 min

P3 – HEAA TIRP from macroinitiator MI-2



P3

The polymerization is conducted as described in section 1.3 general methods "Standard protocols for TIRP" and sample sizes and yields are summarized in Table S1, see p. 19.

^{1}H-NMR (600 MHz, D_2O): δ (ppm) 8.25-8.03 (m, NH), 7.77-7.54 (m, H_{TPO}), 7.17-7.05 (m, H_{Tyr}), 6.97 (s, H_{TPO}), 6.86 - 6.75 (m, H_{Tyr}), 3.75-3.17 (m, $H_{HEAA\text{-side chain}}$), 3.07-2.46 (m, $H_{MI\text{-}2}$), 2.29-1.39 (m, $H_{HEAA\text{-backbone}}$).

GPC: $\overline{M_n}$ = 12.9 ± 0.5 kDa, Đ = 1.15.

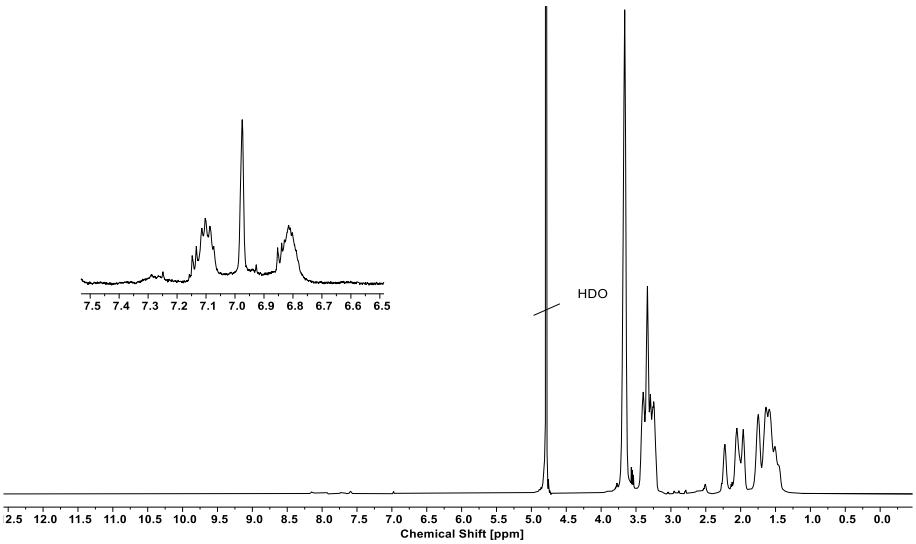


*Figure S23: ^{1}H-NMR spectrum (600 MHz, D_2O) of **P3**. The zoom shows the tyrosine signals of the macroinitiator.*

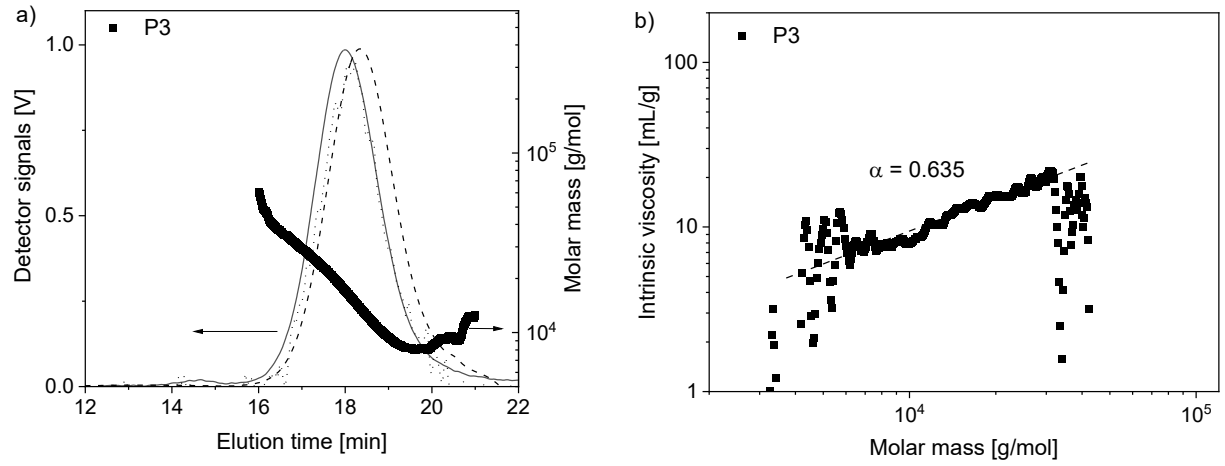


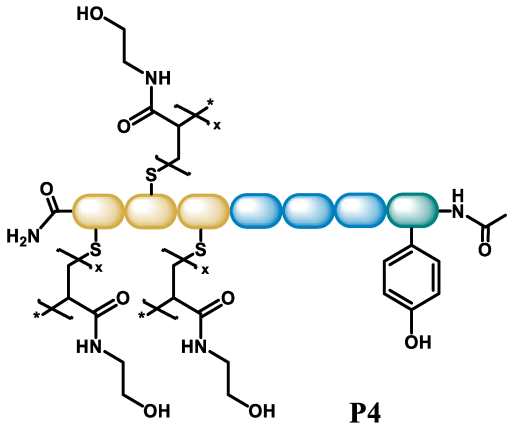
*Figure S24: SEC-D5 studies: a) detector signals (solid line – LS; dashed line – dRI, dotted line – specific viscosity) and molar masses (symbols)vs. elution time; and b) Kuhn-Mark-Houwink-Sakurada plot (intrinsic viscosity vs. molar masses) of **P3**.*

*Table S4: Results of SEC-D5 studies of **P3.***

Measurement	M_n *1 [kg/mol]	M_w *1 [kg/mol]	Đ (M_w/M_n)	R_g *2 [nm]	$R_{h,DLS}$ [nm]	$R_{h,h}$ [nm]
1	12.9	14.8	1.15	n.d.	n.d.	3.2
2	12.8	14.9	1.16	n.d.	n.d.	3.4
3	12.9	14.9	1.15	n.d.	n.d.	3.4
average	**12.9 ± 0.5**	**14.9± 0.5**	**1.15**	**-**	**-**	**3.3 ± 0.1**

*1 calculated by dn/dc = 0.163 ml, experimentally determined, SEC-D5 performed by System 2

P4 – HEAA TIRP from macroinitiator MI-2



P4

The polymerization is conducted as described in section 1.3 general methods "Standard protocols for TIRP" and sample sizes and yields are summarized in Table S1, see p. 19.

^{1}H-NMR (600 MHz, D_2O): δ (ppm) 8.26-8.02 (m, NH), 7.77-7.54 (m, H_{TPO}), 7.17-7.04 (m, H_{Tyr}), 6.97 (s, H_{TPO}), 6.87-6.75 (m, H_{Tyr}), 3.85-3.13 (m, $H_{HEAA\text{-side chain}}$), 3.07-2.43 (m, $H_{MI\text{-}2}$), 2.28-0.91 (m, $H_{HEAA\text{-backbone}}$).

GPC: $\overline{M_n}$ = 25.6 ± 0.3 kDa, Đ = 1.30.

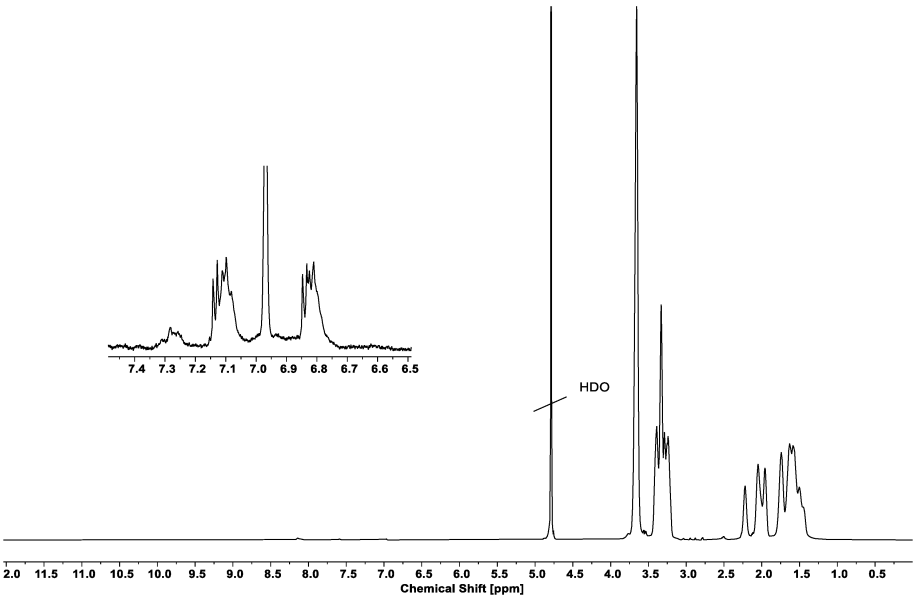


*Figure S25: ^{1}H-NMR spectrum (600 MHz, D_2O) of **P4**. The zoom shows the tyrosine signals of the macroinitiator.*

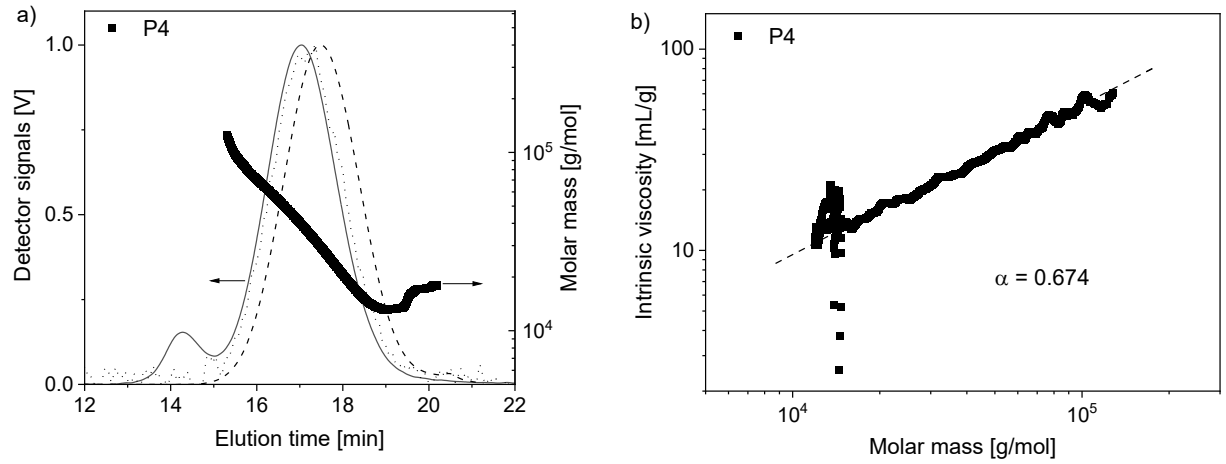


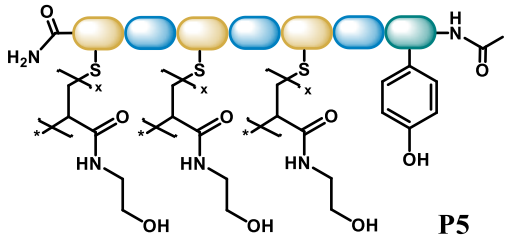
*Figure S26: SEC-D5 studies: a) detector signals (solid line – LS; dashed line – dRI, dotted line – specific viscosity) and molar masses (symbols)vs. elution time; and b) Kuhn-Mark-Houwink-Sakurada plot (intrinsic viscosity vs. molar masses) of **P4**.*

*Table S5: Results of SEC-D5 studies of **P4.***

Measurement	**M_n*1 [kg/mol]**	**M_w*1 [kg/mol]**	**Đ (M_w/M_n)**	**R_g [nm]**	**$R_{h,DLS}$ [nm]**	**$R_{h,h}$ [nm]**
1	25.3	33.1	1.31	n.d.	3.5	5.7
2	25.5	33.2	1.30	n.d.	4.0	5.5
3	26.0	33.3	1.28	n.d.	3.7	5.6
average	**25.6 ± 0.3**	**33.2 ± 0.1**	**1.30**	**-**	**3.7 ± 0.1**	**5.6 ± 0.1**

*1 calculated by dn/dc = 0.163 ml, experimentally determined, SEC-D5 performed by System 2

P5 – HEAA TIRP from macroinitiator MI-3



The polymerization is conducted as described in section 1.3 general methods "Standard protocols for TIRP" and sample sizes and yields are summarized in Table S1, see p. 19.

^{1}H-NMR (600 MHz, D_2O): δ (ppm) 8.25-8.05 (m, NH), 7.78-7.54 (m, H_{TPO}), 7.16-7.02 (m, H_{Tyr}), 6.98 (s, H_{TPO}), 6.88-6.73 (m, H_{Tyr}), 3.76-3.16 (m, $H_{HEAA\text{-side chain}}$), 3.08-2.46 (m, $H_{MI\text{-}3}$), 2.31-1.36 (m, $H_{HEAA\text{-backbone}}$).

GPC: $\overline{M_n}$ = 14.5 ± 0.5 kDa, Đ = 1.15.

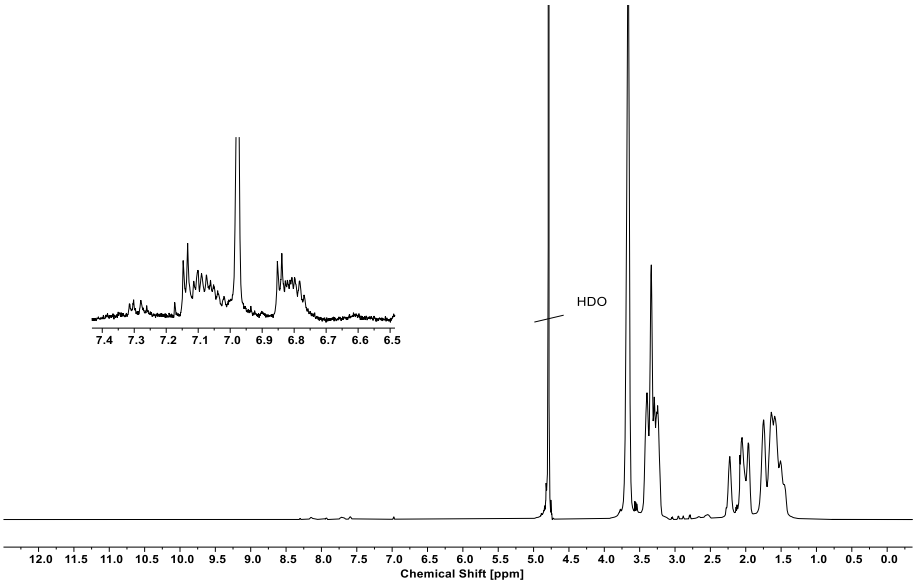


*Figure S27: ^{1}H-NMR spectrum (600 MHz, D_2O) of **P5**. The zoom shows the tyrosine signals of the macroinitiator.*

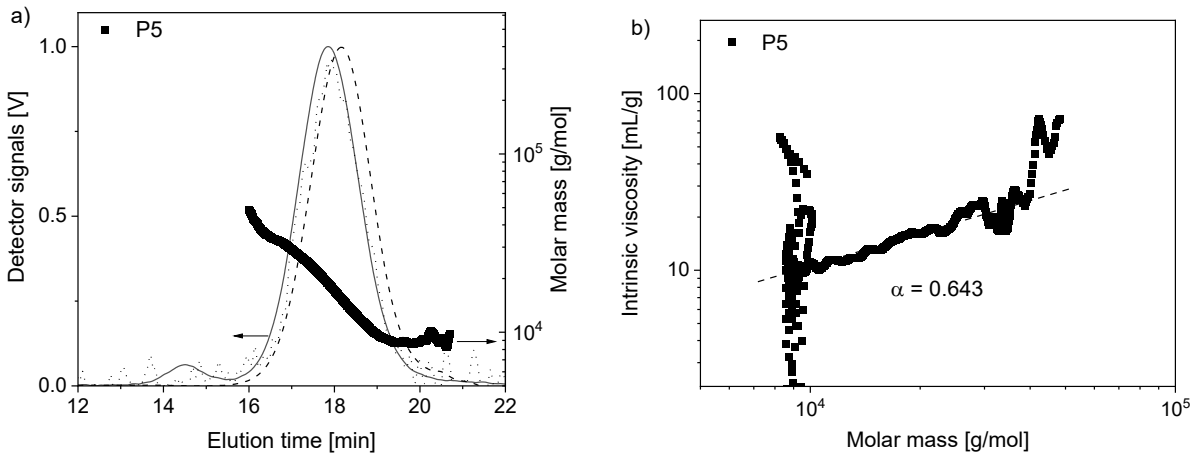


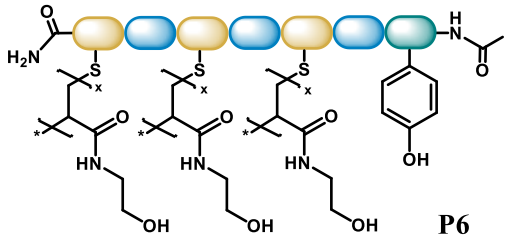
*Figure S28: SEC-D5 studies: a) detector signals (solid line – LS; dashed line – dRI, dotted line – specific viscosity) and molar masses (symbols)vs. elution time; and b) Kuhn-Mark-Houwink-Sakurada plot (intrinsic viscosity vs. molar masses) of **P5**.*

*Table S6: Results of SEC-D5 studies of **P5.***

Measurement	M_n [*1] [kg/mol]	M_w [*1] [kg/mol]	Đ (M_w/M_n)	R_g [nm]	$R_{h,DLS}$ [nm]	$R_{h,h}$ [nm]
1	14.6	16.8	1.15	n.d.	1.7	3.6
2	14.3	16.5	1.15	n.d.	1.9	3.6
3	14.5	16.8	1.16	n.d.	1.7	3.6
average	**14.5 ± 0.5**	**16.7± 0.5**	**1.15**	**-**	**1.7± 0.3**	**3.6 ± 0.1**

[*1] calculated by dn/dc = 0.163 ml, experimentally determined, SEC-D5 performed by System 2

P6 – HEAA TIRP from macroinitiator MI-3



The polymerization is conducted as described in section 1.3 general methods "Standard protocols for TIRP" and sample sizes and yields are summarized in Table S1, see p. 19.

^{1}H-NMR (600 MHz, D_2O): δ (ppm) 8.26-8.02 (m, NH), 7.77-7.54 (m, H_{TPO}), 7.16-7.00 (m, H_{Tyr}), 6.96 (s, H_{TPO}), 6.86-6.72 (m, H_{Tyr}), 3.83-3.14 (m, $H_{HEAA\text{-side chain}}$), 3.06-2.44 (m, $H_{MI\text{-}3}$), 2.29-1.01 (m, $H_{HEAA\text{-backbone}}$).

GPC: $\overline{M_n}$ = 26.0 ± 0.1 kDa, Đ = 1.25.

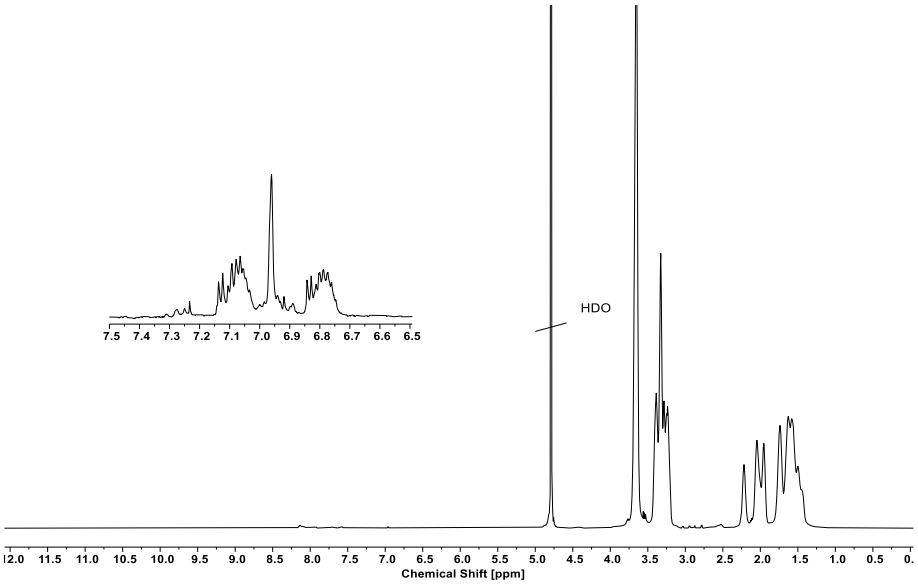
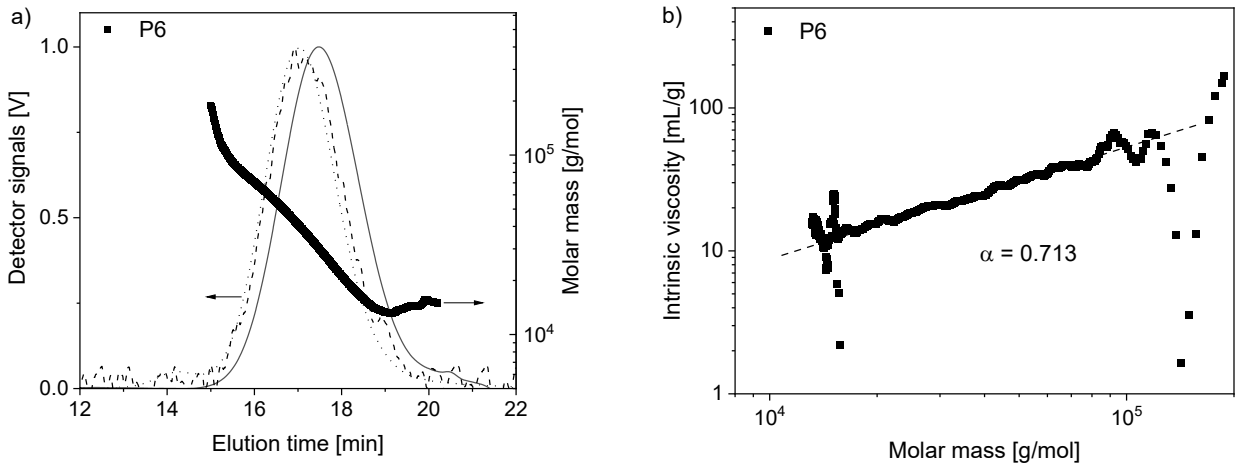


*Figure S29: ^{1}H-NMR spectrum (600 MHz, D_2O) of **P6**. The zoom shows the tyrosine signals of the macroinitiator.*



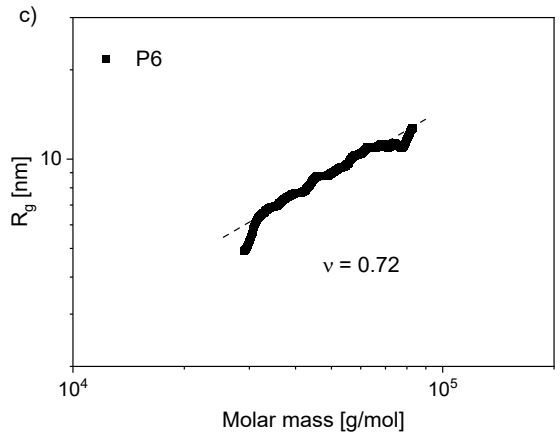


*Figure S30: SEC-D5 studies: a) detector signals (solid line – LS; dashed line – dRI, dotted line – specific viscosity) and molar masses (symbols)vs. elution time; b) Kuhn-Mark-Houwink-Sakurada plot (intrinsic viscosity vs. molar masses) and c) scaling plot (R_g vs molar mass; only elution range from 15.4 – 18 min) of **P6**.*

*Table S7: Results of SEC-D5 studies of **P6.***

Measurement	M_n *1 [kg/mol]	M_w *1 [kg/mol]	Đ (M_w/M_n)	R_g *2 [nm]	$R_{h,DLS}$ [nm]	$R_{h,h}$ [nm]
1	25.8	32.9	1.28	7.3	3.6	5.5
2	26.0	33.1	1.21	8.4	3.7	5.4
3	26.1	33.1	1.27	8.3	3.6	5.4
average	**26.0 ± 0.1**	**33.0 ± 0.1**	**1.27**	**8.0 ± 1.1**	**3.6 ± 0.1**	**5.4 ± 0.1**

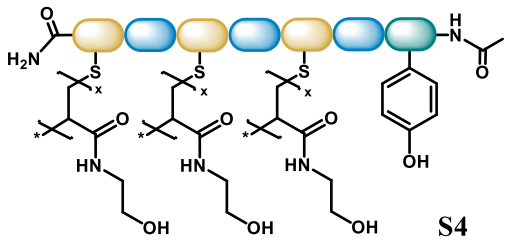
*1 calculated by dn/dc = 0.163 ml, experimentally determined, SEC-D5 performed by System 2, *2 only elution range from 15.4 - 18 min

2.4 TIRP block-polymerization conditions and analytics *S4*, P7-P9

Table S8: Sample values of the used TIRP components and yields of polymers ***S4, P16-P18****.*

No.	macroinitiator [mg]	TCEP [mg]	TPO [mg]	$Ir(ppy)_3$-cat. [mg]	monomer [mg]	yield	
						[mg]	[%]
S4	MI-3  50.12	119.28	28.99	0.817	HEAA 287.45	144	43
P7	MI-3  52.40	18.90	4.51	0.019	Man(Ac)EAA 28.76	33	39
P8	MI-3  34.18	12.09	2.96	0.027	Man(Ac)EAA 37.62	26	31
P9	MI-3  16.10	5.86	1.42	0.040	Man(Ac)EAA 54.64	23	32

S4 – HEAA TIRP from macroinitiator MI-3 as core for block-copolymers



The polymerization is conducted as described in section 1.3 general methods "Standard protocols for TIRP" and sample sizes and yields are summarized in Table S1, see p. 19.

^{1}H-NMR (300 MHz, D_2O): δ (ppm) 8.22-8.03 (m, NH), 7.16-7.12 (d, H_{Tyr} overlap with water), 6.88-6.82 (d, H_{Tyr}), 3.73-3.21 (m, $H_{HEAA\text{-}side\ chain}$), 2.98-2.53 (m, $H_{MI\text{-}3}$), 2.27-1.49 (m, $H_{HEAA\text{-}backbone}$).

GPC: $\overline{M_n}$ = 3.0 ± 0.1 kDa, Đ = 1.73.

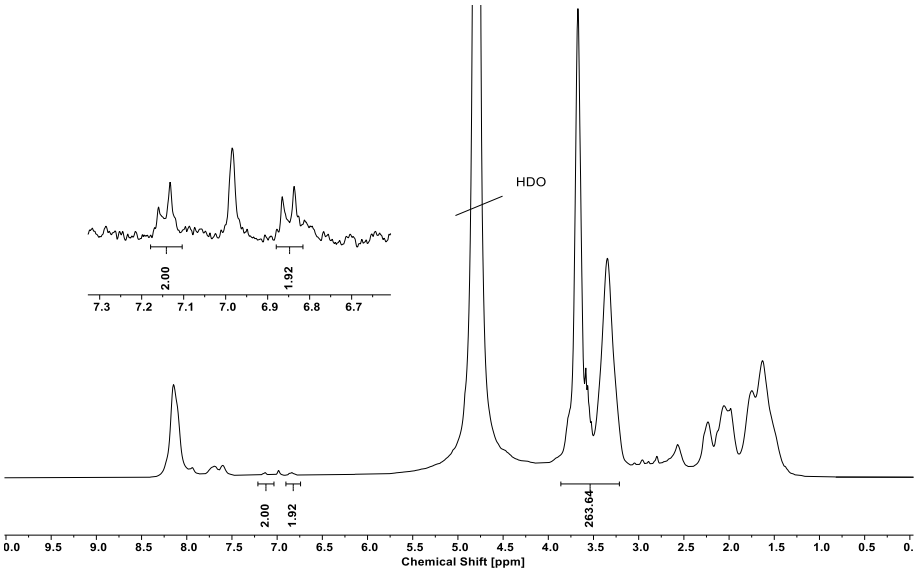


*Figure S31: ^{1}H-NMR spectrum (300 MHz, D_2O) of **S4**. The zoom shows the tyrosine signals of the macroinitiator.*

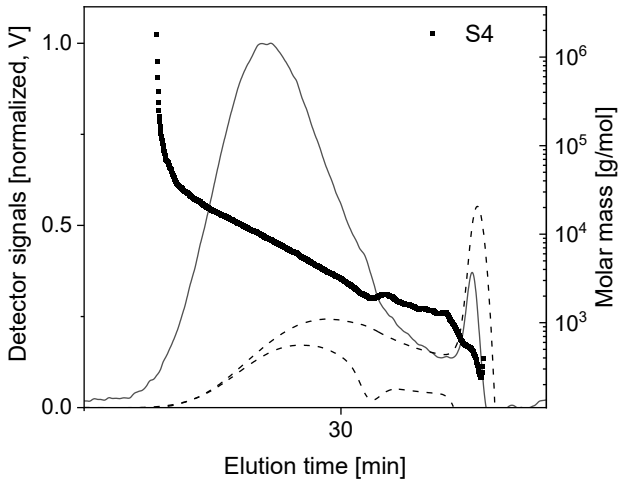


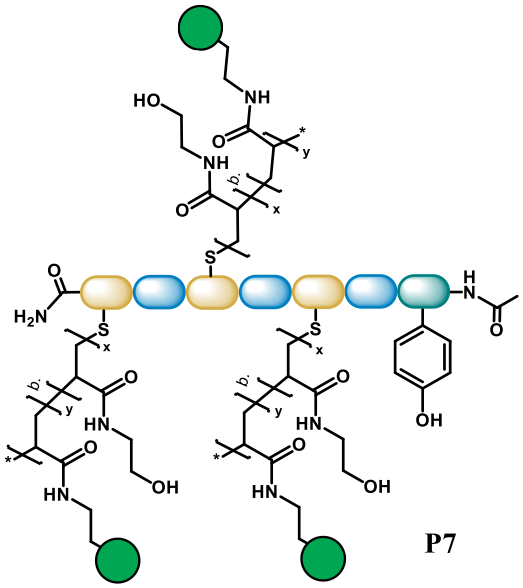
*Figure S32: SEC-D4 studies: detector signals (solid line – LS; dashed line – dRI, dotted line – UV_{280nm}) and molar masses (symbols) vs. elution time of **S4**.*

*Table S9: Results of SEC-D4 studies of **S4.***

Measurement	M_n [*1] [kg/mol]	M_w [*1] [kg/mol]	Đ (M_w/M_n)	R_g [nm]	$R_{h,DLS}$ [nm]
1	2.9	5.3	1.80	n.d.	2.2
2	3.0	5.2	1.75	n.d.	2.1
average	**3.0 ± 0.1**	**5.2 ± 0.2**	**1.73**	**-**	**2.2 ± 0.7**

[*1] calculated by dn/dc = 0.163 ml, experimentally determined, SEC-D5 performed by System 1

P7 – Man(Ac)EAA TIRP block from star-shaped p(HEAA) polymer *S4*



The polymerization is conducted as described in section 1.3 general methods "Standard protocols for TIRP" and "Standard protocol for block-copolymers via TIRP" sample sizes and yields are summarized in Table S8, see p.32.

^{1}H-NMR (300 MHz, D_2O): δ (ppm) 7.11 - 7,04 (m, H_{Tyr}), 6.78 – 6.72 (m, H_{Tyr}), 3.84 - 3.17 (m, $H_{HEAA/ManEAA\text{-}side\ chain}$), 2.31 - 1.31 (m, $H_{HEAA\text{-}backbone}$).

GPC: $\overline{M_n}$ = 17.5 ± 0.6 kDa, Đ = 1.45.

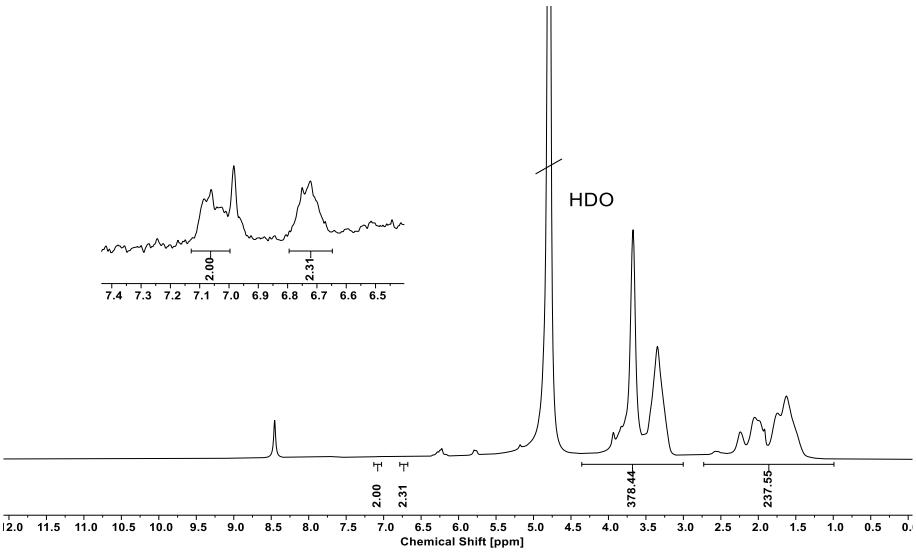


*Figure S33: ^{1}H-NMR spectrum (300 MHz, D_2O) of **P7**. The zoom shows the tyrosine signals of the macroinitiator.*

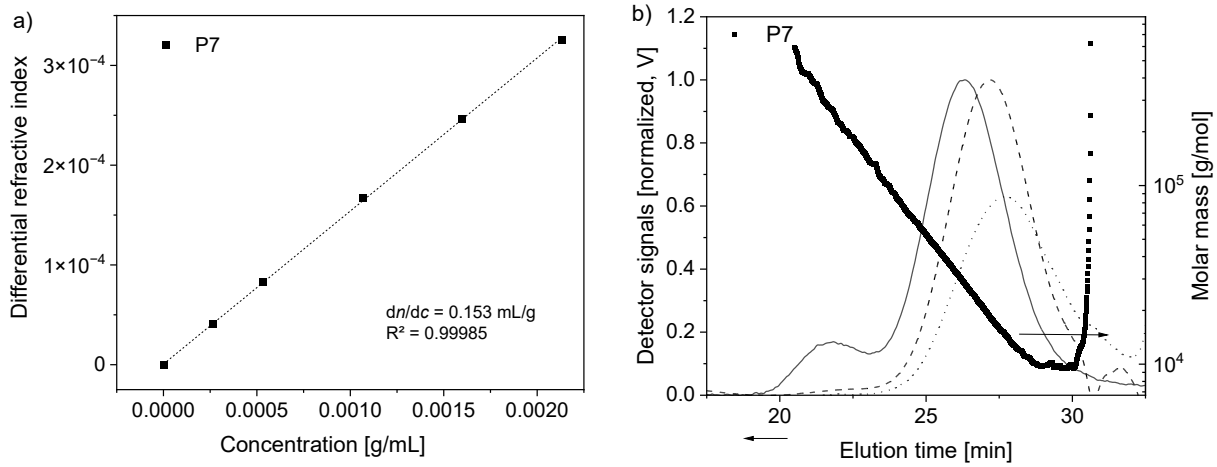


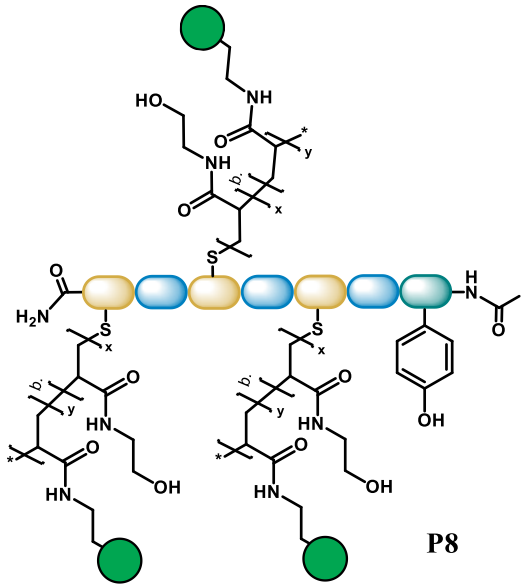
*Figure S34: SEC-D4 studies: a) results of dn/dc determination, dRI vs. concentration, and b) detector signals (solid line – LS; dashed line – dRI, dotted line – UV_{280nm}) and molar masses (symbols)vs. elution time of **P7**.*

*Table S10: Results of SEC-D4 studies of **P7**.*

Measurement	M_n *1 [kg/mol]	M_w *1 [kg/mol]	Đ (M_w/M_n)	R_g [nm]	$R_{h,DLS}$ [nm]
1	17.4	25.5	1.47	n.d.	4.2
2	17.7	25.3	1.43	n.d.	4.0
average	**17.5 ± 0.6**	**25.4 ± 0.8**	**1.45**	**-**	**4.1 ± 0.7**

*1 calculated by dn/dc = 0.153 ml, experimentally determined, SEC-D5 performed by System 1

P8 – Man(Ac)EAA TIRP block from star-shaped p(HEAA) polymer *S4*



The polymerization is conducted as described in section 1.3 general methods "Standard protocols for TIRP" and "Standard protocol for block-copolymers via TIRP" sample sizes and yields are summarized in Table S8, see p.32.

^{1}H-NMR (300 MHz, D_2O): δ (ppm) 7.03 – 6.95 (m, H_{Tyr}), 6.65-6.58 (m, H_{Tyr}), 4.88 (s, $H_{anomeric\ center}$ overlap with water), 3.98 – 3.18 (m, $H_{HEAA/ManEAA\text{-}side\ chain}$), 2.29-1.30 (m, $H_{HEAA\text{-}backbone}$).

GPC: $\overline{M_n}$ = 19.4 ± 0.6 kDa, Đ = 1.41.

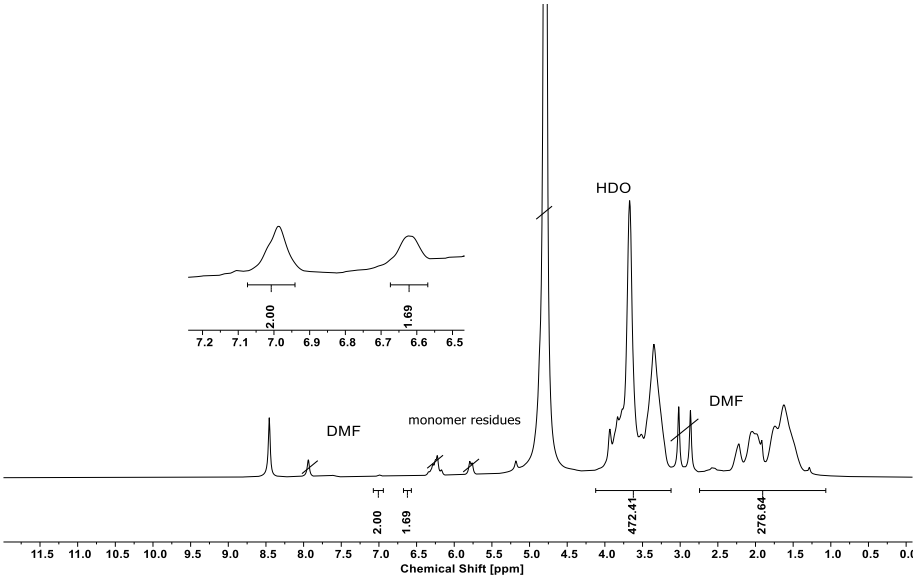


*Figure 35: ^{1}H-NMR spectrum (300 MHz, D_2O) of **P8**. The zoom shows the tyrosine signals of the macroinitiator.*

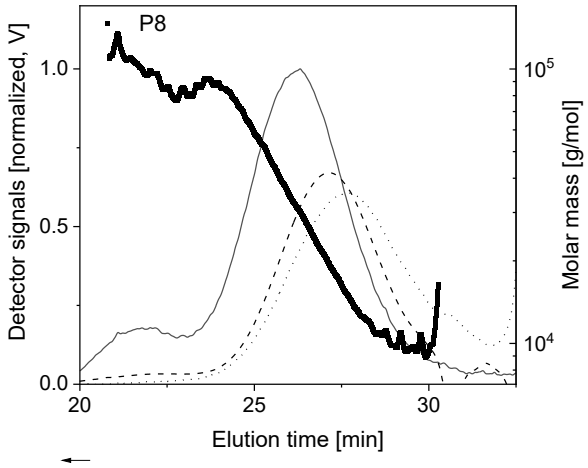


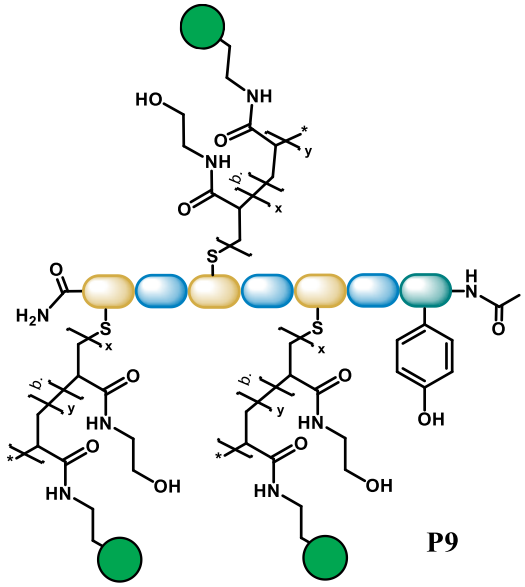
*Figure S36: SEC-D4 studies: detector signals (solid line – LS; dashed line – dRI, dotted line – UV_{280nm}) and molar masses (symbols)vs. elution time of **P8**.*

*Table S11: Results of SEC-D4 studies of **P8.***

Measurement	M_n *1 [kg/mol]	M_w *1 [kg/mol]	Đ (M_w/M_n)	R_g [nm]	$R_{h,DLS}$ [nm]
1	18.4	27.2	1.48	n.d.	4.1
2	20.5	27.4	1.34	n.d.	4.2
average	**19.4 ± 0.6**	**27.3 ± 0.8**	**1.41**	**-**	**4.2 ± 1.5**

*1 calculated by dn/dc = 0.163 ml, experimentally determined, SEC-D5 performed by System 1

P9 – Man(Ac)EAA TIRP block from star-shaped p(HEAA) polymer *S4*



P9

The polymerization is conducted as described in section 1.3 general methods "Standard protocols for TIRP" and "Standard protocol for block-copolymers via TIRP" sample sizes and yields are summarized in Table S8, see p.32.

^{1}H-NMR (300 MHz, D_2O): δ (ppm) 7.16 – 7.05 (m, H_{Tyr}), 6.86 - 6.74 (m, H_{Tyr}), 3.97 - 3.18 (m, $H_{HEAA/ManEAA\text{-}side\ chain}$), 2.41-1.39 (m, $H_{HEAA\text{-}backbone}$).

GPC: $\overline{M_n}$ = 16.8 ± 0.5 kDa, Đ = 1.49.

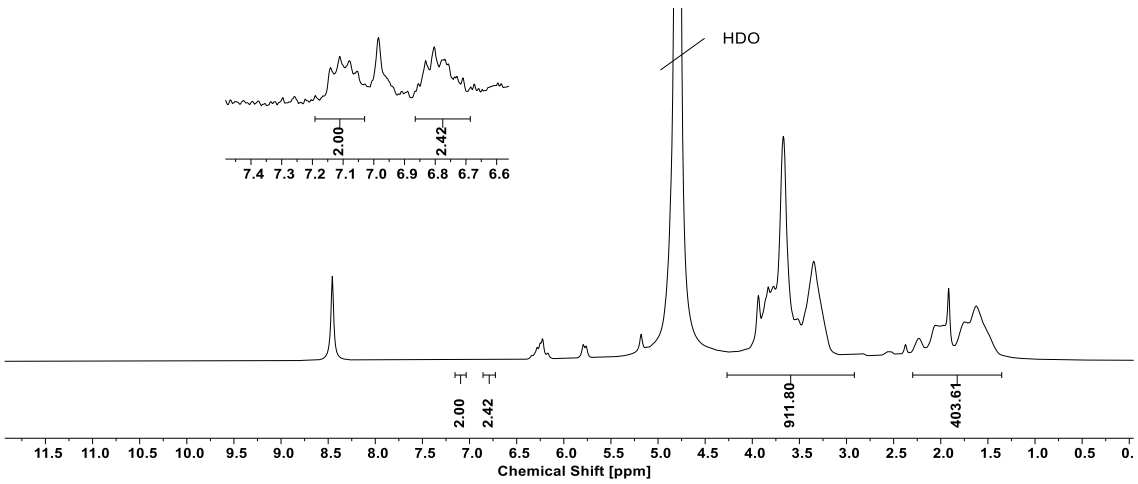


*Figure S37: ^{1}H-NMR spectrum (300 MHz, D_2O) of **P9**. The zoom shows the tyrosine signals of the macroinitiator.*

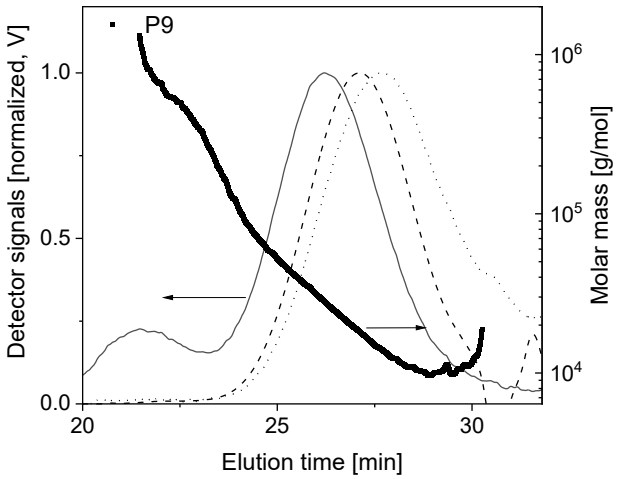


*Figure S38: SEC-D4 studies: detector signals (solid line – LS; dashed line – dRI, dotted line – UV_{280nm}) and molar masses (symbols) vs. elution time of **P9**.*

*Table S12. Results of SEC-D4 studies of **P9**.*

Measurement	**M_n[*1] [kg/mol]**	**M_w[*1] [kg/mol]**		**Đ (M_w/M_n)**	**R_g [nm]**	
1	17.2	25.3		1.47	n.d.	4.0
2	16.4	25.0		1.52	n.d.	4.5
average	**16.8 ± 0.5**	**25.1 ± 0.8**		**1.49**	**-**	**4.2 ± 1.5**

3. Deprotection kinetics

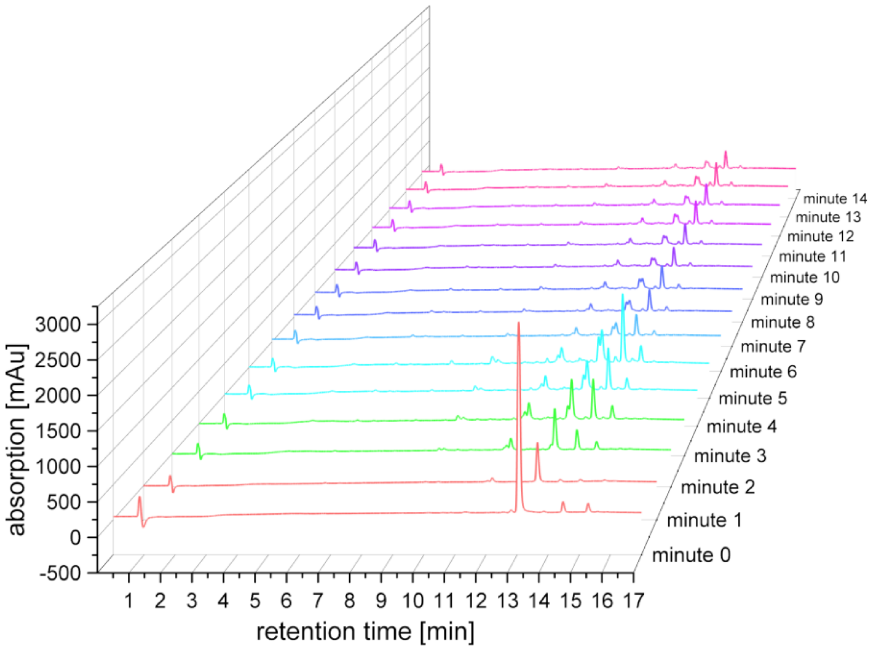


Figure S39: Chromatograms of the RP-HPLC-MS spectra of the Fmoc-Cys(oNv)-OH ***S3*** *building block after one minute steps of irradiation at 365 nm with an intensity of 576.4 mW/cm^2 (linear solvent gradient from 100% A to 50 A in 30 min at 25 °C).*

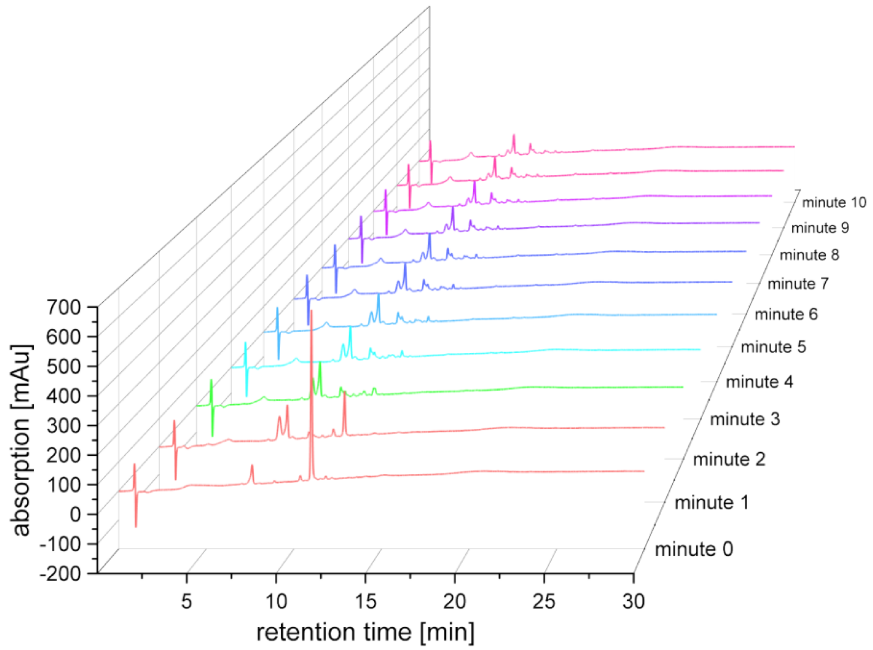


Figure S40: Chromatograms of the RP-HPLC-MS spectra of the ***MI-1*** *after one-minute steps of irradiation at 365 nm with an intensity of 576.4 mW/cm^2 (linear solvent gradient from 100% A to 50 A in 30 min at 25 °C).*

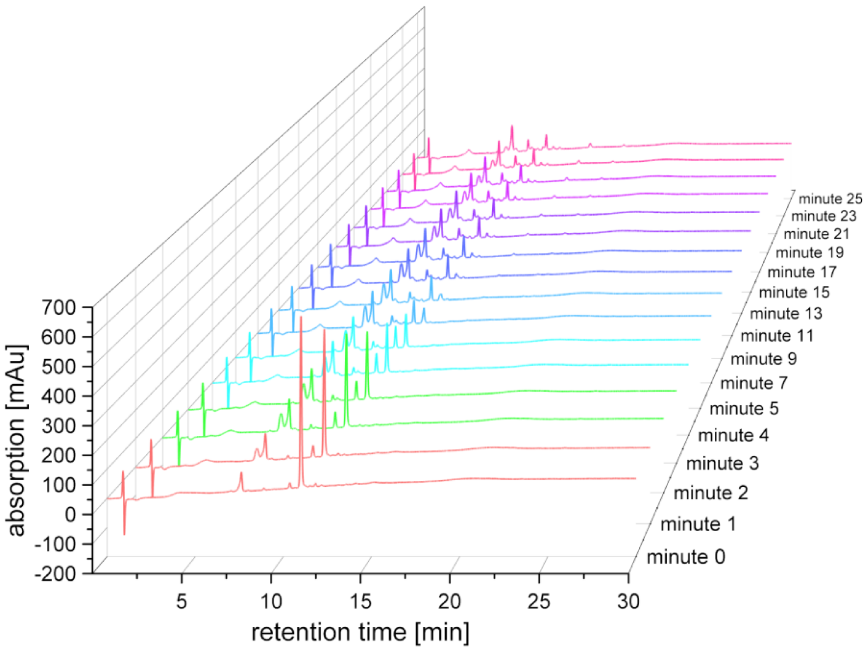


*Figure S41: Chromatograms of the RP-HPLC-MS spectra of the **MI-1** after one-minute steps of irradiation at 405 nm with an intensity of 57.5 mW/cm² (linear solvent gradient from 100% A to 50 A in 30 min at 25 °C).*

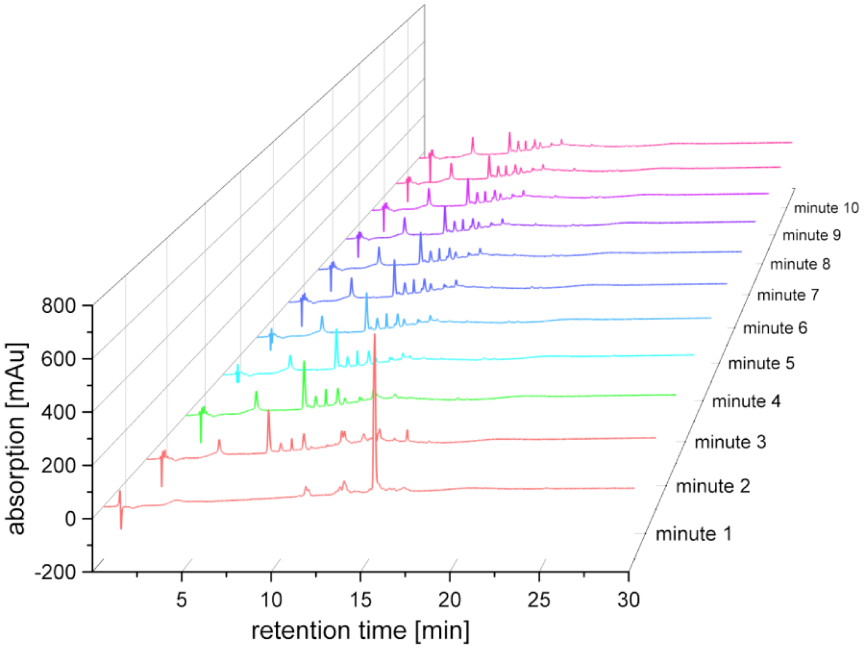


*Figure S42: Chromatograms of the RP-HPLC-MS spectra of the **MI-3** after one-minute steps of irradiation at 365 nm with an intensity of 576.4 mW/cm² (linear solvent gradient from 100% A to 50 A in 30 min at 25 °C).*

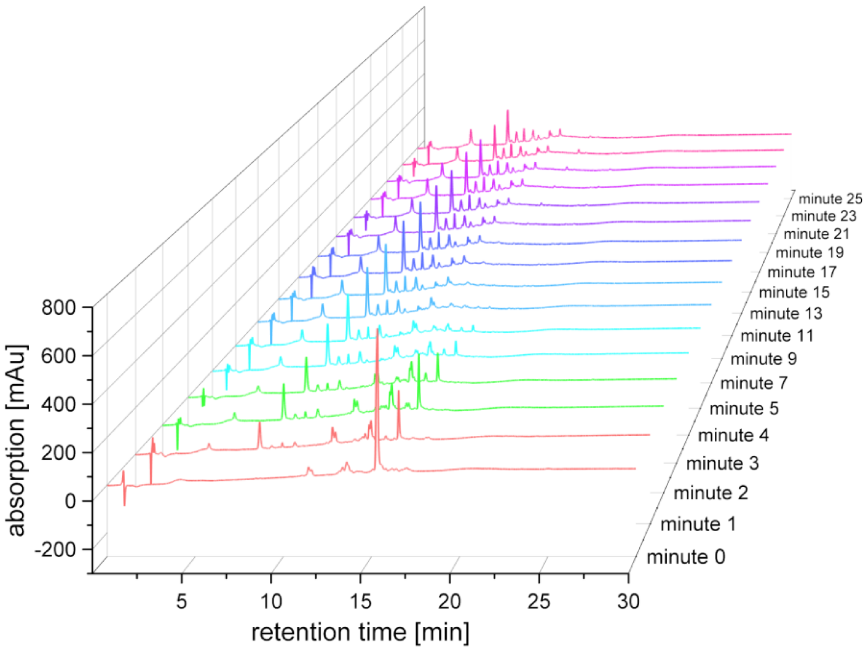


*Figure S43: Chromatograms of the RP-HPLC-MS spectra of the **MI-3** after one-minute steps of irradiation at 405 nm with an intensity of 57.5 mW/cm² (linear solvent gradient from 100% A to 50 A in 30 min at 25 °C).*

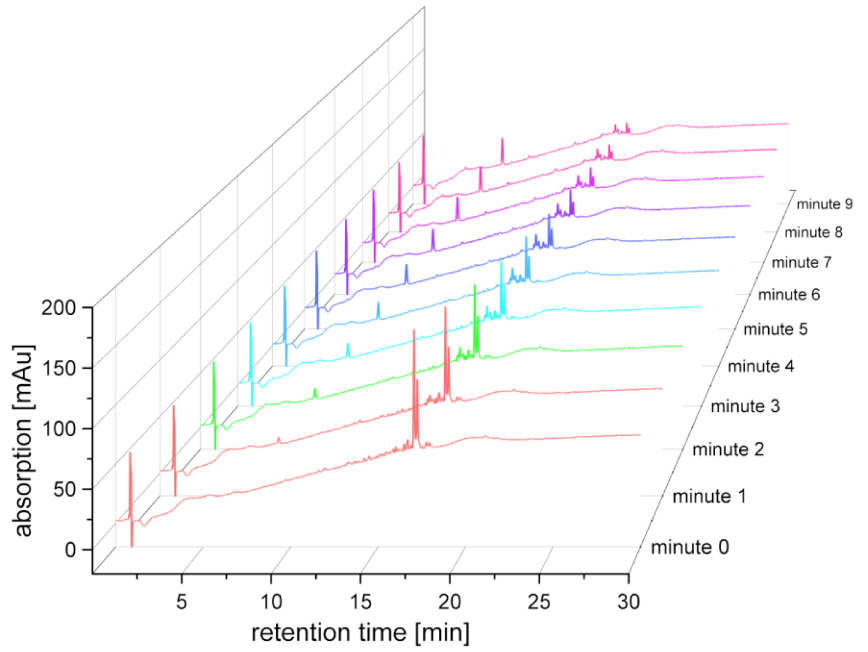


*Figure S44: Chromatograms of the RP-HPLC-MS spectra of the **MI-5** after one-minute steps of irradiation at 365 nm with an intensity of 576.4 mW/cm² (linear solvent gradient from 100% A to 50 A in 30 min at 25 °C).*

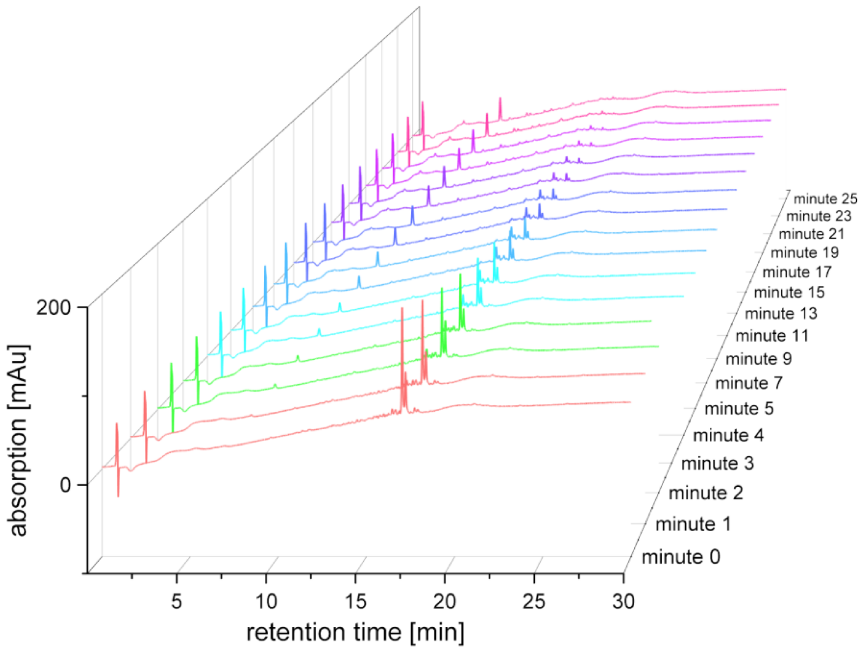
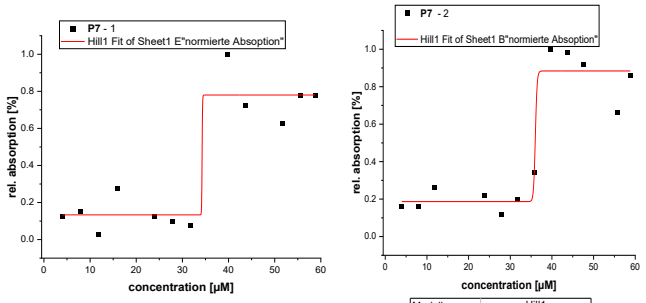


*Figure 45: Chromatograms of the RP-HPLC-MS spectra of the **MI-5** after one-minute steps of irradiation at 405 nm with an intensity of 57.5 mW/cm² (linear solvent gradient from 100% A to 50 A in 30 min at 25 °C).*

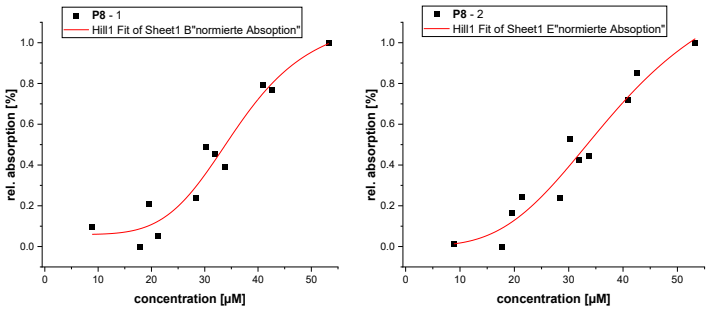
4. Ligand lectin binding studies



Modell	Hill1
Gleichung	y = START + (END - START) * x^n / (k^n +
Plot	normierte Absoption
START	0.13332 ± --
END	0.77994 ± --
k	34.27497 ± --
n	727.63048 ± --
Chi-Quadr Red	0.2754
R-Quadrat (C	-0.61637
Kor. R-Quadra	-1.22251

Modell	Hill1
Gleichung	y = START + (END - START) * x^n / (k^n +
Plot	normierte Absoption
START	0.18667 ± 0.04264
END	0.884 ± 0.05222
k	36.02365 ± 58000.960
n	173.32185 ± 3.82076E
Chi-Quadr Re	0.01091
R-Quadrat (C	0.93932
Kor. R-Quadra	0.91657

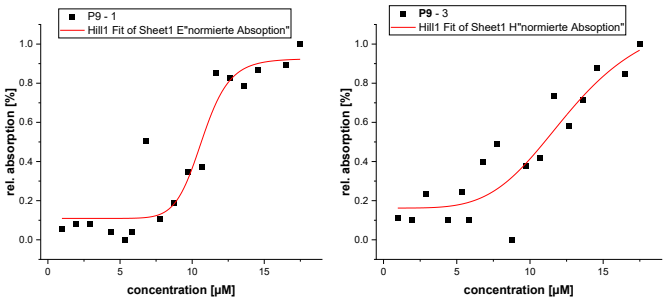
*Figure S46: Compilation of the individual measurements of **P7** (f =3) with corresponding values of the half-maximum turbidity. The mean value of the individual measurements is 35.1 ± 1.2 µM.*



Modell	Hill1
Gleichung	y = START + (END - START) * x^n / (k^n + x^n)
Plot	normierte Absoption
START	0.05926 ± 0.06774
END	1.12987 ± 0.25321
k	36.36186 ± 4.04062
n	5.09252 ± 2.14817
Chi-Quadr Red	0.00856
R-Quadrat (CO	0.94534
Kor. R-Quadrat	0.92192

Modell	Hill1
Gleichung	y = START + (END - START) * x^n / (k^n + x^n)
Plot	normierte Absoption
START	0.00435 ± 0.09591
END	1.40115 ± 0.59637
k	39.85025 ± 10.3666
n	3.36947 ± 1.64307
Chi-Quadr Red	0.00815
R-Quadrat (CO	0.94792
Kor. R-Quadrat	0.92561

*Figure S47: Compilation of the individual measurements of **P8** (f =3) with corresponding values of the half-maximum turbidity. The mean value of the individual measurements is 33.6 ± 0.4 µM.*



Modell	Hill1
Gleichung	y = START + (END - START) * x^n / (k^n + x^n
Plot	normierte Absoption
START	0.10938 ± 0.04972
END	0.92536 ± 0.08618
k	10.71577 ± 0.50679
n	11.32191 ± 5.32611
Chi-Quadr Re	0.01855
R-Quadrat (C	0.89261
Kor. R-Quadr	0.86782

Modell	Hill1
Gleichung	y = START + (END - START) * x^n / (k^n + x^n)
Plot	normierte Absoption
START	0.16229 ± 0.06746
END	1.17439 ± 0.50222
k	12.84754 ± 3.32637
n	4.42999 ± 2.84113
Chi-Quadr Red	0.02027
R-Quadrat (CO	0.83368
Kor. R-Quadrat	0.7953

*Figure S48: Compilation of the individual measurements of **P9** (f =3) with corresponding values of the half-maximum turbidity. The mean value of the individual measurements is 11.2 ± 0.4 µM.*

5. Literature

[1] W. Wang, S. Bo, S. Li, W. Qin, *International Journal of Biological Macromolecules,* 1991, **13**, 281-285.

[2] F. Schröer, T. J. Paul, D. Wilms, T. H. Saatkamp, N. Jäck, J. Müller, A. K. Strzelczyk, S. Schmidt, *Molecules,* 2021, **26**, 263.

[3] aD. Ponader, F. Wojcik, F. Beceren-Braun, J. Dernedde, L. Hartmann, *Biomacromolecules,* 2012, **13**, 1845-1852; bM. Ebbesen, C. Gerke, P. Hartwig, L. Hartmann, *Polymer Chemistry,* 2016, **7**, 7086-7093; cS. A. Hill, C. Gerke, L. Hartmann, *Chemistry–An Asian Journal,* 2018, **13**, 3611-3622.

[4] J. A. Karas, D. B. Scanlon, B. E. Forbes, I. Vetter, R. J. Lewis, J. Gardiner, F. Separovic, J. D. Wade, M. A. Hossain, *Chemistry–A European Journal,* 2014, **20**, 9549-9552.